NUI MAYNOOTH

Ollscoil na hÉireann Má Nuad

Development of A Versatile Multichannel CWNIRS Instrument for Optical Brain-Computer Interface Applications

Christopher John Soraghan

B.E.

A thesis submitted to the

National University of Ireland

for the degree of

Doctor of Philosophy

February 2010

National University of Ireland, Maynooth

Department of Experimental Physics & Department of Computer Science

Faculty of Science and Engineering

Head of Department(s):	Prof. Anthony Murphy (Exp. Physics)
	Dr. Adam Winstanley (Computer Science)
Supervisors:	Dr. Charles Markham
	Dr. Tomás Ward

Abstract

This thesis describes the design, development, and implementation of a versatile multichannel continuous-wave near-infrared spectroscopy (CWNIRS) instrument for brain-computer interface (BCI) applications. Specifically, it was of interest to assess what gains could be achieved by using a multichannel device compared to the single channel device implemented by Coyle in 2004. Moreover, the multichannel approach allows for the assessment of localisation of functional tasks in the cerebral cortex, and can identify lateralisation of haemodynamic responses to motor events. The approach taken to extend single channel to multichannel was based on a software-controlled interface. This interface allowed flexibility in the control of individual optodes including their synchronisation and modulation (AM, TDM, CDMA). Furthermore, an LED driver was developed for custom-made triple-wavelength LEDs. The system was commissioned using a series of experiments to verify the performance of individual components in the system. The system was then used to carry out a set of functional studies including motor imagery and cognitive tasks. The experimental protocols based on motor imagery and overt motor tasks were verified by comparison with fMRI. The multichannel approach identified stroke rehabilitation as a new application area for optical BCI. In addition, concentration changes in deoxyhaemoglobin were identified as being a more localised indicator of functional activity, which is important for effective BCI design. An assessment was made on the effect of the duration of the stimulus period on the haemodynamic signals. This demonstrated the possible benefits of using a shorter stimulus period to reduce the adverse affects of low blood pressure oscillations.

Declaration

I hereby declare that this thesis is my own work and has not been submitted in any form for another award at any university or other institute of tertiary education. Information derived from the published and unpublished work of others has been acknowledged in the text and a list of references is given.

Signed: _____ Date: _____

Acknowledgements

There are many people that have had an impact in different ways over the course of the work. Firstly, I would like to thank my two great supervisors Dr. Charles Markham and Dr. Tomás Ward for their dedication to the project and support in all aspects of the research. In particular I want to acknowledge their approachability and full-time efforts. Thanks are also due to Prof. Ray O'Neill who was closely involved as a supervisor for the first year of the project and was involved in securing the funding. I would like to express my thanks to the postgraduates and staff in Experimental Physics, especially the late Dr. William Lanigan who helped in the development of the electronics early on at the prototype stage. Furthermore, I wish to thank Mr. David Watson, Mr. Ian McAuley, Mr. Pat Serry, Dr. Marçin Gradziel, and Mr. Tully Peacock for their continual suggestions on all aspects of the instrumentation. Appreciation is also due to Ms. Gráinne Roche and Mr. Derek Gleeson for there perpetual assistance in the administrative duties. Contributions also spanned the Departments of Computer Science, Electronic Engineering, and Hamilton Institute where many welcome coffee breaks and conversations were to be had.

However, a close knit circle of colleagues and friends developed early on and persists with possibly the best working environment I could expect with Gerard (aka *the music box*), Aoife (aka *the singer*), Fiachra (aka *the man!*), and Jason (aka *the smooth-ster*). One rarely finds such an environment to work in where there isn't a hint of animosity.

With such a long project however, sacrifices are inevitably made and so I dedicate this thesis to the two great women in my life who saw me through: Caitríona (mo cailín álainn) and my Mam. Caitríona has been my bedrock and I love her dearly. I would also like to thank my family, especially my brothers and sister for always been able to give a lift here or there, a helping hand, or just chat about life and the like.

Finally, I would like to acknowledge the financial contributions of Science Foundation Ireland (Grant Number SFII05/RFP/ENG0089), and the Department of Experimental Physics for supporting this project.

Contents

List of abbreviations

ABI	Adaptive Brain Interface
ALS	Amyotrophic Lateral Sclerosis
APD	Avalanche Photodiode
BOLD	Blood Oxygenation Level Dependent
BCI	Brain-Computer Interface
BI	Brain Interface
BMI	Brain-Machine Interface
BPF	Band Pass Filter
CNS	Central Nervous System
CSF	Cerebrospinal Fluid
DBI	Direct Brain Interface
DOT	Diffuse Optical Tomography
EEG	Electroencephalography
EP	Evoked Potential
EROS	Event Related Optical Signal
fMRI	Functional Magnetic Resonance Imaging
FNIRS	Functional Near-Infrared Spectroscopy
HPF	High Pass Filter
LED	Light Emitting Diode
LPF	Low Pass Filter
MEG	Magnetoencephalography
NIRS	Near-Infrared Spectroscopy
OBCI	Optical Brain-Computer Interface
PNS	Peripheral Nervous System
SCP	Slow Cortical Potential
SSVEP	Steady-State Visual Evoked Potential
VEP	Visual Evoked Potentials

List of publications arising from this work

Conference

Soraghan, C. J. (2009). "Mind Maps and Desktop Research Tools". *Festival of Thought*. 19th June, DIT, Kevin Street, Dublin.

Soraghan, C., Markham, C., Ward, T., Pearlmutter, B. A. and Matthews, F. (2009). "Overview of optical BCI research at NUI Maynooth". *The Association of Physical Scientists in Medicine Annual Scientific Meeting (APSM ASM) 2009.* D. Murphy. 27th February, Hotel Kilkenny, College Rd., Kilkenny, Ireland.

Soraghan, C., Matthews, F., Markham, C., Pearlmutter, B. A., O'Neill, R. and Ward, T. E. (2008). "A 12-Channel, real-time near-infrared spectroscopy instrument for brain-computer interface applications". *30th International Conference of the IEEE Engineering in Medicine and Biological Society,* August 20th-24th, Vancouver, Canada - 1: 5648-51.

Matthews, F., Soraghan, C., Ward, T. E., Markham, C. and Pearlmutter, B. A. (2008). "Software platform for rapid prototyping of NIRS brain computer interfacing techniques". *30th International Conference of the IEEE Engineering in Medicine and Biological Society,* August 20th-24th, Vancouver, Canada - 1: 4840-3.

Soraghan, C., Ward, T. E., Matthews, F., and Markham, C. (2008). "Optical Safety Assessment of a Near-Infrared Brain-Computer Interface". *Proceedings of the IEE Irish Signals and Systems Conference (ISSC) 2008*, June 18th-19th, Galway, Ireland, pp. 174-179.

Soraghan, C., Matthews, F., Markham, C., Pearlmutter, B., O'Neill, R. and Ward, T. (2007). "Biophotonic Methods for Brain-Computer Interfaces". *Photonics Ireland,* Sept 24th-26th, Galway, Ireland.

Soraghan, C., Matthews, F., Kelly, D., Ward, T., Markham, C., Pearlmutter, B. and O'Neill, R. (2006). "Viability of a dual channel optical BCI for use in a gaming environment.". In *Proceedings of the 9th International Conference on Computer Games: AI, Animation, Mobile, Educational and Serious Games,* 22nd-24th November, Dublin Institute of Technology, Dublin, Ireland, pp. 35-39.

Lebid, S., O'Neill, R., Markham, C., Ward, T. and Soraghan, C. (2006). "Near Infrared spectroscopy application in a new generation brain computer interface". *2nd Annual Meeting on Optical Sensors in Physiological Measurements*, London, UK.

Lebid, S., Markham, C., O'Neill, R., Ward, T., Soraghan, C. and Condron, J. (2006). "Steady State Visual Stimulation of the Brain: Optical Study of Task Related Effects". *5th European Symposium on Biomedical Engineering (ESBME 2006)*, 6th-7th July, University of Patras, Greece.

Peer Reviewed Journals

Soraghan, C. J., Markham, C., Matthews, F. and Ward, T. E. (2009). "Triple wavelength LED driver for optical brain-computer interfaces." *Electronics Letters*, vol. 45, no. 8, pp. 392-394.

Matthews, F., Pearlmutter, B. A., Ward, T. E., Soraghan, C. and Markham, C. (2008). "Hemodynamics for brain-computer interfaces." *IEEE Signal Processing Magazine*, vol. 25, no.1, pp 87-94.

Ward, T.E., Soraghan, C.J., Matthews, F. and Markham, C. (2007). "A concept for extending the applicability of constraint-induced movement therapy through motor cortex activity feedback using a neural prosthesis." *Computational Intelligence and* Neuroscience, Article ID 51363.

CHAPTER 1

INTRODUCTION

1.1 Preface

This dissertation describes the design, development, and implementation of a versatile multichannel continuous wave near-infrared spectroscopy (CWNIRS) instrument for brain-computer interface (BCI) applications. CWNIRS has been established as a valid technique for assessing brain state for use in an optical BCI or OBCI recently (Coyle, et al., 2004; Coyle, 2005). CWNIRS is an imaging technique that can assess in-vivo localised cerebral tissue oxygenation and blood flow changes occurring in tandem with localised functional activity (Rolfe, 2000). A BCI is a device that can establish a neural prosthesis for those with severely impaired functional expression, by-passing the normal physiological pathways of the brain (spinal cord and peripheral nervous system) that are used for volitional control of motor function (including facial and eye musculature) (Wolpaw, et al., 2000). While this initial OBCI work provided a feasibility study for predominantly single-channel, but also a dual-channel OBCI implementation, an extension to this work was sought to establish what gains a multichannel implementation could provide. Specifically, the dual-channel implementation lacked distinct spatial coverage of the cerebral cortex, and thus localisation of regions of maximal activation conveyed in spatiotemporal patterns of oxygenation changes. Furthermore, in order to establish multiple mental tasks for use in a BCI it was thought that the increase in spatial coverage may provide more independent regions of

activity that could potentially increase the information transfer rate of the device, which was limited to 6 bits/min.

In order to realise these potential gains (and others - developed in Chapter 4) a versatile multichannel CWNIRS instrument was needed which could also allow flexibility at the modulation stage and significant manipulation at the signal processing element. The following dissertation is a report on the development of such an instrument which could be used in optical BCI applications such as stroke rehabilitation (Ward, et al., 2007).

1.2 Motivations and strategies

With the advent of cerebral interrogation by near-infrared (NIR) light in 1977 (Jobsis, 1977), monitoring of global cerebral changes in tissue oxygenation of predominantly neonates was soon implemented (Cope, 1991). More recently, functional activity has been assessed using various instruments based on the similar notion that increases in oxygenation at the site of functional activity increases the absorption of NIR light (Obrig, et al., 2000). The first demonstration of using these phenomena in an OBCI utilised a simple custom-made single-channel device based on phase sensitive lock-in detection techniques (Coyle, et al., 2004). Others recently contributing to the area have mostly utilised commercial based systems with one group (Bauernfeind, et al., 2008) exploring a single-channel version of Coyle's instrument.

The motivation for the research described in this thesis was as an extension to the device developed by Coyle. However, the expansion of the device using lock-in detectors would not allow much flexibility for the ever-growing fields of NIRS and BCI. Thus, a more versatile instrument based on DSP demodulation and substantial software control of hardware timing, triggering, data buffering, and light source generation was envisaged. During this development a new area for OBCI was conceptualised with an application in stroke rehabilitation (Ward, et al., 2007). This particular form of rehabilitation was suggested as being potentially useful as a forerunner to more conventional constraint induced movement therapy (CIMT) techniques for individuals with no residual movement whatsoever. Thus, to support this work a series of BOLD fMRI experiments to common overt and covert motor tasks were assessed. However, overt motor tasks are used for this BCI type since it is required that the user engages in real-movement and tries to move the affected limb rather than a using a motor imagery process, as is more common in mainstream BCIs. However, some additional covert tasks are performed in the fMRI paradigm and measured using the CWNIRS multichannel system. An assessment of the localisation, lateralisation, and

haemodynamic response to left and right hand overt tasks are considered, which help to emphasise what a multichannel instrument could achieve for these BCI applications. In effect, the malleable multichannel instrument developed has application in multiple fields and not simply OBCI. The ability of the system to facilitate rapid prototyping means the instrument could also be used for muscle oxygenation dynamics studies, although this application isn't considered in the thesis apart from an analysis of blood vessel occlusion and release (Chapter 6) as a means to assess haemoglobin oxygenation status variations in an hypoxic scenario.

1.3 Contributions

For clarity and reference it is desirable to outline the main contributions of the presented work. While the principal contribution can be interpolated from the thesis title, a comprehensive list is presented here:

- The custom design, development and evaluation of a versatile real-time multichannel CWNIRS tool/instrument for BCI-type applications;
- The construction of a stable triple wavelength LED driver. This device also allowed flexibility in the exploration of multiple modulation strategies, e.g. round robin, amplitude modulation, and m-sequences (maximal length sequencies);
- The implementation of flexible, software-based demodulation for light source separation to replace hardware-based phase sensitive detection techniques that were used in the feasibility study;
- A safety assessment of LED-based optical sensors used in such instruments;
- The demonstration of a series of functional magnetic resonance imaging (fMRI) blood oxygen-level dependent (BOLD) studies on overt and kinesthetic imagery of motor tasks. These would be used for localisation of metabolic activity in the cerebral cortex and to validate designed experimental protocols for multichannel OBCI applications;
- An assessment of various mental tasks and of the fidelity of the cerebral activation signals. In particular, transparent single-trial analysis of evoked haemodynamics are reported including a discussion on the 'baseline' of haemodynamics;
- A procedure based on a set of validatory tasks used to assess the ability of a CWNIRS instrument to interrogate physiological phenomena and localised

- An implementation of a dual-channel OBCI application based on overt motor tasks for developing the concept of stroke rehabilitation using biofeedback of NIRS signals;
- The exploration of further applications of OBCI such as a controller for computer games;
- The identification of deoxyhaemoglobin as a more robust indicator of functional activity changes in single-trial tasks for OBCI;
- The identification of the benefits of using a multichannel CWNIRS instrument for OBCI applications, i.e. the ability to determine functional activity localisation and lateralisation;
- Single-trial observations of functional activity changes to motor imagery;
- Single-trial observations of the effect of shortening the stimulus period in overt motor tasks and its potential to reduce the complexity of the haemodynamic response.

1.4 Outline of thesis

An outline of the thesis is illustrated in a mind map shown in Figure 1.1. Since the work described involves irradiating human tissue with NIR light, in particular on the human head and brain, Chapter 2 provides scientific background of anatomy and physiology of the human, a description of functional NIRS (FNIRS), and a relevant selection of pathological conditions (e.g. locked-in syndrome). The anatomy and physiology discussion includes the various extracerebral layers of the human head and brain, blood composition, systemic blood pressure dynamics, and cerebral blood flow and metabolism. A cerebral map is given to aid in identifying anatomical locations of, in particular, motor control sites, (e.g. the hand area on the primary motor cortex on the precentral gyrus).

Chapter 3 considers the current state of the art of BCI apart from optical BCI which is considered in Chapter 4 along with the problem statement. The problem statement develops the research question of why NIRS should be used for BCI and what are the justifications for a multichannel implementation. The methodology outlined in the remainder of the work is also stated here.

Chapter 5 essentially describes the system implemented - the development of the multichannel instrument, along with an exposition of the optical, electrical, and mechanical

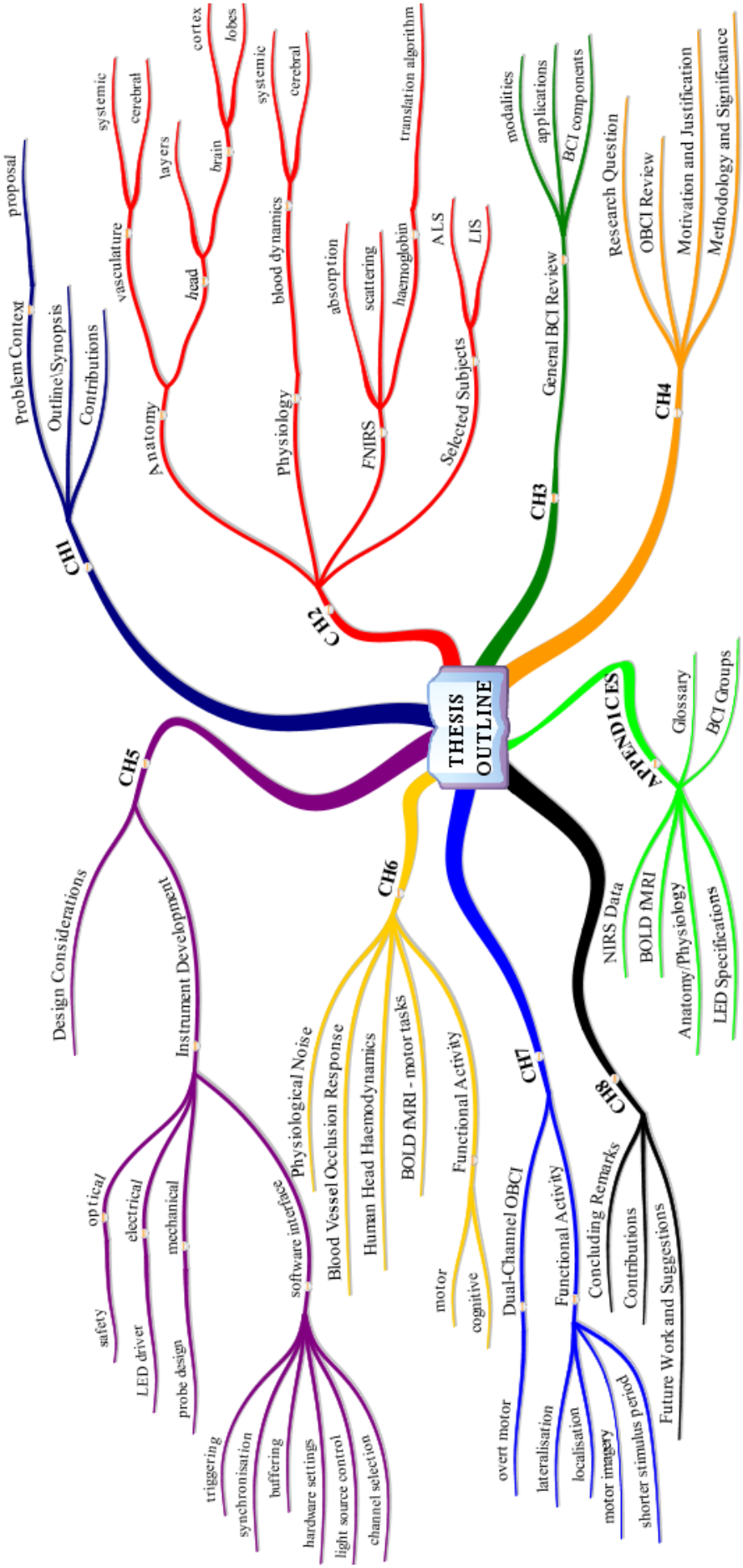

Figure 1.1: Mind map of an outline of thesis dissertation chapters and appendices (image designed using iMindMap® software).

elements of the system including the software interface. A validation of the instrument is given in Chapter 6 which was performed to assess the system's ability to measure haemodynamic patterns of functional activity and identify other physiological phenomena (e.g. cardiac pulse). Chapter 6 also provides a series of experiments with incremental complexity that reveals various measurements from the human head and forearm. Chapter 7 is included to report on an OBCI application for stroke rehabilitation using a dual-channel CWNIRS instrument using instrumentation from previous prototypes. It also includes an analysis of the ability of the new versatile CWNIRS instrument to identify functional activity lateralisation, and to localise regions of maximal activity in a given area of cerebral tissue. Single-trial responses to motor imagery and the effect of shortening the stimulus period in overt motor tasks are also reported.

Finally, Chapter 8 ends the thesis dissertation with conclusions, a recapitulation of the major contributions of the work, and identifies key areas of future work.

CHAPTER 2

SCIENTIFIC BACKGROUND

2.1 Introduction

For a thesis dissertation it is important to convey the necessary terminology and, in this case, physiology, in order that the reader appreciates the subsequent content and arguments proposed in the remainder of the document. For clarity a figure is included below (Figure 2.1) which represents the main human anatomical components which have a bearing on the observed phenomena in the reported experimental work (and which therefore should be understood). Briefly, in these experiments, near-infrared (NIR) light is shone onto a human head which travels into the brain, backscatters, and travels back out through the scalp. This is done to inspect the volitional mental effort by the subject, and this light is perturbed directly or indirectly by various somatic constituents including, the:

- Circulatory system (including the blood, kidneys, and liver);
- Whole head (brain, skull and skin, and various intermediary layers);
- Nervous system;
- Cerebral blood flow and metabolism.

Blood is a connective tissue. Undeniably, the blood's characteristics which are being probed/analysed are influenced by many more faculties of the body, such as the endocrine system; however, a thorough discussion of these is beyond the necessary scope of this thesis.

This phenomenon is true of other aspects that will be discussed, such as the brain, which is constantly probed by almost every action of the body. Nevertheless sufficient detail will be provided in order that the reader appreciates the hypothesis presented. In addition to physiology, a necessary exposition of light propagation in living tissue is discussed along with a description of a selection of pathological conditions e.g. 'Locked-In syndrome'.

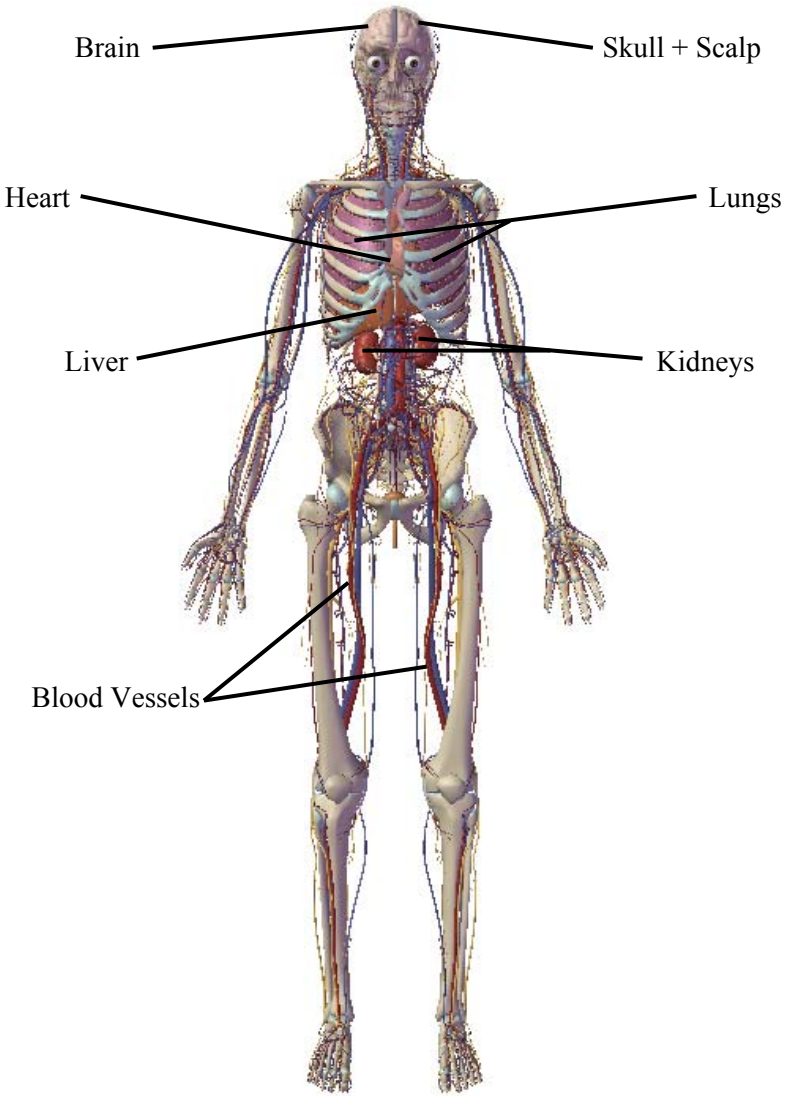

Figure 2.1 : Outline of the main anatomical components which have an influence on the physiological measurements made. Note: The skull and sternum were made transparent and other organs removed to reveal the underlying tissues/organs of interest (Image created using interactive 3-D software at www.visiblebody.com).

2.2 The Human Circulatory System

An introduction to blood composition, the human circulatory system, and systemic blood pressure (BP) control is available in Appendix E. The proceeding section discusses blood pressure oscillations in the body. Arterial pressure (AP) oscillations are manifest in the

body of at least conscious animals (Julien, 2006). From an analysis of the data shown in later chapters these low frequency blood pressure oscillations, known as Mayer waves, introduce what is the most significant signal processing difficulty in near-infrared spectroscopy (NIRS) based BCIs. In this chapter only the hypothesised physiological origin(s) of these signals in the systemic circuit is/are explored, which are as yet not fully understood.

2.2.1 Low frequency blood pressure oscillations

Due to constant internal and external perturbations on arterial blood pressure and indeed heart rate, there exist in the body low frequency oscillations (cardiovascular rhythms) in arterial blood pressure to ensure adequate blood perfusion of all tissues throughout the body. Comprehensive reviews (Seydnejad, et al., 2001; Cohen, et al., 2002; Julien, 2006) of these oscillations still profess the lack of understanding of their physiological origins. Linear and non-linear mathematical models have been proposed but those employing multiple inputs are deemed too complex for direct validation (Julien, 2006). Nevertheless, some experimental evidence has been gathered shedding light on possible physiological contributors, some outlining that no single mechanism is responsible for these homeostatic rhythms.

In humans there are three major components in this autonomous regulation:

- A very low frequency component around 0.04Hz possibly due to vasorhythmicity thermoregulatory control or humoral (bodily fluids) regulations (Seydnejad, et al., 2001);
- Low frequency sympathetic activity and closed-loop control component at ~0.1Hz;
- A respiratory movement rate component at ~0.25Hz.

Of particular interest are the very low and low frequency components at 0.04Hz and 0.1Hz, respectively, known collectively as the Mayer Waves. The very low frequency component is primarily thought to be due to the vasomotor tone or autonomous rhythms of the vascular smooth muscle in the blood vessels of the body (spontaneous rhythmic contractions and relaxations). The origin of the low frequency component at 0.1Hz is mooted to be generated by one or both of the following:

1) The baroreceptor or chemoreceptor feedback system (these receptors are discussed in Appendix E);
2) A centrogenic oscillator in the central nervous system.

The first hypothesis claims that the component is a result of the instability in the arterial blood pressure regulation feedback system. Afferent fibres monitoring circulation gather information to the brain, which then integrates it, and sends commands via efferents to the areas of the cardiovascular system that can induce a compensatory change in arterial pressure, e.g. smooth muscle of blood vessels, and the SA node of the heart. Delays in the afferent-efferent paths introduce latency in blood pressure regulation of ~2.5s, leaving the system susceptible to oscillation. Any external input then is said to be amplified by this resonant circuit. The centrogenic oscillator on the other hand is proposed to be an inherent oscillation in the neuronal discharge patterns of the brainstem. This pacemaker theory is based on empirical observations where oscillations of sympathetic nervous activity or haemodynamics can still be observed at or close to the LF component (0.1Hz) even in the absence of sensory inputs from the body. However after some deliberation it can only be said that under certain experimental conditions the central nervous structures can generate slow sympathetic nervous activity rhythms without peripheral sensory input (Julien, 2006). Julien et al concluded that it can be said that Mayer waves are:

- Oscillations of arterial blood pressure occurring spontaneously at frequencies lower than respiration in conscious humans at ~0.1Hz;
- Tightly coupled with oscillations in sympathetic nervous activity, with enhancement during this activity;
- Possibly not feedback oscillations but rather transient oscillatory responses to perturbed haemodynamics.

The low frequency component of the Mayer wave is said to be fairly stable within a given species. However, as will be seen in the experimental data in later chapters, the amplitude varies greatly, especially with posture. Frequency analysis of posture reveals that amplitude increases when the subject[1] is upright as opposed to being supine (Coyle, 2005).

2.2.2 Gaseous transport in blood

Non-stationary low- and very-low- frequency blood pressure oscillations contribute greatly to the features explored in the experimental results but their presence is, at least for this project, a form of unwanted physiological noise - as will be discussed in later chapters. In NIRS, gaseous transport and exchange via blood are also significant contributors to our signal of interest (e.g. affect blood pressure), so they must be understood and appreciated in order that any spectroscopic analysis carried out has a sound physiological basis.

[1] Unless otherwise stated a 'subject' is a healthy, gender-unspecific human synonymous with a 'person', 'patient', or 'test subject'.

Firstly, there are two forms of respiration of interest: external respiration and internal respiration. The former concerns inhalation and exhalation of air via the lungs to remove CO_2 (a byproduct of metabolism) from the blood and take O_2 into the blood. Internal respiration at the bodies' tissues concerns exchange of gases in the opposite direction by the same method - diffusion. To understand these processes, some basic properties of gases are required.

2.2.2.1 Basic gas theory applied to respiration

Volume changes lead to pressure changes which in turn lead to gaseous flow to equalise the pressure. Dalton's law of partial pressures states that the total pressure exerted by a mixture of gases is equal to the sum of the pressures exerted by each individual gas (its partial pressure) comprising the mixture. In addition, the partial pressure of each gas is proportional to the percentage of that gas in the gas mixture. Oxygen in air (~79% nitrogen; ~21% O_2) entering the lungs has a partial pressure of 0.21atm or 159.6mmHg. Henry's law explains how gaseous exchange occurs in the lungs. When a mixture of gases meets a liquid, each gas will dissolve into that liquid in proportion to its partial pressure. The higher the concentration of the gas in the gas phase the more and quicker that gas will enter the solution in the liquid. However the reverse is also true and so the direction and quantity of each gas depends on the partial pressure in the two phases - gaseous and liquid. It also depends on the temperature of the liquid and the solubility of the gas in that liquid. Figure 2.2 illustrates the typical partial pressure gradients throughout the body facilitating metabolic demands of O_2 and excretion of excess CO_2. It should be noted that although blood in arterioles may pass tissue in need of O_2, only capillaries are suitable for gaseous exchange. This is because the cell membrane is too thick in arterioles, as are membranes of all other blood vessel types except capillaries with cell membranes only one cell thick (epithelial lining ~1mm thick).

Although some oxygen (1.5%) and CO_2 are dissolved in blood plasma (O_2 is poorly soluble in water) and travel the circulatory system around the body, this is not the main mode of travel for these molecules. Indeed, if it were, a cardiac output 15 times normal (or a PO_2 of 3atm) would be required to meet the bodies' demands (Marieb, et al., 2006a). Instead, 98.5% of O_2 is carried around by haemoglobin in a loose chemical combination, within erythrocytes - also known as red blood cells (RBCs).

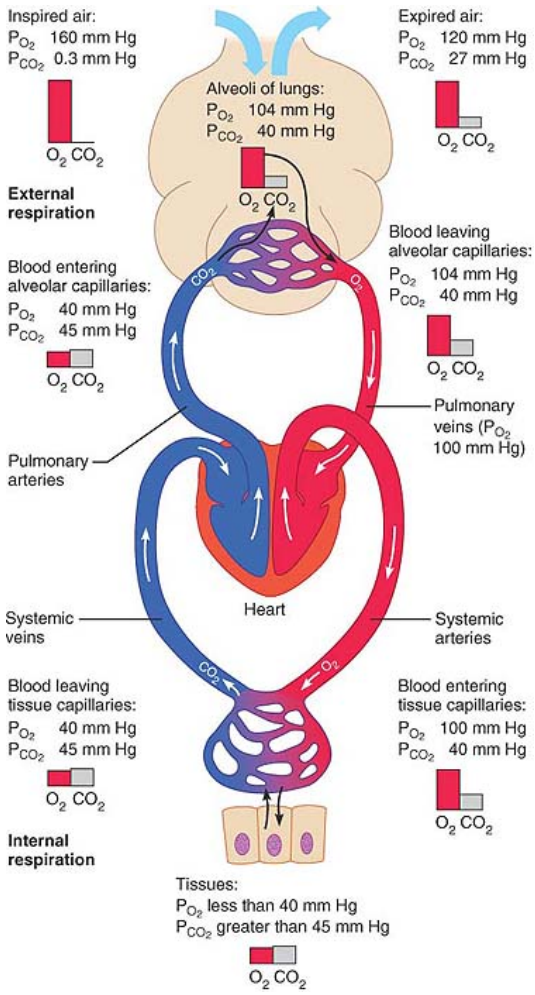

Figure 2.2: Partial pressure gradients in internal and external respiration are used to meet demands for oxygen uptake and carbon dioxide excretion. For example, PO_2 in the alveoli at 104mmHg has a steep gradient (64mmHg) to 40mmHg PO_2 in blood entering and perfusing the lungs. Note: The decrease in pulmonary venous PO_2 is due to a partial dilution of the alveolar capillaries with less oxygenated blood. Also since CO_2 is 20 times more soluble in alveolar fluid and plasma than O_2, a 5mmHg gradient in CO_2 exchange is sufficient for equal amounts of CO_2 and O_2 exchange from tissues (Reproduced from Marieb, et al., 2006a).

2.2.2.2 Erythrocytes (Red Blood Cells) and Haemoglobin

Erythrocytes (*erythro - red; cyte - cell*) or red blood cells (RBC) are dedicated to the task of transporting respiratory gases (O_2 and CO_2) around the body. They carry O_2 from the capillaries in the lungs to supply other tissue cells around the body (diffusion through capillaries). RBCs also carry 20% of the CO_2 released from tissue cells to the lungs for excretion. RBCs pack-in 250 million respiratory pigments called haemoglobin (Hb), and it is these molecules that bind to the O_2 molecules to be carried around the body. In humans, each Hb molecule can potentially bind to 4 oxygen molecules - so that is 1 billion O_2 molecules per RBC (Marieb, et al., 2006a). (Note: later in this chapter (Section 2.5), the change in the oxygenation of haemoglobin in brain tissue is monitored as an indicator of metabolic activity (using NIRS). It is this activity that is used for brain-computer interface applications as local

changes in oxygenation reflect changes in tissue metabolism which causes the optical properties of the tissue to change, i.e. the tissue changes colour.)

The production of RBCs is not due to division of preexisting blood cells in circulation, but instead they are shed into the bloodstream by erythropoietic (blood forming) organs. Starting from the embryo, these are produced from the yoke sac in the embryo, and as it develops, contributions are taken over by the kidneys, spleen, liver, and lymph nodes. Finally in adult life RBC formation takes place in the red bone marrow particularly from the ribs, sternum, vertebrae, and long bones such as the femur and humerus. The number of RBCs in circulation is regulated hormonally by the hormone erythropoietin released by the kidney cells. The result of an increase in this hormone is an increase in RBC production into circulation. Low oxygen tensions such as those at high altitudes can also affect production, where increased tissue anoxia leads to an increase in erythropoietin produced by the kidneys and thus RBCs, with a reaction within the first few hours of exposure. RBCs usually survive ~120 days in circulation. As they mature and age their membrane becomes distorted and they get trapped in various organs, especially the spleen (known as the RBC graveyard), where they are broken down by phagocytes and enzymes.

The structural characteristics of RBCs are in sympathy with respiratory gas transport:

- A biconcave shape gives RBCs a large surface area (30% more than an equivalent spherical cell type). Thus, no point in the cell's cytoplasm is too far from the surface and so is maximally suited for gaseous exchange in the capillaries. Surface proteins such as spectrin ensure the cell membrane can deform, twist and turn so as to squeeze through the slightly wider or narrower capillaries where the exchange occurs;
- RBCs have no mitochondria. Since they generate ATP by anaerobic mechanisms they don't consume any of the O_2 they carry, making them very efficient carriers;
- Disregarding water (dry weight), haemoglobin molecules (which respiratory gases bind to in RBCs) account for 97% of the contents of RBCs.

As previously mentioned the molecule within RBCs that oxygen binds too is haemoglobin or hemoglobin (Hb)[2], which is depicted in Figure 2.3. The 'haem' in the word haemoglobin pertains to the ferrous (Fe^{2+}) iron-containing pigments in the haem groups of haemoglobin which O_2 molecules actually bind to. It constitutes the prosthetic group (non-

[2] Hb is contained within RBCs to prevent direct contribution to blood viscosity and osmotic pressure, and also to prevent broken Hb fragments from leaking through the porous capillaries.

protein component of a conjugated protein) of the Hb molecule. However, the O_2 molecule does not combine reversibly with the haem group on its own. Only when complexed to the globin protein can the haem group achieve this. The iron atom in each haem group makes two links - one to the O_2 molecule being transported and the other to the globin protein. There is a change in shape of the globin protein following attachment of oxygen to the embedded iron atom in its haem group, and it is this very important characteristic that gives Hb tetramers (4 haem-globin monomers bind to form the common Hb tetramer) their impressive physiological properties. The globin linkage also ensures that the iron atom remains in its ferrous state following association with O_2 whereby in a ferric state (oxidised) the molecule would become useless as an oxygen carrier. This is one of the important characteristics of the haem-globin complex, working together to function as an oxygen carrier.

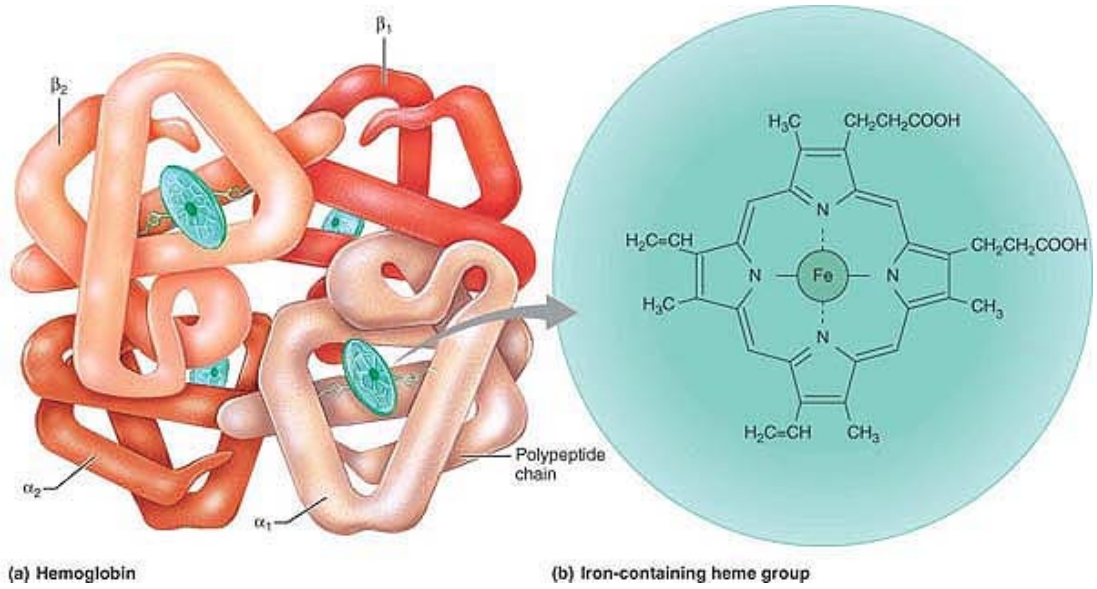

Figure 2.3: Haemoglobin tetramer structure showing the protein globin attached to iron-containing haem groups. Each globin molecule has 4 polypeptide chains (2 alpha and 2 beta) with each bound to one molecule of oxygen. Unlike O_2, CO_2 carried in Hb is only carried in the globin chains reducing competition between the two molecules (Reproduced from Marieb and Hoehn, 2006).

Each monomer in Hb is made up of a single globin with one haem group embedded in it. In the Hb tetramer, the 4 monomers are held together by hydrophobic links between adjacent polypeptide (protein) chains. When a haem group in the tetramer accepts an O_2 molecule, the surrounding globin chain undergoes a small accommodating change in shape: ~0.1nm (Maclean, 1978b). This change affects the other globins in the full Hb complex and they undergo slight changes in structure (allosteric shifts). This affects the potential oxygen affinity (binding strength) of their embedded haem groups and is cooperative. Further conformational shifts due to the 2nd and 3rd subunits (Hb monomers) each binding to an O_2

molecule, lead to the final haem group having a 100 times greater affinity for O_2. This also applies to the release of O_2 into the demanding tissue whereby the first molecule of O_2 is given up quite readily, but subsequent O_2 molecules are released with increasing difficulty, at reduced O_2 tensions (Maclean, 1978a) (see Figure 2.4).

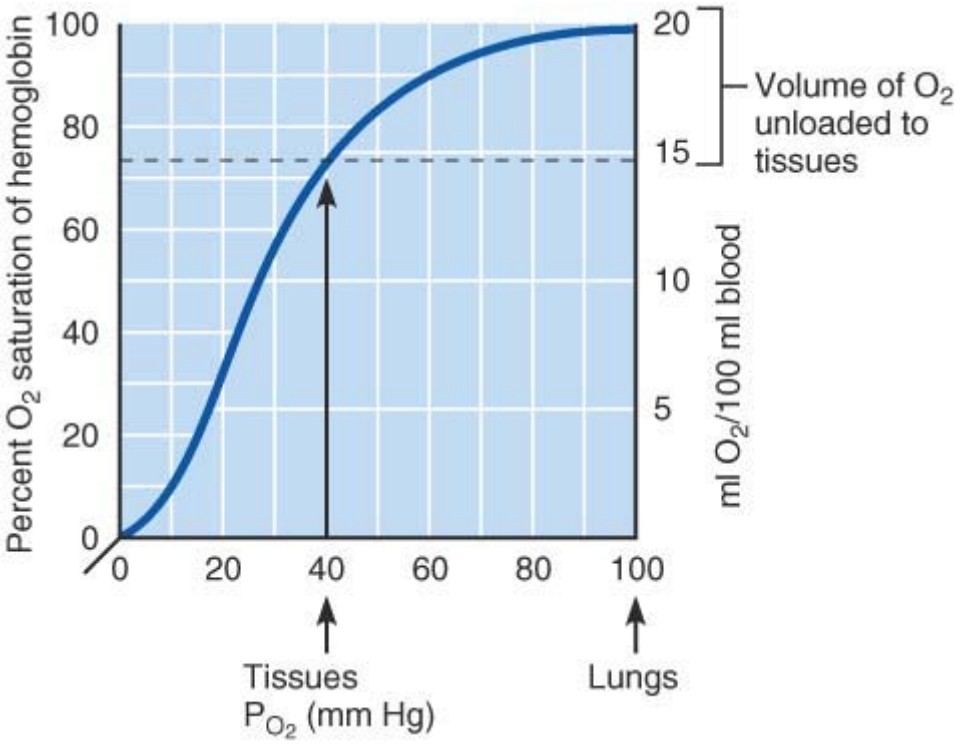

Figure 2.4 : Sigmoidal oxygen dissociation curve with haemoglobin (Reproduced from Marieb, et al., 2006b).

However, as is apparent in Figure 2.3 there are two types of polypeptide chains in human haemoglobin, and for healthy adults over 95% of the haemoglobin in their body is made up of alpha and beta dimers (dimer = two identical monomers), α_2 and β_2 respectively. The importance of having differing dimers within the Hb tetramer can be demonstrated when synthetic Hb homotetramers are generated in the laboratory/test tube (Maclean, 1978b). The oxygen-haemoglobin dissociation curve takes on a hyperbolic form, losing out on the sigmoidal O_2 affinity characteristics of the Hb heterotetramer (see Figure 2.4). If human haemoglobin had this hyperbolic dissociation the result would be that oxygen would be bound at very low tensions and released from the blood too easily and so tissues in greater demand for O_2 supply would suffer (Maclean, 1978a). Thus the sigmoidal form (due to the differing dimers) offers a wider range of oxygen partial pressures to cater for many

environment types: from 40mmHg in the tissues to 100mmHg in the lungs for O_2 replenishing as shown in Figure 2.4[3].

In this study of optical BCIs the main concern is with regard to oxygenation changes in blood, which are seen as changes in concentration of oxygenated haemoglobin or oxyhaemoglobin (HbO_2); and deoxygenated (or reduced) haemoglobin or deoxyhaemoglobin (HbR). To complete the picture of oxygen transport and exchange, it is important to investigate what affects the rate of O_2 loading and unloading. This reversible binding of Hb with O_2 is regulated by not only Po_2[4] but also by blood pH, temperature, and Pco_2, and the concentration of 2,3-bisphosphoglycerate (BPG: produced by RBCs via anaerobic glycolysis).

2.2.2.3 Affectors of O_2 loading and unloading from Hb

Haemoglobin oxygenation saturation for a given Po_2 is determined by:

1) Blood pH;
2) Pco2;
3) Temperature;
4) BPG (2,3-bisphosphoglycerate) concentration.

Under normal conditions a decrease in blood pH (increase in hydrogen ions H^+), and/or an increase in either Pco_2, temperature, or BPG cause an increase in unloading of O_2 from Hb. In general this means that highly active tissues receive higher amounts of O_2 since increased metabolic activity accompanies local temperature increase (by-product of metabolism), increased CO_2 levels and H^+ levels (Bohr affect - from metabolising glucose using O_2), and increased BPG levels (from increased RBC glycolysis). In essence these changes affect Hb's affinity for O_2, by altering the shape of Hb's structure. Graphically, this would be seen as a shift of the normal dissociation curve (Figure 2.4) to the right, essentially enhancing O_2 unloading to demanding tissues. Opposite changes, such as a decrease in temperature, would cause a similar but opposite shift in the curve to the left, inhibiting O_2 unloading from Hb. In order to rule out competition for binding sites on Hb, CO_2 transport and H^+ buffering (carried in RBC rather than in blood plasma) need to be looked at briefly.

---

[3]Interestingly, veins returning to the heart carry a significant proportion (75%) of the oxygen supplied by the arteries, with only 5ml of O_2 used out of the possible 20ml O_2/100ml of blood.

[4] Po_2 is not a measure of the amount of O_2 attached to Hb, but is only indicative of the amount of O_2 dissolved in plasma. Although this only accounts for 1.5% of O_2 transported, it nevertheless is indicative of respiratory state/efficiency.

2.2.2.4 CO_2 transport and pH control

An excellent illustration (from Marieb, et al., 2006b) of the various O_2 and CO_2 transport and excretion mechanisms is shown in Figure 2.5. Cells in the body produce CO_2 and H^+ ions as byproducts of metabolism. CO_2 is produced at a rate of ~200ml/min, which is equal to the rate of CO_2 excretion by the lungs. However, only 7-10% of this CO_2 is transported to the lungs dissolved in blood plasma. A further 20% is carried by binding to the amino acids in globin of Hb (called carbaminohaemoglobin or $HbCO_2$).

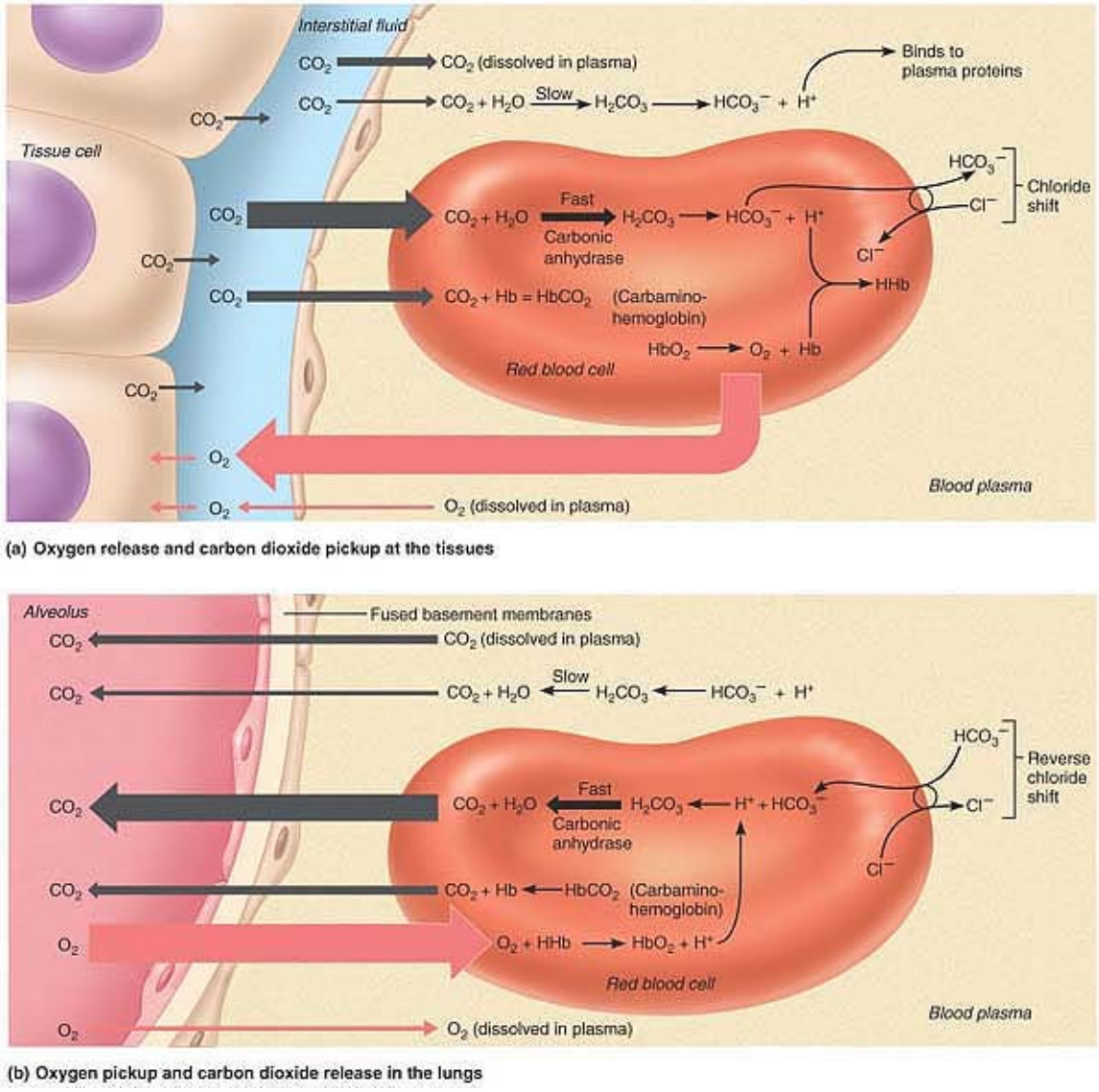

Figure 2.5: Overview of O_2 and CO_2 transport and excretion, including pH buffering. Full description of the exchanges are outlined in the text. Note: HHb in the figure denotes deoxyhaemoglobin but the convention used in this dissertation is to use HbR (Reproduced from Marieb, et al., 2006b).

Note that CO_2 does not compete with O_2 for binding to the iron atom in the haem groups but binds directly to the globin protein itself. However, there is a phenomenon known as the Haldane Effect, which demonstrates that CO_2 combines more readily to HbR (labelled HHb

in Figure 2.5) than to HbO_2. In addition it also implies that more H^+ ions can be buffered and carried in RBCs. To understand this effect fully it is first necessary to explicate the third and final mechanism of CO_2 transport from tissues to lungs, namely via bicarbonate ions (HCO_3^-).

Most (70%) of CO_2 waste is transported as bicarbonate ions in blood plasma. CO_2 exiting tissues quickly move from blood plasma into the circulating RBCs. CO_2 combines with water within RBCs forming carbonic acid (H_2CO_3). This unstable bond dissociates to hydrogen ions (H^+) and bicarbonate ions (HCO_3^-). This occurs in blood plasma also, but within RBCs this process is facilitated and sped up (1000s of times faster) by a catalyst, carbonic anhydrase. H^+ and CO_2 are released and both bind to Hb[5] (which increases O_2 unloading - Bohr Effect). This buffering of H^+ ions means only a slight increase in blood pH (acidic) occurs. Next, the bicarbonate ions slip back out of the RBC to the blood plasma to be carried to the lungs. As a counterbalance, chloride ions move into the RBCs (chloride shift). Finally, on reaching the pulmonary capillaries in the lungs the process is reversed. HCO_3^- ions move back into the RBCs and chlorine ions return back to the blood plasma. Carbonic acid is formed once again (HCO_3^- binding to H^+ ions) which is split by the carbonic anhydrase enzyme releasing water and CO_2 excreted by the lungs under the influence of partial pressure gradients from pulmonary capillary blood to alveoli. O_2 binding at these sites also influences CO_2 release. H^+ ions are released as Hb becomes saturated with O_2. A similar process occurs with bicarbonate ions dissolved in blood plasma, albeit slower in the absence of a catalyst.

The CO_2 in carbaminohaemoglobin is excreted under the influence of the Pco_2 pressure gradient from blood to alveoli in the lungs. CO_2 unloading is also determined by the Hb oxygenation there (Bohr Effect). In addition the CO_2 - simply dissolved in the blood plasma since its release by metabolising tissue somewhere in the body - is excreted under the same pressure gradient. As an aside, hydrogen ions and blood pH are maintained by a carbonic acid-bicarbonate buffer system. Here, increases and decreases in blood pH are dealt with via H^+ ions binding to the bicarbonate ions (forming carbonic acid) in plasma, and dissociation of carbonic acid in the blood, respectively. Blood pH levels can be affected via simple changes in rate and depth of respiration.

Finally in this section, other complexes of haem and globin are considered, which are dependent on development (age), tissue type, ambient conditions, and health.

---

[5] In blood plasma, the released H^+ ions bind to plasma proteins.

2.2.2.5 Other haemoglobin/globin complexes in man

Although haemoglobin has been discussed in terms of its 'ferrying' oxygen around the body there are quite a few other molecules to which Hb can bind to. Some of these render the Hb molecule incapable of carrying O_2 around the body (dyshaemoglobins) but others don't, e.g. carbaminohaemoglobin (although it does influence loading and unloading of O_2 as already discussed). Within the human body there can be:

- Myoglobin

This complex is a sarcoplasmic hemoprotein and is a monomer (not a tetramer like Hb) and so has very different characteristics in comparison to Hb. It is found in high concentrations in the heart and striated muscles that use considerable force and highly repetitive contractions. It can be seen as an intracellular storage molecule for O_2 in those muscles. Unlike Hb-O_2 dissociation, it has a hyperbolic dissociation curve meaning its affinity for O_2 does not change with O_2 binding since it is a monomer. Recent reviews (Garry, et al., 2000; Wittenberg, et al., 2003) have reported that myoglobin is an intracellular facilitator of O_2 transport. Since most of the oxygen pressure gradient is eliminated by the capillary wall on route from the RBC to the mitochondrion of cells, myoglobin rapidly augments the flow of O_2 to the mitochondria. Interestingly, however, using gene disruption technology on mice to remove all myoglobin from their bodies, the authors demonstrated that the mice were still fertile with healthy heart and skeletal muscle function (Garry, et al., 1998) which has perpetuated the debate.

- Fetal Haemoglobin

Haemoglobin F or fetal haemoglobin is used as a carrier of oxygen in the fetus. Instead of having α_2 and β_2 dimers (found in Hb) it has α_2 and γ_2 dimers. As a result it has a higher O_2 affinity (and thus higher than its mother's Hb). The fetal RBCs carrying the molecules are destroyed by the liver shortly after birth, and begin producing adult Hb. It can be called into production in later life pharmacologically in treatment of diseases such as sickle-cell anemia.

- Carbaminohaemoglobin

As discussed, CO_2 binds to the amino acids of the globin protein, carrying ~20% of CO_2 from the tissues to be excreted by the lungs.

- Carboxyhaemoglobin

Carbon monoxide can bind to haemoglobin to form the Hb-CO complex. This silent killer does not display the usual hypoxic signatures: for example cyanosis. Hb has an affinity for CO 200 times greater than for O_2, thus winning binding sites on Hb, even at low partial pressures. Hyperbaric therapy or 100% O_2 are used as treatments to rid the body of CO and free up the Hb which cannot be used for O_2 transport once bound to CO. When CO is bound to Hb it is characterised as absorbing more red light than HbR and even more than HbO_2.

- Metahaemoglobin

Metahaemoglobin, MetHb, is Hb that is oxidised (loses an electron), and is thus useless as an O_2 carrier. As mentioned previously, Hb is kept in a ferrous state, which is maintained by the globin linkage. It accounts for less than 0.6% of total Hb but concentrations can vary throughout the day (Tungjitkusolmun, 1997).

- Sulfhaemoglobin

SulfHb is a result of an irreversible reaction of HbO_2 with sulfide. It is still capable of O_2 transport, though SulfHb has an affinity 100 times less than Hb itself.

- Glycosylated hemoglobin

Haemoglobin can also bind to glucose molecules throughout the 120 days of its RBCs existence. Once bound they remain there. The amount of bound glucose can be monitored and used in diabetes control by inferring glucose metabolism state.

- Cytoglobin and Neuroglobin

Both cytoglobin (CYGB) and neuroglobin are the newest members of the globin family (Dewilde, et al., 2008; Petersen, et al., 2008; Shivapurkar, et al., 2008) and their function is of very recent debate. However, they are said to be found in vertebrates in very low concentrations, with CYGB mooted as being a distant relation to myoglobin, with some recent evidence that CYGB could be a tumour suppressor gene (Shivapurkar, et al., 2008).

The remaining physiology considerations constitute those most important for this study, namely that of the brain and its vascular and neural network; including the central nervous system. The NIRS experimental studies carried out (in Chapters 6 and 7) dealt with spectroscopic analysis of brain tissue, principally the outermost layer: the cerebral cortex

(*"cortex" - latin for bark*). As already mentioned, the brain is influenced by many systems and organs outside of the head. The human head is no different in that various parts of the head affect what occurs in the main tissue of interest: the cerebral cortex. In addition, the brain has some unique vascular and metabolic processes and characteristics not seen in the rest of the body, and so these deserve/require careful study, and are the sole discussion of Section 2.4. Firstly however, brain anatomy and physiology are explicated where a brain 'map' including functional responsibilities is explored.

2.3 Brain Anatomy and Physiology

In order to convey the direction or position of some physiological structure or tissue relative to another, the anatomist uses quite a few terms (e.g. distal, superior), which are very useful and easy to follow once a key is provided. A glossary of these terms is provided at the end of this thesis dissertation in Appendix F. These terms can differ depending on the species being referred to, and in this case the terms are specific to humans.

Many textbooks that describe the anatomy and function of the human brain take a 'bottom-up' hierarchical approach, first describing the low-level microscopic elements and function of for example neurons, followed by the larger macroscopic structures, such as lobes of the brain. In this chapter however, a 'top-down' approach was employed since it was felt that it would be easier to digest, beginning with what every layperson should at least be aware of - the head, scalp, skull, and brain. Following these the less well known descending hierarchical constituents and all the substructure's specific functions are described. It is believed that from the outset this should give a more vivid and tangible understanding to the highly complex human head. It addition, for the experiments in this body of work (in the chapters to follow) near-infrared light initially travels from the light emitter onto and into the scalp, followed by the super-cranial tissues, skull, super-cerebral tissues, and into the brain itself, respectively. Thus, this journey of photons from outside the head inward is mirrored by the sequential description of the anatomical structures that these photons meet along their path. An overview of the major elements of this hierarchy is illustrated in a mind map in Figure 2.6 and described in detail in the next section. In addition to these descriptions and illustrations, functional 'maps' of the brain shown later in Figure 2.13 and Figure 2.14 serve as invaluable tools in developing experimental protocols for BCI applications, which will be dealt with in later chapters.

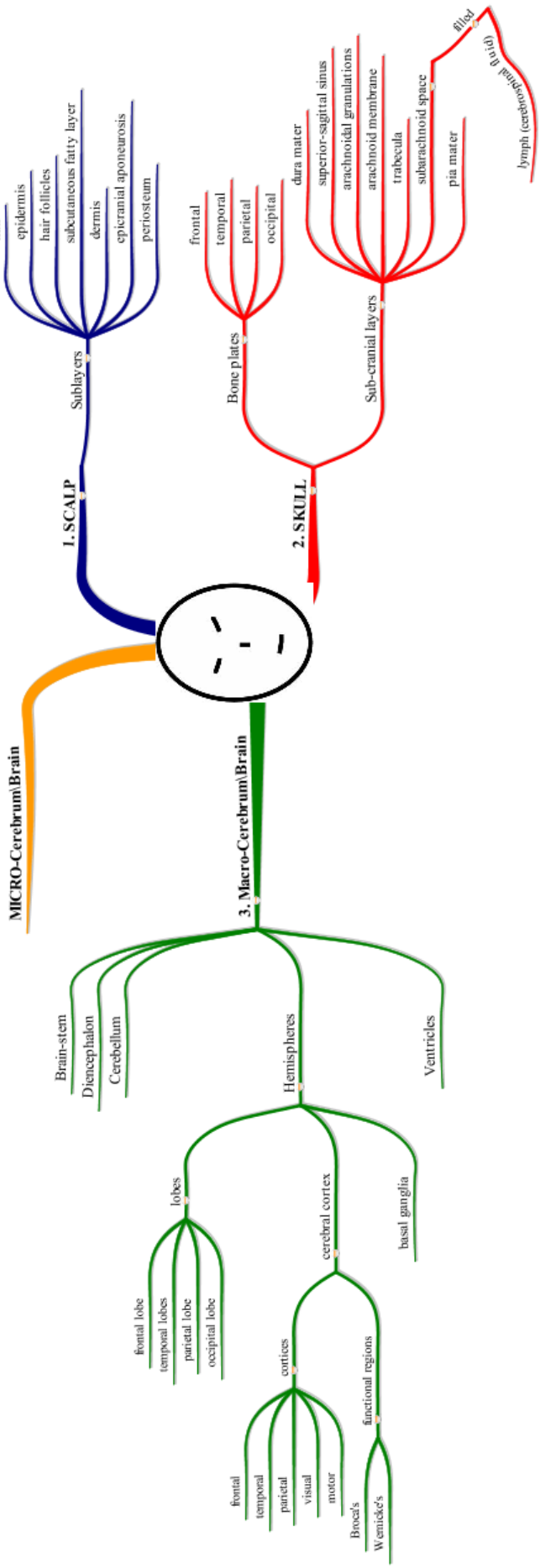

Figure 2.6: Mind map of human cranial structures (designed using iMindMap® software).

2.3.1 Superficial cerebral layers

The superficial layers are dealt with in three stages: those above the skull bone, the skull bone itself, and finally the remaining layers beneath the skull but above the brain.

2.3.1.1 Hair-to-Skull

The description of the human head begins with the most superior tissues, beginning with the hair and skin structures. Figure 2.7 illustrates the tissue layers above the skull which are highly interwoven with nerve endings and indeed blood vessels which become important later on in understanding extracerebral contributions to the oxygenation changes being measured (section 2.5.3.3). The blood vessels in the skin act as blood reservoirs for other organs of the body, called upon to release (vessels constricted) or store (vessels dilated) its supply, depending on specific temporal metabolic demands. Skin colour is as a result of three pigments: melanin (yellow to reddish-brown), carotene (yellow to orange), and haemoglobin (pinkish-red to blue).

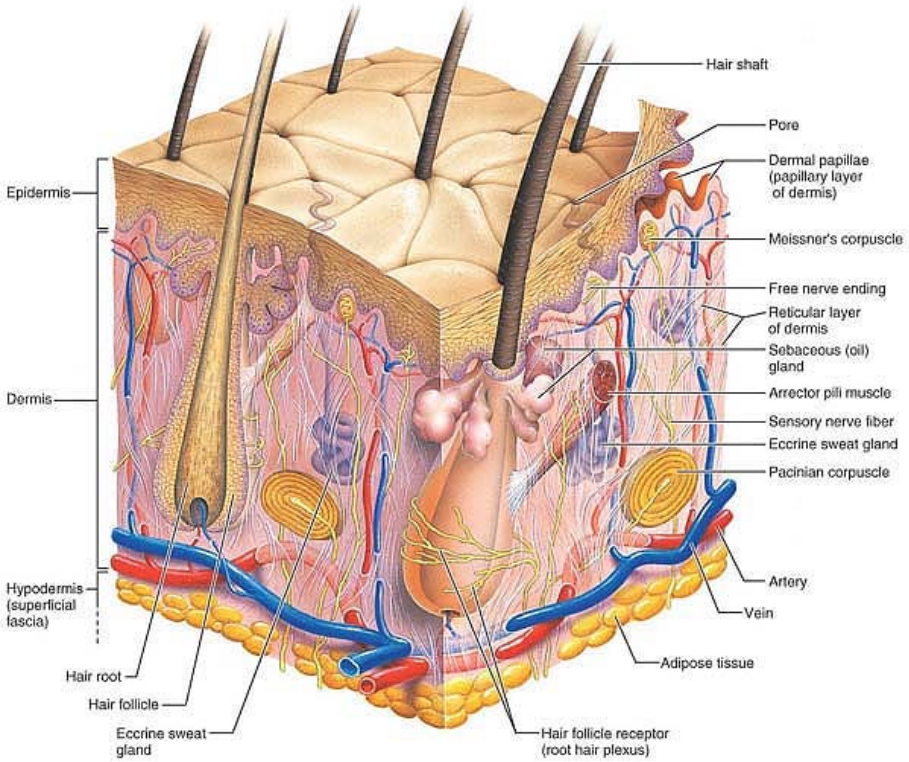

Figure 2.7: Skin structure above the skull. Blood vessels are distributed throughout the dermis and act as blood reservoirs for other organs of the body (Reproduced from Marieb, et al., 2006c).

2.3.1.2 Skull / Cranium

Beneath the skin resides the skull where instead of a seamless encasing of the brain, the cranium (including the facial bones) is made up of 22 bone segments. The main bone segments are outlined in Figure 2.8 and give rise to the naming of the underlain brain lobes (see section 2.3.2.1), e.g. the parietal lobes of the brain lie under the parietal bone pair. These bones are fused together at interlocking joints known as sutures. Apertures (foremen, meatus, and canals) for passageway of blood vessels, nerves, and spinal cord to the brain can be found piercing the cranium at multiple sites.

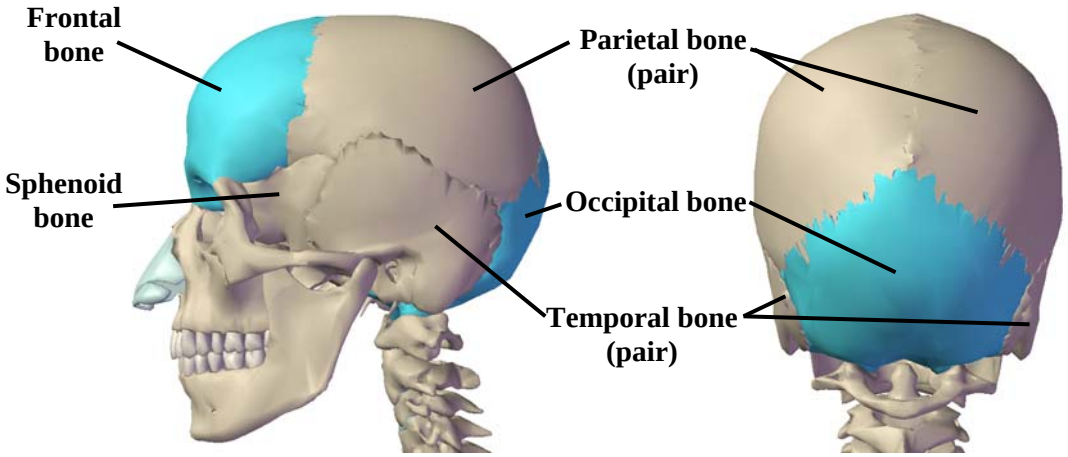

Figure 2.8: Human skull depicting the main bones of the cranium (Image created using interactive 3-D software at www.visiblebody.com).

2.3.1.3 Layers visceral to the skull

Visceral/deep to the skull but superficial (towards the outer surface) to the brain are multiple layers of additional tissues and membranes. Figure 2.9 very effectively illustrates these tissue layers that the NIR optical light sources have to contend with in order to reach the cerebral cortex - the activity of which is of interest for BCI control. The effect of the extracerebral layers on the overall optical attenuation is dealt with in Section 2.5. The sequence of the main tissue layers and obstacles to the cerebral cortex are:

1) Hair;
2) Epidermis;
3) Hair follicles;
4) Dermis;
5) Subcutaneous fatty layer;
6) Epicranial aponeurosis;
7) Periosteum;
8) Bone of skull cap (incl. emissary veins);
9) Dura mater;
10) Superior sagittal sinus (in certain areas);
11) Arachnoidal granulation;
12) Arachnoid membrane;
13) Subarachnoid space (full of lymph fluid);
14) Trabecula, and 15) Pia mater.

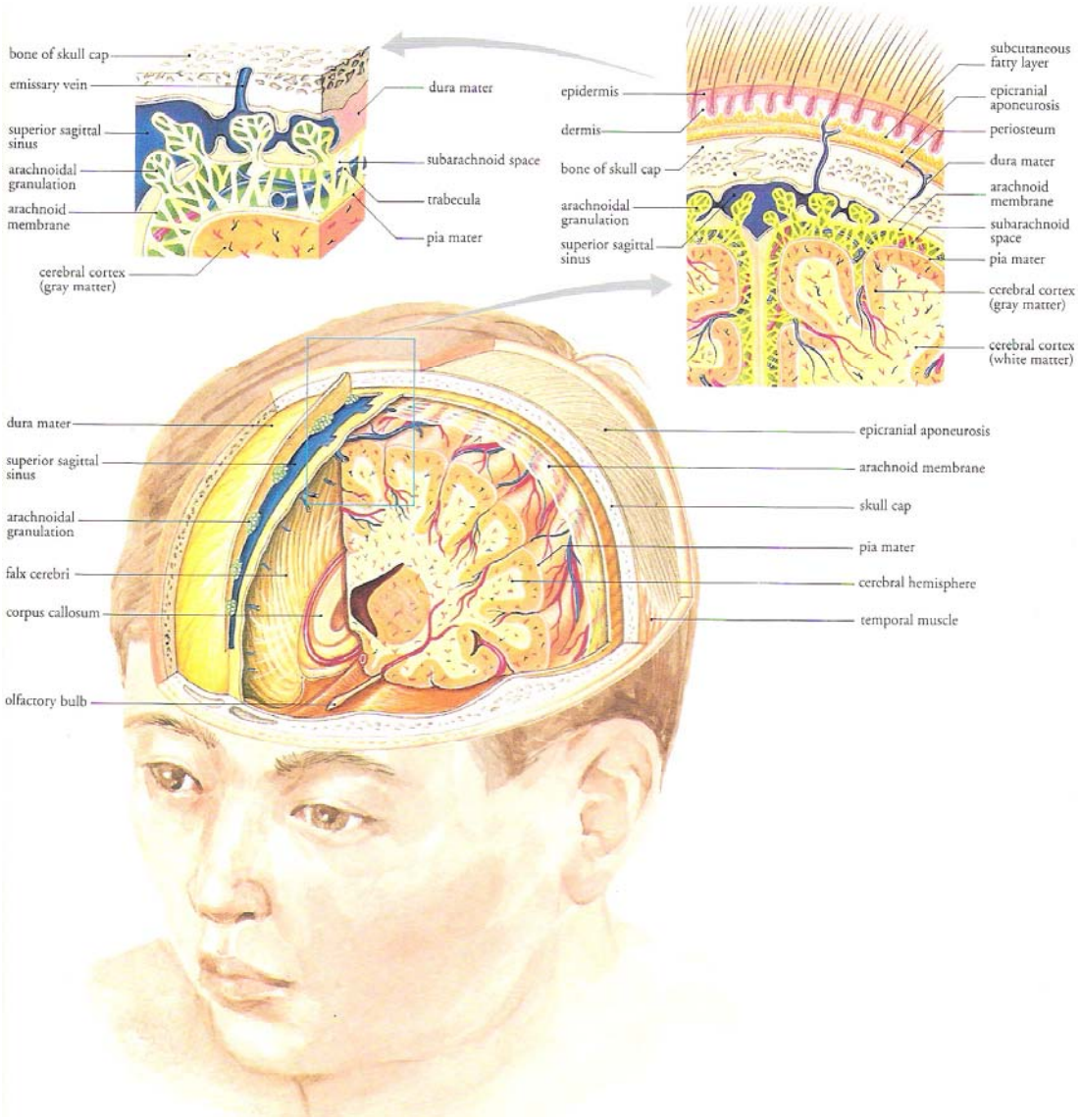

Figure 2.9: Illustration of inferior and superior cranial structures and layers. Numerous vascular and extracerebral tissues' influence on the optical physiological recordings and these are dealt with in Section 2.5 (Reproduced from Takahashi, 1994).

In addition to these main tissue layers various blood vessels, nerve fibres, sweat glands, and some muscles fibres populate the superficial cerebral structures. It can be seen in Figure 2.9 that some of the blood vessels run between the skull bone tissue and the various protective membranes and within the subarachnoid space between the pia mater *("tender mother")* and the arachnoid membrane. The three main protective membranes (meninges) protecting the brain (the skull bone and dura mater *("tough mother")*, the arachnoid membrane, and the pia mater) continue down the spinal cord of the central nervous system. The meninges can be seen as protecting the brain and spinal cord from rubbing off the bones of the skull and spine. The dura mater has two layers: one connecting to the skull (periosteum) and the other (meningeal) covers the outside of the brain. Dural sinuses which

collect venous blood interrupt the fused dura mater layers whereby the arachnoid villi also protrude the dura mater to collect venous blood into the dural sinuses. Cerebrospinal fluid (CSF) fills the subarachnoid space to provide support to the brain. The CSF, formed from blood, is constantly circulating the brain (within the brains ventricles also - see section 2.3.3), and returns to the bloodstream via the arachnoid villi into the dural sinuses, not unlike the venous blood.

Housed within these superficial structures and also extending throughout the body is what is collectively known as the human nervous system. An introduction into the human nervous system and the peripheral nervous system (PNS) can be found in Appendix E. However, of principle interest for this dissertation is the central nervous system (CNS) which encompasses the brain and spinal cord. In keeping with the 'top-down' approach, a look at the brain and how it is apparently organised and 'split-up' into different sections is considered next. Before commencing the description of the brain's several regions it is important to be aware of a few terms which help outline different sections of the brain and give a point of directional reference of one brain section to another. Again, a glossary of these terms can be found in a glossary in Appendix F. For example, 'superficial' relates to tissues towards the surface of the body with respect to a specific deeper tissue.

The main components of the human brain as outlined in the mind map in Figure 2.6 are:

- Cerebral Hemispheres - lobes, landmarks (gyri, fissures, sulci), cerebral cortex, white matter, basal ganglia (nuclei);
- Ventricles;
- Diencephalon - (thalamus, hypothalmus, epithalamus);
- Brain Stem - (midbrain, pons, medulla oblongata), and,
- Cerebellum.

2.3.2 Cerebral hemispheres

The most conspicuous part of the brain is the walnut-like cerebrum. The two cerebral hemispheres shown in Figure 2.10(c) are referred to collectively as the cerebrum. During development from fetus to neonate, the brain constantly morphs, and a significant contributor to this shaping is the lack of space imposed by the surrounding membraneous skull, since it grows relatively slower. As a result, the cerebral hemispheres growing anteriorly are forced back posteriorly and laterally. Consequently, the cerebral hemispheres grow back over the diencephalon and brain stem like an umbrella or mushroom cap over its stalk. The cerebral hemispheres snugly envelop the diencephalon and parts of the cerebellum and brain stem. Convolutions of the cerebral hemispheres occur by week 26 of development

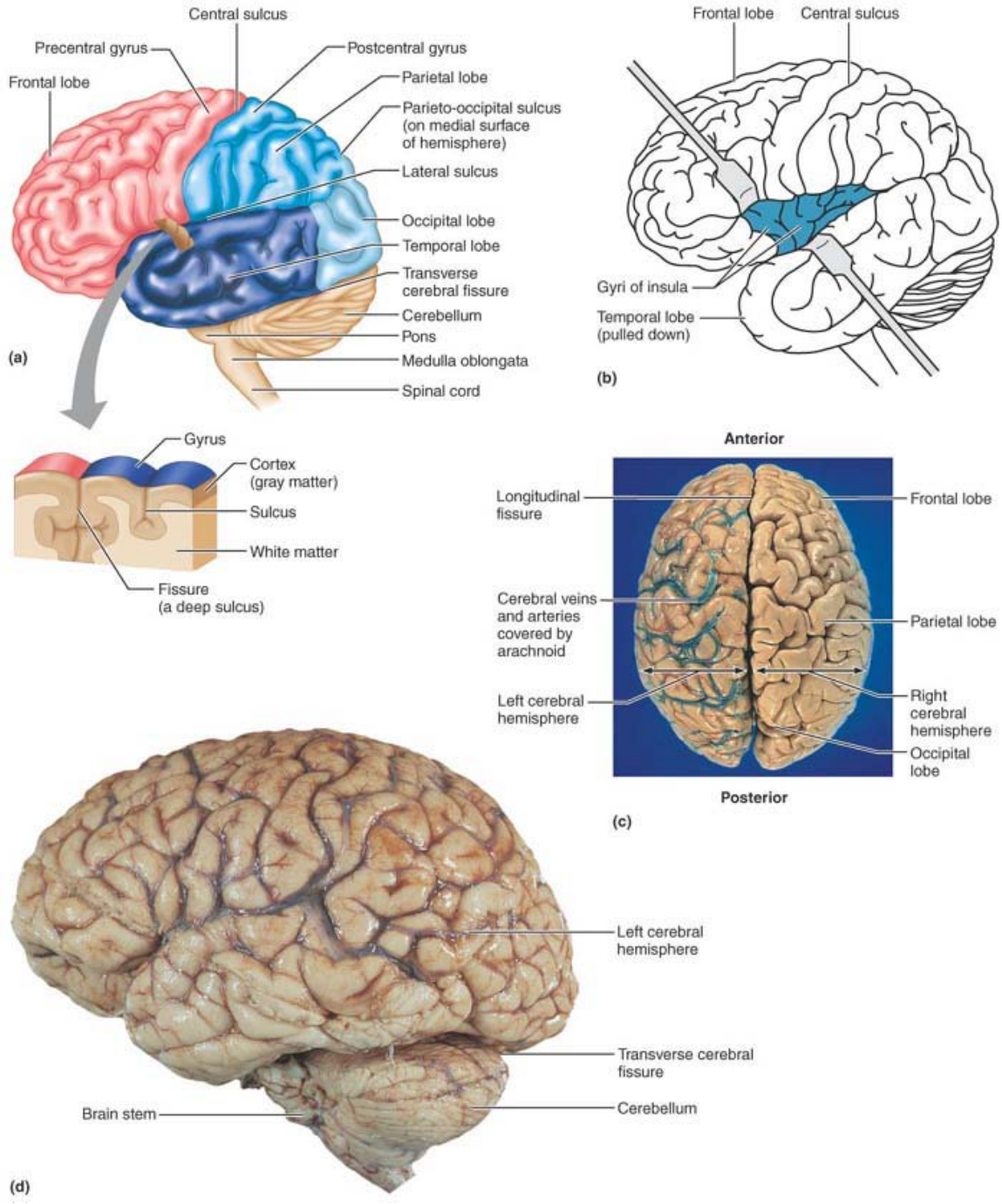

Figure 2.10: Illustration of the brain. a) Brain lobes and major fissures and sulci; b) 5th lobe of the brain, the Insula *("island")*; c) Cerebral hemispheres with blood vessels and arachnoid shown only on the left half of the brain (removed from right hemisphere); d) Photograph of a brain (Reproduced from Marieb, et al., 2006e).

due to continued growth of the cerebrum, increasing the cerebral surface area (hence more neurons are available in the cortex than for a corresponding spherical type).

The many convolutions of the brain act as landmarks to help identify particular regions of the brain. Figure 2.10(a) depicts these with deep grooves or fissures, and shallow grooves

or sulci (*"furrows"* sulcus - singular). The folds of brain tissue are called gyri (*"twisters"* gyrus - singular).

Much of the human body is bilaterally symmetrical in that it has, in general, mirror image left and right halves - if the body was split down the mid-sagittal line. One obvious discrepancy to this symmetry is the appendix, only present in the right half of the abdomen. The cerebral hemispheres of the brain seen in Figure 2.10(c) share this pseudo-bilateral symmetry: corresponding left and right cerebral hemispheres. The median longitudinal fissure (deep groove) separates the two hemispheres. Further sulci and fissures divide the brain into lobes.

2.3.2.1 Brain Lobes

Figure 2.10(a) and Figure 2.10(b) depict the five brain lobes of the human brain. Separated by several sulci, these are the:

1) Frontal lobe;
2) Temporal lobe;
3) Parietal lobe;
4) Occipital lobe, and,
5) Insula lobe.

The first four lobes mentioned are named after their overlying cranial bone segment, shown in Figure 2.8. The gyri of the insula are shown with the temporal lobe pulled down in Figure 2.10(b). The central sulcus shown in Figure 2.10(a) separates the frontal and parietal lobes. Two of the most significant gyri for this BCI study, and indeed in most BCI work, are the gyri immediately anterior and posterior to this sulcus: the precentral gyrus and postcentral gyrus, respectively. These are involved in motor and sensorimotor movement (described in the next section, Section 2.3.2.2). The parieto-occipital sulcus on the medial surface of the hemisphere divides the occipital and parietal lobes. The lateral sulcus traces the edges of the temporal lobe, separating it from the frontal and parietal lobes.

Three main components make up the cerebral hemispheres:

1) The cerebral cortex (gray matter);
2) White matter, and,
3) Basal nuclei (gray matter portions deep within the white matter).

The cerebral cortex *(latin - "bark")* is the outer surface of the brain or the 'bark' of the brain, and is superficial to the inner white matter. The basal nuclei are found deep within the

white matter tissue. The cerebral cortex is described next, and since the optical measurements made penetrate significantly only as far as these outer structures of the brain (Fukui, et al., 2003), it is of particular importance and fundamental understanding for subsequent experimentation and signal analysis. In addition, the cerebral cortex houses the structures involved in higher order brain function such as voluntary motor movement, cognition, and mental arithmetic. Furthermore these can be exploited in BCI applications.

2.3.2.2 Cerebral Cortex

In working with functional activity in the cerebral cortex it is important to have a firm anatomical knowledge, and a firm physiological knowledge base, so as to be in a position to develop experimental paradigms for functional activation studies in the adult human.

The highly complex control implemented by the cerebral cortex (gray matter) is not mirrored by an initial examination of its position and physical dominance on the brain with a thickness of only 2-4mm. However, due to its many convolutions and folds which may initially seem a developmental byproduct and limitation on the potential growth of the brain, these characteristics result in a much larger surface area than would be possible with a spherical model (effectively tripled) (Marieb, et al., 2006e). In addition the cerebral cortex makes up about 40% of total brain volume and contains ~16 billion nerve cells (Jacobson, et al., 2008). Its thickness and structure is not uniform however, and varies across the cerebral hemispheres. The average thickness is 2.5mm, with 4.5mm thickness at the motor cortex and 1.45mm - 2mm for the visual cortex (Jacobson, et al., 2008).

Cortical Structure

The cerebral cortex is composed of blood vessels, neuron cell bodies, dendrites, and associated glia (the structure and function of these micro-cerebral components are reported in Appendix E). Since the thickness of cerebral cortex is non-uniform, it can be viewed in two major groups depending on the number of layers (lamination) a particular cortical region contains:

1) Neocortex *("new bark/rind")* is homogenetic with 6 distinct layers;
2) Allocortex, heterogenetic with 3 layers.

Neocortex (aka isocortex, or neopallium, or supra limbic) makes up about 90% of the cerebral cortex with an estimated 2.78×10^8 synapses per $1mm^3$ of neocortex, 84% of which are excitatory synapses and 16% inhibitory (Colonnier, 1966). The neocortex is differentiated into 6 horizontal layers (as shown in Figure 2.11), according to cell type and neuronal connections:

1) Molecular Layer I - scattered neurons, apical dendrites, axons (horizontal-orientation), glial cells, Cajal-Retzius cells, and stellate neurons. The cell density is low;
2) External Granular Layer II - small pyramidal and stellate neurons. The cell density is high and project to deeper layers, receiving inputs;
3) External Pyramidal Layer III - small-medium pyramidal neurons and non-pyramidal neurons with intracortical (vertical) axons. Apical dendrites stretch to layer I, with axons going to white matter;
4) Internal Granular Layer IV - stellate and pyramidal neurons;
5) Internal Pyramidal Layer V - large pyramidal neurons, with axons projecting to subcortical nuclei;
6) Fusiform Layer VI - some large pyramidal neurons and spindle-like multiform and pyramidal neurons.

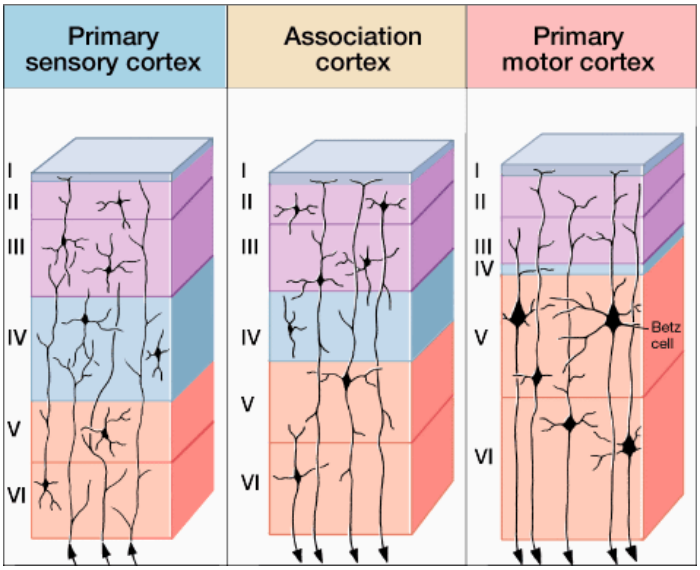

Figure 2.11 : Cerebral cortex layers in the primary sensory, association, and primary motor cortex. Betz cells can be seen in the primary motor cortex (Reproduced from Boon, et al., 2004).

Some of these layers connect afferents and efferents coming from the lower structures (subcortical) of the brain, in particular the thalamus and basal ganglia. The majority, 99% (Braitenberg, et al., 1991), of connections however are to other cortical areas (corticocortical connections), rather than to subcortical regions. Connections are both neuron-type dependent and neocortical-layer dependent. The layering characteristics of the neocortex can be seen in Figure 2.11 and Figure 2.12. Neocortical columns of 200-500 μm in diameter can also be found penetrating the layers vertically, deemed microcircuitry units of the cortex receiving inputs from a specific neuronal population, e.g. from the thalamus (these columns can be seen in the right-most staining of the neocortex in Figure 2.12).

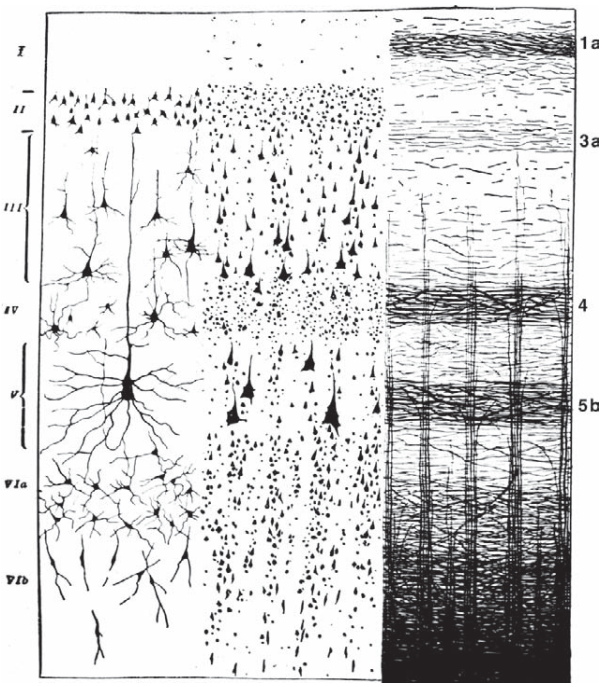

Figure 2.12: Apparent 6 layers of the neocortex (roman numerals) are shown for 3 staining methods. Neocortical columns are apparent in the rightmost image (Reproduced from Jacobson, et al., 2008).

The Allocortex differs from the neocortex group in that it has 3 layers, and never has 6 layers in any stage of development or in adult life. Examples are the hippocampus and olfactory cortex. There are also other auxillary classes other than the neocortex and allocortex, which fall into a category between the two, such as the mesocortex.

In the early 1900's anatomists were able to map the variations in thickness and structure of the cerebral cortex, most notably Korbinia Brodmann who in 1906 produces a map of 52 cortical areas, known now by many as Brodmann areas. Some of the major Brodmann areas are shown in Figure 2.13(a) and Figure 2.13(b). The next chronological step in this mapping of the brain was to append functional labels to specific areas of the cortex, since at that stage a large portion of the anatomy landmarking was complete in Brodmann's work. This functional map is of interest to researchers performing functional activity measurements of the cortex such as in optical BCI.

Functional Cortical Map

The cerebral cortex is in control of many facets of human function such as consciousness, awareness of self, communication, memory, cognition, voluntary movement initiation, and awareness of sensations.

Three functional areas are found in the cerebral cortex: motor areas, sensory areas, and association areas. Interestingly, the motor and sensory functions of each side of the body are

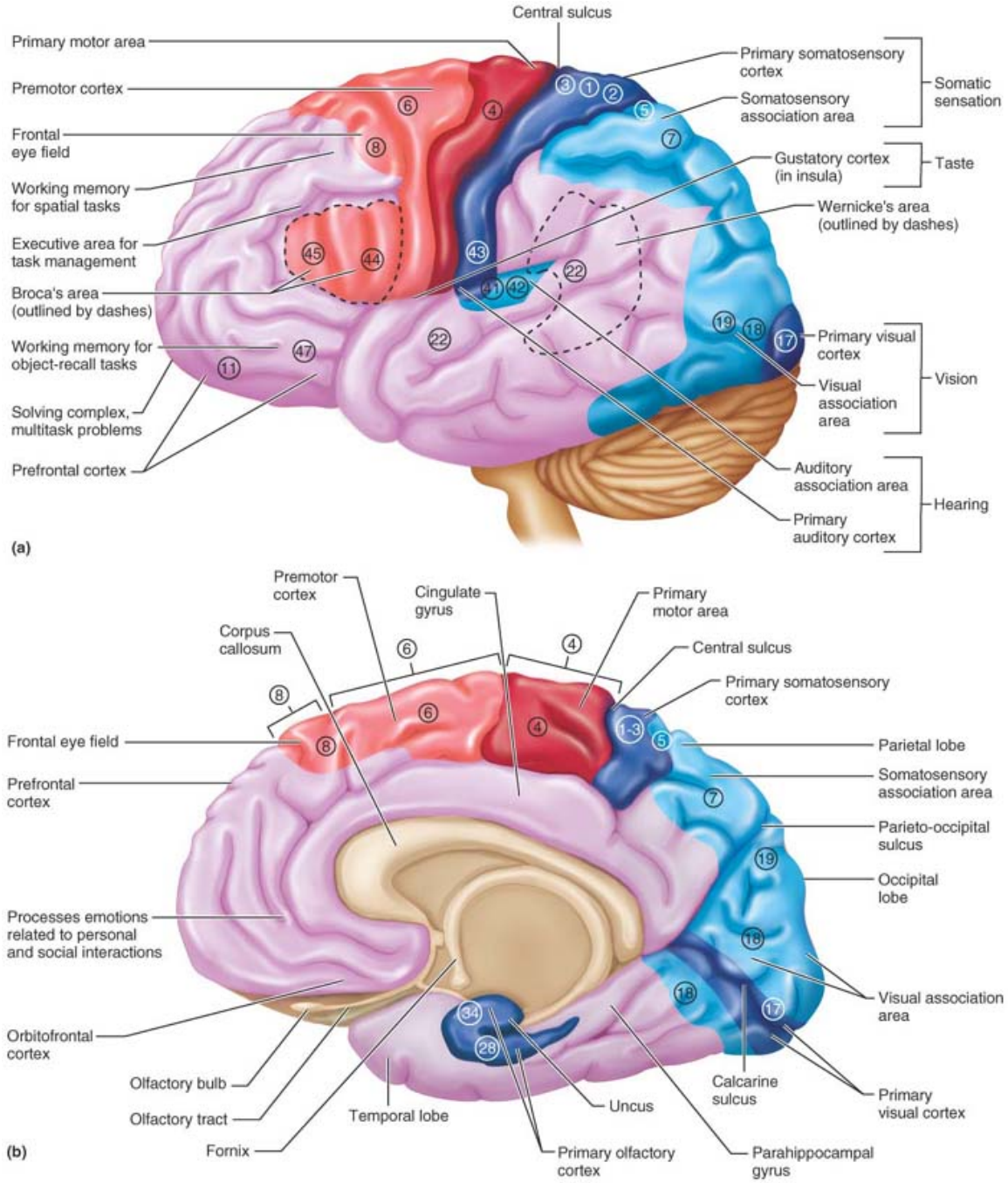

Figure 2.13: Cerebral Cortex - functional and structural map. a) Left hemisphere view of main functional regions of cerebral cortex. Darker colours represent primary structures. Lighter colours represent association areas. (Motor - red; Sensory blue; Violet - multifunction association). Cheif Brodmanns structural areas shown numbered. b) Parasagittal *("beside"* sagittal plane) view of right hemispere, also depicting motor areas located deeper into longitudinal fissure (Reproduced from Marieb, et al., 2006e).

principally dealt with by the opposite hemisphere (contralateral) of the brain, i.e. the left hemisphere integrates the motor and sensory function of the right side of the body, and vice versa. These hemispheres although chiefly functionally-symmetrical do have lateralisation, where functional activity is dominant on one side, depending on the activity. In addition,

although specific functions will be attributed to some cortical regions of the brain, this metabolic activity involves an integration of much more of the brain, with both serial and parallel processing occurring in the brain (these processes are described in Appendix E).

Before divulging the particulars of the motor, sensory and association areas it is worth noting how functional-activity labelling came about, and still does. Three principal methods are used to investigate functional architecture - 1) lesion studies (the first method used Obrig, et al., 2003; Muller, et al., 2006), 2) functional brain imaging, and 3) functional interference studies. A brain lesion *(latin laesio - "injury")* is an abnormal section of brain tissue and may be caused by stroke, cancer, brain injury, blood vessel malformation, multiple sclerosis, and others. Thus if a person is found to have a functional difficulty, such as an inability to move a body part, and subsequently a lesion is found on the brain, it could be inferred that the specimen of cortical tissue where the lesion resides is needed to control that particular body part. Of course this would have been demonstrated in multiple subjects for statistical significance and indeed, the question of mere covariance or causality would arise. Some functions are localised in discrete cortical tissue areas known as domains, e.g. voluntary motor control, and for some functions such as language and memory these domains are spread across the cortex. The particular mental functions used in the experimentation sections of this dissertation are dealt with later in a Chapters 6 and 7. A broad description of the three functional area types is outlined next.

As already mentioned the cerebral cortex has three functional areas, the first of which are **motor areas**. Motor areas are in control of voluntary movements and some studies have suggested that they are involved in the preparation or imagery of movement (Porro, et al., 1996; Porro, et al., 2000) but others have outlined discrepancies (Dechent, et al., 2004). The motor areas of the cerebral cortex, which are shown in Figure 2.13 are the:

1) **Primary motor cortex** - found on the precentral gyrus of the frontal lobe (Brodmann Area 4). Controls most of the bodies' volitional motor movements, illustrated in the left hand side of Figure 2.14;
2) **Premotor cortex** - controls learned motor skills like piano playing, involved in motor movement preparation, coordinates impulses to the primary motor cortex, controls some direct motor activity, and employs movement control dependent on sensory feedback from other cortical areas;
3) **Broca's area** - present in one hemisphere only (usually the left) and involved in controlling muscles for speech production, and possibly the imagery\preparation of these movements;
4) **Frontal eye field** - controls voluntary movement of the eyes.

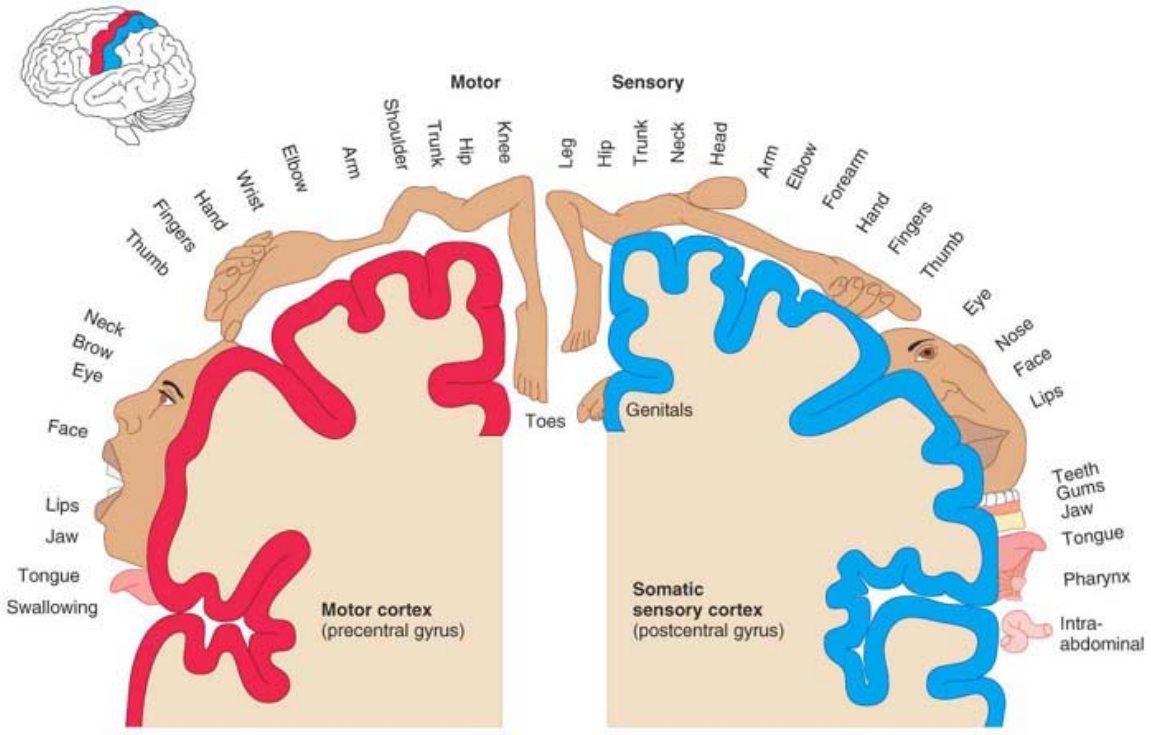

Figure 2.14: Motor and sensory functional map of precentral and postcentral gyri, respectively. Only one hemisphere is shown for each gyrus, located each side of the central sulcus. Both gyri are bilaterally symmetrical for motor cortex functions, and somatosensory functions (Reproduced from Marieb, et al., 2006e).

The primary motor cortex is found on both hemispheres, employing contralateral control: the left hemispherical regions controlling the movements of the right hand side of the body, and the right hemispheric precentral gyrus controlling the left hand side's voluntary movements. A functional map of the precentral gyrus on one hemisphere is shown in the left hand portion of Figure 2.14. Here the somatotopy (spatial map of body parts) is illustrated with an apparent upside-down functionally-fractionated map. In other words the cortical tissue in control of the lower regions of the body such as the feet are found at the superomedial region (top-centre of head) and the cortical tissues dictating control of the head at the inferolateral (lower-to the side) region of the precentral gyrus. The disproportionate size of the body parts next to the cortical tissue in Figure 2.14 is indicative of the amount of cortical tissue that controls their function. For example, the cortical regions of the tongue, hand, and face are found to dominate much of the precentral gyrus, since they require more precise movement than others (Marieb, et al., 2006e). This spatial map of functional control of body parts is important for experiments in the development of the multichannel CWNIRS instrument. In Chapter 6 a series of BOLD fMRI experiments look at the spatial distribution of metabolic activity in relation to motor tasks. Furthermore, in Chapter 7 the newly developed multichannel CWNIRS instrument is validated by assessments of lateralisation and localisation of similar motor tasks for a right-handed subject.

The second of the functional areas of the cerebral cortex are the **sensory areas**. These are concerned with human conscious awareness of sensory input. They are found in the temporal, parietal, occipital, and insular lobes, shown also in Figure 2.13 with the following cortical domains:

1) **Primary somatosensory cortex -** found just posterior to the primary motor cortex, and receives sensory input from the general sensory receptors of the body found in the skin, and proprioceptors (receptors that sense position and movement) sensing skeletal muscle, tendons, and joints. Like the primary motor cortex a general upside-down map of body areas are mapped across the gyrus shown in the right hand illustration in Figure 2.14, and employs contralateral sensing. Again, the amount of cerebral cortex in control of sensing a particular body part is related to the number of receptors of that part (sensitivity) rather than the size of the body part. For example the lips and fingertips are some of the most sensitive parts of the body and thus require a larger dominant portion of cortical tissue on the primary somatosensory cortex;
2) **Somatosensory association cortex -** damage to this area removes the ability to recognise objects by touch, and requires visual senses to do so. It can draw upon memories in its sensory history to perceive objects felt, and can produce understanding such as size and texture. It integrates sensory input from touch and relays this to the primary somatosensory cortex via its multiple connections to it. It is found just posterior to the primary somatosensory cortex;
3) **Visual Areas - Primary visual cortex (striate cortex) & visual association areas -** the primary visual cortex is the largest of all sensory cortices, and is found on the occipital lobe. Much of it is deep within the calcarine sulcus, which may prove difficult for imaging with some methods. It receives input from the retina of the eye resulting from visual stimulation. Again like the somatosensory cortex the visual-space is mapped and relayed onto this cortex upside-down, and employs contralateral mapping. The visual association areas cover a vast region of the occipital lobe and use past visual stimuli to interpret current input - interpreted as colour, form, and movement. This allows for such complex preceptory tasks as face recognition, although much more of the cerebral hemispheres have been shown to be involved in complex visual tasks (Marieb, et al., 2006e);

4) **Auditory Areas - Primary auditory cortex & auditory association area -** primary areas in the temporal lobe interpret pitch, loudness and location of sound from impulses from inner ear receptors. The association areas allow perception of these stimuli, such as speech, music, or screeching brakes of a car. Association areas also act as memory storage of sounds, which can be used as reference for perception;
5) **Olfactory cortex -** deals with sensation of smell, found in the medial part of the temporal lobe. Smell receptors from the superior nasal cavity relay impulses to this region;
6) **Gustatory cortex -** deals with perception of taste, found in the cortex of insula;
7) **Visceral sensory area -** deals with perception of sensations of visceral organs, such as a full bladder, or a sick stomach. It is found in the cortex of insula;
8) **Vestibular cortex -** deals with perception of balance: the position the head in space. It is found in the posterior aspects of the insula, deep to the temporal lobe;
9) **Wernicke's area -** shown in Figure 2.14 this area is critical in language, along with Broca's area on the primary motor cortex and basal nuclei described later.

The last of the three functional areas of the cerebral cortex are the **association areas**. Some association areas have already been dealt with, whereby in general a primary motor or sensory cortex works closely with a corresponding association cortex, e.g. the primary visual cortex and the visual association areas. As you might expect however, much more of the cerebral cortex is complexly connected dealing with multiple inputs and sending outputs down multiple channels. This can be easily demonstrated by examining everyday activities that involve multiple senses such as checking if a food is ripe or rancid: smell, sight and indeed touch play a part whereby an integration of these individual inputs is processed with multiple outputs, perhaps including movement of the food to the mouth if the food is deemed fresh.

A general flow of information from sensory input to a/multiple motor response/s is portrayed in Figure 2.15. The multimodal association areas are where these multiple inputs and outputs are processed. The multimodal areas provide a means to tag meaning onto the information sensed where it can be stored in these areas, and can also be compared to previous experiences, and ultimately a decision can be made as to what action to take. Once

decided, these decisions pass to the premotor regions which in turn communes with the primary motor cortex to drive the response(s). It is in the multimodal cortices that these multiple happenings may become conscious to humans.

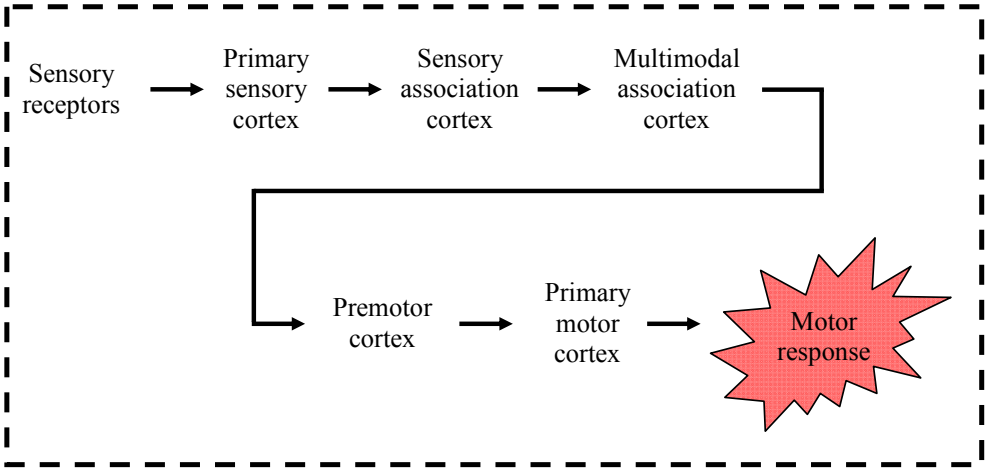

Figure 2.15: Flow chart of general sensory input information flow: from sensory processing to motor response.

The multimodal association areas are divided into three main parts: anterior, posterior, and limbic association areas. The anterior association area is known as the prefrontal cortex (see Figure 2.13) and is involved in mental arithmetic, cognition, and working memory to name a few. The posterior association area is linked to spatial awareness and recognising patterns, such as faces. Understanding language (both written and spoken) is expressed here, including Wernicke's area. It is found in the temporal, parietal, and occipital lobes. Finally, the limbic association area is involved heavily in emotion, and incorporates the hippocampus, parahippocampal gyrus, and cingulate gyrus.

A vast amount of detail on the cerebral cortex and function could be dealt with here but is not within the scope of this dissertation. More detail on cerebral function specific to the imaging modality used is dealt with later, in particular, whilst developing the hypothesis and in the development of suitable experiments to validate the multichannel CWNIRS instrument (Chapters 6 and 7). Since different imaging modalities have varying strengths and weaknesses in terms of say temporal and spatial resolution, it will be important to reflect on the ability of said imaging modalities to be able to "see" the actual activity occurring in the cranial structures. Most important to this study are the vascular activities of the brain. Once these physiological processes are understood, and the capabilities of the imaging modalities used are also understood, the recorded data can be analysed and compared to the actual expected physiological responses - to see if they covary. The reported imaging results should agree with the established anatomy and physiology, or perhaps adequately challenge it, since the area of functional mapping for various imaging methods is still being constantly updated.

Next, the white matter of the cerebral hemispheres and basal ganglia are explored briefly, followed by an overview of various other macro structures of the brain: ventricles, diencephalon, cerebellum, and brain stem. Once accomplished, cerebral blood flow and metabolism are described to complete the reported anatomy and physiology of the human brain.

2.3.2.3 White Matter

The second cerebral hemispheric region after the cortex is known as white matter found deep in the cerebral cortex. The white matter of the cerebral hemispheres is responsible for the communication links between many parts of the brain, in particular links from the cerebral cortex to the lower structures of the CNS. It is made up of mainly myelinated (making it white in appearance) fibres, which are bundled together in large tracts. It has three different types of tracts, classified according to the direction they travel, i.e. which CNS structures they link together: commissural fibres, association fibres, and projection fibres.

Commissural fibres connect corresponding gray matter areas of the two hemispheres (inter-hemispheric) and are horizontally oriented. Association fibres connect multiple parts of the same hemisphere (intra-hemispheric), short types connecting adjacent gyri, and longer ones connecting lobes, and are horizontally oriented. Projection fibres connect the cerebral hemispheres to lower structures of the CNS and spinal cord vertically. They also connect the cortex to the rest of the bodies' nervous system including its receptors and effectors. All these connections allow the brain to work and integrate information seamlessly, with one major link being the commissural fibres of the corpus callosum, shown in Figure 2.13 for one hemisphere.

2.3.2.4 Basal Ganglia

The basal ganglia or basal nuclei form the third basic cerebral hemispheric region, found deep within the cerebral white matter. They receive input from the entire cerebral cortex, and some project via relays through the thalamus to the premotor and prefrontal cortices, and thus influence motor control, although they have no direct access to these motor links. Other functions include attention, cognition, and controlling intensity of movements dictated by the cortex in particular those that are relatively slow such as arm swinging during walking.

2.3.3 Ventricles

The ventricles are hollow chambers travelling up the spinal cord and into the head and are continuous with each other. They are filled with cerebrospinal fluid (CSF) and project into four ventricles in the brain, with apertures to the subarachnoid space filling it with CSF. This provides a fluid filled space surrounding the brain and provides protection from blows

and allows the brain to be buoyant and not crushed under its own weight. An additional function of the CSF then is also for nourishment to the brain (in addition to its blood supply).

2.3.4 Diencephalon

In the analogy used previously of the cerebral hemispheres being like a mushroom enveloping its stalk, the diencephalon would be the superior aspect of the stalk, immediately below the mushroom cap, i.e. immediately below the cerebral hemispheres, as shown in Figure 2.16. It consists of three paired structures: the thalamus, hypothalamus, and the epithalamus. The thalamus *(greek - "inner room")* has many links to the cerebral cortex. Afferents from all body sensors end up at the thalamus and they filter the information before sending on to the cerebral cortex. It functions in mediating motor activities, learning memory, and sensations, acting as a chief gateway to the cerebral cortex.

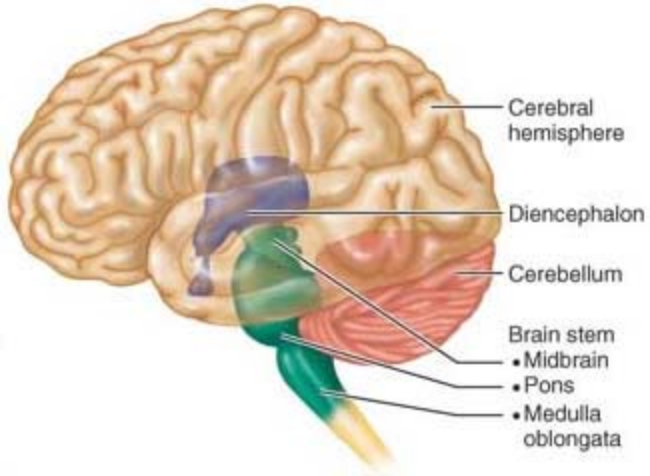

Figure 2.16: Illustration of position of diencephalon, brainstem, cerebellum and spinal cord (Adapted from Marieb, et al., 2006e).

The hypothalamus *(hypo - "below")* is just above the brainstem and below the thalamus. It is heavily involved in homeostasis of most bodily tissues and is the main visceral control centre of the body. It functions in body temperature regulation, regulation of food intake, regulation of sleep-wake cycles, regulation of water balance and thirst, control of endocrine system functioning, and acts as a centre for emotional response. In addition the hypothalamus regulates ANS (autonomic nervous system) activity by controlling the activity in the brain stem and spinal cord influencing blood pressure, eye pupil size, gastrointestinal motility, and the force and rate of heartbeat. The epithalamus aids in regulating the sleep-wake cycle along with the hypothalamus.

2.3.5 Brain stem

The brainstem is made up of the midbrain, pons and medulla oblongata as shown in Figure 2.16, each about an inch long. The brainstem transmits impulses from higher to lower

structures of the brain, and also from the brain to the spinal cord. Much of the body's autonomic responses for survival are housed here controlling breathing, rate and force of heart rate, blood pressure, etc. The midbrain houses structures in control of the "fight or flight" response while the pons *("bridge")* serves as a conduction tracts to the spinal cord, but also act as relays between the cerebellum and the motor cortex. The medulla oblongata is a major region of ANS control for homeostasis including the cardiovascular centres, respiratory centres, and others in control of vomiting, hiccuping, coughing, and sneezing. The hypothalmus relays some of these controls through the medulla areas, which accounts for the apparent functional overlap. A functional brainstem system called the reticular formation is also in place which maintains cortical awareness and filters out repetitive stimuli, also regulating skeletal and visceral muscle activity.

2.3.6 Cerebellum

The cerebellum *("small brain")* controls precise timing and pattern of skeletal muscle control allowing smooth and coordinated movement, which is entirely subconscious. It does this by processing inputs from the cerebral motor cortex, brainstem, and sensory receptors. The cerebellum is notified of the motor cortex's intent to move some body part, via the brainstem nuclei. At the same time the cerebellum receives sensory updates from proprioceptors and other areas (e.g. visual) to establish current position and momentum and then calculates the best way to proceed such as the amount of force and direction of movement. The cerebellum then dispatches these instructions to the cerebral motor cortex and to motor neurons of the spinal cord to carry out the calculated tuned movements.

With a functional map of the cerebral cortex now available from the previous sections in this document, feasible functional experiments could be carried out by imaging the cerebral cortical areas of interest. However, although the macro structures of the human nervous system have been explored and understood it may be desirable to have an understanding of the micro-architecture and histology of nervous tissue, in order to appreciate the fundamental workings of the larger structural units, such as a cortical domain like the primary motor cortex. These descriptions are found in Appendix E, under the heading "Low-level structure and function of the nervous system".

2.3.7 Afterword

An important question still remains unanswered: how does nervous tissue, specifically neurons, receive nourishment from blood in circulation throughout the highly profuse brain? This is of great importance to the optical techniques used in the experimental work, since the measurements made are proportional to cerebral blood flow and metabolism which are

ultimately related to the functional activity that can be exploited in optical BCI applications such as stroke rehabilitation.

2.4 Cerebral Blood Flow and Metabolism

The circulatory system of the human body has been described in detail in Appendix E and throughout Section 2.1, and so the question might be raised, "why is a separate section needed to deal with blood circulation in the brain, or why deal with anything but the brains vasculature and blood dynamics?". Firstly, an overview of the general blood composition in particular the oxygen molecule transport system via haemoglobin is required in order to appreciate the specifics of systemic blood dynamics. In addition, the systemic vasculature can be compared and contrasted with differences in the circulatory subroutine of that of the head. Many other tissues of the body such as muscle tissue may expand and contract with increased or decreased blood perfusion, but the cranial contents are much more delicate and incompressable. Thus, intracranial pressure must be somehow pseudoindependent to the incoming arterial supply from the heart - i.e. the brain's autoregulation. Thus when recording oxygenation of haemoglobin by way of NIRS it might occur to the experimentalist that a measure of blood pressure from the body would be useful for noise cancellation, with the assumption that pressure dynamics of the brain are similar to the rest of the body. All questions specific to the comparability of the head to the rest of the body are not answered, but a good deal of detail is presented in order that physiological constraints to experimentalist's techniques (such as DSP - work ongoing in the group) may be identified.

Blood vessels in the brain are not the same as those of the rest of the body. For example, cerebral veins do not have valves, and so an analysis of the unique irrigation of the brain in terms of its arterial, venous, and capillary systems are dealt with next.

2.4.1 Arterial system

Carotid sinuses are found at the point where the common carotid arteries bifurcate into the internal and external carotid arteries, at the proximal side of the internal carotid arteries. These house baroreceptors used in blood pressure regulation (as discussed in Appendix E). Chemoreceptors are also found nearby at carotid bodies - involved in respiratory rate control. The external carotid arteries supply all head tissues except the brain and the eye sockets (orbits). The internal carotid arteries supply 80% of the blood supply to the cerebrum. Arterial anastomoses are found encircling the pituitary gland, where the anterior communicating artery, posterior communication arteries, and basilar artery join to form the circle of Willis (see Figure 2.17) - conjoining the anterior and posterior supply lines, and

equalising blood pressure between both sides. This affords the blood supply some flexibility, whereby if one of the arteries (carotid or vertebral) becomes occluded, sufficient shunts are available to bypass the hampered vessel. Other anastomoses are found, mainly at the cerebral cortex surface, and not deep in the brain. These again give protection to under perfusion by some vessels, but are not nearly as efficient as the circle of Willis (Edvinsson, et al., 2002)**.** A unique aspect of the arterial supply in the brain is the apparent absence of precapillary sphincters (illustrated for the rest of the body in Appendix E). Instead the brain enforces vascular resistance by arterial and arteriolar segments. Approximately 50% of the aortic pressure is lost at the terminus of the major cerebral arteries, and a further 25% of this pressure is lost at the cerebral cortex surface (Edvinsson, et al., 2002)**.**

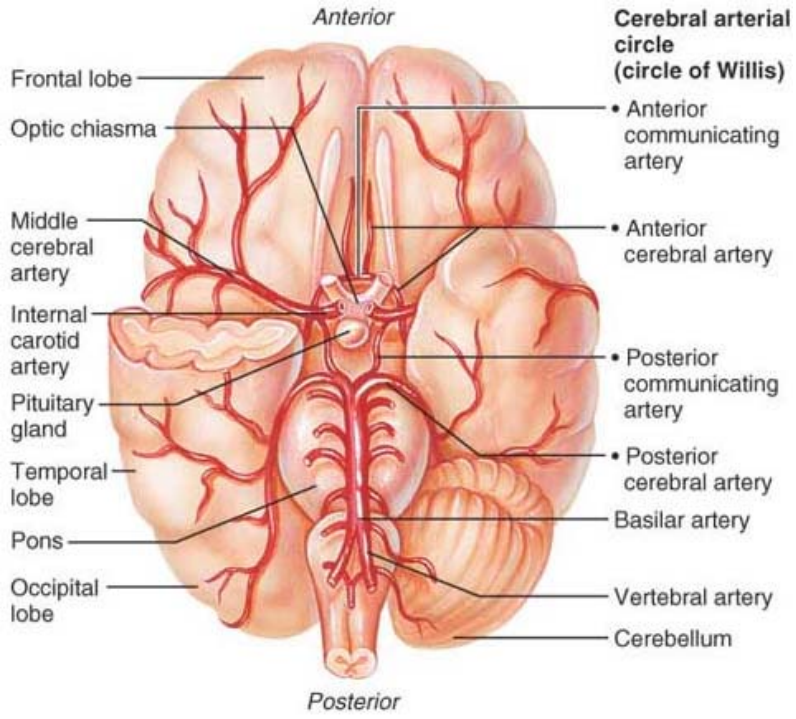

Figure 2.17: Inferior view of lower brain surface irrigation (Reproduced from Marieb, et al., 2006a).

2.4.2 Venous system

The venous drainage of the head has three main veins pairs: external jugular, internal jugular, and vertebral veins. Most of the veins of the head all terminate at the dural sinus. The dural sinuses are a collection of interconnected vessels with no valves, located between the dura mater layers. The internal jugular vein collects blood returning from the sinuses. These vessels do not have valves, unlike systemic veins (Edvinsson, et al., 2002).

2.4.3 Blood-brain barrier and capillaries

Most of the protective measures of the brain have already been discussed: meninges, bone, and CSF fluid. However, a final mechanism, called the blood-brain barrier (BBB),

protects the brain by enforcing only selective crossing of substances from the capillaries to neural tissue in the brain. This further unique aspect of the brain is facilitated by the relative impermeability of the epithelium of capillaries in the CNS. Capillaries in the brain known as continuous capillaries (see Figure 2.18) are more restrictive owing to a lack of fenestrations (found for example in organs requiring rapid filtration such as the kidneys) and more closed tight junctions and intercellular clefts than sinusoidal capillaries (leaky capillaries found in the liver and bone marrow).

The brain requires a tediously robust and constant internal environment since the many chemical variations occurring in the rest of the body, such as those experienced after eating , would overpower the CNS since they would influence for example, neurotransmitter and ion levels that the brain needs independent control over for correct neuronal operation. The sometimes disastrous effect can be seen when a person takes certain drugs that are permeable to the brain's capillary lining.

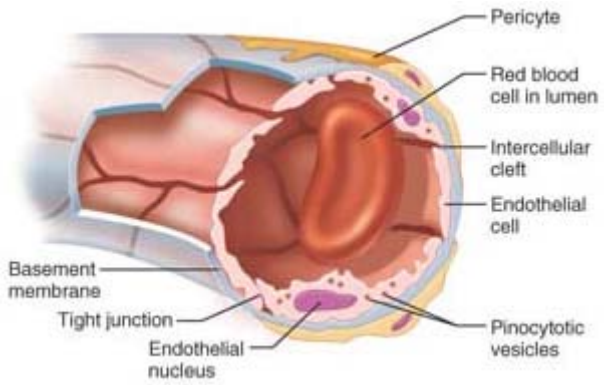

Figure 2.18: Continuous capillaries of the brain with narrow tight junctions and intercellular clefts (Reproduced from Marieb, et al., 2006a).

In addition to the continuous endothelial wall which constitutes most of the BBB, two other factors keep capillary lumen content from neurons and extracellular space: 1) the external face of each capillary is surrounded by a thick basal lamina, and 2) Astrocyte processes cling from neurons to neighbouring capillaries (these structural cells of the CNS are described in Appendix E). Various regions of the brain have more porous capillaries and in some areas the BBB is almost completely absent (such as those adjacent to the 3rd and 4th ventricles). An example of this are regions of the brainstem which sample the blood for poisonous substances, which can initiate a vomiting response (Marieb, et al., 2006e). Nutrients such as amino acids, glucose, and some electrolytes can pass though the cell membrane (facilitated diffusion) but metabolic wastes, toxins, drugs, and proteins are not allowed through. Some substances such as potassium ions and nonessential amino acids are actually pumped from neural tissue through the capillary endothelium. Further substances

can diffuse through the membrane such as fats, CO_2, O_2, fatty acids, and fat soluble molecules - facilitating alcohol, nicotine, and analgesics (Marieb, et al., 2006e).

So how does nutritional exchange occur for the neural tissue? Neurons, neuroglia (especially astrocytes) and vascular cells work together for homeostasis. Arteries arising from the circle of Willis emanate as smaller arteries and arterioles at the surface of the brain across the subarachnoid space. These pial arteries (above and in pia mater) penetrate the brain within a CSF-full space keeping the vessels from the neural tissue. As the vessels penetrate deeper this space disappears and the vascular membrane comes into direct contact with astrocytic (nerve cells) end feet (Girouard, et al., 2006). The density of these capillaries is heterogeneous across the brain and varies with metabolic demand and regional blood flow. It is also proportional to synaptic ending density.

The structure of the brain is such that it facilitates the robust functional activity of the nervous tissue of the CNS. The principal dynamics of blood concerning functional activity and homeostasis are cerebral blood flow (CBF), cerebral blood volume (CBV), and the cerebral metabolic rate of oxygen consumption ($CMRO_2$). Next, these dynamics are examined in terms of the factors that affect their change and how they compensate for potential sabotage on cerebral homeostasis. Note: These three factors contribute to the signals measured in the experimental work - the so called haemodynamic response - which is outlined later in Section 2.4.6.

2.4.4 Factors affecting cerebral circulation

Although making up only 2% of the bodies mass, the brain nevertheless receives 15% of the total cardiac output and so is highly profuse. Blood flow to gray matter is higher than flow to white matter (80ml/100 gm/min, and 20ml/100 gm/min, respectively) with a blood velocity of ~50cm/s in adults (highest values occur in early childhood).

Cerebral circulation is mainly modulated by the following influences: metabolism, PCO_2, PO_2, blood viscosity, and cerebral autoregulation (Udomphorn, et al., 2008). These are outlined next.

- Cerebral blood flow (CBF) coupling to **metabolism** is considered the most important controlling factor of cerebral circulation - meeting the demand. During rest, cerebral metabolic rate of O_2 consumption ($CMRO_2$) is well correlated to CBF. However, during activity CBF exceeds the demand 'asked for' by the increased $CMRO_2$ rate (Fox, et al., 1986). Thus, CBF regulation during neuronal activity is somewhat independent of levels of oxygen in focal tissue

(Udomphorn, et al., 2008);

- CBF is highly sensitive to **changes in PCO_2** with CBF increases of 2-4% per mmHg increase in PCO_2 in the range 25-75mmHg. The potent vasodilation occurs within seconds of the change in PCO_2 and equilibrium occurs after 2 minutes (Udomphorn, et al., 2008);
- Above a **PO_2** of 50mmHg there is minimal change in CBF. Below this value however, CBF will increase to maintain delivery of oxygen to cerebral structures. Nevertheless, PO_2 dynamics have far less influence on CBF than PCO_2, whereby equilibrium of PO_2 can take ~6 minutes after hypoxemia onset;
- A high hematocrit (red blood cell fraction in blood) has the primary bearing on **blood viscosity**. If anemic (low RBC count), CBF is said to increase due in part to the ease in the ability of blood flow (rheology) since it is less viscous, and also to compensate for reduced O_2 delivery to cerebral tissue;
- Finally, **cerebral autoregulation** has been touched on in various sections of this chapter. This is where there is a stark segregation between systemic and cerebral blood pressure and their autoregulation. Cerebral autoregulation is enforced by involuntary processes in the lower brain structures of the brainstem, which dictate dilation or constriction of cerebral arterioles. This maintains a near constant CBF for a range of systemic blood pressures. The desired effect is to have CBF remain constant despite increases in systemic mean arterial pressure (MAP) and even cerebral perfusion pressure. As already mentioned precapillary sphincters are absent in cerebral structures and so instead it is the small cerebral arteries and cerebral arterioles that increase or decrease resistance to filter out pressure changes in the brain, protecting weaker capillary vessels. This mechanism can cope with changes in MAP between 60-160mmHg, and cerebral perfusion pressure changes in the range 50-150mmHg, with little change in CBF. Of course, for various reasons pressures may undesirably stray outside these ranges resulting in hypo- or hyper-tension, for lower and higher pressures, respectively (Udomphorn, et al., 2008).

2.4.5 Neuronal metabolism and neurovascular coupling

The realisation of the relationship of CBF to metabolism did not come overnight. Since the seminal paper in 1890 by Roy and Sherrington (Roy, et al., 1890), many have criticised their two principal outcomes: CBF is regulated by metabolic activity in the brain, and second they deduced (incorrectly) that blood-supply to the brain varied directly with pressure changes in systemic arteries. A reexamination of this work and the chronological advances in literature since then has been documented in 1991 (Friedland, et al., 1991). In particular the

authors outline the difficulties throughout the early 1900's in replicating the CBF response to brain pH change identified by Roy and Sherrington. This inability was suggested as being possibly due to equipment-induced trauma which damaged the integrity of local BBB filtration at the cerebral cortex site which facilitated an undesirable change in brain acidity. In addition it was suggested that subsequent failed attempts to repeat the experiment was because the corresponding authors used inadequate techniques which inadvertantly caused the brain to operate outside its autoregulatory pH range (Friedland, et al., 1991). Nevertheless Roy's hypothesis of regulation of CBF by metabolic activity has been verified, but the nature of the coupling was said to remain an open question (Friedland, et al., 1991). Nevertheless it can be said that neurons and glia release many vasoactive agents that work together to alter CBF (Girouard, et al., 2006). These signals target vascular cells (pericytes, endothelial cells, and smooth muscle cells) which transduce these signals into the adjustments needed to ultimately alter CBF. Moreover, some significant research has identified coupling in microcirculation of cortical columns in the visual cortices of cats (Mayhew, 2003; Thompson, et al., 2003). In terms of this project, the signature haemodynamic response (change in oxygenation) to cerebral metabolic activity is of interest for BCI applications, and this is described next.

2.4.6 Haemodynamic response to neuronal activity

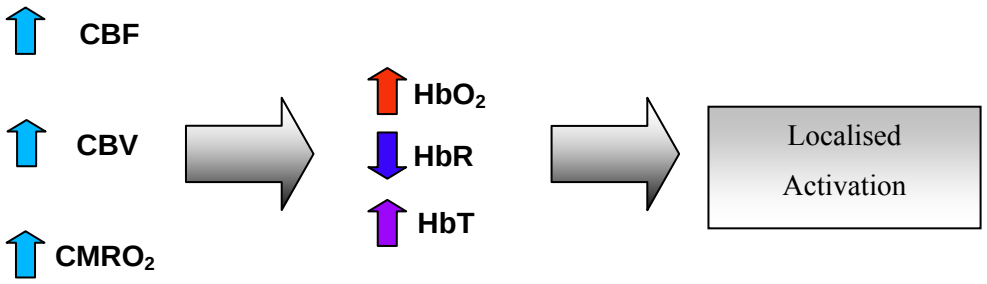

Figure 2.19: Origin of a typical haemodynamic response to localised activity in the brain.

Localised changes in the oxygenation of haemoglobin which are proportional to functional activity are the basis of the experimental imaging technique (FNIRS) which produces a distinct haemodynamic function which is a collective result of changes in CBV, CBF, and $CMRO_2$ as illustrated in Figure 2.19.

Specifically, an increase in CBV leads to an increase in both oxyhaemoglobin (HbO_2) and deoxyhaemoglobin (HbR) since it results in an increase in total haemoglobin (HbT). An increase in CBF however, increases HbO_2 concentration, but decreases HbR. Finally, an

increase in $CMRO_2$ leads to a decrease in HbO_2 and an increase in HbR since more O_2 is being consumed. These superimpose in time to give an overall increase in HbO_2, an overall decrease in HbR, and an increase in HbT - which again is an addition of HbR and HbO_2 concentrations. This haemodynamic feature is what is searched for, for use in optical BCI applications. Two such typical features are shown in Figure 2.20 where during the green segment, a functional event occurred (e.g. finger tapping causing localised activity in the primary motor cortex). Typically, the increase in HbO_2 and decrease in HbR don't occur for 1-3 seconds post stimulus onset, and time to peak is typically ~5-8 seconds. At the cessation of applying the stimulus (in this case finger tapping) both haemoglobin species return to baseline with some overshoot and undershoot. Note: the signals shown are single-trial responses with some simple bandpass filtering applied. These were measured using the instrument described in Chapter 5.

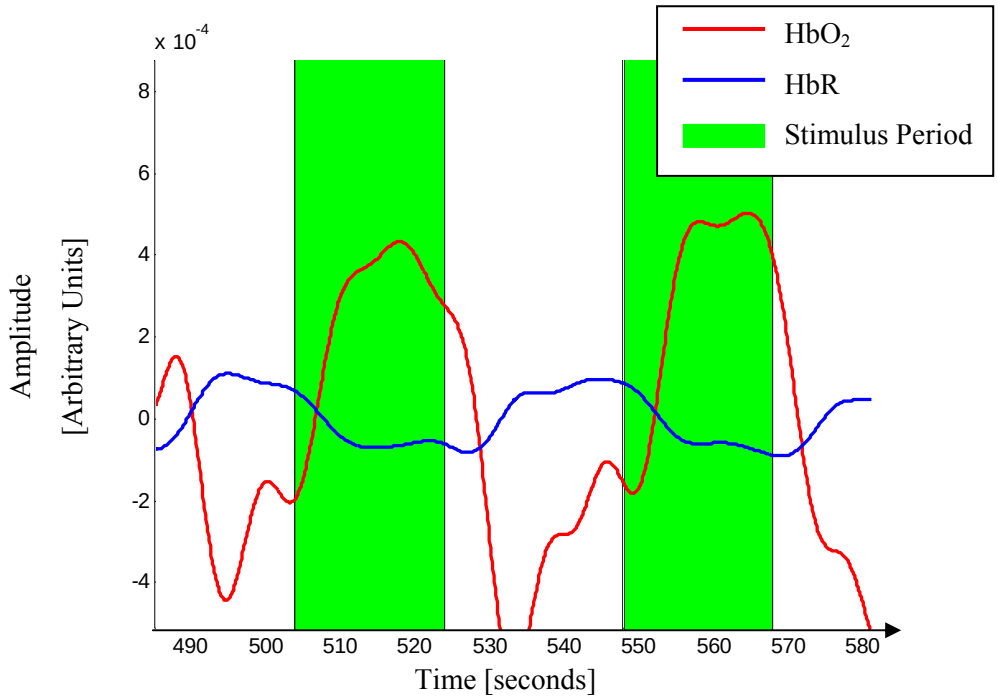

Figure 2.20: Two haemodynamic functions - the response to localised metabolic activity.

2.4.7 Afterword

This concludes the section on the anatomy and physiology relevant to the experimental work. The signals above in Figure 2.20 were measured using FNIRS. This is the imaging modality used in optical BCIs and thus, FNIRS is described next. A description of the theory of light transport in tissue is also provided including the concepts of scatter, and absorption - the effects of photonic propagation in living tissue. In addition, the calculation of haemoglobin (HbO_2 and HbR) concentration changes (e.g. Figure 2.20) for discerning localised functional activity is also explored.

2.5 Functional NIRS (FNIRS)

A principle method for analysing human brain tissue pathology and/or function is via spectroscopy. Crudely speaking, spectroscopy is the study of matter using the electromagnetic spectrum. By having some portion of the EM spectrum meet/interact with the biological tissue being examined and studying the effects (e.g. absorption) that the biological tissue had on the incident energy, one could make a series of deductions on the pathology and perhaps function of the tissue. In NIRS it may not be suprising to find that the experimentalist uses the near-infrared (NIR) portion of the EM spectrum (for tissue ~650nm to 900nm) to study the tissue. However apparently simple this spectroscopy technique may appear at first glance, the thought of using NIRS for analysing brain tissue did not occur until 1977 (Jobsis, 1977). With NIRS we can ascribe measurement of localised cerebral blood volume and haemodynamics of the brain tissue being examined, which are indicators of functional activity in the focal tissue (Wolf, et al., 2007). A variant of NIRS, functional NIRS (FNIRS), is the modality of choice for the optical BCI being described in this dissertation, and so the following section is dedicated to explicating the fundamentals of FNIRS applied to human tissue - the brain in particular. In keeping with the methodology used in other major sections of the dissertation, for conceptual transparency a diagram is included (Figure 2.21) outlining the main components in the discussion to follow including the fundamentals of NIRS theory.

From the diagram in Figure 2.21 the discussion begins with the origins of NIRS, followed by the theory of photonic interaction with matter. Next, NIR photon migration in biological tissue is described including measurement of concentration changes in chromophores[6] whose absorption are proportional to functional activity. The principles of NIRS are then described including the major contributing factors that facilitate the spectroscopist in using NIRS for functional activity measurement. Finally the various techniques within NIRS that are available to the researcher are outlined.

[6] A chromophore is any compound that absorbs EM radiation in the wavelength range being used. In the case of NIRS the chromophore is any compound which absorbs NIR radiation, e.g. HbR.

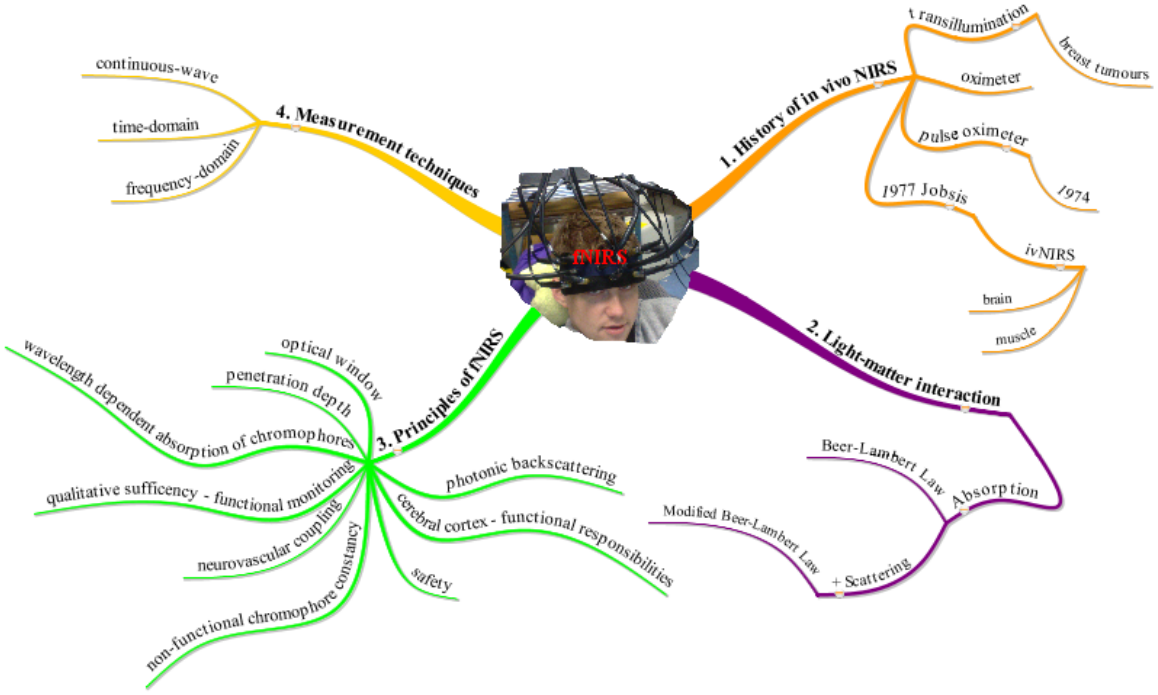

Figure 2.21: Outline of FNIRS section displaying the main components of each subsection in a mind map.

2.5.1 A brief history - the origins of *in vivo* NIRS

Perhaps the first record in history of the application of light to the human body for supposed medicinally related purposes was by Hippocrates (460-370 BC) by putting in place "sun clinics" on the island of Kos in the Mediterranean (Rolfe, 2000). The light penetration into tissue was thought to have medicinal purposes, although the harmful carcinogenic effects and beneficial vitamin D nourishment have been determined since then. A diagnostic application of visible light has been used for centuries and can still be seen in use today with interpretations by the naked eye to detect cyanosis (bluish skin, perhaps carbon monoxide poisoning), liver failure (yellowish eyes/skin), and internal bleeding (red to blue bruising), to name a few. In the earlier part of the 1900's instruments using visible light were used for diagnosis, such as detection of large breast tumors by transillumination (Cutler, 1929). Early techniques in breast imaging with visible light suffered problems with overheating and superficial burning of the tissue, and were thus abandoned for a time. Alongside these developments the field of oximetry was born for invasive and non-invasive measurement of blood oxygenation. Thus, this brand of optical measurement was more specific by attempting to measure the oxygenation status close to the sensor. Along with the vital signs of blood pressure, heart rate, temperature, and respiration rate, oxygenation provides complementary health monitoring, especially in the newborn infant and aiding in the study of neonatal neurodevelopment problems (Cope, 1991).

As described in detail in Section 2.2.2 oxygen is transported around the body via haemoglobin (Hb) molecules, each able to carry 4 molecules of oxygen. Oximetry measures the oxygenation saturation which is the amount of O_2 the haemoglobin is carrying compared to the amount it could carry, expressed as a percentage. The key to oximetry and indeed NIRS is the wavelength-dependent absorption of light by the two types of haemoglobin: oxyhaemoglobin (HbO_2) and deoxyhaemoglobin (HbR). The optical-absorption spectra of HbR and HbO_2 were first measured in 1943 (Horecker, 1943) but it wasn't until the 1970's that the first commercial oximeter was developed by Hewlett-Packard (Merrick, et al., 1976). In 1974 pulse oximetry was developed (Aoyagi, et al., 1974; Severinghaus, 2007) whereby the volume pulse was recorded spectrophotometrically with the assumption that the pulse is caused by arterial inflow of blood -allowing calculation of arterial oxygen saturation. A startling 90% reduction in fatalities related to anesthesia coincided with the introduction of the pulse oximeter (Severinghaus, 2007). Nevertheless, until the 1970's NIR light was not investigated extensively for application in oximetry (Rolfe, 2000) but in 1977 Jöbsis discovered that NIR light could penetrate bone and also penetrate biological tissue deeper than visible light (Jobsis, 1977) and that it could be used to determine brain oxygen sufficiency. Thus in vivo NIRS (ivNIRS) emerged. Early measurements were performed monitoring continuous cerebral oxygenation state of animals (Piantadosi, et al., 1986), and in reflectance mode on the human adult (Fox, et al., 1985) and the neonate (Ferrari, et al., 1986).

2.5.2 The journey of photons through biological tissue

To understand the nature of light transport in biological tissue a description of the potential effects of light interaction with matter are outlined next.

2.5.2.1 Photonic effects

Light propagating through a medium can undergo perturbing effects or travel straight through the medium. To illustrate these effects a simple 3 piece model (light source, a medium, and a detector) is depicted in Figure 2.22.

- The first photon travels straight through the medium unperturbed - a ballistic photon;
- The second photon travels some distance into the medium before it is absorbed. Light absorption is the loss in energy of the incident beam with interaction with electrons, atoms, and molecules. The conservation of energy law demands that this 'lost' energy be converted rather than truly extinct, and in this case it is converted into either heat or light of longer wavelengths (Splinter, et al., 2007);

- The third and fourth photon undergo scattering. The third is scattered in such a way as to still reach the detector, whereas the fourth photon scatters away from the source-detector axis altogether, and so is lost and undetected as a result. There are three classes of light scattering: Raleigh-, Mie-, and Raman-scattering. Rayleigh scattering occurs when the incident light wavelength is much larger than the dimensions of the scattering particle it collides with. Mie scattering occurs in cases where the wavelength is comparable to the particle dimensions. In both Raleigh and Mie scattering the collisions are elastic, whereby only the trajectory of the light is altered, with no energy loss. Mie scattering is the dominant scattering effect in biological tissue, thus scattering in tissue is mostly elastic, with no energy loss. Raman scattering, which is not dominant in light-tissue interaction, induces changes in the trajectory but is inelastic meaning it also causes light to be emitted from the particle at a different wavelength, typically at a longer wavelength (Splinter, et al., 2007).

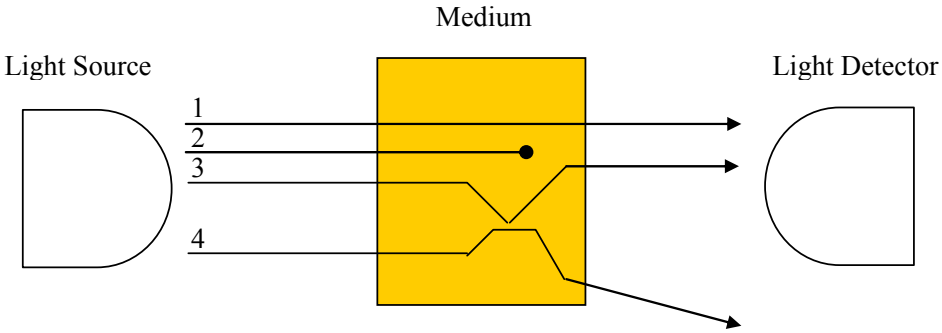

Figure 2.22: Illustration of photonic effects - the cuvette model. Four photons leave the light source. Photon 1 emerges unperturbed known as a ballistic photon. Photon 2 is absorbed in the medium where as 3 and 4 are scattered (arbitrarily). Photon 4 is scattered away from the detector and so is lost from the measurement altogether.

2.5.2.2 Absorption of Light - Beer-Lambert Law

One of the two main effects of photonic interaction with matter is absorption. It has long been established that layers of equal thickness absorb the same portion of an incident beam of light. This logarithmic attenuation of light through an absorbing medium was discovered in 1729 and is known as the Lambert-Bouguer Law:

$$A = \log_{10}\left(\frac{I_0}{I}\right), \tag{2.1}$$

...where A is the light attenuation (dimensionless) given nominal units of optical density (OD). A represents the number of orders of magnitude of attenuation between the incident (I_0) and the transmitted (I) light.

In 1852 August Beer formulated a law stating that the optical density of a non-absorbing medium with a purely absorbing substance dissolved in it is proportional to the concentration of the dissolved absorbing substance. From this the Beer-Lambert Law, which combines the 18th and 19th century laws just mentioned, can be written as:

$$A = \log_{10}\left(\frac{I_0}{I}\right) = \alpha c d, \tag{2.2}$$

... where α is the specific extinction coefficient [units: $mM^{-1}cm^{-1}$], c is the concentration of the absorbing substance [units: mM], and d is the distance between light entry and light exit from the medium [units: cm].

Attenuation by purely absorption effects can be described by the Beer-Lambert Law and can be used for colorimetric analysis (doesn't account for scattering). In the case where there are multiple absorbing compounds in a non-absorbing medium, the Beer-Lambert Law can be applied as a linear summation of the contributions of each absorber/chromophore to the overall attenuation, all multiplied by the distance d between the light entry and exit point to/from the medium. This can be written as:

$$A = \log_{10}\left(\frac{I_0}{I}\right) = \sum_{i=1}^{n} \alpha_i c_i d = (\alpha_1 c_1 + \alpha_2 c_2 + ... + \alpha_n c_n) d, \tag{2.3}$$

The process of solving the above equation to calculate the concentration (c) of each chromophore is as follows:

- Measure the distance d in centimeters between the light entry into the medium and the light exiting the medium;
- The extinction coefficient, α, by each chromophore is a function of wavelength and can be measured. This is usually retrieved from a tabulated list (measured in vitro using laboratory spectrophotometers) of values for chromophores at various wavelengths, e.g. for HbO_2 and HbR at NIR wavelengths (Cope, 1991);
- The attenuation of each wavelength of light used is then measured experimentally. Each wavelength used supplies an equation for the simultaneous

equation set. The number of wavelengths of light used must equal or be greater than the number of chromophores in order to solve the set of simultaneous equations.

The Beer-Lambert Law in the form above cannot be used in tissue spectroscopy because it would require knowledge of the absolute attenuation to calculate the absolute concentrations of the tissue chromophores, e.g. HbO and HbR. This is because of scatter, whereby the incident light is scattered from the original linear path and so this acts as a large source of attenuation (~80% of the total attenuation is due to scattering (Elwell, 1995)). In addition, the actual distance a photon travels (which is required for the calculation) when scattered can be considerable larger, e.g. ~6.26 ($\pm$ 14.1%) times larger than the distance between the light source and detector in the normal adult head for a wavelength of 807nm (Duncan, et al., 1995). Nevertheless, a modified form of the Beer-Lambert Law can be applied to attempt to tackle the issue of scatter and ultimately allow for spectroscopic analysis of biological tissue - since biological tissue induces scatter.

2.5.2.3 Attenuation of Light - Modified Beer-Lambert Law

The modified version of the Beer-Lambert law (MBLL) accounts for the large effect scattering has on the observed attenuation. As already mentioned scatter accounts for 80% of the attenuation and this is partly accounted for by introducing an additive term G for the scattering losses. In addition, a multiplicative term B is included to account for the aforementioned increase in geometric distance between the source and detector due to scattering. These modifications can be written as:

$$A = \log_{10}\left(\frac{I_0}{I}\right) = \alpha c d B + G \tag{2.4}$$

The shortcoming of using this algorithm for colorimetry is that:

1) The scattering losses denoted by G are usually unknown and are dependent on the relative positing of the source and detector, and on the scattering coefficient of the tissue under examination, and,
2) The distance that the light has to travel is larger that the linear distance between the source and detector, and this value is needed for the calculation.

Nevertheless, a differential version of the MBLL can be used to calculate the concentration *changes* of the chromophores. This measurement of changes in the

concentration of a chromophore is sufficient for functional brain measurements (Wolf, et al., 2007). Firstly, an assumption is made that the mean scattering losses and the tissue geometry remains unchanged for a given source and detector position over the time period of measurement. In addition, the differential pathlength factor (DPF) term B is said to remain constant over the brief course of the attenuation measurement. Thus, the differential version of the MBLL for multiple chromophores at wavelength λ_i can be written as:

$$\Delta A(\lambda_i) = \left[\alpha_1(\lambda_i)\Delta c_1 + \alpha_2(\lambda_i)\Delta c_2 + ... + \alpha_n(\lambda_i)\Delta c_n\right] dB(\lambda_i), \quad (2.5)$$

... where $\alpha_n(\lambda_i)$ is the extinction coefficient (absorption) of the nth chromophore in the medium measured at the ith wavelength, and where c_n is the concentration of the (nth) chromophore.

To solve for the concentration changes of the chromophores ($\Delta c's$) in a typical spectroscopic application:

- The geometrical pathlength d is measured;
- The n extinction coefficients for all (i) wavelengths used are gathered from tabulated values: $[(\alpha_1(\lambda_1),\alpha_2(\lambda_1),...,\alpha_n(\lambda_1)), (\alpha_1(\lambda_2),\alpha_2(\lambda_2),...,\alpha_n(\lambda_2)), ...,(\alpha_1(\lambda_i),\alpha_2(\lambda_i),...,\alpha_n(\lambda_i))]$;
- The differential attenuations are measured experimentally using the i wavelengths. This is done by taking an attenuation measurement (recording from a detector) using each wavelength (as a light source) at a moment in time t_0 and again at some time later, t_1. The differences in these attenuations correspond to the change in the chromophore levels. In the case of one wavelength and a single chromophore in the compound an attenuation measurement ($A(t_0)$) corresponds to the concentration of the chromophore at that instant in time, $c(t_0)$. Some time later (t_1) the chromophore concentration has changed and a further attenuation measurement ($A(t_1)$) is made yielding a corresponding chromophore concentration $c(t_1)$. The difference in these attenuations is used to calculate the change in concentration of the chromophore : $\Delta A = (A(t_1) - A(t_0)) = \Delta c \alpha dB$. In practice repeated attenuation measurements are made to monitor changing chromophore levels over the course of an experiment. The concentration levels are not measured directly but

are calculated in the MBLL as part of an inverse problem;

- The DPF (B) remains unknown. Nevertheless, it's value is required for chromophoric measurements to be made (Owen-Reece, et al., 1999). Thus, an approximation of the DPF from tabulated values can be used, or an actual measurement of the DPF can be made with some systems (Elwell, 1995). These are explored more in section 2.5.3.3.

The MBLL can be used in FNIRS in order to calculate the specific chromophore concentration changes that relate to functional activity in the human brain e.g. HbO_2, HbR, and cytochrome-c-oxidase (Wolf, et al., 2007). The calculation will be described in Section 2.5.3.3 as it pertains to the instrumentation reported in Chapter 5, but first the principles of NIRS applied to human head are described.

2.5.3 Principles of NIRS

To aid in visualising and appreciating the principles of NIRS, an overview of the process of photons travelling from the light source, through the cranial tissue, and finishing at the detector is given next.

2.5.3.1 Brief functional NIRS event overview

As portrayed in Figure 2.23 near-infrared light is applied in contact with, and perpendicular to the scalp. The NIR light enters the epidermis and after only a few millimeters becomes highly diffuse due to multiple scattering events due to the refractive index mismatches mostly between extracellular and intracellular boundaries (Madsen, et al., 1999). Scatter will occur wherever there is a change in refractive index (Rolfe, 2000). The further NIR light has to travel in a highly scattering medium, the greater the angle of scattering. From diffusion theory, the more scattering particles there are in a medium the greater the probability that the light will be backscattered - that is that the light travels a net direction of ~180° in reference to the light source injection (Rolfe, 2000). Thus the light is said to travel a random walk path but in a pseudo-arc or banana-like path with decreased photonic emergence from the scalp a few centimeters from the source (as illustrated below in Figure 2.23).

A detector placed approximately 3cm from the source can collected sufficient photons (~10^6-10^7 loss - so 1 out of a million photons) which have travelled through the cerebral cortex - the outer layer of the brain (see Section 2.3.2.2 on the cerebral cortex). It can be claimed that these photons have travelled into the cerebral cortex since photonic penetration into the brain or photonic depth is proportional to the distance between the source and detector, with ~3cm being the standard inter-optode (IOS) distance for cerebral interrogation.

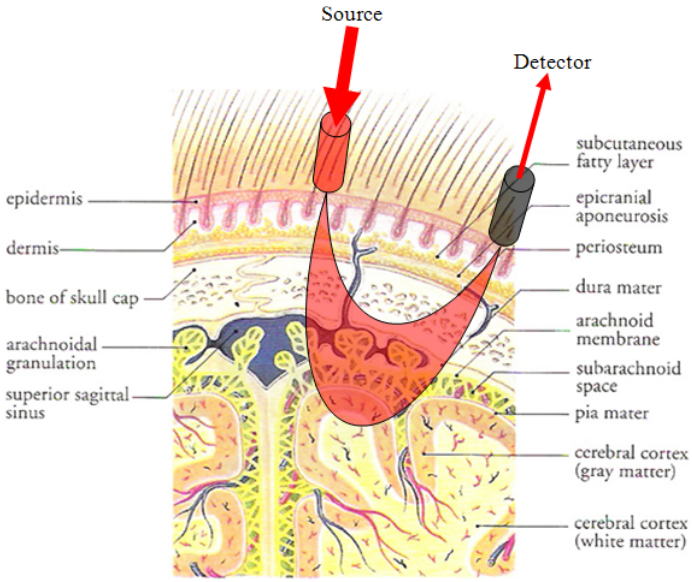

Figure 2.23: Conceptual arc-like NIR light propagation in the human head, penetrating to the cerebral cortex. Notice the many layers that the NIR light has to propagate through to reach the cerebral cortex. Many of these chromophores are assumed constant for the duration of a recording.

In other words, in general NIR light emerging <1.5cm from the source cannot penetrated deep enough to reach the brain (Okada, et al., 2003b; Okada, et al., 2003a) but only interrogates the superficial layers (meninges, skin, bone etc). It is principally the changes in NIR light absorption that provides the crucial information about the functional activity of that localised tissue (which accounts for 20% of light attenuation Elwell, 1995). With a functional event, such as movement of a limb, the brain tissue responsible for controlling that event becomes more metabolically active, and a neurovascular process ensues due to increased metabolism (as shown earlier in Figure 2.20). A focal/regional increase in cerebral blood volume (rCBV), cerebral blood flow (rCBF), and the cerebral metabolic rate of oxygen consumption ($rCMRO_2$) pseudo-superimpose (time evolutions differ) to give a distinct pattern of haemodynamics. This induces a distinct pattern in NIR light absorption which is wavelength-dependent for the two main haemoglobin molecule states: oxygenated (HbO_2) and deoxygenated (HbR) (described in Section 2.4.6). Thus, to resolve changes in HbO_2 and HbR the spectroscopist requires at least 2 wavelengths of light (to solve the simultaneous equations of the modified Beer-Lambert Law described earlier). Specifically, NIR light below the isosbestic point (800nm for HbR and HbO_2 absorption spectra) for HbO_2 and HbR is more sensitive to changes in HbR than HbO_2 (see Figure 2.24 in Section 2.5.3.3 to follow). Similarly NIR light above 800nm is more sensitive to HbO_2 concentration changes than HbR. Thus for example more absorption of the <800nm light source indicates a more distinct change of HbR concentration in the localised tissue. This process will be described in more detail in the following sections, such as the importance of selecting the correct wavelength pair.

2.5.3.2 Facilitating principles of NIRS/FNIRS, specifically for brain imaging

There are many recent apt reviews covering the state of the art of NIRS (Owen-Reece, et al., 1999; Soul, et al., 1999; Rolfe, 2000; Obrig, et al., 2003; Gibson, et al., 2005; Wolf, et al., 2007). Within these reviews common principles of NIRS/FNIRS can be found which *enable* the spectroscopist to analyse, specifically, brain tissue non-invasively and sufficiently for use in optical BCI applications:

1) **The optical window:** There exists an optical-window of biological tissue transparency within a subset (~650nm-900nm) of the NIR portion of the EM spectrum (see Figure 2.24). This is due to the relative transparency of water and haemoglobin within this spectral range. The shorter wavelength boundary (650nm) is set by the high absorbance of shorter wavelengths by tissue constituents, in particular haemoglobin (both HbO_2 and HbR). Above 900nm water, abundant in the body, is a dominant highly-absorbing tissue chromophore thus imputing the longer wavelength boundary of the NIR 'window';
2) **Penetration depth:** Near-infrared light can penetrate a total of 10 optical densities or up to ~8-9cm[7] of tissue (Cope, et al., 1988; Elwell, 1995) In contrast, visible light (400-700nm) can only penetrate biological tissue to a thickness of ~1cm due to strong absorption and scattering by tissue constituents in this wavelength range (Owen-Reece, et al., 1999);
3) **Varied wavelength-dependent absorption of HbO_2 and HbR**: The next significant contributor to NIRS' ability to monitor cerebral oxygenation is the fact that the magnitude of absorption of a particular NIR wavelength by a haemoglobin molecule is dependent on the oxygenation status of that Hb molecule. Thus the oxygenation of haemoglobin can be calculated (at the very least qualitatively) by using two wavelengths of light, one more sensitive to HbO_2 (above 800nm but < 900nm) and the other more unique to HbR (below 800nm but >650nm) (see Figure 2.24). Note: wavelength selection is dealt with in Section 2.5.3.3;
4) **Neurovascular coupling**: Tied into the previous facilitator of NIRS is the notion that a change in the oxygenation of haemoglobin is an indicator of neuronal metabolism, which is the result of a cerebral functional event such as engaging in the movement of an arm. This covariance of neuronal activity to vascular nourishment is known as neurovascular coupling and

[7] The actual distance is greater (~6 times) than this value due to multiple scattering events

provides a physiological basis for NIRS (described earlier in Section 2.4.6);

5) **The cerebral cortex is involved in and reflects functional activity by the brain:** By definition FNIRS should be able to detect functional changes in the brain. There would be little use in using FNIRS for monitoring oxygenation changes of the outer layer of the brain (the cerebral cortex) if the cortex didn't participate in functional activity. Of course in terms of monitoring oxygenation only with no regard for functional information NIRS still has a purpose, but in terms of FNIRS the experimentalist is fortunate perhaps that the cerebral cortex is in control of many high level functions of the brain, for example cognition and voluntary motor control. These cerebral areas are not alone in there elicitation of a particular function but regional areas can be monitored that are at least a significant part of that activity. See Figure 2.14 for an example of a cerebral map of the primary motor cortex for voluntary control;

6) **Chromophoric constancy and superficial tissue contributions:** There are various chromophores (any constituent that absorbs the wavelengths used) found in the human head which the photonic-stream has to contend with in order to reach the cerebral cortex and arrive back at the detector, e.g. water, lipids, cerebrospinal fluid (CSF), melanin (as can be seen in Figure 2.23). However, most of these can be considered constant chromophores for the duration of the experiment and so don't hamper functional activity since FNIRS is engaged in concentration *changes* of chromophores over time. These are considered in more detail in section 2.5.3.3;

7) **Photonic backscattering:** Due to the high scattering nature of the head reflectance mode measurements can be made. Once the source and detector are placed an appropriate distance apart (~ 3cm) and perpendicularly applied to the scalp, the assumption can be made that the photonic flux has engaged the cerebral structures (Franceschini, et al., 1998; Fantini, et al., 2001; Choi, et al., 2004) along the banana-shaped path (see Figure 2.23);

8) **Qualitative sufficiency for functional monitoring (continuous-wave FNIRS):** The ability of continuous-wave FNIRS (CWNIRS) to measure only concentration changes of HbO_2 and HbR rather than quantitative absolute values is sufficient for functional monitoring of cerebral effort. It is the focal change in oxygenation that is the marker of a focal change in cerebral metabolism making CWNIRS an appropriate NIRS technique for

functional brain imaging. The main NIRS techniques available to the researcher are described in Section 2.5.4;

9) **Safety**: The safety of any spectroscopic technique is paramount for human studies. The safety aspects of NIRS/FNIRS are discussed in Chapter 5 but briefly, NIRS is non-invasive and uses non-ionizing radiation, and is suitable for long-term use and is beginning to be used routinely on neonates (Wolfberg, et al., 2006). Thus, FNIRS can be seen as a suitable/safe technique for the functional activity monitoring aspect of an optical BCI as reported recently (Coyle, et al., 2004; Coyle, 2005; Coyle, et al., 2007; Soraghan, et al., 2008).

With an appreciation for the facilitating principles of FNIRS, the calculation of the functionally relevent chromophores is described next, along with an exposition of the various other constant absorbers in the tissue being interrogated.

2.5.3.3 Calculation of functional chromophores in tissue

This section is provided to elucidate how it can be claimed that the light intensity changes measured from a detector (as in Figure 2.23) are related to functional activity in the brain which is indicated by oxygenation changes. In other words, as shown in Figure 2.23, the NIR light travels through many layers of tissue, and yet it is claimed that cerebral oxygenation is monitored. This is possible because of the nature of the chromophores in the head. The main chromophores to consider are: water, lipids, melanin, haemoglobin (HbO_2 and HbR), and cytochrome-c-oxidase. Most of these can be considered constant absorbers, and while, yes, they do attenuate the light, their attenuation *changes* are negligible over the course of an experiment.

Water: As previously stated, water is abundant in the body, with low absorption in the NIR range of interest. Above 900nm, its absorption increases with wavelength. Water concentration is considered constant for the duration of a typical experimental procedure.

Melanin: This pigment found in the epidermis (for UV protection from the sun) and although its levels may increase in the presence of sun producing a tan, it is a constant absorber for the duration of a typical experiment.

Lipids: This chromophore has low scattering effects, and has extinction coefficients similar to water in the NIR range. It can comprise up to 40% of tissue, which is dependent on tissue type. It can be considered a static absorber for the duration of an experiment.

Haemoglobin: The haemoglobin species are a highly variable chromophore in tissue due to their prevalence in metabolic processes for all cells in the body. Even more fortunate in terms of functional activity measurement for BCI, is that the level of oxygenation in either oxy- or deoxy- haemoglobin form can be distinguished due to the distinct extinction spectra for each species - as shown in Figure 2.24 below.

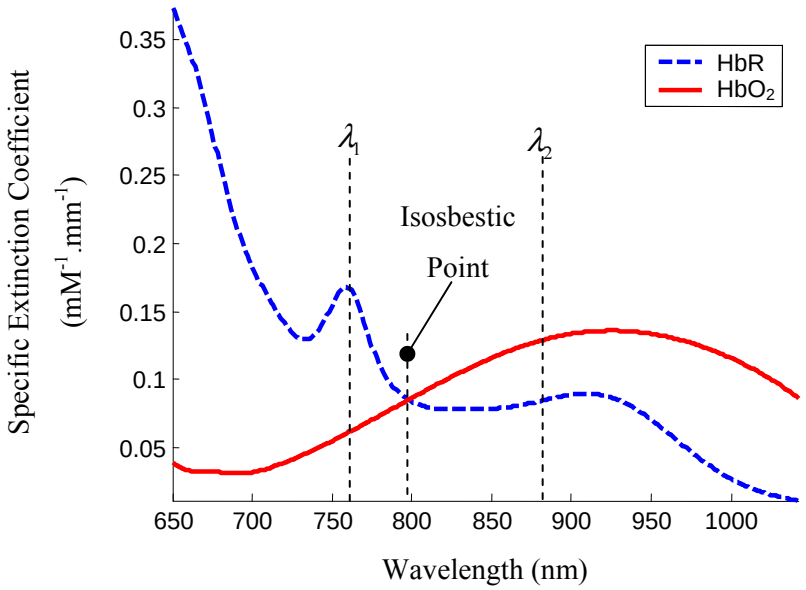

Figure 2.24: Extinction spectra for the haemoglobin species, oxy- and deoxy-haemoglobin (HbO_2 and HbR, respectively). Values taken from (Cope, 1991). The wavelengths used in this project are λ_1 at 760nm and λ_2 at 880nm.

As discussed in Section 2.5.3.1 in order to resolve dHbR and $dHbO_2$, at least two wavelengths in the NIR range are needed, one either side of the isosbestic point at ~800nm (the isosbestic point is where absorption from both HbR and HbO_2 are equal). The variation of these chromophores is also seen in systemic blood pressure oscillations not specific to a preformed task, which is dealt with more in Chapter 6. The wavelengths used for this project are at 760nm and 880nm[8]. Again, these light sources and their selection etc are dealt with in Chapter 5 which considers the design constraints and development of the versatile multichannel CWNIRS instrument.

Cytochrome-c-oxidase:

[8] The longer wavelength is continually referenced as 880nm, but deviation from the manufacturer specification place the true value at 868nm. The resulting differences are negligible (see Chapter 5).

Cytochrome-c-oxidase (Cyt-ox) is a terminal enzyme of the respiratory chain found in the mitochondrial membranes. It is mooted as being available as an intrinsic 'contrast agent' in the body which could indicate metabolic effort (on an intracellular-metabolic level) however controversy into whither a measured response may be a factor of crosstalk between chromophores is still under scrutiny (Uludag, et al., 2004). Unlike haemoglobin, the total amount of the enzyme doesn't change but rather change in redox state could be measured by NIRS. Thus, a difference spectrum of extinction coefficients is used (i.e., oxidised minus reduced Cyt-ox) to assess this difference with a peak in extinction coefficient (absorption) around 830nm. Moreover, it has a larger absorption spectrum than haemoglobin but concentrations in tissue are an order of magnitude less than haemoglobin - thus it is more difficult to measure.

Numerical Solution of the MBLL for 760nm and 880nm:

An analytical solution of the MBLL algorithm for calculating chromophore concentration changes was demonstrated in Equation (2.5). Haemoglobin concentration changes need to be calculated to determine functional activity. The method requires at least two wavelengths of light to solve for concentration changes in HbR and HbO_2, which in this dissertation are denoted dHbR and $dHbO_2$, respectively. Wavelengths 760nm and 880nm are used in this project (further characteristics are assessed in Chapter 5). Thus from Equation (2.5) two equations (simultaneous equations) are used to calculate dHbR and $dHbO_2$:

$$\Delta A(\lambda_i) = \left[\alpha_1(\lambda_i)\Delta c_1 + \alpha_2(\lambda_i)\Delta c_2 + \ldots + \alpha_n(\lambda_i)\Delta c_n\right] dB(\lambda_i),$$

$$\Delta A(\lambda_{760}) = \log_{10}\left(\frac{I_0(\lambda_{760})}{I(\lambda_{760})}\right) = \left[\alpha_{HbR}(\lambda_{760}).\Delta c_{HbR} + \alpha_{HbO_2}(\lambda_{760}).\Delta c_{HbO_2}\right] d.B(\lambda_{760}), \quad (2.6)$$

...and

$$\Delta A(\lambda_{880}) = \log_{10}\left(\frac{I_0(\lambda_{880})}{I(\lambda_{880})}\right) = \left[\alpha_{HbR}(\lambda_{880}).\Delta c_{HbR} + \alpha_{HbO_2}(\lambda_{880}).\Delta c_{HbO_2}\right] d.B(\lambda_{880}),$$

...where $\Delta A(\lambda_{760})$ and $\Delta A(\lambda_{880})$ are the measured *changes* in the detected light intensity (attenuation) from the 760nm light source and the 880nm light source, respectively. These are not measured directly but from Equation (2.4) recall that these changes are the logarithm (to the base 10) of the input light intensity divided by the output light intensity for the respective light source (wavelength) - i.e. I_0 and I respectively at either 760nm or 880nm. Both these light intensities are measured from the detector and are used in the logarithmic equation. Next, $\alpha_{HbR}(\lambda_{760})$ is the specific extinction coefficient for HbR at 760nm;

$\alpha_{HbO_2}(\lambda_{760})$ is the specific extinction coefficient for HbO_2 at 760nm; $\alpha_{HbR}(\lambda_{880})$ is the specific extinction coefficient for HbR at 880nm; and $\alpha_{HbO_2}(\lambda_{880})$ is the specific extinction coefficient for HbR at 760nm. These extinction coefficients are taken from (Cope, 1991) as illustrated in Figure 2.24. Furthermore, Δc_{HbO_2} (or $dHbO_2$) and Δc_{HbR} (or dHbR) are the changes in concentration of HbO_2 and HbR, respectively (which are being solved for). The term d is the geometric distance in units of [cm] between the source and detector. $B(\lambda_{760})$ and $B(\lambda_{880})$ are the normalised differential pathlength factors for the 760nm and 880nm wavelengths where these are normalised to a DPF at 780nm ($B(\lambda_{780})$) (Duncan, et al., 1996) where:

$$B(\lambda_{780}) = 5.13 + 0.07Ay^{0.81} \tag{2.7}$$

...where Ay is the age of the subject, since the DPF is age dependent (Cope, 1991). The extinction coefficients and normalisation factors are displayed in Table 2.1 below.

Wavelength [nm]	*HbR extinction coefficient [$mM^{-1}cm^{-1}$]*	*HbO_2 extinction coefficient [$mM^{-1}cm^{-1}$]*	*$B_{normalise}$*
760	1.6745	0.6096	1.12
880	0.8412	1.2846	0.84

Table 2.1: Wavelength dependent optical parameters for use in the MBLL algorithm. Values from measurements performed in (Cope, 1991).

This algorithm is used later in Chapters 6, and 7 to calculate haemodynamic responses (dHbR and $dHbO_2$) to functional tasks.

2.5.4 Measurement techniques

Until recently, multichannel instruments that have been developed operate on mostly continuous wave NIRS or CWNIRS techniques (Wolf, et al., 2007). However there are three main techniques which are based on the same principles of absorption and scattering of NIR light and these are outlined next.

2.5.4.1 Continuous Wave NIRS

CWNIRS is perhaps the least demanding method in terms of hardware, optics, and speed of data processing, and it has the greatest potential for miniaturisation, even to a wireless system (Muehlemann, et al., 2008). Only changes in light intensity (attenuation) are measured with this technique, whereby the light sources are turned on continuously, or

modulated at low frequencies - a few kHz. At present they are the most common NIRS imager (Wolf, et al., 2007) due perhaps to the flexibility of the modality, although the technique can only resolve qualitative information on the changes in concentration of the various chromophores, e.g. oxyhaemoglobin. Quantitative measures are impossible with this technique due to the highly scattering (mostly elastic) nature of biological tissue whereby the pathlength of the light is extended to typically six times the distance between the source and detector. This term, the differential pathlength factor (DPF) cannot be measured directly in CWNIRS and so tabulated values (Cope, 1991; Duncan, et al., 1995) are used for typical tissue models, e.g. the adult head, and different wavelengths (i.e. the DPF is tissue- and wavelength dependent). Nevertheless, CWNIRS is suitable for functional studies where concentration changes in chromophores are sufficient for determining functional activity (Strangman, et al., 2002; Wolf, et al., 2007). For quantitative measurements where absolute levels are required such as in neonatal cerebral oxygenation monitoring, two principle methods can be used - time resolved- and phase resolved spectroscopy (Rolfe, 2000).

2.5.4.2 Time-Resolved (time-domain) Spectroscopy

In order to determine the mean optical pathlength ($\overline{L_O}$) of light travelling through tissue, time-resolved spectroscopy (TRS) delivers a short pulse of light (~2ps-5ps) which can then be detected with a suitably fast detector. The tissue scattering these photons cause the delta pulse to broaden, such that a histogram of arrival times of photons is developed. The time it takes for photons to traverse the tissue is called the time-of-flight (TOF), and is the time difference between the incident light pulse peak-intensity and the peak of the transmitted light temporal point spread function as depicted in Figure 2.25. The $\overline{L_O}$ can then be calculated based on this TOF (Rolfe, 2000), and is written as :

$$\overline{L_O} = \frac{c_v}{n_t}\bar{t} \tag{2.8}$$

...where c_v is the velocity of light in vacuo, n_t is the tissue's refractive index, and $\bar{t}$ is the mean arrival time of the photons (time where the maximum light intensity occurs relative to the incident pulse). Thus the attenuation measurement incorporating scatter and absorption is now:

$$
\begin{aligned}
A = \ln(\frac{I_o}{I}) &= \mu_a dB + \mu_s dB \\
&= (\mu_a + \mu_s) dB \\
&= (\mu_a + \mu_s) \overline{L_O} \\
&= (\mu_a + \mu_s) \frac{c_v}{n_t} \bar{t}
\end{aligned}
\tag{2.9}
$$

... where μ_a and μ_s are the absorption and scattering coefficients of the tissue, respectively, d is the distance between the source and detector, and *B* is the DPF.

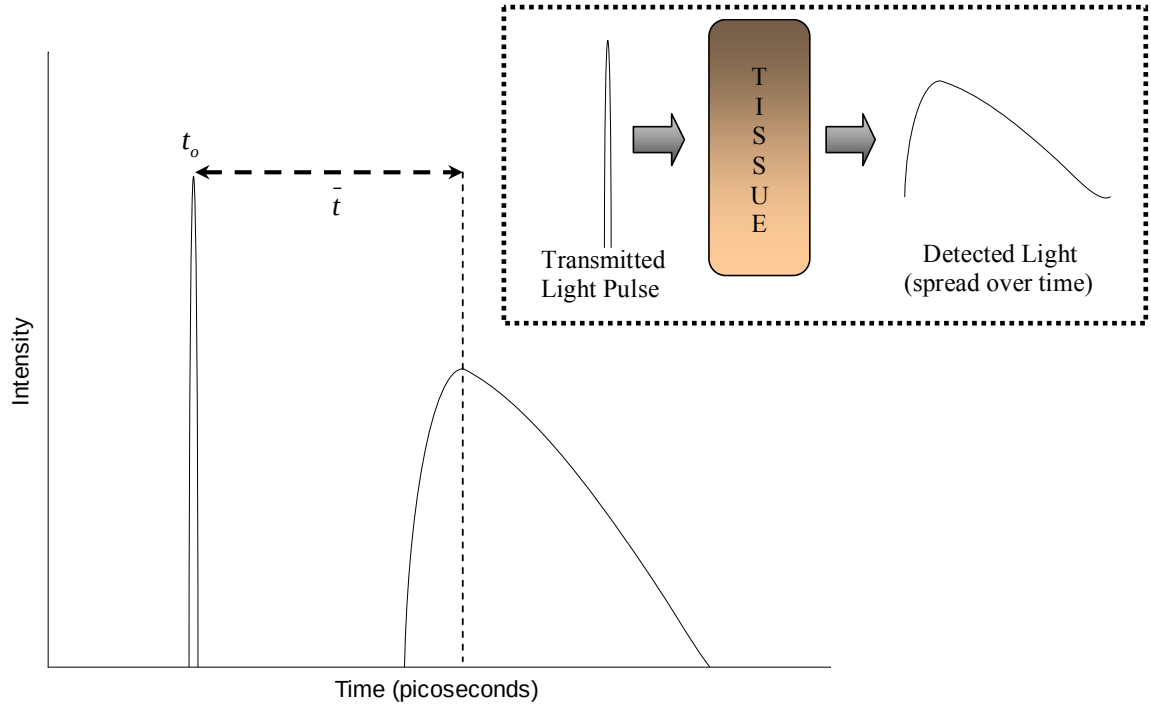

Figure 2.25: Graph depicting relative temporal broadening of incident pulse of light due to scatter in a time-resolved spectroscopy. The inset illustrates that the medium (tissue) produces the temporal point spread function.

2.5.4.3 Phase-Resolved (frequency domain) Spectroscopy

Instead of measuring time of flight directly, a frequency based temporal calculation of the propagation delay of photons due to scatter is possible by assessing the phase shift of a light source whose intensity is modulated in the range of hundreds of MHz (Chance, et al., 1998). The absorption due to the tissue can also be measured by an assessment of the AC and DC attenuation of the detected light intensities (at the intensity modulation frequency) as shown in Figure 2.26. The average time of flight of the photons is thus related to the phase shift, and the differential pathlength can be written as:

$$B = \frac{\phi c}{2\pi f} \tag{2.10}$$

...where ϕ is the measured phase shift, c is the speed of light within the medium, and f is the intensity modulation frequency of the light source. The various instrumentation and calculations used for this technique are reviewed in (Chance, et al., 1998).

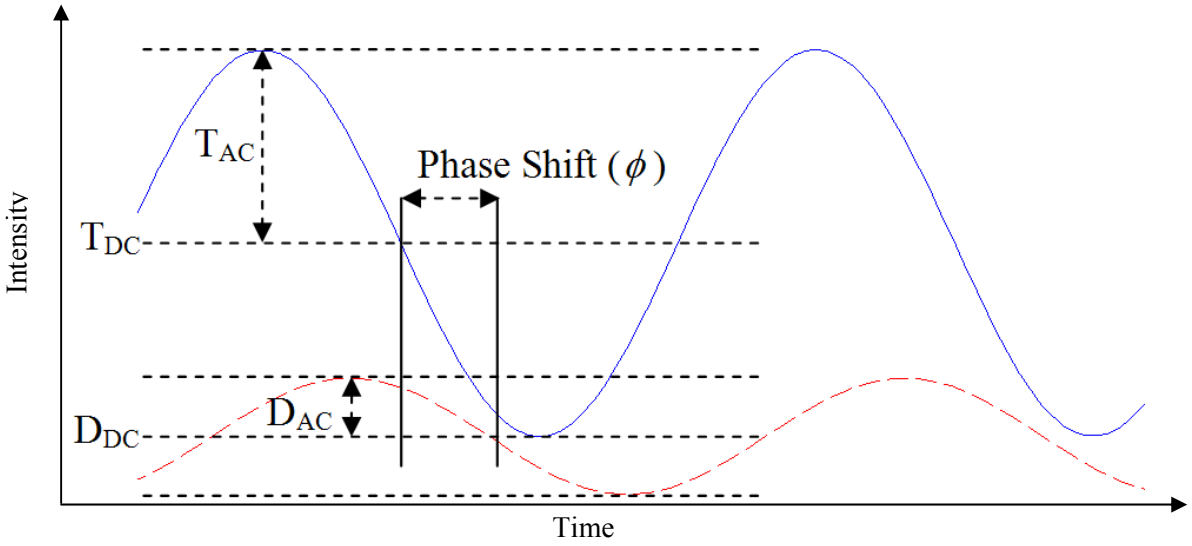

Figure 2.26: Phase shift and AC and DC measurements for phase resolved spectroscopy. The blue solid trace is the transmitted intensity with AC and DC values (T_{AC} and T_{DC}); The red broken trace is the detected light intensity with associated AD and DC parameters (D_{AC} and D_{DC}).

Having completed the section on FNIRS principles and techniques, the next (final) section reports on some of the human pathological conditions relevent to BCI such as locked-in syndrome.

2.6 Selected Human Pathology

The research carried out as described in this dissertation was aimed principally at developing a multichannel CWNIRS instrument for applications in BCI. In particular a new application of optical BCI was conceptualised by the group recently in stroke rehabilitation (Ward, et al., 2007) which is considered in Chapter 7. However, one of the main areas of BCI is as a communication aid for the severely disabled for those individuals who for a number of reasons are not able to interact with their environment at all or at least in a very limited way. A review of BCI is reported in Chapter 3, most of which concern such communication aids Thus, it was felt fitting that the main debilitating disorders that these people face should be described. The principal pathological condition of "locked-in

syndrome", along with the various contributing diseases that can cause it are mentioned, in particular, amyotrophic lateral sclerosis (ALS).

2.6.1 Locked-In syndrome

Locked-In syndrome (LIS) refers to a state of paralysis of voluntary muscular control as a result of a disease causing de-efferentation of the motor system. The term 'locked-in syndrome' was first coined by Plum and Posner in 1966 which refered to a neurological condition of infarction of the ventral pons (pons in the brainstem that is). However, in a review in 1986 of 139 cases of ALS (Patterson, et al., 1986), many more etiological origins were reported, labelled as either vascular or non-vascular. Vascular origins included pontine hemorrhage, embolic phenomenon, and infarction of the midbrain. Non-vascular etiology included those caused by tumor, trauma, heroin abuse, and multiple sclerosis, to name a few. In the study, the non-vascular group were reported as having a more rapid functional recovery in its survivors compared to the vascular etiology group (Patterson, et al., 1986). Although there are various other names by which it is known such as pseudocoma, three principle varieties were identified in 1979 (Bauer, et al., 1979): Classical-, Incomplete-, and Total- locked-in syndrome.

The three catagories are identified according to the level of functional impairment the subject sustained. The *classical* version resembles those signs (reported by physician) and symptoms (reported by patient) as outlined in the foremost publication by Plum and Posner (Posner, et al., 1966), with manifestations of quadriplegia, lower cranial nerve paralysis, and mutism. However, the subject preserves vertical eye gaze and upper eyelid voluntary control. *Incomplete* locked-in syndrome includes the same manifestations and voluntary controls as the classical version except that the subject has additional remnants of volitional control apart from those of eyelid and vertical eye movement. Finally, the *totally* locked-in state (TLS) is a version where the patient is completely immobile, with no voluntary motor ability whatsoever.

The main subgroup that BCIs have a unique duty to establish a working communication strategy for is the TLS variety. This is because other varieties with some form of voluntary control can avail of other ultimately better techniques of control using whatever residual voluntary control they have, be it eyeblinking, eye tracking, etc. However, it has also been suggested (Naito, et al., 2007) that to increase the chances for successful communication in the TLS state, the patient in question should be 'trained' in the use of the device whilst still in the classical or incomplete state. This is because since the expectancy is that the disease will progress to the TLS variety. In the event of the patient only beginning to use the device in the TLS state, the outlook is grim (Birbaumer, 2006).

The life expectancy after diagnosis of the syndrome ranges from months to less than 15 years in the case of the aforementioned study (Patterson, et al., 1986). One neurological disorder called amyotrophic lateral sclerosis (ALS) can lead to the locked-in state and is highly reported in BCI literature. ALS is the most common neurodegenerative disease, involving progressive degeneration of motor neurons which can lead to complete paralysis of the patient, i.e. the TLS version of LIS.

2.6.1.1 Amyotrophic lateral sclerosis (ALS)

Amyotrophic lateral sclerosis (ALS) also known as Lou Gehrig's disease was first described in 1869 by Jean-Martin Charcot, a french neurologist. It is called Lou Gehrig's disease after the famous American baseball player Lou Gehrig, who retired after contracting ALS in 1939 (ALS_Association, 2008).

The term amyotrophic lateral sclerosis can be split into different segments to clarify its definition. 'A' refers to negative or no, 'Myo' refers to muscles, and 'trophic' refers to nourishment. Thus - a lack of nourishment to the muscles leading to muscular atrophy or muscles wasting away. 'Lateral' refers to the fact that ALS affects lateral areas of nerve cells in the spinal cord that signal and control the muscles. Finally, 'sclerosis' refers to the hardening of the affected areas, not unlike scarring of the skin. ALS specifically is a neurodegenerative disease which affects mostly upper (in the CNS) and lower (in the spinal cord and to the PNS) motor neurons, leaving afferent or sensory motor areas unaffected. Although the heart and digestive system are under involuntary control, and are thus not directly affected by ALS, the lung's muscular control is under threat since their associated musculature can be voluntarily controlled. Thus, a high cause of death is from pulmonary complications, mainly pneumonia, as was also demonstrated in the previously mentioned review for general LIS patients (Patterson, et al., 1986). A further high incident cause of death for those LIS patients was the extension of the brainstem lesion. In any case the ALS disease is quite variable with a spectrum of progression rates and survival times for ALS sufferers. Typically, death by respiratory failure is said to occur 2-5 years after disease onset (Schmidt, et al., 2009). Early symptoms of ALS include increasing muscle weakness especially of the arms, legs, speech related musculature, and those of breathing and swallowing.

2.6.1.1.1 Forms of ALS

In the USA, 5,600 are diagnosed with ALS each year (15 per day), with 30,000 people estimated to have the disease at any given time there (ALS_Association, 2008). It mostly affects 40-70 year olds being 20% more common in men. Apart from classification within the realm of LIS, ALS can be divided into three chief subgroups:

- Sporadic ALS (SALS);
- Familial; (FALS);
- And, Guamanian ALS.

Most (90-95% in the USA) of all ALS cases are of the sporadic ALS (SALS) type, meaning that it can affect anyone, anywhere, with no direct familial link. Familial ALS (FALS) occurs in 5-10% of ALS cases with an inherited predisposition to the disease. One known susceptible gene responsible is the SOD1 gene on chromosome 21, although this only accounts for 20% of the total FALS patients. The other 80% of FALS cases are caused by unknown familial linkage and so testing for FALS is not as significant an indicator as a thorough family history. Guamanian ALS occurs in Guam and the Trust Territories of the Pacific where a high occurence of ALS was found there in the 1950's (ALS_Association, 2008). ALS is not contagious and doesn't fall into any racial, socioeconomic, or ethnic boundaries. In 1995 the FDA approved the use of a drug Riluzole which is aimed at prolonging a patient's life by slowing the progression of the disease. Other efforts have been sought to aid or reduce the risk of ALS such as stem cell therapy (Lunn, et al., 2009) and intake of vitamin E with polyunsaturated fatty acids (Veldink, et al., 2007).

2.6.1.1.2 Cognitive ability in the ALS patient

A recent question being considered is whether the patient with TLS-ALS has any/enough cognitive control to take part in a communication system employing cognitive tasks in order to control an augmentative device (Hinterberger, et al., 2005, Fuchino, et al., 2008). As reported in (Kiernan, 2009) it was thought in the past that cognitive areas were completely unaffected by ALS. Kiernan then continues to cite research demonstrating that ALS sufferers can develop overt dementia syndrome, but others only manifest less severe cognitive defects. Nevertheless, some BCI studies have been performed on TLS-ALS subjects (Naito, et al., 2007**)** although the outlook for controlling a BCI for a TLS-ALS subject with no prior BCI training before entering that final state is, for the moment, very poor (Birbaumer, 2006)**.**

2.7 Chapter Summary

NIRS for BCI applications brings together many fields of science and thus a variety of scientific background for the project was described. The main contributors to the recorded NIRS signal of interest are scattering and absorption of the incident light by highly inhomogeneous cranial tissue. The presence of a 2mm cerebrospinal fluid layer (a low absorption, non-scattering fluid layer with low-scattering arachnoid trabeculae) sandwiched

between the pia mater and the arachnoid membrane have been shown to facilitate NIR light penetration into the cerebral cortex (Okada, et al., 2003a). Thus a description of brain anatomy and physiology was considered along with an analysis of blood composition and blood pressure dynamics (homeostasis). Haemoglobin (and its oxygenation) is the main chromophore of interest in this work for assessing functional activity in the brain and so its application to oxygen transport was reported. Furthermore, cerebral blood flow and metabolism are markedly different from systemic perfusion dynamics and so the cerebral vascular network was outlined as well as a report on neurovascular coupling. A description of NIRS and its application to functional activity monitoring via the modified Beer Lambert Law was considered along with NIRS principles and measurement techniques. Finally, a look at some of the most highly reported subject population for BCI (ALS and LIS subjects) were reviewed briefly. In the proceeding chapter a review of BCI using non-optically based techniques is reported to assess the current state of the art of this expanding field of research.

CHAPTER 3

BRAIN-COMPUTER INTERFACING: REVIEW OF THE CURRENT STATE OF THE ART

3.1 Chapter preamble

The purpose of this chapter is to bring together the recent advances in brain-computer interfacing (BCI). This discussion establishes the notion of what a BCI is including its various elements in order to demonstrate the variety of modalities and outline current limitations in the field. It establishes a framework, which optical BCIs also need to adhere to, i.e. Figure 3.1, and the potential applications that it may be suitable for. The first implementation of an OBCI was reported in 2004 (Coyle, et al., 2004) and so this particular BCI modality is still very much in its infancy, but the principle optical technique (NIRS) used in all current OBCIs has been around since 1977 (Jobsis, 1977). Nevertheless, the current NIRS technology is constantly developing and so it is not simply a matter of applying NIRS to the realm of BCIs as a blind imaging tool. For example, the analysis of single-trial FNIRS measurements is rarely found in literature since most applications of FNIRS can afford offline analysis and post-processing generally including averaging of multiple trials to increase the signal-to-noise. The perpetual development of NIRS is similar to the development electrophysiological based recordings, whereby the application of those measurement techniques has been one of the principle driving forces of its technological advancement - for example BCI applications (see Allison, et al., 2007). In other words, the

persistent need to 'listen-in on'[1] and exploit the brain's functional and adaptable neural network drives the progression of the measurement technique and also its clinical applications, e.g. pathology and psychology. The sections to follow discuss the various methods, principles, successes, and limitations of current BCIs. However, Chapter 4 includes the discussion of OBCI, whereas a general BCI review is considered here. An overview of the current state of the art of all BCI technologies (except optical BCIs) needs to be reported to establish current BCI trends, its development, and what current issues are being reported by the BCI community. This provides impetus to the justification in the succeeding chapter which will ultimately establish (in addition to chapter 1) the reasoning and potential benefits of developing a flexible real-time multichannel CWNIRS instrument capable of measuring user-induced activity from multiple cortical regions for BCI-type applications, e.g. motor areas and cognitive regions.

3.2 Introduction - a general BCI Review

The major fundamental questions that should be answered in a review of BCI include the following:

1) What is a BCI and how has it emerged from its earliest implementation, chronologically?
2) What would a generic BCI look like and what do the individual constituents of the generic model represent?
3) What physiological signals are available that reflects functional intention in the human brain?
4) How are these brain signals recorded, processed, analysed, characterised and used?
5) Who are the potential users of the resulting BCI devices?
6) What learning or training is involved?
7) What are the applications?
8) What does the future hold for BCI development, and are there any serious limitations, gotchas, or insurmountable issues?

[1] This analogy is not really accurate to BCI, although it will suffice for conceptual purposes. In reality for most BCIs (especially electrophysiological types) a BCI is a 'new' output channel for the brain - a new skill that the brain must master like learning the piano, rather than utilisation of current rigid neural networks. Brain plasticity will determine a new neural substrate for this new 'function' and thus produce perhaps unexpected signal features (spatially, etc).

9) Has the advancement plateaued and have there been significant implementations of the BCI to improve human capabilities?
10) What groups are involved in BCI worldwide and how do the BCI implementations they have developed and used compare?

These items will be addressed in the review to follow, starting from the first question of "What is a BCI and where are its origins?"

3.3 Origins of BCI

A BCI is a device (usually electronic) which provides its user with an alternative means of communicating with their external environment independent of voluntary muscular control. It is typically necessitated by a severe motor disability which has rendered its user unable to utilise the normal output pathways of his\her brain and spinal cord (peripheral nerves and muscles). The field of study of BCI is known by many other terms such as Brain-Machine Interfacing (BMI), Brain Interfacing (BI), Direct Brain Interfacing (DBI) and Adaptive Brain Interfacing (ABI), cognitive neural prosthesis, a neural interfacing system, and brain actuated control. These terms are considered essentially equivalent in regard to the technologies used in their high-level design (Mason, et al., 2007). All incorporate a communication and control system that uses bio-signals originating from the CNS, which do not depend on peripheral input (Wolpaw, et al., 2000a; Allison, et al., 2007).

The first account of a BCI project emerged in 1971 (Vidal, 1973) asking the question as to whether sustained electrical fluctuations recorded at the scalp could be used in "man-computer" communications or to control prosthetics? Could the computer be used as a prosthetic extension of the brain? These bio-potentials or electroencephalograph (EEG) recordings were pioneered by Hans Berger 80 years ago (Berger, 1929) but are still the dominant (83%) neurological phenomena utilised by the BCI community (Mason, et al., 2007). Since Vidal's initial exploration further interest saw other early publications (Farwell, et al., 1988; Wolpaw, et al., 1990; Sutter, 1992) utilising similar electrophysiological correlates of neural activity (e.g. P300 potentials and visual evoked potentials - described later). Since then there has been a surge of research into BCI development (different approaches will be discussed later in this section) and this rapid increase in BCI research has been reported (Daly, et al., 2008) as been due to:

- Knowledge that activity-dependent plasticity occurs in the CNS (physical adaptability of neural tissue) throughout a lifetime and so a measure of it can be

used to determine the functional implications of, for example disease and trauma;

- Increased understanding of the particulars facets of physiological signals (e.g. physiological origin of different frequency bands) in particular those from the CNS, as well as how these might be used and exploited in a BCI. This was gathered from decades of research into animal and human studies;
- Advances in hardware and software for recording and analysing CNS activity in real-time, as well as the reduced cost of these tools;
- Less naïve knowledge of the needs, ability, and potential of people with seriously impaired functional expression, such as those with neuromuscular diseases.

In order to obtain a more gestalt-like\holistic BCI research community, and to monitor progression of BCI research, three international BCI meetings have taken place over the last decade. These reported that only 6 BCI groups were known of in 1995, but by the first international BCI meeting in 1999, 22 groups met to review the state of the art in BCI. Its purpose was to define the aims of basic and applied BCI research, to identify key technical issues, and finally to consider standardisation of assessment and research procedures (Wolpaw, et al., 2000a). The 2nd international meeting of June 2002 in New York saw 38 groups (98 researchers) from China, Europe, USA, and Canada with the main aim of summing up advances in the field and to host discussion of major issues with 6 panels debating key themes of BCI research up to 2002 (Vaughan, et al., 2003). In the most recent BCI meeting 53 groups participated, again focusing on the most recent advances in BCI technology covering the full spectrum of disciplines involved (Vaughan, et al., 2006b). However, it could be inferred from these meetings that only a subset of international BCI groups attended and there are possibly many more in operation. Nevertheless in a recent review of the literature (including both conference and journal publications) Mason et al identified 54 groups engaged in BCI research worldwide - at least those published up to January 2006 (Mason, et al., 2007)[2] although Wolpaw reflects that over 100 groups are involved (Wolpaw, 2007) globally.

As part of the discussion at the international meetings the major components of a BCI were outlined, in particular during the 1st international BCI meeting, establishing a generic BCI with components like that of any control system: the input, the translation algorithms,

[2] An adapted list of these groups from that particular review by Mason et al can be found in Appendix A of this dissertation.

and the output. A generic model of a BCI is described next. This model also applies to the optical BCI developed and used in the experimental work, which will be described in the chapters to follow.

3.4 Overview of a generic BCI

The chief components of a generic BCI are shown in Figure 3.1 below.

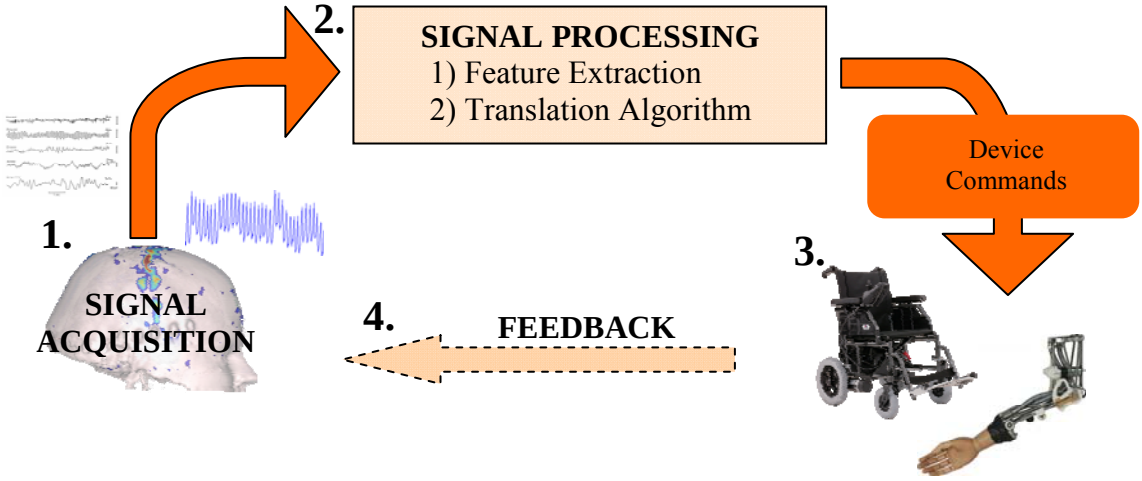

Figure 3.1: Generic BCI model. The principle components of a BCI are realised in four stages: 1) the *input* - which are the physiological signals acquired (including the methodology used); 2) the *processing* of the input signals to reveal time/frequency domain components which are decoded and translated into device commands; 3) the commands (*output*) are used to arrogate augmentative devices such as a cursor on a computer screen or a neuroprosthetic arm; and 4) *feedback* to reinforce learning and adaptation which may induce activity-dependent brain plasticity processes vital for certain applications such as those used in stroke rehabilitation.

The following is a brief overview of the generic model: data flow begins at the user (1), where his/her brain activity is recorded and used as the *input* to the model, which is then *processed* (2) to produce *output* (3) commands to control an external device such as a wheelchair or a cursor on a computer screen. *Feedback* or *biofeedback* (4) of this progress, whether discrete or continuous, is used to complete the BCI loop and is a vital element of any BCI that requires user training\learning.

In more detail then, the inputs to the BCI are the physiological signals acquired from the head and should reflect spatiotemporal brain activity. Traditionally, exclusively electrical correlates of brain activity such as EEG were used as the input (up until ~7 years ago) although now the signals recorded need not be electrical in origin but are only required to be manifestations of brain activity such as magnetic or vascular correlates of neurological

symphony. These signals may be evoked (by external externally stimuli) by the BCI or be spontaneous - requiring no external stimulus. The signals are then possibly amplified, and then digitised. The digitised signals are then processed to extract relevant features and remove physiological noise where the features are used to decode the user's intent. The translation algorithm generates output commands from these features (time or frequency domain) to control the external device. The final stage of the BCI is the feedback stage which is very important for enhancing the potency and efficacy of the device, as well as the aforementioned possible plasticity inducing effects.

Each of these four stages is outlined over the next few sections (from section 3.5 to section 3.12).

- Stage 1 - The input. The physiological signals used as the input to the BCI are outlined in section 3.5 and the various BCI types which are categorised by the measurement modality (e.g. EEG) are described from section 3.6 to section 3.8 covering BCIs based on EEG, MEG, and fMRI;
- Stage 2 - Signal Processing. The feature extraction and translational algorithm signal processing element s are reviewed in section 3.10;
- Stage 3 - The output. Applications of BCI derived from the output commands to control some device are described in section 3.11;
- Stage 4 - Biofeedback and training. The learning and feedback stage are explored in section 3.12.

For ease of navigation of these stages in the pages to follow, the beginning of each of these four sections is marked with a reduced-size image of the generic BCI system shown in Figure 3.1 with the particular stage highlighted in white, with the rest of the image blurred. The remaining sections of this chapter concern remaining questions in the BCI review, such as the potential users and future prospects of BCI research.

3.5 Physiological brain signals for BCI and transducing techniques

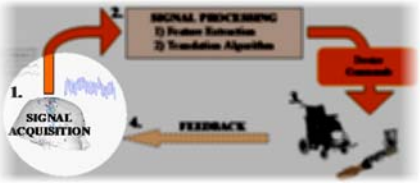

The signals used in a BCI can be electrical, mechanical, magnetic, or metabolic. Mechanical and non-cerebral events are considered outside of the realm of BCI and fall into the category of assistive technologies, or more conventional interfaces. In some cases a hybrid device is utilised supplementing the user's remaining voluntary muscular control with cerebral signals used in

a BCI. Below is a mind map of the main physiological signals used in BCIs along with a listing of the non-cerebral methods that aren't true BCI methods and so aren't discussed.

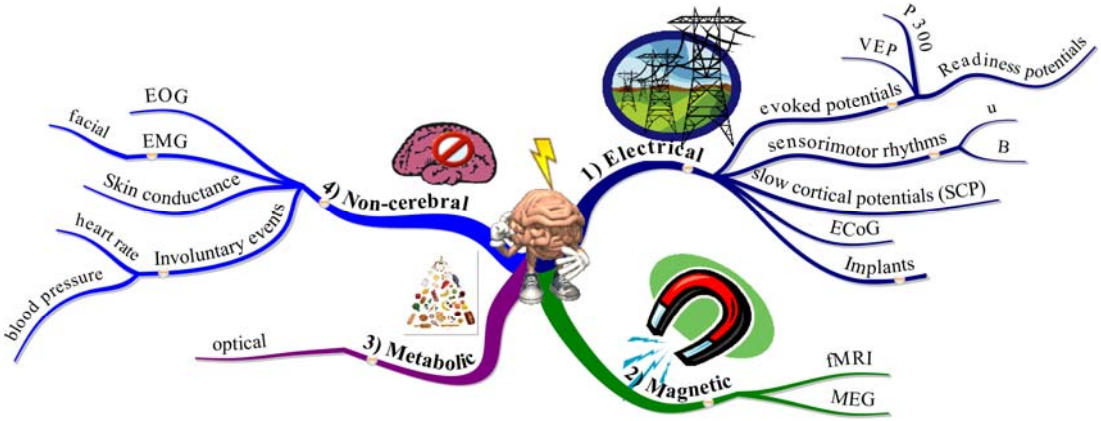

Figure 3.2: Mind map of the physiological signal types used for use in brain-computer interfaces. (Note: involuntary events cannot be directly controlled to operate a BCI). *Acronyms:* magnetoencephalography (MEG), functional magnetic resonance imaging (fMRI), visually evoked potential (VEP), electrocorticography (ECoG), electrooculography (EOG), electromyography (EMG) (designed using iMindMap® software).

The measurement of these signals is performed with various sensors, depending on the modality used. The different sensor locations are illustrated in Figure 3.3 also depicting the invasive (implants), intermediately invasive (ECoG - subdural and epidural), and non-invasive (EEG, NIRS, MEG, fMRI) aspects of the various modes. Invasive BCIs use sensors that are placed inside of the body boundary (brain, dura layer), whereas non-invasive BCIs use sensors located outside of the body (e.g. scalp EEG). They are described in more detail in the sections to follow but are listed next. The various brain signals currently used in BCIs can be categorised as either invasive or non-invasive (see Mason, et al., 2007 for a comprehensive review of bio-signals used by the BCI community):

- **INVASIVE**
  - Implanted microelectrodes\arrays - recording signals from action potentials (neural spike trains) from nerve cells or nerve fibres;
  - Extracellular microelectrodes - recording synaptic and extracellular field potentials;
  - ECoG - using subdural or epidural electrodes.
- **NON-INVASIVE**
  - Scalp EEG oscillations
    - sensorimotor rhythms (mu and beta rhythms) - oscillations or SMRs;
  - Slow Cortical Potentials (SCPs) - DC shifts from self-regulation;

- Evoked potentials (P300, VEP, SSVEP (steady-state VEP), AEP) - time- and phase-locked events;
- Metabolic changes in oxygenation:
  - Oxy- and deoxy- haemoglobin - NIRS;
  - Deoxy-haemoglobin correlate (magnetically susceptible) - fMRI;
- MEG - magnetic correlates of electric fields generated from functional activity.

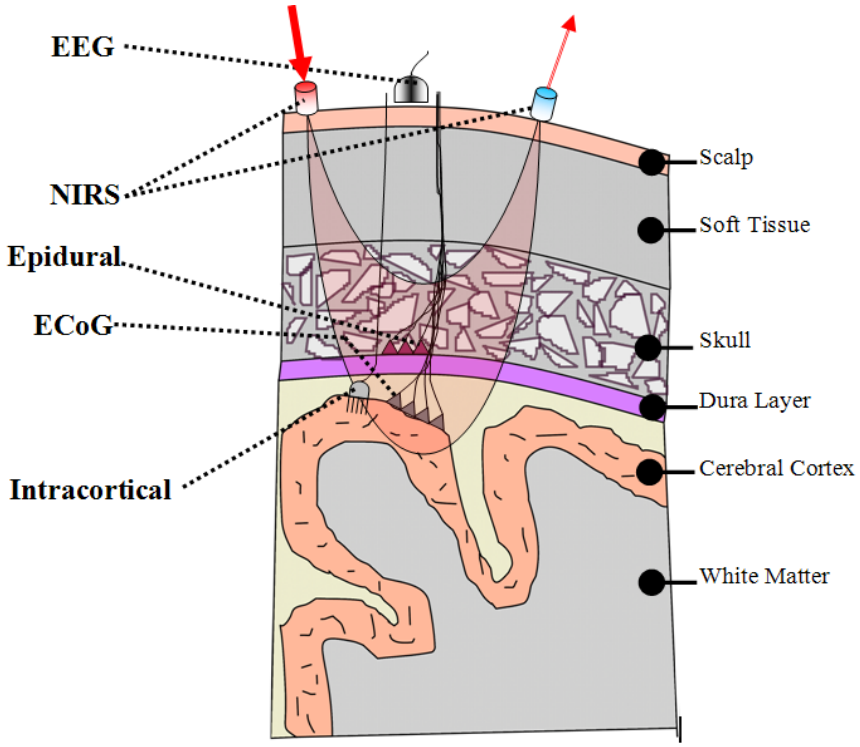

Figure 3.3: Sensors used in BCIs to extract the spatiotemporal information correlated to functional activity. The illustration demonstrates the relative placement of sensors from non-invasive (e.g. NIRS) to highly invasive intracortical electrode arrays. NIRS sensors penetrate the cortex with NIR light (red hue). Scalp EEG electrodes (SCP, mu/beta rhythms, evoked potentials) record mostly postsynaptic potentials. Subdural and epidural electrodes (ECoG) can record rhythms or local field potentials. Intracortical electrodes record signals from groups of neuronal action potentials/spikes or single neurons. MEG and fMRI sensors (not shown) are outside of the body and magnetic field changes are recorded in large controlled environments.

A further categorisation of BCIs is to group them according to whether they are exogenous (where the arousing stimulus arises from outside the body - flashing icons, sounds, etc) or endogenous (stimulus arises from inside the body - self-regulated EEG, modulation of existing neurological oscillations or metabolic markers). For various reasons, such as to avoid subject irritation, internal neurological stimuli are the dominant type in the BCI community (~83% up to January 2006) (Mason, et al., 2007). BCI types are explored next, according to the features measured, so as to investigate current performance and specialities of the various methods, i.e. while a P300-BCI may have one of the highest

information transfer rates it may not be suitable for some individuals who may prefer an endogenous SCP-driven BCI. This will indirectly elucidate clues as to whether the extracted neurological features from a multi-channel optical BCI could augment other techniques or perhaps establish a BCI realm of its own, e.g. as a short training length, endogenous BCI with high spatial specificity - owing to the measurable metabolic activity of focal cortical tissue.

3.6 EEG-based BCI

An EEG recording is the sum of postsynaptic potentials from the cortical tissue examined with oscillations in the range 4Hz-200Hz, and also includes transient event-related potentials (ERPs). EEG-based BCIs were the only considered BCI modality until recently with only tenuous mention of alternatives up to the first international BCI meeting (Wolpaw, et al., 2000a). Initially EEG was considered for clinical diagnosis and examining brain function but research for using EEG in BCIs in humans began in 1971 (Vidal, 1973). EEG-based BCIs still captivate 83% of all BCI groups internationally (Mason, et al., 2007) possibly due to its relatively low cost, portability, and non-invasive properties. Two principal forms of EEG activity occur - those that occur due to some external sensory stimulation (exogenous), and those from self-regulation and operant conditioning (by virtue of presenting reinforcement contingent upon the occurrence of the operant response). The former applies to ERPs (time-locked and phase-locked, i.e. evoked) whereas the latter corresponds to event related synchronisations (ERS) and event related desynchronisations (ERD) of cortical rhythms (time-locked but not phase-locked, i.e. induced). BCIs based on these EEG rhythms are discussed next, followed by those based on ERPs, SCPs, intracortical electrophysiology, and finally ECoG-based BCIs.

3.6.1 Sensorimotor rhythms (SMR) BCIs

These features are measured over the sensorimotor cortices with different frequency bands of EEG oscillations: μ rhythms (8-12Hz) and β rhythms (18-26Hz). If a person engages in movement, motor imagery, or even sensation it tends to affect the amplitude of these oscillations (attenuation - ERD; enhancement - ERS) (Pfurtscheller, et al., 1997). Users can learn to control these amplitudes for use in a BCI to control some external device. They have been used for basic word processing, and 1-D, 2-D (Wolpaw, et al., 2004) , and 3-D cursor control (McFarland, et al., 2008).

Pfurtscheller's group were the first to employ a BCI for subjects suffering from high spinal cord lesion controlling delivery of electrical stimulation to arm muscles using SMR

increase and decrease (Pfurtscheller, et al., 2005). The subject was able to grasp a glass and raise it to his mouth with successive activation of electrical stimulation of muscles in his had and arm. An example of mu rhythm activity dominating the right sensorimotor cortex is shown in Figure 3.4 part (B) below.

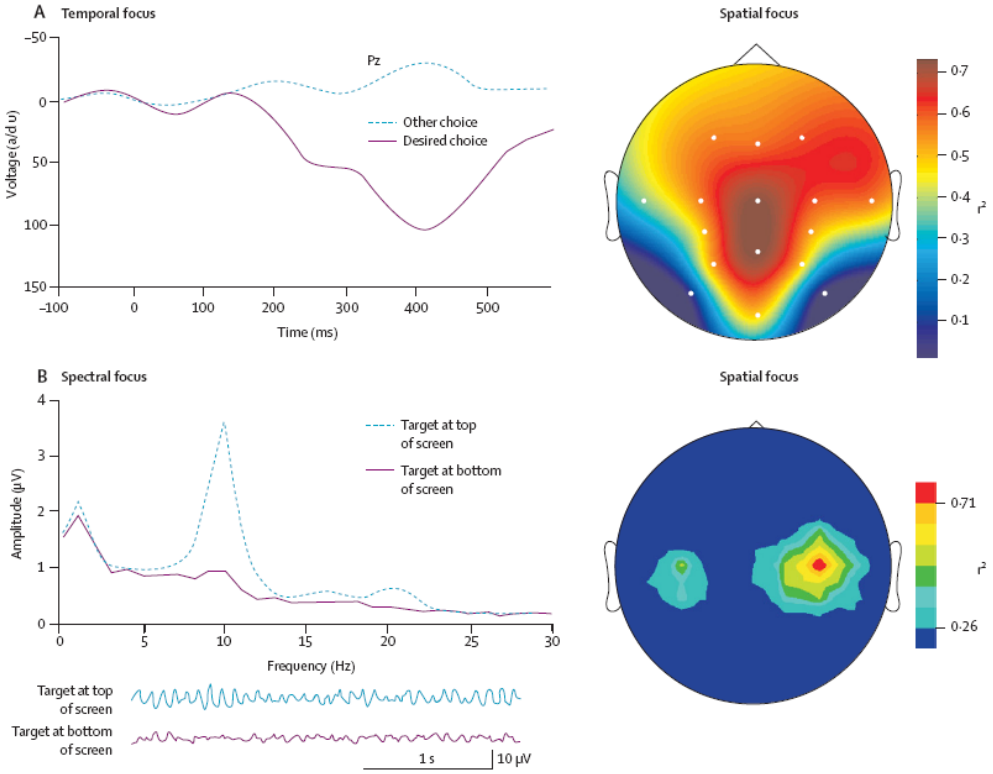

Figure 3.4: A) P300 potential demonstrating a large peak at the centro-parietal cortical region for the desired choice versus some other choice, which were displayed in succession. B) Sensorimotor activity recorded from scalp EEG showing a response from a user trained in utilising mu rhythm activity (8-12Hz range in this case). The topographical illustration on the right demonstrates larger activity over the right sensorimotor cortex (Reproduced from Daly, et al., 2008).

Recently the Blankertz group in Berlin using their Berlin Brain Computer Interface (BBCI) reported that out of 10 untrained subjects, 9 could operate a 1-D cursor control with 91.7%± 5.4% accuracy, but the subjects were staff members that took part in feedback studies in earlier versions of the BBCI (Blankertz, et al., 2007). In order to clarify any bias in the results a further study was performed on BCI novices with no prior training or involvement except some calibration and feedback runs for the experiment. Out of 14 subjects, 8 performed with >84% accuracy and a further 4 subjects, >70%. This success was reported as not being due to superior training but instead to optimisation of EEG analysis for individual subjects and advanced machine learning techniques with 55 sensors (Blankertz, et al., 2008). This is in stark contrast to the investigation by Guger and Pfurtscheller's group in

2003 where ~57% of naive subjects achieved less than 70% accuracy during feedback, although they only used a 2 bipolar-channel system (4 electrodes) (Guger, et al., 2003). Only 17% achieved rates over 80%. Interestingly the results reported that performance was worse using feedback than those trials that did not use feedback. This is suggested as possibly being because BCI novices are overwhelmed with such a device at first and perhaps frustration arised from incorrect feedback and it may induce insufficient attention to the imagery tasks.

A curious reality at present that has been reported is that this non-invasive modality currently equals or exceeds the performance of that achieved by invasive BCIs (Daly, et al., 2008) in terms of speed and precision of multidimensional control of a neuroprosthetic limb in humans (Kennedy, et al., 2000; Wolpaw, et al., 2004; Birbaumer, 2006; Hochberg, et al., 2006; McFarland, et al., 2008). Future technological advancement may see invasive BCIs becoming superior, although some groups suggest that non-invasive technologies may hold more promise than first expected.

3.6.2 Event related (evoked) potentials

Exogenous responses occur in the body in reaction to an externally applied stimulus such as the auditory evoked potential (AEP). The neurological response to a short auditory click is shown in Figure 3.5. The commonly reported peaks are labelled in the graph.

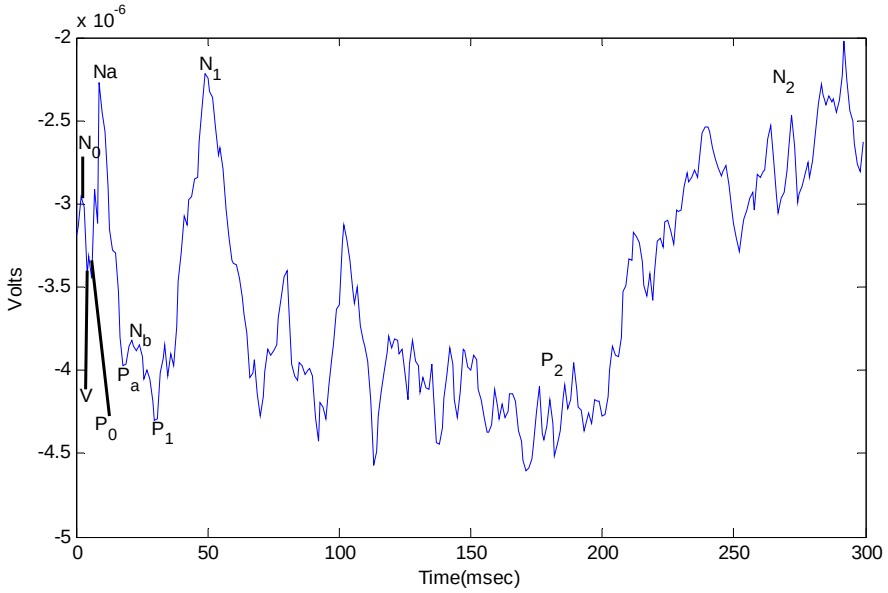

Figure 3.5: AEP from aural click stimulus applied monaurally (right ear) via an Eartone 3A insert earphone driven by the line out port of an M-Audio Duo D/A converter connected to the computer via USB.

BCI technology includes the use of event related responses such as VEP, SSVEP, P300 oddball response (both visual and auditory types), and preparation for movement (readiness

potential). One distinct advantage is that these intrinsic endogenous responses require relatively little or possibly no training, unlike the aforementioned oscillatory neurological phenomena (SMR) (Wolpaw, et al., 2000a). These BCI types are outlined next along with the current state and potential of these modalities.

3.6.2.1 VEP/SSVEP-based BCI

VEPs are measurable neurological phenomena resulting from an applied visual stimulus such as a reversing checkerboard, e.g. reversing at a rate of 1Hz. The response can be seen dominating the occipital lobes of the brain (visual cortex) as these regions integrate the retinal input (although some responses have been found more prominent in posterior parietal areas - Beverina, et al., 2003). The general practice is to provide multiple options (e.g. icons) on a screen each flashing at a different rate, whereby the subject is asked to gaze at the target of interest (e.g. one of four flashing virtual buttons). The resulting EEG spatiotemporal pattern can then be used to decode the users' selection. The signal is characterised by a negative peak around 100ms (N1) with a positive peak at 200ms (P2). Early BCIs operated on these principles with some success (Vidal, 1973; Vidal, 1977; Sutter, 1992). A more recent conference publication reports on a VEP-BCI (Guan, et al., 2005) utilising the N2 component (negative peak between 0ms-300ms) using a support vector machine (SVM) classifier. They reported an accuracy of 90.5% for single-trial VEP for one subject but two further subjects had an accuracy of ~75%. In addition a new transient VEP-BCI technique is reported whereby a low frequency stimulus and non-direct gaze can be employed to ultimately minimise any aversive contributions by the device, e.g. high flashing rate stimuli (Yoshimura, et al., 2008). However by far the more common visual-based BCI is one that uses steady state visually evoked potential (SSVEP) (Mason, et al., 2007).

SSVEP differ from transient VEP in relation to the stimulus repetition rate: transient VEP occur at <2Hz to allow for a rest period between successive evoked potentials, whereas SSVEP occur for stimuli above 6Hz. SSVEP demonstrate an increase in EEG activity at integer multiples of the frequency of the applied stimulus. Parameters such as rate, contrast, and spatial frequency all determine SSVEP amplitude and phase (Regan, 1989). However, these BCIs (and VEP-BCIs) have previously been classified as dependent BCI since extraocular muscular control and output pathways of cranial nerves are supposedly required to alter gaze direction during selection (Wang, et al., 2006). However, recently SSVEP-BCIs with attentional\cognitive\covert gaze control (non-muscular) report that a so-called independent SSVEP-BCI is possible - i.e. one that a completely paralysed individual could benefit from (Allison, et al., 2008). One technique implemented is to have two overlapping images in the users' passive field of view flashing at different rates, and the user is asked to

consciously fix there *attention* on the desired target (rather than moving there eyes at all). However, currently there are issues with this modality suiting only some individuals - 50% in one study (Allison, et al., 2008) - since decoding differences in frequencies were possible but not large enough to allow for effective control. This subject-specific success has also been reported by another group (Kelly, et al., 2005) although they didn't use overlapping images. This BCI modality is still however undeveloped with questions of what stimuli frequency to use (can be subject specific) and what attentional gaze techniques can be used for healthy subjects viewing the stimuli. In addition best practices for stimulus display, feedback, and training are still under investigation (Allison, et al., 2008). In so-called dependent BCIs however bit rates of 68 bits/min have been achieved in at least in one subject (Gao, et al., 2003). It has been suggested however that this single subject's superior performance was discovered from a previous study - i.e. the subject was preselected\screened - and that in that prior work (Cheng, et al., 2002) a bit rate as low as 0.76 bits/min was found for some subjects (remarked by Allison, et al., 2008). There is also another neurological feature, a type of ERP, represented within decoding of visual stimuli, arousing a potential about 300ms after the stimulus applied, i.e. the P300 potential, aka the oddball response. This also occurs for other sensory stimuli.

3.6.2.2 P300 potential - oddball response for BCIs

When rare/significant stimuli are applied (visual, auditory or somatosensory) interspersed with frequent/routine stimuli, a neurological response is evoked - a positive peak with a latency of ~300ms (post stimulus up to 1s for more complex stimuli) (Beverina, et al., 2003). A typical P300 response is shown in Figure 3.4(A) with relatively large amplitude around Cz-Fz electrode positions. The amplitude of the peak is proportional to the unpredictability of the stimulus. It makes up one of the earliest (Farwell, et al., 1988) and most successful exogenous BCI modalities due to the fact that it requires little or no training (intrinsically due to exogenous stimulus), and has demonstrated high information transfer rates (ITR) (Lenhardt, et al., 2008). The user is typically asked to select an item of choice from a list or matrix of possibilities by simply having consciously decided to do so, and as that item is highlighted in some fashion the potential is evoked. Interestingly a larger matrix size for selection is said to invoke a larger P300 peak amplitude (Allison, et al., 2003).

One limitation of the visual P300-BCI is that a visually impaired individual would not be able to use the device and so an auditory modality can also be used (Furdea, et al., 2009; Kubler, et al., 2009). It was argued however, whether such as BCI could achieve high enough bit rates to provide useful communication, but a recent study (Klobassa, et al., 2009) has demonstrated that successful levels can be obtained (an average of 1.86 bits/min in a

speller). In addition this auditory P300-BCI would be classified an independent BCI model since the visual musculature or associated voluntary motor control is not required.

A recent study was undertaken to investigate how many from the 100 subjects tested, could operate a P300-BCI using a 36-character matrix speller to spell a five letter word with only 5 mins training (Guger, et al., In Press, Uncorrected Proof). Nearly 73% of users achieved accuracy of 100% in one paradigm with flashing of individual rows and columns, and 89% achieved success of >80%. A further paradigm with individual letter flashing saw ~56% achieving success of 100% indicating that the row/column flashing paradigm was superior. The hypothesis then was to demonstrate that the P300-BCI was superior to the motor imagery based modalities in terms of limited training data and assuming the goal is to quickly achieve good statistics, which is supported by the reduced success in a previous study in 2003 using motor imagery on 99 subjects (this study was already discussed in section 3.6.1) (Guger, et al., 2003). Nevertheless the results may perhaps not be directly comparable since the newer study used more channels - 8 electrodes (2 bipolar channels in the 2003 study), and superior active electrodes instead of the previous gold plated type. Perhaps in future comparisons (time permitting) the authors could use the same equipment and perform both the P300-BCI and the motor imagery based BCI on the same subjects serially but in the same sessions to rule out bias.

A further promising BCI-modality has recently claimed high temporal resolution for subjects using the readiness potential, although this approach has been implemented with a focus on multimedia applications rather than for the chronically disabled. This BCI modality is discussed next.

3.6.2.3 Readiness potential-based BCIs

In preparation for motor movement the brain conjures a negative readiness potential (RP: a form of SCP) occurring up to 1-second pre-movement and occurring before EMG onset. This RP could perhaps be used in time-critical applications where the user may wish to speed up reaction times, perhaps for gaming or rapid (faster than motor response) breaking in a moving vehicle (Krauledat, et al., 2004). Several brain areas are said to contribute to the negative shift. However, in unilateral movement (finger or hand) a more focal negative shift is found in the corresponding motor area of the frontal lobe, maintaining contralaterality as with standard movement-related neurophysiology of the motor cortex. This allows for discrimination of right versus left hand movement in multi-channel EEG recordings using the lateralised readiness potential (LRP). The Berlin Brain Computer Interface (BBCI) adapts this biopotential as an input signal with the main purpose of reducing user training by

using advanced machine learning techniques while at the same time striving to improve classification performance. Since a BCI requires two adaptive controllers it aims to unevenly distribute the workload, enforcing more adaptation on the machine and less on the user. Futhermore, in the same publication, a combination of LRP and ERD features were used as inputs to the BBCI and the results indicated significant improvements in most subjects.

LRPs can be measured in both overt and imagined motor movement, although in the case of an amputee, motor imagery of the missing limb is different than in a healthy subject since a "veto" signal is required in the healthy subject to prevent the movement (inhibition). Because of this, the BBCI is said to focus on preparation of real movement for BCIs (Krepki, et al., 2007). Interactive gaming and robotic arm control are demonstrated by the group. In a further study half the subject population attained ITRs of 35bits/min and in a subsequent study with one subject using a mental typer, the user achieved 4.5-8 letters per minute (including corrections for errors) (Blankertz, et al., 2006). Another electrophysiologically-based BCI typical employing slower brain signals is the SCP-based BCI.

3.6.3 Slow cortical potentials (SCPs) based BCIs

SCPs are self-regulated slow changes in cortical potential (DC) that can last from 300msec to several seconds (~<1Hz, max. 4Hz), but are fluctuations rather than oscillations, since they are arrhythmic EEG (He, et al., 2009). A positive SCP is said to reflect cortical inhibition whereas a negative SCP occurs with preparation and depolarisation (e.g. movement) of the assessed cortical tissue (as supported by fMRI analysis), and both can be used to control a BCI for navigating the internet, and basic word processing (Birbaumer, et al., 1999; Birbaumer, et al., 2000; Hinterberger, et al., 2004b). However in some cases training with positive SCPs (inhibition) proved to be superior for locked-in/paralysed subjects (Birbaumer, et al., 1999; Pfurtscheller, et al., 2005). Measurement is typically made using electrodes around Cz or between Cz and Fz of the 10-20 international electrode placement system, but may vary. It has been reported that posterior parietal and occipital regions do not provide SCP regulation sufficiently - relative to more anterior cortical regions. One of the leaders in the field of SCP-BCIs is Dr. Birbaumer's group at the University of Tubingen with many publications for their Thought Translation Device (TTD). They have used this device to have users such as locked-in patients to self-regulate their SCPs using operant learning and using visual and auditory feedback and positive reinforcement of SCPs. It is said that the technique does not require continuous feedback of the response (can be discrete) but rather a reward for achieving the required amplitude - be it positive or negative polarity - and that this is the main element in the learning process (Pfurtscheller, et al., 2005). Thus it can be seen as a melding of operant and conditional

learning with only functional intactness of cortical systems (e.g. frontocortical basal ganglia attentional regulation system; motor and premotor cortical and subcortical systems) and motivational rewards being critical, i.e. intelligence factors, and motor imagery ability or strategies are not critical for this modality (Pfurtscheller, et al., 2005; Birbaumer, et al., 2007). For example, deficits or lesions in frontal lobe tissue (i.e. non functional intactness) can imply an inability or delay in regulating SCPs such as in children with an attention deficit disorder (ADD) and users with schizophrenia.

The principal contribution of the SCP-BCI is its level of clinical application having been extensively investigated for and used in subjects with late-stage ALS (no residual motor control), affording them communication prosthesis. However another hallmark of this technique is the lengthy training (sometimes months) and operation time required (~1min/letter) for proficient use (>70% of trials correct constituting proficiency) (Birbaumer, 2006) with ALS patients. Nevertheless, its stability and independence makes it retain its importance for the totally locked-in (TLS) patient.

BCIs using implanted electrodes may seem like the BCI modality of choice due to various negative characteristics of non-invasive systems: noisy signals, electrode-skin problems over long recording time periods, long training periods, etc. However as already mentioned, this invasive BCI presents its own difficulties rendering them only comparable to non-invasive BCI performance, at present.

3.6.4 Intracortical BCIs

As already illustrated in Figure 3.3 sensors have been used within the body boundary epidurally, subdurally (placed on the cortex but not penetrating it), and intracortically to support invasive BCIs. Intracortical electrodes report on single cortical neurons and their firing rates or spike trains (action potentials). This direct neuronal recording began in the 1960s with metallic microelectrodes applied to animals (Evarts, 1966) and research moved to determine if animals could learn to control neuronal firing rates. In the 1970's monkeys learned to control discharge of neurons in their motor cortex using operant conditioning (Fetz, et al., 1975), and so work has been ongoing to determine if humans could achieve control with this possible independent BCI modality. However, the apparent delay in applying this technique to humans was one of safety and long-term stability, and still persists today. Better electrodes were required since those earlier ones incurred tissue scarring and recording deterioration due to poor neuronal coupling. A solution to this came with the development of hollow glass cone electrodes with neurotrophic factors residing in the electrode cone, where these factors probe neurons to extend their processes into the electrode

cone (Kennedy, 1989). With this in place, action potentials could now be recorded for the neurons whose processes resided in the cone.

Kennedy and his coworkers developed these cone electrodes and tested them on monkeys (Kennedy, et al., 1992; Kennedy, et al., 1997) with stable recordings for up to 16 months. In a further study they applied the Neurotrophic Electrode with 2 wires coming back out of the head in humans (Kennedy, et al., 2000) on 3 ALS patients. The first patient died from her underlying condition 76 days after the implant but achieved binary control prior to death. Studies on the second subject revealed that his neural signals stabilising after 3 months and he could achieve spelling rates up to 3 letters/min (~15bits/min) after a few months training, and the implant worked for at least 17 months (to the publication time - so perhaps more). It's also suggested that his learning to control the cursor on screen was perhaps a result of plastic processes of the surrounding neural tissue where he may have developed "cursor-specific" neural tissue as a result of training and biofeedback (visual and auditory) of the cursor movement. Kennedy and his group carried out a further study this time using local field potentials (LFPs) (not action potentials/fast transients) in 2004 on presumably the same patient (JR) with an implanted system.

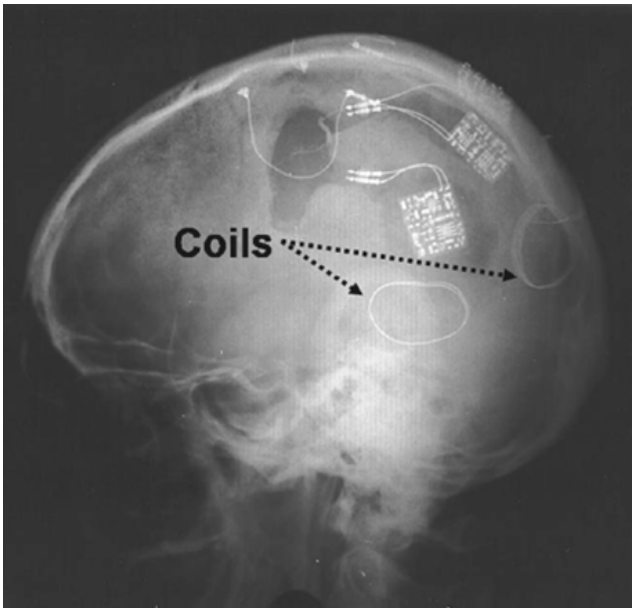

Figure 3.6: X-Ray of implanted electrode system (Two coils, board mounted FM transmitter) from a study using LFPs on a male ALS patient. The two implanted coils are indicated with dashed arrows and these provide power to the implanted circuitry by induction (induction system cemented to the skull). Coils on the implanted circuit boards (between the cranium and scalp) transmit signals (30-40MHz) to an FM receiver on the scalp surface (reproduced from Kennedy, et al., 2004).

Figure 3.6 is an X-Ray of the subjects head showing the implanted electronics and coils, with an induction coil to power the implanted electronics via implanted coils of wire. Each

cone electrode had 2 wires and these could be independently controlled by the subject to encode horizontal and vertical direction of a cursor. When asked what his mental strategy was he reported via the BCI that he simply *thought about the desired direction*. This study is demonstrated that control using LPFs for this subject could compare to previous direction encoding in single-neuron action potentials, for the same subject.

Finally, a study in 2006 by Hochberg and co-workers published in *Nature* magazine is worth mentioning (Hochberg, et al., 2006). The study involved a pilot clinical trial on a subject with spinal cord injury (tetraplegic), unable to move or sense his limbs. Within a few training sessions he was able to use M1 (primary motor cortex) neuronal ensemble spiking activity to control a 2-D cursor even three years after the injury using an implanted 96 microelectrode array. With the device he could open email and operate a television even during conversation. Supplementary videos with the publication demonstrate the significant success of this intracortical BCI even though it is comparable to rates achieved by a non-invasive sensorimotor BCI controlling multidimensional cursor movements (Wolpaw, et al., 2004).

The current problems in the widespread dissemination of these devices is still one of long term safety, long term stability of recordings, the need for expert oversight, and the technical requirements of these recordings where it has been suggested that the degree of practicality and potential improvement are unclear, even with good signal fidelity (Daly, et al., 2008; Schalk, 2008). Reaction of the tissue to the implanted system is also a concern possibly inducing tissue damage and infection. Most intracortical studies have been performed on animals but also in some humans as already outlined above. Finally for intracortical methods to receive widespread use the control offered needs to significantly exceed the capabilities of non/less invasive BCIs since they are currently comparable. Kennedy et al suggest an order of magnitude would be needed to justify intracortical measures (Kennedy, et al., 2000). However there is a saving grace - although it may have seemed apparent that only action potentials or field potentials from implanted systems can convey complex aspects of neurons such as speed and direction of hand movements, evidence is available to suggest otherwise, using electrocorticograms (ECoG). Detailed decoding may be possible through ECoG - measurements from above or below the dura layer - which are less invasive and have many benefits over other techniques such as EEG.

3.6.5 ECoG-based BCIs

ECoG recordings measure electrical potentials typically acquired above the dura mater or subdurally on the cerebral cortex surface using electrode arrays (for example, Figure 3.7).

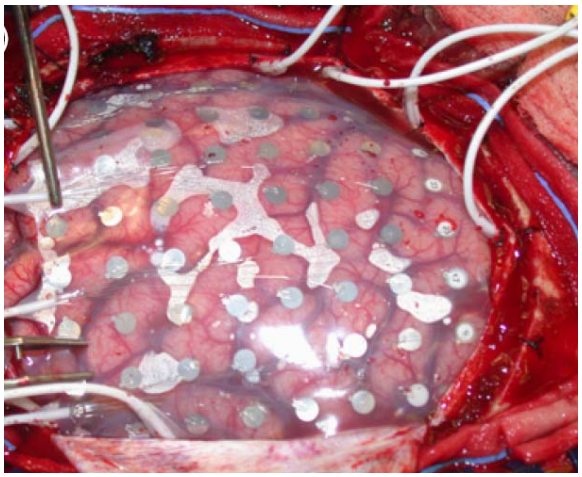

Figure 3.7: ECoG electrode array applied subdurally on the exposed cerebral cortex (Reproduced from Schalk, et al., 2008).

Since the electrodes do not penetrate the cortex they present a less invasive modality than single neuron or LFP recordings by intracortical sensors. This could likely provide them with better long-term stability (Yuen, et al., 1987; Margalit, et al., 2003) and without penetration they present less tissue damage or tissue reaction. They can detect μ-rhythms, β-rhythms, higher frequency γ-rhythms (30-200Hz), and beyond - up to 500Hz (compared to 0Hz-50Hz in EEG). Spatial resolution is higher too with tenths of millimeter resolution compared to cm's in EEG. ECoG is also less susceptible to EMG, EOG artefacts (Fatourechi, et al., 2007), ambient noise, and other non-brain signals and returns a higher voltaic amplitude 50uV-100uV compared to EEG (10uV-20uV). A further benefit is that training is much shorter than many other BCI-types taking only minutes to control a cursor using rhythms from motor imagery (see study in next paragraph). However issues at present that impede ECoG as a method for BCI applications are that most candidates (at present) for testing and development in humans is confined to pre-surgical patients - for example intractable epilepsy patients. In addition, exposed cerebral areas for imaging (placement of electrodes) are determined by the regions of interest for the surgery and not any way preselected for the BCI itself - which may not present much diversity for BCI control.

The first 1-D cursor control using ECoG was demonstrated in 2004 (Leuthardt, et al., 2004). In a more recent study the same group (Schalk, et al., 2008) reported on 2-D cursor control on 5 subjects (no previous BCI exposure) going for surgery to remove regions of epileptic foci. Subdural electrodes were put in place for 1-2 weeks primarily to localise the seizure foci using between 26-64 electrodes. Recordings were made on one hemisphere only for 4 of the five subjects and features for control included μ-rhythms, β-rhythms, and γ-rhythms. However, most control was achieved by a large increase in amplitude of frequencies in the gamma range (especially >70Hz in Brodmann's areas 1-6) in response to

overt or imagined motor movement (resulting signals for imagined movement were the same as overt topographically but lower in intensity). Three stages were identified and took place to learn for 2-D control: first was to identify the best feature for the subject (locations of sensors varied for different subjects), second training was carried out for 1-D cursor control, and finally third, 2-D cursor control was attempted. With brief training (12-36 minutes), accuracies between 53%-73% were obtained in a four target centre-out task with a proposed chance rate of 25% for this task. Tasks were identified in pairs that were spatially independent and frequency independent, and more prominent to control both horizontal and vertical cursor movement using one hemisphere alone. This typifies the success of the study whereby previously it had been thought by some that intracortical sensors on single neurons was needed for such degrees of freedom in controlling a 2-D cursor (rather than an integration of field potentials) (Schalk, et al., 2007).

The future for this technology (ECoG) for BCI looks good with the former demonstration acquiring faster control of a 2-D cursor than a seminal EEG counterpart (Wolpaw, et al., 2004; Schalk, et al., 2008). However ECoG-based BCIs are not without serious limitations at present such as the low subject population for testing, as well as current difficulties in determining best ECoG features since the bandwidth is much greater than EEG. There may also be a need to track features and adapt the system as they (features) change over time. Animal studies to test long-term safety of ECoG-implanted systems, optimum electrode placement, and a fully implanted wireless telemetry system are items of topical discussion for development of this technique for BCI use (Schalk, et al., 2008). Some recent work has advanced the classification techniques for motor imagery in ECoG for BCI using support vector machines (Demirer, et al., 2009).

Like ECoG, another BCI modality apart from EEG which is gaining more attention in BCI research is magnetoencephalography (MEG) (Kauhanen, et al., 2006b; Mellinger, et al., 2007; Waldert, et al., 2008) which although it may be impractical for widespread BCI use at the moment, it may have significant contributions for rehabilitation (e.g. stroke) (Birbaumer, 2006) which has become a major 'spin-off' of BCI research. This concludes the section on EEG-based BCIs.

3.7 MEG-based BCI

With the presence of neuronal activity in the cerebral cortex for example, localised electric and magnetic fields are produced (from electric current dipoles) which can be measured: EEG for the electric fields and MEG for the magnetic fields. However, EEG

suffers from spatial smearing/blurring and filtering of the electric signal due to affects from the scalp, skull and intracerebral fluid. In contrast, MEG does not suffer from these problems (inherent to the magnetic fields) and has a high spatial specificity or uniqueness as a result, i.e. it can measure localised magnetic fields pertaining to spatially specific tissue. However, the magnetic fields that MEG measures are those from a group of neurons rather than individual cells, since the fields produced would be too weak. The magnetic signals are acquired from SQUIDS (superconducting quantum interference devices) - the highly sensitive detector used in MEG. The resulting equipment is rather bulky and expensive and requires a magnetically shielded room due to possible contamination from environmental disturbances (e.g. radio, geomagnetic field fluctuations of the earth) which can be 6-orders of magnitude higher than the signal of interest (Kauhanen, et al., 2006a).

The first MEG-based BCI with biofeedback (Lal, et al., 2005) strove to demonstrate that learning in an MEG-environment was easier compared to EEG (with proof by way of a reduced error rate in MEG over EEG using the same machine learning algorithm). Furthermore it was suggested that MEG-based BCIs could be used for initial screening and training with a view to moving the subjects to an EEG-based BCI after training (due to lack of portability of MEG system) (Mellinger, et al., 2007). Success rates ranged from chance up to 92% using tongue and left little finger imagined movement as tasks in 10 healthy subjects with a 150 channel system (offline). Four out of 5 subjects in an online implementation were able to spell a short name 4.25 letters using imagined movement in the first session. Imagined movements were represented by μ-rhythms (similar to EEG) in MEG recordings of 8-12Hz and 18-22Hz, which were reduced in intensity during activation in the sensorimotor cortex. Another recent publications proposes MEG-based BCI feasibility and efficiency in user training (Mellinger, et al., 2007) specifically taking 32 minutes for self control of rhythms in feedback training in real-time on 6 subjects.

A further study in 2006 (Kauhanen, et al., 2006a) used both single-trial EEG and MEG recordings on 3 right-handed male tetraplegics. A 306 channel (102 locations - triple sensor units) whole head MEG system was used simultaneously with a 58-channel EEG system. Six MEG locations and 6 EEG electrodes located over the sensorimotor cortices were used in the classification of 10Hz and 20Hz rhythms. Tasks included attempting to move left and right index fingers in isolation, together, or not at all. Both rhythms were suppressed during attempted movement for all subjects in both MEG and EEG (but without the contralateral rebound[3] found in healthy subjects). Interestingly they found comparable classification rates

[3] A rebound is a short-lasting power increase of a particular frequency rhythm

for both EEG and MEG techniques even though MEG has multiple superiorities (more localised; not affected by scalp/skull blurring, etc). In a further experiment (offline), features for slow potentials (0.5Hz-3Hz) yielded better rates than the higher frequency potentials (3-7Hz) in both modalities with short training periods, and a dynamic classifier obtained higher rates than a batch-trained classifier for the slow potentials.

Hand movements and direction along with other desirable increases in the degrees of freedom in the same appendage have been a topic of interest lately, to increase the symbol rate for BCIs. In a recent MEG study (Waldert, et al., 2008) small hand movements were determined on a single-trial basis with a success rate of 67%. This MEG study along with EEG recordings has added to the debate about invasive-recording necessity for detection of directional movements of the same extremity (directional decoding). In the study, four distinct reaching movements of the same extremity were discernable using both EEG and MEG, i.e. non-invasively, which holds promise for multidimensional control of an external effector, e.g. robotic arm for a so-called BMI (brain-machine interface).

The final BCI type using cerebral signals for consideration is the functional magnetic resonance imaging (fMRI) based BCI which has only come to the fore of late, although like MEG it is unlikely that it could be used in the long-term for BCIs other than perhaps for localisation, pathological considerations, and perhaps for training.

3.8 FMRI-based BCI

Magnetic resonance imaging (MRI) is a widely used clinical imaging technique providing detailed anatomical "images" of various body parts, including circumscribed regions such as the brain. FMRI is a MRI paradigm capable of determining functional activity indirectly.

Haemoglobin: The fMRI signal, the so called blood-oxygen level dependent or BOLD signal, reflects changes in metabolism identified by changes in local haemodynamics which induce local changes in magnetic susceptibility, i.e. magnetic susceptibility differences between oxyhaemoglobin (HbO_2) and deoxyhaemoglobin (HbR) in microcirculation (Ogawa, et al., 1990). HbO_2 is diamagnetic and has similar magnetic susceptibility to the surrounding tissue (Sutton, et al., 2009), due to the presence of the attached oxygen molecule in haemoglobin. In the case of HbR that attachment is not there and HbR is thus paramagnetic meaning there is a difference in blood vessel- and tissue- magnetic susceptibility in the presence of HbR which extends beyond the blood vessel wall. In the

event of a localised activation of neural tissue an increased delivery of HbO_2 is routed to the area, which reduces HbR in the area, thus reducing the magnetic HbR affect and this leads to an increase in the BOLD signal (Sutton, et al., 2009).

Spin, Precession, and Nutation: When placed in the magnet of the MR scanner, somatic protons (mostly hydrogen protons of water) align parallel to the main magnetic field. Somatic nuclei are said to have a magnetic moment and thus spin or rotation. These protons also precess around the MR scanner's main magnetic field axis, at a rate determined by the magnetic field strength and a gyromagnetic ratio (also enabling spatial encoding by varing field strength and phase). A short radio frequency (RF) pulse tilts (nutation) them from there natural alignment on the axis of the main magnetic field. Once the RF pulse ceases, they release the RF energy at their resonant frequency and the relaxation times of the precessing protons is used to determine the metabolic extent of that focal tissue, due to the level of blood oxygenation. This energy is detected by surrounding RF coils. Mostly water hydrogen protons of the tissue surrounding the blood vessels which have incurred a change in oxygenation are affected by the microscopic magnetic field variation, resulting in a loss in coherence of the precession frequency (loss of phase coherence leads to signal cancellation and thus decreased signal intensity) (Sutton, et al., 2009). Thus, the BOLD signal increases with increasing oxygenation, since HbO_2 has similar magnetic susceptability to the surrounding tissue (isomagnetic), compared to HbR, which induces signal loss.

BOLD fMRI was developed in 1990 for potential functional brain imaging (Ogawa, et al., 1990). The first real-time fMRI-based BCI with feedback to the subject was developed only recently (Weiskopf, et al., 2003). One subject was asked to increase and decrease the BOLD signal for BCI control using emotional valence and arousal, which was intended to activate the circumscribed areas of the anterior cingulate cortex (ACC). The BOLD response for two subdivisions of the ACC and head motion tracking were fed back to the subject where a learning effect was said to occur over time with increased control over the rostral-ventral subdivision of the ACC. Feedback delay was two seconds from acquisition of images to feedback of the time series. Yoo et al (Yoo, et al., 2004) developed an fMRI-BCI for 2-D control of a cursor through a maze, using four tasks - mental calculation (frontal and anterior cingulate gyrus), mental speech (temporal), and right and left hand motor imagery (somatosensory areas in pre- and post- central gyri). Classification was based off reference templates from previous studies showing typical activations and regions of interest. Four subjects took part and listened to a 900Hz monotone during rest periods to maintain attention throughout the experiment. One major drawback of the BCI was that command generation took 135 seconds each owing to a 111 second scan time. Two of the three subjects navigated

to the end of the maze without error, in 12 steps requiring 3 of each task in a random order. Errors in one subject were expressed as being due to overlapping regions of interest leading to misclassification. Subjects closed there eyes during the task with feedback constituting seeing the movement through the maze at the end of each task. In a very recent publication by the same group (Lee, et al., 2009) control of a robotic arm (horizontal and vertical control - range and direction) was demonstrated in a real-time fMRI-BCI using hand motor imagery from both hemispheres.

An fMRI image sequence (32 slices) for a subject performing a task of right hand imagined movement is shown in Figure 3.8. A larger response (shown in red) is seen over the contralateral (left) cerebral cortical areas and supplementary motor area (SMA). The response appears first 9 slices in (slice 1 at bottom left, slice 10 bottom right, and slice 11 middle-row right, and so on) which are areas on the cerebral cortex. The author carried out these experiments in conjunction with Rutgers University in Newark, New York in a 3 Tesla Siemens MR scanner. The study was performed to validate the protocols used in the NIRS experiments for OBCI applications (described further in Chapter 6).

Currently MEG-BCIs and fMRI-BCIs suffer from many limitations\disadvantages: firstly they are very bulky requiring specialised shielded rooms to dominate their magnetic environment. In addition they are expensive, require complex technical requirements, and are not portable or suitable for long term use. For fMRI, the intrinsic nature of the haemodynamic signal taking 4-5 seconds to peak appears to cap its potential, although there are potential applications within the realm of BCI that it can provide. Due to its applicability for assessing functional activity of circumscribed neural substrates and using biofeedback it could be used as a training ground for other more portable BCI modalities. It could also be used for optimisation and localisation of regions of interest for invasive BCIs. Much like the specificity of near-infrared spectroscopy (NIRS) and its applicability to stroke rehabilitation (Ward, et al., 2007) it would be perhaps useful to utilise this metabolic BCI in rehabilitation where other imaging modalities such as NIRS and EEG cannot reach the deeper CNS areas of interest. Nevertheless the field of fMRI is continually developing with the original standard BOLD fMRI approach becoming obsolete (Sutton, et al., 2009). Current challenges impeding functional activation determination are venous contributions to the signal, bulk magnetic susceptability losses (due to non-uniformity of the magnetic field due to varing magnetic susceptibility of various body tissues), and indirect coupling to the neural response, which is still under debate (Sutton, et al., 2009).

The next section provides a brief look at the area of biofeedback which training in contemporary BCI has extended.

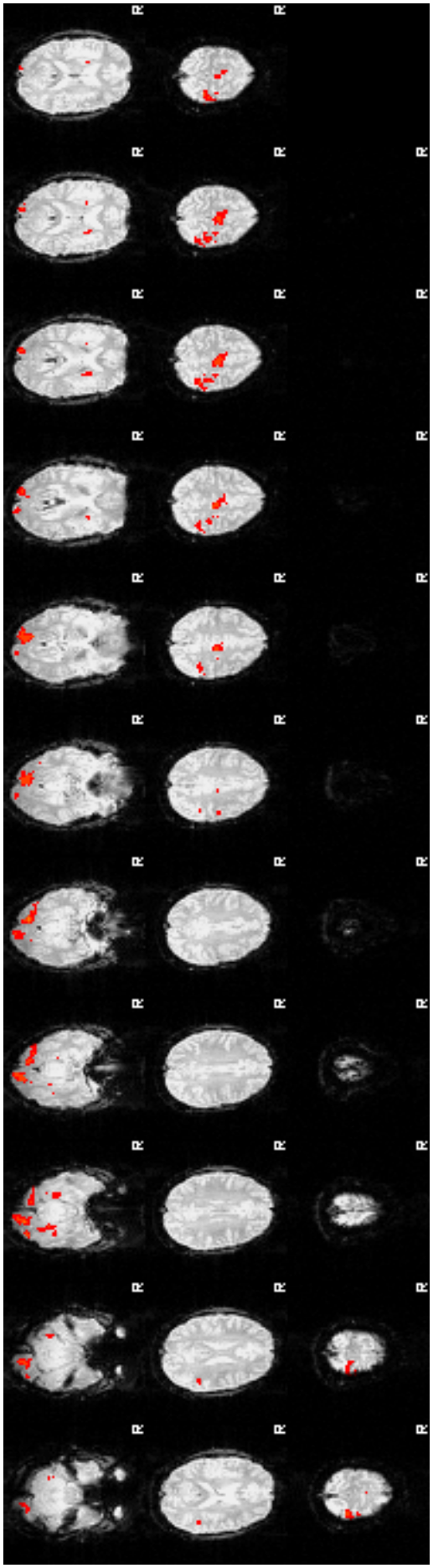

Figure 3.8: FEAT fMRI report for imagined right hand movement from a researcher at NUI Maynooth. Larger activity in the first few slices is seen over the contralateral (left) cerebral cortex areas and SMA. (These experiments were performed to validate the protocols used in the NIRS experiments for optical BCI applications - described further in Chapter 6.)

3.9 Biofeedback

Like all developments in neuroscience, BCI has roots. The area of biofeedback for neurological operant conditioning and activity-induced plasticity has its origins in attempts to apply operant conditioning - rather than accept classical (Pavlovian) conditioning alone - to supposedly involuntary controls of the body, i.e. the autonomous nervous system (ANS). Some early results (Miller, 1978) appeared to provide promise to instrumental visceral conditioning of for example heart rate and blood pressure, to perhaps alleviate hypertension and cardiac arrhythmias. However after years of failure in trying to replicate the work satisfactorily, it was thought that operant methods were lacking the homeostatic effect of the reward (reviewed in Birbaumer, 2006). Recently however there has been a demonstration of ANS activity accompanying mental control of beta oscillations in a tetraplegic patient (preparatory-induced heart-rate acceleration terminated by a deceleration of 10-20 bpm) suggesting that cardiovascular nuclei in the brain stem accompany activation of motor structures in cortical areas (Pfurtscheller, et al., 2007). Nevertheless from the earlier attempts of direct ANS control there was some success in the area of operant conditioning using neurological feedback, which training in contemporary BCIs has extended. However, autonomic control of visceral organs seemed impossible.

The next stage of the generic BCI model from Figure 3.1 is the second stage or the signal processing stage, aiming to extract and translate notable features of the physiological signals recorded - be it EEG, fMRI, or NIRS etc. This crucial element is described in the next section.

3.10 Signal Processing

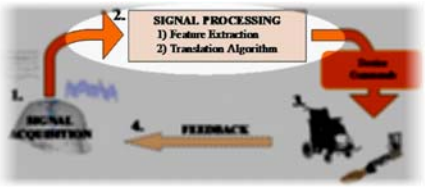

The next element in the BCI chain after the signal acquisition - which incidently is how a BCI type is identified, e.g. an MEG-BCI uses MEG signal acquisition - is signal processing. The signal processing element of the BCI is generally the workhorse of the BCI with the most temporally demanding processes occurring at this stage - usually DSP. Widely accepted by the BCI community (Wolpaw, et al., 2000a), there are two sub-elements in this stage - feature extraction and translation algorithms, and the distinction is important for percipient progression in BCI (these differences are explored further in Section 3.10.1 and Section 3.10.2). The aim of this signal processing stage is to generate signals and device commands

from analysis of the input signals, in order to control the external BCI device, and perhaps allow for adaptation of its algorithm due, for one, to the highly non-stationary nature of physiological signals. An effective signal processing stage can substantially reduce or eliminate training times which can have a large bearing on the success rate and indeed the effective ITR of the device (Dornhege, et al., 2004; Blankertz, et al., 2008).

From the signal acquisition stage (the input) the researcher has acquired a mixture of exogenous noise, endogenous/physiological noise, physiological signals of interest (known), and other physiological signals which are as yet not usable (perhaps non-linear phase information). The researcher will at some level have used preprocessing at the acquisition stage along with perhaps analog signal processing using filters and amplifiers to offer the DSP section more physiologically-specific data and higher signal-to-noise. Still, classification algorithms are generally not fit to cope with the plethora of features in the data set and so specific features must be isolated at the *feature extraction* stage of the signal processing element of the BCI. The translation algorithm takes the features from the feature extraction stage and decodes those features to present the external BCI device with commands to carry out, such as translating an increase in $dHbO_2$ concentration to move a cursor horizontally by some predetermined amount. The various signal processing techniques used by the BCI community have been reviewed recently (Mason, et al., 2007).

3.10.1 Feature Extraction

These features are typically either time domain or frequency domain signals (perhaps spatially specific). Another important aspect of this stage is not to define or confuse a feature with the product of some analysis method. A feature should be reflective of brain anatomy and physiology as specified at the first international BCI meeting (Wolpaw, et al., 2000a). For one, this is to foster better appreciation for tackling artifacts (undesirable EMG) that may be somehow masked by more abstract algorithms which don't necessarily aim to identify a specific physiological feature, e.g. autoregressive parameters which are dependent on the specifics of the analysis algorithm (Wolpaw, et al., 2000a). Time domain features include P300 potentials, SCPs, action potentials of signal cortical neurons, and amplitudes of other techniques. Frequency domain features include EEG μ and β rhythms, MEG rhythms, haemodynamic spectral features of fMRI (BOLD signal) and FNIRS (cerebral blood flow, low blood pressure oscillations, rate of oxygenation-concentration change from HbO and HbR). Firing rates of neurons, band powers, wavelets, Hjorth parameters (mean power, mean frequency, and bandwidth in EEG), and autoregressive models are also determined as features in various BCI modalities (Pfurtscheller, et al., 2005). After these features have been

extracted they are passed to the translational algorithm stage to determine the output of the BCI.

3.10.2 Translation algorithms

It is the job of the translation algorithm to determine what the feature should achieve such as letter selection in a menu matrix. These can be based on linear equations or more complex ones such as neural networks or support vector machines (SVMs) (Daly, et al., 2008). As part of the adaptive capabilities of a working BCI controlling a cursor on a screen the translation algorithm should accomodate for selection of the entire range of the pc screen, say 1uV-6uV for cursor movement from the left to the right hand side of the screen. It should also cater for *changes* in the user's capability such as may result from fatigue or diurnal change (day and night differences). Thus if the users range expands beyond the 1uV-6uV to say 1uV-10uV, then the algorithm should reset the cursor limits similarly. The next stage after translation of the features to commands is the output (stage 3 of 4) - to drive some device or application.

3.11 Applications of a BCI

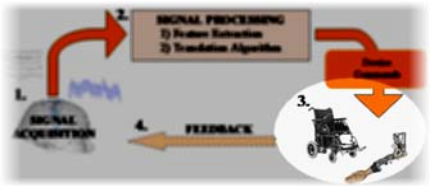

There are several BCI output devices and applications in current BCI implementations. They range from simple binary switches to control of neuroprosthetic arms with various degrees of freedom. These commands might be used to carry out one of the following (Mason, et al., 2007):

- Answers to yes or no questions;
- Select from an iterative menu (matrix/table of options);
- Control of a computer (cursor control, browse the internet, check email, send message to a social network (such as Twitter));
- Word processing (typing);
- Control an electric wheelchair (with perhaps extra sensors on the chair to detect objects etc);
- Household environment control (lighting, temperature, switches, television, music player, air conditioning, other common appliances);
- Navigate through a virtual environment;
- Mobile robots;
- Robotic arms (mechanical neuroprosthesis);
- Functional electric stimulators or orthoses;

- Full motion flight simulator;
- Neuroprosthetic arm (multidimensional control mostly developed for invasive BCIs but may also be controlled using non-invasive BCIs such as EEG - as mentioned in the signal acquisition section for EEG).

The historical BCI application methodology which is still prominent today is for the user to use brain signals to control some device, some options of which have just been listed. However, more recently applications have been sought to *restore* motor function (rather than replace it with artificial prosthesis) using the phenomenon of activity-dependent brain plasticity which could positively affect motor learning skills (Daly, et al., 2008). This may promote sensory input that influences plasticity. Another motor learning paradigm is used also which is simply to have the user produce more predetermined normal brain signals. However, Daly et al (Daly, et al., 2008) have reported that there is so far no evidence that this type of training (feedback of signals alone) will fix or improve motor areas that have been affected by stroke, for example.

Further applications of BCIs have been developed such as BCIs to reduce epileptic seizures by self-regulation of for example SCP and other implementations in order to reduce the potency effect in attention deficit hyperactivity disorder (ADHD), using appropriate feedback. One of the major upsets in a lot of these applications is the ongoing (expensive) need for technical support. A 47-year-old neuroscientist with ALS has been shown to be able to run his BCI independently using a P300-based BCI in a matrix speller application and to check email and has found it better than eye gazing dependent BCIs. Promisingly his caregiver is able to put on his EEG cap daily and he doesn't need technical personnel (with data updates going to the lab via the internet) (Vaughan, et al., 2006a). However, many of these applications require months of training and more in some cases. This is the final stage in the BCI model shown in Figure 3.1 - the feedback and learning stage.

3.12 Learning, training, and mental strategies

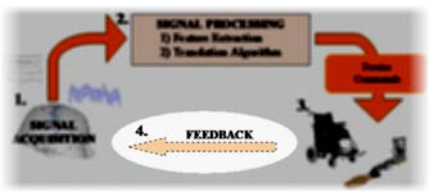

Of all the numerous BCI types that are available which have been discussed in previous sections, most require some form of training in order to learn the 'new skill' required to control the BCI effector. There are some BCIs such as the P300-based BCI which typically don't require training due to the exogenous nature of the applied stimulus and the fact that they evoke a more natural innate bio-potential. In most BCIs however, the need for training can be due to the nature of the

control being sought which initially is a new, unnatural process such as learning to modify SMRs amplitudes. However, after a certain period of time (which can be months Birbaumer, et al., 1999; Pfurtscheller, et al., 2005) the process is said to become more natural, like many acquired skills where the user no longer needs to focus on the specifics of the task (Wolpaw, et al., 2004)) - he/she "just does it". However the training procedure is not to be taken lightly (Wolpaw, et al., 2002) - there are procedures and reported methods to use and others to avoid. For example, the method of using a virtual reality feedback system is said to decrease the error rate in at least one group's research (Ron-Angevin, et al., 2009a) with a significant implementation of walking through a virtual street using foot imagery in another study (Pfurtscheller, et al., 2006). Much of this training is based on essential biofeedback - which can be continuous or discrete, i.e. constantly showing the user his\her progress (continuous) or perhaps only after a certain period of time, such as at the end of the task (discrete).

Biofeedback is perhaps synonymous with the early work of Neal Miller (Miller, 1978) as already mentioned briefly in Section 3.9. In 1974 biofeedback to control SMRs (specifically mu rhythms) was implemented by Sterman (Sterman, et al., 1974). Biofeedback essentially provides the contingent of the volitional thought or action, which serves to reinforce learning. In includes both the information on the level of success in controlling the particular brain signal, and it also indicates the (necessary) reward (Birbaumer, et al., 2007). The feedback to the subject can be visual, auditory, or even tactile. This feedback process requires the determination of 2 things: 1) the task to be performed; and 2) the training protocol (Ron-Angevin, et al., 2009b).

3.12.1 Task Selection

The mental strategies that can be performed to elicit a significant functional brain-signal are potentially limitless, but thus far in the literature the typical strategies utilised are listed in the table (Table 3-1) below.

Overt Tasks	*Cognitive Tasks (non-overt)*
Eye gaze for visual stimuli (P300, VEP, SSVEP)	Motor imagery (hand, feet, tongue)
Overt movement (hands, feet, tongue)	Mental arithmetic (at least 2-digit numbers)
	Mental rotation of geometric objects
	Non-verbal fast signing
	Non-verbal slow signing (during rest periods)
	Mentally counting sheep (during rest periods)

Table 3-1: Typical mental tasks for controlling a BCI effector.

The majority of BCIs apply only two mental tasks for control, although there have been cases with far more, up to eight (Mason, et al., 2007). However, some studies have suggested that increasing the number of tasks (classes) tends to decrease the classification accuracy due to design protocol complexity trade-offs (Kronegg, et al., 2007), where a maximum of three was determined by another study to be optimum (Obermaier, et al., 2001) - at least for the more common EEG-based BCI. However, the method of selecting the best mental task for a subject appears to be agreed across studies - stipulating that it is highly subject-dependent and needs to be optimised/adapted for each subject (Obermaier, et al., 2001). A further example demonstrates that at least for untrained subjects, it may be more prudent to start off with tasks maximally dissimilar to the user, e.g. instead of left vs right hand in a two task paradigm, being with an easier combination of tasks, e.g. right hand as the first task and the rest-state as the second task (Ron-Angevin, et al., 2009b). Furthermore, the case is potentially even more complex when dealing with the disabled since the commonly used neural substrates (e.g. motor cortical areas) may have been affected by the disease or trauma, and thus are unsuitable for malleable functional activity (Daly, et al., 2008). In this case (motor) other brain signals could be used (e.g. P300 potentials). Either way the feedback used will be determined by the task selection, i.e. feedback of the success of completing the task correctly. The second element that determines what feedback to use is the training protocol, e.g. timing and how the feedback is presented (for example, visual, auditory, or tactile).

3.12.2 Training Protocol and biofeedback

As previously mentioned training for effective use of a BCI (especially using endogenous stimuli) can take up to months (Birbaumer, et al., 1999; Wolpaw, et al., 2000b). Strategies should take psychological factors into account which can affect a subject's ability to navigate their brain signals - frustration, motivation, fatigue, and concentration. The training paradigm considers timing (duration of session and trials, number of trials, and inter-trial duration), and presentation of feedback (continuous or discrete; visual, auditory, and/or tactile). These are outlined next.

Timing: The paradigm can be either self-based (asynchronous) or cue-based (synchronised to some timestamp) although cue-based methods are by far the more utilised due to difficulties with false positives and the 'idle' problem - i.e. how to instruct the BCI that you don't wish to use it, and other times when you do (the 'on' and 'off' switch). Asynchronous BCIs would be more favourable since it would be always 'on' but the idle problem needs to be fully addressed for a particular BCI. In general, it is favourable to have a shorter trial time period, i.e. the quicker the selection or process of control, the higher the

potential bit rate of the device. The number of trials is largely determined by the constraints due to subject fatigue although asynchronous BCIs would have potentially limitless trials - that is until the device was voluntarily turned off by the user's idle response.

Presentation of feedback: Finally, consideration needs to be given to the choice of feedback presentation. Visual feedback serves most of the BCI implementations to date (Mason, et al., 2007). However, some disease and trauma can affect the subject's visual system where they may no longer be able to fix their gaze willingly, such as can occur in ALS, and so alternative feedback presentation methods are needed. Auditory feedback has been used with some success, but it has been found that auditory feedback alone (e.g. increase and decrease of pitch in piano tones) performs significantly worse than visual implementations alone (Hinterberger, et al., 2004a), in this example using a SCP-based BCI, on 54 healthy subjects. Furthermore, a combined visual and auditory feedback paradigm showed the smallest learning affect, actually impeding learning (perhaps due to limited\competitive attention resources) - although perhaps a longer training period could help a user to improve performance. In order to control an advanced neuroprosthetic device it would be critical to have a tactile feedback system. In a study, motor imagery modulating mu rhythms conveying 1-D control demonstrated an average accuracy of 56% with 15% being an accuracy percentage for chance. There are potential drawbacks to this feedback method however, where it was found in the same study that vibrotactile sensor placement (such as on the ipsilateral or contralateral bicep (to motor imagery task)) had an influence on provided bias to the control, effectively modulating the mu rhythms due to this sensory input. Training and further signal processing levels are said to help in overcoming this bias (Chatterjee, et al., 2007).

Training approaches: A recent publication has demonstrated however, the potential for BCI proficiency with little user training by even naïve BCI users by using powerful machine learning algorithms. While it is accepted that there are two adaptive controllers at play (the user and the BCI software), in this case an extra workload is placed on the BCI software relative to the user (Blankertz, et al., 2008). For the intracortical BCI (single neuron or local field potential) the process of learning is to define the neuronal activity that occurs with standard limb movement, and then to use this for control of cursor movements. Finally, the last step is to demonstrate that mental activation alone without overt movement can be used similarly to control the device (Daly, et al., 2008). In terms of adaptability, it should also be remembered that activity can change over time - perhaps represented as a reduction of the observed responses - since neural tissue is highly plastic. However, this plasticity with operant conditioning and biofeedback should strive to adapt to the users intensions forming

new connections for the newly acquired skills. This should be seen in non-invasive approaches also. The user receiving feedback as the output of the BCI (such as the reward of cursor movement) in turn affects the user's brain activity, which then influences subsequent BCI output, closing the loop.

The full BCI loop from data acquisition (input), through signal processing (feature extraction and translation algorithms and classification), through to device control and finally feedback, have been described. However, for any study it is worth outlining the target applications that the research intends to provide and pursue. The next section provides a brief look at the target population of BCI research, broken down into applications for the disabled, then specifically for motor restoration, and finally other applications for the healthy population.

3.13 Potential BCI Users

BCIs have three potential target application areas: 1) as a communication device for the disabled or to control external devices (environment); 2) therapy or treatment for ailments such as epilepsy, stroke, ADHD, anxiety, other psychiatric conditions by using biofeedback of self-regulation bio-signals; and 3) to enhance the cognitive performance of healthy humans (Angelakis, et al., 2007). Most BCIs are aimed at enabling the millions of disabled users that would benefit from such a device to offer them a lifeline to express their full potential.

3.13.1 Disabled Community

- Locked-In syndrome (LIS);
- Amyotrophic Lateral Sclerosis (ALS)
  Suffers of this disease usually require artificial ventilation to prolong their life and give them a chance at restoring some communication with a BCI, due to the almost certain degenerative nature of the disease;
- Sever cerebral palsy
  In severe cases no useful muscle control remains and so a BCI is a suitable alternative to a conventional device which requires at least some residual motor control;
- Spinal cord injury (SCI)
  In cases of say high spinal cord injuries, the user may prefer a BCI device over a more conventional one which utilises EMG from facial muscles or eye gaze etc;
- Neuromuscular disorders;

- Brainstem stroke
  Subjects suffering from this disease which may lead to locked-in syndrome may retain only minimal eye movement control;
- Muscular dystrophy
  Hereditary disease of the muscular system with characteristics of weakness or wasting of skeletal muscles;
- Multiple sclerosis
  Chronic progressive nervous disorder - loss of myelin sheath around (certain) nerve fibers;
- Acute disorders leading to extensive paralysis
  e.g. Guillain-Barré syndrome - acute inflammatory demyelinating polyneuropathy (AIDP) in the most common form is an auto-immune disorder which affects the peripheral nervous system (PNS) - part of the larger peripheral neuropathy group;
- Severe polyneuropathy;
- Mitochondrial myopathy
  Not attributable to nerve dysfunction but rather affecting the 'energy factories' or mitochondria of muscle cells.

In order for BCIs to be accepted by user groups which have some residual control such as eye movement, a number of elements in BCIs need to be improved. The device's precision of control, speed, reliability, convenience, and complexity of applying sensors and using applications will need to be addressed. In addition, the cosmetic aspects of a BCI can be an issue, i.e. how the subject looks with the device in place (Daly, et al., 2008). BCIs that restore movement of limbs, although usually termed BMIs, are also possible with the first SMR-BCI (sensorimotor rhythm) demonstration by Pfurtscheller in 2005. The patient learned how to encode hand and arm movements through various stages of electrical stimulation of those limbs (via SMR increase and decrease) to grasp and lift a glass (Pfurtscheller, et al., 2005). Nevertheless observations of the literature on the success of BCIs (usually embodied by their ITR) need to be taking with a certain level of scepticism since it has been reported that in many cases potential subjects are pre-screened before a narrow selection is made, excluding poor performers or other factors negatively affecting ITRs (Jackson, et al., 2006). However, a good competitive ground for at least the signal processing contributions by BCI groups internationally has been provided over the last decade with BCI competitions (4 so far) for various BCI types, e.g. motor imagery, MEG-BCI, intracortical BCI (Blankertz, 2008). The question of how slow or successful a BCI needs to be in order to be considered at all is difficult to determine though. An anecdotal message of how important and relevant even the slowest BCI can be for the totally

muscularly impaired and how options are needed for matching the best BCI to the user was observed recently (Allison, et al., 2008). An eye surgeon in a locked-in state was able to dictate that he was going blind due to negligence by a nurse who forgot to administer regular eye drops and he then went further and prescribed the medicine he needed to alleviate the infection. This was achieved with a <0.096bit/min ITR with 60-80% classification using a galvanic skin response interface, where other BCIs and groups failed with this subject. Thus, the key issue for practical application of BCIs is to have a range of options, not just the fastest available at that time.

An understanding of the illness or disease is important when considering a BCI for a subject. Although it was previously accepted that ALS subjects remain largely cognitively sound with the disease affecting only the motor structures, more recent reports demonstrate that ALS can lend to cognitive dysfunction and there are reported techniques to identify these cognitive defects such as analysis of ERPs (Hinterberger, et al., 2005; Kiernan, 2009; Ogawa, et al., 2009; Raggi, et al., 2009). Furthermore a startling issue up to 2006-07 at least, was that no ALS patient who has entered into the totally or completely locked-in state (TLS/CLIS) has ever gained control of a BCI *unless* they have had previous training while in the less severe locked-in state (reported in Birbaumer, et al., 2007). There was one exception in the literature of a CLIS subject using a pH-based BCI for 3 hours into the CLIS state, but no control thereafter. However, using a recently developed optical BCI (which is the modality used in this dissertation) a group performed a study on 23 LIS subjects and on 17 CLIS subjects. Over 70% of the LIS demonstrated cerebral blood volume changes during cognitive tasks such as mental arithmetic, but only 40% of those in the CLIS (Naito, et al., 2007). The authors suggest that it may be due to consent or interest by these subjects (even though they gained consent from family members) but perhaps it may be an issue with cognitive dysfunction in some subjects (up to 50% in some studies) (Kiernan, 2009).

In regard to ALS patient depression, however, it may have been assumed (incorrectly) by a patient's family or health carers that patients with severe motor impairment would have relatively increased probability of depression and a desire to opt out of life. Recent research has shown that they are no more likely to have depression than healthy individuals and with a proper communication strategy they can lead lives that they consider happy and productive (Robbins, et al., 2001; Lule, et al., 2005; Birbaumer, et al., 2007).

In addition to the restoration of communication, there are two other groups that BCIs are being applied to - 1) the area of restoration of movement and neurorehabilitation, and 2) applications for the general public for gaming and novel computing.

3.13.2 Movement restoration and Neurorehabilitation

Another important area of BCI research that has been investigated recently is the ability of a BCI to train a subject to gain back some degree of motor competency, perhaps after a stroke. A huge area that affects and costs millions every year is stroke. In this case, the subject is under pressure for time with possible cerebral atrophy in under-utilised cerebral tissue and associated nervous areas that have been affected by the stroke such as the motor cortex. A user must train to regain control over these motor commands. An exciting facet of neural tissue is its plasticity and adaptation continually across a lifetime - or more specifically activity-dependent CNS plasticity (at the level of synaptic, neuronal, or microcircuitry of the CNS). This is not limited to healthy individuals but is also possible in subjects who endure disease or trauma. However, this plasticity can have a negative impact as well as a positive one, whereby if abnormal movements are made repetitively, this could effectively train the motor area incorrectly, perhaps even making it worse, promoting abnormal motor function (Daly, et al., 2008). Thus, there are particular strategies, usually training of the upper and lower periphery, to restore normal motor function. However, BCIs can intervene here in two ways. One is where the subject is asked to continually generate motor specific brain signals such as mu rhythms with feedback, and the other is using those signals to control a device that assists movement of the affected limb. These techniques are mooted as being able to induce more normal activity-dependent CNS plasticity to restore normal motor function. Biofeedback using an optical BCI has been conceptualised in a recent paper here at Maynooth (Ward, et al., 2007) (explained further in Chapter 7).

3.13.3 Other users and the general population

The general public are also likely to be excited with the possibility of controlling their environment with a BCI. However, in addition to the novelty aspect of such BCIs for the general population there are further applications of BCI in serious gaming (Soraghan, et al., 2006; Nijholt, 2009) (which was explored here at Maynooth Soraghan, et al., 2006), brain based biometric authentication (Palaniappan, et al., 2007), and automobile monitoring (Ruei-Cheng, et al., 2004).

Whatever the current users of the system, the area of BCI is rapidly growing in techniques, approaches, and classification methodologies. In fact, at the 3rd international BCI meeting in 2006 it was reported that over half of all peer-reviewed BCI publications had been published in the preceding 2½ years (Vaughan, et al., 2006b). Thus, the question needs to be asked, what are the current issues and future prospects of this thriving scientific community.

3.14 Future prospects

There are many issues to be dealt with in BCI research, perhaps the most significant of which is to develop BCIs that can be used in the home by completely immobile users, and who can do so independent of technical laboratory professionals - which ultimately would be too costly and unfeasible in the long term. This and other issues are outlined briefly in the following subsections. First, the current issues and limitations in BCI research are revealed, followed by future expectations in the field.

3.14.1 Current issues and limitations

The current issues should (and do) reflect those questions arising and debated at the international meetings and workshops. A brief description is given of the major issues:

What signals and methods are most optimal for BCI use?

Currently various signal-possibilities are available to the starting-out BCI researcher, the most likely of which to use are the EEG-based signals according to recent reviews. However, there are limitations with EEG-based signals in comparison to those other methods mentioned earlier, e.g. spatial resolution. It should be noted that at present there is no absolute preferred method, whereby in fact it may be suitable to combine methods for greater statistics, or perhaps jointly applied during the training period as seen in the sections above, e.g. MEG for training and EEG as the final, portable BCI (since they share the same electrical signal characteristics). Metabolic BCIs such as fMRI and NIRS-based BCIs are of current interest reflecting metabolic activity which may perhaps reflect physiological characteristics in the disabled that electrical based BCIs cannot, although this needs to be substantiated. The current state of the art of NIRS-BCIs will be expanded upon in the next section, leading into the necessity to develop a flexible multichannel OBCI. There is also a need to have choices for the user where some methods may not work (Allison, et al., 2008) for a variety of reasons, e.g. trauma or disease affecting the signals of interest. A comparison of methods is shown in Table 3-2.

How best to advance signal processing methods?

With the community expanding, many techniques are being developed and in order to reduce redundancy in the BCI community (i.e. unnecessary replication) it would be useful to have a forum of sorts to share ideas and established methods. Of course, replication of another's work is not always 'redundant' since it may raise important criticisms or indeed appraisals (e.g. in early biofeedback, Neal Miller discovered that initial claims of ANS

mediation using operant conditioning were unsustainable over further studies). Another forum is the scientific literature, although this is expanding rapidly, which can make it more difficult to be thoroughly aware of signal processing advancement. However there are at least four areas that can and are attributing to advancement in this area: 1) International BCI meetings and workshops (Wolpaw, et al., 2000a; Vaughan, et al., 2003; Vaughan, et al., 2006b) - these provide an invaluable communion of ideas and reports emerging from these are equally invaluable, especially to those who were not in attendance; 2) General purpose software and online forums - BCI2000 (http://www.bci2000.org/wiki/index.php/Main_Page) and 'www.bci-info.org', respectively; 3) special issue publications in BCI - these allow for focused publication of the current state of the art. Four have emerged in IEEE publications so far:

- IEEE Signal Proc. Magazine, 25(1), 2008;
- IEEE Trans. Biomed. Eng., 51(6), 2004;
- IEEE Trans. Neural Sys. Eng., 11(2), 2003;
- IEEE Trans. Rehab. Eng., 8(2), 2000.

The fourth (4) area enabling advancement in the area are the BCI competitions that have taken place (Blankertz, 2008). To foster advancement in the BCI community, to date four BCI competitions (in June 1999, 2003, 2005, and 2008) have been held (Blankertz, 2008) each with specific goals by the organisers but all aiming to validate signal processing and classification methods for use in BCIs. The 1st competition deliberately included only a small community of applicants as a first implementation to test how such an event could work. Subsequently, 59 applications submitted to the (international) 2nd competition using data sets from 4 EEG-based BCI groups. In 2005, 99 applications to the 3rd meeting incorporated 5 data sets from 5 BCI groups, and finally many more applications to the 4th BCI competition based on 5 data sets from four BCI groups. The 4th competition included data from motor imagery for EEG, directionally modulated low frequency MEG activity for wrist movements in four directions, and ECoG for individual flexions from five fingers. All details and links to all the competition's goals, data sets, results, organisers, review publications of the competitions, and other references can be found at the website hosted by Benjamin Blankertz (Blankertz, 2008). It could be said that perhaps a lack of bias and a greater level of assuredness is achieved by these competitions since results are more representative of international BCI state of the art. They also allow for advancement in BCI-areas not as accessible by most researchers since datasets are made available for multiple biopotential types, for example MEG and intracortical recordings.

Invasive or non-invasive?

As has already been covered in previous sections this is a question that for the moment has been answered, that is: currently non-invasive BCIs operate comparably with invasive approaches (Wolpaw, 2007). In a study in the paper just cited an invasive and non-invasive group's highest performing users were compared in a 2-D cursor centre out task control. Both produced ataxic-like (jerky) movements, expressed by Wolpaw as being like a user with a cerebellar deficit trying to control a joystick in a 2-D cursor session. In addition movement time, precision, and hit rate (~90%) were very similar. However, invasive BCIs may have more potential since they have access to lower level neural structures, e.g. the ability to measure single unit recordings from neurons. Nevertheless, current research in ECoG-based BCIs seem to hold promise as a intermediately\less invasive technique with capabilities perhaps thought only possible with intracortical electrode recordings - i.e. local field potentials can be used for multidimensional control of a neuroprosthesis with decoding of subtleties such as arm direction also possible.

However some success with completely non-invasive techniques has been reported for MEG and EEG based BCIs, in decoding movement direction for the same effector (MEG - Waldert, et al., 2008; EEG - Gu, et al., In Press, Corrected Proof). For invasive-BCIs to be widely used and accepted they have to first contend with questions of safety, convenience, reliability over long-term use, stability of the signal, and ultimately significant advancement over non-invasive techniques, such as an ITR closer to that of normal human capabilities, e.g. reading. See (Wolpaw, et al., 2000a; Vaughan, et al., 2003; Birbaumer, 2006) for more on the discussion of invasive versus non-invasive techniques.

Unsupervised BCI applications in the home?

The question of advancement of an area is personified in practical, real world applications for those in most need (Vaughan, et al., 2006a). Indeed, the last international BCI meeting (Vaughan, et al., 2006b) was themed 'Making a difference' highlighting the need to move from the laboratory to the home with minimal technical intervention. This has been carried out to some degree by at least one group (Wadsworth, Albany, New York), as mentioned in previous sections. More applications should be developed over the next decade to realise the initial vision of Vidal in the 1970's.

BCIs for the totally locked-in\wholly paralysed?

Although Birbaumer et al argue (Birbaumer, 2006; Birbaumer, et al., 2007) that no

Bio-Recording Technology	*Temporal Resolution*	*Spatial Resolution*	*Signal Source*	*Advantages*	*Disadvantages*
Scalp EEG	<1ms	~1cm	Postsynaptic Potentials	Non-Invasive; portable; Low cost;	Low spatial resolution
Intracortical	<1ms	Single neuron	Neurons AP	Excellent spatial resolution	Limited spatial coverage; highly invasive; currently unknown long term stability, reliability, and extent of tissue damage
ECoG	<1ms	1mm	Postsynaptic Potentials	Low cost; extended bandwidth	Invasive; limited to surgical direction - spatial coverage
MEG	<1ms	5mm	Magnetic fields from brain activity	Non-invasive	Very expensive; limited resolution for deep structures; bulky
fMRI	~1s	3mm	HbR paramagnetic	Excellent spatial resolution	Very expensive; bulky; Slow haemodynamic response
NIRS (slow)	100ms	~3cm	HbR and HbO_2 changes	Non-invasive; portable;	Slow haemodynamic response
NIRS (fast - neural)	ms		Neuronal firing (optical)	High temporal and spatial resolution	Requires many averages; Currently elusive from the scalp

Table 3-2: BCI comparisons (by bio-recording technology) for common characteristics such as spatial resolution, temporal resolution, signal source, and the advantages and disadvantages of the various modalities.

CLIS subject can utilise a BCI without prior training in the LIS, it is still an open question that needs to be confirmed by more research groups with a wider subject population with perhaps more studies using optical\metabolic BCIs (Naito, et al., 2007).

Training time length?

The length of training time is key question in BCI research. It is known that many BCIs require hours and months of training (e.g. Birbaumer, et al., 1999; Spinney, 2003) but some recent research with advanced machine learning algorithms (Blankertz, et al., 2008) has perhaps called to question the demand been placed on the user in some implementations that require this lengthy training period. Nevertheless, there are other techniques that are more natural to the user and require almost no training, e.g. P300-, SSVEP-, and perhaps metabolic BCIs (fMRI and NIRS). However, these are either deemed dependent BCIs (P300, SSVEP), are impractical at present, or are currently underdeveloped (NIRS). Neuroplasticity takes time and so perhaps true learning of this new skill with independent BCIs will require training.

Speed and performance - information transfer rates (ITR)?

There are three key markers of BCI transfer rate: speed, accuracy, and number of selections (Cheng, et al., 2002). However, speed in a BCI is almost always seen as synonymous with the performance of a BCI. To this end, the then current performance rate reported at the first international BCI meeting was 5-25bits/min (Wolpaw, et al., 2000a). Some 7-9 years later similar average rates are reported (up to 35bits/min) in review papers (Nijholt, et al., 2008; Schalk, 2008) but up to 30bits/min in P300-based BCIs (Daly, et al., 2008). Nevertheless, an account of the ITRs achievable by humans using normal means (mouse, reading, morse code) are described illustrating current BCI rates of 0.41bits/sec (not bits per minute) with the lowest normal communication rate by other means being between 1-50bits/sec with reading being two orders of magnitude higher (~41bits/sec) than BCI rates. The argument can be made though that although this is a reason to contemplate BCI's potential, very low rates of more than an order of magnitude lower than 0.96bits/min have been used for the locked-in subjects where no other means were possible (Allison, et al., 2008). The same article sites other groups who have witnessed users continuing to use BCIs that have very slow rates allowing less than one yes\no answer per minute or one word every five minutes. However, higher ITRs are generally more favourable, at least as an option to the user.

User illiteracy and high-performance variability?

Although the aim of any research in BCI is to have every user be able to use the BCI device with good performance, there is considerable evidence that there is high variability between subjects and even within a subject (inter and intra subject variability), and that some users will not be able to use a BCI at all (Nijholt, et al., 2008). Performance can change across days, sessions, and between trials (Wolpaw, 2007). In terms of asynchronous BCIs it has been reported by Popescu and Blankertz in (Nijholt, et al., 2008) that they estimate that 20% of subjects do not have strong enough mu rhythms for BCI control, with 30% having a performance of <20bits/min, and 50% of subjects with performance in the currently moderate-to-high range (20-35bits/min). The proposed solution to maximise potential is to calibrate for subject specific tasks and frequency bands or features, since anatomical differences may hinder detection of some signals, e.g. EEG is more sensitive to signals originating from cortical folds/gyri, and not to tangential cortical tissue (w.r.t. scalp electrodes).

'Idle\rest' class in asynchronous BCIs?

The final issue (although there are more (Wolpaw, et al., 2000a; Wolpaw, et al., 2002; Vaughan, et al., 2003; Birbaumer, 2006; Vaughan, et al., 2006b; Birbaumer, et al., 2007; Nijholt, et al., 2008) dealt with here is that of the idle class, specifically pertaining to asynchronous BCIs. It is simply the question as to how the user can indicate to the BCI when to stop responding to his\her brain signals - i.e. how to turn it on and off (Nijholt, et al., 2008). Two main solutions that have been looked at are: 1) to trigger the switch by resting for a period, thereby inducing elevated and sustained alpha waves which can be detected by the signal processing unit. However issues of involuntary variation of alpha in physiology as opposed to experimentation settings (e.g. during fatigue) and alpha induced drowsiness hamper its use. This solution pertains to frequency bands specifically for electrophysiological signals but correlates may be usable for other biopotentials which reflect rest in a subject. 2) The second solution is the use of an active task in control of the on\off switch, but could be seen as a large waste of potential performance of the device since it would have the effect of reducing the number of classes\tasks available for BCI operation.

Other issues in BCI research include: calibration procedures; stability of the brain's existing activity patterns; false activation of the BCI when using overt tasks; effects of the BCI on the user's mood; quality of life; productivity; extent to which a users desires and personal environment are being met; set-up and other costs; amount of ongoing technical support needed; continual online adaptation of the user and BCI software; sensor application

and lifetime; user-attention span, and the comparability and adoption of standards by the BCI community (Mason, et al., 2005; Jackson, et al., 2006; Mason, et al., 2007).

3.15 Chapter Summary

BCIs still have many unresolved issues for widespread dissemination for the disabled and even more so for the healthy user where BCIs have to provide information transfer rates closer to more conventional devices, e.g. the computer mouse. Nevertheless, there have been significant trials and some clinical applications and even home applications of BCIs that have enabled severely disabled users to communicate. The question still remains - which methodology is the best: EEG SMR, auditory-P300, visual-P300, VEP, SSVEP, fMRI, MEG, or NIRS based BCIs? However there are distinct differences and trade-offs between these and perhaps the best answer is to state that the user should be supplied with alternatives or choice, e.g. perhaps training in the more rigid types such as MEG and fMRI, to be later moved to more portable modalities, e.g. EEG or NIRS, respectively. Or perhaps some systems will not work for some users perhaps due to tissue damage or poor signal strength, where other techniques may be able to interrogate more areas, e.g. EEG SMRs can be affected by poor determination of signals from cortical folds, where perhaps NIRS can interrogate those areas more directly.

There are many users and applications that BCIs can support along with the recent topic of neurorehabilitation which relies on the activity-dependent brain plasticity phenomenon. More specifically it is interesting to consider this plasticity and the role of the cerebral cortex, as outlined in a report recently (Wolpaw, 2007). In this publication, Wolpaw reports that the CNS's output is not the cerebral cortex, but rather the cortex is simply an intermediate part of the whole process within the CNS - especially for motor tasks. While the cerebral cortex being activated is significantly correlated to the motor tasks, it may not have the smooth, refined possibilities of a resilient CNS using filtering and adaptive processes from the cerebellum and basal ganglia (to name a few) and more terminally, the spino-motor neurons. Thus, the plasticity process in the cortex needs to occur in such a way that the cortex can act as a CNS output device, as if it is bypassing all the lower CNS structures. It is suggested by Wolpaw that this may be a reason for the current ataxic control in 2-D cursor control for both non-invasive and invasive methods, even with extensive training.

Along with the issues just reviewed, there is in particular one question which this dissertation is posed towards - that of the potential of multichannel NIRS methods for BCI - or an optical BCI. In particular it is of interest to investigate the contribution of a versatile

multichannel CWNIRS instrument for optical BCI (OBCI) applications, and what it can offer in terms of perhaps increased spatial coverage of the cerebral cortex over the single\dual channel OBCI developed by a predecessor here at NUI Maynooth, Ireland (Coyle, et al., 2004). The next chapter deals with optical BCIs and how they have emerged since 2004 to the present time, what the current issues are, and which ones are being addressed in this project. It considers the research question posed by this dissertation.

CHAPTER 4

PROBLEM STATEMENT: THE NEED FOR A VERSATILE MULTICHANNEL CWNIRS INSTRUMENT FOR OPTICAL BCI APPLICATIONS

4.1 Introduction and Research Question

The following chapter considers (along with Chapter 1) the problem statement of the body of work presented. The nascent area of optical BCI research has only been established in the past eight years, and significant questions still remain even in the field of NIRS such as the processes behind neurovascular coupling - although recent research has brought some closure to cerebral microcirculation at the level of cortical columns (Mayhew, 2003; Thompson, et al., 2003). The proposed hypothesis for this current work is that a multichannel CWNIRS instrument for optical BCI can improve on the single\dual channel device first developed by Coyle (Coyle, 2005). The main contribution of the current dissertation is the design, development, and detailed exposition of a multichannel real-time CWNIRS system as an instrument for BCI applications.

The chapter starts with a brief review of the history of OBCIs, and then the motivation and challenges of a multichannel OBCI are described. Finally, the methodology, contribution, and significance of the work are outlined. Note that the fundamentals of NIRS, FNIRS, and CWNIRS have already been dealt with at the end of Chapter 2.

4.2 The History of Optical BCI

The first peer review journal publication of an optical BCI was published by Coyle et al in 2004 (Coyle, et al., 2004). Coyle essentially sought to assess the feasibility of using optical measures of functional brain activity as a control channel for a BCI. In this work she utilised elevations in concentration changes in oxyhaemoglobin ($dHbO_2$) during predefined stimulus periods (synchronous BCI) that were above the mean $dHbO_2$ level in the preceeding rest period - i.e. above the most recent baseline. Levels of deoxyhaemoglobin (dHbR) were not considered since they were more difficult to determine, potentially due to a lack of localisation (due to the limited number of channels) and lower optical power output from the 760nm light source (LED) used (the shorter wavelength is more sensitive to changes in HbR than HbO_2). Furthermore, localisation was difficult with only a single channel device. A further exposition of the work by Coyle was presented in her PhD dissertation (Coyle, 2005) with various studies assessing motor imagery control signals. It also demonstrated an OBCI in a so-called 'Mindswitch' with binary selection of one of two coloured boxes which took approximately 1 min. Throughout this work various stages of assessing appropriate signals for optical BCI, physiological noise removal, and other related issues were reported (Coyle, et al., 2003a; Coyle, et al., 2003b; Coyle, 2004b; Coyle, 2004a; Coyle, et al., 2005). During 2006 Soraghan and Matthews (Soraghan, et al., 2006) explored the possibility of using a dual-channel instrument based on motor imagery in a gaming environment (using a 3-D graphics engine). Detected $dHbO_2$ and dHbR were used to control the arm movements of an avatar on screen. The user was required to elevate the arm to a predefined level based on predetermined threshold levels. At the end of 2006 Sitaram et al (Sitaram, et al., 2007) explored left and right motor imagery classification techniques offline (Support Vector Machines (SVMs) and Hidden Markov Model (HMM)) with a commercial multichannel system reporting average accuracies of 73% and 89% for the models, respectively. In a further publication by Coyle et al (Coyle, et al., 2007) they reported on work carried out for dual-channel experiments reported in her dissertation on the 'Mindswitch' OBCI application. Like other BCI modalities (e.g. EEG), optical BCI has extended from a pure communication tool and was proposed for neurorehabilitation purposes in 2007 as a means to extend the applicability of constraint-induced movement therapy using biofeedback of motor cortex activity (Ward, et al., 2007). This has potential applications for stroke sufferers who have no residual motor control of for example an effected limb, and requires a more direct measure of fundamental functional cerebral activity in control of that body part (see experiment and discussion in Chapter 7).

The first application of an OBCI applied to disabled users, specifically ALS, was reported in (Naito, et al., 2007). A communication means for these subjects was attempted using only measures of cerebral blood volume utilising only one wavelength of light and one detector on the frontal lobe using various mental strategies such as mentally singing a fast song. They used dynamic measures of changes in amplitude and phase of CBV (cerebral blood volume) and reported that subjects in ALS but not TLS (totally locked-in) achieved rates of 70%. Moreover, ALS-TLS subjects were shown to have poor accuracy rates of 40% which for the moment appears to coincide with findings in EEG-based BCIs for this subject base - i.e. user's in the TLS who have not had previous BCI training before being in the TLS state have shown to have no success in controlling a neural prosthesis (Birbaumer, et al., 2007). The device used by Naito is very similar to that developed by Coyle (Coyle, et al., 2004). In 2008 a further device similar to Coyle's was also used by Bauernfeind et al (Bauernfeind, et al., 2008). This group (Graz, Austria) utilised a commercial multichannel device to compare functional responses to mental arithmetic tasks from this instrument against the single-channel system they developed based on Coyle's OBCI architecture. Of particular interest in that work was an analysis of the FNIRS frontal lobe response (particularly at 10-20 electrode position Fp1) to mental arithmetic. In most subjects an inverted response relative to that found at the motor cortex for activity (a decrease in $dHbO_2$ and an increase in dHbR at the frontal lobe) was recorded from most subjects by both the single-channel and the multichannel system. This finding is also reported by the author (see Chapter 6), with both responses (inverted and non-inverted) occurring in different experiments, potentially due to either activation or deactivation in the cortical tissue analysed (see Chapter 6 for discussion).

Most other publications arising since then concern signal processing methods used in optical BCI to remove physiological noise and classify events which have been reviewed recently (Matthews, et al., 2008a). Matthews is currently researching signal processing methods for optical BCI in tandem with the OBCI instrumentation developed by the author (Soraghan, et al., 2008a; Soraghan, et al., 2009), which is being reported in this dissertation. Further recent publications have arisen which utilise commercial multichannel NIRS instruments - e.g. ETG-4000, Hitachi Medical Corporation - for detecting functional activity with the goal of controlling an OBCI (Tsubone, et al., 2008; Utsugi, et al., 2008). Thus, the area of OBCI has begun to emerge with various groups contributing mainly to the signal processing aspect of OBCI. However, the dissertation reported here aims to address the hypothesis of a multichannel system extending\improving on specifically the dual-channel custom-made OBCI device developed by Coyle.

4.3 Problem Statement and Motivation

Up to the year 2000, BCI was almost exclusively pursued utilising electrical measures of cortical activity - mostly from the intact scalp, i.e. using EEG (Wolpaw, et al., 2000). Recently, more BCI modalities have arisen such as MEG-based BCIs and the metabolic oriented fMRI-based BCIs, although EEG-based systems are still the dominant choice by research groups (Mason, et al., 2007). This is perhaps due to the practicality, portability, bedside usability of EEG, and due to the technological development it has received since Berger's pioneering work (Berger, 1929). Subsequently Coyle introduced NIRS-based BCI to the BCI community (Coyle, et al., 2004) developing a single\dual-channel custom-made instrument for BCI. One justification for an fMRI-based BCI and indeed MEG-based BCI were that they are postulated as being potential training grounds for BCIs. In particular MEG-based BCIs were directly comparable to EEG-based BCIs since the recorded features of cerebral effort were similar and thus interchangeable (Mellinger, et al., 2007; Waldert, et al., 2008). Ultimately a BCI should be portable and have use at the bedside, which makes MEG and fMRI based systems currently impractical, but are nonetheless useful additions to BCI research. Moreover, fMRI has a correlate with NIRS-based systems (in HbR) and potentially if needed, could also be an interchangeable training ground (or perhaps simply for localisation) for portable NIRS-based BCI. For this project, fMRI work on functional motor activity was conducted to reveal neural substrates that were both independently and simultaneously activated (see Chapter 6). This millimeter spatial resolution offered by fMRI could be used to determine an intended user's cortical regions of maximum activity and this information could then be utilised in a NIRS-based BCI. Nevertheless for single-trial NIRS, specific events may vary to those determined from grand averages established from fMRI, although fMRI can and has been used in a single-trial implementation (Yoo, et al., 2004; Weiskopf, et al., 2007).

4.3.1 Why NIRS?

A NIRS-based BCI offers many potential advantages for BCI and these will be mentioned shortly. However, the most commonly reported limitation of a NIRS-based BCI is that it is intrinsically limited by the time taken for a functional response to be elicited (~5 seconds). Thus, typically a functional response is determined by a large increase in HbO_2 and a significant but smaller decrease in HbR, taking approximately 4-8 seconds to peak, with a similar time to return to baseline. Thus, the potential bit rate for a single channel NIRS-BCI using this haemodynamic feature is ~6 bits/min. However, there are four key points (but also other advantages listed later in this section) in favour of this relatively slower technique:

1) **Sufficient Speed:** Although in general greater speed is favoured in terms of computer processing and essentially the time it takes to carry out a computational task, these desires may not always be similar for such an essential communication tool as a BCI. Recently, Allison et al reported how a 0.96bit/min device can still allow affective communication and they review that even slower systems have been continued to be used by patients (Allison, et al., 2008);
2) **Alternative Channels - choice:** Continuing from the previous point of speed is the element of choice. Although a certain BCI may emerge with the highest bit rate (e.g. the SSVEP-BCIs with up to 68 bits/min (Gao, et al., 2003)), some require the application of external stimuli (extraneous) which can be a cause of irritation for the user. Thus, choice should feature in the selection of a BCI that perhaps reflects a user's preference. A NIRS-based BCI offers an alternative passive (endogenous) channel for BCI research;
3) **Specificity:** Certain neural substrates could become impaired as a result of the particular disability of the user such as severe cerebral palsy (Daly, et al., 2008). As such NIRS offers high parameter specificity of the haemoglobin species being measured (Obrig, et al., 2003) and can exhibit distinct (independent) functional activations such as motor and visual evoked responses (Plichta, et al., 2006). Thus, as reported by Daly et al, BCI techniques most effective will depend on the underlying CNS abnormality. They also specify that certain signals (e.g. SMRs) may be absent in some users due to the cerebral impairment and so alternative signals would be required. Thus, NIRS-based BCIs may be able to provide this alternative. This again links to the idea of variety and choice for BCI. Furthermore, a hybrid EEG-NIRS device could be effective in this case to establish alternatives, since NIRS optical signals would not interfere with the EEG recording, i.e. it is electrically isolated using photonic energy for interrogation of cerebral tissue;
4) **Outlook:** Finally, it should be noted that there are optical signals found from invasive studies (Thompson, et al., 2003) that are localised to cortical columns and others reporting high temporal responses on the order of milliseconds (Obrig, et al., 2003). These have been mooted as being measurable non-invasively using a 1000 averages or more (Gratton, et al., 1997; Wolf, et al., 2004) for a 0.07% change in signal intensity (Franceschini, et al., 2004) although other groups have reported an

inability to reproduce some of these results (Obrig, et al., 2003). However, it is restated here that further advances in technological development to enhance the SNR of in vivo NIRS (ivNIRS) to detect these signals related to neuronal cell swelling, may provide an avenue for a faster optical BCI.

As an aside, it should be noted that many researchers state that NIRS has a low temporal resolution - it does not. Temporal resolution for NIRS is on the order of ~100msec, but what is meant\intended really is that NIRS has a haemodynamic feature that has a large time constant - i.e. a concentration change in HbO_2 and in HbR takes 4-8 seconds to peak. In addition, there are potentially earlier transient features that could be utilised such as the elusive initial dip, sometimes found in fMRI (Buxton, 2001; Buxton, et al., 2004) but more research is needed to investigate this in single-trial NIRS.

Optical BCIs have further advantages such as: 1) practicality, 2) providing a low-cost alternative relative to other metabolic BCIs (e.g. fMRI), 3) portability (including potential wireless implementations Muehlemann, et al., 2008), 4) suitability for the bedside (required for BCI), 5) being non-invasive, 6) suitability for long-term use, 7) being safe, 8) having a high temporal resolution (~100msec), 9) user-friendliness (sensors don't require gel as in EEG), and 10) requiring less training (Coyle, et al., 2007) since the functional activity is from a more natural (direct) mental procedure compared to the intense learning required in some BCIs - e.g. SCP-based BCIs. Months of training can be required for such devices, leading to frustration and perhaps abandonment of the device since the user doesn't normally have control over these signals - they are learned (Spinney, 2003).

4.3.2 Justification for multichannel-OBCI

Many commercial multichannel NIRS instruments are available (Wolf, et al., 2007) but as reported by Wolf, they are typically built with specific applications in mind - such as a time-domain instrument for quantitative assessment of neonatal cerebral oxygenation monitoring. Thus, these systems tend to limit the flexibility that a custom device could achieve for BCI such as access to the unprocessed light levels from the detector and being able to develop advanced modulation schemes which may improve signal-to-noise ratios, which is paramount for highly attenuating tissue spectroscopy (i.e. seven to ten orders). Furthermore, most of these instruments are based on laser diodes and pose a potential risk (e.g. retinal damage) due to coherency effects. As will be discussed in Chapter 5, LEDs are sufficient for use as a light source in CWNIRS since the short transport scattering length of NIR light in tissue means any beam (e.g. from a laser diode) effectively becomes diffuse after the first few millimeters of penetration. Moreover, cerebral tissue of interest is 2-4 cm

below the scalp surface. Thus, for long-term BCI applications with unlimited exposure an LED-based solution is more satisfactory especially for vulnerable immobile populations such as ALS subjects. Furthermore, LEDs have a longer lifespan (~80,000 hours), and are more straightforward to modulate.

A multichannel implementation of an OBCI is hypothesised to increase the potential performance over what a single channel device can obtain. That is:

- Since more spatial coverage of the cerebral cortex (from the scalp probes) is obtained by increasing the number of channels, potentially more features are expected to be available to the BCI researcher that could be used for control of the device. Furthermore, visual, auditory, motor, and cognitive features have been measured using FNIRS and some of these could potentially be used for volitional control of an augmentative device. (However, most researchers have considered grand averages of these to examine the integrated effect of multiple instances of some task, e.g. finger flexion. Thus, a single-trial assessment of some of these features are explored in Chapters 6 and 7);
- With increased spatial coverage comes the possibility of localisation of regions of maximal activity to a mental event. These can only be reliably explored with a multichannel device, and thus the multichannel device developed in this dissertation facilitates those investigations (see Chapters 6 and 7);
- A multichannel instrument could be used for effectively overcoming anatomical differences between subjects, which could introduce inter-subject variability in BCI performance;
- Lateralisation of events for BCI is important and could be assessed. Since multi-regional functional activation to tasks, e.g. motor events stimulating cognitive areas or vice versa, or indeed bilateral activation from motor imagery (Coyle, 2005; Wriessnegger, et al., 2008) may increase classification difficulties, additional channels may be useful to compare signal strength from one hemisphere to the other. This is explored in Chapter 6 and 7 for mostly overt motor tasks;
- Additional channels also allow the researcher to develop noise cancellation techniques, especially immunity to global haemodynamic effects. The BCI group at NUI Maynooth is currently working on adaptive cancellation techniques to remove physiological noise and other artefacts (Matthews, et al., 2008a) based on the provision of multiple channels and instrumentation from this currently reported dissertation;

- A custom-made multichannel device also allows for exploring ways to reduce set-up time and perhaps deliver more computational time to fewer channels after an initial calibration. In other words, if multiple channels can identify similar localised functional activity, it may be possible to reduce the redundancy and remove some of those channels - if they are not necessary, e.g. they may be used for noise cancellation. This reduces the equipment placed on the subject and perhaps allows for more advanced online signal processing (although not reported in this dissertation) since more time could be allocated if fewer channels were being analysed;
- More channels assessing more functional cerebral events may allow for improvements in the potential data rate of the device from that of a single-channel device (6 bits/min). Furthermore, one cerebral region of tissue which is activated could be allowed to rest (return to baseline) while another basal-state region of tissue essentially takes over straight away, thus reducing the time needed for each event to be identified.

In Section 4.2, the chronological publication record of optical BCI was reviewed. In its 8 years, a custom-made dual-channel device was developed by Coyle (Coyle, et al., 2004; Coyle, 2005; Coyle, et al., 2007). Most others implemented signal processing techniques operate on the back of a commercial NIRS instrument, except for Bauernfeind (Bauernfeind, et al., 2008) whose essentially developed a single-channel version of the design from Coyle to compare against a commercial multichannel instrument. However, the design from Coyle was never intended to be a unit to be extended (i.e. modular), using multiple lock-in detectors etc. For BCI, a more flexible scheme was and is envisaged and is developed in this dissertation. Flexible in the sense that firstly, demodulation was moved completely into software using high-end *National Instruments* acquisition and generation cards and a data management scheme to ensure data buffering and triggering in a PCI eXtensions for Instrumentation (PXI) model. Moreover, for improved spatial specificity, multiple wavelengths were integrated into single high-power LED packages, custom designed and produced by *Opto. Diode Corp.* Thus, the proposal and methodology for the various design features of the versatile multichannel OBCI instrument are described next.

4.4 Methodology, Contribution, and Significance

The multichannel CWNIRS instrument developed for OBCI in this work consisted of a number of individual elements that make up the final instrument. The contributions of this

work were outlined in Chapter 1. However, the methodology for implementing such a device is considered next and is described over the following chapters.

Chapter 5 describes the design considerations and choices in detail for each stage of the instrument, such as the light sources, detectors, data acquisition, generation, triggering and buffering, to name a few (Soraghan, et al., 2008a). The optical drivers to supply the sources and a safety assessment of the sources used are also considered as reported in recent publications (Soraghan, et al., 2008b; Soraghan, et al., 2009). The modulation strategies and software interface are also developed as a means to interact with the hardware and optics (Matthews, et al., 2008b). The flexibility of the system to allow for multiple modulation schemes is one of the significant features of the device. The software interface also allows for rapid prototyping of functional tasks and prompts to the user, some of which were developed with a colleague at NUI Maynooth (Matthews, et al., 2008b). Flexible software control of the light sources is also employed for calibration at the pre-experimental checks stage of a measurement, as well as a facility to identify channels that are causing the most significant saturation on a detector, (e.g. when light has been directed toward the detector without having to go through the tissue, as would be the case if a probe holder was incorrectly fitted to the subject). Furthermore, optical probe holder configurations are considered for different functional tasks, e.g. motor and frontal activity.

Chapter 6 considers a validation of the instrument along with various measured physiological phenomena being reported - cardiac pulse from the head, haemodynamic spatio-temporal pattern to blood vessel occlusion in the forearm, and haemodynamics from the human head. These measures provide some validation of the ability of the instrument and intervening software to be able to identify haemodynamic events over time. A series of fMRI experimental protocols for common motor tasks used in BCI are reported in order to validate some of the protocols that would be used in a NIRS-based BCI including overt tasks for neurorehabilitation. Subsequently functional activity from the human head using the multichannel CWNIRS instrument in response to motor activity and cognitive tasks are recorded and analysed. The motor activity measured using fMRI were used as an aid to identify regions of maximal activity, which could be used as a cross-modal confirmation of the ability to evoke distinct patterns of metabolic effort.

Chapter 7 looks at preliminary optical BCI experiments to motor activity using biofeedback to control a robotic arm. This experiment was part of a study in the use of NIRS for stroke rehabilitation. The study is also considered in light of an OBCI experiment on four subjects with biofeedback to overt motor tasks commensurate with a variant of constraint induced movement therapy using a neural prosthesis. The ability of the multichannel

CWNIRS system to assess localisation and lateralisation of motor tasks is also presented, which would feature important for OBCI implementations since a bilateral activation may limit the potential data rate of such a BCI. Responses to motor imagery and shorter stimulus periods are also reported. Finally, Chapter 8 concludes with a discussion of the contributions of the work and some thoughts on possible future developments.

CHAPTER 5

DESIGN AND DEVELOPMENT OF THE MULTICHANNEL CWNIRS INSTRUMENT

5.1 Introduction

The central element of this project was the design, construction, and development of a flexible multichannel CWNIRS instrument capable of determining specific cerebro-vascular characteristics which are correlated to cerebral functional activity. There are many commercially available near-infrared imagers (Wolf, et al., 2007), whereby different devices are designed with different applications in mind (and different tissue types). Thus, some imagers may only be suitable for certain study groups, e.g. for neonatology less sensitive detectors are needed due to the relative transparency of the neonatal head (Wolf, et al., 2007). In addition, more sensitive detectors may be unsuitable where ambient light interference would hamper measurements, such as in a clinical setting, although perhaps these may be compensated by optical shielding, filtering, or perhaps DSP.

In the case of functional brain imaging studies for BCI using FNIRS, relative concentration *changes* in chromophores, i.e. functional detectability, are sufficient for use in an optical BCI. A more thorough description of the design considerations specific to a multichannel CWNIRS instrument for BCIs is required, and is reported in the sections to follow.

The first prototype built at NUI Maynooth (Coyle, et al., 2004; Coyle, 2005; Coyle, et al., 2007a) established the applicability of FNIRS in accessing functional activity in the brain in a single-channel NIRS system specifically for BCI. However, as already described, a multichannel system presents an opportunity to extend the potential of such a modality for BCI. However, the first prototype design was not intended as a modular unit which could be extended to increase the number of channels. In other words, it would not be practical to have many of the same hardware-based lock-in amplifiers to increase channels (along with associated cabling, electronics, and software) as the resulting system would be rather bulky, expensive, difficult to miniaturise, and not portable.

Instead a flexible software-based demodulation scheme is employed, allowing significant scalability even beyond the number of channels currently in place. The sections to follow in this chapter expand upon this design and are broken down into the various component groups of the constructed multichannel CWNIRS instrument:

- Optical components (Section 5.3);
- Electrical components (Section 5.4);
- Mechanical components (Section 5.5), and,
- Software interfacing and DSP components (Section 5.6).

The safety aspects in human interfacing using NIRS are also dealt with throughout the chapter. Firstly, however, the system nomenclature and a system overview are presented (Section 5.2) highlighting all the major components of the system.

5.2 System Overview

A NIRS instrument is typically named after the number of channels it possesses and perhaps what type of signal recovery it uses: continuous wave, frequency domain, or time domain (as discussed in Section 2.5.5). A *channel* is a pairing of a *detector* and a *light source* that the detector can "see". So if a detector can see six light sources that makes for six channels.

5.2.1 NIRS-system nomenclature - Channels and Sources

It is also possible to have a system where each detector can "see" multiple light sources, so determining the number of channels an instrument has is not straightforward - it is dependent on the source-detector geometrical configuration on the scalp. Thus, in some cases a theoretical maximum is given for the event of every detector being able to receive

light from every light source. A more immediately useful specification is to report the number of sources and detectors in the system. The instrument developed at NUI Maynooth for this project is a CWNIRS instrument with 12 light sources and 7 detectors. A typical source-detector configuration used in the experiments of this work allows for each detector to receive light from 4 sources, and thus makes up a 28-channel system (7 detectors * 4 sources). It should also be noted that some systems report a channel as a wavelength-detector pair, and not a source-detector pair. A source in NIRS is usually made of 2 wavelengths of light in the same package, in order to determine, for example, oxy-haemoglobin and deoxy-haemoglobin (although many more can be used to either increase the accuracy of haemoglobin species calculation or to calculate concentrations\concentration-changes in other metabolic species, e.g. cytochrome-c-oxidase). These two wavelengths can simply be two separate light sources put side-by-side, such as two light-emitting-diodes (LEDs) fixed together, e.g. used in (Coyle, 2005). However, to ensure both wavelengths irradiate approximately the same tissue they should be integrated into a single unit, e.g. using a bifurcated fiber optic bundle or a dual-wavelength LED. A configuration of a single-channel on the head - with one source and one detector - is also called an *optode*, whereas a configuration of a single detector with multiple sources (at least 2) we have termed an *optet* (Soraghan, et al., 2008b). The *inter-optode spacing* (IOS) is the distance in centimeters between a light source and its neighbouring detector, and is critical for ensuring cerebral penetration (i.e. IOS $\propto$ the penetration depth of NIR light detected). An image of the whole CWNIRS system is given next, followed by a description of a single iteration of the system - from light generation, to detection of the (unabsorbed) light exiting the head, to DSP on the PC. In the proceeding sections, each component is expanded upon and described in terms of why it was used including a justification for the choice.

5.2.2 Full instrument schematic

The illustration shown in Figure 5.1 depicts the multichannel CWNIRS system developed at NUI Maynooth, with 7 light detectors and 12 NIR light sources. The data stream begins in LabVIEW (a *National Instruments* graphical programming language) where software controlled sinusoidal carrier signals (up to 32) are generated from the analog output on the PXI-6723 card which drives the light sources (NIR LEDs) via the custom built LED driver (voltage-to-current conversion). The LEDs then irradiate the tissue and NIR light exiting the tissue is collected by fiber optic bundles (F1:F7). The light exiting the fiber optic bundles is filtered by 830nm glass band-pass filters which are housed within light-collecting aluminium buckets. NIR light then enters the detectors (APDs - avalanche photodiodes)

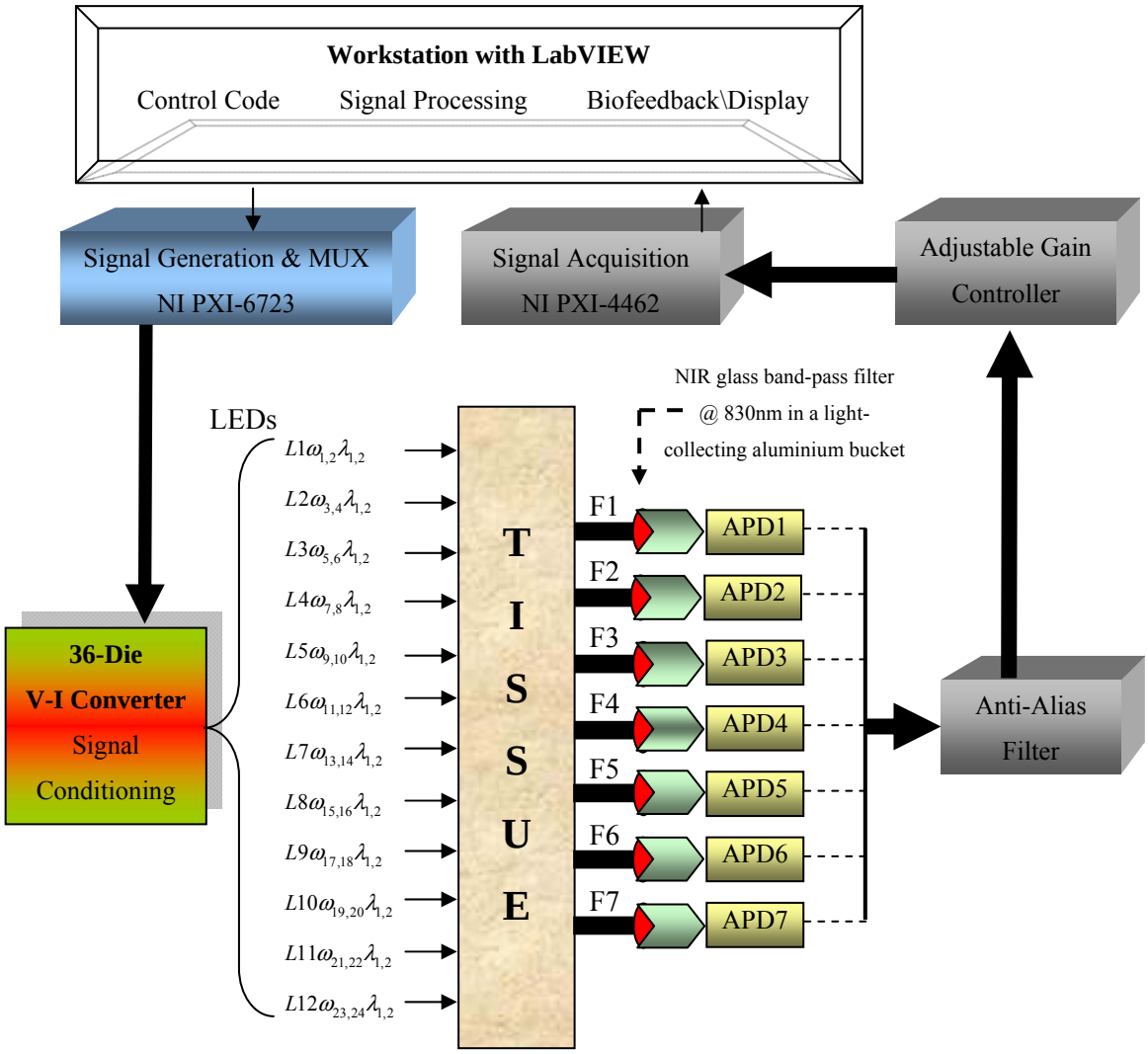

Figure 5.1: Multichannel CWNIRS system at NUI Maynooth (7 detectors and 12 sources). $L1\omega_{1,2}\lambda_{1,2}$ denotes LED1 with wavelength λ_1 (760nm) and λ_2 (880nm) with kHz carrier waves ω_1 and ω_2, respectively.

which transduce (linearly) the light detected to potentials (~0 to -10V). BNC cabling carries these signals to the signal acquisition cards (PXI-4462) with onboard anti-alias filtering and adjustable gain (analog amplification - software controlled in LabVIEW). The sampled data is then processed and demodulated in software on the main workstation computer in LabVIEW (based on the carrier signals from the analog output stage (PXI-6723)), and a display\biofeedback is presented to the user based on the processed signals of concentration changes in HbR and HbO_2. This completes an iteration of the data loop. A 12 channel implementation of the system was described in (Soraghan, et al., 2008a).

Next, the system is described in terms of its optical, mechanical, hardware, and software components. For any in vivo NIRS (ivNIRS) system there are four main elements which make up these components: the source of energy of the impeding beam along with the choice and number of wavelengths; the technique of coupling this energy to the analysed medium

(e.g. tissue), such as using fiber optic light guides; the method of acquisition, processing and calculation of variables from signals; and finally the detector choice (Rolfe, 2000).

5.3 Optical Components

The optical components of the system are perhaps the most important in determining the critical characteristics and capabilities of the imaging system such as the spatial and temporal resolution along with dictating potential crosstalk and noise. Furthermore, the light source and the detector's fiber bundles are the points of contact with the user\tissue (see Figure 5.1) and so comfort and safety are paramount at this stage of the design.

5.3.1 Light source

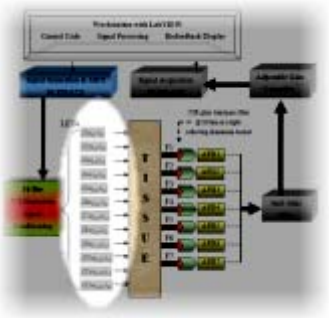

The light source for the ivNIRS instrument is characterised by physical size, wavelength and number of wavelengths used, spectral bandwidth, optical output power, wavelength integration (e.g. into a single package), coupling to the tissue, beam angle, irradiance pattern, and finally safety implications. These specifications and constraints need to be satisfied in the instrument design. The design constraints are developed next followed by a description of the chosen device. Finally the safety concerns and enclosure design for the optical sources are addressed.

5.3.1.1 Choice of light source - design considerations

Design considerations for the light sources used in an OBCI are dependent on the NIRS theory specific to brain studies. The specifications from the previous paragraph are now developed further for ivNIRS with human subjects.

The *size of the device* is perhaps dependent on how the NIR energy is coupled to the head, i.e. if the source is to be placed in contact with the head then a reduced package size is required to make room for others in order to maximise the spatial coverage on the scalp for appropriate imaging. However, if fiber optics are used to couple light to the head (e.g. generally used for NIR laser diode sources), then the actual light source can be considerably larger, but with implications on the overall system size (bulkiness) - which is determinant of portability.

The *number and choice of wavelengths* are determined by the functional imaging desired, as described at the end of Chapter 2. At least two wavelengths of light are required

within a sub-range of the NIR wavelength range - 650nm to 950nm (bound by relatively large absorption by haemoglobin below 650nm and that of water above 950nm - both abundant in the body). These two wavelengths should be chosen either side of the isosbestic point (~800nm) in order to allow for spectroscopic determination of both HbR and HbO_2 (and incidentally HbT [= HBR+HbO_2] which is proportional to cerebral blood volume).

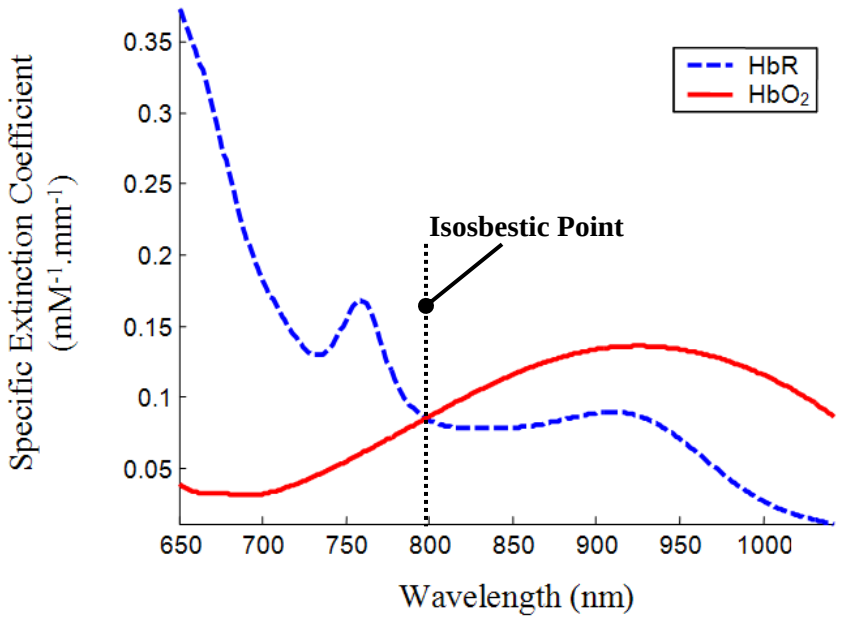

Figure 5.2: Absorption spectra in the near-infrared range for oxyhaemoglobin (HbO_2) and deoxyhaemoglobin (HbR). Values taken from (Cope, 1991).

Okui et al (Okui, et al., 2005) describe how it was originally thought that minimising the difference in the wavelengths either side of the isosbestic point was favourable since the scattering coefficient in cortical tissue increases with decreasing wavelength. Thus, in previous systems a 780nm-830nm pair was commonly used. Okui et al continue to reiterate that crosstalk was revealed to be proportional to the difference in the relative partial pathlength (ratio of actual partial pathlength to the one used in the MBLL algorithm) for the two wavelengths. Specifically, the wavelengths chosen should also have similar partial optical pathlengths in cortical tissue to minimise crosstalk (Okui, et al., 2005) but this is said to be difficult to define due to tissue effects (e.g. scatter) which differ within and between subjects (inter and intra subject dependence) - for example, skull thickness and CSF layer thickness. Nevertheless, a rule of thumb is to have the shorter wavelength below 780nm, ideally in the range 690nm-750nm (Okui, et al., 2005) with improvements in SNR for lower values (Sato, et al., 2004). A good description of wavelength selection and pathlength effects can be found at (Okui, et al., 2005).

More wavelengths can be employed to either increase the measurement species specificity or to determine other chromophores with less dominant absorption effects, e.g. cytochrome-c-oxidase. These wavelengths should also be separated in the spectral range, in order to avoid crosstalk between the haemoglobin species (see Figure 5.2 of spectra of absorption coefficients). Crosstalk from HbO_2 to HbR increases when the shorter wavelength is longer than ~750nm, and crosstalk from HbR to HbO_2 increases when the shorter wavelength is less than 690nm (Okui, et al., 2005). In addition the *spectral bandwidth* of each source wavelength should be as narrow as possible to avoid overlap.

The *optical output power* of the light source should be high enough for sufficient photons to penetrate through the head and be detectable by a suitably sensitive detector. Attenuation of NIR wavelengths is approximately 7 to 9 orders of magnitude for a 4cm IOS with light detectable after traversing up to 8cm of tissue (Elwell, 1995). However, an upper limit of output power is imposed by *safety specifications* (described in Section 5.3.1.4 to follow). The *beam angle* should be as narrow as possible in order to deliver maximum energy to the cerebral tissue - light at grazing angles is less likely to reach deeper cerebral structures (Sliney, et al., 1980). Finally, the light source should suit the NIRS modality used - e.g. for CWNIRS the light source should cater for modulation from DC up to several tens of kHz, whereas for time-domain spectroscopy a picosecond source is required for time of flight measurements (Rolfe, 2000).

These constraints present three possible NIR light sources for CWNIRS in functional brain studies for OBCI applications:

- NIR LEDs;
- NIR laser diodes, and,
- Broadband sources (with appropriate optical filters).

Laser diodes are excellent candidates for NIRS studies and are employed in many commercial instruments. However, they impose safety issues which have led to some researchers using LEDs for more vulnerable subject groups such as in neonatology (Bozkurt, et al., 2004). Laser diode coherency makes them hazardous, in particular to the eyes, with possible retinal damage. The invisible nature of NIR light increases the risk since the subject would be unaware of the potential danger. Furthermore, laser diode modules are generally large and typically require optical fibers to couple light to the head. Broadband sources (e.g. tungsten lamp) can be used but require optical\NIR filters to divide light into separate discrete wavelengths. A more suitable source for safe, long term use is the inexpensive high powered NIR LED. It also allows for direct coupling to the scalp, and doesn't have the

coherency-specific safety concerns of the laser diode. A coherent source is not required due to the nature of NIR scattering in tissue optics. The short transport scattering length (the distance over which a collimated beam effectively becomes diffuse) of NIR light in tissue means that laser diodes and LEDs at these wavelengths are indistinguishable after the first few millimeters of penetration, and tissue of interest lies centimeters from the source.

5.3.1.2 NIR LEDs - the light source solution for OBCI

NIR LEDs satisfy the many design considerations mentioned in the previous sections. They are rugged, small in size (e.g. TO-39 package) and allow for direct coupling to the head rather than using lossy fiber optic bundles. Wavelengths are available in the range of interest although those closer to 700nm are more difficult to manufacture (Opto Diode Corp. - personal communication). Nevertheless, NIR wavelengths of ~760nm and ~880nm were chosen, with minimal overlap (FWHM of $\pm$ 30nm and $\pm$ 80nm, respectively). The selection of wavelengths was commensurate with the specifications and guidelines outlined in the previous subsection. The 760nm die is relatively more absorbed by increases in the concentration of HbR, whereas the 880nm die, the opposite side of the isosbestic point (~800nm), is more absorbed by HbO_2 concentration increases. Nevertheless, both NIR wavelengths are absorbed by both haemoglobin species - HbO_2 *and* HbR - the amount depending on their absorption spectra (Figure 5.2) and so measurements can be used in a simultaneous equation set involving the modified Beer-Lambert Law (MBLL) as described at the end of Chapter 2. (Note: this algorithm is used in the experiments in Chapters 6 and 7.) The FWHM of both sources allows for minimal spectral overlap of these sources (see Figure 5.3). It should be noted that recent studies have paired 690nm with 830nm as improving signal-to-noise ratio (Sato, et al., 2004), and these are used in very recent commercial CWNIRS instruments (Wolf, et al., 2007). As mentioned previously though, these wavelengths are difficult to manufacture in LEDs, especially at the high powers required (~10mW).

A specification list of the custom-designed light source used for ivNIRS studies in this project is shown in Table 5.1. In the first prototype single wavelength LEDs were used but for better spatial specificity and imaging applications, wavelengths integrated into a single package[1] with a narrow beam angle were required. The second iteration included a triple wavelength device with an additional wavelength at 800nm for determining HbT - however

[1] In order to avoid confusion, from here an "LED package" refers to a semiconductor device that contains multiple (more than one) wavelength of light, i.e. multiple LEDs within the same package.

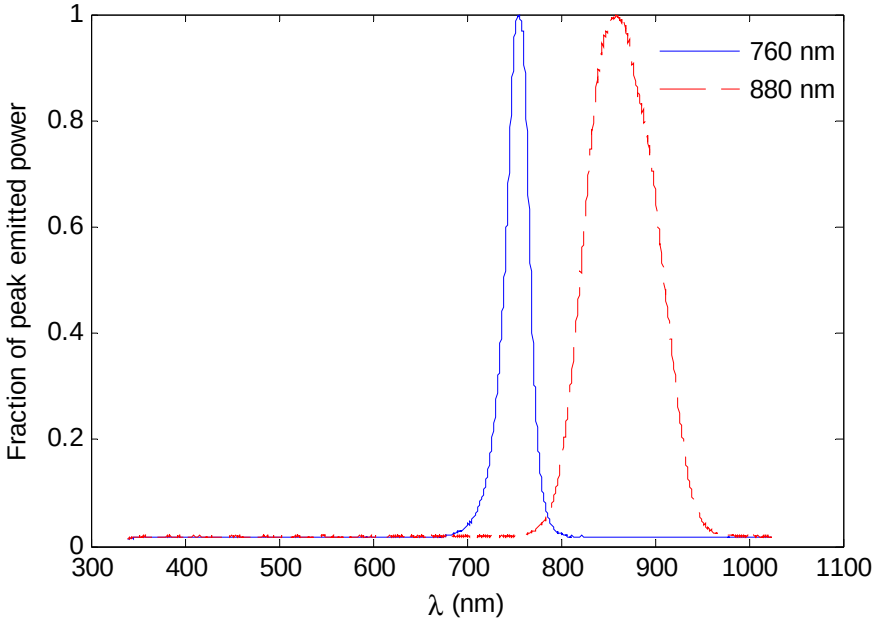

Figure 5.3: LED emission spectra at low current (~30mA) showing central wavelengths at ~755nm and ~ 860nm, with little overlap. Due to the large difference in optical output power between the two, the 755nm source was set at a lower power during acquisition of these spectra.

Specification	*Description (Typical)*
Manufacturer	Opto Diode Corporation, Newbury Park, California, USA
Custom LED Name	OD-1894
Wavelength	5-die dual wavelength LED (4 * 760nm and 1* 880nm)
Package	4+1 lead[2] TO-39 header with lensed cap (10° FWHM); Common Anode (case)
760nm die (high efficiency)	760nm ± 10nm ; 30nm FWHM ; 2 leads - 2-die parallel per lead; 40 ± 10mW (for 4 die @ ~10mW per die) @ 400mA
880nm die	880nm ± 10nm ; 80nm FWHM ; 1 lead; 16 ± 1mW @ 100mA;
Beam Angle	10°

Table 5.1: Dual wavelength high power NIR solution for ivNIRS. Specifications are given for the individual die used (760nm and 880nm) where 4 of the latter and one of the former are integrated into a single common-anode TO-39 package, with lensed cap. (See Appendix B for a more detailed specification sheet.)

the optical output powers of the 760nm die in the triple wavelength package[2] were low (~5mW). The shorter wavelength is also more susceptible to absorption than the longer wavelength further compounding the power issue. Thus, a dual wavelength design was implemented, in a solution with four 760nm-die plus one 880nm-die, yielding an effective

[2] Each wire exiting an LED package is called a lead, or pin, or wire. These are used interchangeably in the remainder of the document.

power excess to the 760nm (whose power can be adjusted\reduced). This was important since changes in the concentration of the HbR species is said to reflect more localised activity relative to changes in the concentration of HbO_2 (Hirth, et al., 1996). In addition, HbR is said to be correlated (spatio-temporally) to the BOLD signal in fMRI which may have use in future concurrent studies. The increased power of the 760nm chip also allows for easier source placement since lower powers in earlier designs required more tedious scalp preparation (e.g. hair parting) to achieve adequate power levels. The final design can be seen below in Figure 5.4. Die 1 and die 2 share the same cathode pin, and die 3 and die 4 also share another common cathode pin. All 5 LEDs share a common anode (also connected to the package case\chassis), which incidently are connected to ground (note: the driving electronics are described later in Section 5.4.1).

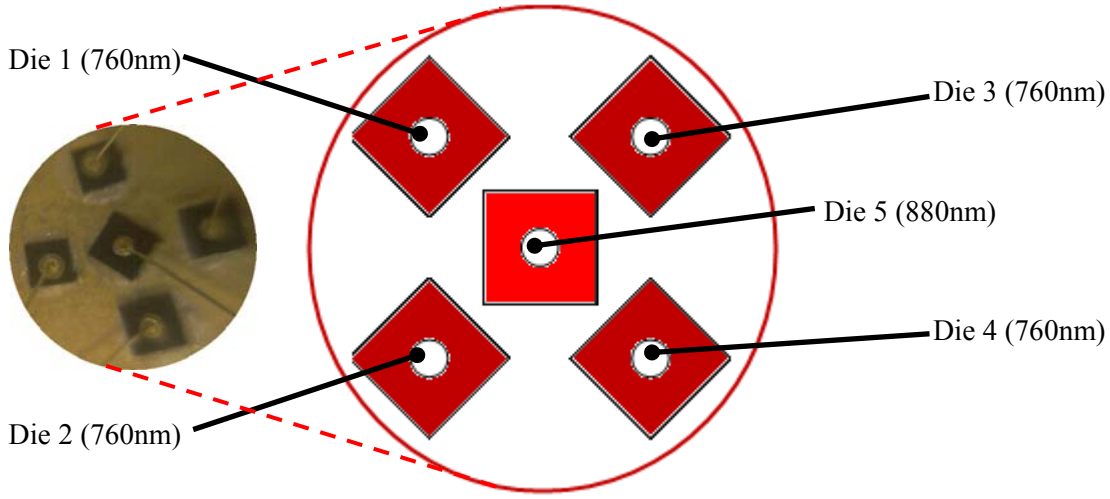

Figure 5.4: Distribution of LED chips (die) within the dual wavelength LED TO-39 package (OD-1894). The view of the LED package is from the top-down - the left image is a photo taken through the LED lens. Having 2-die on the same lead (2*760nm) in a parallel configuration is possible whereby voltages are matched intrinsically for the pair by having the manufacturer select 2 adjacent die from the same semiconductor wafer.

Note: An acceptable reduction in power of the central 880nm die was intrinsic to the design. Each LED chip emits from all surfaces (sides as well as top) and each sit on a gold-plated surface which reflects the side-emissions forward - contributing to the overall optical output. In this die configuration the 760nm chips actually absorb some of the 880nm output whereby the light coupled into the output beam from the 880nm chip was reduced from ~16mW to ~11mW (Opto Diode Corp. manufacturer - personal communication).

In order to calculate concentration changes in haemoglobin species, it has been shown already that at least two wavelengths of light are needed - preferably two monochromatic sources. Two narrow band light sources with known peak emission wavelengths (λ_p's) are

sufficient. Thus, it is a requirement to know the wavelength peak for each source - i.e. in this case 760nm and 880nm - although in reality manufacturing limitations mean that variance occurs in the peak emission wavelengths across different die. The next section deals with the issue of variance in LED spectral power distribution (SPD) and drift in the wavelength emission due to thermal effects at high operating temperatures of the p-n junction of each diode.

5.3.1.3 LED wavelength variance and drift

Variance: The variance in wavelength was analysed for all twelve light sources for each individual wavelength (or wavelength pair in the case of 760nm) driving each with a low DC current (~30mA) and recording their SPD with a spectrophotometer (Ocean Optics Inc. USB2000). It was found that for the 760nm die, the mean peak emission wavelength ($\mu\lambda_p$) was 755.33nm with a standard deviation of 0.5265nm between sources - see Figure 5.5. Similarly, for the 880nm components, the $\mu\lambda_p$ was found to be 860.3342nm with a standard deviation of 0.8642nm - see Figure 5.6. However, all the 880nm LED components had a notch in SPD between 870nm-890nm. An analysis of the FWHM ($\Delta\lambda$) suggests a central peak emission (weighted mean in Figure 5.6) at 866nm for a Gaussian-shaped model. The notch is from manufacturing limitations, which have been seen in other LEDs that the company manufacture (Opto Diode Corp., personal communication).

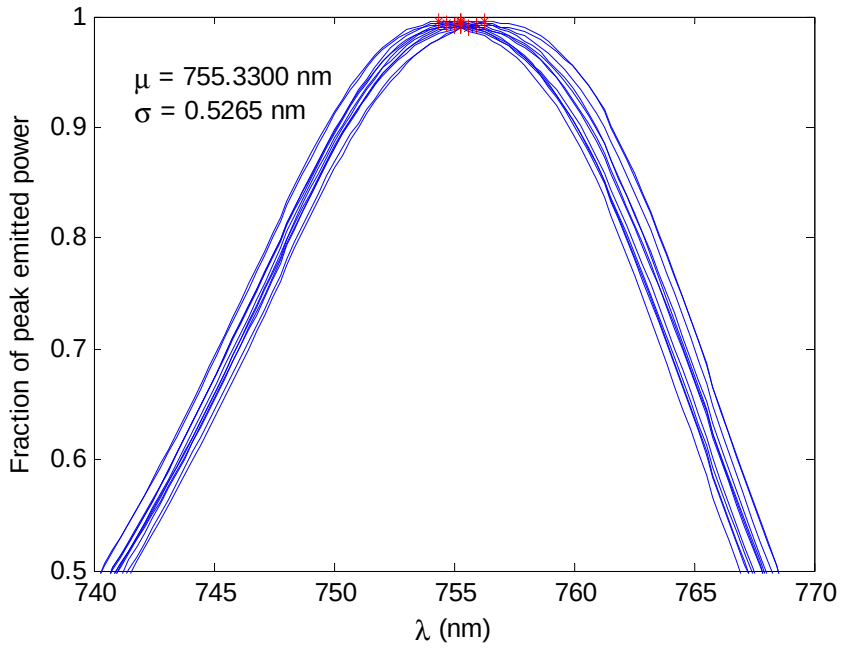

Figure 5.5: Normalised peak emission wavelength of twelve 760nm die pairs within the twelve OD1894 LED packages. These die have a mean peak emission wavelength of ~755nm with a standard deviation of ~0.53nm. The FWHM ($\Delta\lambda$) is ~27nm (741nm-768nm).

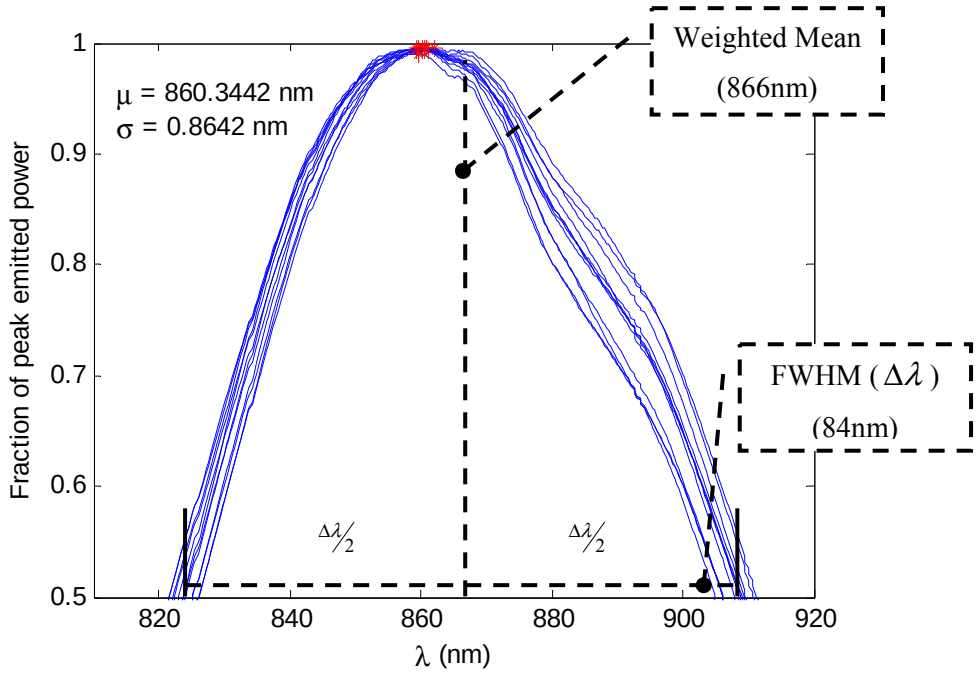

Figure 5.6: Normalised peak emission wavelength (λ_p) of twelve 880nm die within the twelve OD1894 LED packages. The device was found to have a mean peak emission wavelength ($\mu\lambda_p$) of ~860nm with a standard deviation of ~0.8642nm. The FWHM ($\Delta\lambda$) for the die is ~84nm (824nm-908nm) though, suggesting a central peak emission (weighted mean) of 866nm which is masked due to the notch (common for all 880nm die) on the right of the spectrum between ~870nm-895nm.

Although the LEDs are quasi-broadband with $\Delta\lambda$ of ~27nm for the 760nm LED and $\Delta\lambda$ of ~84nm for the 880nm LED they can nonetheless be considered as monochromatic light sources. This can be demonstrated by comparing the resulting haemoglobin calculations when treating the LEDs as monochromatic versus their actual spectral spread. This test is reported in Appendix D.

Drift: A further adjustment to the design specifications on the peak emitted wavelength for the LEDs is due to drift in the wavelength of the die. The wavelength of light from an LED can be described by the following equation:

$$\lambda = \frac{hc}{E_g}, \tag{5.1}$$

...where λ is the wavelength of light emitted from the LED, h is Planck's constant, c is the speed of light in a vacuum, and E_g is the band gap (energy gap) in units of electron volts (eV). Thus, E_g determines the wavelength of light emitted and is a function of the semiconductor materials used to construct the LEDs, where gallium aluminium arsenide (GaAlAs) is used to produce the NIR wavelengths (with different ratios) for the LEDs used

here[3] (Held, 2008). However, E_g is also a function of the temperature at the p-n junction, whereby E_g typically decreases with increasing temperature (Varshni, 1967). Thus, from Equation (5.1) it can be seen that wavelength will increase with decreasing E_g due to increasing temperature. It should also be noted that optical output power decreases with increasing power due to a reduction in quantum efficiency due to thermal losses (see Section 5.4.1.3 to follow). Thus, higher currents are expected to yield a drift (increase) in wavelength for the LEDs.

A series of recordings were made for a single LED package over two hours for the 760nm LED component (4 die) and over one hour for the 880nm LED component. The LEDs were driven using the maximum power settings used in a typical experiment (discussed later in Section 5.4.1) driving the sources with a sine-wave carrier signal with 90mA-RMS current peak for each 760nm pair, and 142mA-RMS peak for the 880nm die, all with a duty cycle of 50%.

From Figure 5.7 it can be seen that the 760nm LED incurred more wavelength drift. A closer analysis of the two sources in Figure 5.8 demonstrates that the 760nm LED drifts by almost 2nm over the two hour period to 760.92nm. Moreover, the first recording was made at the instant that the high current (90mA-RMS per 760nm pair) was applied, with a λ_p of 758.95nm. This supposed baseline (before drift) is almost 4nm higher than that recording from a low driving current shown in Figure 5.3. Thus, the temperature drift affect from the p-n junction occurs instantly when a relatively higher current is applied (~4nm for the 760nm LED) as well as the relatively slower drift shown in Figure 5.7. This longer time constant is due to ambient temperature affects and the increased temperature due to limitations in the rate of heat dissipation. These also have a bearing on the LED performance in terms of its wavelength drift and decrease in optical power output (the optical output power drift in discussed further in Section 5.3.1.4). Nevertheless, the majority of the wavelength drift was found to occur in the first thirty minutes of recording as shown in Figure 5.8 (left hand graph). In contrast 880nm component settles quickly (<5 mins) and drifts <0.1nm over the course of 1 hour.

[3] Gallium arsenide (GaAs) is also commonly used for creating infrared LEDs whereas many other materials are used for visible LEDs, e.g. gallium phosphide for pure green (Held, G. (2008). Introduction to Light Emitting Diode Technology and Applications, Auerbach Publications.).

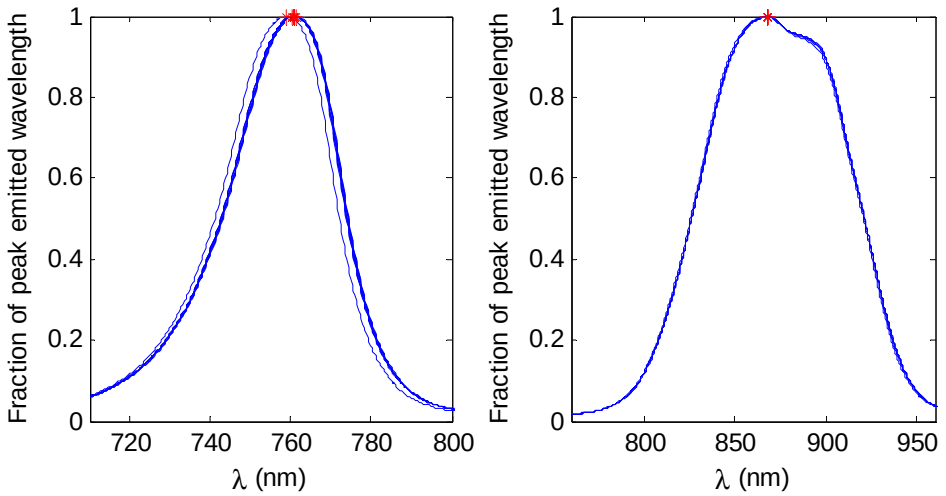

Figure 5.7: Drift analysis of the 760nm wavelength component (4 die) and the 880nm component of the OD1894 LED package. Recordings were made over 2 hours for the 760nm component and 1 hour for the 880nm component (since it incurred less drift).

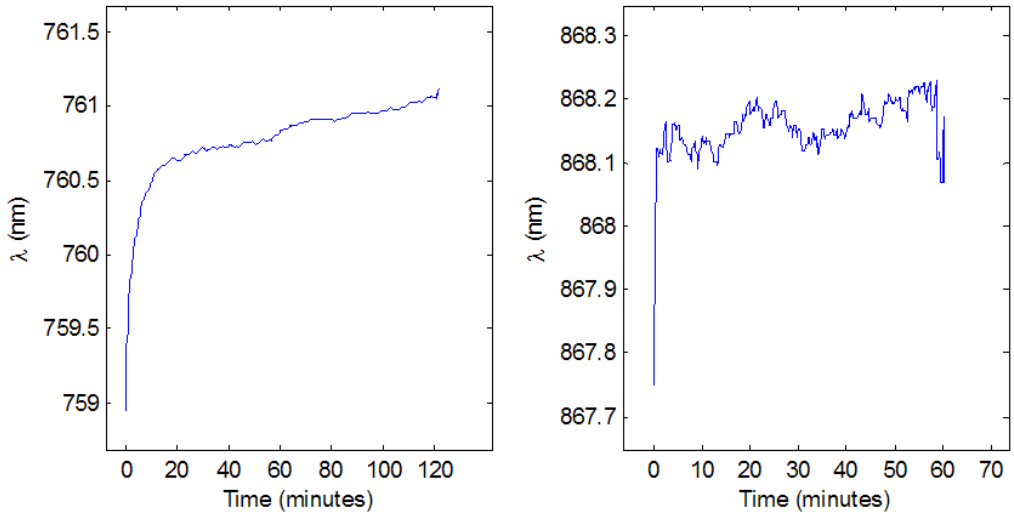

Figure 5.8: Wavelength drift over time for the 760nm die (left) and the 880nm die (right).

Drift in the *optical output power* (not wavelength) are dealt with in Section 5.3.1.4 (which also considers the safety assessment of the optical sources) and in Section 5.4.1.3 (on the LED driving electronics). However, the significance of the *wavelength* drift reported in this section is that it has a direct affect on the calculations of the changes in concentration of the haemoglobin species (HbO_2 and HbR) since the MBLL algorithm used to calculate these dynamics assumes a constant peak emission wavelength, using specific extinction coefficients from Figure 5.2. Thus, the solution to overcoming these adverse affects is simply to allow the LEDs to operate at a high current and 'settle' in wavelength for at least ~35 minutes (this is considered more in the proceeding section).

As an aside, it should be noted that the modified Beer Lambert Law algorithm developed in Chapter 2 considered the manufacturer-specified wavelengths of the two LED die used: 760nm and 880nm. However, from the analysis in this section, the central wavelengths are at ~761nm and ~868nm. However, when haemoglobin calculations were performed using values for 868nm with 761nm, and 880nm with 760nm the differences are negligible, where a plot of haemoglobin calculations and the values used in the MBLL using these two criteria is reported in Appendix D.

A significant parameter in the selection of a source is that they should be safe to use, and in this case LED sources have two potential concerns: 1) heat generated in tissue due to the NIR irradiation applied, and 2) heat from the operation of the semiconductor junction. These are considered next, completing the section on light source selection. (Note: The driving electronics will be dealt with in the electrical components section - Section 5.4.1.)

5.3.1.4 LED source safety

The chief safety concerns of the sources used in this project have been presented recently (Soraghan, et al., 2008b). NIR energy is non-ionising and is thus suitable for potentially limitless cerebral 'scans' (Strangman, et al., 2002). It also has the added benefit of being non-coherent, reducing the risk of for example retinal damage. Nevertheless, the technique is not a passive one like, for example, EEG is. An external source of photons is actively sent into the tissue and the redetected photonic flux exiting the head is analysed to detect changes in cerebral metabolism. Some literature carelessly uses the term "injected photons" which may conjure up invasive notions. However, to put it in perspective, interestingly NIR-tissue interaction is currently being investigated for wound healing (Whelan, et al., 2003) and therapeutic benefits (Schmidt, et al., 1996).

The principal concern with using NIR LEDs is skin damage as a result of heating effects. This can take place by two mechanisms: 1) skin absorption of radiated NIR energy, and 2) the thermally conducted energy arising from the p-n junction of the LED during operation. Irradiated energy heating effects deal with in two sub-issues - first the geometrical significance of the source-detector probe (optet configuration) is considered, followed by the general irradiance effects. Finally the thermal conduction effects due to the p-n junction operation are described.

Source-detector geometrical probe set-up: Firstly, the optet design can have a bearing on the heating effects from radiated energy. This means that if many sources are radiating the same or close to the same tissue, then exposure should be calculated based on the additive photonic flux and not simply calculated for a single source alone. However, the

design of optets used in this work such as the point measurement optet shown in the inset of Figure 5.9 allows for treating exposure rates of these light sources as individual contributors, i.e. they don't contribute additively. Since source positions are typically 3cm from an adjacent detector and more importantly since sources are greater than a few centimeters apart from each other, there is minimal overlap between flux patterns and sufficient tissue between source sites to minimise thermal focus. An empirically study (Ito, et al., 2000) expressed that sources can be treated independently for inter-optode spacings (IOS) greater than a few millimeters.

LED Radiated Energy: The second potential heating issue is that irradiance of NIR light does induce some heating of the tissue as it absorbs the energy (mostly by water, abundant in the body). Heating is greater for longer wavelengths in the NIR range. However a study has demonstrated that for typical CWNIRS systems this radiated energy results in a temperature increase of $<0.5\,^{\circ}\mathrm{C}$ (Ito, et al., 2000). Tissue also dissipates heat as a function of depth thus ensuring deeper tissues are even less susceptible. Skin thermoreceptors also provide compensatory reflexes from sensed temperature increases. Skin is also a better thermal conductor with a higher specific heat capacity perhaps explaining the lesser heating effects of the human model compared to the less conductive polystyrene model (Table 5.2) in a study carried out for this project's light sources. Nevertheless, there is a lack of standards for exposure rates of NIR LEDs and so the practice has been to take the conservative approach or treating the LED as a laser source as outlined in (Coyle, 2005; Soraghan, et al., 2008b). The International Commission on Non-Ionizing Radiation Protection (ICNIRP) and the International Electrotechnical Commission (IEC) specify maximum exposure duration limits that need to be adhered too (British Standards 1994; ICNIRP Guidelines 2000). LEDs are categorised between incoherent broadband and coherent laser sources (ICNIRP Guidelines 1997) since they lack the lasing process and effective optical gain compared to a laser diode. State-of-the-art LEDs are limited to <40% quantum efficiency with typically 20% quantum efficiency due to lattice vibrations (non-radiative processes) that convert much of the energy to heat (Held, 2008). The (ICNIRP) recommends that LED sources adhere to guidelines for incoherent sources (ICNIRP 1997). Nevertheless, the IEC includes LEDs in the same category as lasers for safety guidelines, and so that approach is adopted for this project. The specifications for a coherent source in the range 700-1400nm has a Maximum Permissible Exposure (MPE) on skin of:

$$MPE = 2000.10^{0.002(\lambda - 700)} \qquad \left[W/m^2\right] \tag{5.2}$$

... where λ is the LED centre wavelength, for an exposure time t: $10^3 s < t < 3\times10^4 s$.

Wavelengths used in the light sources are at ~760nm and ~880nm. Calculating for a laser at these wavelengths, an MPE for these wavelengths would be 2.6mW/mm^2 and 4.6mW/mm^2, respectively. NIR energy from the LED light sources used which are coupled directly to the scalp radiates an area of ~20mm^2. Within a single LED source are 5 LED 'die' - 4 at 760nm, and 1 at 880nm (see Figure 5.4). The NIR energy although resulting from spontaneous emission and thus incoherent, is focused using a lens for each light source package facilitating a 10 degree beam angle. Thus, a linear addition of the non-coherent NIR energy from all LED die is assumed when they are all emitting light (since photons are out of phase). From Table 5.1 it can be seen that 40±10mW is achievable from the 760nm component of the source (i.e. the total from four 760nm die) and 16±1mW for the single 880nm die in the same source package. This gives a potential output power of 56±11mW of NIR energy from a single source. Thus, for the 760nm component a maximum exposure of 2.5mW/mm^2 is possible (at maximum 50mW). The 880nm component has a maximum exposure of 0.85mW/mm^2. Each of these is below the MPE for corresponding coherent sources (as a conservative benchmark). A total exposure of 3.35mW/mm^2 is possible. However, in reality even though exposure is below the MPE for a comparable coherent source, these LED sources are not in the same category. Furthermore, due to non-radiative processes, the LED package would heat up considerably if this much power was actually used. Thus for practical reasons, the OD1894 LED source is powered to a level much lower than the theoretical maximums just proposed. As will be seen in the LED driver section for this instrument, the 760nm die are set at powers approximately half their maximum, but the 880nm die at its maximum (due to previously mentioned power reduction from the surrounding 4 die in the LED package). In essence it was found that the 880nm die operated at a maximum of 13mW, not 17mW. Thus, a calibrated light source of 38mW (25mW+13mW) contributes to an exposure of approximately 1.9mW/mm^2 (for a radiation area of 20mm^2 per OD1894 light source). This is well below the specified MPE for wavelengths in the NIR range for a coherent source. A useful comparison is to consider that irradiance due to sunlight on the earth's surface is ~1mW/mm^2 (and this is more efficiently absorbed than NIR light) (Ito, et al., 2000). It should be noted that all light sources are sinusoidally modulated with a duty cycle of 50% which would be expected to further reduce the output power (0.7071 times the peak power) and exposure. However, this power reduction was exploited in the design process to increase the output power of the 880nm die specifically, since signal-to-noise in the NIRS system overall is greatly dependent upon the source output power. This will be dealt with in the LED driver section but briefly, a 100mA-DC is specified for the 880nm die for typical operation. However, a peak of 100mA-RMS using sinusoidal modulation with a duty cycle of 50% is effectively only 70% (RMS) of the specified 100mA-DC. Thus a maximum of ~142mA-RMS can be employed to match the

100mA-DC (for a 13mW output power from the 880nm die) specified driving current for the device.

A study examining maximum heating effect in skin via irradiance for a NIRS measurement demonstrated a 7.93x10-6 °C/mW/mm^2 at 0.5mm below the skin surface, and even less temperature changes at greater depths (Ito, et al., 2000). From an irradiance standpoint it can be concluded that the NIRS sources used can be considered safe since tissue damage occurs at 41°C, with normal skin temperature around 31°C (depending on the ambient environment). The final heating consideration for the optical sources is that due to thermal conduction due to LED semiconductor junction operation, which incidently reduces quantum efficiency of the sources, reducing the output power (lost energy to heat).

Thermal effects of LED-skin contact: A more significant source of heating that is usually limited by appropriate driving currents is due to the flow of current across the semiconductor junction. The LED will heat-up depending on the current applied, and for DC currents they can heat significantly such that superficial burns are possible (Murphy, et al., 1990). These effects were reported in the literature recently (Bozkurt, et al., 2004) and a safety assessment was carried out for this project (Soraghan, et al., 2008b) by way of monitoring temperature change over time (using an IC temperature sensor - LM35) on a polystyrene head phantom, and a human head. It was found that at no time did the temperature ever exceed 41°C under the optet. The temperature change over time for the polystyrene head phantom was used to implement a worse-case scenario since polystyrene is a very poor heat conductor, and temperature changes were expected to be higher. A graph of the temperature profile for the polystyrene head phantom is shown in Figure 5.9, and for the human head in Figure 5.10. From Table 5.2 it can be seen that the polystyrene head phantom increased more in temperature for the same time period (40 minutes) which was expected, and it took longer to peak. The head model shows a peak in temperature of 36.4°C after ~30 minutes. In all measurements a 7-source and 1-detector optet was used as shown in the insets of the temperature profile graphs, as would be typical for NIRS experiments carried out. The temperature profiles recorded are from previously used LED light sources with output powers of 5mW for 760nm and 17mW for 880nm, in a triple wavelength LED (only 2 wavelengths used - 800nm die was never used). The same dies are used in the current light sources from the same manufacturer, although there are 3 additional 760nm die per package and they are twice as efficient (10mW instead of 5mW). However, similar measurements were made on these sources where currents were adjusted (approximately half power for the 760nm die), keeping temperature below 39°C.

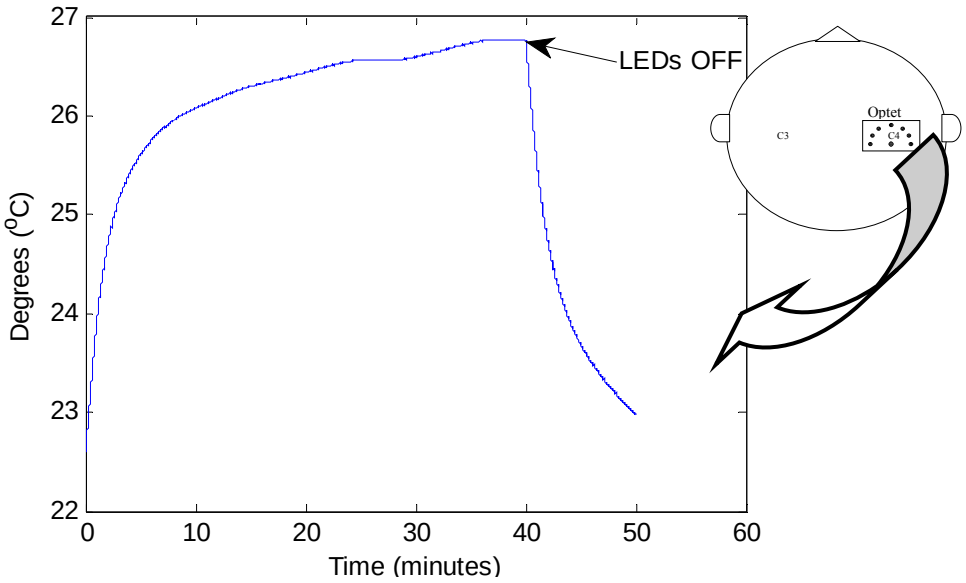

Figure 5.9: Temperature profile of a polystyrene phantom of a human head in contact with the LED. This demonstrates an extreme case of temperature effects - polystyrene is a poor heat conductor. Temperature sensor (LM35) was placed in contact with the LED case under a 7 source + 1 detector optet (see inset).

Phantom	*Duration (mins)*	*$T_{initial}$ (°C)*	*Peak Time (mins)*	*T_{final} (°C)*	*ΔT (°C)*
Polystyrene head	40	22	38	26.75	+4.75
Human head	40	33	30	36.4	+3.4

Table 5.2: Temperature profile of LED in contact with the polystyrene phantom and a human head. In both cases temperature never exceeded 41°C - temperature onset of tissue damage.

Some additional design features were added to aid in dissipating more heat from the high power NIR sources. The LED was housed in a brass cylinder and filled with non-electrically conductive heat sink epoxy resin (see inset, part (C) of Figure 5.11). In addition, the lens side of the light source was sealed into the brass tube with clear epoxy resin around the border of the lens for three reasons: 1) to reduce subject-LED contact to only the glass-lens window of the LED; 2) to fix the LED to the rigid brass tubing, so that the LED does not move in its brass housing as it makes contact with the scalp (i.e. to ensure the photonic pathlength doesn't change over time due to movement artefacts of the light source), and 3) to ensure a smooth surface contact to the subject's scalp.

Conclusions:

It is known that >95% of photonic energy in the NIR spectrum interacts with the epidermis in the vicinity of the light source (Strangman, et al., 2002). The safety

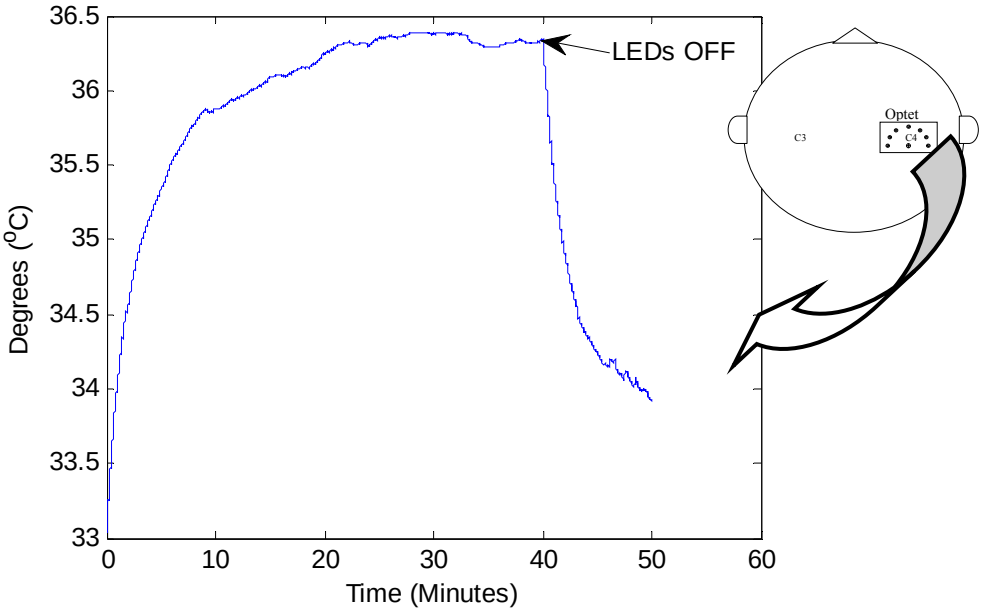

Figure 5.10: Temperature profile of a human head in contact with an LED. The temperature sensor (LM35) was placed in contact with the LED and the human head under a 7 source + 1 detector optet (see inset).

concerns of the CWNIRS instrument were shown to be issues of heating effects. The irradiance-specific heating effects have been shown to be safe for this system and the thermal conductance effects from the operation of the p-n junction of the LEDs were described and at no time do the light sources rise above 39°C where damage is said to occur at 41°C. The safety concern of heating was controlled by effectively controlling the parameters of the driving current. A current limit for each light source is employed in order to maximise signal-to-noise contributions from the LEDs but all the while maintaining a sufficient temperature and keeping below irradiance values bound by maximum permissable exposure rates for coherent sources. Indeed, for these light sources, they could never exceed those MPE, since they are intrinsically limited - unlike laser diodes. Furthermore, sinusoidal modulation reduces the effective output power for the LEDs although this was harnessed for the 880nm die.

The final section on the optical sources is the LED package's additional enclosure design (outlined next in Figure 5.11), which needs to provide rigid coupling to the subject within a mechanical holder or 'optet holder', while at the same time maintaining subject comfort. This comfort is important not only for ethical reasons, but also since subject distress can bias results - usually negatively (Coyle, et al., 2003).

5.3.1.5 NIR LED enclosure design

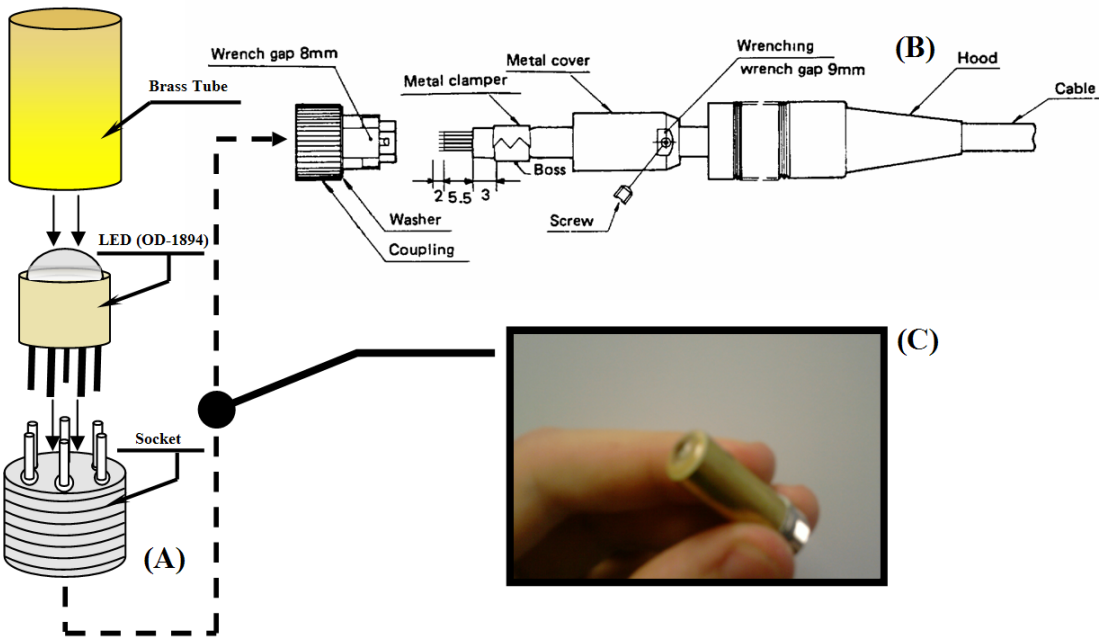

Figure 5.11: Light source housing for a single LED package (OD-1894). (A) The LED package fits into a chassis mounting socket and a brass tube encloses the LED, apart from the protruding LED lens; (B) The housed light sources are detachable from the connecting electronics; (C) A photograph of the assembled light source (detached from jack in (B)) where the three items from (A) are assembled. (Note: LED case\chassis which is connected to common anode is also connected to ground).

The driving electronics and strategies for signal recovery of light exiting the head is dealt with later in a section on the electrical components of the CWNIRS system (Section 5.4.1). One other design issue however, was the housing and ensurance of rigid coupling to the head. Figure 5.11 illustrates in three parts (A, B, and C), the light source housing assembly. In order for the LED to be illuminating it requires current which comes from the LED driver. Connected to the LED driver for each LED package is a 4-core cable about a meter in length - one core for ground (common anode), one for the 880nm die cathode, and two cores\wires for each 760nm pair cathode. This 4-core cable connects to the male jack (SR30-10JE-6S HIROSE jack) (part (B) in Figure 5.11). The LED package in the chassis mounting socket (SR-30-10R-6S, HIROSE socket) shown in part (C) of Figure 5.11 slots into this jack, and a threaded collar fixes\couples the two together in a rigid connection. This effectively means that LED packages can be removed and new ones put on in the event of a failure of one of the LEDs. It also allows for the use of future LED wavelengths with perhaps different wavelengths for resolving further chromophores such as total haemoglobin (HbT: at the isosbestic point ~800nm) or the more elusive cytochrome-c-oxidase (a respiratory enzyme with an absorption peak at 830nm). The LED driver (described later) was specifically made to be flexible in this regard, where three optical drivers are provided for

each LED package. However, in this case two parallel die[4] are used for one driver (discussed further in Section 5.4.1 on the LED driver), with the provision of a change in the current suppled (software configurable).

The LED socket is used to give the LED a firm base and to allow for easy detachment from the jack in part (B). Non-electrically conducting heat sink epoxy resin (blue) is put inside the brass tubing and surrounds the LED (but below the LED lens window) to dissipate heat more effectively from the LED package. This epoxy also has the affect of fixing the LED package to the brass tube. An additional film of clear epoxy around the circumference of the lens window also ensures that the LED package doesn't move with respect to the surrounding brass tube when placed on the subject's scalp - thereby not contributing to a change in the optical pathlength as the subject moves. The final stage in ensuring good coupling to the subject is to have a matching optet holder (frame) to fix the light sources and detectors to the subject's head, while maintaining comfort. Before explaining the optet configuration design, the detectors used in the system, and their associated optics, especially fiber optic bundles, have to be described since these fibers are fixed into the mechanical holders (or optet holders) alongside the sources - ideally applied perpendicularly to the head for maximum light delivery and detection.

5.3.2 Light detector

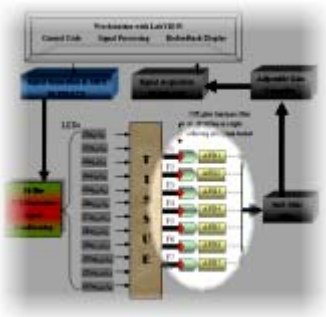

As NIR photons leave the irradiated tissue they can be retrieved from the scalp surface using sensitive detectors, sometimes requiring coupling fiber optic cables. The following section deals with the design considerations for selection of an appropriate detection device for a CWNIRS system.

5.3.2.1 Light detector - design considerations

There are various detectors used in NIRS which are chosen depending on the application, but the choice is primarily dependent on the NIRS modality used, i.e. continuous wave, time domain, or frequency domain NIRS. A NIRS detector should satisfy the following constraints:

- It must be sensitive to photons in the **NIR wavelength range** - typically 650nm

[4] Parallel configurations are possible if the manufacturer chooses die from the same wafer with matched potential drops.

to 950nm, but specifically for LED sources used in this project (LED specifications in Table 5.1) - taking into account the broadband nature of the LEDs' wavelength - sensitivity should cater for 745nm-775nm for the shorter wavelength LEDs (30nm FWHM) and from 840nm-920nm for the longer wavelength LEDs (80nm FWHM);

- It should have a **high sensitivity** for this wavelength range - with consideration for both (a) the 7-9 orders of magnitude loss from NIR photons traversing the head, and (b) the capabilities of the light source primarily optical output power, i.e. how much light remains after exiting the head will depend on the tissue's absorption and scattering effects and on the amount of photons emerging from the light source in the first instance. Thus, the detector should be sensitive enough to detect the remaining photons;
- It have an appropriate **speed** (rise-time and fall-time, i.e. time constant) - depending on the mode of NIRS used the detector may have to respond to very fast pulses, e.g. during time-of-flight measurement for time-domain systems. For CWNIRS, detectors should be able to detect signals in the DC-to-several kHz range. The modulation strategy used (described later in Section 5.4.1 and Section 5.4.2) operates with sinusoidal carrier signals up to 16kHz, so a detector with response rates capable of detecting these signals is needed. Furthermore the detector should only have a bandwidth sufficient for the measurement made since anymore lets in more noise (Johnson noise). However, there is a trade-off in the design in terms of complexity, cost, portability, and other issues such as e.g. photomultiplier tubes are more fragile;
- **Coupling** - the detector should be able to retrieve light from the head. Nevertheless many systems use coupling fiber optics to carry the light to remote detectors, with varied distances in different designs. However, there are losses involved in this coupling technique. Thus, losses should not be more than the detector can afford for the photonic flux exiting the head.

Four types of detectors are generally used (Rolfe, 2000; Strangman, et al., 2002). Charge-coupled devices (CCDs); photomultiplier tubes (PMTs); silicon photodiodes (SiPDs); and avalanche photodiodes (APDs). PMTs may require cooling and need a high bias potential, as mentioned above, and are not very portable. They also require high voltages and protection from high currents to prevent them being damaged. These have been used in a single-channel photon counting system at Maynooth (Lebid, et al., 2004) with the aim to detect the fast signal (event related optical signal), since they can be configured to be highly-sensitive fast detectors. CCD devices could be used when there are many wavelengths

of light to collect, such as with a tungsten lamp. The wavelengths can be dispersed using a prism, spreading light of different wavelengths across the CCD surface. SiPDs can be used and placed in direct contact with the scalp, making them useful for effective portable probes. Nevertheless they are less sensitive than APDs, since APDs achieve electrical gain via the amplification from the high electric field applied to the depletion layer of this semiconductor detector. This yields higher quantum efficiency for the device. In addition, onboard temperature modules can be used to keep the APD gain constant. APDs on the other hand cannot be placed in direct contact with the scalp (due to the high voltage electronics for these modules) but they can be highly effective when used with coupling fiber optics, since their sensitivity is appropriate for low light levels emerging from the head. Thus, APDs were chosen as the light detector. Furthermore these devices are also used by others in the NIRS community, especially in CWNIRS devices (Koizumi, et al., 2003; Coyle, et al., 2004; Joseph, et al., 2006).

5.3.2.2 Avalanche photodiode (APD) detection for CWNIRS

The major specifications of the APD detector used in this project (full list at Hamamatsu_Photonics_K.K., 2009) are outlined in Table 5.3. Seven APDs were used for the complete multichannel CWNIRS instrument, as illustrated earlier in Figure 5.1.

Specification	*Description*
Manufacturer	Hamamatsu Photonics K.K., Japan
Device Name	C5460-01 APD
Wavelength Range	400nm to 1000nm (peak sensitivity @ 800nm)
Sensitivity	$-1.5*10^{8}$V/W
Active Area	ϕ3.0mm (diameter of circular photodiode)
Bandwidth	DC to 100kHz
Noise Equivalent Power (NEP)	$0.02\text{pW/Hz}^{1/2}$
Minimum Detection Level	0.005nW (RMS)
Maximum Input Level (light)	$0.06\,\mu$W

Table 5.3: Avalanche photodiode (C5460-01) detector used in the CWNIRS instrument.

It can be seen from the specifications above that this device satisfies many of the requirements of a detector for CWNIRS with the LED light sources used. Firstly, the wavelength range is adequate with a central peak at 800nm which is at the centre of the LED wavelengths and the isosbestic point for the haemoglobin species. The bandwidth of the

device is also suitable up to 100kHz. An analysis of the light detection level limits (minimum and maximum) can be seen as suitable for cerebral interrogation. The 760nm component (four die) of each LED package outputs approximately 25mW and the 880nm die 13mW. With the high absorption of cranial tissue (~10^7) it can be crudely assessed that 2.5nW and 1.3nW reach the detector, a combined total of 3.8nW which lies within the detectors range (0.005nW - 60nW). The active area of the detector is also an important factor - the larger it is the more light can be detected. However, for increased spatial specificity a smaller active area may be required. Given the difficulties with hair follicles and hair absorbing light it is a trade-off between size and what is practical for applications on a subject's scalp, principally signal-to-noise ratio. Hair can be brushed aside and clear up to 10mm of 'free' scalp typically, and so an area less than say 8mm would suffice - here an active area of 3mm is employed in this APD detector. Furthermore, a fiber optic bundle (see later in Figure 5.13) of 6.35mm diameter (ϕ) was used to increase the SNR of the instrument compared to the first prototype by Coyle et al at Maynooth (Coyle, 2005). It was anticipated that perhaps software-based demodulation techniques would not be as good (in terms of SNR of the demodulated signals) as hardware-based phase-sensitive lock-in detection techniques (examined later in Section 5.6.2) used in that first prototype previous to this project - where Dr. Coyle used a ϕ3.175mm light guide (Coyle, 2005). (These light guides are described in the next section - Section 5.3.2.3). Apart from these specifications the APD module also has a temperature-compensation bias circuit (to keep APD gain constant at ±2.5% at an ambient temperature of 25±10˚C) and a high-speed current-to-voltage converter (linear) in order to have the light levels recordable from the BNC output (as a potential difference). A block diagram of the APD board is shown in Figure 5.12 below. The high-voltage generator (+12V to +200V) is needed for the amplification process.

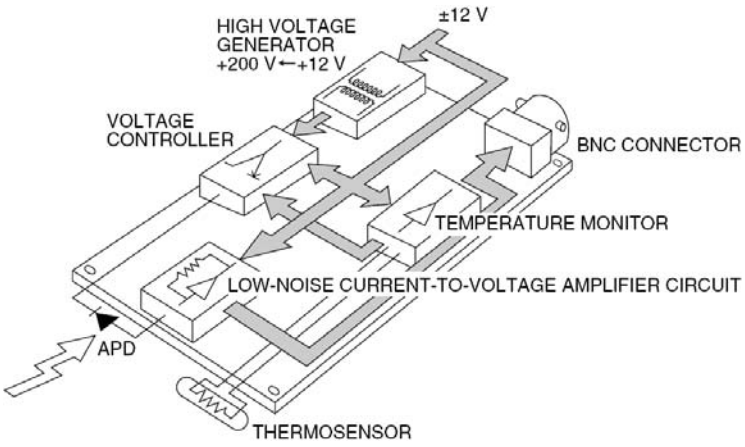

Figure 5.12: C5460-01 APD block diagram showing the main components for transducing light levels linearly to recordable potentials (~ 0V to -10V) from the BNC output.

5.3.2.3 APD coupling optics and signal conditioning

The APD module from Hamamatsu comes as shown in the previous block diagram, with a connection for the DC power supply. A design issue then is how to couple the light from the head to the APD's ϕ3mm active area. Fiber optics bundles can be used as light guides although there is a trade-off between losses and fiber cable length (evaluated later). In addition, if the diameter of the light guide is larger than the active area then a focusing lens of some sort is required to couple as much light as possible to the APD. Again, there are some other design considerations in selecting a light guide: 1) it should have good transmission for the NIR wavelengths used; 2) to maximise photons collected, it should have a large acceptance angle; 3) the length of the light guide should be as short as is practical to minimise losses, or incur acceptable ones; 4) the bend radius of the fiber bundle should allow for practical application of multiple light guides onto a subject's head for a multichannel CWNIRS instrument; and 5) it should be possible to fix the fiber cable to the subject's head and to the APD at the other end securely, to minimise artefacts arising from motion of the subject\light guides. This would also have the affect of changing the optical pathlength in an experiment if there is some artefact introduced (subject motion). The modified Beer-Lambert Law is not well equiped to handle these motions due to it being an ill-posed inverse problem.

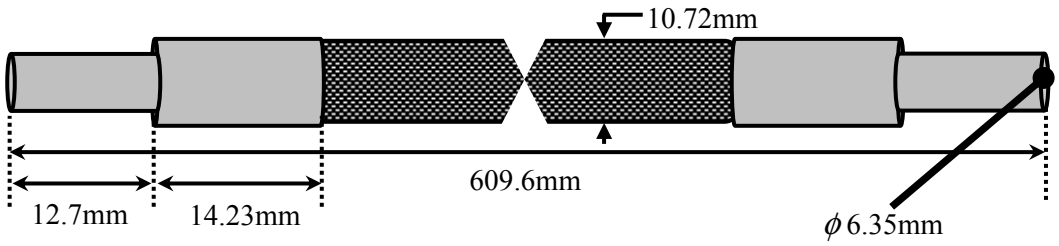

Figure 5.13: Fiber optic bundles (glass light guides) used to couple light from the scalp to the active area of the APD detector (not to scale).

The optic fiber bundles used for this project have an acceptance angle of 68° (with a numerical aperture of 0.55) with approximately 12,800 fibers per bundle for the 6.35mm diameter light guide used (Edmund Optics - NT42-346), with individual fibers 50 microns in diameter. The fiber bundle ends are polished and sealed with stainless steel ferrules. For this light guide, ~70% of light enters with losses of 6% per 300mm. Thus, for this light guide, ~60% of the light makes it through the fiber to the detector. They also have a minimum bend radius of 38mm.

Two other optically related accessories were added to the detection system. First, the light guide used has approximately twice the diameter of the active area of the APD, calling for some additional lensing apparatus. However, due to the spatially extended light coming

from multiple fibers in the fiber bundle, an aluminium bucket was used to collect the light. The aluminium bucket was also designed to allow for better, more secure coupling to the APD. This is illustrated in Figure 5.15. The aluminium bucket design also catered for rigid application of a second accessory - a NIR glass bandpass filter (NT46-082:Edmund Optics, UK; RT830; 12mm diameter with a central wavelength at 830nm and a FWHM of 260nm; 2.5mm thickness). The transmission spectrum for this filter is shown in Figure 5.14. This filter was put in place so as to protect the detector from saturation (ambient light) and reduce noise in the system from stray light arising from lack of secure fitting of the APD to the light guide, i.e. the photodiode is fastened with screws to the aluminium bucket and the light guide is flush with the opposite side of the glass BPF (the assembly is shown in Figure 5.15). Since the detector is sensitive in the wavelength range of 400nm-1000nm, the main effect of this filter is to reject visible light, i.e. <~700nm and, also those infrared sources above ~960nm.

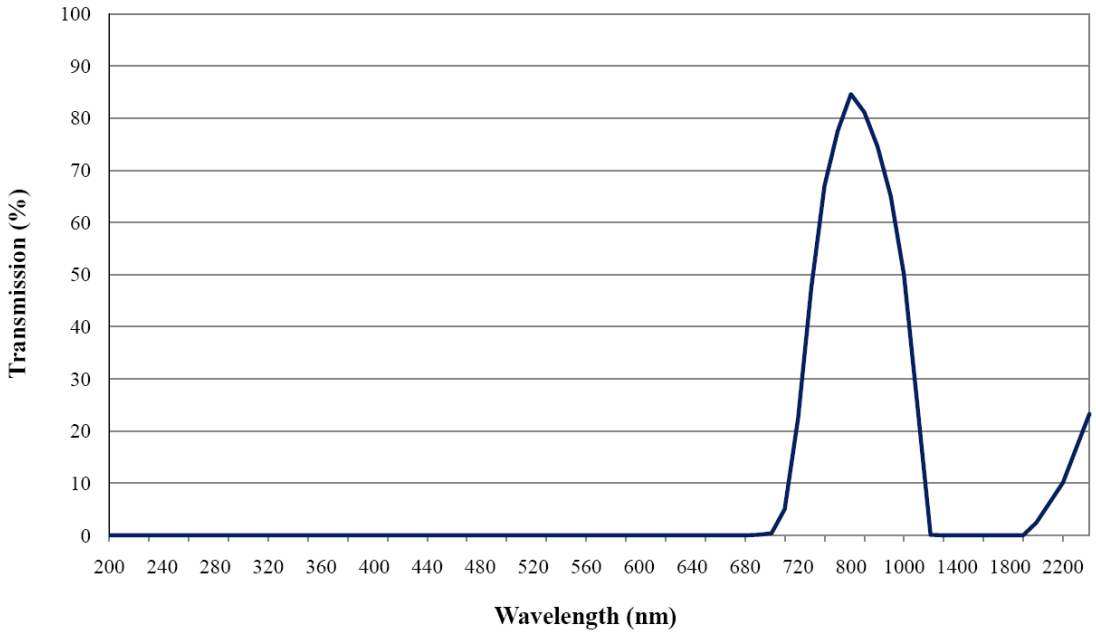

Figure 5.14: NIR glass bandpass filter with central wavelength at 830nm (Adapted from Edmund_Optics, 2009)

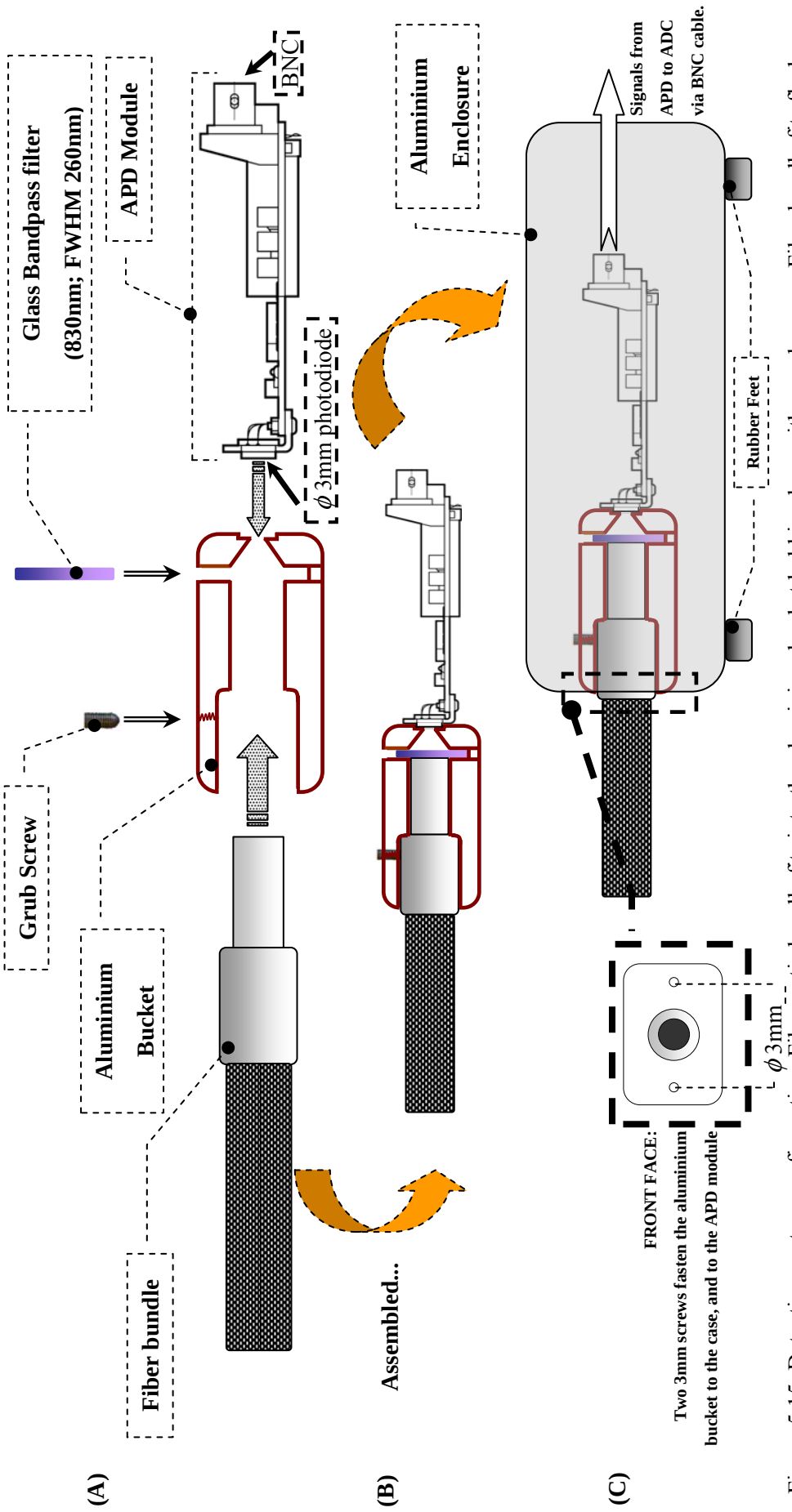

Figure 5.15: Detection system configuration. Fiber optic bundle fits into the aluminium bucket held in place with a grub screw. Fiber bundle fits flush against the glass BPF, which is slotted in a tight groove in the aluminium bucket. APD is held tight against the aluminium bucket on the right hand side via two 3mm diameter screws which secure the APD module, aluminium bucket, and the aluminium enclosure case (shown in "front face" inset).

5.4 Electrical Components

The electrical components of the CWNIRS instrument include:

- The signal generation card (PXI-6723) for creating signals to drive the LEDs;
- The circuits designed to provide linear voltage-to-current conversion to drive the LEDs, using the signals generated from the analog output of the PXI-6723 card (with additional design considerations such as input DC coupling);
- Auxiliary stand-alone power supplies to supply the APDs ($\pm$12 volts), and provide ~3 amps to supply the optical drivers or LED drivers;
- Analog-to-digital conversion (ADC) cards for acquisition of transduced optical signals from the detectors (APDs) via BNC cables (two 4-channel PXI-4462 cards with associated on-board analog anti-alias filters and analog amplifiers);
- Data buffering, multi-instrument triggering and synchronisation, and interfacing with the main workstation PC running LabVIEW - using the PXI-1033 Chassis and associated cabling;
- Finally, processing of these signals within the PC.

The LED driver is described next, followed by the signal acquisition and generation unit (for the optical sources), which operates under the supervision of a custom LabVIEW platform to implement data buffering and storage, triggering, biofeedback display, along with all real-time data processing (an account of the software interface is reported in Section 5.6).

5.4.1 LED driver

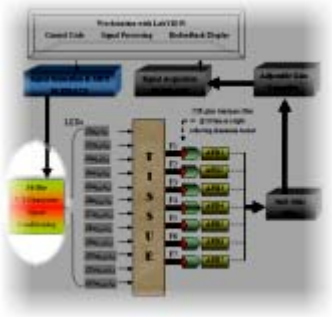

The optical BCI requires a circuit to control the NIR light sources. A triple wavelength LED driver for optical BCIs has been published in *Electronics Letters* recently (Soraghan, et al., 2009) which is effectively the same driver used to power the dual wavelength sources used here. The light sources used - LEDs - are current driven devices. The current through them is directly proportional to the optical output power they deliver (note: this demonstrated later in Figure 5.21(a)). Preferably, these devices should be voltage controlled. Thus, a stable voltage-to-current converter - which essentially provides voltage-to-light intensity (linear) conversion - is required. A further requirement is that for CWNIRS, the driver must allow for modulation of the light output from DC to several kHz. This is to allow separation of the light sources after being detected, i.e. each LED will be

modulated at a different frequency allowing for amplitude demodulation (AM) of each source. (This demodulation strategy is described later in Section 5.6.2.) In addition, input DC coupling is required to facilitate multiple modulation strategies such as time division multiplexing (TDM). As previously mentioned, to ensure maximum light entry into the head at a focused point on the scalp, both wavelengths should be housed within the same LED package. Without common anode/cathode configuration, this would require at least 6 leads from the device, making the resulting system bulky (1 anode and 1 cathode for the 880nm die (thus 2 leads) and similarly for each pair of 760nm die (thus 4 more leads)). Thus the custom-made common-anode (ground) dual wavelength LEDs used (OD1894- Opto Diode Corp.) place an extra constraint on the LED driver design: the common-anode connection must be grounded. This favourable common-ground configuration also has a potential safety benefit, since the LED package case (chassis) is also connected to ground. Indeed, it also allows shielding right up to the active component (LED die). A photograph of base of the common anode LED package and its leads is shown in Figure 5.16 below for reference. Lead 5, the common anode for the die at zero volts - ground - can be seen soldered onto the case behind lead 1 in the image.

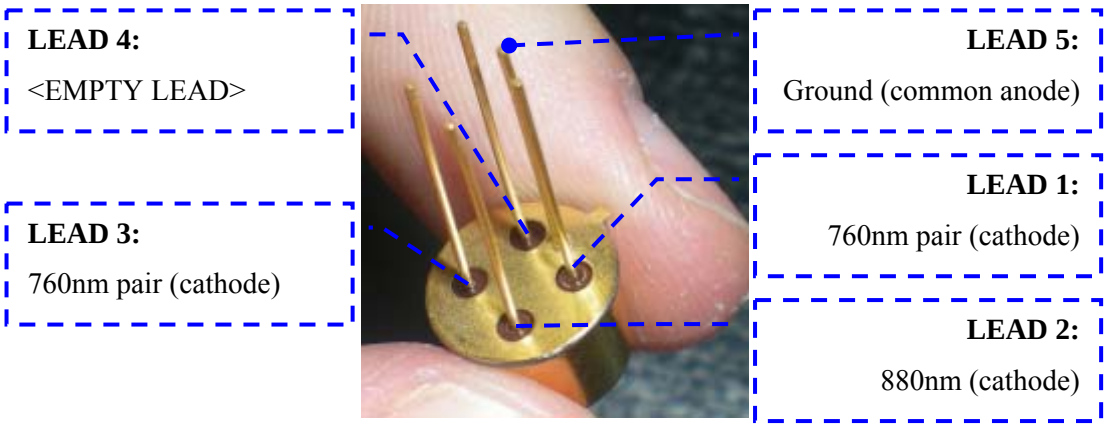

Figure 5.16: Photograph of base of LED package showing 4+1 leads. As mentioned in Section 5.3.1.2 one lead is empty. Two of the leads serve the four 760nm die in 2 pairs. The final lead serves the 880nm die. All die (5) share a common anode (case).

In terms of an LED driver, the popular design in Figure 5.17 has the potential for lower inherent noise, but nevertheless it cannot satisfy the common-anode ground constraints which are satisfied by the driver design presented in Figure 5.18. The necessary modifications from the standard active driver design (Figure 5.17) are PNP transistors for current amplification (for high power LEDs), a differential op-amp, resistors to reduce the gain in the second stage (required to suppress oscillations in the output - discussed next), and capacitors to decouple the supply rails. The differential op-amp stage facilitates grounding of the common-anode leads. This op-amp provides a feedback signal which is related to the potential drop across the LED's current limiting resistor (1W, 47Ω) in order to sense the

current driving the LED. Thus, this negative feedback control ensures linearity in the voltage-to-light intensity output by each LED and is the basis for the V-I conversion stability (linearity shown later in Figure 5.21(a)).

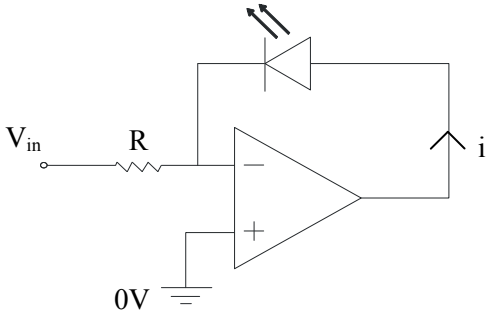

Figure 5.17: Standard active V-I converter design, employing a single operational amplifier (op-amp).

The circuit in Figure 5.18 is used to drive one 880nm die or a 760nm die pair, i.e. one cathode in an LED package. Thus, for a full LED package with two 760nm die pairs and a single 880nm die, three of these subcircuits are needed (as illustrated in Figure 5.19). The circuit in Figure 5.18 is specifically for the 880nm die, whereby for each 760nm pair, the current limiting resistor, *R1*, is 26Ω (rated at 2 watts) instead of 47Ω (rated at 1 watt); since twice as much current is required to drive the pair of 760nm die (200mA). *Vin* is set in software and is independent to every die\die pair (cathode) connection, thus allowing for

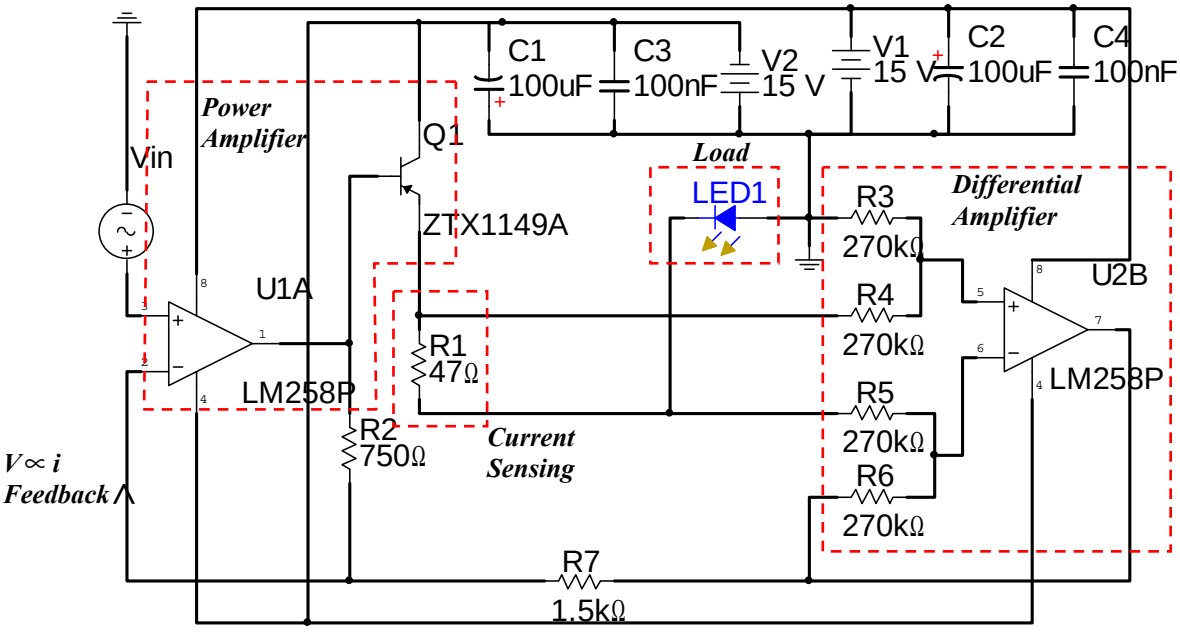

Figure 5.18: LED driver sub-circuit schematic. Three sub-circuits are required per OD1894 package - 1 per 760nm die pair (of which there are 2 pair per OD1894 package) and 1 sub-circuit for the 880nm die.

setting individual current levels. The transistors used (ZTX1149A) have heat sinks and non-electrically conductive heat sink epoxy to enable dissipation of more heat from these E-line transistor packages.

As illustrated in Figure 5.19 all five die in a single LED package share a common anode (ground), but have separate voltage inputs (Vin_1, Vin_2, and Vin_3). It can also be seen that each 760nm die pair (parallel) shares the same Vin. Note also that in practice Vin_2 is set equal to Vin_3. This means that potentially four times the output power at 760nm leaves the single LED package than is achievable from a single 760nm die. Moreover, these inputs could be driven independently with simple alterations to the electronics.

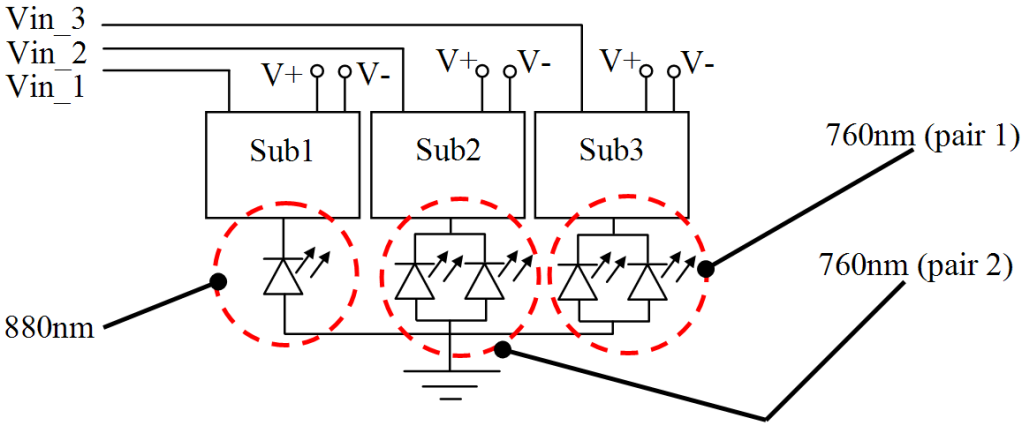

Figure 5.19: Complete circuitry for a single LED package (OD1894). The schematic illustrates the modularity of the subcircuits from the single schematic shown in Figure 5.18.

In the design process of the optical drivers, a source of contaminations was found appearing as high frequency oscillations in the output (across the current limiting resistor, R1). These are described next.

5.4.1.1 Stabilisation of control loop

In the original design, resistors R2 (750Ω) and R7 (1.5kΩ) were not used, in comparison to the final design schematic shown in Figure 5.18. However, in this reduced design, oscillations (~0.333MHz) in the output were observed in an *Electronics Workbench* (Multisim) simulation of the circuit and also in practice, which are shown in Figure 5.20. The cause of these oscillations was identified as being due to propagation delay between the first and second stage op-amps in the circuit. The solution was to reduce the gain in the first stage op-amp. This was achieved by introducing feedback resistors R2 and R7 (750Ω and 1.5kΩ respectively), effectively reducing the gain to a half. This removed the oscillations in the software simulation and in practice. The graph in Figure 5.20 demonstrates the

suppression of these oscillations contaminating an applied 3kHz carrier wave signal modulating an LED (measurement across the current limiting resistor, R1 (47 Ω)). In order to prevent other common aberrations, such as clipping (waveform distortion) in the event of applying inadequate power levels, careful consideration is needed in applying the correct input signal. Thus, the common settings for the LEDs and associated circuitry are discussed next.

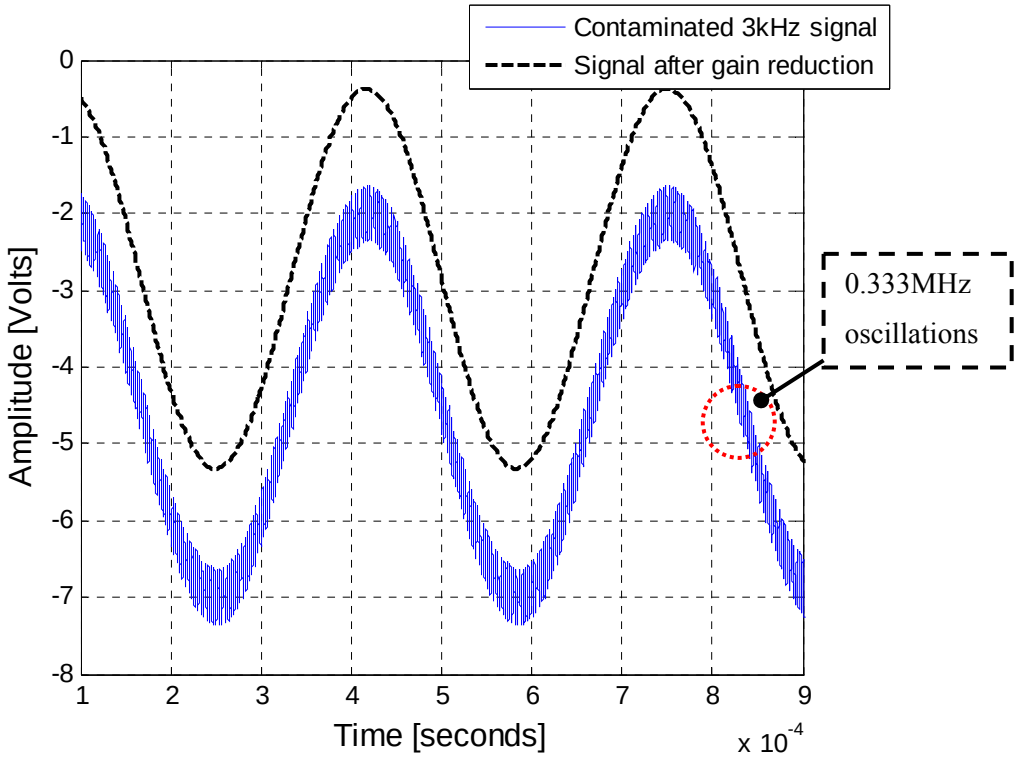

Figure 5.20: Oscillations across the current limiting resistor due to propagation delay between the first and second stage of the dual op-amp. The contaminated 3kHz signal (blue solid trace) applied to the light source is cleaned (black broken trace) using feedback resistors to reduce the gain in the first op-amp stage.

5.4.1.2 LED driver settings

The circuitry for a full LED package was shown in Figure 5.19. Op-amp rails are set at ± 15V (V+ and V-). Each LED package (OD1894) is almost modular, requiring the same circuitry for each die in the package (except for a single resistor, R1). A flexible software interface (Section 5.6.1.3) allows the potential (which is ∝ current for this circuit - see Figure 5.21(a)) to be adjusted for each die. In the LED package, the 880nm die requires a maximum ~140mA RMS forward current, and each 760nm die pair could be set up to twice that current - although these levels are never used due to the thermal conduction issue dealt with in Section 5.3.1.4. The typical settings for an LED package are shown in Table 5.4 below. All LEDs (12 sources * 2 wavelengths) are modulated in the range 8kHz to 16kHz with inter-modulation values (frequency gaps) of ~200Hz, i.e. all frequencies are kept within

one octave to avoid harmonic crosstalk. The modulation technique used is dealt with in Section 5.4.2.4 (analog signal generation) and Section 5.6.2 (software demodulation). Finally, *Vin* for each source was set to modulate those sources at each separate frequency between a maximum and a minimum potential. The minimum voltage is bound by having LEDs operate on the linear slope of forward current (see Figure 5.21(a)), and the maximum voltage is bound by thermal conductance levels (<41 °C - as discussed in Section 5.3.1.4) and satisfactory optical output power for acceptable SNR at the detector. A channel is deemed sufficient for recording with the acquisition of the cardiac pulse from the arterial contribution of the imaged cerebral tissue (discussed in the next chapter). Commissioning of the optical driver (LED driver) has been reported recently (Soraghan, et al., 2009) and is described next.

OD1894 LED LEAD	*Current [mA-RMS]*	*Modulation Frequency [kHz]*
LEAD 1 (880nm)	142	8
LEAD 2 (760nm (die 1 & die 2))	90	8.2
LEAD 3 (760nm (die 3 & die 4))	90	8.2
LEAD 4 (Ground - common anode - LED Case)	N\A	N\A

Table 5.4: Common settings for individual die within the LED Package (OD1894). Note: all 760nm die are driven with the same voltage input in an LED package, which is why cathode LEAD 2 and LEAD 3 have the same modulation frequency - they are physically connected to the same cable.

5.4.1.3 Commissioning the optical driver

Commissioning of the optical driver (Soraghan, et al., 2009) involved analysis of the frequency response, linearity, and step response of the device. Figure 5.21(a) demonstrates the voltage-to-light intensity mapping (using an optical power meter (Model: Ando AQ-2105)) showing a linear response, with a slope of -0.8995 ± 0.0006 [mW/V] and an intercept of -1.0634 ± 0.0027 [V]. The offset (non-zero intercept) in the graph is due to the potential drop by the feedback resistors R2 and R7 (required to reduce the aforementioned oscillations). This offset is catered for by maintaining a dc offset (equal to the intercept) at the input, to ensure the LED is always on. Without it the LED waveform would be clipped as the LED turns off (not forward biased).

The frequency response of the LED driver (~40 kHz range) is shown in Figure 5.21(b) which is suitable for CWNIRS studies. In addition, the step response (sampled at 204.8 kHz) is illustrated in Figure 5.21(c). Finally, total harmonic distortion of 0.95% was recorded at

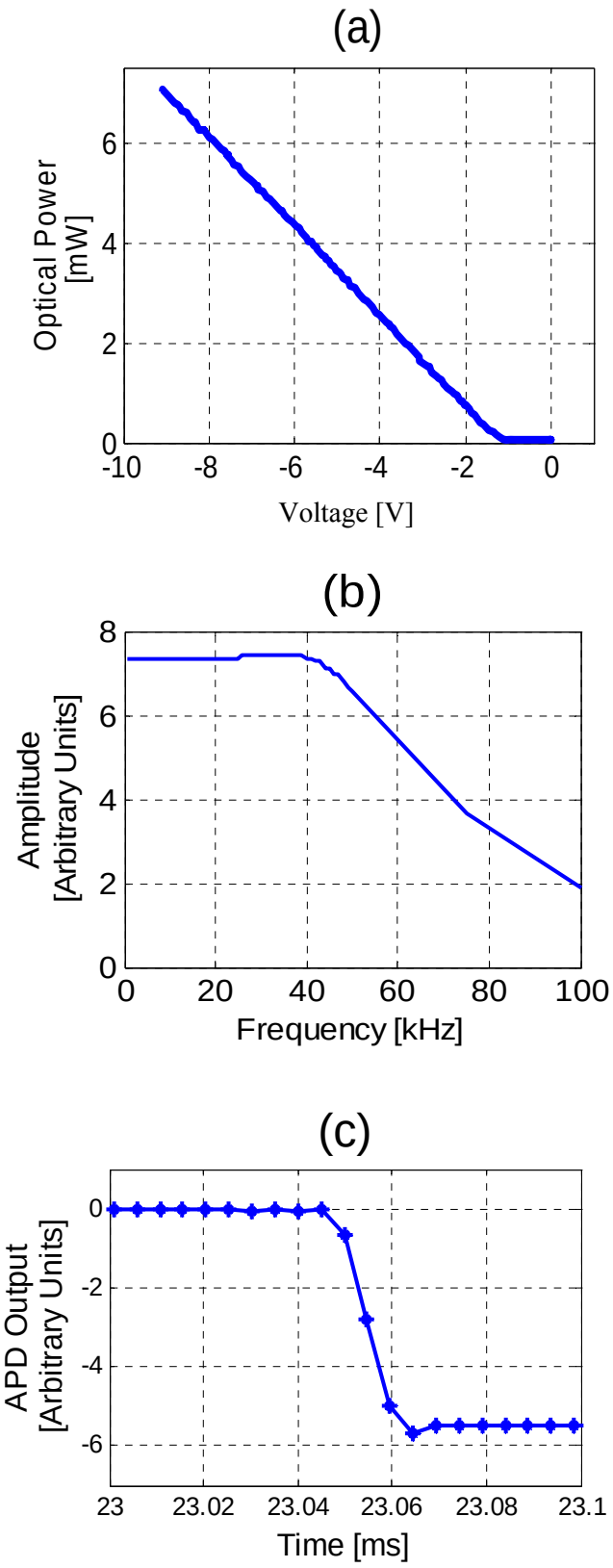

Figure 5.21: LED driver characteristics (using a 760nm die): (a) Optical power output linear response to change in DC input voltage (slope = - 0.8995 ± 0.0006 [mW/V]); (intercept = -1.0634 ± 0.0027 [V]); (b) Frequency response of LED driver (~40 kHz range); (c) Step response of LED driver.

the detector output, using a LabVIEW virtual instrument.

It can be seen from Figure 5.21(a) that the LED operates in a linear fashion in the range of ~ -2V to -9V. Note: the optical power values in this figure are for a relatively low power single 760nm die that was used in the commissioning of the LED driver. Thus, for different LEDs and wavelengths used, the drive signal will differ slightly (but within the 0V to -10V range) but the operation of the LED driver remains the same, i.e. the characteristics pertain to the LED driver. For example the LEDs are capable of emitting light in the MHz range (Held, 2008), and so the frequency response in Figure 5.21(b) is a characteristic of the LED driver circuitry - not the LEDs.

Conclusions:

The LED driver described caters for scaling an OBCI to a multichannel device which is needed to improve localization and throughput\data rates of the BCI device. Since the input design is DC coupled it also enables the group and other researchers to test and establish different modulation strategies such as time-division multiplexing and pseudorandom binary sequences making the device more flexible for different research needs (Matthews, et al., (Under Development)). It should be noted that the LEDs require at least 35 minutes settling time before use so as to sufficiently stabilise their optical output (as well as wavelength - as was discussed in Section 5.3.1.3). Drift in the optical output is shown in Figure 5.22.

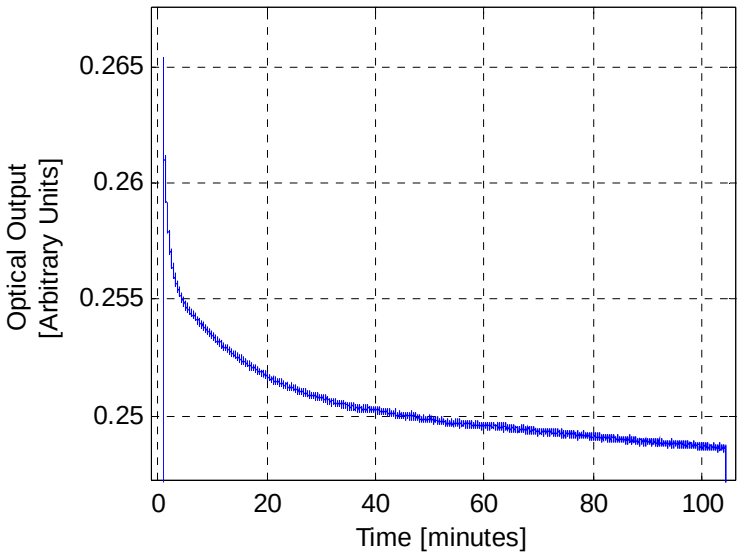

Figure 5.22: Drift profile of an LED over ~ two hours. At least 35 minutes should be allowed for the LEDs to settle their optical output.

The drift shown in Figure 5.22 reflects the temperature drift in the optical output (Soraghan, et al., 2008b) displayed previously in the temperature profiles in Figure 5.9 and Figure 5.10 (temperature increase is proportional to output power decrease - thermal losses). Care should also be taken to avoid clipping (introduces harmonics and thus poor demodulation) - i.e. driving signals should be set within the linear range depicted in Figure 5.21(a).

The next electrical component of the CWNIRS instrument refers to the data acquisition and processing unit of the device. The generation of a carrier signals for the LED drivers and the data sampling of the APD detectors are performed using various *National Instruments* PXI cards and associated electronics. These instruments are all under the control of a powerful and flexible software platform (LabVIEW). These instruments and their integration into the CWNIRS system are described next.

5.4.2 Data acquisition and processing unit

The entire CWNIRS system is integrated into a single workstation pc running LabVIEW which controls signal generation for the optical sources (sinusoidal signals), data acquisition from all 7 APD detectors, including data buffering and data synchronisation (triggering between devices), as well as all online (during an experiment) and offline (optional post-processing) signal processing. The LabVIEW software interface (described in Section 5.6 to follow) works with a *National Instruments* PXI Chassis (NI-PXI-1033) which houses two data acquisition cards (NI-PXI-4462) and one signal generation card (NI-PXI-6723) - as illustrated in Figure 5.23 for a three detector system (note: the full instrument uses seven detectors and twelve light sources as depicted in Figure 5.1, but only three of each are shown in this figure for clarity). The inset in Figure 5.23 is a photograph of the PXI chassis with the ADC and analog output cards in place in the chassis. In this section (5.4.2), firstly the design considerations for data acquisition and carrier wave generation are discussed, followed by an exposition of the choice of instruments and their characteristics. Finally, the workstation used is described.

5.4.2.1 Design considerations

Data Acquisition Considerations: Specific design considerations for the data acquisition system were that it should allow for sampling of up to 7 detectors with signals up to 16kHz. Shannon's sampling theorem dictates that the sampling rate should be at least twice the highest frequency found in the sampled signal to avoid aliasing - i.e. prevent the introduction of signals that are not present in the measured signal. Thus, this would require a sampling of at least 32kHz for a 16kHz signal. However, for a 16kHz sine wave modulating

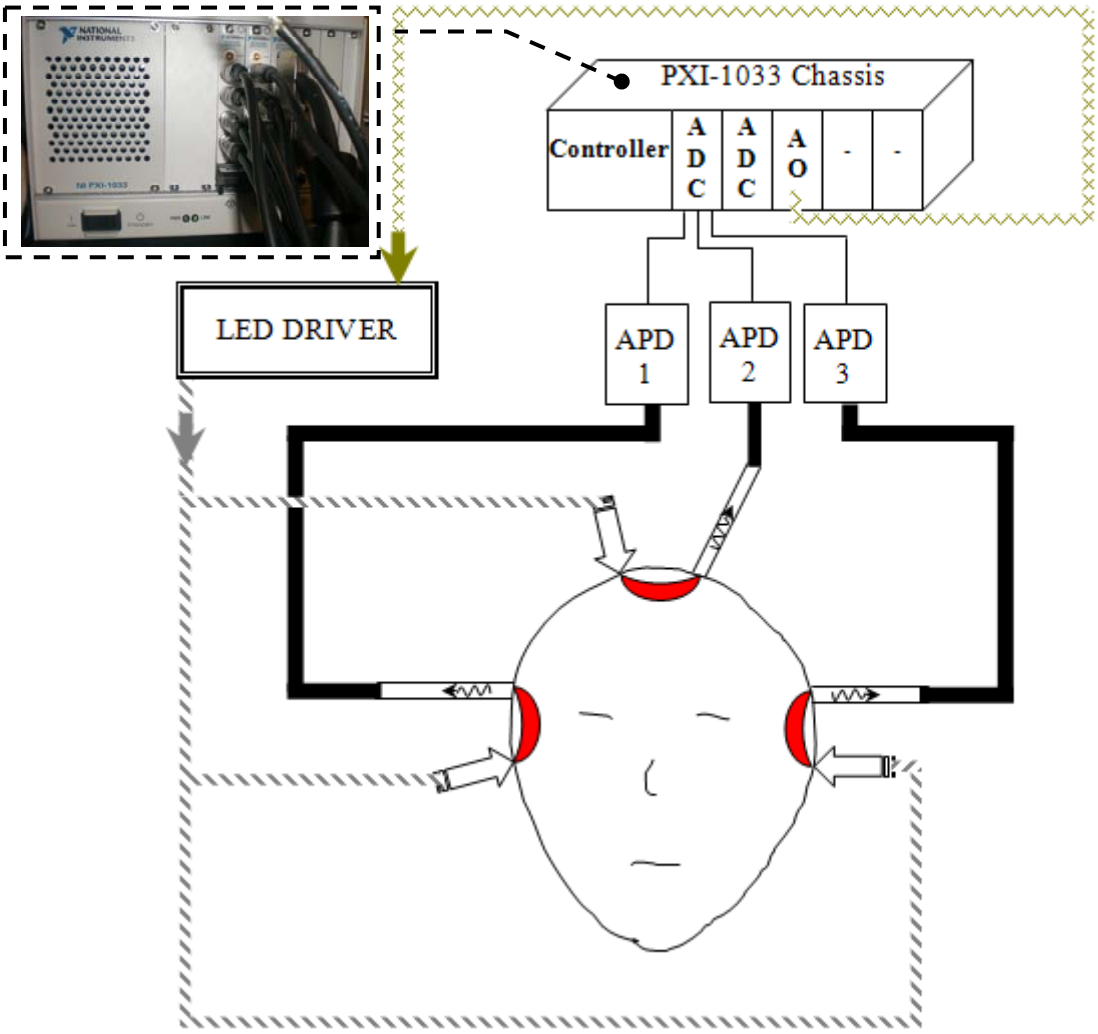

Figure 5.23: Data acquisition (analog-to-digital converters - ADCs - *NI-PXI4462*) and signal generation (analog output -AO - *NI-PXI6723*) integration and housing within the *NI-PXI-1033 Chassis*.

a light source, this sampling rate would only produce two samples per period of the 16kHz signal. Thus, in practice for better waveform reconstruction (more samples per period) a sample rate of perhaps 10 times the highest frequency (thus 160kHz) is favourable. This issue is illustrated in Figure 5.24 below demonstrating the difference between sampling at two samples per period versus ten sampled per period.

A further design feature for this system was to have an analog amplifier after the APD before sampling to use the full dynamic range of the APDs. This offers increased SNR to the digital signal processing (DSP) stage where demodulation takes place, and better use of the bit resolution (24-bits) of the ADC cards since the amplitude range of the detected signal is maximised to match the ADC card's voltage range (typically $\pm$ 10V).

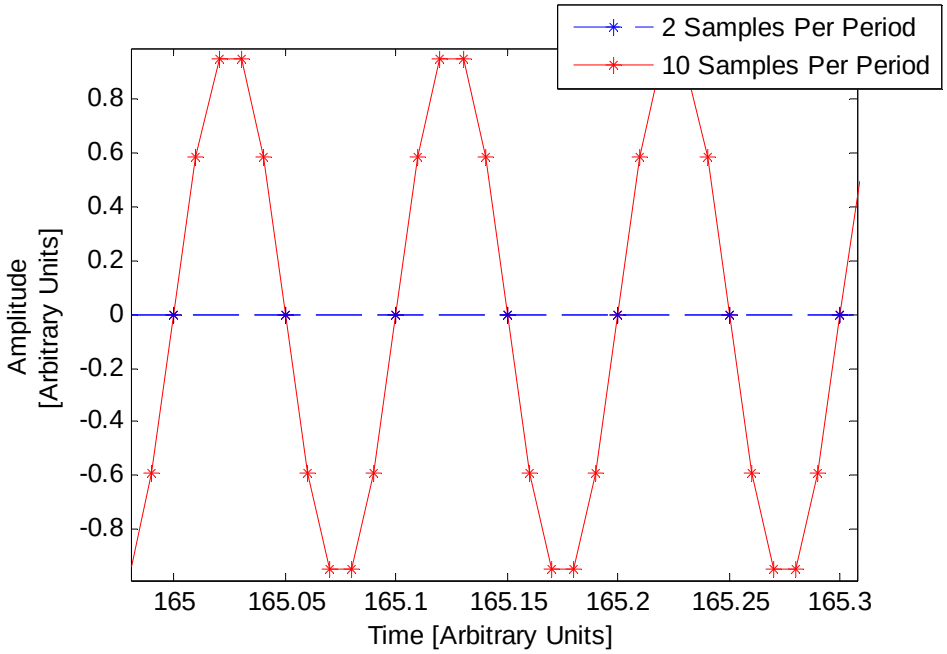

Figure 5.24: Sampling rate affect on a sinusoidal signal - two samples per period (blue broken trace) versus 10 samples per period (red solid trace).

Signal Generation Considerations: The design considerations of the analog signal generation are that it should provide at least 24 analog output signals in the range ~0V-10V since this is the voltage range required for linear operation of the driver as presented in Figure 5.21(a). It should also cater for generation of sinusoidal signals in the range 0 to 16kHz, as stipulated in Section 5.4.1.2.

Signal Synchronisation Considerations: The design constraints for the signal acquisition and generation just described were considered along with how they may be interfaced with a LabVIEW software environment. Consideration was also needed into how the triggering and data buffering may be handled since the multichannel system demanded a significant volume of data to be recorded, generated, and processed. The solution was to have all data acquisition cards and signal generation cards integrated into a *PXI chassis* which overcame many potential difficulties in the overall design and provided:

- Simultaneous data sampling capabilities;
- Data synchronisation (to a shared clock) and triggering (starting and stopping cards);
- Buffering of data to ease the workload on the PC, and,
- Flexible cabling with single BNC connections to all signal generation and acquisition channels.

5.4.2.2 PXI- Chassis: NI-PXI-1033

For seamless data transfer, a PXI chassis to house all data acquisition and signal generation cards was integrated into the CWNIRS system. PXI (PCI eXtensions for Instrumentation) is a modular electronic instrumentation platform from National Instruments (originating in 1997) and allows for rigid timing, synchronisation, and triggering, with increased provision for single-slot cooling and power delivery, than a PCI (Peripheral Component Interconnect) counterpart. A 'PCI Express-to-PCI bridge' on the PCI-express card (which is plugged into the PC's PCI-express slot) allows the modules (e.g. a data acquisition card) in the chassis to appear like separate PCI cards in the computer (see Figure 5.25). The added benefits are more power and cooling to individual slots, an increase in the number of slots available (for one PCI-express slot), and synchronisation features. Phase sensitive techniques were originally desired for data demodulation and so data synchronisation and triggering between various modules was required. The NI-PXI-1033 chassis (dimensions: L*W*H ~25cm*22cm*18cm) along with PXI data acquisition (Section 5.6.1.2) and generation cards (Section 5.6.1.3) chosen also have the advantage of being optimised for interfacing with LabVIEW, i.e. National Instrument hardware (PXI) used with National Instruments software (LabVIEW). This allowed for triggering between modules (cards) on a common 10MHz clock running on the backplane of the chassis, which is configurable in software. Thus, cards can be set to initialise at the same moment in time and can be phase synchronised with the use of the 10MHz clock - specifically on a RTSI 1 bus (Real-Time System Integration bus) configured using the NI-DAQmx driver - described in Section 5.6 on software interfacing.

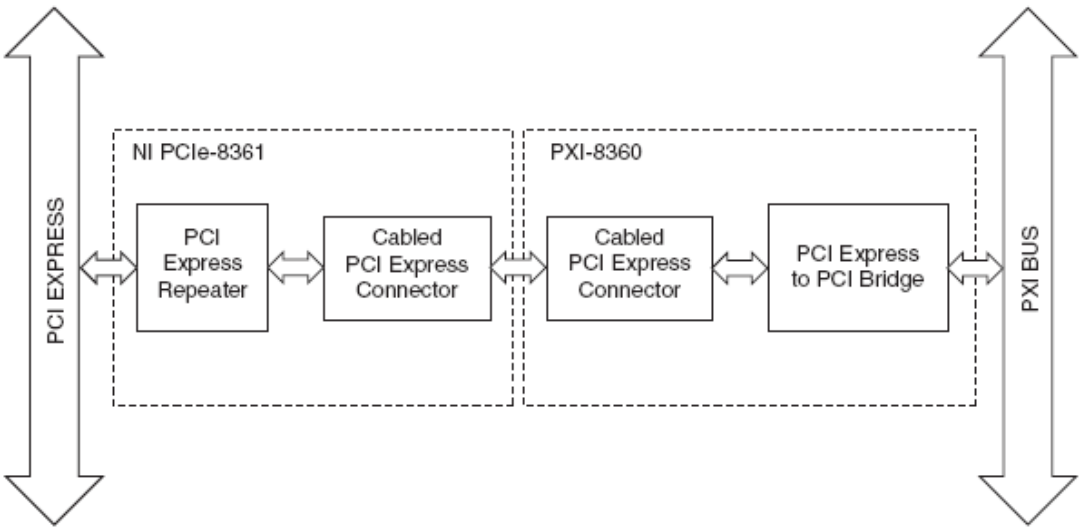

Figure 5.25: MXI-Express block diagram. The NI-PCIe-8361 connected to the PCI express slot in the pc is connected via a PCI express cable to the PXI-8360 card in the PXI-1033 chassis.

Another favourable aspect of the PXI system was the availability of a suitable PXI data acquisition card with onboard programmable gain and anti-aliasing filters. The PXI chassis is integrated with the PC via an MXI-Express remote controller (in the chassis) with 110MB/s throughput and a high bandwidth PCI-express card (NI-PCIe-8361-connected to the chassis controller via a 3m cable). This connection is illustrated in Figure 5.25. Next, the data acquisition solution is described which meets the design constraints reported in Section 5.4.2.1.

5.4.2.3 NI-PXI-4462 ADC

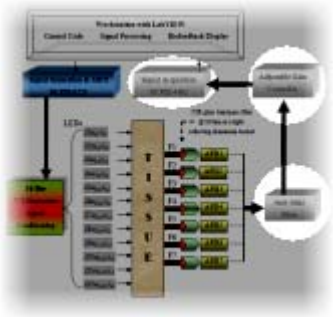

The NI-PXI-4462 data acquisition card (24-bit resolution with 118dB dynamic range) was selected due to its simultaneous-sampling capability across all four of its input channels at a maximum rate of 204.8kHz (kS/s) per channel - thus providing almost 13 samples per period for a 16kHz signal (the maximum carrier wave frequency from the LEDs). Many data acquisition cards use multiplexing techniques, sampling in a time multiplexing fashion across channels, whereby as the number of channels being sampled increases the maximum sampling rate is reduced for all channels. Two of these 4-channel NI-PXI-4462 ADC cards are used in the NI-PXI-1033 chassis thus allowing data acquisition for up to eight detectors (APDs) with the possibility for further expansion (2 empty slots - depicted in Figure 5.23). Again, the key is that increasing the number channels acquired can be achieved without a reduction in sampling rate (although software timing may be affected due to the sheer amount of data being processed in real-time - dealt with later in Section 5.6).

Onboard anti-alias (AA) filtering is also provided in two stages using analog filters:

- An fixed analog AA filter to remove frequencies beyond the ADCs range (maximum rate of 204.8kS/s); and,
- Digitally controlled AA filters, whereby their cut-off frequency is adjusted automatically to remove components above half the programmed sample rate (set in software).

As a result an alias-free bandwidth (passband) of ~92.8kHz is maintained (DC to 0.4535*fs: fs max 204.8kS/s).

Six gain settings for the analog amplification (pre-amp) allow for various input voltage ranges (full-scale range V_{pk}) from the minimum range of $\pm$316mV to the maximum range of

±42.4V (gain selection -20 to +30dB in 10dB steps). This pre-amp range is set in software (LabVIEW) and each input channel gain is independently software selectable. Since the light detector's output potential ranges between 0V and -10V, this pre-amp gain is set to that range (0 to -10V) using the full dynamic range offered by the ADCs. Data acquisition inputs can also be programmed for either AC or DC coupling which is important for allowing different modulation strategies to be used. Finally, this card can be synchronised with other cards in the NI-PXI-1033 chassis (digital trigger and clock) or indeed with an external trigger for, for example, phase sensitive detection techniques (with <0.1° phase mismatch). This triggering and synchronisation is utilised on all three cards in the chassis - two NI-PXI-4462 and the signal generation card (NI-PXI-6723), discussed next. The operation of the ADCs are fully realised in the software interface section (Section 5.6), outlining the specifics of timing and typical settings used for the experimental work. Next, however, the signal generation card in the PXI system is described.

5.4.2.4 NI-PXI-6723 AO

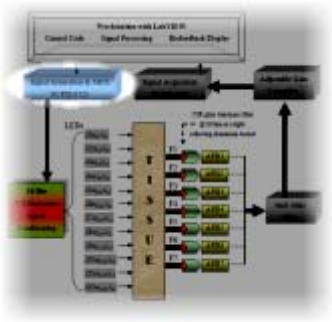

A signal generation card was required to supply the LED driver with 24-sinusoidal carrier wave signals up to 16kHz, but with the high power\current coming from stand-alone power supplies connected to the LED driver directly. The NI-PXI-6723 provides 32-analog output channels and is housed in the NI-PXI-1033 chassis. It has a 13-bit output resolution with an output voltage range of ±10V, satisfying the necessary 0V to -10V range needed for linear operation of the LED driver (demonstrated earlier in Figure 5.21). The PXI card used is a multifunction digital-to-analog converter (DAC) with an update rate of 45kS/s when generating signals on all 32 analog output channels. However, when generating only on 24-channels (as is needed for 24 LEDs) an update rate of ~60kS/s is achievable, using the host PC memory. The data flow from the signal generation in the AO card through to the LED driver and the LEDs is shown in Figure 5.26 below, with some break-out boxes in between.

Signal generation starts within the PC in LabVIEW whereby all individual signals (for each separate LED wavelength) are software configurable to adjust LED power levels.

1) The output signals are generated from the 24 analog outputs on the NI-PXI-6723 card (Figure 5.26(1));
2) All signals from the 24 channels are carried via two cables (2 meter 68-pin D-Type Connector - SH68-C68-S 68-pin VHDCI to 68-pin) to two noise-

rejecting, shielded BNC break-out boxes (BNC-2110 and BNC-2115), with additional multifunctional capabilities (Figure 5.26(2)), e.g. digital output channels and triggers;

3) One meter (1m) BNC cables carry signals from these National Instruments break-out boxes to a custom break-out box (Figure 5.26(3)) to convert from BNC to a 37-Way-D connector;

4) This 37-Way D connector relays the signals to the LED driver (Figure 5.26(4)). From here, ~1.5-meter 4-core cables relay signals to the LEDs - shown beneath the LED driver in Figure 5.26(4).

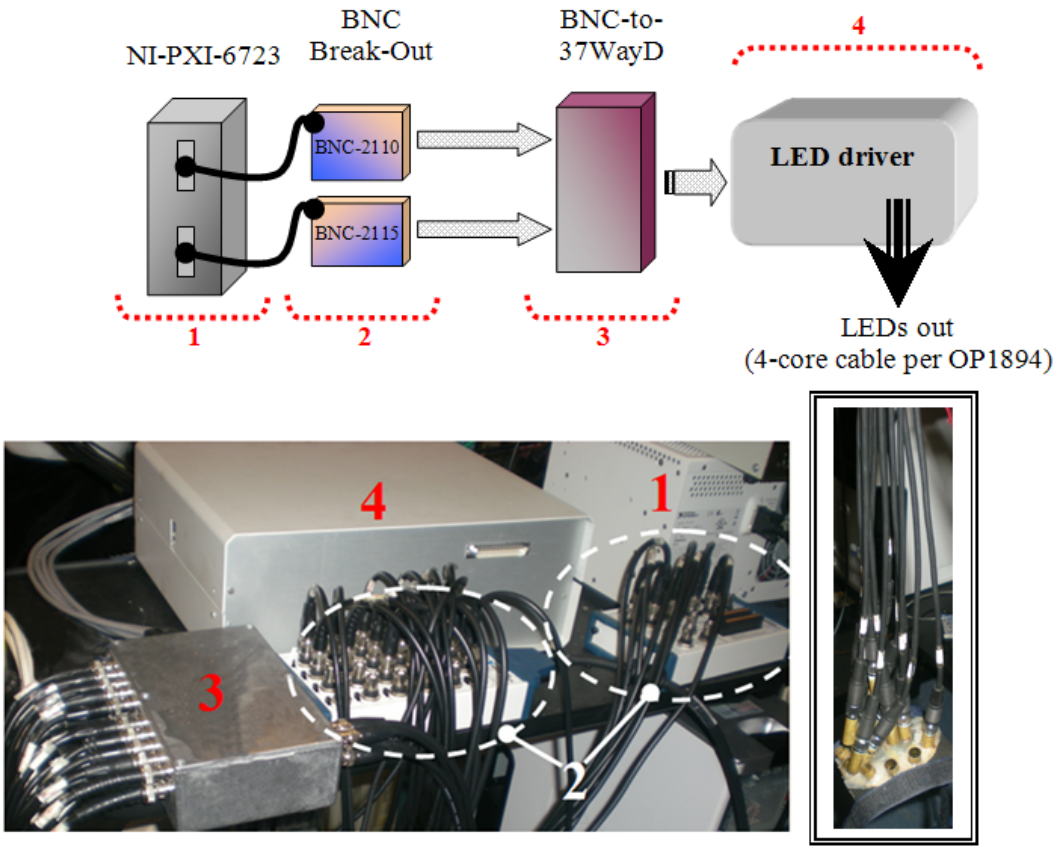

Figure 5.26: Analog signal path from signal generation to LED output. 1) The NI-PXI-6723 analog output generates 24 carrier waves; 2) Two 68-pin cables carry the signals to the break-out boxes; 3) A further break-out box converts from BNC to a 37-Way-D connector, and 4) signals are relayed to the LED driver which power the LEDs at the opposite end of 1-meter, 4-core cables.

This concludes the complete signal generation loop used to drive the LEDs. However, like the ADC cards, the operation of this signal generation card requires some software configuration which allows for flexibility in the overall CWNIRS instrument, e.g. software control is used to adjust LED power levels. The software interface element for signal generation is discussed in Section (5.6.1.3) where its integration into the whole CWNIRS instrument is illustrated in terms of timing, modulation strategies, and operation principles.

The final element of the PXI system is its integration to a PC with properties to cater for, for example, fast data processing. The workstation used is described next.

5.4.2.5 Workstation PC

Although the PXI-1033 chassis along with the ADC and DAC cards dominate data buffering and synchronisation, a powerful workstation PC was required for real-time data processing in LabVIEW, especially for online frequency analysis at the demodulation stage (described later in Section 5.6.2). The major specifications for the workstation are listed in the table below.

Workstation Feature	*Specification Value*
Workstation Model	Dimension 9200
Operating System (OS)	Windows Vista Business
Processor	Quad Core (2.4GHz, 8MB Cache)
RAM	3GB (3*1024MB;667MHz DDR2)
Hard Drive (HDD)	500GB (2*250GB Serial ATA 7200rpm)
Graphics	256MB ATI Radeon X1300 PRO
Monitor	20" Wide Flat Panel (LCD)
Other	No anti-virus installed; Not networked

Table 5.5: Main workstation pc specifications for all digital signal processing and biofeedback display. To maximise performance no anti-virus scanner is installed, and to prevent security issues, the machine is not networked.

A wireless mouse and keyboard were used to allow for better flexibility in controlling the PC in an experimental session, where the use of these close to the main monitor would obstruct the user's view. A second monitor was used for some experimental sessions, whereby biofeedback (LabVIEW generated graphics) was exported to this monitor for the user to observe during trials.

This concludes the section on instrumentation for data acquisition and generation. Next, the protection of the instruments and electronics is described.

5.4.3 Equipment protection

Protection of the equipment from power surges and associated electrical issues is catered for by the integration of an isolation transformer (Radionics, [1:1] 240-240 VAC; 4.2A) and a residual current circuit breaker (RCCB) - acting as an intermediary between the mains power (240VAC) and all BCI instrumentation, including the power supplies and pc workstation (see Figure 5.27 below). Thus, in the event of current leakage, the complete instrument is disconnected from the mains via the RCB. Furthermore, the isolation

transformer decouples (no electrical connection; blocks DC signals) the instrumentation from the main power supply.

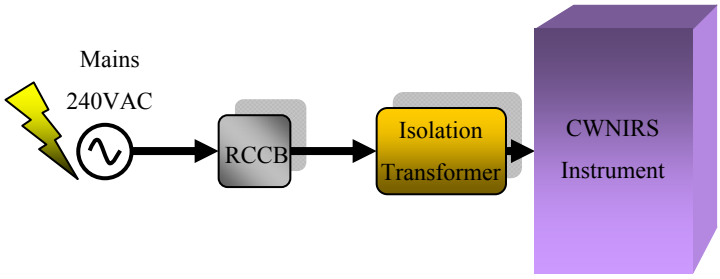

Figure 5.27: CWNIRS Instrument protection. The 240VAC-mains flows through a residual current circuit breaker and is decoupled at the isolation transformer (240-240VAC) before reaching the main CWNIRS instrumentation.

Thus far, the optical and electrical components of the CWNIRS Instrument have been discussed. The mechanical components of the instrument play an under-emphasised role in the overall efficacy of the device, where crucial SNR can be lost with poor coupling of the optical components (sources and detector fiber optic bundles) to the subject's head. Mechanical harnessing of the instrumentation is dealt with in the proceeding section.

5.5 Mechanical Components

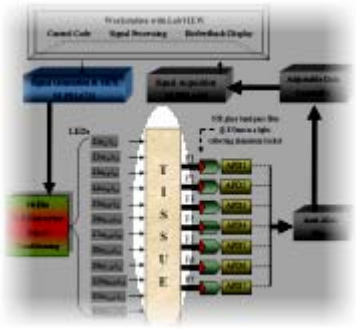

The mechanical components of concern in the CWNIRS instrument (highlighted on the left) are all related to couping the light sources and detectors to the subject's head. However, this is not simply a cosmetic concern, i.e. it has a substantial bearing on the signal integrity due to absorption effects, changes in photonic pathlength (which cause calculation errors), subject comfort (capable of causing undesirable haemodynamic arousal), and spatial resolution of optical imaging. The various design considerations for these mechanical components are outlined in a mind map in Figure 5.28 for a better holistic view of the many contributing factors. These factors are described in this section.

5.5.1 Components - sources and detectors

As mentioned previously, it is required to have the sources and detectors placed in contact with the head - to shine NIR light onto the scalp and to pick-up the remaining light (with a detector) exiting the head a few centimeters from the location of light entry (see

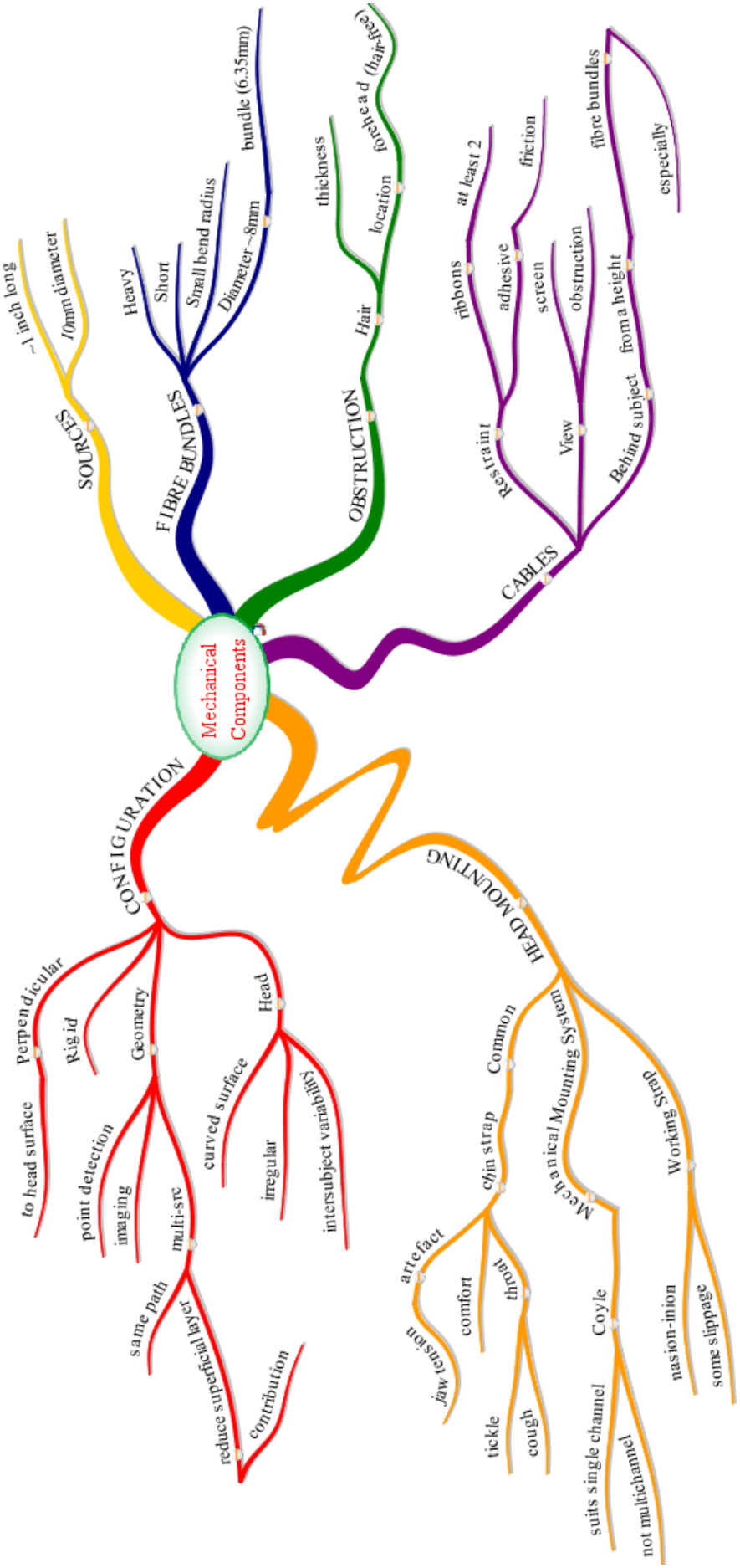

Figure 5.28: Mind map of the considerations for the mechanical components in the CWNIRS instrument design, especially those pertaining to harnessing cables and coupling optics to the head (image designed using iMindMap® software).

Figure 5.30 for a single-channel template). These are the only components of the CWNIRS instrument that need to be placed on the subject's head. However, the detectors (APDs) used have fiber optic bundles to couple the light remotely (~60cm away) instead of being in direct contact with the head (due to the power electronics needed for the APD, as well as improving the source detector electrical isolation). This also has the desirable effect of decoupling the subject from the detector electronics (glass fiber bundles). The grounding of the LEDs within the brass collar tubing (Figure 5.11) has the added effect of subject decoupling and improved safety (Soraghan, et al., 2009). Thus, the light sources (shown in Figure 5.11 and a group of sources shown in the inset of Figure 5.26) and the fiber bundles (see Figure 5.13) need to be fixed to the surface of the head. In addition, these should be applied perpendicularly to ensure maximum light entry into the head (to maximise the potential SNR) (Sliney, et al., 1980). The light sources are not wireless and so the associated cabling (see Figure 5.26 inset) needs to be harnessed appropriately and out of the subject's view of the monitor which is providing cues and\or biofeedback. Thus, the design of the mechanical coupling and harnessing of the optical components has to contend with four key elements which are developed in the following subsections:

1) Physical coupling to the head (including subject comfort and safety) (Section 5.5.1.1);
2) Non-haemodynamic photonic obstruction, (e.g. hair) (Section 5.5.1.3);
3) Cable harnessing (Section 5.5.1.2), and,
4) Optet configuration (Section 5.5.1.4).

To satisfy visualisation of a typical probe holder[5] (as a 'flash-forward') and for better appreciation of the design considerations yet to be described, an image is given below in Figure 5.29 of a typical optet holder designed during this project, specifically for BCI tasks utilising frontal cortex activity (e.g. mental arithmetic). This probe holder is secured to the head by the central strap (with velcro) which is fixed transversally around the head, i.e. horizontally from the inion to the nasion (see inset in Figure 5.29), and with four smaller straps - two above and two below the main strap. The specifics of probe fabrication will be dealt with later in this section.

[5] A *probe* is a general term for either a source or a detector. An *optical probe holder* (or probe holder, optet holder, or simply holder) is the term given for a mechanical structure used to rigidly fix the probes in place to a subject's head.

Figure 5.29: "Frontal probe holder". Optical probe holder for BCI tasks utilising activity from frontal cortex tasks, e.g. mental arithmetic. The four cylindrical brass tubes in the middle row house the fiber bundles for 4 APD detectors (D1, D2, D3, D4). Each detector can 'see' NIR light from 4 neighbouring light sources (OD1894 LED packages; S1, S2, ... , S10) surrounding the fiber in a square formation (example shown for detector D1 and sources S1, S2, S6, and S7). The image to the right illustrates the placement of the optical probe holder on a subject's head, for frontal cortex studies.

5.5.1.1 Physical coupling - fixing probes to the head

Attaching the optical components or probes to the head is one of the more testing elements of the CWNIRS instrument design (or for any NIRS instrument for that matter, e.g. time-domain imager). One of the challenges is that the head is curved with many irregular ridges that hamper rigid connection to the head and make perpendicular application of probes difficult. Furthermore, these differences can vary across subjects and in addition hair not only absorbs NIR light significantly but it makes provision for movement of overlying optical components with respect to each other (slippage). This causes changes in the mean optical pathlength (as well as obscuring the source and detector) which can have a significant negative affect on the recorded signals analysed in an ill-posed inverse problem, i.e. the modified Beer-Lambert Law used to calculate haemodynamic concentration changes.

Strangman et al lists solutions to date of modified cycle helmets, fibers embedded in rubber forms, and subject-specific (individualised) thermoplastic moulds (Strangman, et al., 2002). David Boas' group along with a commercial company (TechEN, Inc.) selling instruments developed by Dr. Boas and his colleagues have many different variations in probe design over years of development shown at their Photon Migration Imaging (PMI) Lab webpage (http://www.nmr.mgh.harvard.edu/PMI/research/probe-gallery.htm), which epitomise the range of currently available probes. Earlier probes can be seen to apply the fiber bundles perpendicular to the scalp, but more contemporary versions have fibers arriving parallel to the scalp surface, using a prism to steer light 90° (Elwell, 1995) or simply having fibers bent in a 90° arc at the fiber terminus (personal communication, TechEN, Inc. (CEO), Arthur Dimartino).

The fiber bundles used in this dissertation have a metallic ferrule at their terminus, thus allowing for support of the bundle with this 12.7mm-long and ~8mm-diameter fixture (see Figure 5.13). The LEDs are housed in a brass cylinder (see Figure 5.11), and so the brass caters for rigid support of the LEDs. Thus, a series of rigid 'sockets' and a frame is needed to hold the probes in place. A concept-template for a single source and a single detector is shown in the illustration above (Figure 5.30).

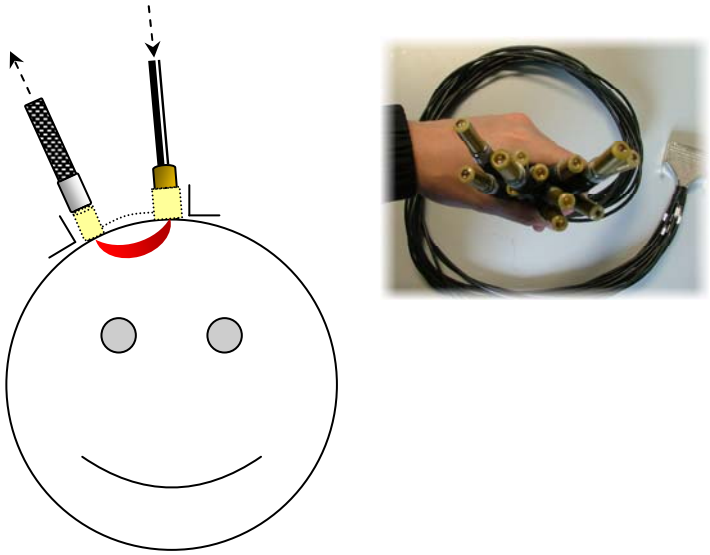

Figure 5.30: Probe application template for a single source and detector. Inset on the right shows the full light source cable suppling 12 LED packages from a 37-Way-D connector which receives carrier wave signals from the LED driver.

In the figure, the dashed sockets and dashed frame hold the probes in place at right angles to the head surface. Note that even for the same optode (with a single source and single detector place 3cm apart) the curvature of the head differs for each probe position relative to each other, and so the frame of the holder needs to be curved and rigid - yet flexible enough for differences in inter-subject *and* intra-subject head curvature. 1) Cables suppling current to the LEDs, and 2) the fiber optic bundles coupling NIR light to the detectors, need to be harnessed apart from this socket-frame. This is done in order to reduce the load bearing-down on the subject's head and the load on the optical probe holder itself, i.e. the cables for the optical probes need to be held above the height level of the subject.

5.5.1.2 Cabling harnessing

With twelve ~1.5 meter long cables for the light sources (coming from one 37-way-D connector from the LED driver) and seven fiber optic bundles, a considerable amount of weight and pressure would be exerted on the probe holder and may cause the subject's head to tilt, also shifting the fiber bundles and sources from the required perpendicular coupling to the scalp. In addition, the fiber bundles have a minimum bend radius of 38mm and so they

should not exceed this bending in order to prevent fiber damage. Appropriate positioning of these 610mm long fiber optic bundles should ensure this doesn't occur (such as their positioning shown in Figure 5.31). Support of light source cabling and fiber optic bundle cabling and their relative positioning to a subject is also shown in the image in Figure 5.31. A polystyrene head is used to demonstrate subject position.

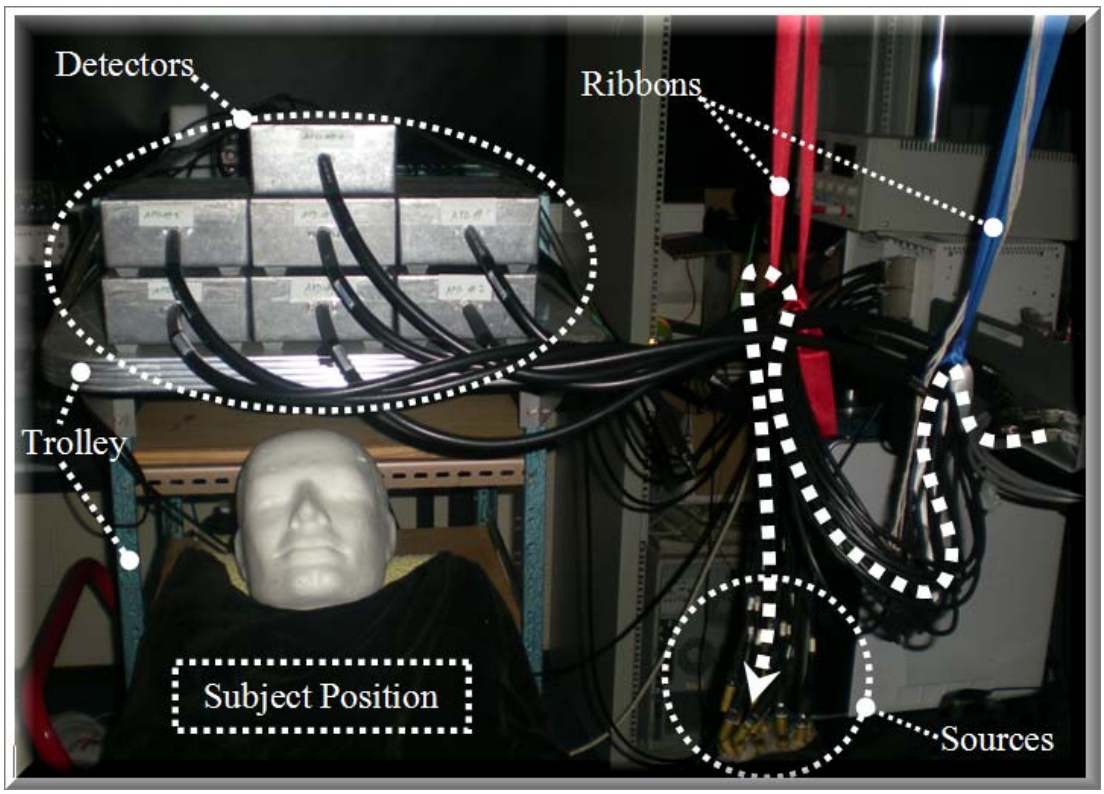

Figure 5.31: Practical positioning and harnessing of light source cabling and fiber optic bundles (cables).

In the image, the light source cables exit the LED driver (on the right) where a broken arrow is used to clearly indicate how the LED cabling is supported by 2 ribbons suspended from a height. The use of 2 ribbons is important (instead of just 1) as the loop of cables between the ribbons contributes to most of the weight and prevents cable movement relative to the subject when in place in the probe holder. Also, double-sided adhesive tape is used at lowest part of each ribbon (where the ribbons meet the cables) to add friction-support so as the cables remain in place. However, they are not tied to the ribbons and so they can be adjusted easily to suit subject height and seating position. The 7 APD detectors are housed in 7 die-cast aluminium boxes (circled in the image). The 7 fiber optic bundles exiting the boxes hang over the subject's head at a height suitable for easy placement and minimal bending of the bundles (to avoid fiber damage and also to avoid strain on the probe holder which would be placed on the subject's head). The detectors are fastened securely to a panel that juts-out from a trolley which has wheels for ease of repositioning of the whole detector

unit (this detector unit may need to be adjusted depending on the subject's relative waist-to-head length).

Having just dealt with the general design considerations for fixing the optical probes to the head (Section 5.5.1.1) and securing the associated cabling (Section 5.5.1.2 - the current section), there are still a few design considerations of the mechanical components of the CWNIRS instrument. These relate to the *density* of optical probes used in a single location on the head, and the specific optet geometry (how probes are positioned relative to one another) used for functional activity recording. Firstly, the issue of ambient light and other photonic obstruction and interference is dealt with, specifically those that concern design of an optical probe holder. Following that, the geometry of the sources and fiber bundles relative to each other is discussed which ultimately establishes the final design constraints for optical probe holders in the CWNIRS imager.

5.5.1.3 Photonic absorption and interference

It may seem like a full-head mould would be a suitable scaffolding to direct and hold the optical probes to the subject's head, but a large contaminant of NIR light is from the hair of the subject, with significant absorption in the NIR range. Hair follicles are also an unavoidable absorber, although in the absence of hair (i.e. a short haired subject), these follicles generally only affect measurements to a small degree. With hair in place however, much of the set-up time of an experiment is simply preparing the subject and setting hair aside, so that the light sources and more importantly the light detectors (since significantly less light exits the head, than enters from the light sources) can be placed in contact with the naked scalp (or as much as is possible). Hair also incurs dynamic (not just a constant\offset absorption) contamination whereby if it moves under the optical probes it can distort any functionally-specific haemodynamic changes being detected, i.e. it masks functional activity during an experimental trial. Thus, the probes need to be fixed securely in contact with the scalp throughout an experiment to avoid this potential contamination. In the set-up stage, a long blunt object is usually used to sweep hair out from under where the source or detector will be placed - and this is repeated for each probe. Unfortunately, as found in practice, this preparation of parting hair cannot be done all at once before applying any probes since probe points are relatively close together, and parting hair in one direction would just move that obstructing-hair into the site of the neighbouring probe point. In conversations with multiple researchers in the NIRS imaging field (e.g. IEEE EMBS conferences 2007/2008), many seem to use this method. There are other methods however, such as the use of fiber brushes which are placed between hair strands - although the difficulty is holding these in place and not damaging the fiber brushes (Luo, et al., 1996).

Care must also be taken to ensure light travelling from the source does not leak directly to the detector without having to travel into the head. If it does it may either saturate the detector or introduce errors into the analysis, since this light has not interrogated the cerebral tissue of interest. This is prevented using black NIR absorbing foam surrounding the detector fiber bundles on the probe holder. The foam also serves to cushion the probe holder attached to the head which is important for subject comfort. In practice too, the amount of ambient light is kept at a minimum (lights dimmed\off) in order to reduce error and saturation of the detector. In a multichannel imaging system ambient light reduces the dynamic range of the detector adding a DC offset to the detected signals. Thus, less signal dynamic range (and more susceptibility for saturation) would be available for the multiple light sources each detector can 'see'.

The configuration of the geometrical positioning of the optical probes (source and detectors) relative to each other is the final and important design consideration, since inappropriate positioning can lead to interrogation of perhaps only superficial layers of tissue. These are considered next.

5.5.1.4 Optet configuration

The most basic NIRS measurement uses a single light source (typically 2 wavelengths) and a single detector in a 1-channel system, which could use a probe holder like that one shown in the top row of Figure 5.34. Such a set-up, although the most basic for NIRS, has been used for successful BCI implementations (Coyle, et al., 2004; Coyle, 2005). In addition a system using a single-wavelength source and a single detector has been used which could analyse cerebral blood volume dynamics to investigate the possibility of frontal cortex control in ALS patients for communication (Naito, et al., 2007). The geometrical constraints of this simple probe are:

1) To ensure the source and detector are a sufficient distance apart for interrogating cerebral tissue ~2.0cm - 5.5 cm (Germon, et al., 1999) but usually 3cm (as is used in all probes in Figure 5.34); and,
2) To ensure that the probes are applied perpendicularly to the scalp and remain relatively motionless throughout the experiment. This second constraint also means that the geometry should allow for fixing the probes to the head, such as can be achieved using Velcro straps (discussed later).

A two-channel system offers the next level of complexity for a NIRS system, which can use two single channels at different locations on the head, which has been used for early optical BCI work (Coyle, et al., 2007b) using a mechanical framework to hold the optical

probes (Coyle, 2005; Coyle, et al., 2005). Such a dual-channel system has also been applied for assessing the viability of simple, serious gaming in this project (Soraghan, et al., 2006). However, there are limitations to these optical probe geometries in a single- or dual-channel system. The main issue is that of poor spatial coverage of cerebral tissue. Since there can exist anatomical differences between subjects, the international EEG 10-20 electrode placement system (as used in EEG recordings) is usually employed to estimate locations of neural substrates, such as the primary motor cortex (as outlined in Figure 2.13 in Chapter 2). The source and detector are usually placed either side of the common electrode positions in order to interrogate tissue that lies below the electrode position, e.g. probes placed each side of electrode position C3 to interrogate right-hand movement\imagery.

Coyle et al proposed a more reliable positioning template based on the EEG-10-20 system (Coyle, 2005; Coyle, et al., 2007b) and the author uses it here (depicted below in Figure 5.32).

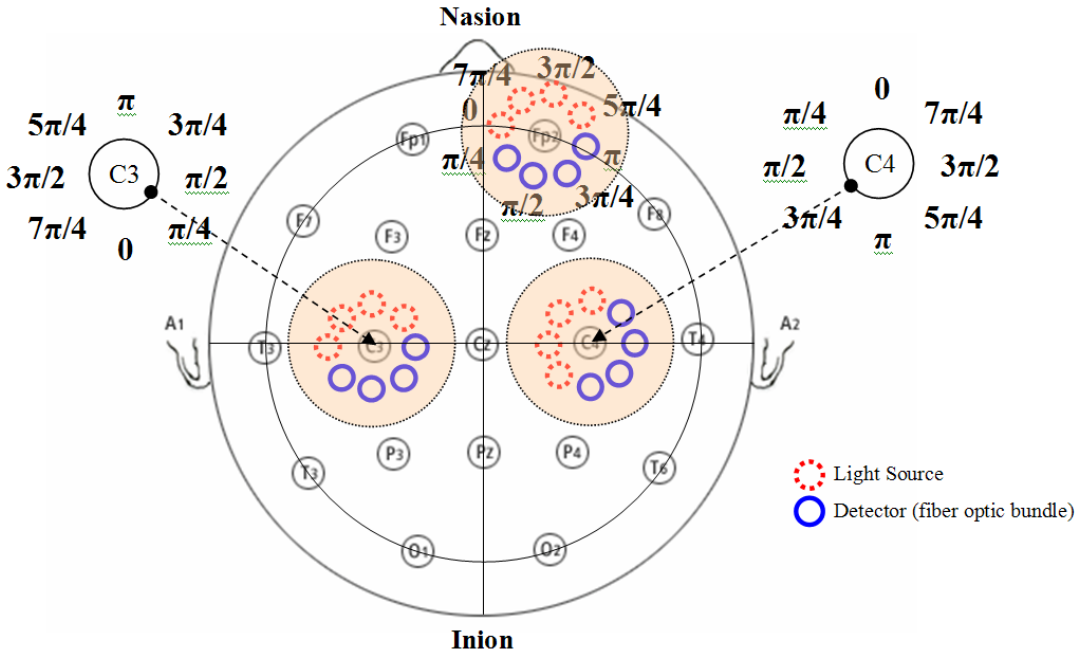

Figure 5.32: Adaptation of the 'Optode Placement System' first proposed by Coyle (Coyle, 2005), based on the conventional EEG 10-20 electrode placement system.

Since there are at least two probes used in a NIRS channel and not only 1 (electrode) as in EEG, the relative position of these probes to each other and some landmark on the head is needed for repeatability of experiments and knowledge of the true positions for the research community worldwide. Coyle et al used the vertex as the cranial landmark reference where probes are labeled depending on their angle with respect to (w.r.t) the vertex, electrode position Cz. Polar coordinates for sources and detectors around C3, C4, and Fp2 are shown in Figure 5.32. The labelling for a NIRS channel at C3 with IOS of 3cm where the light

source (say, source seven S7) is at $3\pi/2$ and the detector (say, detector five D5) is at $\pi/2$ would be C3:1.5($3\pi/2$) and C3:1.5($\pi/2$), respectively. Thus, the labelling convention is:

- <Electrode position>:<distance between probe to electrode position>:<polar coordinate w.r.t the vertex at Cz>.

In Figure 5.32 the sources and detectors are indicated by the red dashed circles and blue circles, respectively. The position of these in the figure is not standard and is only meant as an example configuration, i.e. they can be configured in many ways such as shown in an optical probe holder in Figure 5.38.

Nevertheless, even with this placement system, anatomical differences still occur, and so regions of interest or regions of more concentrated activity in the cortex may be missed simply because the probes were positioned at the wrong location. Thus, a multichannel system can achieve more spatial coverage and less chance of missing regions of activity. In a single-channel system, to find this active region may require repositioning of the probes many times to locate the optimal response (if at all), which is very time consuming, and frustrating for the subject. In addition, a multichannel system provides potential to increase the number of functional tasks that can be monitored simultaneously for use in a BCI. For example, in a single-channel system, cerebral tissue of the frontal cortex cannot be analysed at the same time as the motor structures of the cental sulcus.

The multichannel configuration can use a straightforward extension to the single-channel system (as demonstrated in Figure 5.30) and make use of the dynamic range of each detector. This can be demonstrated in the comparison with the optical probe holders in Figure 5.34 - comparing the top row holders to those on the bottom row. In the top row, detector D1 sees only source S1 and similarly detector D2 sees only source S2. In the multichannel probe holder, detector D1 can be used to analyse tissue irradiated from sources S1, S2, S3, S4, S5, S6, and S7. Similarly, detector D2 can analyse tissue on the path of sources S8-S14[6]. In addition, cerebral tissue in the arc between the detectors and the sources is analysed rather than the single site in a single-channel system. This probe holder using multiple sources and a single detector is known as a single point-measurement (Strangman, et al., 2002) rather than true imaging. However, such single-point measurement geometry is effective nonetheless and is used in some of the studies in Chapters 6 and 7 in this dissertation.

[6] Although there are only 12 light sources, additional probe positions are catered for in some probe holders for better flexibility in the experiment and wider spatial coverage - see caption in Figure 5.34.

The imaging solution (2-D - topography) using a multichannel optical probe holder is demonstrated in Figure 5.37 and Figure 5.38 whereby some sources are decoded from multiple detectors (Strangman, et al., 2002). The probe holder for frontal cortex studies is shown in Figure 5.37 and that for motor tasks is illustrated in Figure 5.38. The probe designs used throughout the project are outlined next.

5.5.2 Optet designs

Figure 5.29 and Figure 5.31 have already alluded to the optical probe holders and geometry used throughout the project. However, there are many designs that have been developed and used, depending on the prototype-stage of the device and on the mental tasks being analysed for BCI control, e.g. tasks involving motor, visual, or cognitive processes. These probes are illustrated and a description of each is given in the figure captions from Figure 5.34 to Figure 5.38. In practice the probes in Figure 5.36 were most straight forward and quicker to implement, and these are used in the experiments in Chapter 6 and 7. However, the frontal probe holder was also used for assessing motor imagery on the motor cortex in Chapter 7, due to this probe's conformation to the subject's head.

In order to obtain a more realistic probe holder that can conform to the curvature of the human head, a head mould was developed to shape these holders to a typical human head curvature (Figure 5.33).

Figure 5.33: Head mould of a subject for fabricating curved optical probe holders.

Figure 5.34: (TOP ROW) Early optical probe holders for single-channel (one source and one detector) measurements, and (BOTTOM ROW) single-point multichannel measurements. In all probe holders, the detector is 3cm away from the source(s). *Sources S13 and S14 would be empty if both probe holders on the Bottom row were used since there are only 12 sources. For even\uniform distribution sources would be more spread out, e.g. at least S1, S3, S5, S7, S8, S10, S12, S14 would be used with the remaining 4 sources distributed between the probe holders - two for each probe holder.

Figure 5.35: fMRI-compatable optical probes for concurrent fMRI-FNIRS studies carried out in collaboration with Rutgers University in Newark, New Jersey. Probe sockets are the same diameter for both source and detector since two large fiber bundles were used: one bundle to deliver light from remote sources; the other to carry light to remote detectors, pass the 5 gauss line. All probes are non-ferrous and non-ferric (acrylic glass) to avoid magnetic susceptability and thus imaging errors.

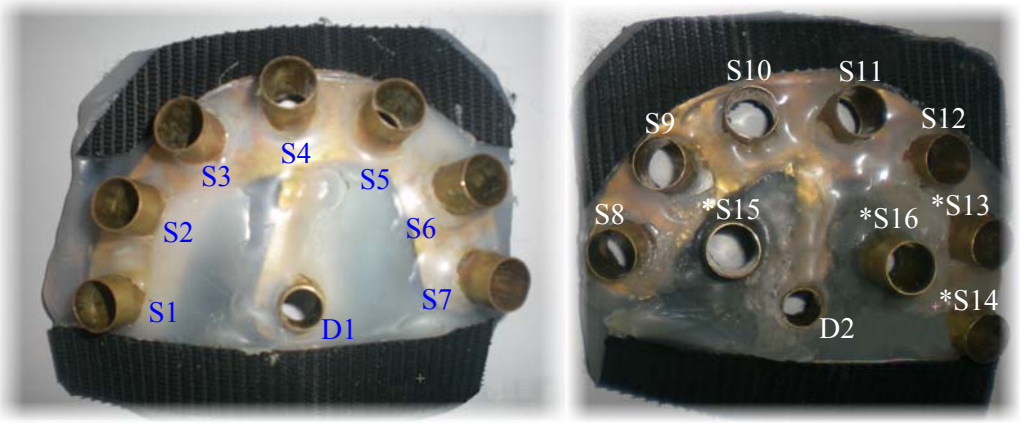

Figure 5.36: Single-point multichannel imaging probes (4cm IOS). The probe holder on the right has two additional source positions (9 in total) close to the detector (2cm). These would be used for noise cancellation where work is ongoing in the group to access such adaptive noise cancellation of superficial signals and blood pressure oscillations.

Figure 5.37: "Frontal optical probe" for multichannel imaging (3cm IOS) with sockets for 10 light source and 4 detectors. Central strap ensures detectors make good contact with the subject's skin (forehead).

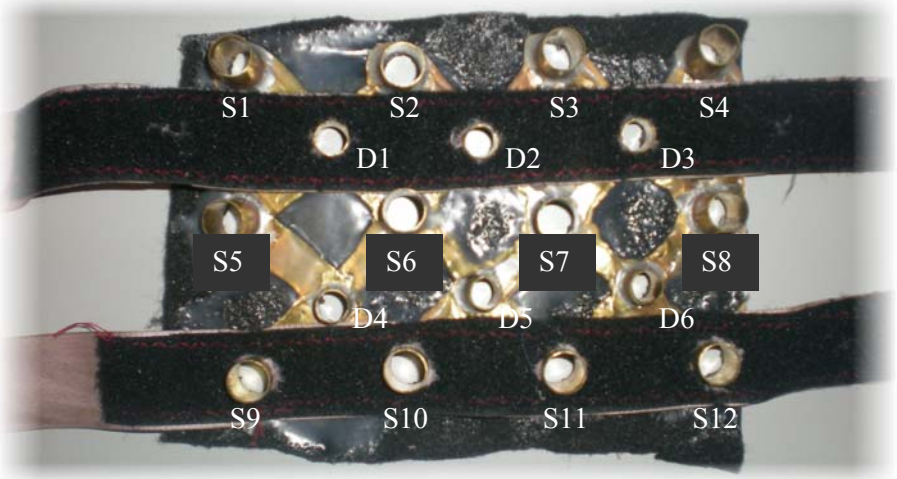

Figure 5.38: "Motor Cortex" optical probe holder for multichannel imaging (3cm IOS) with sockets for all 12 light sources and 6 detectors.

Strapping: Fixing the optical probe holders to the head is typically done using straps such as those built into the probe design in Figure 5.37 and Figure 5.38. Although the design in Figure 5.37 allows for the strapping to be placed from inion to nasion, the motor cortex probe holder has to be placed on the top of the head and so strapping needs to be applied vertically. The common option used in EEG caps is to have the strap come together under the chin using embedded Velcro patches. However, this has the unfavourable affect of introducing severe artefacts into a NIRS recording, due to the movement of the probes when the patient swallows. Also, due to the weight of the probes in NIRS compared to EEG, the chin strap is very uncomfortable and can introduce discomfort, possibly affecting recordings due to ANS arousal (Coyle, et al., 2003).

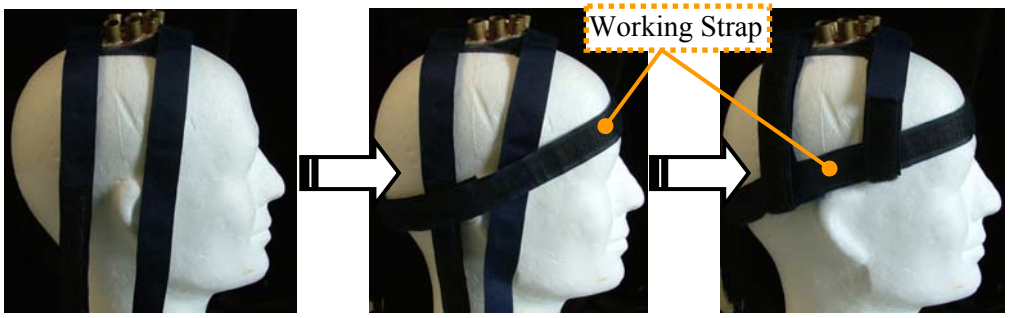

Figure 5.39: Strapping technique to hold optical probe holders in place for interrogating motor structures. Horizontal strap acts as an anchor for the two vertical straps used to secure the probe holder.

The strapping method shown in Figure 5.39 has been shown to be successful in the experiments carried out in this project, which uses a horizontal strap (from nasion to inion) to act as an anchor or base for the motor probe holder's straps to tightly fix to. Velcro pads are embedded in the straps and on the probe holders to secure the strap-to-strap coupling. The horizontal strap is not permanently fixed to the vertical straps (e.g. by sewing) since different head geometries require different lengths of strapping from the vertical straps. In practice, a foam lining is used on the inside of the horizontal strap to increase subject comfort as it acts as the 'working' strap around the circumference of the head, as indicated in Figure 5.39.

The final component group of the multichannel CWNIRS instrument is the software interface, dictating programmable hardware variables such as timing, synchronisation, triggering, and data buffering.

5.6 Software Interface

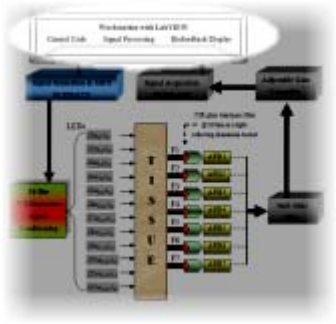

The software interface element of the CWNIRS instrument is integrated in a LabVIEW platform running on a Windows Vista Business Workstation PC with the specifications listed in Table 5.5. Many functions, or *virtual instruments* which they are known as in LabVIEW, were used to specify instrument variables and to process the haemodynamic data. The benefits of using LabVIEW are many as have been outlined in a recent conference publication (Matthews, et al., 2008b). Although LabVIEW can be used to interface with 3rd party hardware, it has an additional benefit of being dedicated to National Instruments hardware such as the devices used in this project (NI PXI-Chassis-1033, NI-PXI-4462, and the NI-PXI-6723).

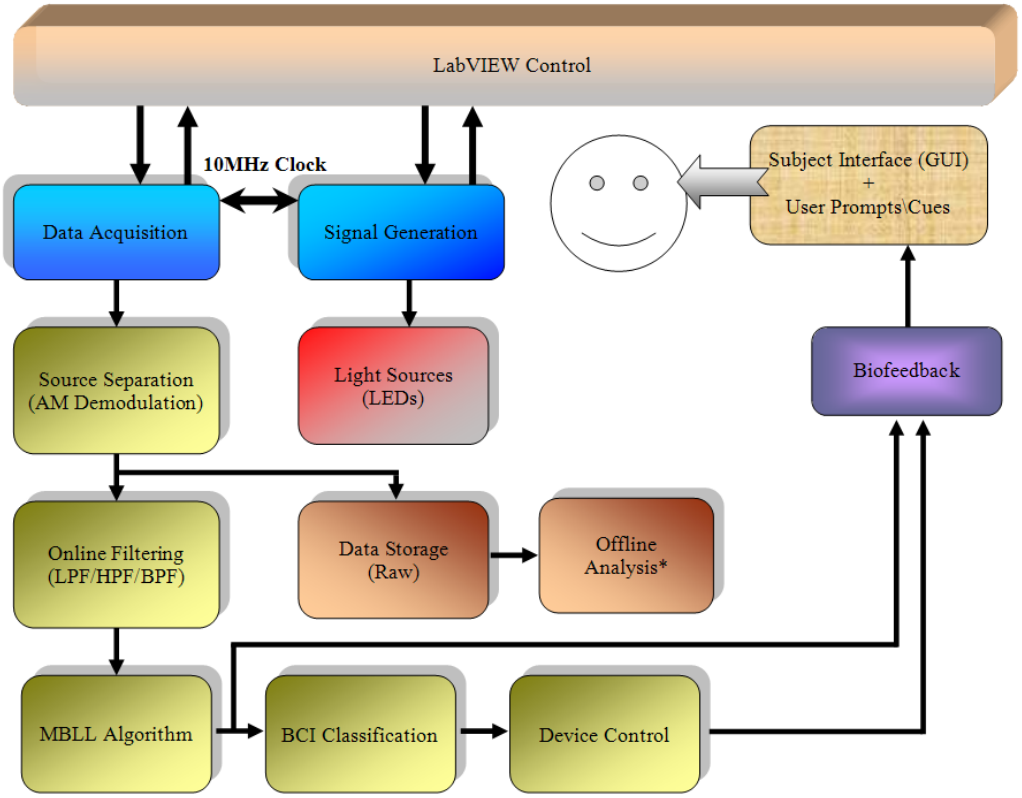

Figure 5.40: Software flow diagram of the CWNIRS instrument adapted from (Matthews, et al., 2008b).

Figure 5.40 illustrates the software flow diagram to demonstrate the complete operation of the CWNIRS instrument in an optical BCI application. Firstly, software interfaces with the hardware to control signal generation for the LEDs and data acquisition from the detectors. Once data is acquired, it is passed onto a source separation routine to extract all

individual channels by AM demodulation. These data are then stored on disc for possible offline analysis prior to filtering. In addition, these data are filtering in real-time (point-by-point) using a 3rd order lowpass Butterworth filter lowpass with a cutoff frequency of 0.2Hz. Each channel then iterates through the modified Beer-Lambert Law (MBLL) algorithm to calculate real-time concentration changes in HbO_2 and HbR, which is fed back to the user. At the same time, a BCI classification routine is performed on the data and used to implement some device control. This device control is also fed back to the user (visually). Throughout the experiment the user receives visual (and possibly auditory) cues in a synchronous BCI routine, with pre-defined time periods for performing the tasks, such as mental arithmetic.

The author worked closely with a colleague on the software development for classification and online DSP, whereas the hardware-software interfacing element was the main contribution here, and is described next. The specific biofeedback, DSP filtering and other online signal processing are dealt with as they are used in the proceeding two chapters.

5.6.1 Hardware control

Some of the hardware control has already been dealt with in the sections describing the National Instruments hardware used for data acquisition, and also for signal generation for the LED driver (Section 5.4.2). However, as was mentioned in those sections, some software configurable settings are needed to control the software interfacing of the hardware modules, and these are outlined next: first the settings for the PXI chassis, then the ADC cards, and finally the AO card.

The programme in LabVIEW (known as a *Virtual Instrument* or VI) for initialising and setting up these PXI modules and chassis is shown in two parts in Figure 5.41 and Figure 5.42. Data lines A, B, C, and D exiting to the right of the first part of the VI enters the second part (from the left) in Figure 5.42 as indicated by arrows in the figures. The VI's are briefly described in eight steps as indicated in the figures. Note: the purple data lines (carrying task information) and the yellow lines (carrying error reports) ensure the data flows in a sequence from left to right since LabVIEW is a parallel programming language. Sequence frames can also be used to force the data flow such as in part 5 of Figure 5.42 for starting the triggering of the various cards. After the brief eight step description of the VI, the settings used for the cards are reported.

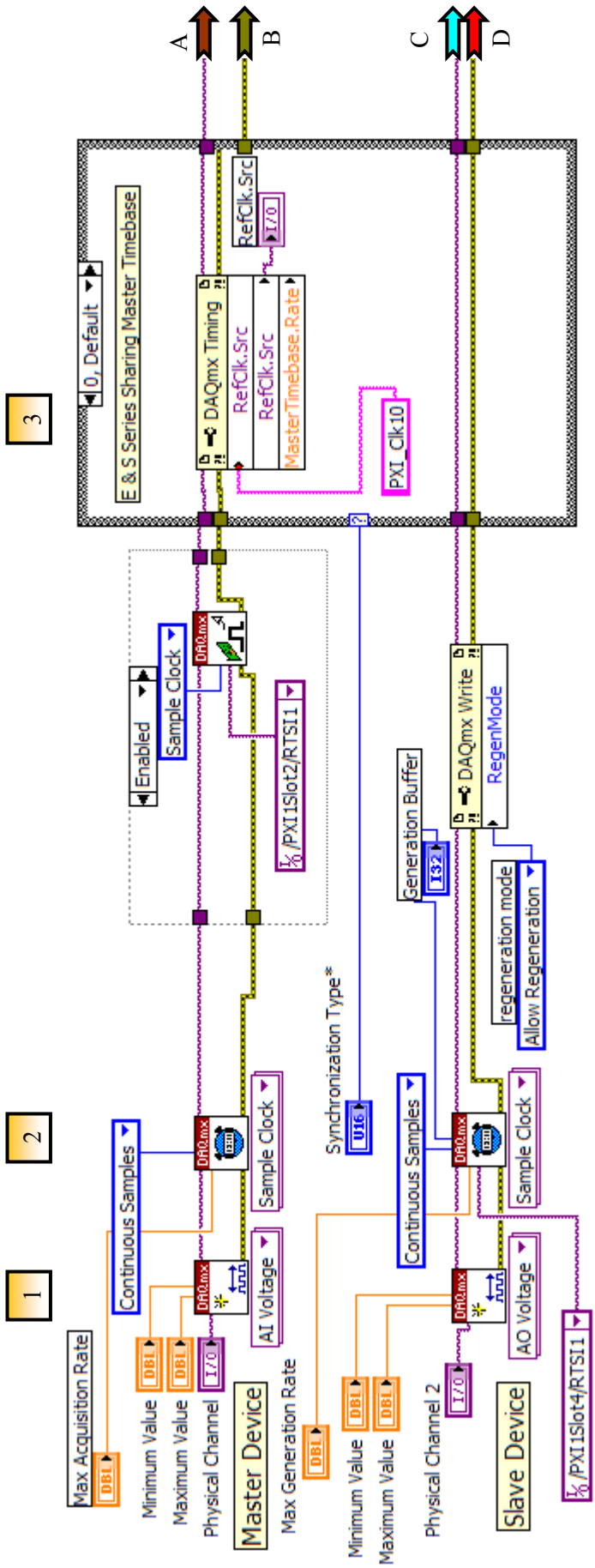

Figure 5.41: Data acquisition and signal generation (Part I): Creation of physical channels, setting the shared trigger on the RTSI1 line bus based on the PXI_Clk10 clock via the backplane of the PXI1033 Chassis. (Data lines A, B, C, and D enter Part II of the VI on the next page).

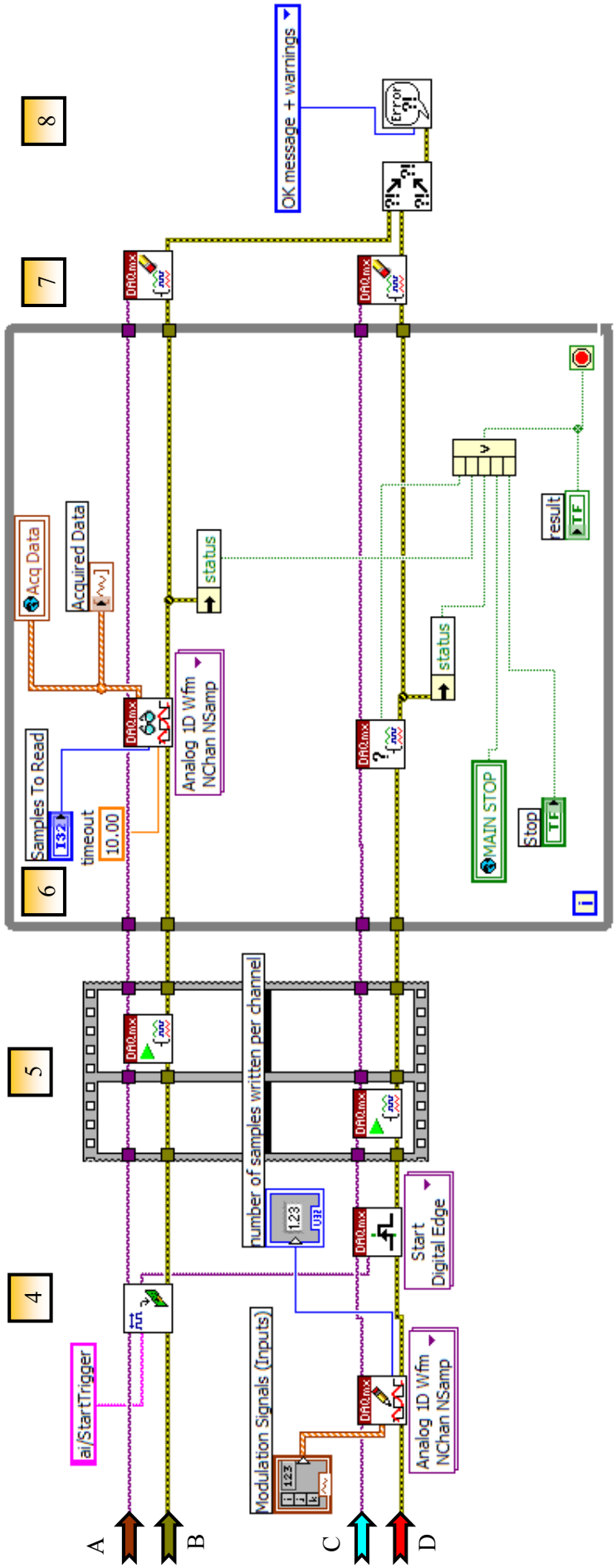

Figure 5.42: Data acquisition and signal generation (Part II): Triggering cards (StartTrigger), setting data acquisition for multiple channels, setting signal generation for multiple channels, error handling, and clearing physical channels once the programme has been stopped. (Data lines A, B, C, and D come from Part I of the VI on the previous page. In reality they are actually connected in a single VI in LabVIEW.

1) Create the Analog Inputs (acquisition), and Analog Outputs (signal generation) and specify maximum and minimum values (which is sets the analogue amplifier for the ADC cards). ADC #1 is the Master device;
2) Setting timing parameters. The source of the Sample Clock for the AO card is from the RTSI1 bus for this card (PXISlot4) which is from the Master Device (sample clock signal from the master device is exported onto the RTSI1 line connected to PXISlot2). Sample mode is set to continually sample. Maximum Acquisition and Generation rates are set independently. The generation buffer is set here to 2500 samples. The data generation is set to allow regeneration of samples where buffers of data are repeatedly output from the AO cards channels for the LED drivers;
3) The two AI ADC Cards are synchronised sharing the reference clock (PXI_Clk10) on the PXI1033 backplane as a master timebase;
4) The trigger from the Master Device (ai/StartTrigger) is used as the source for the Slave's Trigger. This will ensure both devices start sampling at the same time. Also, the Analog Output is set up for a specified number of channels (depending on LEDs used) and a number of samples to output (buffer of 2500 in this case). The "Modulation Signals (inputs)" contains an array of data specifying carrier frequencies, offsets, and amplitudes for all LEDs being used;
5) The Start VI is called to start the acquisition. The flattened sequence structure is used to ensure the slave device is armed before the Master so that the slave device does not miss the trigger from the Master Device. Thus all cards begin acquiring\generating data;
6) A while loop ensures the signal acquisition and generation keep running until a stop condition is reached. A number of samples (buffer size 10000 samples) is read for all channels and sent to a global variable "Acq Data" where it is further processed in buffers of 10,000 samples. Also, if any device reports an error (from Status) or the user presses the 'Stop' button on the front panel, the while loop will exit terminating the acquisition\generation;
7) The Clear Task VI is then used to stop the acquisition and clear the tasks once the while loop is exited;
8) Popup dialog box is used to display an error, if any.

5.6.1.1 Data timing and triggering (NI-PXI 1033 Chassis)

In software, all cards in the PXI chassis are running on the same 10MHz clock (PXI_Clk10 in Figure 5.41) which is shared on the backplane over the RTSI1 (real-time system integration) bus lines for the cards. The first PXI-4462 data acquisition card is set as the Master Card, and in software it is initialised, and the other 2 cards, one ADC and one AO card trigger 'on' to sample\generate as soon as the master card begins\is triggered 'on' ('StartTrigger' in Figure 5.42). Thus, phase distortion is kept at a minimum between the cards ($<0.1^\circ$), allowing for potential phase sensitive demodulation techniques.

5.6.1.2 Data acquisition configuration (NI-PXI 4462)

For data acquisition, the following settings are configured in software:

- the number of acquisition channels (1-4 per card);
- the sampling rate (typically set to 100kS/s);
- the data buffer size (number of samples), and,
- the trigger line.

Up to four channels per card can be used and the software program is configurated in such a way that changing from a single data acquisition channel to up to 8 channels requires only a change in one line of code. The sampling rate is set at 100kS/s (kHz), which is the same for all acquisition channels, i.e. simultaneous sampling. No change in the sampling rate is enforced by using additional channels, i.e. they are not multiplexed. This is one key feature to the software and hardware design, and allows for flexible scalability of the instrument. There are additional time constraints introduced by having more channels since there is simply more data to analyse. However, this is dealt within a timing loop in a VI whereby each buffer of data is analysed every <50msec. The data buffer is set to the number of samples that are analysed at anytime in the whole DSP loop. A buffer of 10,000 samples is typically used. The trigger line as mentioned already is the line that shares the 10MHz clock on the backplane of the chassis, and is the RTSI1 line on "slot 2" for the data acquisition cards.

5.6.1.3 Signal generation configuration (NI-PXI 6723)

For signal generation, the following settings need to be configured in software:

- the number of signal generation (analog output) channels (1-24 typically);
- the signal generation rate (45kS/s for 24 analog output channels);
- the signal generation data buffer (number of samples output at a time), and,

- the trigger line for synchronisation.

Up to 32 signal generation channels can be produced from this card, although in the current design, only 24 are used - 12 LED packages * 2 wavelengths. Again, the configuration in software is such that only a change to a single line of code is required to change the number of output channels. In addition, some channels provide signal generation for all four 760nm die in the same LED package. However, the large driving current needed to have the LEDs operating at high output power is supplied by auxillary power supplies connected to the LED driver, and so the current\power drawn from the analog outputs is miniscule compared to the actual driving current needed for the high power NIR LEDs. In effect the software sets a potential which is relayed to the LED driver circuit with the effective gain being produced by the PNP transistors (see schematic in Figure 5.18). The signal generation rate (update rate) is the number of samples per second that each channel should generate which is 60kS/s when generating on 24 channels for this generation card. The generation buffer is set to 2500 samples. The trigger line for the generation card is the RTSI1 bus line on "slot 4" which synchronises with RTSI1 bus line from "slot 2" (master card) for both ADC cards, which in turn synchronises with the 10MHz clock on the PXI trigger bus on the PXI backplane (see the VI in Figure 5.41).

When using multiple light sources in the same region of tissue, where a detector may see more than one light source, a method is needed to separate the sources after detection by the APDs. Some systems utilise time-division multiplexing (which is analysed later), but the method used here allows all light sources to be on at any moment in time, using a frequency division multiplexing routine or amplitude modulation. This technique was inspired by the work of Everdell et al (Everdell, et al., 2005) in which each light source is modulated at a different frequency and later recovered\demodulated in software. This demodulation technique is described in the next section, but first, the settings used to drive the sources are outlined.

Adjusting the LED optical output power: For maximum flexibility, each wavelength in each LED package is programmable in terms of its optical output power by setting amplitude and offset potentials also in accordance to the linear V-I conversion demonstrated in the LED driver section (see Figure 5.21(a)). The frequencies and maximum amplitude potentials and maximum offset potentials are saved in a '.csv' (comma-separated-value file format - csv) file called *"max.csv"*. There are two main stages to setting up an experimental trial:

1) The first aims to establish the light source output powers needed for each channel beginning with the maximum values from "*max.csv"*;
2) These values are then tweaked and optimised depending on multiple criteria such as saturation of a detector. The final optimised values are then saved to a second csv file -*"optimised.csv"* - which is used for the experimental trial, which is the second stage.

Thus, two files are used to set the LED values, the first is the maximum that the LEDs should produce, and the second is a weighted version of the values in that file - either equal to or less that the maximum value set in the first file. The frequencies are set between 8kHz and 16kHz with a minimum frequency gap of 200Hz. The frequencies are kept within one octave to avoid harmonic crosstalk of the sinusoids. Offsets (VDC - including intercept compensation) are set between -4.2V and -4.7V, and amplitudes of the sine waves (VAC pk-pk) generated are set between ± 1.3V and ± 1.5V in the *"max.csv"* file. The scaling\reduced weighting of these values is generated by an affective multiplication of the values between 0 and 1 - 0 meaning the LED is off, and 1 meaning the LED is producing the maximum value specified in *"max.csv"*. A screenshot of the front panel of the virtual instrument (VI) is shown in Figure 5.43. The VI allows for setting values for each individual die separately, or each wavelength collectively (i.e. all 760nm or all 880nm die), or all die (every 24 die both 760nm and 880nm) at the same value. A slider ranging between 0 and 1 is used to set the output power between 0 and 1 times the maximum set in the *"max.csv"* file. This set-up scheme ensures that LEDs cannot be set above their maximum allowed value, whereby if a value greater than 1 is entered into any of the input boxes, an error is generated. Once the values have been determined, the "Commit Values" button should be clicked by the researcher, carrying onto the next screen which is used to determine what sources a detector should demodulate for. Note that the final values committed are used as the "Modulation Signals (input)" array shown in the VI in Figure 5.42.

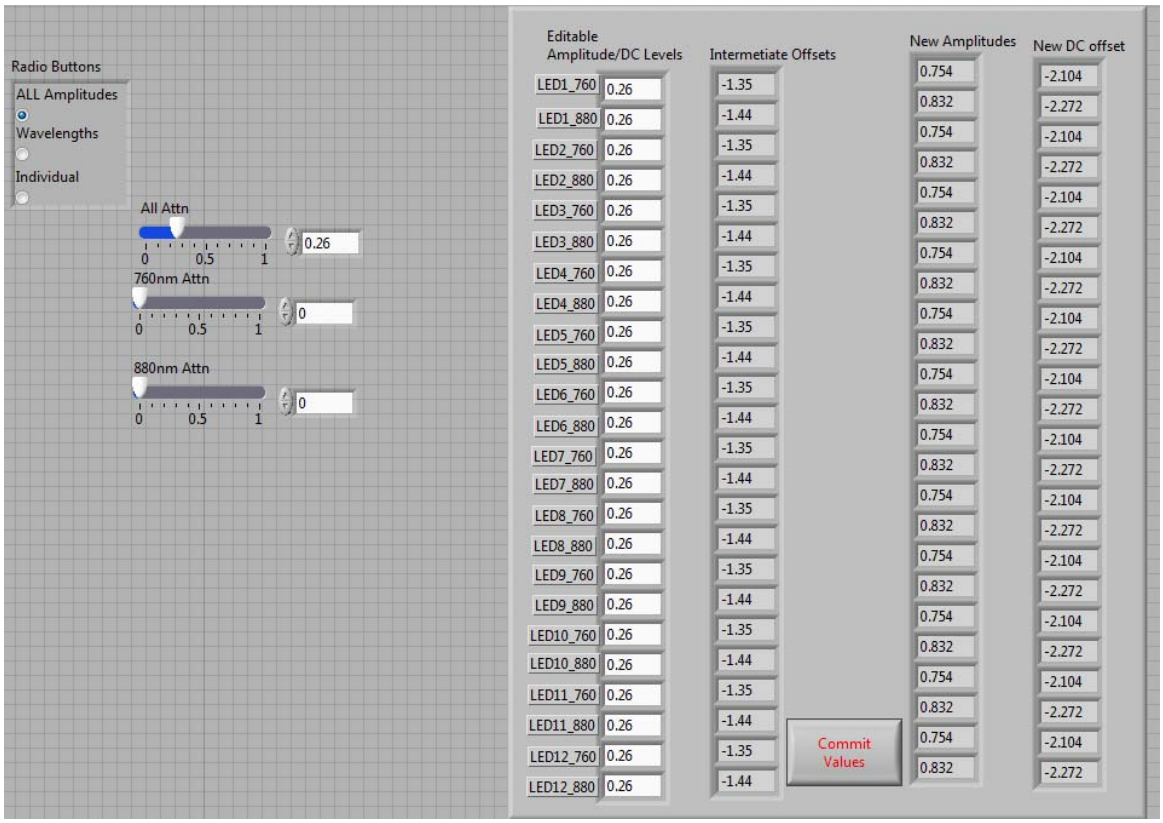

Figure 5.43: Optimisation of LED power levels with options to set values for individual die ('Individual' radio button); wavelengths ('Wavelengths' radio button) - to set all 760nm or 880nm to the same value; and finally, all light sources ('All Amplitudes' radio button). In the case above, all die are set to 0.26 times their maximum (which is taken from the *"max.csv"* file).

5.6.2 Light source separation (software-based demodulation)

In the first single- and dual-channel systems employed by Coyle et al at NUI Maynooth (Coyle, et al., 2004; Coyle, 2005; Coyle, et al., 2007b), hardware-based lock-in detectors were used to separate multiple light sources irradiating tissue and being detected by a single detector. Phase sensitive lock-in detection was used to maximise the output from the amplitude demodulation stage. However a key element to the multichannel CWNIRS instrument developed for this project was the discarding of this bulky, expensive hardware and to move demodulation completely into software for increased flexibility. This also proposes to be a more scalable cost effective design, where more channels can easily be catered for.

The software demodulation technique can best illustrated using an example whereby a single APD receives NIR light from multiple LEDs. The APD is sampled by the ADC (NI-PXI-4462) and inserts the samples into the data acquisition buffer. The data is then retrieved in windowed blocks of 10000 samples, into software. A Hanning-windowed FFT (Fast Fourier Transform) is applied to the data block producing a complex spectrum. A frequency search LabVIEW VI is then applied to the complex spectrum to search for a single frequency

specified in the LED set-up file *"optimised.csv"*. The bin width for the frequency search is determined as a percentage of the sampling frequency - a 200Hz bin in practice. This search retrieves the amplitude for the specific carrier frequency and corresponds to the detected light level for the LED emitting a carrier wave at that frequency. This search is repeated for all specified frequencies for that detector. The data is then stored for further processing, e.g. lowpass filtering (Matthews, et al., 2008b).

5.6.3 Detector saturation

During pre-experimental checks, it is often required to known the signal strength that each APD is receiving and specifically to analyse if an APD detector is saturated. The GUI in Figure 5.44 analyses in groups of four APDs, if any one of those APDs is saturated. A green Boolean (single column at the center and to the top of the VI) is ignited in the case of saturation. Also, on the left of the GUI, the right hand column is a sorted order of the contributions of each LED to the overall signal collected by a single APD. This list allows the researcher to quickly locate which LED is contributing the highest signal, and potentially saturating the APD. This high signal is usually caused by light leaking directly from the source to the detector where the probe holder hasn't been fastened to the head appropriately. A toggle menu is available to change the APD that is being analysed and sorted in the '*Saturated APD No.#*' menu of the GUI.

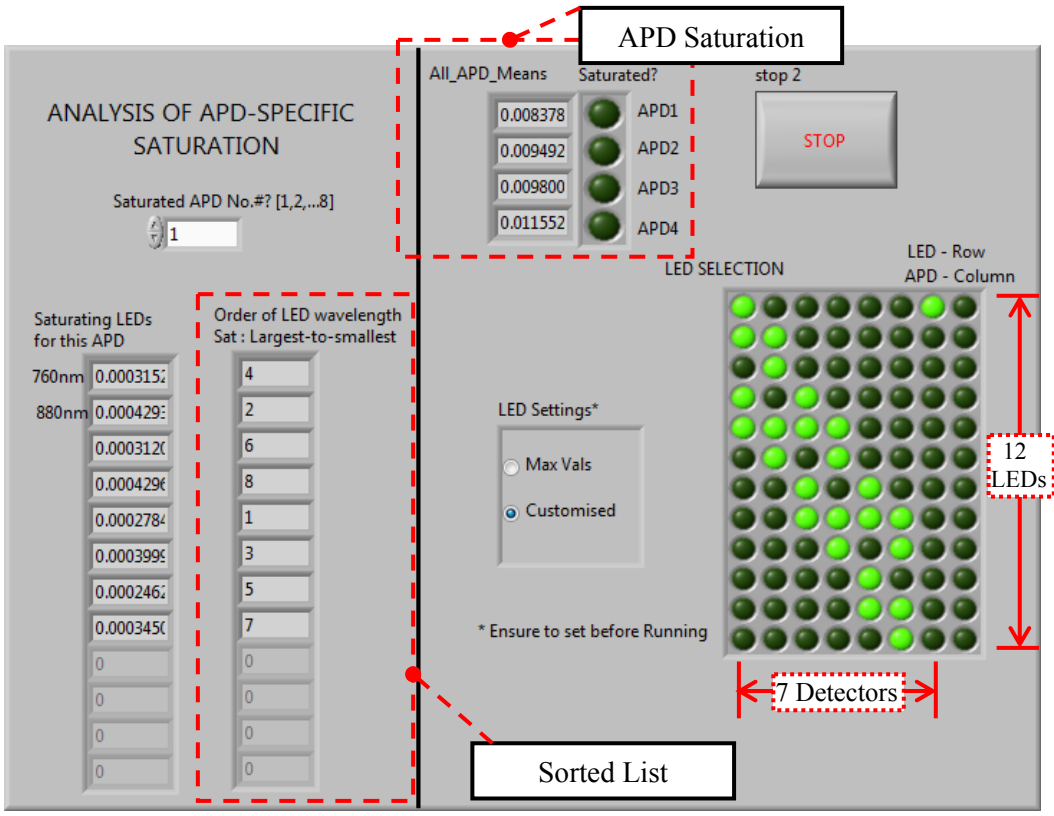

Figure 5.44: Analysis of APD saturation. Rough channels are ordered in the highlighted sorted list. Note: the column\list on the far left is not part of this sorting; only the highlighted column is. LED pairing to detectors is also shown on the right.

On the lower-right of the GUI is a panel of radio buttons indicating which LEDs each APD is demodulating for. The 12 light sources are represented by the 12 rows, and the 7 APDs take up the first 7 columns (the last column is not used but represents the final ADC channel on the second NI-PXI-4462 card). It can be seen that APD1 is demodulating for LEDs 1, 2, 4, and 5 whereas APD4 is demodulating contributions from LEDs 5, 6, 8, and 9. The order of this APD-LED panel is based on the specific geometry of the APDs to LEDs in the optical probe holder used. In the case of the probe holder shown earlier in Figure 5.38, APD detector D3 would demodulate for its neighbouring LEDs 3, 4, 7, and 8 and these would be represented in the panel of the GUI in Figure 5.44 as the boolean radio buttons 3, 4, 7, and 8 highlighted for the third column, i.e. the third APD detector.

The instrument also allows for multiple demodulation techniques to be implemented due , for example, to the LED driver design and the simultaneous sampling capabilities of the ADCs with high 24-bit resolution and high sampling rate of 204.8kS/s. The software platform developed in LabVIEW also allows for rapid prototyping of these modulation strategies (Matthews, et al., 2008b) (along with other filtering and classification techniques on the DSP element of the instrument which are ongoing in the BCI group at NUI Maynooth).

5.7 Provision for Multiple Modulation Strategies

One of the constraints placed on the LED driver design was to allow for multiple modulation strategies, especially time domain techniques such as round robin, where the optical driver design needed to cater for DC coupling (Soraghan, et al., 2009). Three modulation techniques (being compared in Matthews, et al., (Under Development)) are considered here: round robin, amplitude modulation, and m-sequences or maximum length sequences. These are reported here to demonstrate the ability of the instrument to cater for the various techniques. AM modulation has already been described and so round robin and M-sequences are described next.

5.7.1 Round robin - Time Division Multiplexing (TDM)

Round-robin is a modulation technique whereby each LED wavelength (24 in total) is turned on independently for a short period of time (~10ms) at the maximum current for the LED beginning at LED 1 then 2, 3, and so on. Thus, only one LED is on at any given time and so the signal from the APD at that time can be considered as coming exclusively from that single LEDs channel, with perhaps other noise and stray light. Thus, a single iteration of each LED for 10msec takes 240ms. So thus, each LED turns on for 10ms every 240ms.

However, although this technique removes potential cross talk between LEDs, each source is on for less time and thus there is a reduction in the signal from each source leading to a reduced SNR. Hence, the optical power per wavelength is dependent on the number of wavelengths used, with increased reduction in power with the number of wavelengths used.

5.7.2 M-Sequences

In telecommunications spread spectrum techniques use pseudorandom binary sequences (spreading codes) known to both the transmitter and the receiver to communicate multiple signals over a common channel, also known as code division multiple access (CDMA). Using different sequences, simultaneous transmission can be achieved and the bandwidth can be shared. Maximal length sequences or M-sequences are a type of spreading code and are used here in a spread spectrum modulation technique for FNIRS. A 63-bit sequence was used, where each source's (wavelength) sequence was the original m-sequence shifted (lag) by the source number. The resulting sequences have an autocorrelation of 1 for zero-lag but almost zero for all other lags - thus ensuring minimal crosstalk between sources on different sequences. They also have other specific properties such as the number of ones in the sequence is greater than the number of zeros by one (Matthews, et al., (Under Development)). Note: the purpose of implementing this technique here was to demonstrate the ability and facilitation of the instrument to allow such flexibility where perhaps a lower specification signal generation card could be used to generate the binary signals instead of the more complex series of carrier signals at various frequencies used in AM. A new channel could be simply use a lagged version of the primary binary sequence, thus facilitating ease of scalability (increased channels) for this modulation technique.

5.7.3 Demonstration of the modulation techniques

The phantom and associated mount and DC motor used in Chapter 6 in Section 6.2.1 was used to demonstrate the modulation techniques. The fluid in the phantom was stirred with the arched hose-pipe spinning on the DC motor to simulate a cardiac pulse (seen in normal studies on the human head) producing sinusoidal absorption patterns of the NIR light at ~0.8Hz. Thus, each modulation technique was used to reconstruct the absorption pattern in the channel between a light source and a detector. The absorber used was "Dettol" - an amber-coloured household antiseptic liquid (parachlorometaxylenol) which turns milky-white when added to water. Sufficient absorber (~27ml) was added to the phantom of water (~2.5l) to avoid saturation of the light detector (APD). For round-robin and m-sequences, the LEDs were pulsed at 100mA maximum, whereas in AM modulation the LEDs were illuminated with sinusoidal carrier waves (<16kHz) up to 142mA-RMS maximum. Each technique was carried out independently (not at the same time). A section of ten seconds of recovered signal from each modulation technique is shown in Figure 5.45 below. Note that

the amplitudes are in arbitrary units and are not comparable across techniques. Also in all three techniques every second pulse is of lower amplitude. This is because the hose-pipe turning in the phantom enters into the pathway of the LED and the detector twice every revolution. The lower amplitude in the second pulse is where the hose-pipe is closer to the LED and thus further from the APD on the opposite side of the phantom - i.e. more light is absorbed\blocked when the hose-pipe is closest to the detector. As an observation is can be seen that there appears to be more noise in the round robin implementation, which is expected since the LED is on for less time than the other two techniques. A further exposition of these comparisons along with a look at M-sequences on simulated data is currently being reported by the group (Matthews, et al., (Under Development)).

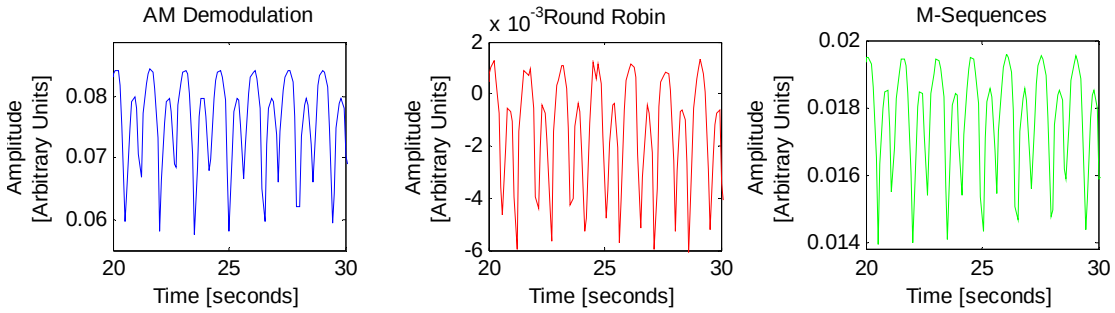

Figure 5.45: Demonstration of demodulation techniques recovering simulated cardiac-like pulses from a phantom.

In terms of the versatility of the multichannel CWNIRS system developed, implementation of these modulation strategies was easily facilitated since all techniques incurred only a change in a portion of the software code used. This flexibility would be welcome where perhaps only a basic signal generation card was available, only needing to generate simple binary sequences rather than a range of carrier signals varying in frequency for each light source. Further observations are being reported by the group (Matthews, et al., (Under Development)), whereas here it is simply observed that these techniques are facilitated by the instrument developed in this chapter.

5.8 Chapter Summary

A versatile multichannel CWNIRS instrument was described for optical BCI applications based on PXI data acquisition and generation technology operating in a flexible LabVIEW platform. The development of the system was broken down into the various optical, electrical, and mechanical components as well as the software interface (Soraghan, et al., 2008a). LEDs were outlined as the light source of choice, avoiding the potential retinal damage that a laser diode source may cause, especially for long term use on vulnerable

subjects, e.g. locked-in patients. A particular design feature was to have considerable increase in power output from the shorter wavelength at 760nm (compared to the initial prototypes (Coyle, et al., 2004; Soraghan, et al., 2006)) which is more sensitive to concentration changes in HbR and may be a better marker of localised metabolic activity than HbO_2 - which is discussed and investigated over the proceeding two chapters. An analysis of the drift in wavelength and optical power output due to thermal effects addressed the need to allow the sources to heat up for at least 35 minutes before experimentation. A safety assessment of these sources was carried out in terms of thermal conduction from the semiconductor junction and irradiance of the NIR light. Both were within or kept within the permissable exposure limits as described elsewhere recently (Soraghan, et al., 2008b). APD detectors with low noise and high dynamic range were chosen for light recovery and amplification with coupling fiber optics, glass filters, and aluminium buckets to couple maximum light from these light guides to the active areas of the APDs. A stable triple die LED driver was described with a suitable 40kHz bandwidth for CWNIRS systems (Soraghan, et al., 2009). It was designed to allow for constraints of common-anode multi-wavelength LEDs and with DC coupling in order to facilitate multiple modulation strategies such as CDMA (using m-sequences). These instruments required a substantial data processing system to simultaneously sample up to 7 detectors and generate signals on 24 channels for the light sources. The strength and flexibility of these systems was to replace the hardware-based lock-in detectors where now demodulation was moved completely into software. This along with the optical drivers facilitated multiple modulation techniques some of which were addressed at the end of the chapter. Furthermore, the software interface was designed to assess detector saturation and identify rogue channels in descending order of contamination (e.g. light escaping from the LED directly to the detector). An interface was also developed to allow adjustment of LED power (as a fraction of 1) for individual LEDs, collectively for wavelength groups, or all die in the system. This facilitates examination of various tissue types since for example cranial interrogation would require more optical power than forearm tissue would due to larger scattering and absorption coefficients of cranial tissue. Data synchronisation, buffering, and triggering was native to the *National Instruments* PXI chassis and associated cards which provided the researcher with a rapid prototyping platform in LabVIEW for different experimental paradigms. Further DSP routines and interfacing is ongoing in the BCI group at NUI Maynooth, (Matthews, et al., 2008a; Matthews, et al., 2008b; Matthews, et al., (Under Development)). Finally, the mechanical components which can have the most significant influence on the resulting SNR for a channel were addressed with various optical probe holders designed to fit to a subject's head. However, as will be seen in the chapters to follow, one of the more successful probe designs due to its conformity to the head and quicker set-up time was the seven light source

and one detector probe shown in Figure 5.36. The proceeding chapter considers an assessment of the physiological signals recorded from the body using the multichannel CWNIRS instrument and validates the ability of the system to assess functional activity from cerebral structures.

CHAPTER 6

INSTRUMENT VALIDATION AND OBCI EXPERIMENT PREPARATION

6.1 Introduction

In order to validate the instrument and its performance and assess how the instrument applies to functional activity monitoring and subsequent exploitation of these signals for use in a BCI, there are a few preparatory steps that were undertaken. These steps are presented next, roughly in increasing order of complexity, i.e. each step can be considered milestones in the validation of the instrument:

1) Detection of physiological phenomena using the instrument -

- Synthetic cardiac-like pulse in a phantom (Section 6.2.1);
- Cardiac pulse from the human head (Section 6.2.2);
- Physiological vascular features found via frequency analysis, e.g. Mayer Waves (Section 6.2.3).

2) Haemodynamic analysis -

- Spatiotemporal haemodynamic patterns from blood-vessel occlusion and release using a blood pressure cuff on a human arm (Section 6.3.1);

- Real-time assessment of haemodynamics from the human head (Section 6.3.2).

3) Functional activity detection -

- Blood Oxygen Level Dependent (BOLD) fMRI analysis of motor tasks used in FNIRS paradigms for BCI applications (Section 6.4.1);
- Typical CWNIRS signals related to motor activity - single trial analysis (Section 6.4.2);
- Typical CWNIRS signals related to cognitive activity - single trial analysis (Section 6.4.3);
- Multi-channel topography - HomER® offline analysis (3rd party NIRS data analysis software, (Section 6.5).

These assessments are demonstrated over the proceeding sections in this chapter. These preparatory steps allow the researchers to assess the ability of the developed CWNIRS instrument to be able to measure functional activity from the brain. Subsequently they allow for the experiments in Chapter 7 in the knowledge that the system can indeed report on functional haemodynamics, which ultimately could be used for BCI applications. Functional activity localisation and lateralisation to motor tasks are explored in Chapter 7 which outline the benefits of using the versatile multichannel instrument for BCI applications.

6.2 Physiological phenomena - initial assessment

In order to determine if an NIR source and detector are working appropriately (correctly aligned, appropriate light source power delivery, etc), initially many researchers tend to take the same approach in assessing 1) if there is sufficient SNR in a channel, 2) if the light being detected has travelled into the cerebral structures. The method is simply to analyse if a clean cardiac pulse can be found in this channel (Coyle, 2005) providing the source and detector are greater than ~2.5cm apart (Rolfe, 2000; Strangman, et al., 2002a). This cardiac pulse is seen as a non-stationary ~1Hz pulsatile signal due to the pulsation of arterial blood. During each cardiac stroke, relatively more blood (volume) exists in the area beneath the source and detector where the smooth muscle of the arteries expands (dilation). At the same time, the orientation of the disc-shaped red blood cells (RBCs) (which contain the absorbing chromophore haemoglobin) is flow-dependent (Visser, et al., 1976). During systole (typically 120mmHg - peak pressure) the RBCs are densely packed with their long axis perpendicular to the direction of flow. During diastole (typically 80mmHg - resting pressure)

the RBCs are packed less densely, and are orientated with their long axis parallel to the direction of flow. The result is that at systole, light absorption is at a maximum, and during diastole absorption is at a minimum, with intermediate absorption in between the extremes. Other physiological signals are present such as low- and very low blood pressure oscillations some which tend to absorb in tandem with the vasotone of the smooth muscle of the blood vessels (Franceschini, et al., 2000; Obrig, et al., 2000a). Thus, an assessment is carried out in the proceeding subsections to analyse this cardiac pulse initially from a synthetic model (see Figure 6.1), and then from a human head. Other physiological features are then examined (Section 6.2.3) to complete the initial stage of signal integrity analysis.

6.2.1 Synthetic cardiac pulse using a phantom

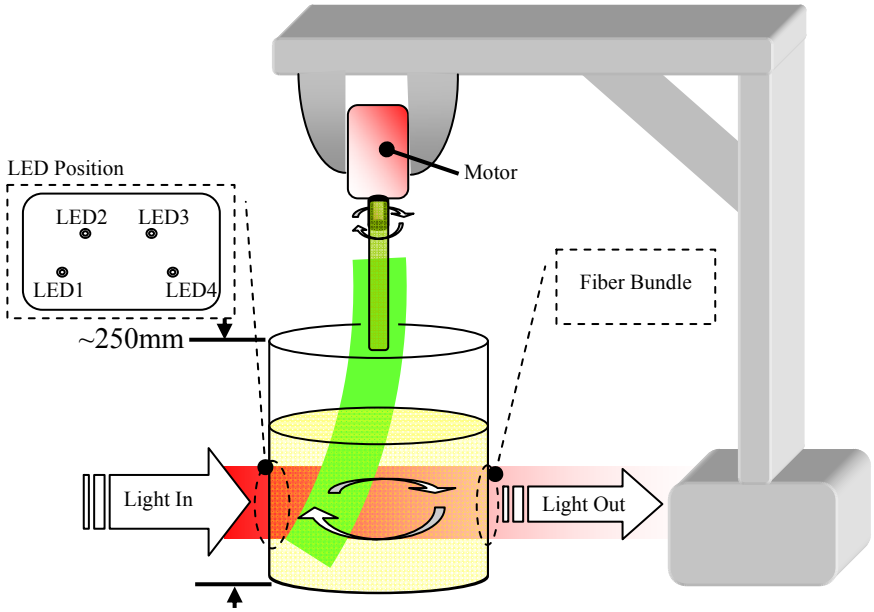

Figure 6.1: Synthetic cardiac pulse from a phantom of water + absorber (Dettol® antiseptic) with a bent hosepipe turning on a DC motor (red block fastened to the grey mount).

The apparatus in Figure 6.1 is useful for early calibration studies (e.g. testing demodulation strategies, investigating faults) as a means to simulate a heartbeat signal using a bent hosepipe turning in an absorbing phantom. The cardiac-like pulse is seen in all channels in Figure 6.2 (in this case for each individual wavelength) and slight temporal differences occur depending on the geometrical position of the hosepipe within the phantom. The absorption signal over time can be seen as periodic variations in the amplitude of each of the carrier signals detected using a real-time fast Fourier Transform (FFT), not dissimilar to a Mexican wave. This occurs in the FFT because adjacent LEDs are at incremental carrier frequencies and because the hose passes each one at incremental moments in time. The use of the apparatus in Figure 6.1 negates the need to have the LEDs and fiber optic bundles (for the APDs) attached to a human subject for long studies, i.e. some studies may be run for a

few hours which may require no movement of the optical probes - which would be impractical for a human subject. In addition, this basic set-up helps to establish a working system inferring that each LED-detector channel is operational - in preparation for human interfacing studies. The next stage in the practical assessment of a working NIRS apparatus is to retrieve a cardiac pulse from the body, and then from the head of a human subject.

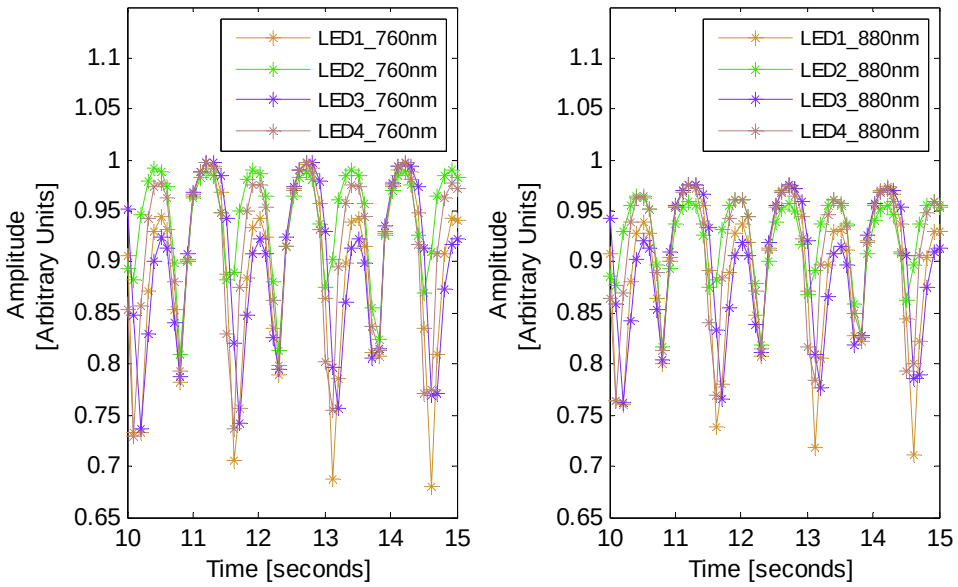

Figure 6.2: Synthetic cardiac pulse from an absorbing phantom and hosepipe on a DC motor. Absorbance increases as the hose passes between the path of each LED and the detector.

6.2.2 Cardiac pulse from the human head

The *cardiac pulse* measured using NIRS from the human head is not the same as an electrocardiogram (ECG). An ECG is a measure of the electrical potentials generated from the beating heart whereas the cardiac pulse from the head using NIRS is akin to the blood volume change specifically after left ventricular (serving the head and body) contraction in the heart (Marieb, et al., 2006a). The comparison is best described with an example of a single heartbeat where in Figure 6.3:

1) the top graph demonstrates an ECG measured from a 21-year old subject. It shows the typical PQRST-wave measured using BIOPAC® instrumentation. This instrumentation includes an amplifier with a gain of 5000, UIM100C Interface Module, MP100 ADC sampling at 1kHz, using 3 electrodes (2 shielded electrodes placed either side of the chest, and a ground electrode placed on the front of the tibia (or shinbone));
2) the bottom graph, below the ECG, is a proposed (based on values from Marieb, et al., 2006a) ventricular volume change where it can be seen that

shortly after onset of ventricular contraction (R-wave) the left ventricle ejects ~60ml of blood out through the Aortic artery. In the graph, end diastolic volume (EDV) and end systolic volume (ESV) are the volumes of blood in the ventricle at the final stage of diastole (rest just before ventricular contraction) and systole (the end of ventricular contraction), respectively.

Thus, the measured NIRS cardiac pulse is expected to have a similar timescale to the left ventricular volume dynamics, since unprocessed light levels from a CWNIRS measurement (even before calculations of haemodynamics) are correlated to cerebral blood volume (CBV) due to attenuation of the light by total haemoglobin (HbT - equal to HbR plus HbO_2) (Obrig, et al., 2003).

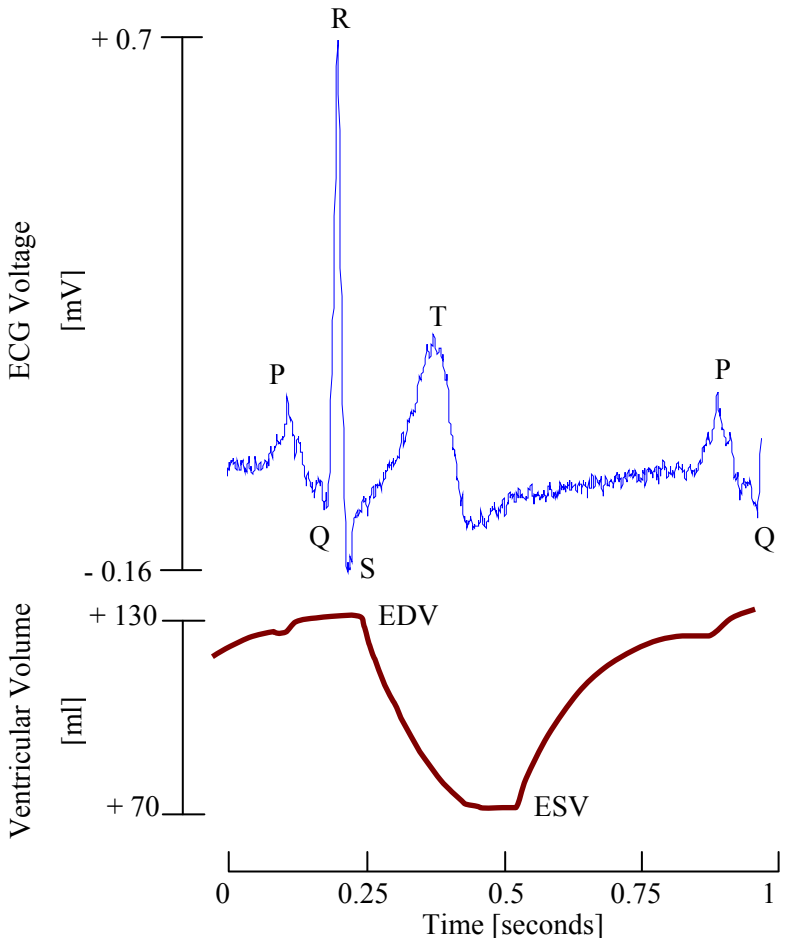

Figure 6.3: Electrocorticogram (21-yr old subject) compared to the proposed left ventricular volume for a heartbeat, (EDV - end diastolic volume; ESV- end systolic volume).

As previously mentioned, the cardiac pulse is typically the first benchmark for determining sufficient SNR in a recorded channel, where a clean quasi-sinusoidal waveform

is the objective. In the event of a poor channel due to perhaps inefficient optical probe coupling to the subject's scalp, the result is generally either a noisy, low-amplitude signal or a cardiac pulse but with additional, sporadic noise sources deforming the waveform. Typical channels showing clean cardiac pulses are shown in Figure 6.4 for seven channels (fourteen individual LEDs) in a NIRS recording.

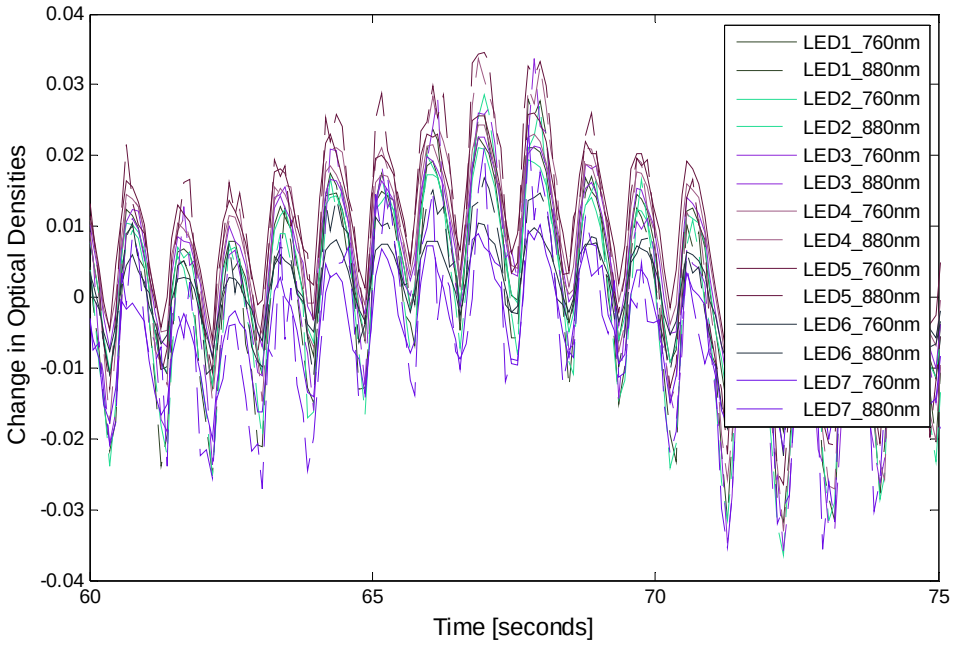

Figure 6.4: Cardiac pulse from the human head from fourteen individual LEDs (7 LED packages).

The graph reports on units of changes in optical density (ΔOD) which is a measure of the change of optical absorption expressed on a logarithmic scale:

$$\Delta A = \log_{10}\left(\frac{I_o}{I}\right) \tag{6.1}$$

... where I_o is the output light intensity baseline (from the tissue at rest), and I is the output light intensity for all other recorded samples (for each channel). For functional studies in a CWNIRS instrument, the output light intensity (I_o) baseline is set as the intensity of light where it is assumed that no 'significant' functional activity is occurring. Thus, the first sample recorded from each channel can be used for each individual channel's baseline. However, for the logarithmic ratio, we use a mean of some initial rest period (baseline over 60 seconds or longer) instead of the first sample, since the baseline is meant to reflect a model of the resting state. The change in attenuation (ΔA) is also a parameter in the MBLL calculation for haemodynamics (observed later in this chapter). The logarithmic operation on

the data ensures that offset differences between the channels are removed since it is a ratio of the first sample (or mean of some baseline) in a channel to the remaining samples.

Futhermore, as will be identified later, for real-time processing of single-trial activity in a BCI, there can be considerable drift and oscillations with similar magnitude to the stimulus response (Hoshi, et al., 1997; Franceschini, et al., 2000; Obrig, et al., 2000a), which may remove the validity of using the first sample, or even an initial baseline mean. In these cases, a new light intensity (for I_o) is calculated based on a mean of the preceeding rest period to an active period, since in NIRS the haemoglobin species do not have sufficient time to return to a true baseline, but are reduced by some degree (also called deactivation (Obrig, et al., 2000b)). This makes it easier on the classification routines used, which will be addressed in the next chapter. Further physiological signals that may indicate at least successful cranial (perhaps systemic) interrogation are discussed next.

6.2.3 Physiological features measured from the human head

A number of physiological signals can be found by performing a frequency analysis of a few minutes of data, as shown in Figure 6.5 below.

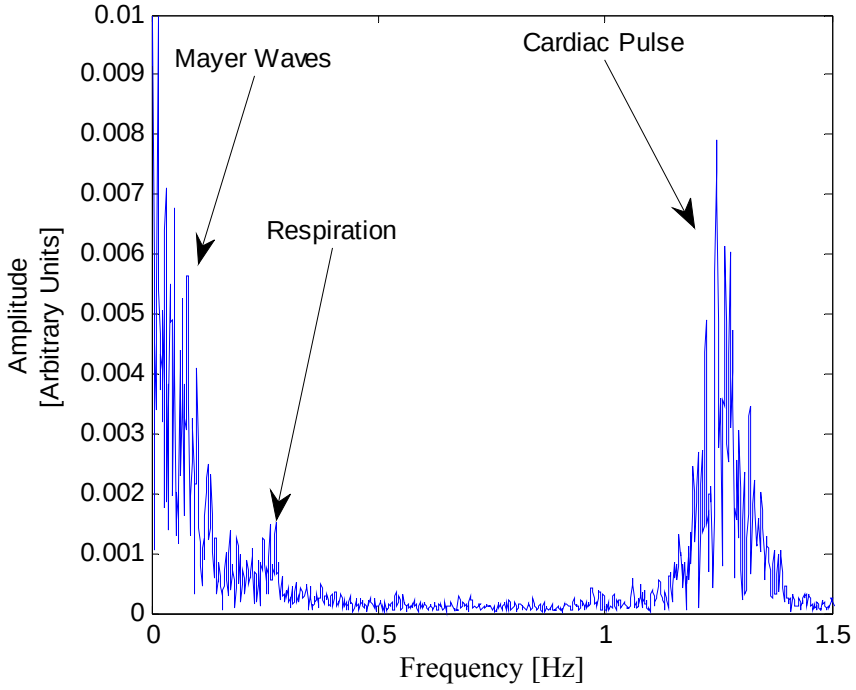

Figure 6.5: Physiological NIRS signal spectra from the head of a human subject. The signals in this case are at ~0.1Hz (Mayer Waves), 0.26Hz (Respiration rate), 1.26Hz (cardiac pulse).

The spectra can be represented in three main frequency bands of cardiac pulse, respiration rate, and very low- and low blood pressure oscillations. In the figure, cardiac

pulse is centered around 1.26Hz but with a typical range of 0.5Hz-2Hz; respiration in the figure is around 0.26Hz but with a typical range of 0.2-0.4Hz; low blood pressure oscillations are shown around 0.1Hz with other very low oscillations below these at ~0.04Hz (Franceschini, et al., 2000).

- The **cardiac pulse** is due to the arterial pulsations, as described earlier in Section 6.2.2.
- The oscillations occurring at the frequency of breathing (**respiration rate**) are due to venous pooling and respiratory sinus arrhythmia (RSA) during inhalation (Elwell, et al., 1994; Franceschini, et al., 2000).
    - RSA is a natural variation in heart-rate (HR) that persists during the breathing cycle - where typically HR increases during inhalation and decreases during exhalation. It is thought that RSA allows for more efficient gaseous exchange or matched timing of alveolar ventilation and alveolar blood perfusion. Thus, RSA may act to conserve energy by eliminating unnecessary heartbeats during exhalation and to increase HR for better alveolar perfusion during inhalation (Yasuma, et al., 2004). These operations are mediated by parasympathetic control via the vagus nerve to the cardio-centers in the medulla oblongata.
    - Blood pooling occurs from a respiratory process modulating cardiac output. During an inhalation intrathoracic pressure falls (due to the diaphragm moving downward) and this has an affect on the thin-walled low-pressure right ventricle of the heart. Increased venous return leads to increased blood volume ejected into the pulmonary circuit. Pulmonary vasodilation magnifies this effect and the left heart system remains unaffected for a time. This leads to blood pooling in the lungs and stroke volume falls, where HR does not compensate for it during inhalation and so cardiac output falls. During exhalation however, intrathoracic pressure increases, affecting the right side of the heart and squeezing blood from the pulmonary circuit to the left atrium, increasing stroke volume. HR does not compensate for this immediately and so cardiac output increases, thus contributing to these respiratory-based blood pressure oscillations (Elwell, et al., 1994).
- Origins of the **low blood pressure oscillations** were already discussed in Chapter 2, but briefly, signals < 0.05Hz are related to thermoregulation. Those in the range 0.05Hz-0.10Hz are due to cyclic increases and decreases in arterial blood pressure and HR, and also perhaps spontaneous fluctuations due to *local*

vasomotion (Hudetz, et al., 1998).

A time series analysis of a short segment of data shown in Figure 6.6 reveals the apparent nature of the cardiac pulse and in many cases, Mayer Waves, but less conspicuous respiration and very low frequency oscillations. Moreover, it is suggested that these signals may synchronise with haemoglobin fluctuations, in particular concentration changes in HbO_2, suggesting the potential for better localisation using concentration changes in HbR (Franceschini, et al., 2000).

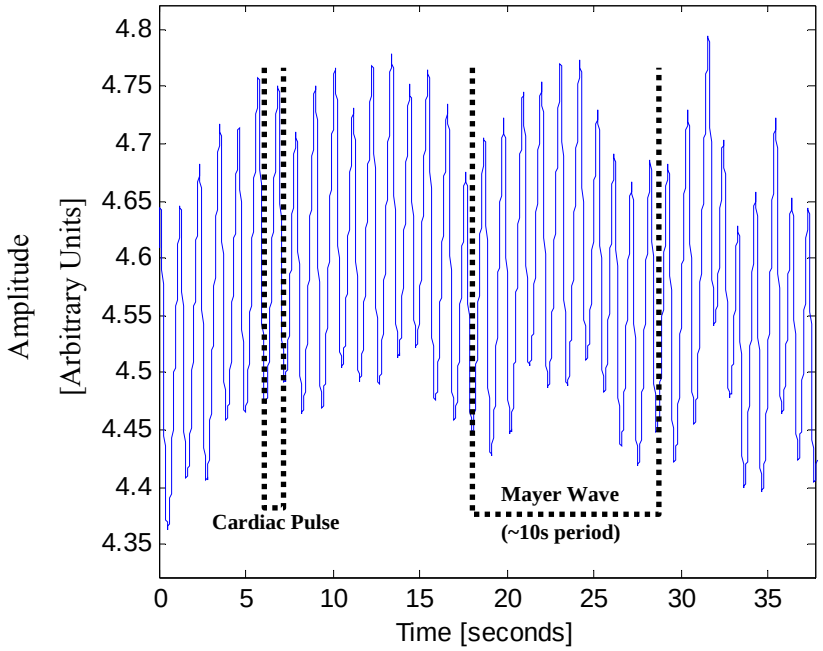

Figure 6.6: Time series analysis of physiological signals from the head. Easily identifiable in every data set is the pronounced cardiac pulse. Conspicuous identification of Mayer wave oscillations varies across subjects and even within a subject, depending on various factors such as posture. Respiration rate features are not so readily identifiable in a time series observation, and they are typically, relatively less pronounced in a frequency analysis such as in Figure 6.5.

For the most part, all of these features are considered noise sources to the signal of interest, which lies in the same frequency band as the spontaneous low frequency blood pressure oscillations around ~0.1Hz. It takes approximately 4-8 seconds for the haemodynamic response (discussed in Section 2.4.6) to peak, and a similar amount of time to return to a baseline (Benaron, et al., 2000) (or at least some lower degree of concentration change). It should also be noted that the low oscillations are more prevalent in $dHbO_2$ than dHbR (~10 times larger) as reported in (Obrig, et al., 2000a), and as we find in our data (see Figure 6.8). Mayhew et al (Mayhew, et al., 1996) also demonstrated that the 0.1Hz signal was prevalent not only in arterial and venous vessels, but also capillary beds of the

intervening regions of brain parenchyma (in an invasive study). Moreover, the signal is said to be neither spatially nor temporally homogenous which makes filtering using a single reference site less potent. Obrig et al reveal phase differences (~2s but subject-dependent) between the haemoglobin species (Obrig, et al., 2000a) which could potentially indicate cerebral interrogation since the phase shift only occurred when imaging the cortex (rather than just superficial layers), as is ensured with a large IOS (>2.5 cm). The power of the 0.1Hz and 0.04Hz signals are also said to change with functional activation, with statistical significance for the 0.04Hz signal increasing power in HbO_2. This will be considered further in Section 6.4 on functional activity analysis of cerebral tissue.

A further important point of interest to note about these signals is that they vary across subjects and even within a subject during an experiment, in phase and amplitude. Indeed, during functional activity such as during motor tasks and even motor imagery, respiration and HR are said to increase (immediately) due to the preparatory effort (Decety, et al., 1993). HR decrease was also proposed as occurring during motor imagery in an EEG-based BCI (Pfurtscheller, et al., 2006), but with occurrences of HR increase in certain subjects, which suggests that neocortical structures involved in motor imagery affect the cardiovascular brainstem nuclei in control of HR. In addition to these functional-activity-induced effects, low blood pressure oscillations measured in NIRS are shown to be posture dependent, with a reduction in their potency in a more supine position of the subject (Tachtsidis, et al., 2004; Coyle, 2005). Thus, subject positioning can be thought of as an analog pre-processing filter for the most menacing physiological noise source (Mayer Waves) - since cardiac pulse in particular, and respiration to a certain degree, are more easily filtered using a simple infinite impulse response (IIR) lowpass filter (typically 3rd order Butterworth) (Soraghan, et al., 2006; Matthews, et al., 2008).

As important as it is to attain a clean cardiac pulse to ascertain sufficient SNR, this signal is mostly contributed from the arterial vessels, which are ~99% oxygenated at all times (since they lack the ability to allow gaseous exchange due to their large cell-wall thickness). The capillary vessels (where gaseous exchange to metabolically active tissue occurs) and venous vessels (where blood enters from the capillaries) are of interest to assess functional activity and mental effort in NIRS (Culver, et al., 2005). The signals - indicating mental effort - occur with a longer time constant (with ~>10 seconds period), and it is generally these haemodynamic signals that are investigated and that represent functional activity (Villringer, et al., 1997). Thus, haemodynamics from the forearm and then from the head are assessed in the proceeding section as a next step in the NIRS-signal analysis for

experiment preparation and validation of the instrument, the process of which could be mirrored by others constructing a multichannel optical BCI.

6.3 Haemodynamics from the human forearm and head

When dealing with a complex organ like the brain with rigid pressure homeostasis and constant oxygenation changes in response to multiple stimuli such as covert thinking, mental arithmetic, movement, and memory allocation, it is prudent to first assess a cruder oxygenation exchange in more extreme circumstances, such as blood vessel occlusion, which has been used to examine NIRS instrumentation by others (Vaithianathan, et al., 2004; Haensse, et al., 2005). Since this occlusion study is not appropriate to the brain (since disruption to cerebral blood flow for a few seconds can lead to unconsciousness and ischemia for a few minutes can lead to brain damage (Berne, et al., 2000)) it was performed on the arm of a human subject, which is described next. Following this, the haemodynamics of the head are analysed without regard to the specific task being carried out. The calculation of deoxy- and oxy- haemoglobin concentration changes (Δc_{HbR} and Δc_{HbO_2}, respectively[1]) were described in Chapter 2.

6.3.1 Venous and Arterial Occlusion - Pressure Cuff Measurements

Analysing the affect of occluding blood vessels is a useful technique to examine a NIRS system's ability to monitor haemodynamic spatio-temporal patterns (Vaithianathan, et al., 2004; Haensse, et al., 2005; Muehlemann, et al., 2008) and instil confidence for the more challenging task of monitoring cerebral haemodynamics. The differential pathlength factors used for forearm measurements are different than those of the head due in part less light scattering and so values of 4.48 (for 760nm) and 3.81 (for 870nm) were used, as used in (Muehlemann, et al., 2008) based on values from (Duncan, et al., 1995). The three stages of the pressure cuff measurement and the timing sequence are shown in Table 6.1. For this test, one detector and seven light sources (14 die) were used. The relative position of the pressure cuff, and the sources and detector are shown in Figure 6.7(B). The pressure cuff was placed around the biceps/triceps of the left arm, just above the elbow on a healthy male volunteer (the same experiment was carried out on a second subject whose results are reported in Appendix D). The NIRS optet was placed with loose strapping around the arm just below the elbow (spanning the brachioradialis, pronator

[1] These concentration changes are also termed dHbR and $dHbO_2$ in this document.

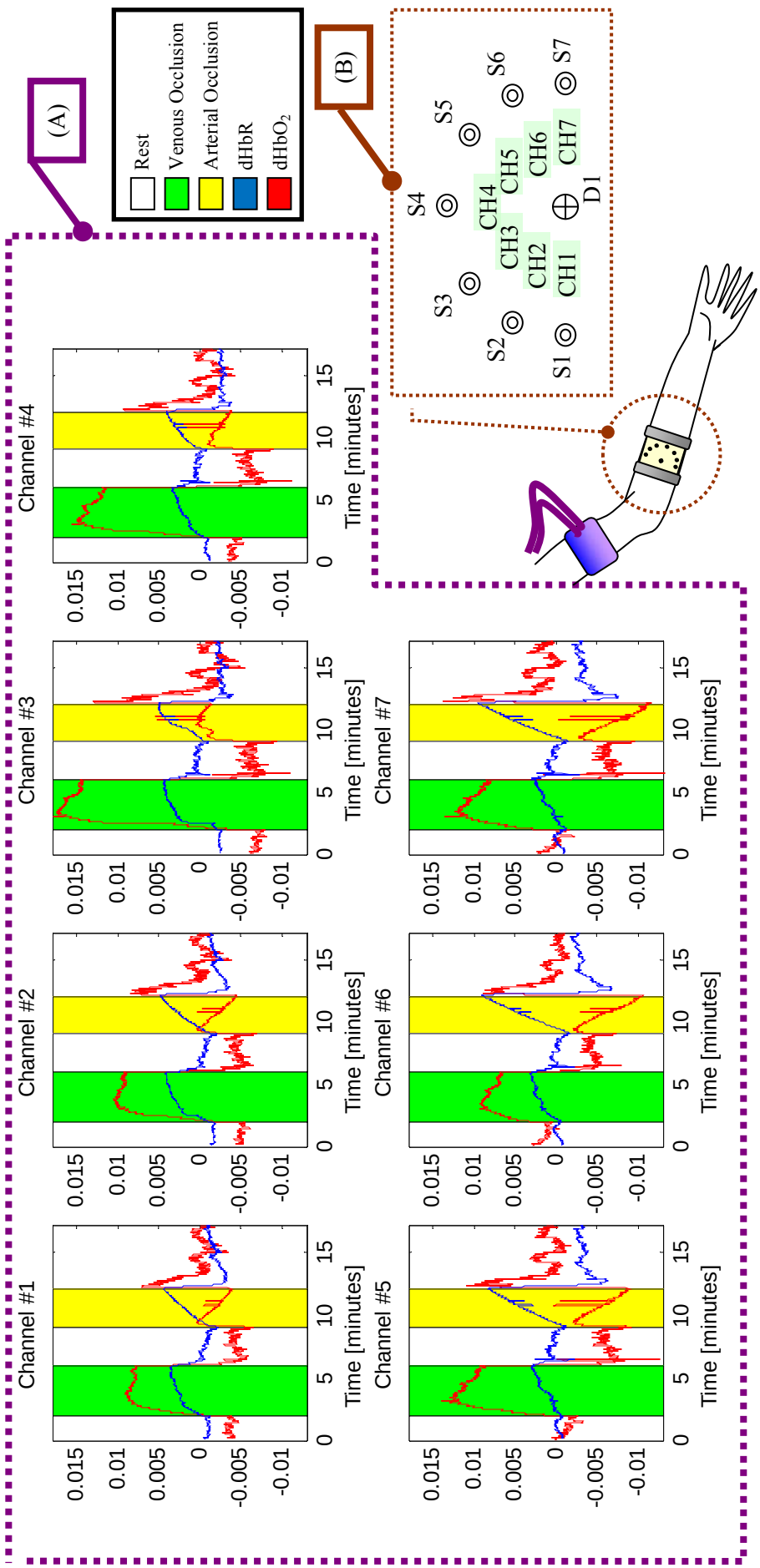

Figure 6.7: Hemodynamics from blood vessel occlusion using a pressure cuff. (A) The time series analysis demonstrates an initial 2 minutes rest followed by venous occlusion (at 40 mmHg) for 4 minutes (green segments); followed by rest for 3 minutes, then arterial occlusion (at 200 mmHg) for 3 minutes (yellow segments), finishing with rest for 3 minutes. (B) Illustration of arm with pressure cuff and the relative positioning of each channel (CH), which lies between a source (S) and the detector (D1). Note: All y-axes are in units of [ΔmM], i.e. Concentration Changes.

teres, and flexor carpi radialis muscules). The arm was positioned on a resting platform at the same height level as the heart. For the measurement, each light source was set at less than half maximum power, to avoid detector saturation which was due to the relatively shorter pathlength of NIR light in arm tissue compared to the cranial NIRS measurements (Duncan, et al., 1995). The haemodynamics as a result of the cuff occlusions are shown in Figure 6.7(A) (and in Appendix D for the second subject). The results match well with the expected concentration changes in HbO_2 and HbR for these cuff occlusions observed by others (Vaithianathan, et al., 2004; Haensse, et al., 2005; Muehlemann, et al., 2008).

Stage	***Timing (Seconds)***	***Pressure (mm Hg)***	***Expectation***
Rest (baseline)	0-120 (2 mins)	0	Baseline of haemodynamics
Venous Occlusion	120-360 (4 mins)	40	Increase in both dHbR and $dHbO_2$; Blood Pooling
Rest (recovery)	360-544 (~3 mins)	0	Decrease in both dHbR and $dHbO_2$ back to baseline
Arterial Occlusion	544-724 (~3mins)	200	Increase in dHbR with reciprocal decrease in $dHbO_2$;
Rest (recovery)	724-1030 (~5mins)	0	Sudden inrush of blood (Reactive hyperaemia); Decrease in dHbR and increase in $dHbO_2$ back to baseline

Table 6.1: Paradigm (timing and pressure values) for haemodynamics measurement from the arm under different stages of blood vessel occlusion using a pressure cuff.

1) The first stage - rest - establishes a *baseline* for haemoglobin concentration changes;
2) The second stage (green segments in all subplots of Figure 6.7) of *venous occlusion* reports an expected increase in both dHbR and $dHbO_2$ as blood pools within the limb - since arterial blood is still flowing into the limb at a cuff pressure of 40mmHg but venous return is restricted.
3) In the third stage, the concentration changes *return to baseline* quite abruptly as blood rushes out of the limb (resumed venous return).
4) In the next stage (yellow segments in all subplots of Figure 6.7), *arterial occlusion* at 200mmHg ensures no blood enters or exits the limb at all. Thus, oxygen is still being consumed, but reserves are not being

replenished and so $dHbO_2$ decreases, and dHbR increases as a result. Also obvious, is the lack of cardiac pulse in the data during arterial occlusion.

5) In the final stage, *rest and recovery*, hyperemia (sudden inrush of blood to the limb) is clearly visible, as well as a return to baseline of $dHbO_2$ and dHbR.

The next successive stage to these cuff occlusion demonstrations is to assess the ability of the instrument to measure haemodynamics from the human head. Subsequently, measurements can be made to assess volitional functional activity in the brain which could be used in multichannel optical BCI applications.

6.3.2 Continuous real-time haemodynamics from the human head

During the normal operation of the system, the modified Beer Lambert Law (MBLL) can be applied in real-time on buffers of 10,000 samples every 50 milliseconds for each APD detector in LabVIEW. Low frequency oscillations from blood pressure changes would be clearly visible in the resulting haemodynamic signal for all channels. Although functional activity can be measured using the CWNIRS technique, it should again be noted that the affective 'baseline' in CWNIRS has significant fluctuations, which can have a magnitude comparable to signals that are evoked by mental tasks (Hoshi, et al., 1997; Franceschini, et al., 2000). Thus, it makes it more difficult to attain an asynchronous BCI, i.e. BCI control at a user specified time and not to some pre-determined time periods (although perhaps with some adaptive filtering/classification methods this could be achieved - ongoing work in the group (Matthews, et al., 2008)). Thus, some type of filtering is typically needed in order to improve the signal prior to classification for online BCI control. Low blood pressure oscillations dominant the DC-0.1Hz frequency band where the haemodynamic signal of interest lies (~5seconds to peak and similarly to return to baseline). Thus, it is typical to see a lowpass filter used to filter the cardiac pulse (Matthews, et al., 2008). However, the Mayer Waves, blood pressure oscillations, and respiratory-related signals are more difficult to remove without distorting the haemodynamic signal. Thus, some preventative measures are taken: 1) the subject is laid in a supine-like position to reduce the size of the Mayer Wave (Coyle, 2005); 2) the timing of the paradigm for mental tasks is pseudo-randomised in order to reduce the likelihood of synchronising with this physiological noise, since they could affectively mask the haemodynamics signal (Soraghan, et al., 2008a). The specific filtering techniques used will be discussed in the experimental results where they apply and some are reviewed elsewhere (Matthews, et al., 2008). For immediate consideration however, an unfiltered recording (having been processed using the MBLL translational algorithm for calculating haemodynamics - see Chapter 2) is shown in Figure 6.8 showing $dHbO_2$, dHbR, and dHbT (total haemoglobin, a sum of the two haemoglobin species). For this dataset, some

mental tasks were performed which contribute to some of the large low frequency signals seen in the data, however, they are not considered here yet. One purpose of Figure 6.8 is to demonstrate continuous haemodynamics from the head recorded by the instrument, as it is sometimes frustrating to see in many publications the lack of an illustration of a complete data-set - pre-filtering.

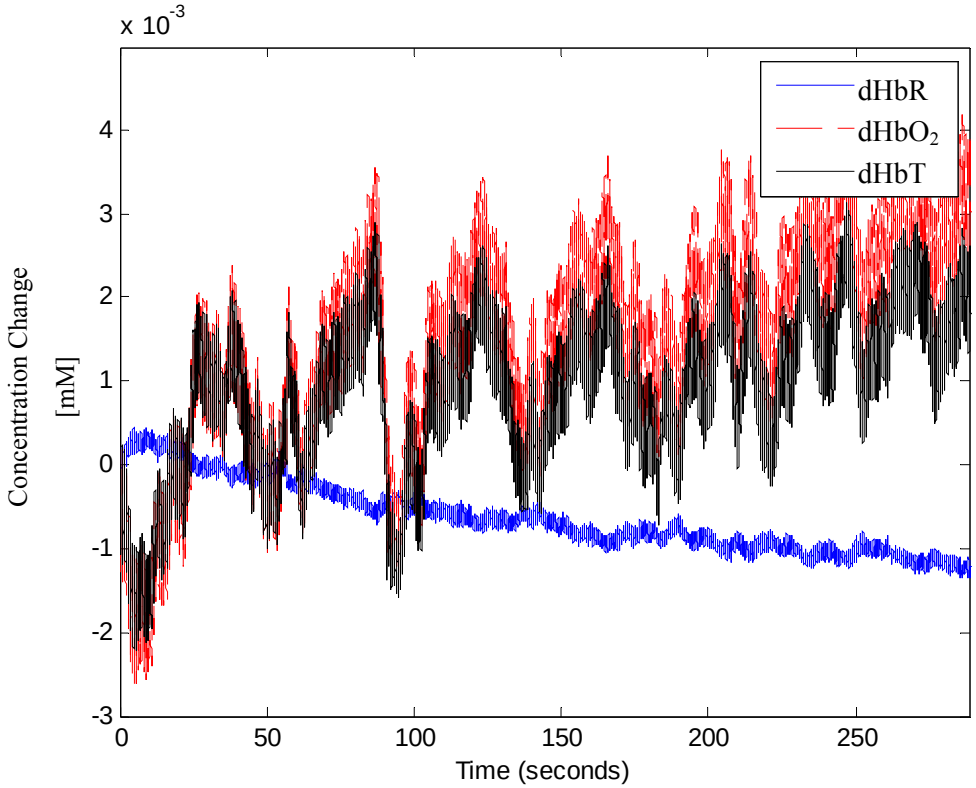

Figure 6.8: Continuous haemoglobin calculation showing $dHbO_2$, dHbR, and dHbT. Data is unfiltered.

The proceeding section considers functional activity from the brain and potential mental tasks that could be used in a FNIRS-BCI, some of which have been published recently (Soraghan, et al., 2006; Ward, et al., 2007; Soraghan, et al., 2008a). First, the common protocols used for BCI are validated in a series of BOLD fMRI recordings, and then these functional activations in the brain are measured by the CWNIRS instrument.

6.4 Functional Activity from the Brain

Functional activity measurement has been documented in various imaging modalities, including FNIRS. Typically NIRS recordings are shown as grand averages of data in the

final analysis. The FNIRS technique has been used to measure functional activity related to motor (Toronov, et al., 2000; Sato, et al., 2006), visual (Jasdzewski, et al., 2003), auditory (Kennan, et al., 2002), and cognitive (Herrmann, et al., 2003) tasks. Thus, some of these reported tasks could possibly be utilised for optical BCI control. The most common mental task group used in BCI is the motor task group (Mason, et al., 2007) and these have been piloted for single-dual channel optical BCI successfully recently (Coyle, et al., 2004; Coyle, 2005; Coyle, et al., 2007). However, in these studies it was mooted that multichannel optical BCI could perhaps have additional benefits such as faster localisation (of active cortical tissue) and better spatial coverage of the cerebral cortex (assessed in Chapter 7).

BOLD fMRI has also been established as a functional neuroimaging tool, and as previously mentioned, it has a correlate with FNIRS in HbR due to its magnetic susceptability (Obrig, et al., 2000b; Strangman, et al., 2002b; Sassaroli, et al., 2005; Huppert, et al., 2006b). Thus, as a means to validate the protocols (timings) and mental tasks used in the FNIRS experiments, a series of fMRI recordings (using a Siemens MAGNETOM Allegra 3T MR Scanner (Siemens-AG, 2009)) were carried out in New Jersey, USA in collaboration with the Cognitive Studies Laboratory in Rutgers University and the University of Medicine and Dentistry of New Jersey (UMDNJ). These studies are considered next, followed by an analysis of motor and cognitive tasks whose responses were recorded using CWNIRS. These fMRI findings establish the use of these tasks in optical BCI applications, also reenforced with previous feasibility studies by Coyle et al (Coyle, et al., 2004), and indeed the peer reviewed publications by the group since then.

6.4.1 BOLD fMRI studies for verifying protocols and mental tasks

BOLD fMRI allows for the identification of regions of activity in the brain in response to some functional activation such as motor movement or motor imagery of a limb. These tasks have also been used in fMRI-based BCIs (see Chapter 3, e.g. Yoo, et al., 2004). One key motivation or outcome from our BOLD fMRI studies was for functional activity localisation and to see if the protocols we used evoked distinct cortical metabolic responses in the brain. This determination of the spatial extent of the elicited activation also aids in understanding the extent of crosstalk in ipsilateral cortical areas or between different tasks (body parts). This information would be useful for the FNIRS experiment design (in addition to the documented cases in the literature) and in particular for placement of the optical probes.

6.4.1.1 Procedure

For all tasks the subjects were asked to perform a specific motor (overt or imagined) event. A visual prompt/cue for each task (in the form of plain text at the center of the display

using *PyEPL*) was sent to a projector in a space a few meters behind the magnet. The projected image was directed to a small mirror just above the subject's nose which was attached to the RF coil of the MR scanner. The protocols for all these experiments consisted of a stimulus duration of 16 seconds and a rest period of 30 seconds in a predetermined sequence. Four stimuli/tasks sets were included (design matrix shown in Appendix C):

- Both feet (Overt Movement and Imagery);
- Left Hands/Fingers (Overt Movement and Imagery);
- Right Hands/Fingers (Overt Movement and Imagery);
- Tongue (Overt Movement and Imagery).

For each session a high resolution T1-weighted anatomical MRI scan was performed with 1mm slice thickness. The functional BOLD axial scans, or T2*-weighted functional scans (related to dephasing of the susceptible precessing hydrogen protons) were acquired with a slice thickness of 2mm. Much of the fMRI protocol set-up was performed by a collaborator (Dr. Halchenko) at the facility, using *PyEPL* (http://pyepl.sourceforge.net/ - library for coding psychology experiments in Python) for presenting the visual stimuli/prompts and for recording these timing events. Eight trials of each task, both overt and imagined, were performed - thus 64 trials in total - with tasks pseudo-randomised.

6.4.1.2 Results

The results from a single subject for left handed tasks for overt- and imagery of movement are shown in Figure 6.10 and Figure 6.11, respectively. Similarly, those for right handed tasks for overt and imagery of movement are shown in Figure 6.12 and Figure 6.13, respectively. Each figure contains 32 axial BOLD slices, in three rows. A representation of the ordering of slices in those figures is shown in Figure 6.9. The superior scalp slices begin at the third row for the tenth column (the rightmost image in this row is blank) for all figures. Slices 2, 3, 4, ... to 10 are in a sequence in the third row to the left of the first slice. Slice 11 is shown in the second row for the eleventh column, and so on.

32	31	30	29	28	27	26	25	24	23	22
21	20	19	18	17	16	15	14	13	12	11
10	9	8	7	6	5	4	3	2	1	

Figure 6.9: Representation of BOLD fMRI slice layout, with the most superior first slice at the scalp, Slice 1, in row three, column ten.

In the BOLD images, the right hand side of the subject is indicated by the letter "R". The subject's forehead (eyes) is facing downwards and so the observers view is inferior to

superior, i.e. not looking from the scalp downward but from under the head. Activations are marked in red-to-yellow against the grey anatomical brain background. The activation intensity is shown in the side colour-bars for each figure, all on the same scale.

Clearly seen in all BOLD responses is activity in the occipital regions possibly related to vision. However, of interest are cerebral regions that are activated in relation to movement. These are expected to be in the sensorimotor, primary motor, and premotor cortices, including the supplementary motor area (SMA) related to preparation of motor movement. In terms of comparisons to NIRS, only slices a few millimeters (< 1cm) into the brain are penetrable due to the conduit effect from the cerebrospinal fluid area and the highly scattering cranial tissue and superficial layers (Okada, et al., 2003a; Okada, et al., 2003b). Nevertheless, as already mentioned, the cerebral cortex controls many of the high level functions such as its involvement in motor control in the aforementioned cortices. Significant activations for left hand overt movement are found (see Figure 6.10) in contralateral regions of the primary motor cortex with some ipsilateral activity. Some activity is found in the SMA, but left handed imagery produces a more significant response in the SMA shown in Figure 6.11. Furthermore, the activity from imagery in the primary motor cortices is less intense. Similar comparisons for overt and imagery of right handed tasks are seen in slices in Figure 6.12 and Figure 6.13. However, apparent is the higher intensity and larger spatial distribution of activation due to right handed overt motor tasks - this is the subject dominant hand - determined using the Edinburgh Handedness Inventory (Oldfield, 1971).

6.4.1.3 Discussion:

The results described demonstrate the localised metabolic responses in cortical areas related to motor movement, with some bilateral activation for the tasks assessed. The larger responses found for right handed dominant tasks are considered in Chapter 7 using the developed CWNIRS instrument (on the same subject as performed the BOLD fMRI reported here). It should be noted that NIRS can only penetrate a few millimeters of cortical tissue. Thus, slices 1 up to perhaps 11 can be assessed using NIRS. However, activations on the fringes/edge of the brain for deeper slices such as the visual activations may be interrogated with NIRS so long as those deeper slice activations occur close to the brain surface. Thus, activations in the center of the deeper slices which may show activity in fMRI cannot be measured using reflectance NIRS. Activations to feet and tongue movement and imagery are shown in Appendix C along with the tasks here for right and left motor tasks. Work is ongoing in the group to assess the possibility of using such tasks in optical BCI applications.

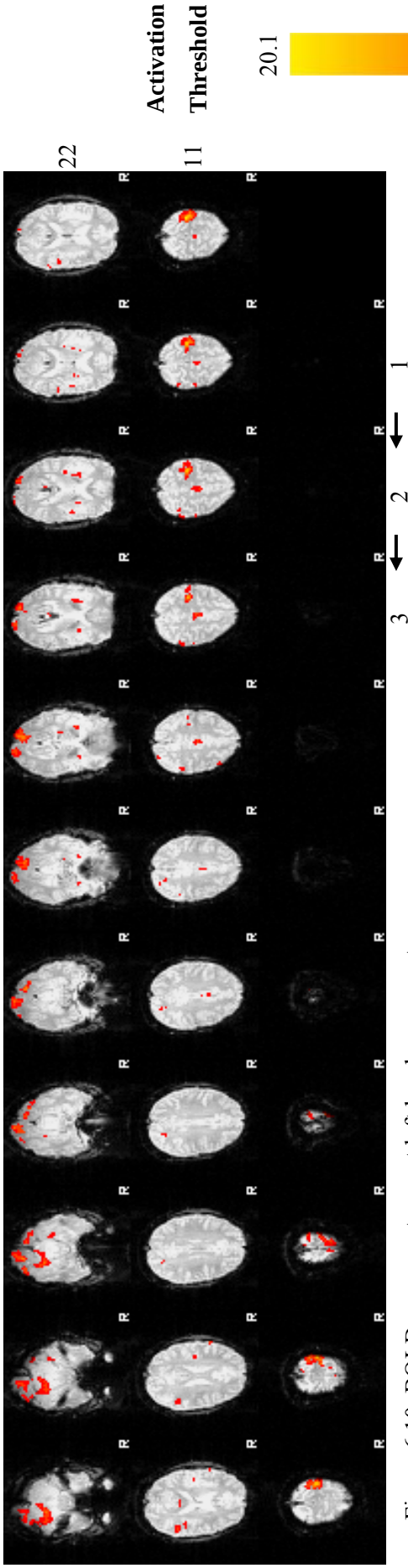

Figure 6.10: BOLD response to overt left hand movement.

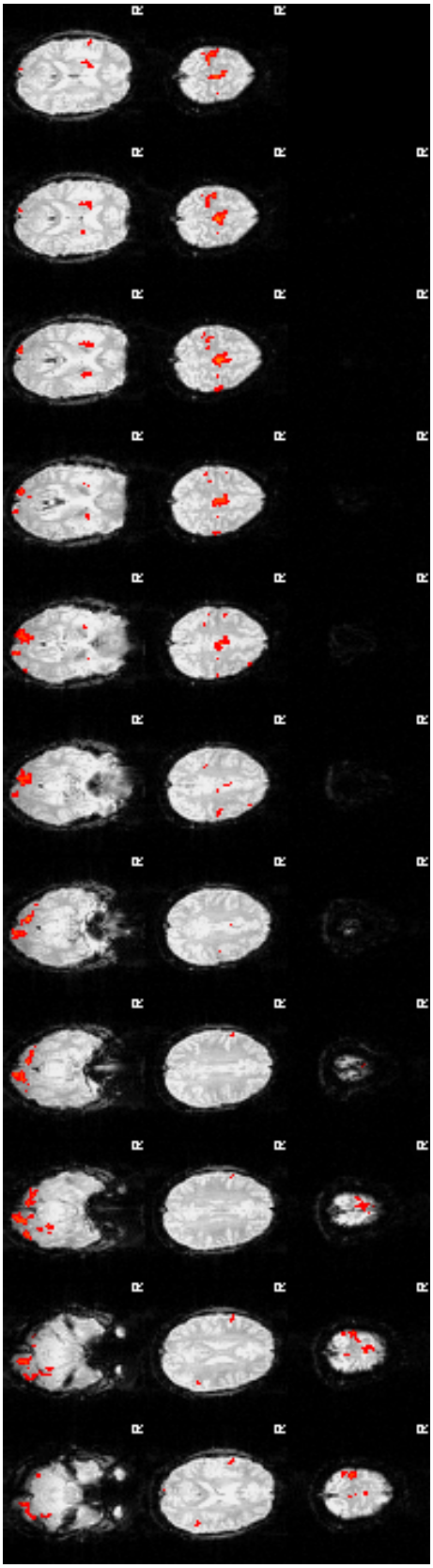

Figure 6.11: BOLD response to imagined left hand movement.

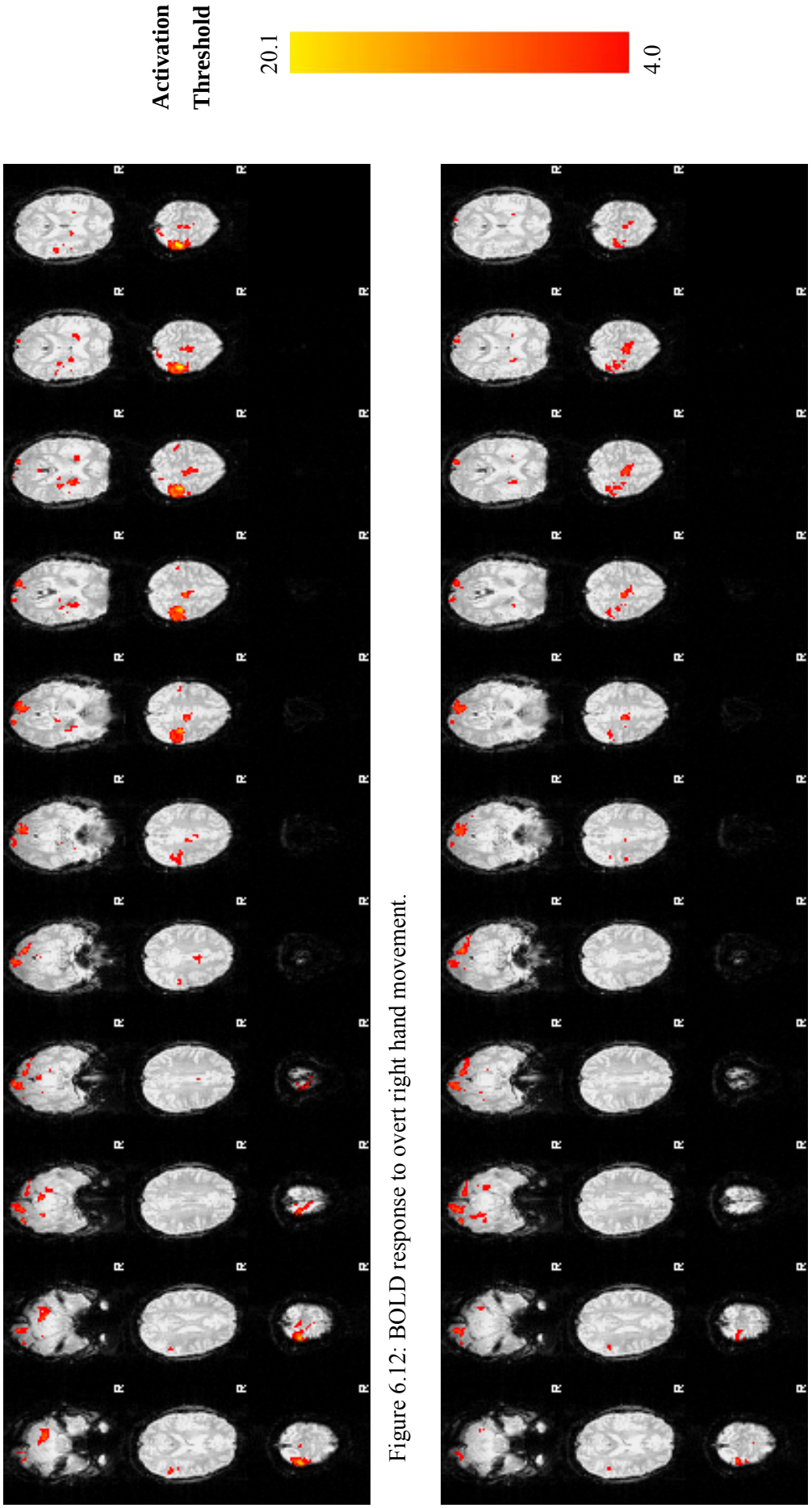

Figure 6.12: BOLD response to overt right hand movement.

Figure 6.13: BOLD response to imagined right hand movement.

6.4.2 Overt Motor Tasks

After having established regions of activity in fMRI for motor tasks (overt and imagery) which correlate well with dHbR in FNIRS, it is of interest to observe motor tasks in FNIRS directly. Moreover, this will provide a validation of the ability of the newly developed multichannel instrument to measure and record such cerebral activity. In the next chapter, these overt motor tasks will be utilised in a biofeedback experiment controlling unilateral movement of a robotic arm.

Finger tapping/opposition tasks are commonly used to evoke metabolic responses in the contralateral cortical tissue of the primary motor cortex (M1) in control of the hand used (Obrig, et al., 2003 - see table of stimuli). However, as previously mentioned, the reported responses are usually grand averages of trials, in order to get a better representation of a typical response and reduce physiological noise. For BCI, single-trial responses need to be decoded in real-time to invoke a neural prosthesis, especially since the haemodynamic response function has such a large time constant, requiring 4-5 seconds to peak. A distinction also needs to be made of the use of the term single-trial - in some of the literature it is reported as meaning a single action of the limb, e.g. single finger flexion, which can then be averaged over multiple trials (Obrig, et al., 2000b). For an optical BCI, a single-trial involves evoking a response within one predefined time period (for a synchronous based BCI), typically less than 20 seconds.

Short Experiment: A finger opposition task of the right hand was carried out on a subject, whereby each finger was opposed to the thumb, switching fingers at a rate of-2Hz (2 finger oppositions in 1 second). For the experiment, seven light sources and 1 detector were used in an optet placed over the C3 region of the motor cortex. The procedure was as follows:

- The LEDs were turned on/heated for 1 hour;
- The optet (see optet in Figure 6.15) was placed on the subject, and the subject was lain in a supine position (to reduce Mayer Wave oscillations);
- The timing protocol consisted of an initial baseline of 300 seconds, followed by five intermittent stimulus and rest periods. The stimulus periods were fixed at 20 seconds, whereas the rest periods were pseudo-randomised between 15 and 30 seconds;
- The subject monitored visual prompts on a screen - ~1 meter away from the subject's head;
- The rest period was indicated by the word "RELAX" and the stimulus period by

"RHO" meaning right hand overt finger opposition task. During the rest period the subject fixated on the word "RELAX" and was asked not to engage in movement-related tasks (or imagery of these tasks).

Discussion: The modified Beer-Lambert Law (MBLL - see Section 2.5.2.3) algorithm was implemented to establish concentration changes in HbO_2 and HbR. The data were then filtered with a 0.01Hz 5th order highpass filter to remove baseline drift and a moving average smoothing filter with 10-point span was applied to remove some of the cardiac pulse, but not completely - so as to reveal some of the true features for comparison to the initial baseline. The resulting haemodynamics from channel 2 are shown in Figure 6.14.

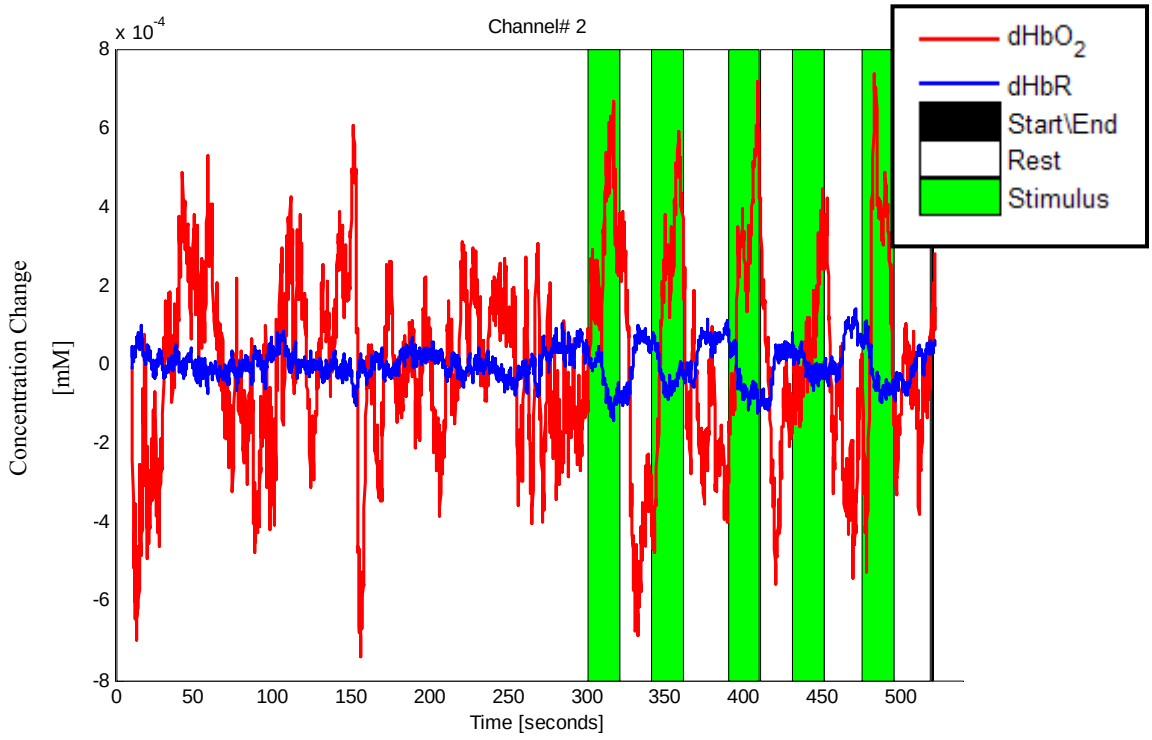

Figure 6.14: Haemodynamic response from the left primary motor cortex to right hand finger opposition task (stimulus). Green sections indicate stimulus periods.

A baseline was established over an initial 300 seconds to demonstrate the dynamic range of, in particular, $dHbO_2$ which (as mentioned previously) is known to include more background blood pressure oscillations than dHbR (Obrig, et al., 2000a). Thus it can be seen in Figure 6.14 that the baseline's dynamic range is similar to that of the stimulus (green) periods. In these stimulus periods however, there is a distinct increase in $dHbO_2$ and a decrease in dHbR, as expected for these motor tasks. Of particular significance is the decrease in dHbR which is said to be more indicative of localised cerebral activation. For comparison all seven channels were filtered using a bandpass filter (0.01Hz to 0.09Hz) after the MBLL algorithm was applied, and are shown overlain in Figure 6.15 below. In

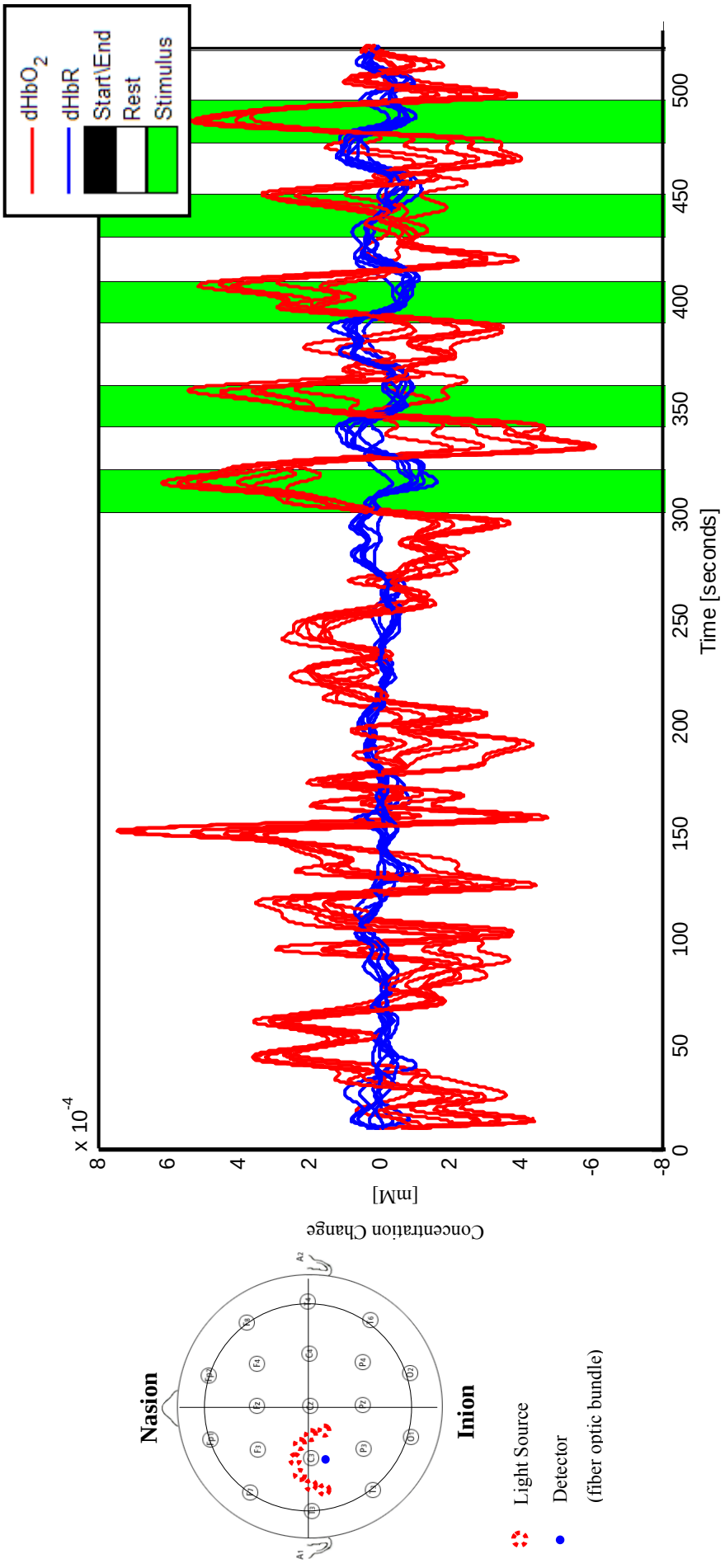

Figure 6.15: Seven channels from one optet overlain to demonstrate relative differences in amplitude and rise time of peaks in $dHbO_2$ and troughs in dHbR during stimulus periods. Differences are found mostly in the fourth stimulus period. The left (inset) depicts the optet used with 7 sources and 1 detector placed over C3 (of the 10-20 EEG system).

Figure 6.15 some of the variations in rise times of $dHbO_2$ during the stimulus periods (green sections) can be seen. During the fourth stimulus period, differences can be seen where it appears certain channels have more distinct increases in $dHbO_2$, perhaps due to variation in the spatiotemporal activation for that time period. This signifies the importance of a multichannel instrument for detecting functional activity since some channel's activity may be weaker and indeed more difficult to classify. In particular channel 2, as shown by itself in Figure 6.14, displayed more significant dips in dHbR and peaks in $dHbO_2$ than the other 6 channels. Localisation is considered further in Chapter 7.

Responses vary from the more conspicuous responses to overt motor tasks, to the less-well defined responses to cognitive effort. Functional activity has been demonstrated in response to cognitive tasks such as during the verbal fluency task (Herrmann, et al., 2003) and mental arithmetic (Soraghan, et al., 2008a). The author has seen (described in the next section) that the HbR and HbO_2 concentration changes in response to mental arithmetic may be inverted compared to other cortical regions (e.g. motor areas) and this finding has been reported by others (Bauernfeind, et al., 2008) and also in concurrent PET-NIRS experiments (Hoshi, et al., 1994). Thus, cognitive tasks are examined in the next section as they are potential tasks for use in optical BCI applications. Again, these assessments are part of a series of validatory experiments to report on the ability of the multichannel system to measure such activity, rather than a thorough analysis of the responses themselves.

6.4.3 Cognitive Tasks

In a recent publication (Soraghan, et al., 2008a), the authors used a mental arithmetic cognitive task to assess a 12-channel prototype of the CWNIRS instrument, but using 2 detectors and 12 light sources (24 LED die) and the software-based demodulation and interfacing equipment reported in Chapter 5. The triple wavelength LED package (APT0101) was used for this experiment but with only the 880nm and the 760nm die being turned on.

Short Experiment: As shown in Figure 6.16 two optets were placed on the frontal cortex with one detector and six light sources each. The results from channel 3 are depicted for ten trials of mental arithmetic. The subjects were asked to perform these mental arithmetic exercises during synchronous predetermined trials which simply entailed successively subtracting (for each subtraction the minuend is the result of the previous subtraction) two whole randomised numbers (the minuend was a 4-digit number, the subtrahend a 2-digit number between 16 and 22) - (e.g. 1011 - 16 = 995, 995 - 18 = 977, etc.). The timing protocol used entailed the following:

- An initial rest period was fixed at 30s to establish a resting haemodynamic baseline (or at least to relax the subject);
- The remaining rest periods were randomised between 15s-30s in an attempt to curtail habituation, stimulus expectation, and low blood pressure oscillation (Mayer Wave) synchronisation (Mayhew, et al., 1996);
- Stimulus periods were fixed at 15s (more than sufficient to establish the haemodynamic response - requiring 4-8s to peak);
- Each subject performed 2 sets/runs of 10 trials within the same session.

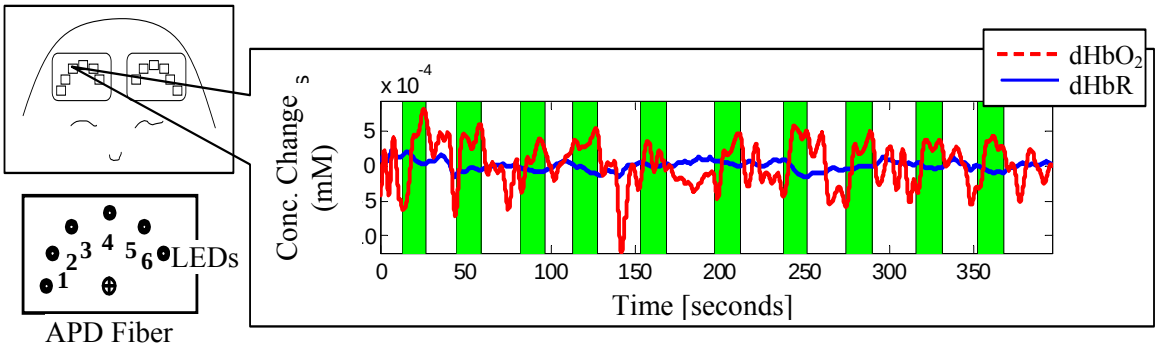

Figure 6.16: Ten trials of mental arithmetic tasks from subject 1 on channel 3. The optet arrangement used is shown on the left (from Soraghan, et al., 2008a).

Figure 6.16 shows the non-averaged response from Subject 1 on channel 3 after bandpass filtering (0.05Hz-0.2Hz). During the stimulus periods (green regions), activity in the right frontal cortex is indicated by increased haemodynamics, in particular, an increase in $dHbO_2$ and a decrease in dHbR. However, a single trial non-averaged response for the six channels on the left-hand-side optet (subject's right) is shown in Figure 6.17. All channels have the same y-axis scaling (minimums and maximums) and are in units of ΔmM. At first glance, channel 1 and channel 2 appear to produce the largest response with the largest $dHbO_2$ peak during the mental task. However, channel 3 (as demonstrated in Figure 6.16 for all ten trials) is more significant since it presents an HbO_2 concentration change increase *and* a decrease in the concentration change of HbR during the mental task. Although many researchers report on $dHbO_2$ as the main indicator of localised functional effort, HbR has been reported as being a better indicator of localised functional activity (Obrig, et al., 2000b; Obrig, et al., 2003). Nevertheless, as stated previously, the haemodynamics of the frontal cortex appear to have more complex distribution patterns with possible inverted responses (see Figure 6.18) from the classical ones from the motor and visual cortices. Furthermore there is also the possibility of both versions (inverted and non-inverted) in the same recording at different locations on the frontal cortex - as were also identified by others recently (Hoshi, et al., 1994; Sakatani, et al., 2006; Bauernfeind, et al., 2008).

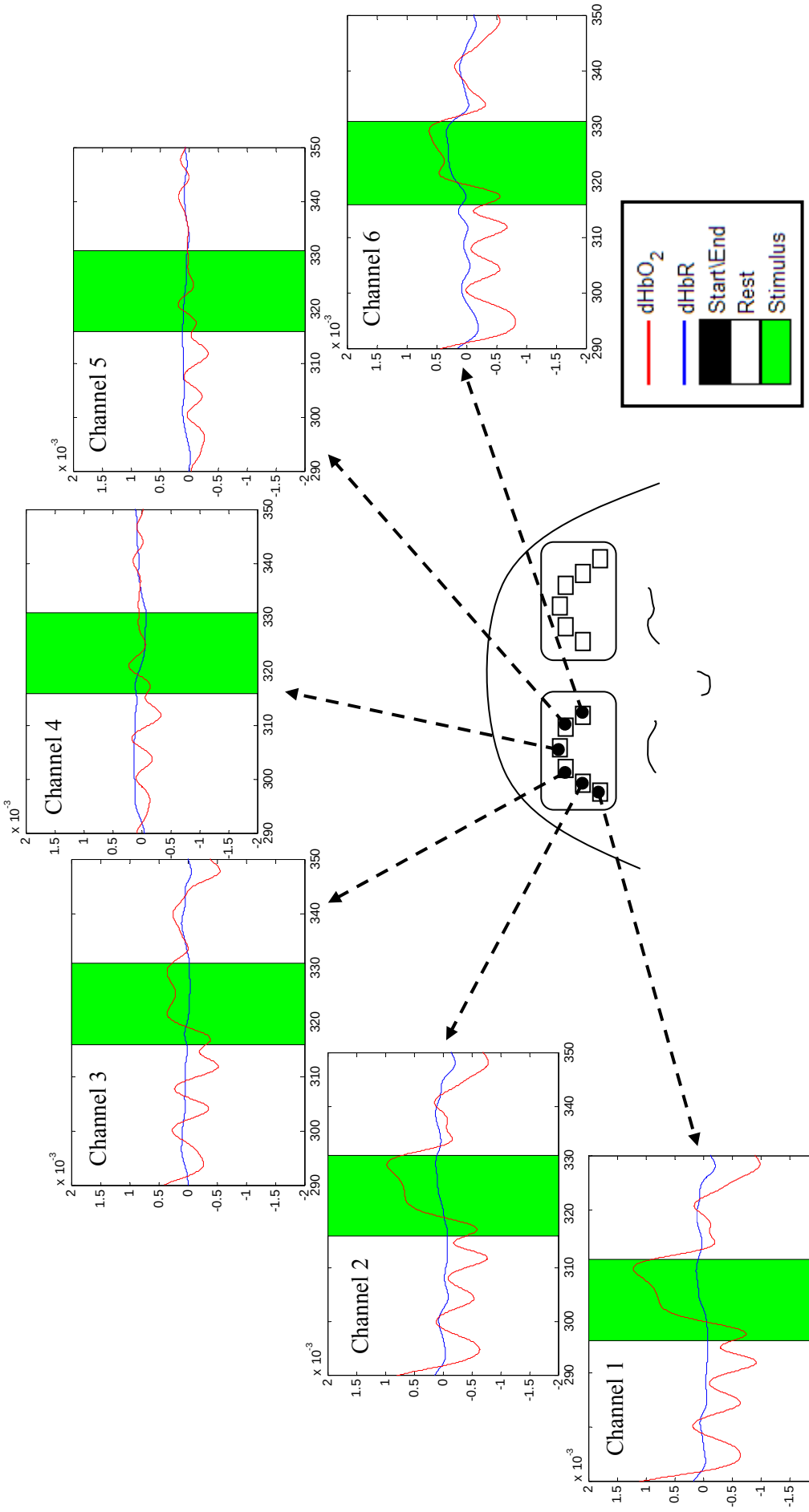

Figure 6.17: Frontal cortex activity to mental arithmetic tasks from an optet on the subject's right forehead. Green sections indicate activation periods. All y-axis (Concentration Change) scalings are the same, and in units of Δ mM. The abscissa for all plots is in seconds.

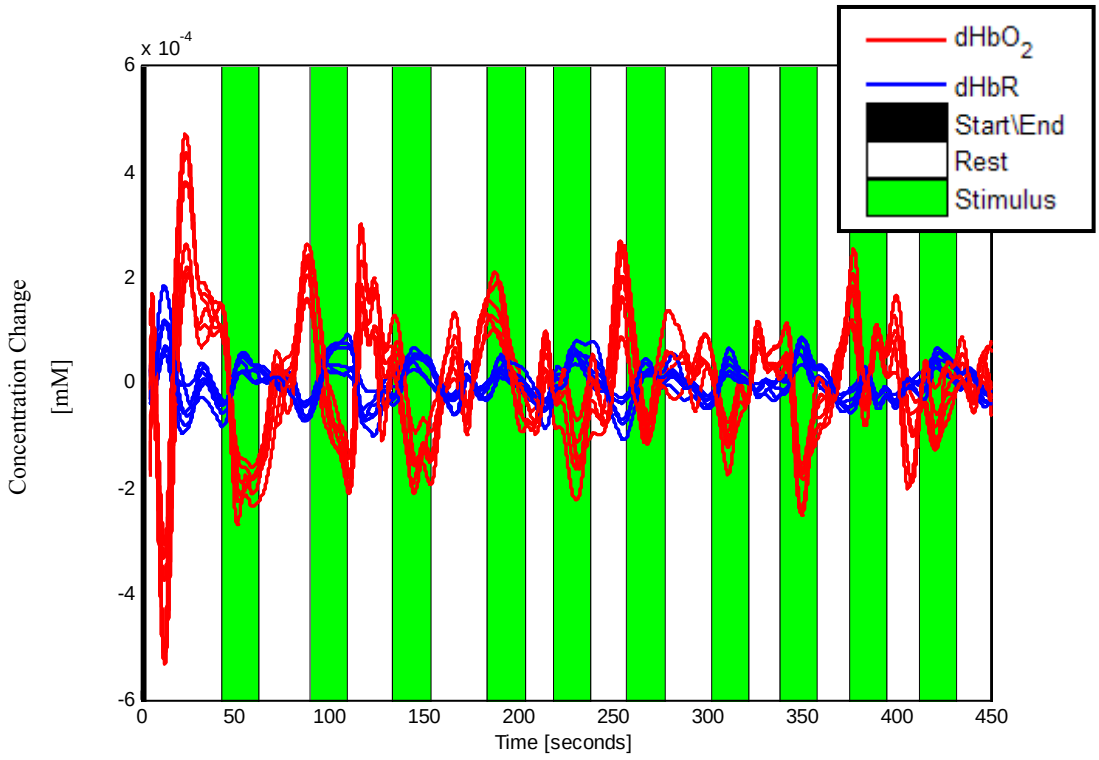

Figure 6.18: Example of inverted responses during ten trials mental arithmetic for the same subject but on a different day. The optet used was the same as in Figure 6.17, with 6 sources and 1 detector over the subject's right frontal cortex (around F8-Fp2).

The physiological origin of such an inverted response has been mooted as being indicative of a decrease in regional cerebral blood flow (rCBF), whereas the expected "activation" typically denotes an increase in rCBF (Obrig, et al., 2003). The decrease in rCBF then does not seem to typify an "activation" but more a "deactivation", where perhaps neighbouring tissue (or perhaps deeper structures since vessels are at right angles to the cerebral surface) may be influencing the periphery's haemoglobin oxygenation pattern - although this claim is not substantiated here. Furthermore, Sakatani et al (Sakatani, et al., 2006) discuss briefly that the process of deactivation is unclear, and that the proposal that "more demanding tissue is robbing the analysed tissue of blood flow", is perhaps unlikely since BOLD fMRI studies by others reported no activation in prefrontal cortical areas that are supposedly draining CBF from the deactivated tissue. A second suggestion is that there may be a suppression of neuronal activities from the action of diffuse projecting systems, e.g. dopamine, or from a reduction of thalamic signals to the cortex during such attention-demanding cognitive tasks. Both haemodynamic patterns of activity were found by Sakatani et al for different tasks- activation patterns (increase in $dHbO_2$ and decrease in dHbR) for verbal fluency tests, but deactivation (decrease in $dHbO_2$ and an increase in dHbR) during driving simulation (Sakatani, et al., 2006). Nevertheless, as a solution for implementing an optical BCI, if these physiological features are reproducible, and are thus useable for

controlling a BCI device, the physiological origin is still required but perhaps not immediately paramount.

In addition to the inverted response, areas of increase in both $dHbO_2$ and dHbR are apparent in some channels in Figure 6.17, e.g. channel 1 and channel 2, which could be indicative of an increase in CBV. This effect (increase in both) can also be seen during a movement artefact or contributed from some change in systemic or extracerebral haemodynamics (e.g. Valsalva maneuver - forceable exhalation against a closed airway), but should be seen in all compartments of the sampling volume (global) (Obrig, et al., 2003) - which they are not here. An increase in both species was also seen in the arm haemodynamics in Figure 6.7, but this was related to venous occlusion. Such mental tasks have been used in an fMRI based BCI for spatial navigation of a maze (Yoo, et al., 2004). However, the question now lies in what response to use for mental arithmetic that is indicative of functional effort? It is felt by the author that both are correlated to the event, and so both features could be added to the classification routine, i.e. the feature of 1) an increase in dHbR and decrease in $dHbO_2$, or else 2) an increase in $dHbO_2$ with a corresponding decrease in HbR. Also of interest in the finding in literature that the cognitive activities have been found to activate regions in the parietal lobe (Richter, et al., 2009), thus increasing the amount of cerebral tissue or mental tasks that could be utilised for in an OBCI. However these may increase the likelihood of an event activating tissue over many areas of the brain making it more difficult to separate tasks (by the classifier).

Having considered and demonstrated some of the mental tasks that could be used in an optical BCI, the next section in this chapter demonstrates the use of topographical reconstruction or imaging of a cortical area. This reconstruction is used for offline analysis of data but is as yet unsuitable for real-time online single-trial analysis for an optical BCI.

6.5 Topographic reconstruction

For offline analysis it is useful to analyse topographic reconstruction of the multichannel data which can be achieved using a third party software called *HomER* (Huppert, et al., 2006a) - although this is not implemented in real-time. It can however, be useful for preparatory experiments where data can be processed through the GUI and return a topographical colour-indexed map registered to the source- and detector positions used. An example of its use was presented by the group recently (Soraghan, et al., 2008b) and is reproduced in Figure 6.19 below. The task carried out was overt motor activity of the subject's right hand, using one detector (o1) and seven sources (x1, x2, ..., x7). The most

significant activity is marked by an increase in $dHbO_2$ (termed HbO in HomER) and a decrease in dHbR (as dealt with in Section 6.4.2 and Section 6.4.3). This is seen dominating channels between the detector (o1) and the sources 'x5' and 'x6' (labelling convention used in HomER). However, a further hypothesis is that cerebral blood volume maps can produce better spatially resolved maps than dHbR or $dHbO_2$ (Culver, et al., 2005), where CBV is proportional to HbT - which would suggest the channel between detector o1 and source x1 produces the most significant metabolic effect in Figure 6.19. Changes in CBV have been utilised in a single-channel, single-wavelength optical BCI (Naito, et al., 2007) although the use of CBV as a marker of activity is perhaps a result of the constraint on the system used, since at least two wavelengths of light are needed to determine haemodynamic (HbO_2, HbR, and HbT) data.

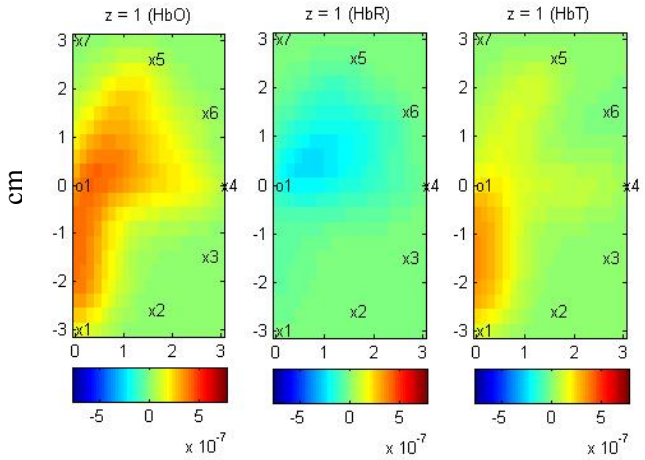

Figure 6.19: Topographical reconstruction of $dHbO_2$, dHbR, and dHbT from multichannel data processed in HomER. The most significant activity from this motor task can be seen in channels between detector 'o1' and sources 'x5' and 'x6' (conventions used in HomER). All abscissa and y-axis are in units of cm. (Soraghan, et al., 2008b).

6.6 Chapter Summary

In order to trial a CWNIRS instrument, it was useful to have a series of practical experiments, with incrementally challenging tasks, to investigate the validity and performance of the instrument. Initially, a non-human phantom was useful in conjunction with a rotating absorber, to mimic a cardiac pulse to test the hardware and software of the instrument. Following this the cardiac pulse was examined from the body and then from the human head. A subsequent frequency analysis of a few minutes of data from an FNIRS channel revealed an abundance of physiological noise apparent in the recordings (even in

time series analysis), such as the cardiac pulse, respiration rate, and low- and very low blood pressure oscillations - the most signficant (filtering challenge) of which are in the region of the haemodynamic response of ~0.1Hz. The next incremental stage, was to determine the system's ability to assess haemodynamics, first from the less absorbing forearm tissue (analysing dramatic haemodynamic responses to blood vessel occlusion), and then from the human head. BOLD fMRI investigation of motor (overt and imagined) tasks (the BOLD signal which is correlated to dHbR) allowed for observation of localisation and ipsilateral activity to right and left hand motor tasks. These examinations established the protocols used in the proceeding NIRS experiments. The FNIRS responses to motor and cognitive tasks were subsequentially assessed with a discussion on the temporal and magnitude changes in $dHbO_2$ and dHbR. In particular it was revealed that motor tasks elicit the more common activation feature representing an increase in rCBF, but in cognitive tests for mental arithmetic on the same subject, both activation and deactivation patterns were found. Finally, an offline topographic illustration of multichannel data for a motor task was demonstrated, discussing the potential of utilising either dHbR or dHbT maps that may represent more localised functional activity in the human cerebral cortex.

The importance of the resulting haemodynamic responses to the mental tasks used in this chapter was to demonstrate the ability of the newly developed multichannel CWNIRS system to be able to detect such metabolic activities in the brain, i.e. it is an assessment of the instrumentation and rather than a rigorous investigation of mental responses to such tasks. Thus, the experiments reported in this chapter cannot really say much about the mental responses to motor and cognitive tasks since they were reported on very few subjects and few trials. In the proceeding chapter, a dual-channel optical BCI is implemented using overt motor tasks and analysing cerebral activity resulting from these as a concept for stroke rehabilitation - an emerging area of BCI research. Further contributions of the multichannel CWNIRS instrument are assessed in a series of studies investigating the ability of the system to detect functional activity localisation and lateralisation in single-trial responses to motor tasks. Furthermore the potential of dHbR being a more robust, stable marker of functional activity for optical BCI applications is discussed.

CHAPTER 7

ASSESSMENT OF FUNCTIONAL TASKS FOR BCI APPLICATIONS USING THE MULTICHANNEL CWNIRS INSTRUMENT

7.1 Assessment Synopsis

In Chapter 6 a series of assessments were made to validate the multichannel CWNIRS instrument developed in this dissertation. This chapter begins with an implementation of an OBCI using an dual-channel system based on similar equipment developed by Coyle (Coyle, 2005). This is described in Section 7.2.

In this initial study, a new optical BCI application was proposed by the group (Ward, et al., 2007). The proposed concept was for extending the applicability of Constraint-Induced Movement Therapy (CIMT) through motor cortex activity feedback using a neural prosthesis. The basic tenet of the work aimed to propose a neurorehabilitation technique for the target group of severe stroke sufferers with little or no perceptible movement. It was perceived that this initial, temporary neurorehabilitation technique/process could allow biofeedback of concealed motor cortex activity for the affected limb. Subsequently, when some motor function returns as a consequence of this neurorehabilitation technique, the patient could then use more conventional CIMT techniques aimed at evoking appropriate neural plasticity processes. As part of this proposal a series of biofeedback experiments

based on responses to attempted (overt) motor tasks were carried out using an optical BCI to control movement of a robotic arm. This study utilised a dual-channel CWNIRS device with classification of HbO_2 concentration changes ($dHbO_2$) only (due to lack of significant changes in dHbR owing to limitations of the instrumentation from the old prototype: lower power 760nm LEDs).

Based on findings from Study 1, justification in moving to multichannel was found since it was thought that some of the subjects may have benefitted from the possible localisation abilities of a multichannel device. Thus, functional activity studies using the newly developed multichannel CWNIRS instrument were sought to assess the potential additional benefits a multichannel implementation could provide for such BCI applications. Thus, Study 2 (see Section 7.3) was carried out to access the ability of the instrument to localise functional activity from motor tasks that could be used in BCI applications. Study 3 (see Section 7.4) was performed to assess the ability of the multichannel system to measure lateralisation of activity rather than global haemodynamic changes in the cerebral cortex. Throughout these experiments it became apparent that HbR concentration changes are potentially a better indicator of focal metabolic activity changes since they are less prone to blood pressure oscillations (and are more localised than $dHbO_2$). A further study, Study 4 (see Section 7.5), was aimed at identifying if shortening the activation period for motor tasks could be achieved in a single-trial basis, and if the haemodynamic responses could be measured by the multichannel CWNIRS device. This was implemented because shorter activation periods could effectively allow for an increase in the potential information transfer rate (ITR) for an optical BCI. Furthermore, perhaps a shorter stimulus period could reduce the influence of non-stationary low blood pressure oscillations on the haemodynamic signals of interest, aiding successful classification of regional functional effort.

The latter studies using the multichannel device also give an exposition of single-trial haemodynamic responses which are of significant interest to BCI research since immediate biofeedback is required for applications such as neurorehabilitation for stroke suffers. In a final study, Study 5 in Section 7.6, observations were made of single-trial functional activity changes to interspersed motor tasks and motor imagery of those tasks. These covert tasks could be used in the more common BCI application of augmentative communication for the severely disabled, e.g. ALS patients.

7.2 Study 1: Dual-channel OBCI - Biofeedback of Overt Motor Tasks

Overt motor tasks were employed for this study since imagined activity was not required or even germane for the neurorehabilitation envisaged. It also allowed the experimenter to determine the motor areas that are active during such tasks and to eliminate poor subject participation that would be reflected in the results. The control signals elicited arise from bilateral activation in the motor areas which are used to determine biofeedback.

7.2.1 Procedure

Instrumentation:

- For this study, a previous dual-channel OBCI prototype was used. Two light sources (with wavelengths 760nm and 880nm - Opto Diode corp., Inc., APT-0010/OD-880F, Calif, USA) were used with a narrow 8° beam angle, spectral bandwidth at 50% of 30nm and 80 nm, respectively. Each LED was modulated with a low kHz carrier wave.
- The same APDs described in Chapter 5 were used (Hamamatsu C5460-01) as the light detection solution with a 3mm diameter active (circular photodiode) region. One meter long, fiber optic bundles guided light output from the scalp to the APDs, and BNC cables carried the transduced output potentials to lock-in amplifiers (Signal Recovery, model 7265).
- The LEDs and fibre bundles were placed in contact with the scalp as shown in Figure 7.1. The BiopacUIM100C interface module in tandem with a Biopac MP100 (analogue-to-digital converter) was used to collect the four analogue channels of raw NIRS data to disc (two wavelengths, two sites) from the lock-in amplifiers at 16-bit resolution.
- A further two analogue channels of data were collected by the MP100: the respiration pneumogram and digital photoplethysmograph (PPG) using Biopac amplifiers modules RSP100C and PPG100C ,with gains of 10 and 100, respectively. PPG100C settings comprised a low-pass filter of 10Hz and high-pass filter of 0.05 Hz. RSP100C settings implemented a low-pass filter of 10 Hz. These were collected for possible future offline processing and are not used in determining biofeedback.
- Feedback was provided through unilateral movement of a robotic arm (Figure 7.2) in sympathy with sustained elevation in $dHbO_2$ levels during the motor execution tasks. A 12-bit National Instruments USB-6008 DAQ was used to

drive the robotic arm in tandem with detected motor activity. This was determined by analysis of data sampled by the same 12-bit DAQ which sampled the outputs from the lock-in detectors (as well as the Biopac instrumentation). Online and real-time processing for dHbR and $dHbO_2$ was performed using the MBLL algorithm in C#. The robotic arm was driven when haemodynamic activity exceeded rest period levels. This protocol is described next.

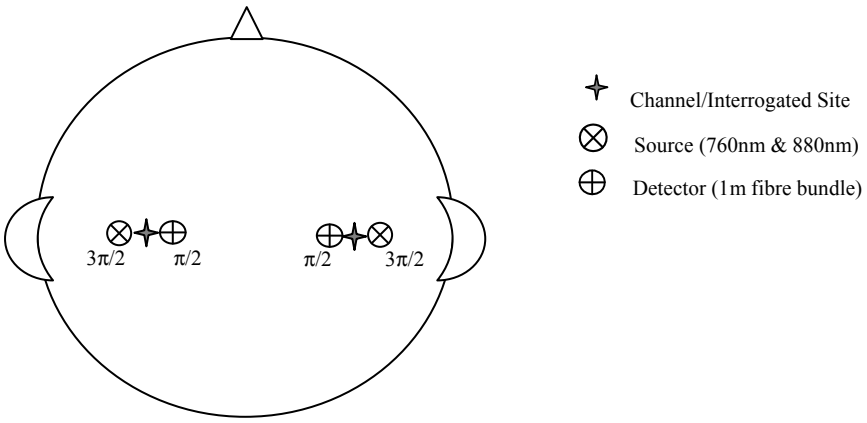

Figure 7.1: Illustration of relative source and detector positioning in two optodes.

Figure 7.2: The Armdroid 1 robotic arm used for biofeedback. The arm performed a unilateral movement in response to motor activity.

Experimental Protocol:

- *Subjects:* Five healthy subjects (4 males and 1 female) were used in this experiment, 2 left handed and 3 right handed - determined using the Edinburgh Handedness Inventory (Oldfield, 1971). Subjects were in the age range 23-25 years old. The female subject was removed from the analysis due to poor SNR and optode placement issues. The remaining four subjects were included in the online biofeedback analysis;

- *Preparation:* Each subject was seated in a near supine position to reduce the effects of low-frequency blood oscillations (Mayer wave) and the experiment took place in a dimly lit room. Subject's head measurements were taken to locate positions C3 and C4 and the source and detector positions are as depicted in Figure 7.1. These 10–20 system positions are approximately over primary motor cortex centres in the brain responsible for right- and left-hand movements. The IOS was 3cm. (Note: a description of the polar coordinate-based optode placement system was given in Section 5.5.1.4.) Channel 1 had a source position C3:1.5(3π/2) and a detector position C3:1.5(π/2); Channel 2 had a source position C4:1.5(3π/2) and a detector position C4:1.5(π/2). Following head measurements, the probe locations were prepared, but individually - not all at once. Hair was parted under the optical probes (light sources and fiber optic bundles) to leave ample hair-free scalp. The optical probes were inserted into cushioned pads in contact with the subject's scalp. The subject's hands were placed under restraining straps on a flat surface in order to facilitate isometric exercise during the stimulus trials;
- *Instructions:* Prior to the experiment each subject was informed about the nature and purpose of the experimental study and given precise instruction as to the task required of them. To reduce artefact, subjects were asked to minimise head and body movements as well as given instructions to breathe gently and regularly;
- *Timing Paradigm:* The timing and stimulus paradigm for performing the overt motor task is illustrated in Figure 7.3. Each experimental run began with 30 seconds initial rest period to establish a baseline. This was followed by intermittent periods of motor stimulus fixed at 25 seconds (which were isometric maximal voluntary contractions—MVCs of the indicated forearm, pivoting at the elbow on a rigid support surface); and rest fixed at 15 seconds. Each experimental run consisted of 10 trials of motor task. A total of 80 online trials for each the right and the left arm were carried out and used in the final analysis - i.e. each of the four subjects carried out two sessions (10 * 2) on each arm, thus a total of 20 stimulus periods per arm per subject;
- *Subject Cues:* Audio and visual cues indicating the task and rest periods were presented via speakers and an LCD monitor to the subjects;
- *Biofeedback:* Feedback was provided in two forms:
    - 1) A symbolic-visual form - on the LCD monitor a change from a black rectangle to an upward-pointing arrow occurred when $dHbO_2$ levels in excess of the previous rest period's level were present, and,

- 2) A real form where the robotic arm physically moved under the same conditions, which could be seen and heard by the subjects.

  If the $dHbO_2$ levels dropped below the threshold during the motor task period, the icon reverted to the black rectangle form and motion of the robotic arm ceased. If during the same period the levels exceeded the threshold again, then the robotic arm would being moving yet again, and the visual feedback of the arrow would reappear.

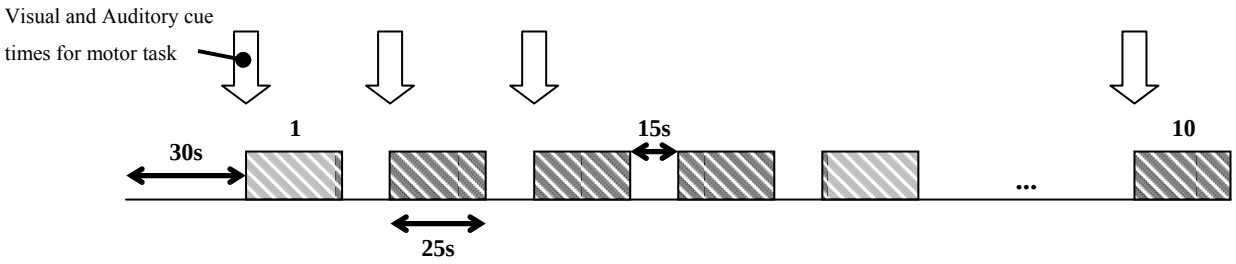

Figure 7.3: Experiment timing paradigm. Shaded boxes indicate motor task periods, 10 in total per experimental run.

Classification:

- Signals from the lock-in amplifiers were sampled at 10 Hz using a 12-bit USB DAQ, and the HbR and HbO_2 concentration changes were calculated in real-time, on a sample-by-sample basis;
- For filtering, simple 10-point moving average filters were used in all experiments to reduce the effects of the cardiac pulse in real-time;
- Neither dHbR nor dHbT levels were used as an information signal in the online experiments - only $dHbO_2$ levels. For the detection of significant activity during the activation period, a simple thresholding scheme was employed whereby a data point was calculated from the preceding rest period. This datum consisted of the average $dHbO_2$ level during the 15 seconds of the rest period. The 10-point running average of the $dHbO_2$ signal calculated during the motor task period was thresholded against this reference signal. When the level was exceeded during this period, significant motor cortical activity was inferred and appropriate feedback was presented. In summary, activation occurs where $s[i]-\bar{r}>0,$

$$s[i]=\frac{1}{W}\sum_{j=0}^{W-1} dHbO_2[i+j] \quad for\, i=1,...,N \tag{7.1}$$

- where, s[i] is the derived control signal at the i^{th} sample; W = 10 (samples); N is the number of samples acquired during the motor task; $\bar{r}$ is the average $dHbO_2$ signal during the rest period. So long as the stimulus moving average was greater than the rest average, activity was sensed and the robotic arm was activated, as well as the visual feedback of the upward-facing arrow.

7.2.2 Results and Discussion

The results of the BCI experiment are presented in Table 7-1. The table indicates the percentage of time that the subjects were able to successfully move the robotic arm during the motor execution task. Each subject was able to gain some control of the robotic arm. The columns indicate the arm being used in the motor cortex task appended with either '1' or '2' to indicate either the first or the second experimental run for that subject. For example, Subject 1 during the second experimental run using left arm movement, was able to keep the robotic arm moving for >90% of the time when engaged in left forearm movement (during all 10 trials for this run). However, Subject 3 demonstrated the poorest performance, only realising movement of the robotic arm ~60% of the time. It was felt that insufficient SNR from this subject contributed to poor activations. A previous x-ray scan from the subject had also found that this subject had a relatively thick skull which is known to reduce the partial mean optical pathlength in cerebral tissue (Okada, et al., 2003). Furthermore, the sensors may have been placed on a scalp location away from the area of maximum activation for this subject due to anatomical differences, i.e. the measured C3 area for the subject may not be exactly over the primary motor areas for hand movement. Thus, this added justification to moving to a multichannel system for better localisation of the maximum haemodynamic response to functional activity in the brain for these tasks. (Note: Multichannel localisation is assessed in Study 2 in Section 7.3.)

Nevertheless, the success measures presented here are rather conservative as they indicate the percentage of time by which the threshold was exceeded during the motor task. In certain BCI applications a goal oriented task could classify activity based on a significantly sustained activation and use this as a binary "Mindswitch" such as the that proposed in Coyle, 2005 which simply uses a threshold. If the results were reworked to indicate the percentage of motor task periods (trials) where the robotic arm was activated at all, then the results reported would be improved. However, a threshold is difficult to implement for NIRS based signals (in terms of reducing false positive and true negatives) as seen from the signals presented for motor activation tasks in Chapter 6, simply because blood pressure oscillations are known to have a similar dynamic range (Franceschini, et al., 2000; Obrig, et al., 2000a). This is further recognised by the various signal processing

methods that are being examined for NIRS-BCI (Matthews, et al., 2008). Nevertheless there are further distinct features that can typify a response in the motor areas using FNIRS - which are increases in HbO_2 and decreases in HbR during the stimulus period.

Subject	Left 1 (%)	Left 2 (%)	Right 1 (%)	Right 2 (%)	Subject Average (%)
1	87.2 ± 23.9	90.4 ± 11.0	91.8 ± 15.9	95.4 ± 5.1	91.2 ± 13.9
2	82.4 ± 20.2	88.2 ± 13.4	73.5 ± 25.9	82.0 ± 25.2	81.5 ± 21.2
3	74.7 ± 25.8	64.3 ± 21.7	63.7 ± 33.6	46.8 ± 38.7	62.4 ± 29.9
4	96.7 ± 3.2	98.4 ± 2.9	90.2 ± 19.1	86.5 ± 23.6	93.0 ± 12.2

Table 7-1: Success rate in moving robot arm. Figures indicate the percentage of time subjects were able to keep the robot moving during each trial. That is, Subject 4 successfully moved the robot 96.7% of the time during all 10 stimulus trials for the first session of left-arm maximum voluntary contraction (left 1). Reproduced from (Ward, et al., 2007).

Figure 7.4 shows the averaged responses (including standard deviations) for two paradigmatic subject tests during both the motor task and rest periods. The top row (A and B) of graphs is from Subject 1, and the bottom row (C and D) from Subject 2. The left column (A and C) shows activity during the motor task between 0 seconds and 25 seconds. The right column (B and D) shows the haemodynamics during the proceeding rest (deactivation) period, between the dashed vertical lines (0 to 15 seconds, after activation). All results are from channel 1 around 10-20 position C3 (see Figure 7.1). The figure was generated in the Matlab-based NIRS analysis tool (HomER) (Huppert, et al., 2006a) and illustrates mean and standard deviation levels that indicate consistent differences between rest and activation. The smoothness of the plot is attributable both to averaging over all trials from both channels and-a 3rd order lowpass Butterworth filter with cutoff frequency of 0.7Hz implemented before calculating averages and standard deviations.

The classic increase in $dHbO_2$ (Obrig, et al., 2000b) can be seen for both subjects taking a few seconds to reach the initial peak (~4 seconds). The amplitude is sustained (or increased in the case of Subject 2) until the activity is ceased at 25 seconds where the expected decrease in $dHbO_2$ ensues. The expected decrease in dHbR (Obrig, et al., 2000b) is seen significantly for Subject 1, but not Subject 2 (top, left side graph) indicating inter-subject variability which has been reported by others (e.g., Huppert, et al., 2006b). The right hand side of the graph (B and D) demonstrates the nature of the recovery of the NIRS response. Whereas it might be assumed that the NIRS response returns to a baseline in reality there is a recovery time period as well as the confounding blood pressure oscillations which can be modulated (amplitude and phase) with functional activity (Obrig, et al., 2000a).

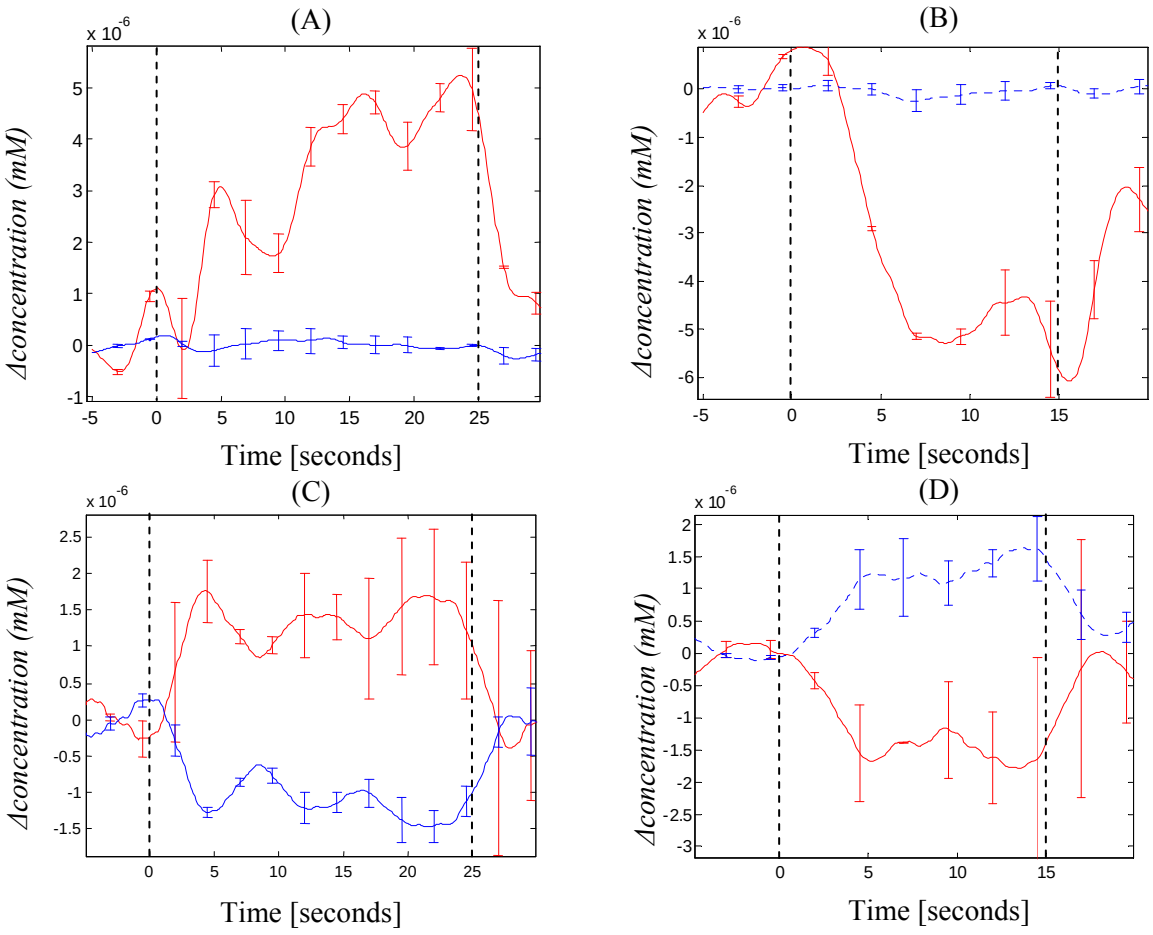

Figure 7.4: FNIRS responses from overt motor movement. The top row (A and B) shows the average dHbR (dashed trace) and $dHbO_2$ (solid trace) levels ± standard deviation for Subject 2. The bottom row (C and D) shows average readings for Subject 1. The left hand column (A and C) shows activity during the motor task (between vertical dashed lines) while the right hand column (B and D) shows haemodynamics during the proceeding rest\deactivation period. The abscissa for all plots is in seconds (Ward, et al., 2007).

As an aside, cortico-regional differences in the haemodynamic response have been reported in the literature, whereby motor activity may be seen as a double peak in $dHbO_2$ compared to the visual cortex activity whereby $dHbO_2$ is said to have more sustained amplitude for the duration of the performed task (Jasdzewski, et al., 2003). This has potential implications for classification of tasks whereby if motor and visual areas were being used in an optical BCI, the motor cortex may provide additional features for the classifier (multiple peaks) compared to the visual areas, although this needs to be investigated for single-trial responses.

7.2.3 Conclusions

The functional activity changes shown in Figure 7.4 demonstrate inter-subject differences in terms of dHbR in particular. However, these differences may be due to inefficient probe placement where the probes are not placed over areas of maximum

localised activity. This is suggested because dHbR for Subject 2 (results shown in A and B in Figure 7.4) did not vary significantly with the task in comparison to dHbR for Subject 1 (results shown in C and D in Figure 7.4), and also since HbR is said to be more localised to the metabolically activated tissue (Franceschini, et al., 2000). These results indicated the need to design a flexible multichannel device capable of localising this activity since a multichannel implementation offers increased spatial coverage of the cerebral cortex than that of a single\dual channel device. This would have the benefit of reducing the set-up time needed to locate regions of maximum activity, or improve true positive classification (since a weaker signal is generally more difficult to detect\classify).

7.3 Study 2: Multichannel Localisation of Functional Tasks

It was of interest to investigate the ability of the instrument to determine localisation of functional tasks. The study was not to check for this localisation across a number of subjects but rather to investigate if the instrument could identify it at all in a single subject.

7.3.1 Procedure

The flexible multichannel CWNIRS instrument described in this dissertation (in Chapter 5) was configured to have seven LEDs and a single detector (7 channels in a single optet) with C3 located (approximately) at the center of the optet. A series of right hand finger opposition tasks were carried out (5 trials) on a single subject (right handed according to the Edinburgh Handedness Inventory - Oldfield, 1971). All data were filtered with a bandpass filter: 0.001Hz - 0.5Hz in HomER but 0.01Hz-0.3Hz for time series data.

Experiment 1: After an initial rest period, five stimulus periods (fixed at 20 seconds) were interspersed with rest periods pseudo-randomised between 15 and 30 seconds.

Experiment 2: The same experiment was performed (as Experiment 1) using right hand finger opposition tasks, with the same timing paradigm, but for 10 trials.

Experiment 3: In this experiment the whole optet was moved a few centimeters from its position in the previous experiment along the coronal plane, towards Cz 10-20 electrode position. Thus, the expectation was that using the same motor tasks, the activation may remain in the same cerebral location and thus appear in different CWNIRS channels, i.e. shifted to the left (since the optet was moved to the right toward Cz). The same timing protocol was used as in Experiment 1 and 2, but with five stimulus periods.

7.3.2 Results and Discussion

Seven channels of data were recorded for each experiment and topographic maps were generated for concentration changes in HbO_2, HbR, and HbT using HomER (NIRS data analysis software). Figure 7.5 illustrates a topographic map for the first experiment where C3 is close to the center of the optet. The largest change in all three haemoglobin species was for channels between the detector and sources 2, 3, and 4. The topographic map for the second experiment is shown in Figure 7.6. The average maximum activation for these ten trials remains localised to cerebral tissue around position C3. This experiment was carried out to test if the activation was robust and localised between experiments as well as trials. Figure 7.7 demonstrates that when the optet was moved with respect to C3, the activation remained in that cerebral tissue, i.e. activation appears apparent in channels to the left of the center of the optet (between the detector and source 4, 5, and 6). It was also an attempt to see if more activity could be found across the entire optet since it appeared cerebral areas to the left of C3 were dominant. Nevertheless, the significance of this result is that the functional activity changes in response to the motor task were found to be localised for this subject over a number of trials.

Note that intensity scales are the same for all topographic maps in all figures (Figure 7.5, Figure 7.6, and Figure 7.7) for better comparison. Using the same scaling has the effect of demonstrating the relatively larger increases in $dHbO_2$ and dHbT, but dHbR seems more dispersed and less significant. This reduced affect is expected since the increase in $dHbO_2$ is reported in literature to be ~4 times larger than the decrease in HbR. However, as reported in Chapter 6, dHbR appears to be a more reliable measure of localised activity for single trial tasks, which are important for BCI applications using this instrument. This was simply because dHbR varies less with respect to the baseline (dynamic range) than $dHbO_2$, due to the dominant affect of low blood pressure oscillations on $dHbO_2$. This can be best represented by an observation of time series data from a single channel.

The channel between light source 3 and the detector in Experiment 2 appeared to produce the most signficant change in dHbR during the task and is shown in Figure 7.6. A comparison of the time series features confirms this. The author feels that this feature (dHbR) may be easier to classify than $dHbO_2$, especially if the aim was to realise an asynchronous optical BCI. The key characteristic of the change in dHbR in Figure 7.8 appears to be the negative slope of the initial decrease in dHbR during the first 3-5 seconds of the activation periods (in green). A threshold could also potentially be used but the author feels that the initial slope may be more robust - from observations of many data.

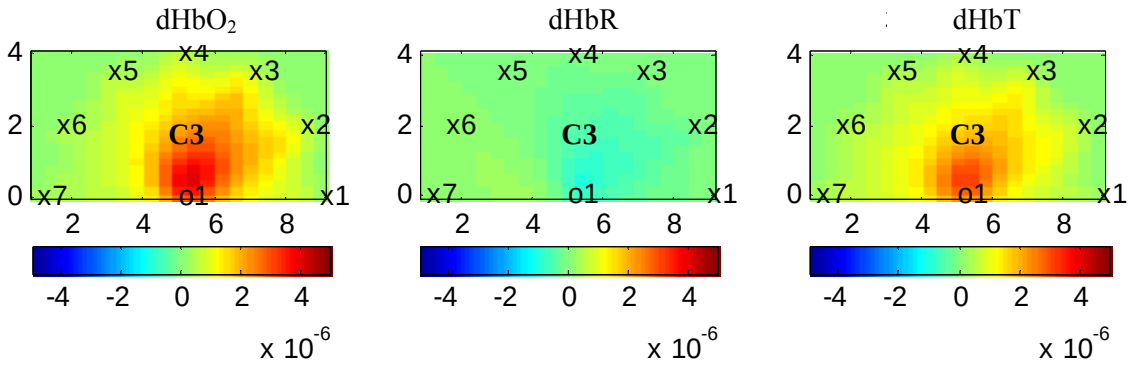

Figure 7.5: Average of haemoglobin species' concentration changes ($dHbO_2$, dHbR, and dHbT) from five finger tapping tasks. Optet was placed around ~C3 toward T3. Maximum metabolic activity is around C3. All x- and y-axes are in units of cm.

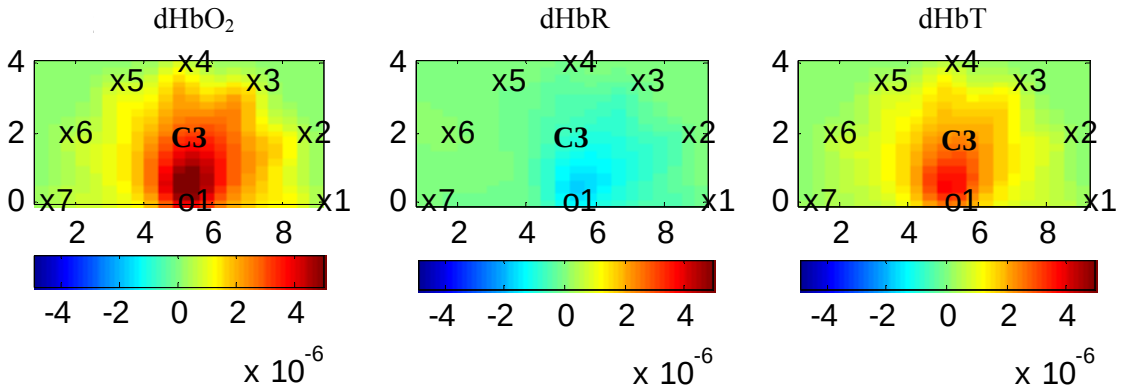

Figure 7.6: Average of haemoglobin species' concentration changes ($dHbO_2$, dHbR, and dHbT) from ten finger tapping tasks. Optet remained in the same location as in Experiment 1. The maximum activation appears to remain localised around C3. All x- and y-axes are in units of cm.

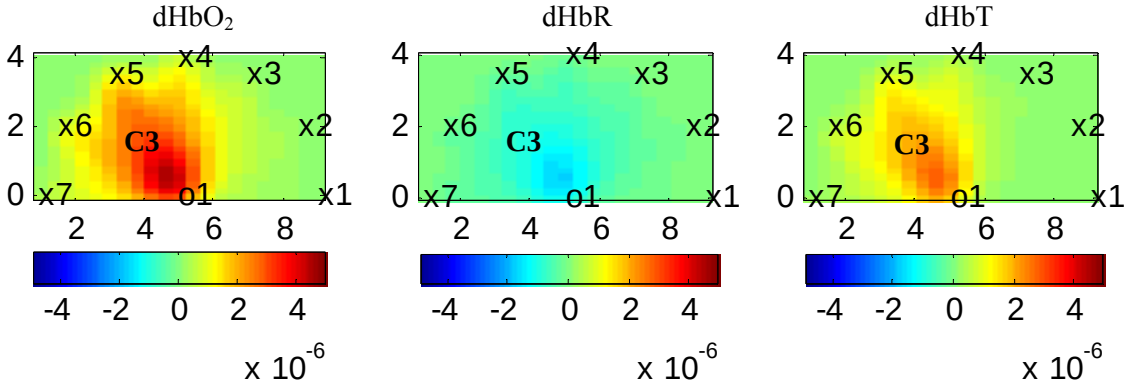

Figure 7.7: Average of haemoglobin species' concentration changes ($dHbO_2$, dHbR, and dHbT) from five finger tapping tasks. Optet was moved toward Cz by a few cm from its position used in Experiment 1 and Experiment 2. The maximum activation remains around C3. All x- and y-axes are in units of cm.

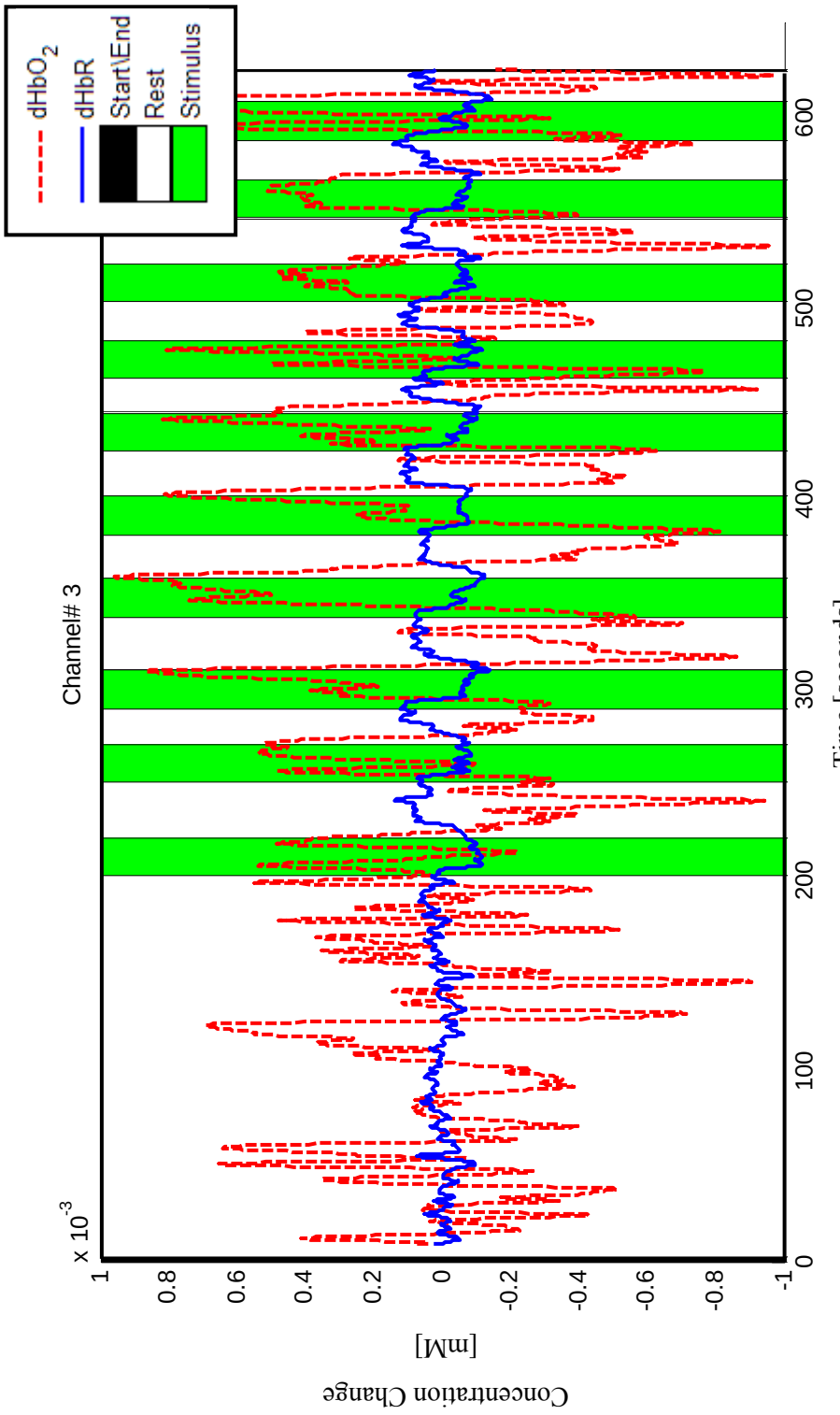

Figure 7.8: Single-trial time series analysis of Channel 3 from Experiment 2 (see Figure 7.7). Apparent decreases in dHbR are seen during the activation periods (in green) with a return to baseline for every intervening rest period (white).

This is emphasised by observing Figure 7.9 where dHbR is compared across the seven channels from Experiment 2. For easier viewing and comparison, an offset is added to each trace. Channels 2, 3, and 4 appear to have the largest and most consistent decreases in dHbR during the stimulus periods. Notice, for example, that in Channel 7 (CH#7) during the third stimulus period (circled in red in the figure) a decrease in dHbR occurs, but is not apparent in other stimulus periods during the experiment, thus illustrating variability in a channel. However, for Channel 3 and 4 the decrease is consistent across all 10 trials, but with subtle differences and transience across trials (stimulus periods).

A final analysis from Experiment 2 was to compare $dHbO_2$ across all seven channels, which is shown in Figure 7.10. More global interference from blood pressure oscillations is apparent. There are differences between channels, with Channel 3 having the largest activations but these are not as easy to identify as activations demonstrated by dHbR (in Figure 7.9). However, reducing the high cut-off frequency of the bandpass filter to 0.1 or 0.2 Hz has the effect of emphasising differences between channels (see graph in Appendix D). In particular, during the 5th stimulus period, Channels 3, 4, and 5 increase more sharply compared to other channels. Thus, features from $dHbO_2$ do represent functional activations but incur more physiological noise compared to dHbR. Thus, the author tends to agree with the literature that dHbR is more localised (Franceschini, et al., 2000).

7.3.2.1 Demonstration of dHbR as a BCI signal

While an in-depth analysis of FNIRS signals and classification are beyond the scope of this dissertation, it was of interest to demonstrate the viability of dHbR as a BCI signal using some analytical support. Perhaps the simplest classification of dHbR signals would be via a threshold paradigm. In particular, a comparison of the mean of the current stimulus period and the mean of some recent rest period could give an indication of activity (as was used in Study 1).

Thus, to demonstrate dHbR as a viable BCI control signal, the most conspicuously-active channel in Study 2 (Channel #3) is plotted in Figure 7.11 with:

1) The mean of the final 60 seconds of initial rest period (IR) plotted (superimposed) in blue asterisks, and,
2) The mean of each of the subsequent ten stimulus periods, superimposed in red asterisks.

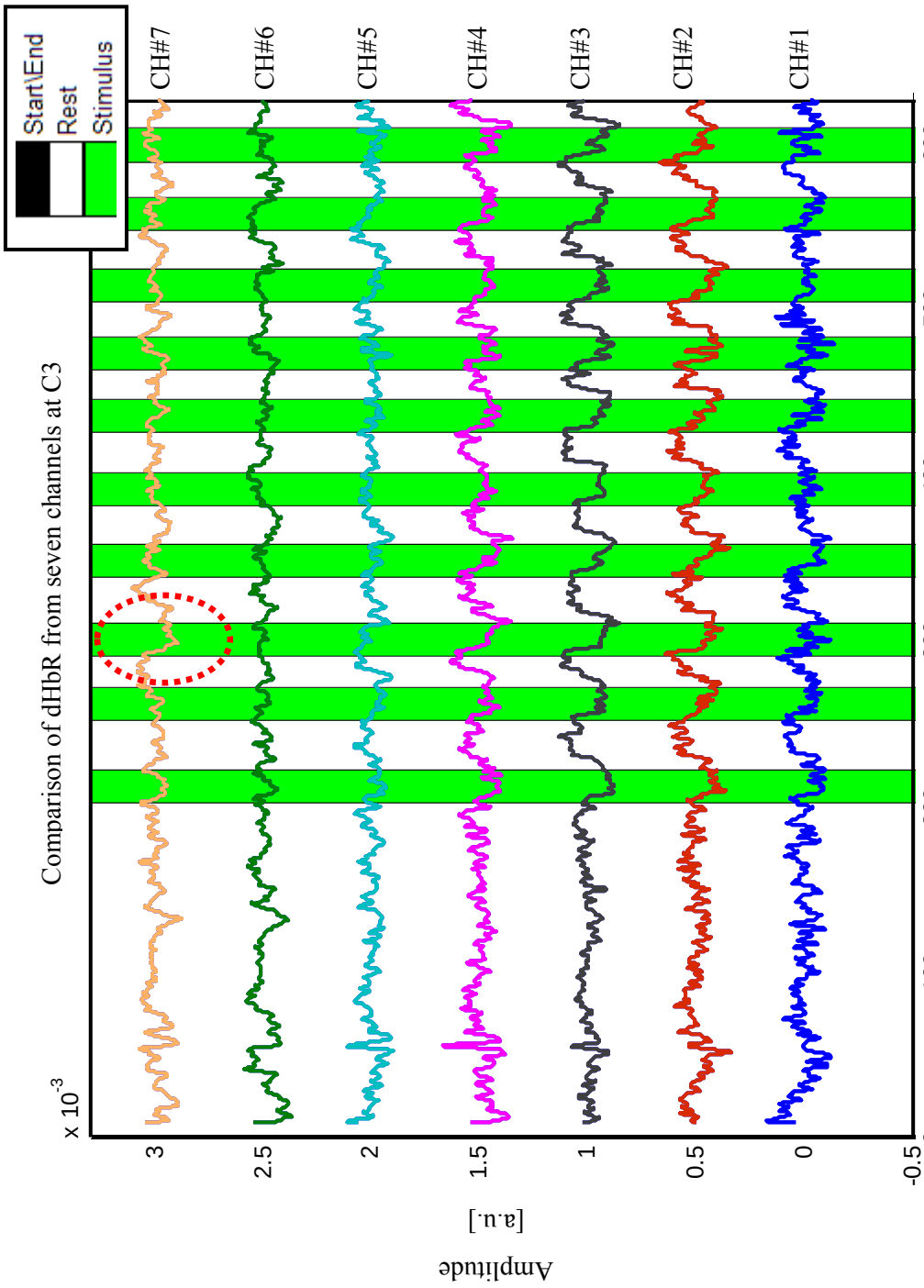

Figure 7.9: Comparison of dHbR across seven channels from Experiment 2. Most significant decreases in dHbR are in channels 2, 3, 4.

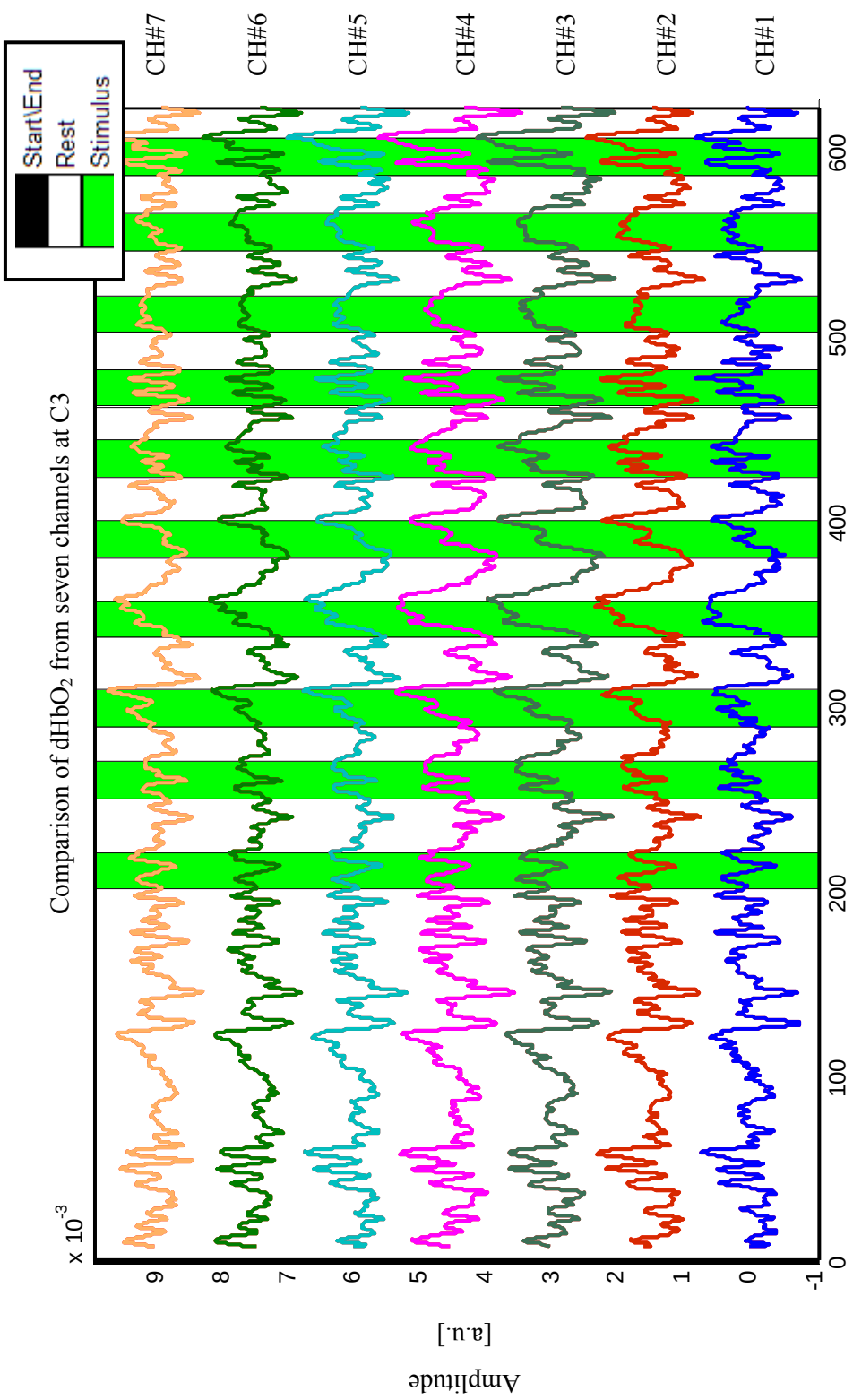

Figure 7.10: Comparison of $dHbO_2$ across seven channels from experiment two. Activations are more distributed across channels with significant contamination from blood pressure oscillations, seen in the dynamic range of the baseline compared to the activation periods.

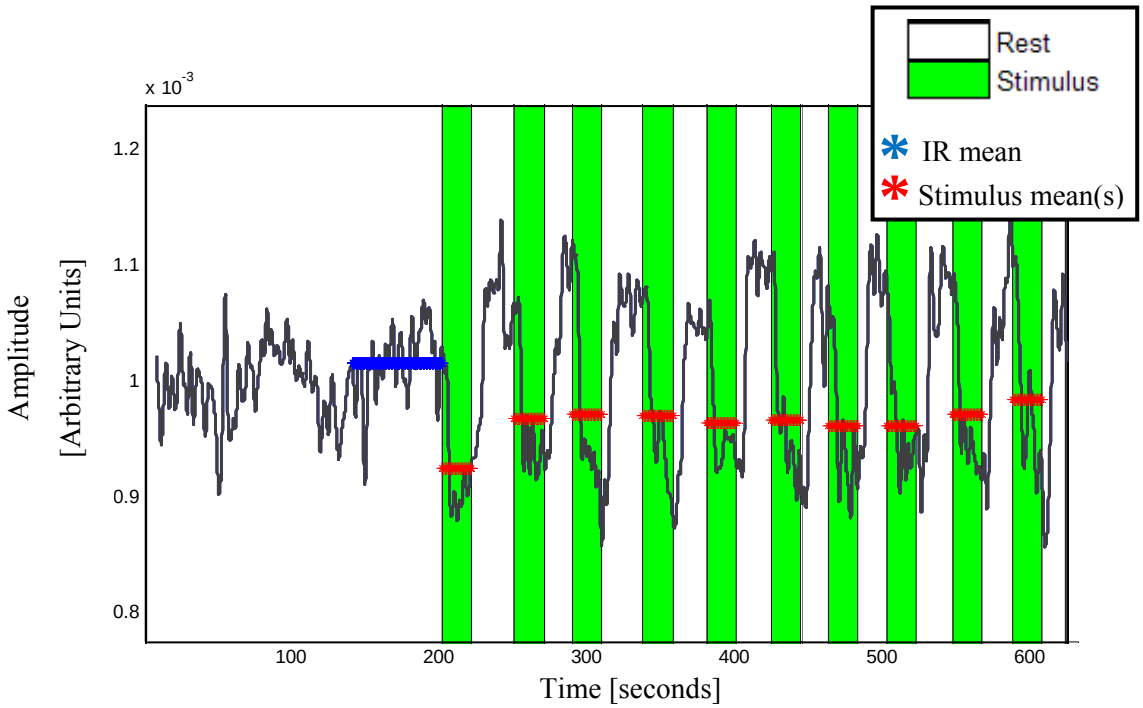

Figure 7.11: Demonstration of dHbR as a BCI signal (data from Channel #3 of Study 2). Deoxyhaemoglobin (dHbR) data is superimposed on the mean of the initial rest period (IR) shown in blue (asterisks), and the mean of each stimulus period shown in red (asterisks). A negative mean for a stimulus period relative to IR indicates activity during that stimulus period.

The mean values of the initial rest periods (IR) for all seven channels of this study (Study 2) are shown in the second column of Table 7-2. Also shown in Table 7-2 are the ten stimulus period mean values for each channel.

Activation during a stimulus period is indicated by a decrease in dHbR below the initial rest period level. Looking at the plot in Figure 7.11 and comparing with the data in Table 7-2 for Channel #3, the mean of all stimulus periods (Stim1 to Stim10 - see Table 1) are less than the mean from the 60 seconds of initial rest period (IR) for this channel. This subtraction of means is shown in Table 7-3 whereby it can be seen that Channel#3 shows 100% activity - seen as ten positive signs as a result of these subtractions. In other words, if the sign from the subtraction is positive then that stimulus period mean was less than the IR mean and thus indicates significant activity under this classification model. Conversely, if the sign from the subtraction is negative then that stimulus period mean was greater than the IR mean and thus indicates no significant activity. Larger values in the Table 7-3 indicate larger differences in mean values and hence indicate potentially larger stimulus events. Note, negative values are shown in red in Table 7-3.

For this study, Channel #6 and Channel #7 show the least activity (30% and 60%, respectively) whereas Channel #3, Channel #1, and Channel #2 demonstrate 100% activity - i.e. activity in all ten stimulus periods. Furthermore, Channel #3 mean differences in Table

7-3 are larger than any other channel except during Stim 3 and Stim 10. Interestingly, during Stim 3, Channel #7 indicates the largest activity which is encircled in red in Figure 7.9.

Note, in practice, the baseline haemodynamics may drift more significantly than is shown for this dataset and thus the simple mean-subtraction classifier used here may not be sufficient. In such cases more substantial signal processing, feature extraction, and classification techniques would be needed such as those being currently investigated by the group at NUI Maynooth. However, for the sake of demonstrating the viability of the dHbR signal as a BCI control signal using the instrumentation described in this dissertation, the example above is sufficient in outlining the key aspect that the dHbR signal can be a robust marker of cerebral effort. Note that in other classifiers, the rest period immediately preceeding each stimulus period could be used for comparison (instead of the initial rest period for a channel). The proceeding rest period could also be incorporated to identify the pattern of "rest"-"activation"-"recovery" cycle, where the proceeding rest period would be the "recovery" period of the cycle. This method is one such technique that could be used to compensate for drift since the rest and recovery periods either side (temporally) of a stimulus period may be less influenced by low frequency drift than the initial baseline. For example, the preceeding rest period was used as the rest/baseline data in the experiments of Study 1.

7.3.3 Conclusions

The short experiments carried out in this study demonstrate the ability of the CWNIRS instrument to determine localisation as seen in the topographic reconstructions. However, an analysis of single-trial time series data revealed that dHbR is a better marker for localised cerebral metabolism, mainly because of the substantial affects of low blood pressure dynamics on the HbO_2 species. Moreover, within an ~8cm by ~4cm optet some channels showed little activation during any trials (e.g. CH#7), illustrating the benefits of using the multichannel CWNIRS instrument to locate cortical areas of maximum activity. It is the author's suggestion, that the feature of a negative slope in dHbR in the first few seconds of the activation period may be significant for classification in a BCI application (discussed in future work in Chapter 8). This may also have the affect of speeding up classification, since this slope is consistent throughout trials (insofar as this study has determined) and may effectively mean the activation period could be reduced to <10 seconds since the slope feature occurs within this time period. A brief consideration of this is reported in Study 4 after the lateralisation study, which is described next. Note: A further contribution of this study and the studies to follow is in the analysis of single-trial FNIRS data since it is rare in FNIRS literature, where grand averages are usually used for functional studies of the brain.

Channel	*Initial Rest (IR)*	Stim 1	Stim 2	Stim 3	Stim 4	Stim 5	Stim 6	Stim 7	Stim 8	Stim 9	Stim 10
#1	*9.63*	*-40.44*	*-9.58*	*-11.27*	*-26.74*	*-7.44*	*-6.79*	*-20.73*	*-6.60*	*-21.73*	*17.87*
#2	*13.66*	*-61.43*	*-24.50*	*-24.95*	*-21.78*	*-34.80*	*-15.98*	*-30.21*	*-32.35*	*-24.99*	*3.77*
#3	*15.79*	*-74.65*	*-32.47*	*-28.78*	*-30.16*	*-36.04*	*-33.33*	*-38.31*	*-38.07*	*-28.22*	*-16.20*
#4	*11.79*	*-50.60*	*-23.23*	*-9.77*	*-24.43*	*-20.04*	*-34.31*	*-12.83*	*-21.40*	*-7.34*	*-26.32*
#5	*5.25*	*-20.88*	*-23.15*	*38.17*	*-5.52*	*27.23*	*-7.54*	*-0.14*	*-7.07*	*20.36*	*-7.71*
#6	*5.93*	*-6.55*	*6.52*	*14.96*	*8.43*	*33.11*	*-2.22*	*4.65*	*13.58*	*31.36*	*6.32*
#7	*5.32*	*-13.16*	*0.60*	*-45.82*	*11.98*	*10.47*	*-0.71*	*3.26*	*3.87*	*11.20*	*19.77*

Table 7-2: Table showing the amplitude level of dHbR*10^6 (arbitrary units) for each channel (#1 to #7), during the initial rest period (denoted "IR") and during each stimulus period.

Channel	IR - Stim1	IR - Stim2	IR - Stim3	IR - Stim4	IR - Stim5	IR - Stim6	IR - Stim7	IR - Stim8	IR - Stim9	IR - Stim10	Positive Signs	Channel Activity (%)
#1	50.07	19.21	20.91	36.38	17.08	16.42	30.36	16.23	31.37	-8.24	9	**90**
#2	75.10	38.17	38.62	35.45	48.46	29.64	43.87	46.01	38.65	9.89	10	**100**
#3	90.44	48.26	44.57	45.95	51.83	49.12	54.11	53.87	44.01	31.99	10	**100**
#4	62.39	35.02	21.56	36.22	31.84	46.10	24.62	33.19	19.13	38.11	10	**100**
#5	26.13	28.40	-32.92	10.76	-21.98	12.78	5.39	12.31	-15.11	12.96	7	**70**
#6	12.49	-0.58	-9.02	-2.49	-27.17	8.15	1.28	-7.65	-25.43	-0.38	3	**30**
#7	18.48	4.72	51.14	-6.66	-5.15	6.03	2.06	1.45	-5.88	-14.45	6	**60**

Table 7-3: Calculation of the activity level of a channel by subtracting the mean of each stimulus period for a channel, from that channel's initial rest period (IR), e.g. [IR - Stim2] would be the 'mean dHbR amplitude from stimulus period 2', subtracted from the 'initial rest period' for a specific channel.

7.4 Study 3: Lateralisation of Functional Tasks

For many BCI applications it is desirable to use tasks that activate independent regions of cortical tissue with minimal activation distribution across the cortex. Thus, in the event of performing a right hand finger opposition task such as in Study 2, neural tissue around C3 is activated (contralateral activity) but it is known that there can exist a bilateral response with these motor tasks (Coyle, 2005). Thus, cortical tissue around C4 (ipsilateral) may be activated. In this study, it was of interest to investigate the ability of the instrument to determine lateralisation of functional tasks, i.e. if a functional task induces metabolic activity in a single hemisphere, or both hemispheres. The study was carried out on a single subject to see if the CWNIRS system could detect lateralised patterns or if global haemodynamics dominated all channels. It is essentially a study to investigate the CWNIRS system's capability in this regard which could prove useful for BCI applications.

7.4.1 Procedure

The multichannel CWNIRS instrument was configured using two optets. Optet 1 was placed over position C4 with light sources 1, 2, 3, 4, 5, 6, and 7 and a single detector. Optet 2 was placed over position C3 with light sources 8, 9, 10, 11 and another single detector[1]. Recordings were made from both optets simultaneously, i.e. a total of 11 channels covering C3 and C4. The position of these optets is shown to the left of the graphs of the results, i.e. Figure 7.12 and Figure 7.13. A series of right- and left hand finger opposition tasks were carried out (4 trials of each, the order of which was randomised) on a single subject (right handed according to the Edinburgh Handedness Inventory - Oldfield, 1971). After an initial rest period, the eight stimulus periods (fixed at 20 seconds) were interspersed with rest periods pseudo-randomised between 15 and 30 seconds. All data were filtered with a bandpass filter: 0.01Hz - 0.3Hz (lowpass 4th order Butterworth; highpass 3rd order Butterworth) with forward and reverse filtering to remove any phase distortions introduced by filtering.

7.4.2 Results and Discussion

In light of the results from Study 2, only the dHbR levels were investigated due to the higher localisation of this metabolic indicator. The dHbR levels for Optet 1 over C4 are displayed in Figure 7.12; levels for Optet 2 over C3 are displayed in Figure 7.13. An offset was added to each trace to compare channels. In the event of complete lateralisation for the finger opposition tasks the following results would occur:

[1] Note: one of the 12 LEDs was not used due to a temporary fault for that LED.

1) Right hand tasks should activate tissue under Optet 2, i.e. position C3. Thus, green segments in Figure 7.13 should show activation.
2) Right hand tasks should not activate tissue under Optet 1, i.e. position C4. Thus, green segments in Figure 7.12 should not show activation.
3) Left hand tasks should activate tissue under Optet 1, i.e. position C4. Thus, yellow segments in Figure 7.12 should show activation.
4) Left hand tasks should not activate tissue under Optet 2, i.e. position C3. Thus, yellow segments in Figure 7.13 should not show activation.

In Figure 7.12, channels are numbered on the right hand side of the graph. Channel 6 and 7 show no significant activation for any of the tasks. Activations are found in all other channels shown as decreases in dHbR, during certain stimulus periods. However, a distinct lateralisation effect is found for Optet 1 at position C4, with activations occurring only during left handed (yellow segments) finger opposition tasks (the subject's non-dominant hand). Right handed tasks (green segments) don't elicit a significant response under this optet. The effect is most prominent in Channel 3 with significant decreases in dHbR during left handed tasks (yellow segments) only.

However, in contrast is the apparent bilateral activation during some tasks under Optet 2 (at C3, left precentral gyrus) shown in Figure 7.13. In particular, Channel 8 shows activation during left handed tasks (yellow segments). Channel 8 also demonstrates the largest decrease in dHbR during right handed tasks (green segments). It should be noted that this is the user's dominant hand (right handed). This coincides with the fMRI results in Chapter 6 (for the same subject) showing larger activation and greater activation spatial distribution for the subject's dominant hand.

7.4.3 Conclusions

The chief contribution from this study is the ability of the developed multichannel CWNIRS instrument to measure lateralisation affects in a single-trial basis. This ability is important for BCI applications in order to isolate cortical tissue that is highly lateralised. For instance, Channel 9 and 10 from Optet 2 demonstrated slightly less bilateral activity than Channel 8. Thus, multichannel implementations like this may improve localisation and lateralisation than would be possible using a single or dual channel device which was used in (Coyle, et al., 2007). However, it should be noted that this lateralisation study cannot say anything conclusive about hand dominance, lateralisation etc since it was only an observation for a single subject in a very limited number of trials. Nevertheless, it provides a suitable validation for the multichannel CWNIRS instrument developed in this thesis..

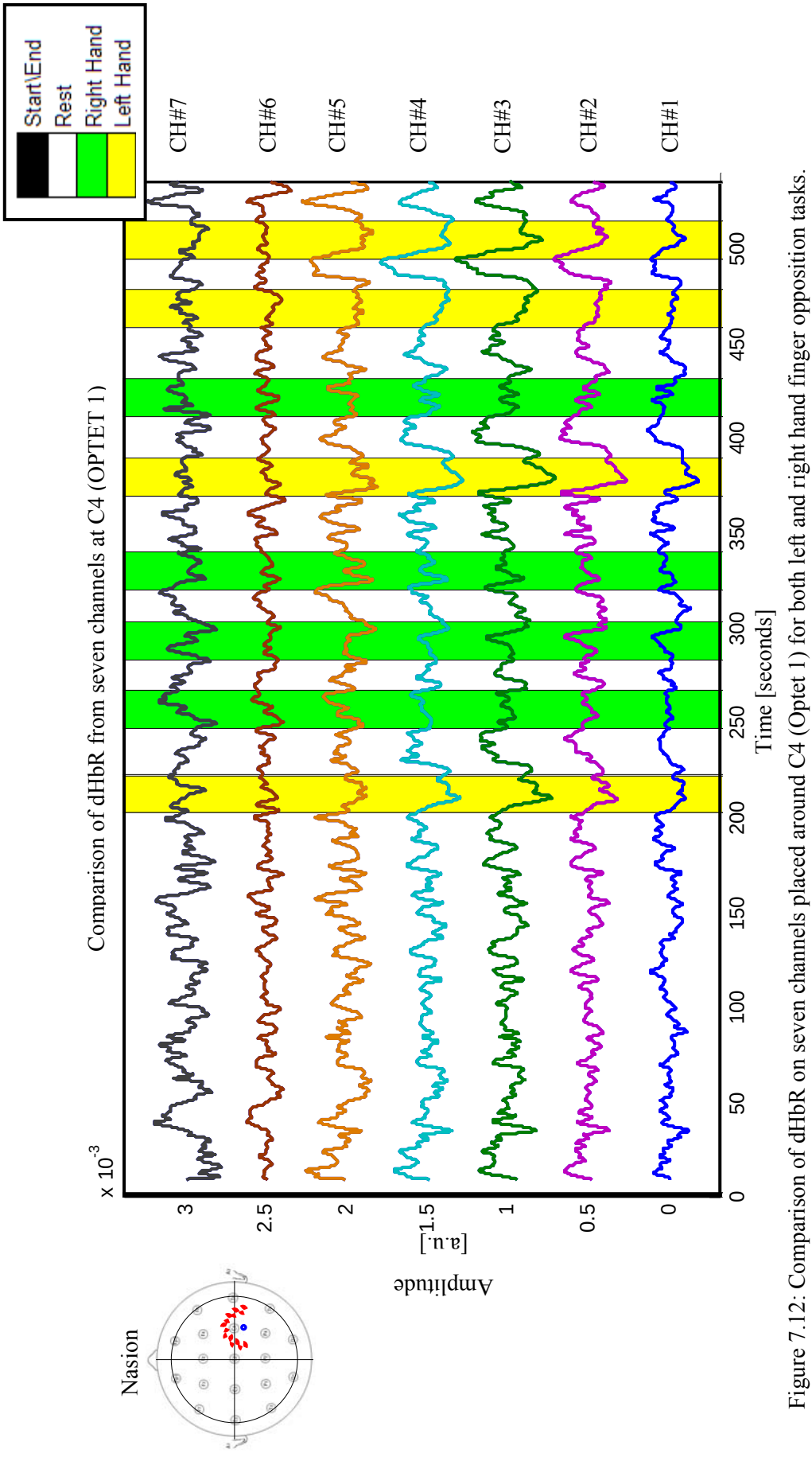

Figure 7.12: Comparison of dHbR on seven channels placed around C4 (Optet 1) for both left and right hand finger opposition tasks.

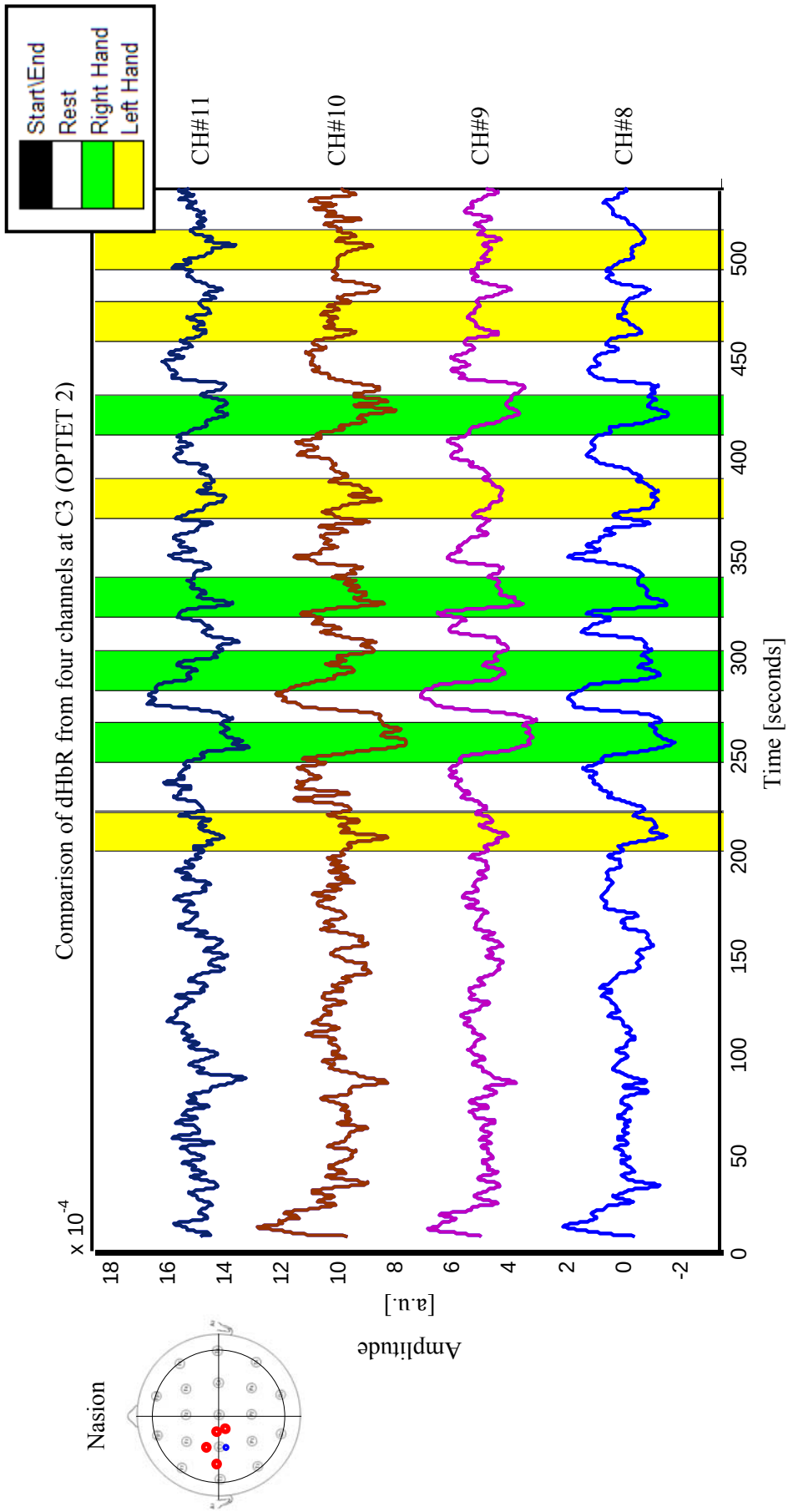

Figure 7.13: Comparison of dHbR on four channels placed around C3 (Optet 2) for both left and right hand finger opposition tasks. An offset was added to each trace for easier comparison.

7.5 Study 4: Shortening the Activation Period

A short experiment was carried out to test if a shorter activation period (8 seconds) could allow for similar dHbR activation features displayed in Studies 1, 2, and 3 which used activation periods of 20 seconds.

7.5.1 Procedure

The same set-up used in Study 3 was used for this study with seven channels over C4 and four channels over C3, all measured simultaneously. The same bandpass filter as used in Study 3 was applied to all data in this study.

7.5.2 Results and Discussion

The concentration changes in HbR for the optet placed over C4 are displayed in Figure 7.14 and those for the optet at C3 are displayed in Figure 7.15. Firstly, carrying on from the theme of the previous two studies, both optets show high lateralisation, but less localisation. There appears to be significant decreases in dHbR on many channels for both hemispheres for their respective contralateral finger opposition tasks. In particular, activation to right hand finger opposition tasks at C3 appears across all channels, but perhaps less so in Channel 11. To answer the question of whether shorter 8 second activation periods can elicit a distinct response, the answer is apparent - yes it can. More than that, it is felt that these shorter activations may be favourable for other reasons than speed alone. Perhaps lengthy 20 second periods of finger opposition add to the complexity of the homeostasis to the increased blood flow and volume. For instance, it has been reported (Obrig, et al., 2000a) that increased metabolic activity in a region of cerebral tissue causes amplitude and phase changes of the local low blood pressure oscillations or Mayer waves. Thus, it is considered here that perhaps limiting\reducing the amount of time that the action is being performed may reduce that affect.

7.5.3 Conclusions

Shortening stimulus periods to eight seconds reveals that distinct decreases in dHbR still occur and are consistent across trials. This was the main concern since it would have been obvious from the previous studies that of course the large negative slope would be apparent in the first few seconds of the activation period. It was of interest to investigate if these more rapid responses had some habituation effect or if they were consistent. For this limited study they appear to be consistent and may have benefits outside of speed alone - such as potentially reducing blood pressure interference effects.

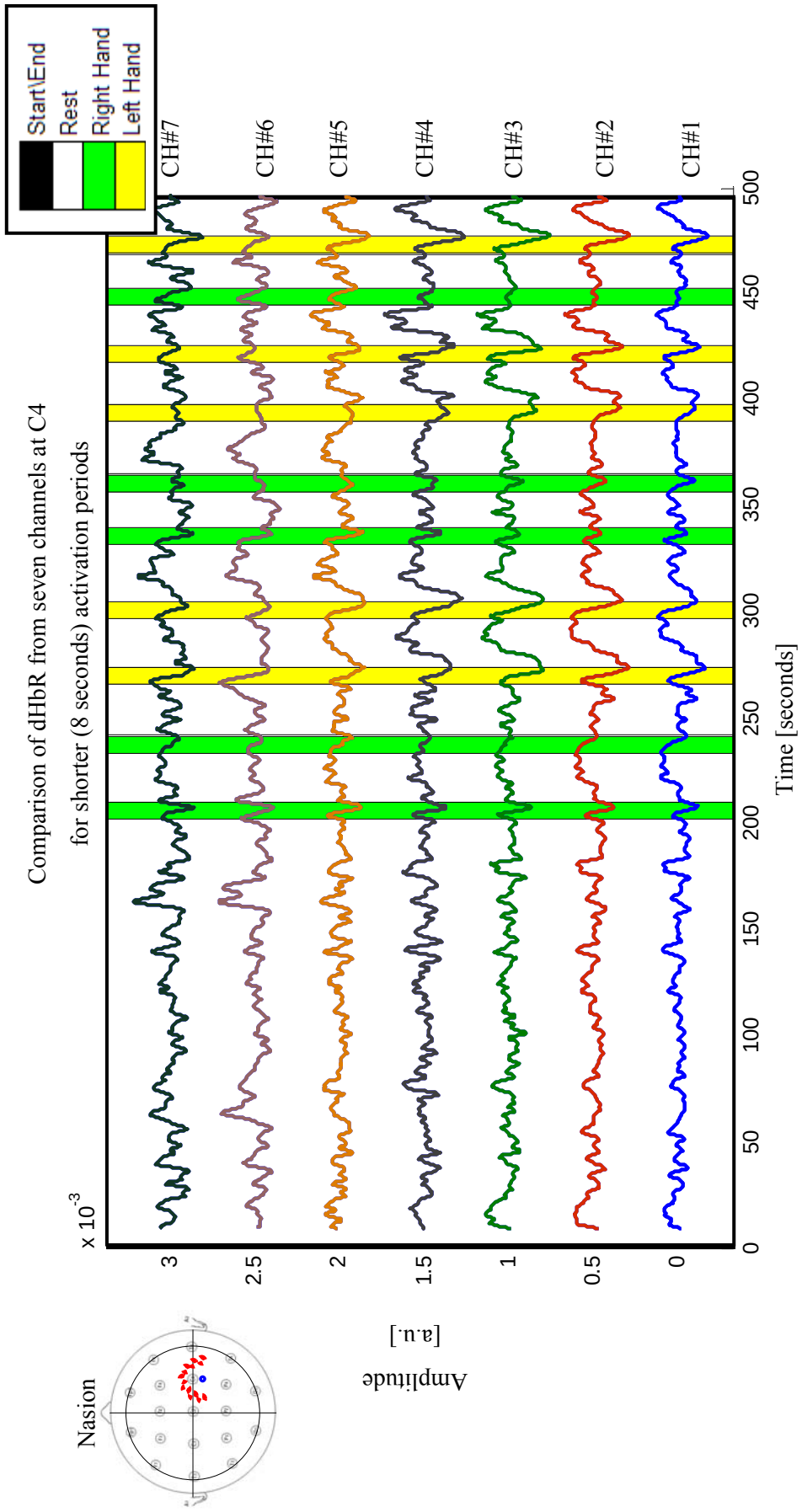

Figure 7.14: Comparison of dHbR (seven channels at position C4) to shorter activation periods (8 seconds). The conspicuous negative slope appears in all trials for some activation periods.

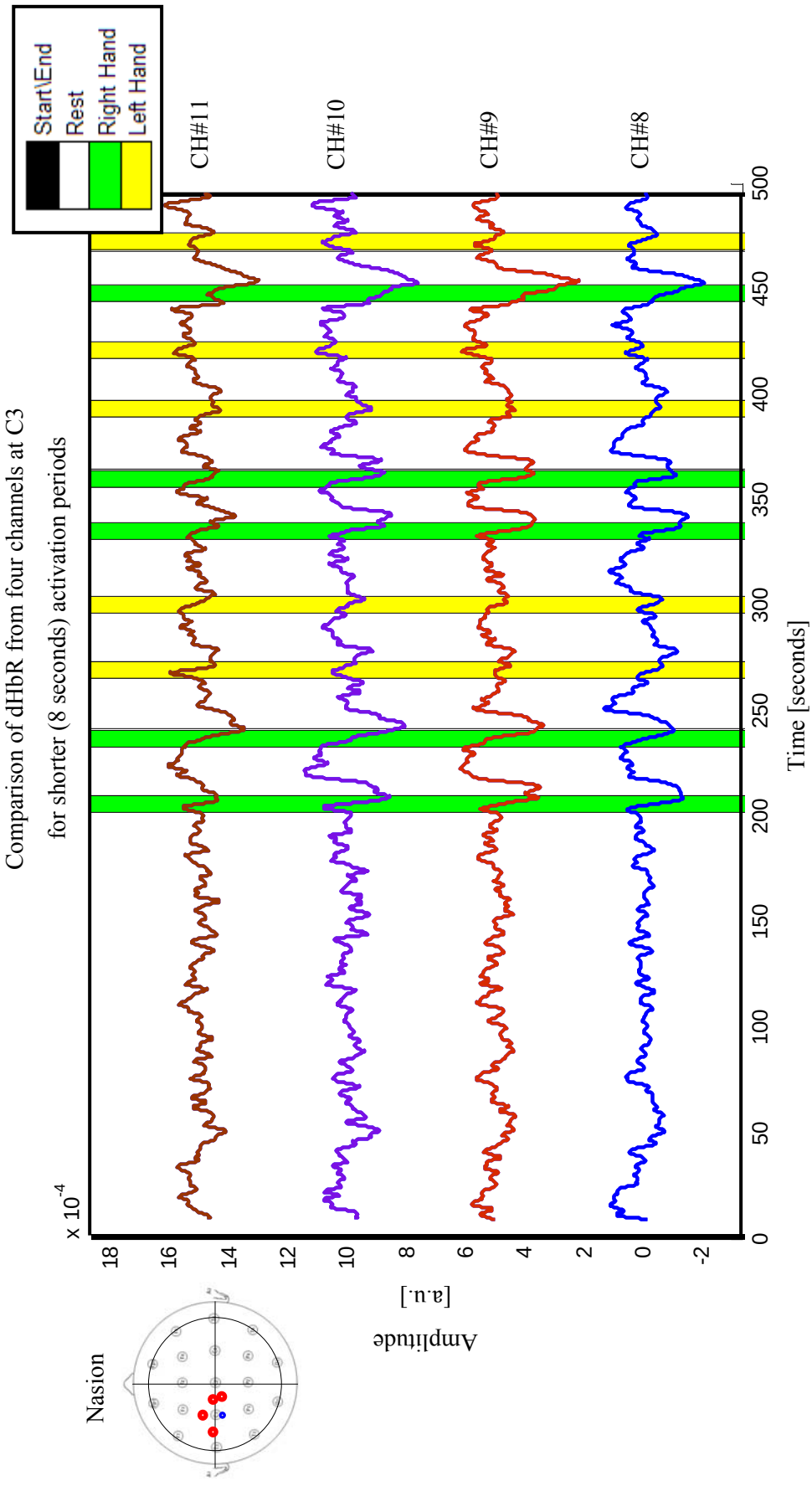

Figure 7.15: Comparison of dHbR (four channels at position C3) to shorter activation periods (8 seconds). The conspicuous negative slope appears mostly during right handed finger opposition tasks (contralateral activation).

Covert tasks such as motor imagery are predominantly used in BCI applications and have been suggested recently as having an onset time lag due perhaps to the added complexity of imagining performing the motor task, rather than simply carrying it out overtly (Wriessnegger, et al., 2008). Furthermore, motor imagery is said to be less lateralised, especially with respect to the non-dominant hand (Coyle, 2005; Wriessnegger, et al., 2008). Thus, although this study and most of the studies in this chapter were used to assess the various abilities of the instrument on a single-trial basis, BCI applications for augmentative communication may have many feature (activation) differences than those from the overt tasks reported in this and earlier studies (i.e. Studies 2, and 3) - e.g. time lags and maximum amplitude changes. Thus, it was of interest to observe haemodynamic changes to covert motor imagery tasks, and this is reported next.

7.6 Study 5: Motor Tasks: Overt and Covert Responses

Recapitulating, the aim of this dissertation was the design and development of a flexible multichannel CWNIRS instrument for BCI applications. As such, as a means to assess its ability to measure functional tasks and specific characteristics of those tasks (e.g. lateralisation) a series of studies were performed in this chapter using attempted movement tasks. However, it was of interest to observe signals recorded from covert motor tasks (imagery). Indeed, these assessments have been addressed first by Coyle (Coyle, et al., 2003; Coyle, et al., 2004) and more recently by (Wriessnegger, et al., 2008) across a number of subjects. However, of interest in the study presented next in this dissertation are the single-trial assessments of such responses rather than a grand average across subjects.

7.6.1 Procedure

A left-handed subject (according to the Edinburgh Handedness Inventory Oldfield, 1971) participated in the study and this subject had previous experience participating in previous experiments such as in Study 1 in this chapter. Initially, the optet (probe holder) used in Study 2, 3, and 4 was used with an inter-optode spacing (IOS) of 4cm. However, this recording produced insufficient SNR (low signal and noisy cardiac pulse) due to optode placement issues and hair obstruction. Thus, eventually a 3cm multi-optet holder which was reported in Chapter 5 was used (see probe holder photograph in Figure 5.27). The probe holder was placed across the motor cortex strip (see Figure 7.16) with channels over C4 and close to T4 of the 10-20 placement system. Position C4 was the subject's dominant hand area (left handed) on the primary motor cortex. Four LEDs and two detectors were used in this study, with a total of 6 channels, i.e. one detector demodulates light from all four sources

whereas the other detector demodulates from two of these light sources. The probe holder set-up and geometrical channel positions are shown in Figure 7.16 below.

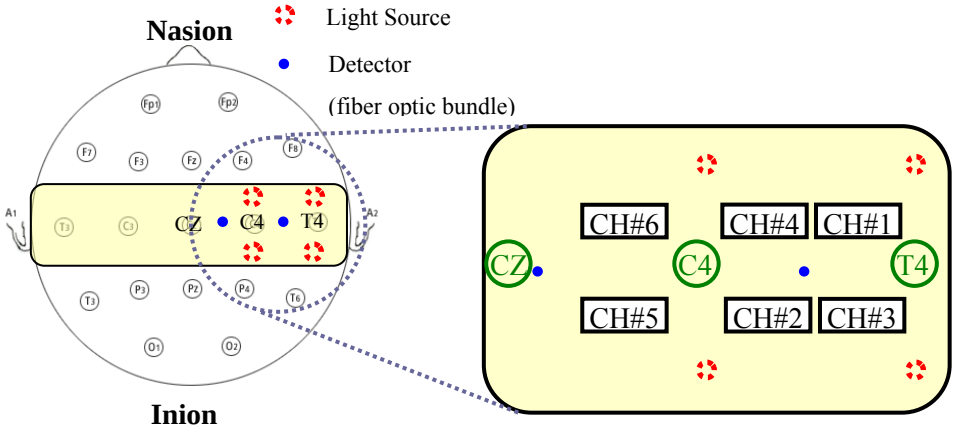

Figure 7.16: Optical probe positioning for overt and covert left-handed finger tapping motor tasks. IOS is 3cm for all channels of this probe holder.

The subject was seated in a supine-like position on a reclined chair with armrests. The experimental paradigm was as follows:

- The subject was asked to observe the LCD monitor which relayed visual cues to either, rest (where a "+" sign appeared); to perform overt left-handed finger tapping (where "Left Hand Overt" appeared); or to perform kinesthetic motor imagery of left-handed finger tapping;
- The subject's hands were kept with palm facing the arm rests to facilitate the imagery tasks, since hand posture commensurate with the actual overt action has been shown to improve imagery (Vargas, et al., 2004);
- The experiment paradigm consisted of an initial rest period of 150 seconds, followed by alternating periods of stimulus and rest;
- The experiment consisted of 20 stimulus periods: 10 for overt finger tapping, and 10 for motor imagery of the task. The order of the tasks (either overt or imagery) was randomised;
- Rest periods were pseudo-randomised between 15 and 30 seconds. Activation periods were fixed at 15 seconds.

As in previous studies, all data were filtered with a bandpass filter: 0.01Hz - 0.2Hz (lowpass 4th order Butterworth; highpass 3rd order Butterworth) with forward and reverse filtering to remove any phase distortions introduced by filtering.

7.6.2 Results and Discussion

ASIDE: As was just mentioned the probe holder was changed from a holder with an IOS of 4cm to one with 3cm (the 3cm IOS "motor cortex probe" from Chapter 5) due to low light levels. However, when the probe in Figure 7.16 was initially placed it was incorrectly applied and resided more anteriorly to C3. As such, the haemodynamic responses to the motor tasks were lacking (data not shown). Subsequently, the probe was moved posteriorly just in front of C3. This saw channel 3 (CH#3) with the most significant responses in dHbR (data not shown). The shape of the subject's head was found to be less conforming to this probe and so the "frontal probe holder" from Chapter 5 was used (shown in Figure 7.16). This probe holder was moved to the final position, over C3, as shown in Figure 7.16. Thus, this emphasises the notion that the placement of the probes is one of the more challenging tasks, due to differences in head shape, hair, etc. Moreover, this initial exercise demonstrated the localisation of functional activity to the overt motor tasks used. Recall also that this localisation was demonstrated for another subject in Study 2 in Section 7.3. The results of the current study to overt and covert tasks are described next.

The concentration changes for all six channels are displayed in Figure 7.17 - again with an offset added to each for easier viewing. Note the relative geometrical position of these channels in the probe holder in Figure 7.16 - for example channel 1 (CH#1) is located beside channels CH#3 and CH#4. However the channels are displayed in a sequence from CH#1 to CH#6 in Figure 7.17. Notice in the results that each channel shows activity for both overt and imagined motor movement. Overt tasks took place during the time periods indicated by the green segments whereas the imagery tasks for left handed finger tapping took place during time periods indicated by the yellow segments. It is not immediately apparent which channel displays the most significant activation (decrease in dHbR - in particular the initial negative slope during the initial 3-5 seconds of the stimulus period).

However, interestingly during the stimulus periods, channels CH#1 and CH#3 are seen as an *increase* in dHbR rather than the classical decrease. This occurs throughout all activations for channel CH#1 and is highly regular and significant. For motor imagery (yellow segments), channels CH#5 and CH#2 appear to display the most consistent activations - which are posterior to position C3, i.e. approximately between the primary motor cortex and the primary sensorimotor cortex. This is most obvious during the last three motor imagery stimulus periods in Figure 7.17. Furthermore some of the dHbR responses to motor imagery appear to be of similar magnitude to overt motor tasks: on CH#2 particular. A comparison was made of the responses in channels CH#1 and CH#5 to observe the activation differences since CH#1 saw a significant increase in dHbR whereas CH#5

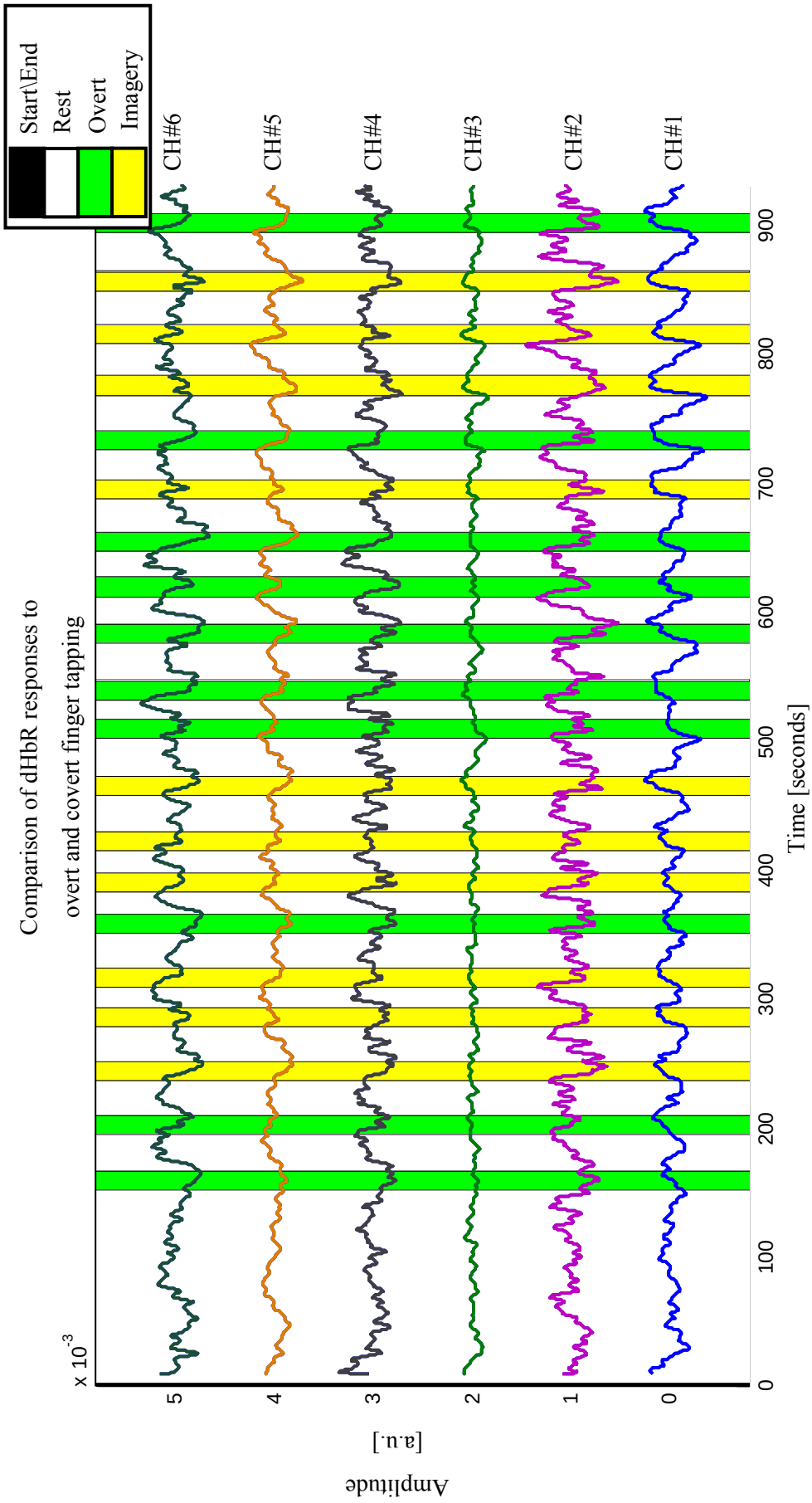

Figure 7.17: Concentration changes in HbR for overt and imagery of left handed finger tapping tasks.

displayed a decrease. Thus, dHbR and $dHbO_2$ are displayed in Figure 7.18 with a negative offset added to CH#5 for easier viewing and comparison to CH#1. For this figure only, the $dHbO_2$ were filtered with a smaller high cut-off frequency, i.e. a bandpass filter between 0.01Hz - 0.09Hz, since $dHbO_2$ have more significant oscillations than dHbR, as mentioned in earlier studies. Apparent in the result in Figure 7.18 is that on CH#1, dHbR *and* $dHbO_2$ both increase during *every* single activation period - to both overt and imagery tasks. This cannot be a simple blood pressure oscillation since the initial rest period is void of these signals. Furthermore, the pseudo-randomisation of the rest periods was put in place to ensure the activation periods did not synchronise to background physiological noise. An increase in dHbR and $dHbO_2$ is indicative of an overall increase in HbT, and thus and increase in cerebral blood volume. It cannot be attributed to a global increase due to some pressure enhancing activity (e.g. Valsalva maneuver) since it does not appear in the all channels, but only in CH#1 (and neighbouring tissue at CH#3 - data for dHbR only for this channel was already shown in Figure 7.17). CH#1 also has less blood pressure oscillations than CH#5, since both channels were filtered with the same bandpass filter. Nevertheless, the decrease in dHbR in CH#5 and in certain activations a large increase in $dHbO_2$ are also seen for the some of the motor (overt and imagery) tasks, which is said to be more indicative of functional activation (Villringer, et al., 1997). A further point to note is that the subject reported\said that he increased the rate at which he performed the overt motor tasks and motor imagery of tasks in the trials at the latter end of the experiment. It is interesting to note that the latter trials appear to incur larger activations which is supported in fMRI literature (Yousry, et al., 2001).

7.6.3 Conclusions

The initial anecdote in this study reflected on the localisation of the dHbR response to motor tasks for this subject (the probe holder had to be repositioned). The chief finding of this study is that functional activity to overt and covert tasks can be assessed using the multichannel instrument, and provides possibilities to develop BCI applications such as those for stroke rehabilitation or indeed the more common augmentative communication aid for the severely disabled (using motor imagery). Futhermore, the results add to the debate about single-trial responses to overt motor tasks and motor imagery of the same tasks. However, again, the author is again aware that this study was performed on a single subject only and with a limited number of trials for overt and covert motor tasks. Thus, the study cannot state anything definitive about the haemodynamic responses to motor imagery in general using FNIRS on humans. Moreover, this was not the intention of the study.

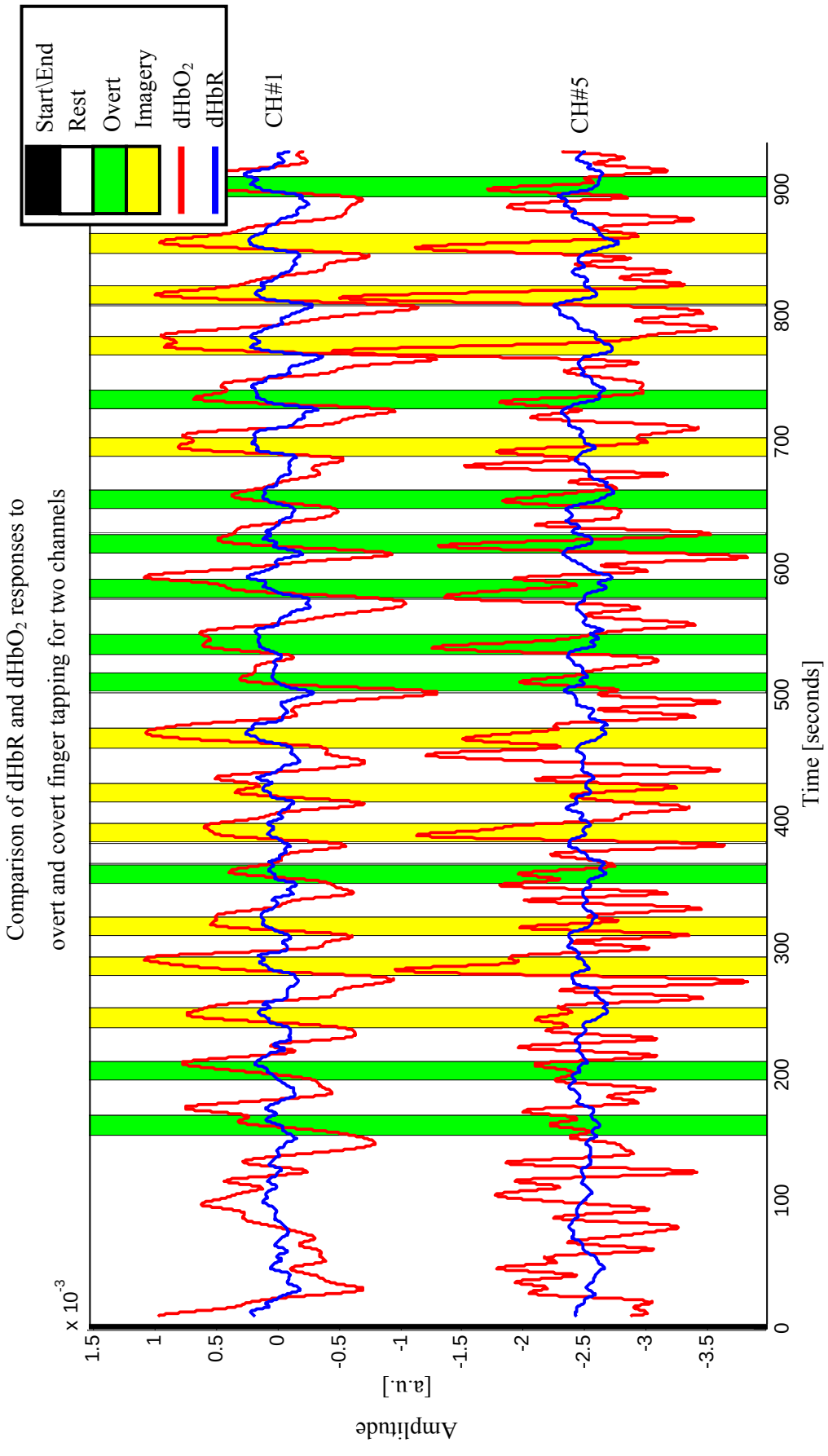

Figure 7.18: Concentration changes in both HbO_2 and HbR for overt and imagery of left hand finger tapping on Channels CH#1 and CH#5.

7.7 Chapter Summary

A new avenue of optical BCI research has been conceptualised recently with a potential application in stroke rehabilitation using biofeedback of motor cortex activity for use as a neural prosthesis. An optical BCI implementation was carried out on four subjects where they moved their arm against a restraint and motor cortex activity based on $dHbO_2$ was utilised to move a robotic arm which acted as biofeedback. Subjects achieved success rates of approximately 91%, 82%, 62%, and 93% which was a measure of the percentage of time they were able to move the robotic arm throughout the entire activation period and over all trials. It was felt that the newly developed versatile multichannel CWNIRS instrument could benefit this new OBCI application by addressing localisation and lateralisation of cerebral functional activity of motor tasks. The instrument has shown an ability to measure such phenomena and was used to identify the benefits of using dHbR as an indicator of localised functional activity changes rather than $dHbO_2$ alone. Subsequently, a short experiment was carried out to assess activation features in the event of shortening the activation period to eight seconds. The dominant negative slope in dHbR was consistent throughout all trials in some channels and was pronounced on the user's dominant hand area (contralateral - left primary motor cortex) which matches well with fMRI experiments carried out on the same subject reported in Chapter 6. In a final study, overt and covert motor tasks were performed by a single subject, which recovered the expected feature of a decrease in dHbR during stimulus periods for both motor imagery and overt motor tasks. However, additional features were found in other channels potentially indicating increases in CBV in tandem with the tasks. However, the principal finding of this study was the ability of the newly developed versatile multichannel instrument to be able to identify functional activity changes in response to motor imagery, which could be harnessed for BCI applications. Finally, it was expressed that the collection of studies in this chapter, with the exception of Study 1, were carried out to assess the ability of the multichannel CWNIRS instrument to recover markers of functional activity from activated cerebral structures. Therefore, this instrument could be used in a multichannel OBCI, such as the OBCI implementation in Study 1 for stroke rehabilitation.

CHAPTER 8

CONCLUSIONS AND FUTURE WORK

The following chapter reviews the main contributions of the thesis and addresses potential avenues for future work in the area of optical BCI.

8.1 Objectives and contributions

The main objective of the work presented was the development of a multichannel CWNIRS instrument for use in BCI applications and the subsequent analysis of the potential gains it could provide. As with any project, the main objective was addressed through a series of milestones. Thus, in the process a number of achievements were attained, and these are listed next.

- The construction of a multichannel CWNIRS device capable of measuring changes in the concentration of haemoglobin species from the human body, including the cerebral cortex;
- Investigation of FNIRS recordings for BCI by assessing the localisation of concentration changes of deoxyhaemoglobin (dHbR) as well as oxyhaemoglobin ($dHbO_2$);
- The design and implementation of a suitable, stable linear driver for the light sources used, as well as a safety assessment of such optical sources for human

interfacing (Soraghan, et al., 2009) This flexible circuit also catered for the implementation of additional modulation strategies such as code division multiple access (CDMA) using m-sequences;

- A demonstration of single-trial haemodynamic responses to common functional tasks, and the subsequent discussion on the suitability of dHbR for determining lateralisation using the multichannel CWNIRS instrument;
- The implementation of a series of fMRI BOLD experiments to validate the protocols used for FNIRS experiments;
- The publication of a number of journal and conference papers covering optical BCI for stroke rehabilitation, circuit design for optical drivers, optical BCI for gaming, development of a 12-channel prototype of the final CWNIRS instrument, a review of signal processing methods for optical BCI, software design for rapid prototyping of BCI applications (see page XI and XII at the beginning of this dissertation for a full list of publications arising from this work).

8.2 Future Work

While this thesis addressed the development of a tool for BCI applications there remain a number of potential enhancements for optical BCI that could be achieved using the multichannel tool described in this dissertation. This section provides some suggestions for further development of BCI applications.

8.2.1 Signal Processing for Online BCI Control

In the series of single-trial experiments performed in this thesis, the non-stationary nature of haemodynamics could be casually observed. In addition, observations were made of the dominance of background blood pressure oscillations in the recorded signals, especially in calculated changes in $dHbO_2$. Furthermore these complex physiological signals are said to change in phase and amplitude during functional tasks (Obrig, et al., 2000) and are found in all blood vessels. Thus, adaptive noise cancellation techniques are needed to maximise the response due to focal activity in the cortex. Work is ongoing in the BCI group to address this issue (Matthews, et al., 2008a) as a means to develop an online BCI using the multichannel instrument developed in this thesis.

8.2.2 Clinical applications

There is now a growing development of techniques for neurorehabilitation using BCI (Birbaumer, et al., 2007) in order to restore movement. The optical BCI work in this thesis

proposed multichannel CWNIRS as a candidate for subjects with severe motor impairments due to stroke (Ward, et al., 2007). However, further investigation needs to be carried out on actual stroke sufferers in a clinical setting to assess the extent of cerebral metabolic activity in the affected tissue, that can be recorded from such patients. Work is ongoing in the BCI group at NUI Maynooth for such applications.

8.2.3 Minimally invasive optical BCI

As was discussed in Chapter 3, invasive BCIs that record spike trains or local field potentials present the risk of infection and have a number of further issues such as long term stability of the signals and the sensor. However, it is envisaged by the author that a minimally invasive optical BCI may be possible using thin optic fiber bristles embedded in the skull cap of the subject. The partial optical pathlength of NIR light travelling in the arc-like projection through the head is mostly contributed from the scalp and skull (~50%) (Okada, et al., 2003a; Okada, et al., 2003b). Thus, this has the effect of increasing scatter and absorption of the NIR light. These embedded fibers may potentially provide a permanent\fixed, lightweight alternative to current NIRS models with further potential for increased spatial resolution, having avoided a certain amount of scatter from the scalp and from some thickness of the skull bone. Nevertheless, the technique would be invasive.

8.2.4 Further applications

Many BCI modalities that provide tools for communication for the severely disabled find further applications such as neurorehabilitation (Birbaumer, et al., 2007), biometrics, and gaming (Nijholt, 2009). Thus, optical BCI could potentially provide computer game control using volitional mental tasks and have been addressed by the BCI group recently (Soraghan, et al., 2006).

8.2.5 Increasing the spatial resolution

Certain application such as stroke rehabilitation may benefit from improved spatial resolution compared with what is typically available using nearest-neighbour channels only. The spatial resolution for such a device is similar to the source detector distance, i.e. the inter-optode distance. For the work carried out in this project a 4cm and 3cm IOS was used - thus a spatial resolution of similar values. Nevertheless, using channels with more than one source or detector placed at different distances apart may provide increased resolution (Joseph, et al., 2006). For example, for a given detector, a source could be placed at say 2cm and another at 4cm. Thus, the channel utilising the 2cm source and the detector can be used as a model of superficial haemodynamics since typically an IOS > 2cm is needed to penetrate the brain. Thus, this nearest-neighbour channel (with IOS of 2cm) could be used to subtract superficial haemodynamics from the second-neighbour channel (with an IOS of

4cm). However, this places constraints on the dynamic range of the detector electronics and so a time-multiplexing scheme working along with a frequency multiplexing scheme could be used (Joseph, et al., 2006). These adjustments could be investigated with the flexible multichannel instrument developed in this thesis, since it would require changes to the software only. A probe such as that shown on the right hand side of Figure 5.36 in Chapter 5 of this thesis could be used. Work is ongoing in the group to assess these modulation strategies for noise cancellation (Matthews, et al., 2008a; Matthews, et al., 2008b; Matthews, et al., (Under Development)).

8.2.6 Multimodal BCIs

Multimodal BCIs have become topics of interest recently due to the potential for one modality to contribute certain advantages that another modality cannot achieve. For example MEG-based BCIs have been used with EEG-based BCIs whereby the increase spatial resolution of MEG could be used to more effectively train a user for BCI using cortical signals that are common to both modalities, i.e. both EEG and MEG (as discussed in Section 3.7). Thus, an optical BCI may be used concurrently with, in particular, EEG-based systems since the optical technique would not interfere with the electrical measures of EEG. Thus, although the optical responses (haemodynamic function) are slower in comparison to EEG features, optical measures could provide additional channels and could be used as a class for the idle response, i.e. to inform the BCI when to monitor cerebral activity from the user asychronously or to 'turn off'\become idle (Nijholt, et al., 2008).

8.2.7 Alternative Calculation of Functional Activity

Obrig et al. (Obrig, et al., 2003) report how the modified Beer Lambert law used to calculate the concentration changes in HbR and HbO_2 can be used for functional activity measurements in the brain. However, they also report that the algorithm is nonetheless based on a series of simple assumptions. Firstly, scattering losses can be ignored as long as a change in concentration is assessed using the MBLL. This assumption is shown to be sufficient to the relatively larger change in absorption compared to scattering (coefficients) during a functional activation in the brain. However, the second assumption is that the tissue being analysed is homogenous - which it is not. This leads to poor spatial resolution in NIRS recordings (typically equal to the inter-optode distance). An additional source of error arise from the third assumption that the change in the volume sampled is homogenous within the sampling volume. This leads to an underestimation of the activation due to the partial volume affect (since only the cerebral structures are activation and not the whole volume sampled). Thus, diffuse optical tomography has been suggested as a potential technique that doesn't use the MBLL but rather is based on diffusion theory. Furthermore it can be used on a CWNIRS instrument and for increased spatial resolution (Joseph, et al., 2006) for certain

BCI applications, DOT may be employed in future implementations. Nevertheless, an initial improvement for MBLL based calculations is simply to have the source and detector close to the region of maximum activity in the cerebral cortex. This is achieved by using a multichannel implementation of a CWNIRS instrument, such as the one described in this dissertation and the subsequent localisation experiments carried out in Chapter 7.

8.3 Concluding Remarks

This thesis describes the design, development, and implementation of a flexible multichannel CWNIRS instrument for BCI applications. Furthermore, it reports on the advantages of using multiple channels for increased localisation and detection of functional characteristics from the brain such as lateralisation of motor tasks. These features are important for BCI applications that require multiple independent features of cerebral activity.

APPENDIX A

WORLDWIDE BCI GROUPS

The following list of worldwide BCI groups is an adaptation from the list produced in [Mason, S. G., Bashashati, A., Fatourechi, M., Navarro, K. F. and Birch, G. E. (2007). "A comprehensive survey of brain interface technology designs." Ann Biomed Eng 35(2): 137-169].

Anderson, C	Department of Computer Science, Colorado State University, Fort Collins, CO, USA.
Andersen, R.	Division of Biology, California Institute of Technology, Pasadena, CA, USA.
Aunon	Department of Electrical Engineering, Colorado State University, Fort Collins, CO, USA.
Babiloni	Human Physiology Institute, University ''La Sapienza'', Rome, Italy.
Bayliss	Rochester Institute of Technology, Rochester, NY, USA.
Birbaumer	Institute of Medical Psychology and Behavioral Neurobiology, University of Tübingen, Tübingen, Germany.
Birch	Neil Squire Society, Vancouver, BC, Canada.
Borkowski*	Applied Science and Engineering Laboratories, A.I. duPont Institute, Wilmington, DE, USA.
Cabral*	Department Telecommunications and Control, Escola Polite´cnica, Sa˜o Paulo University, Sa˜o Paulo, SP, Brazil.
Donchin	Department of Psychology, University of South Florida, FL, USA
	Cyberkinetics Neurotechnology Systems, Inc., Foxborough, Massachusetts, and
Donoghue	Department of Neuroscience, Brown University, Providence, RI, USA.
Erfanian*	Department of Electrical Engineering, Iran University of Science and Technology, Tehran, Iran.
Gao, S.	Department Electrical Engineering, Tsinghua University, Beijing, China.
Garcia	Swiss Federal Institute of Technology, Lausanne, Switzerland.
Glassman*	Department of Electrical Engineering, Massachusetts Institute of Technology
Huang*	Institute of Biomedical Information and Control, Huazhong University of Science and Technology, Wuhan, China
Hsieh	Department Medical Research and Education, Taipei Veterans General Hospital, Taipei, Taiwan.
Inokuchi	Graduate School of Engineering Science, Osaka University, Osaka, Japan.
Kennedy	Department of Neurosurgery, Emory University School of Medicine, Atlanta, GA, USA.
Kipke	Department of Biomedical Engineering, University of Michigan, Ann Arbor, MI, USA.
Kostov	Faculty of Rehabilitation Medicine, University of Alberta, Edmonton, AB, Canada.

	Department of Physical Medicine and Rehabilitation and Department of Biomedical Engineering,
Levine	University of Michigan, Ann Arbor, MI, USA.
Ward	Biomedical Eng. Research Group, Department of Electronic Engineering, National University of Ireland Maynooth, Kildare, Ireland.
Prasad	ISRC, Magee Campus, Univ. Ulster, Northern Ireland. (BCIAT research team)
McMillian	Fitts Human Engineering Division, Armstrong Laboratory, Wright-Patterson Air Force Base, OH, USA.
Meng*	Department of Electrical Engineering, Stanford University, Stanford, CA, USA.
Millan	Dalle Molle Institute for Perceptual Artificial Intelligence, Martigny, Switzerland.
Moran	Department of Biomedical Engineering, Washington University, St. Louis, Missouri, USA
Morradi*	Department of Biomedical Engineering, Amir Kabir University of Technology, Tehran, Iran.
Muller	Fraunhofer, FIRST (IDA), Berlin, Germany
Nakashima*	Faculty of Medicine, Tottori University, Yonago-city, Japan
	Collaborative project between Department of Neurobiology, Duke University, Durham, NC, USA,
	Department of Physiology, State University of New York, Downstate Medical Center, Booklyn, NY, USA, and
Nicolelis/Chapin/Principe	Department of Electrical and Computer Engineering, University of Florida, Gainesville, FL, USA.
O'Leary*	Department of Organismal Biology and Anatomy, University of Chicago, IL, USA.
Pfurtscheller	Institute of Biomedical Engineering, University of Technology Graz, Graz, Austria.
Pineda	Department of Cognitive Science, University of California, San Diego, La Jolla, CA, USA.
Qin*	Institute of Automation Science and Engineering, South China University of Technology, Guangzhou, China
Reilly	Department of Electrical Engineering, National University of Ireland, Dublin, Ireland.
Ritter*	Faculty of Technology, Neuroinformatics Group, Bielefeld University, Bielefeld, Germany.
Roberts/Penny/	Department of Engineering Science, University of Oxford, Oxford, UK, Wellcome Department of Imaging
	Neuroscience, University College London, London, UK, Research Department, Royal Hospital for Neuro-disability, London, UK,
Stokes/Curran/Owen	MRC Cognition and Brain Sciences Unit, University of Cambridge, Cambridge, UK,

	Dept. Law, University of Keele, Keele, UK.
Rosa*	LaSEEB–ISR– IST, Lisboa, Portugal.
Saiwaki*	Department of Systems and Human Science, Graduate School of Engineering Science, Osaka University, Osaka, Japan.
Schwartz	Department of Neurobiology, University of Pittsburgh, Pittsburgh, PA, USA.
Seung*	Department of Brain and Cognitive Sciences, Massachusetts Institute of Technology, Cambridge, MA, USA.
Shahabi*	Department of Computer Science, University of Southern California, CA, USA.
Sohn*	Department of Psychology, Chungnam National University, Taejon, Korea, and Electronics and Telecommunications Research Institute, Taejon, Korea.
Sundaresan	Department of Electrical and Computer Engineering, University of Houston, TX, USA.
Sutter	The Smith-Kettlewell Eye Research Institute, San Francisco, CA, USA.
Trejo	NASA Ames Research Center, Moffett Field, CA, USA.
Vicente*	Department of Electrical and Computer Engineering, Florida International University, Miami, FL, USA.
Vidal	Department of Computer Science, University of California Los Angeles, CA, USA.
Wilson*	Department of Electrical and Computer Engineering, University of New Hampshire, Durham, NH, USA.
Wolpaw	Wadsworth Center for Laboratories and Research, Albany, NY, USA.
Yom-Tov	Department of Electrical Engineering, Technion, Israel Institute of Technology, Haifa, Israel.

APPENDIX B

FURTHER SPECIFICATIONS AND CHARACTERISTICS OF THE LIGHT-EMITTING DIODES

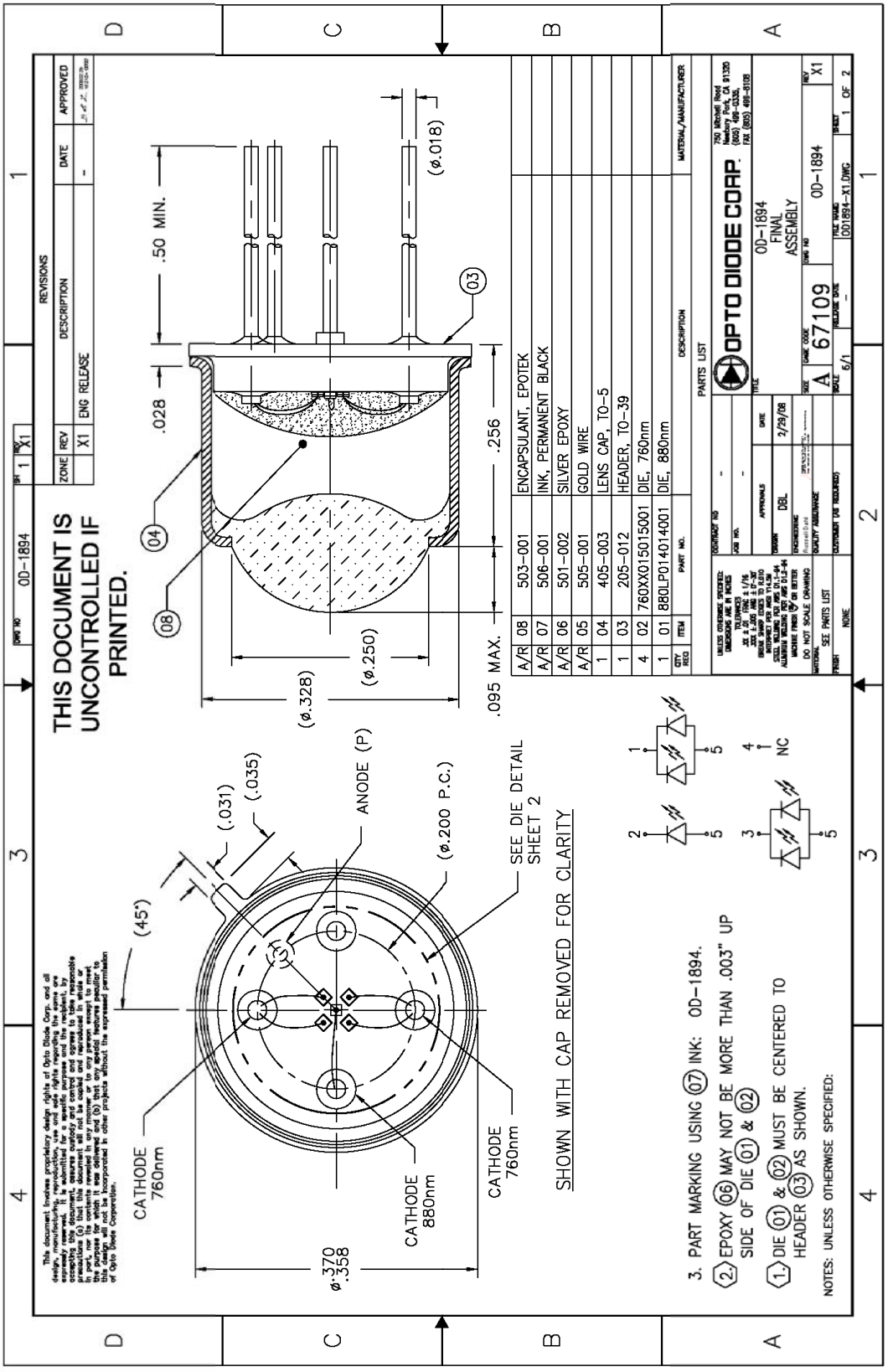
THIS DOCUMENT IS UNCONTROLLED IF PRINTED.
REVISIONS
ZONE REV DESCRIPTION DATE APPROVED
X1 ENG RELEASE -
DWG NO 0D-1894
SHT 1 REV X1
PARTS LIST
QTY REQ ITEM PART NO. DESCRIPTION MATERIAL/MANUFACTURER
A/R 08 503-001 ENCAPSULANT, EPOTEK
A/R 07 506-001 INK, PERMANENT BLACK
A/R 06 501-002 SILVER EPOXY
A/R 05 505-001 GOLD WIRE
1 04 405-003 LENS CAP, TO-5
1 03 205-012 HEADER, TO-39
4 02 760XX0150015001 DIE, 760nm
1 01 880LP014014001 DIE, 880nm
OPTO DIODE CORP.
750 Mitchell Road
Newbury Park, CA 91320
(805) 499-0335
FAX (805) 499-8108
0D-1894
FINAL
ASSEMBLY
SIZE A
CAGE CODE 67109
DWG NO 0D-1894
REV X1
SCALE 6/1
RELEASE DATE -
FILE NAME 001894-X1.DWG
SHEET 1 OF 2
CATHODE 760nm
CATHODE 880nm
CATHODE 760nm
ANODE (P)
(.031)
(.035)
(45°)
(ø.200 P.C.)
SEE DIE DETAIL SHEET 2
SHOWN WITH CAP REMOVED FOR CLARITY
ø.370
ø.358
(ø.328)
(ø.250)
.095 MAX.
.256
.028
.50 MIN.
(ø.018)
04
08
03
3. PART MARKING USING (07) INK: 0D-1894.
(2.) EPOXY (06) MAY NOT BE MORE THAN .003" UP SIDE OF DIE (01) & (02)
(1.) DIE (01) & (02) MUST BE CENTERED TO HEADER (03) AS SHOWN.
NOTES: UNLESS OTHERWISE SPECIFIED:
NC

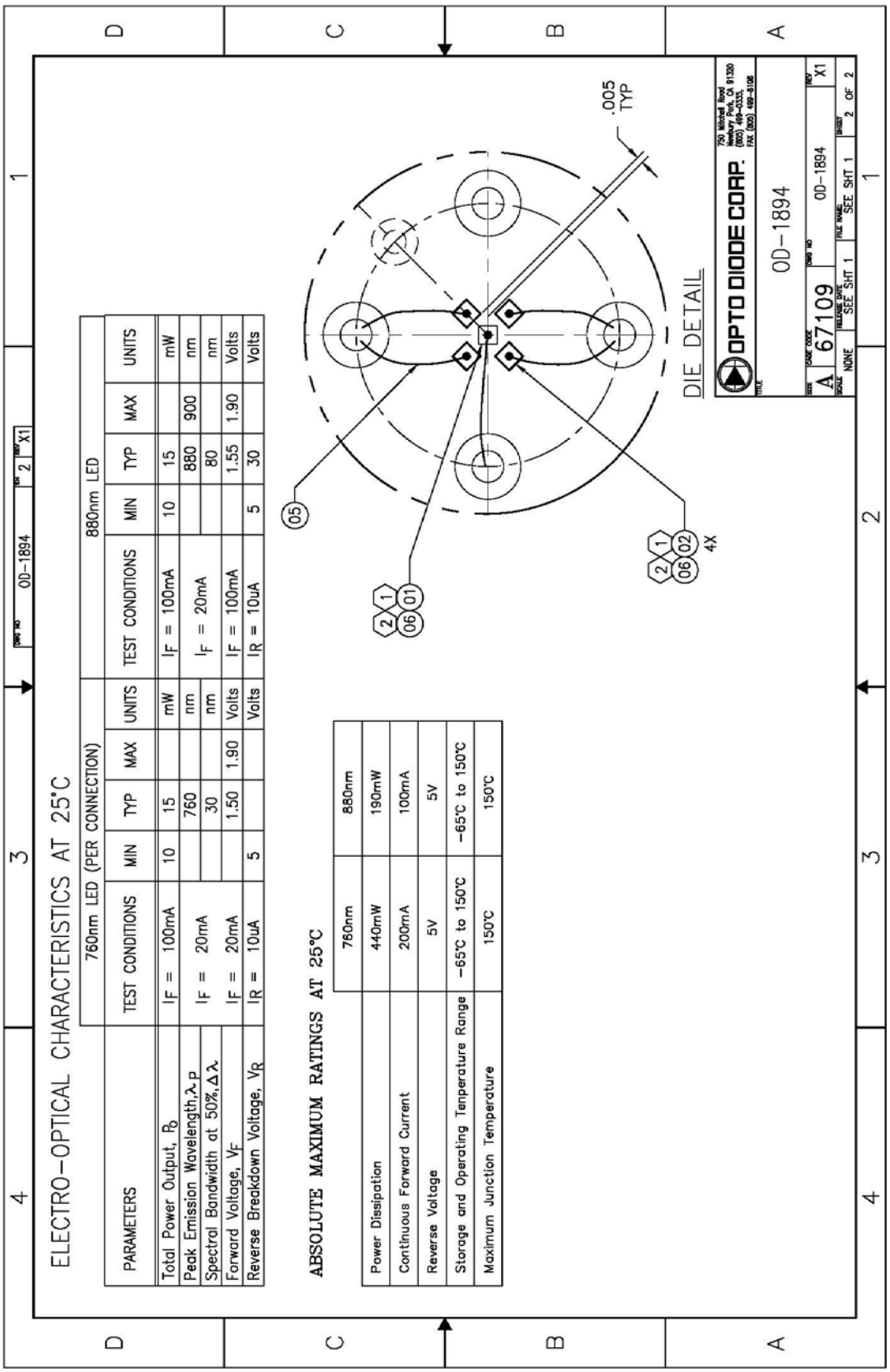
ELECTRO-OPTICAL CHARACTERISTICS AT 25°C
760nm LED (PER CONNECTION)
880nm LED
PARAMETERS
TEST CONDITIONS
MIN
TYP
MAX
UNITS
Total Power Output, Po
IF = 100mA
10
15
mW
IF = 100mA
10
15
mW
Peak Emission Wavelength, λp
IF = 20mA
760
nm
IF = 20mA
880
900
nm
Spectral Bandwidth at 50%, Δλ
IF = 20mA
30
nm
80
nm
Forward Voltage, VF
IF = 20mA
1.50
1.90
Volts
IF = 100mA
1.55
1.90
Volts
Reverse Breakdown Voltage, VR
IR = 10uA
5
Volts
IR = 10uA
5
30
Volts
ABSOLUTE MAXIMUM RATINGS AT 25°C
760nm
880nm
Power Dissipation
440mW
190mW
Continuous Forward Current
200mA
100mA
Reverse Voltage
5V
5V
Storage and Operating Tenperature Range
-65°C to 150°C
-65°C to 150°C
Maximum Junction Temperature
150°C
150°C
DWG NO 0D-1894
REV X1
.005 TYP
DIE DETAIL
4X
05
01
02
06
OPTO DIODE CORP.
750 Walnut Road
Newbury Park, CA 91320
(805) 499-0335
FAX (805) 499-8108
0D-1894
SIZE A
CAGE CODE 67109
DWG NO 0D-1894
REV X1
SCALE NONE
RELEASE DATE SEE SHT 1
FILE NAME SEE SHT 1
SHEET 2 OF 2

APPENDIX C

ADDITIONAL FUNCTIONAL MAGNETIC RESONANCE IMAGING (FMRI) DATA AND INSTRUCTIONS

➢ BOLD fMRI Experiment and Results:

The following are the results of a series of movement-related tasks carried out within a 3-Tesla (3T) Siemens Allegra MR scanner.

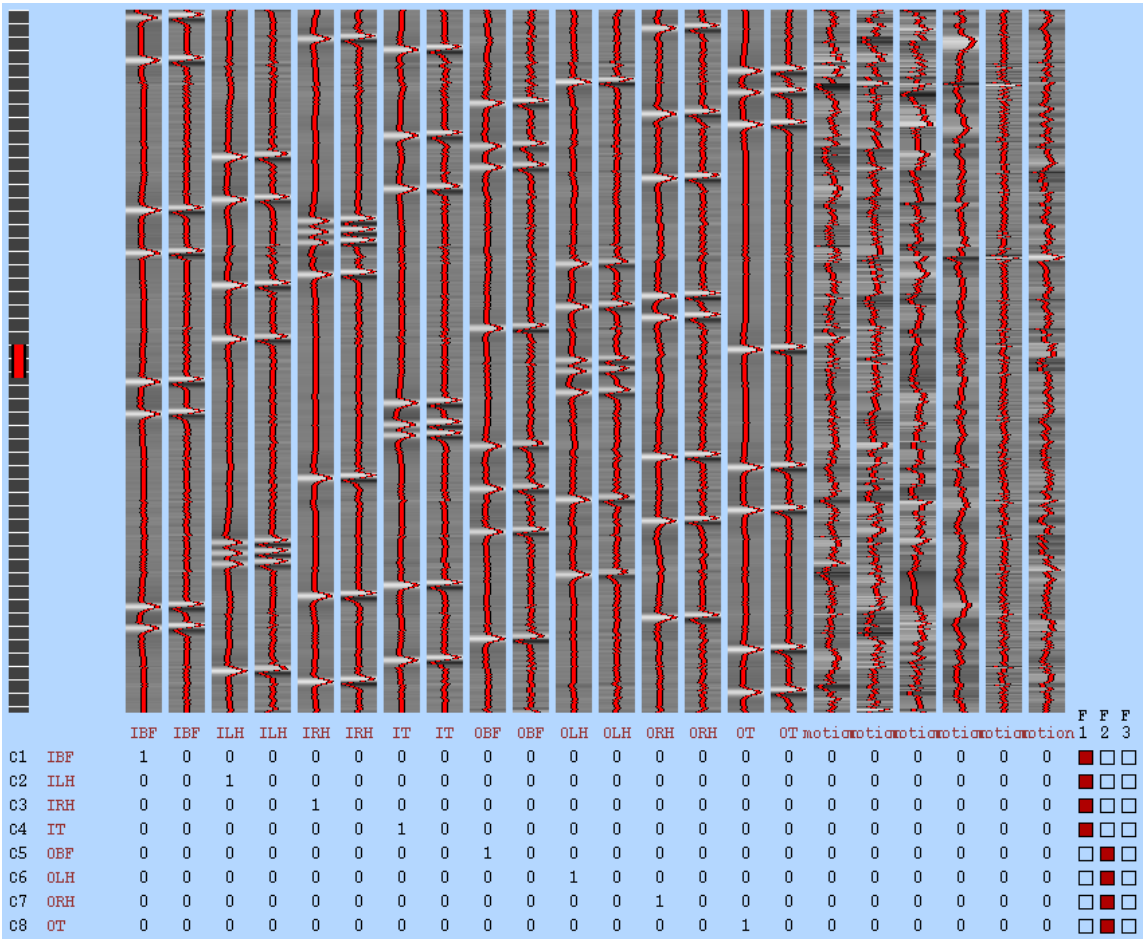

Figure 1: Design Matrix for fMRI protocol. Eight trials of each task were performed, pseudorandomised.

NOTE: All the proceeding fMRI images are results for a single subject participating in the motor-related tasks.

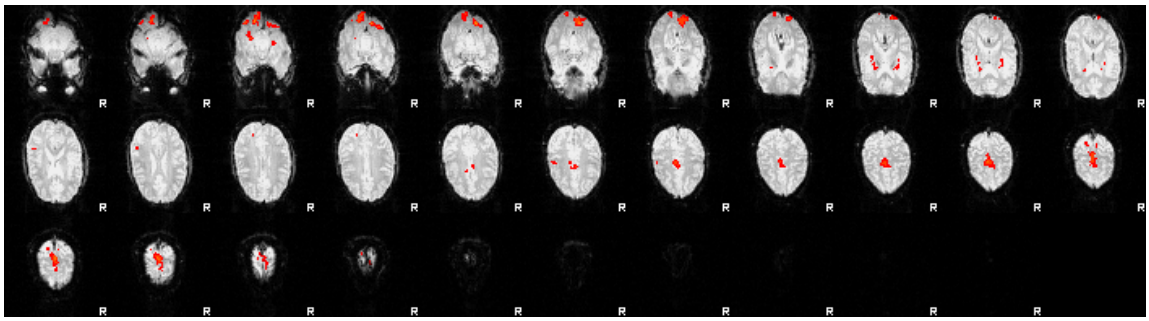

Figure 2: Task C1 - IBF (Imagery Both Feet). Subject performing motor imagery of moving both feet.

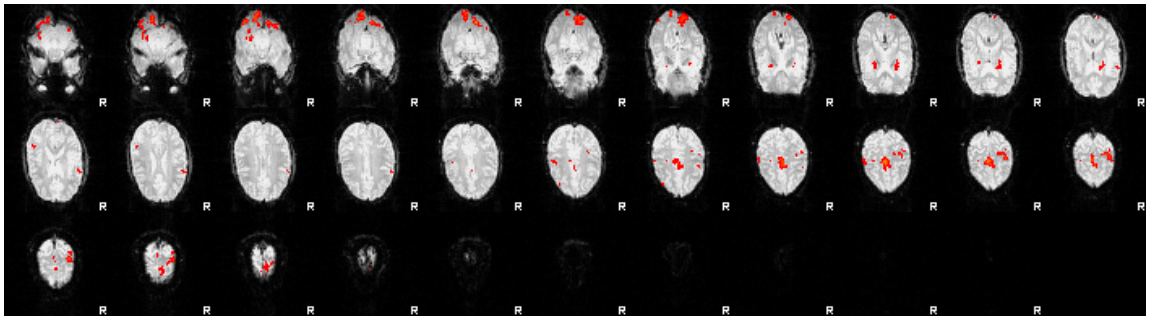

Figure 3: Task C2 - ILH (Imagery Left Hand). Subject performing motor imagery of moving the left hand.

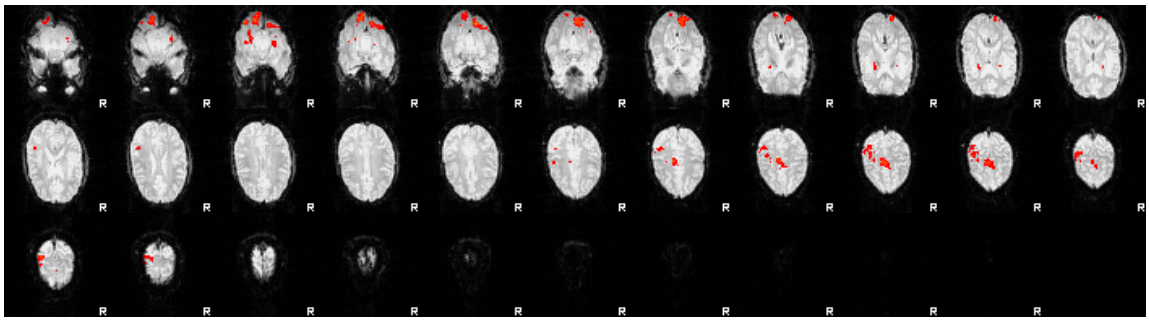

Figure 4: Task C3 - IRH (Imagery Right Hand). Subject performing motor imagery of moving the right hand.

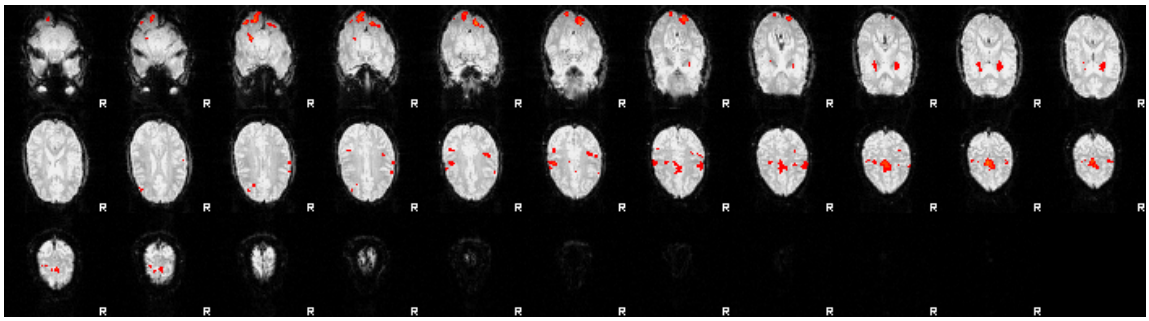

Figure 5: Task C4 - IT (Imagery Tongue). Subject performing motor imagery of moving the tongue.

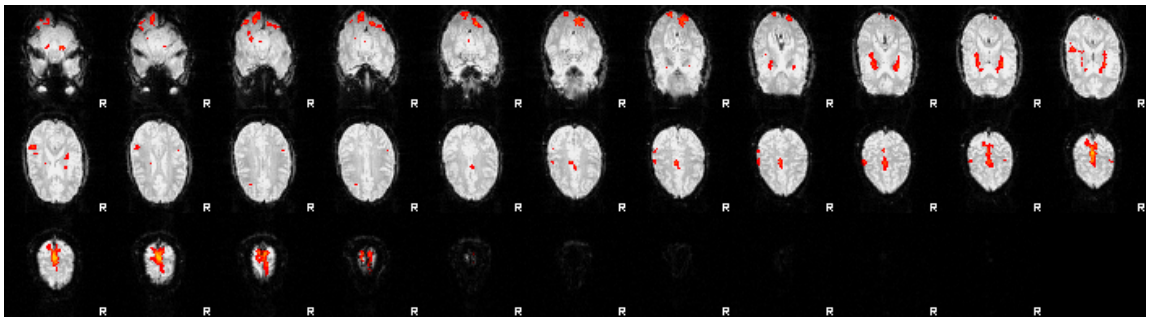

Figure 6: Task C5 - OBF (Overt Both Feet). Subject performing overt motor movement of both feet.

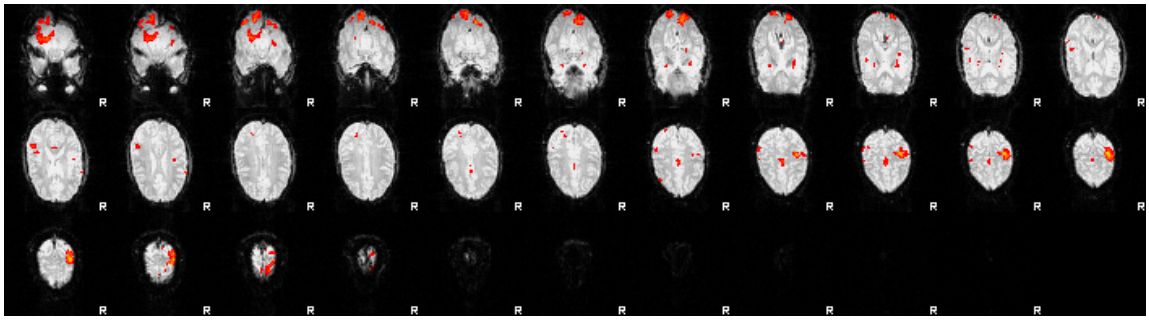

Figure 7: Task C6 - OLH (Overt Left Hand). Subject performing overt motor movement of the left hand.

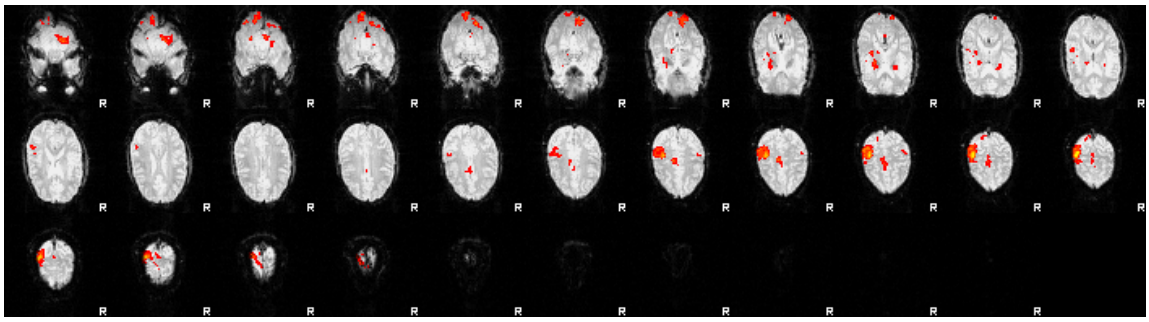

Figure 8: Task C7 - ORH (Overt Right Hand). Subject performing overt motor movement of the right hand.

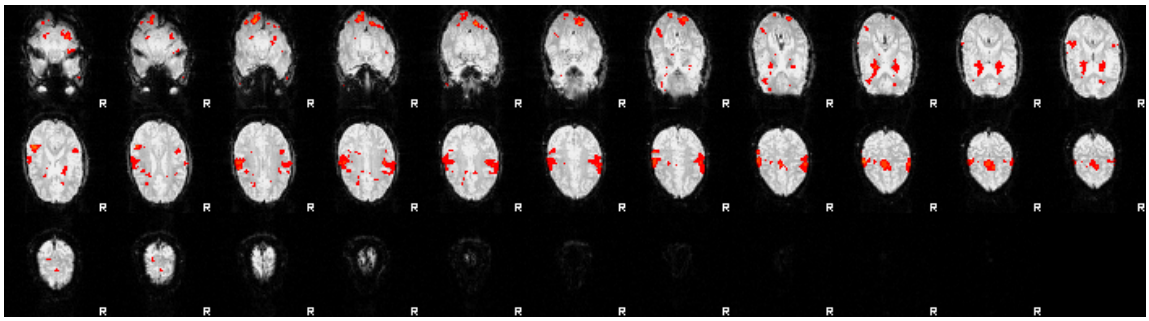

Figure 9: Task C8 - OT (Overt Tongue). Subject performing overt motor movement of the tongue.

APPENDIX D

FURTHER FNIRS DATA

It was felt that certain additional data from various experiments would have interrupted the flow of the main document and so they are appended here, and referenced within the main document.

➢ Compensation for LED spectral spread (Chapter 5)

From Chapter 5 the LEDs at 760nm were shown to have a FWHM of ~27nm and the 880nm components a FWHM of ~84nm. Compensation for the spectral spread of the light sources could be achieved by utilising the spectral profile of each source. To calculate for concentration changes in HbO_2 and HbR, at least two wavelengths are needed and these are used in the modified Beer Lambert Law. However, the MBLL can accept more wavelengths to calculate these haemoglobin species. Thus, each LEDs spectral profile can be treated as a series of discrete wavelengths with decreasing weight from the central wavelength (i.e. at 761nm and 868nm). Therefore, all discrete wavelengths for each LED were used with varing weights across the FWHM for each LED - 82 for the 760nm component and 270 for the 880nm component (since 880nm has a larger FWHM). The specific extinction coefficients for all these wavelengths for both HbR and HbO_2 were retrieved (Cope, 1991) and used in the MBLL. The same differential pathlength factor of 6 was used for all wavelengths.

A cross correlation (using the crosscorr.m function in Matlab) of concentration change in HbO_2 with a single discrete wavelength (monochromatic) compared to that retrieved using the 352 discrete wavelengths (broadband) gave a correlation of 0.99995 at zero lag. Similarly for concentration changes in HbR a coefficient of 0.99975 at zero lag was found. For inspection of the actual differences in the time series data, Figure D.1 shows a graph of the haemoglobin concentration changes for both cases: when treating the light sources as monochromatic or broadband. The various features of the haemodynamics are considered in Chapter 6 and are simply observed here to display time series comparisons.

The calculated haemodynamics are very similar by correlation and by visual inspection of the time series data. Thus, in order to reduce the computational demand (~ three orders of magnitude longer when performed on a full data-set for a single channel - 10.5 seconds compared to 0.011 seconds) in real-time calculations the light sources can and are treated as monochromatic. This of course also explains how LEDs can be used as a light source for NIRS and so the result is not that suprising.

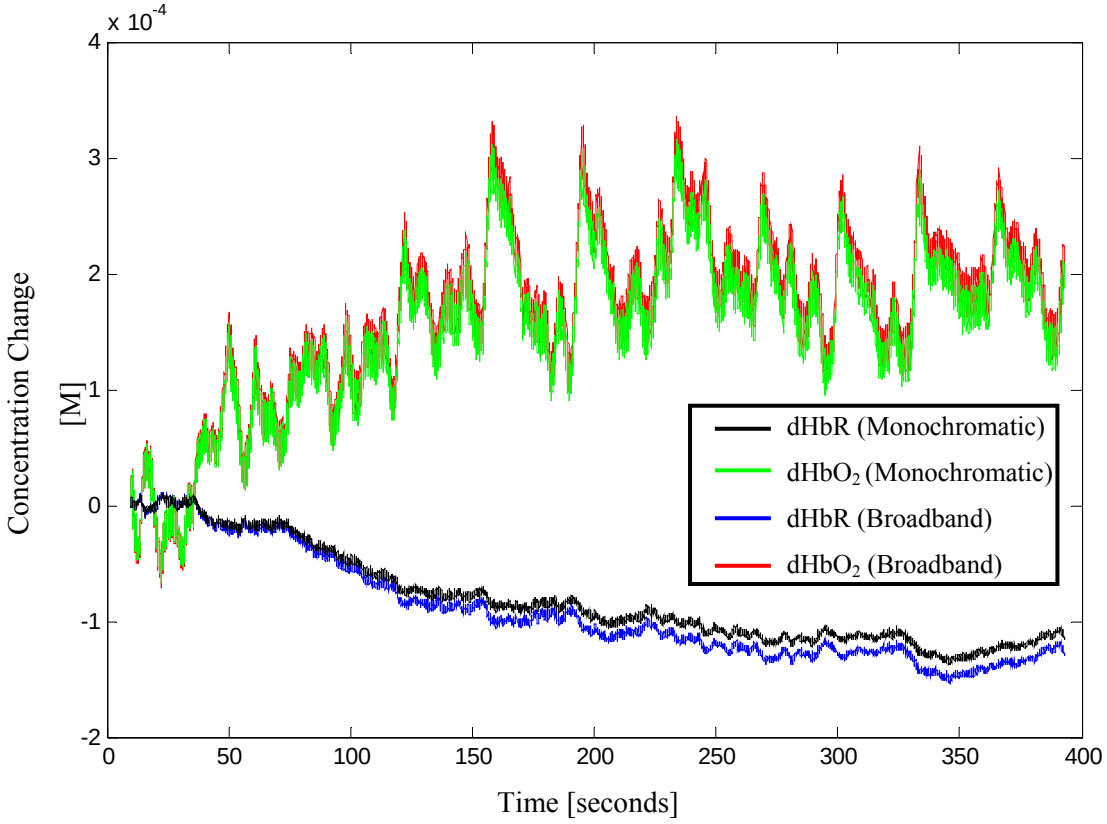

Figure D.1: Comparison of concentration changes in HbR and HbO_2 treating light sources as monochromatic or broadband (containing 352 discrete wavelengths weighted and spread within the LEDs FWHM).

- **Comparison of haemoglobin concentration changes using different wavelengths. (Chapter 2)**

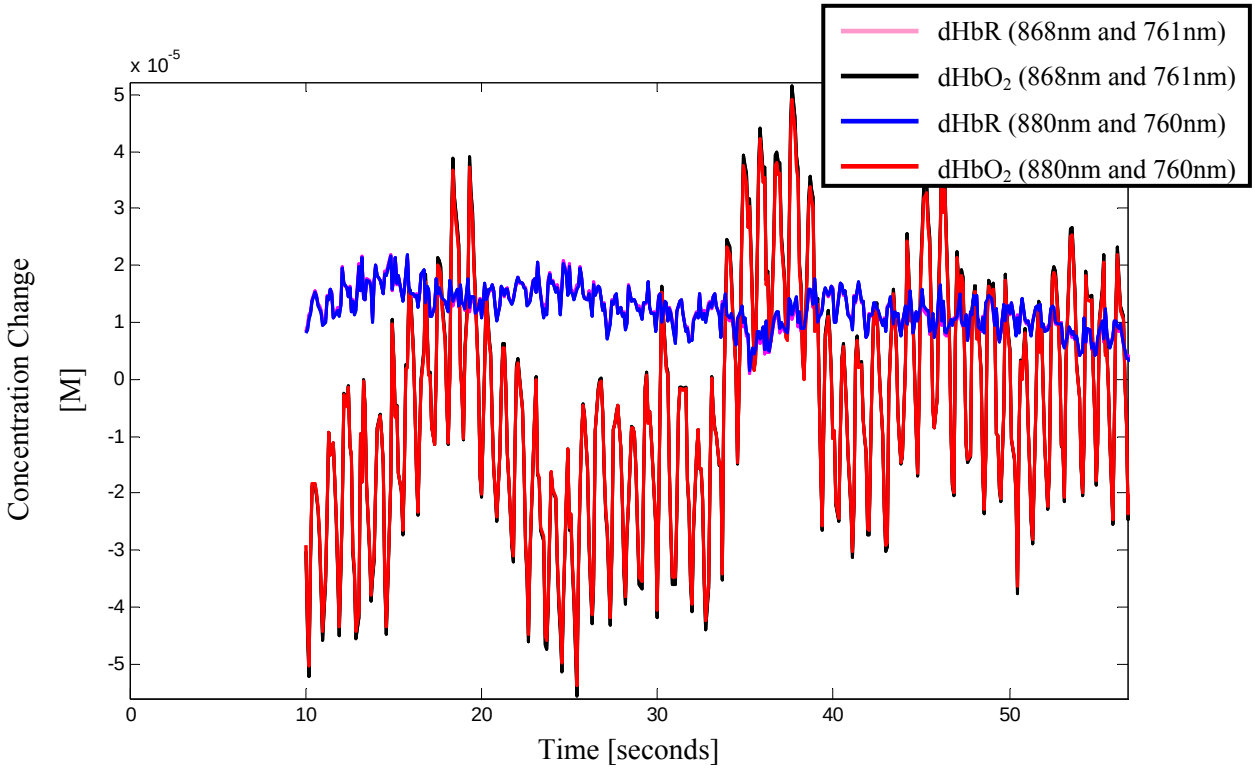

Figure D.2: Comparison of using different wavelength pairs in the Modified Beer-Lambert Law. LEDs were at 868nm and 761nm after being allowed to settle (1 hour). Using extinction coefficients for these wavelengths and for 760nm with 760nm produce miniscule differences, mostly only seen in cardiac pulse peaks and troughs.

Wavelength [nm]	*HbO_2 [α (λ)] $cm^{-1}/(mol/l)*10^3$*	*HbR [α (λ)] $cm^{-1}/(mol/l)*10^3$*
760	1.48658650	3.84370700
880	2.76060610	1.92461710
761	1.49176825	3.83334350
868	2.68000110	1.86013310

Table D-1: Extinction coefficients used for HbO_2 and HbR for various wavelengths used to calculate concentration changes of the haemoglobin species.

➢ **Blood Vessel Occlusion from Subject 2 (Chapter 6)**

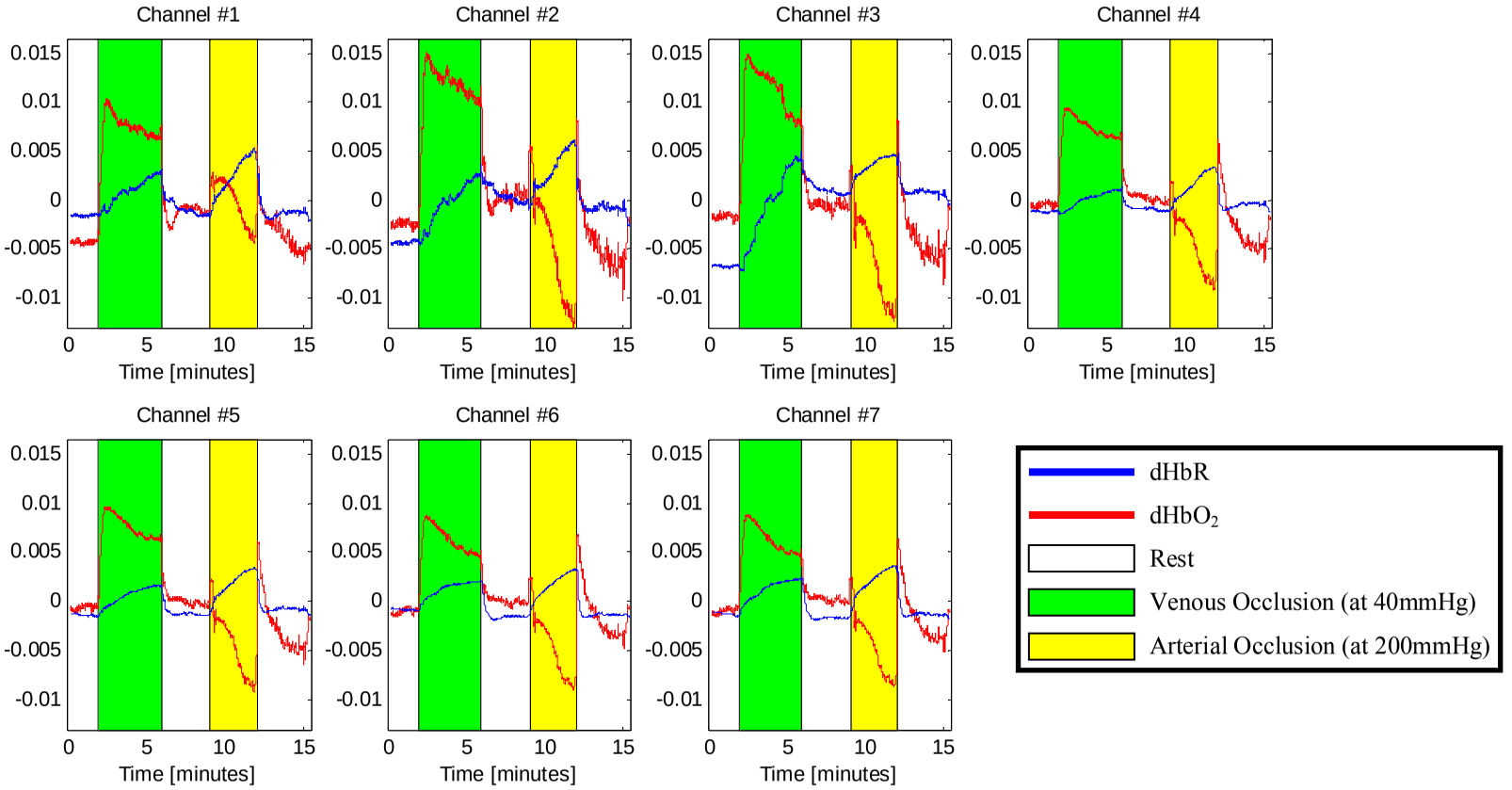

Figure D.3: Blood vessel occlusion haemodynamics from Subject 2. All y-axis are in units of "Concentration Change [mM]". Arterial and venous occlusion responses follow the haemodynamic signatures expected for these occlusions, i.e. an increase in both dHbR and $dHbO_2$ during venous occlusion; and an increase in dHbR but a decrease in $dHbO_2$ during arterial occlusion.

➢ **Comparison of $dHbO_2$ using lower cut-off frequency (Chapter 7)**

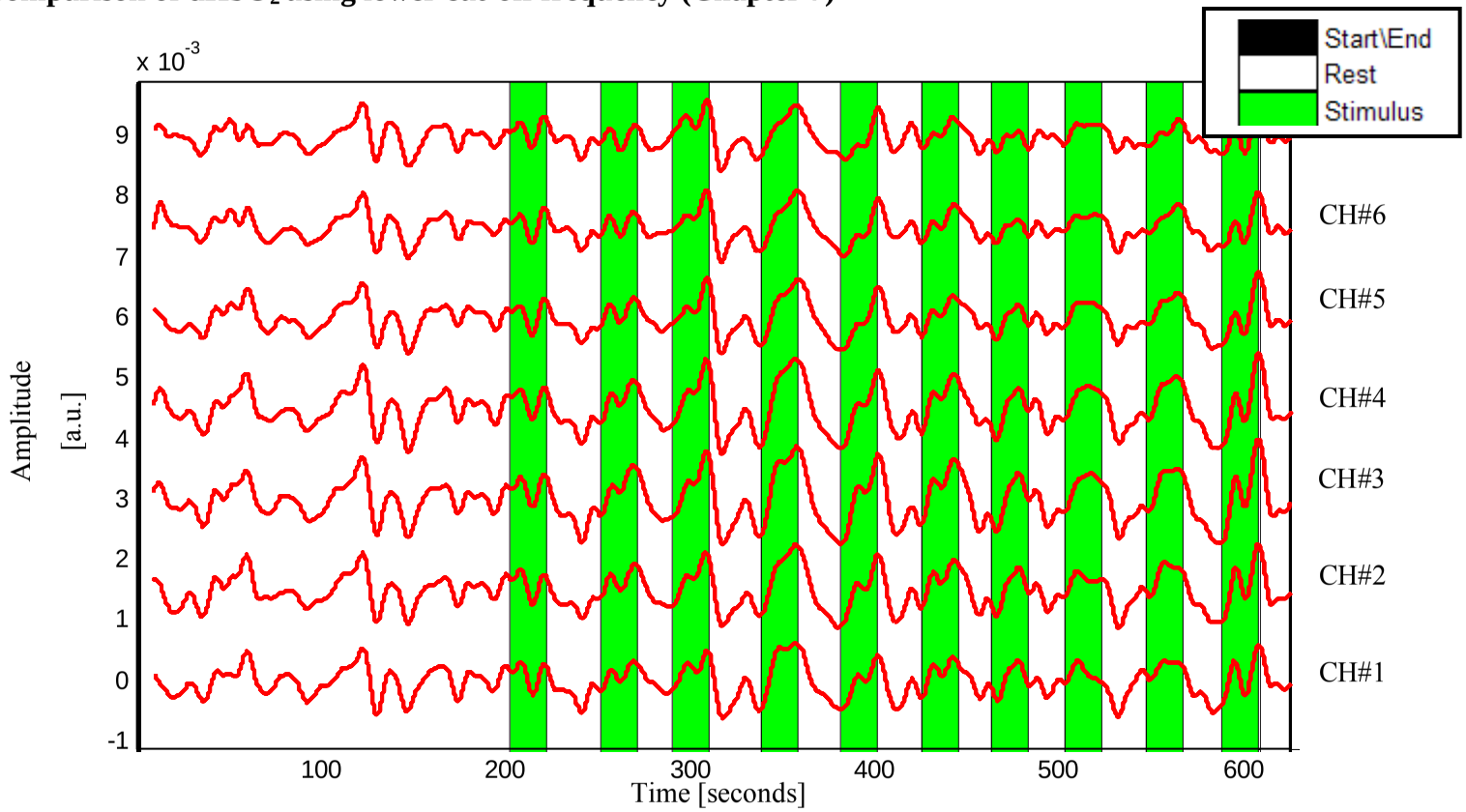

Figure D.4: Comparison of $dHbO_2$ for seven channels in an optet over position C3 for right hand finger opposition tasks. This data was to show the beneficial effect of increased filtering with the following bandpass filter: 3rd order highpass with cutoff at 0.01Hz; 4th order lowpass with cutoff at 0.1Hz.

APPENDIX E

ANATOMY AND PHYSIOLOGY

Certain concepts in the main document may be facilitated by additional knowledge of some of the fundamentals of for example, blood composition. These short introductions to blood composition, systemic blood vessels, systemic blood pressure, the human nervous system, and the low level structure or histology of nervous tissue are reported in this Appendix.

E.1 Introduction to Blood Composition, the Human Circulatory System, and Systemic Blood Pressure Regulation

E.1.1 Blood Composition

Blood, the only fluid tissue found in the body, is composed of ~55% plasma, ~45% erythrocytes (red blood cells or RBCs), and <1% leukocytes (white blood cells or WBC) and platelets. Blood plasma is mostly water (~90%) and includes over 100 different dissolved solutes (hormones, nutrients, waste, gases, proteins, and electrolytes). Plasma proteins play an important role in osmotic pressure regulation, maintaining water content in blood and body tissues. WBCs, RBCs, and platelets make up the formed elements (living blood cells) of blood. Leukocytes (*leuko=white; cyte=cell*) found in blood are merely using it as a transport system to travel to the affected areas where they provide an immune/inflammatory defence. Unlike RBCs, WBCs can slip in and out of the blood stream via capillaries by diapedesis ("leaping across"). They move through tissue spaces by amoeboid motion following a chemical trail released by damaged cells or other WBCs (positive chemotaxis). Platelets are cytoplasmic fragments with granules that contain an array of chemicals (e.g. serotonin) important in blood clot formation.

Erythrocytes ($\sim 7.5\mu m$ in diameter) are the most significant blood constituents in terms of understanding NIR light propagation in tissue since they house the oxygen molecules whose dynamics indicate functional mental activity. Strictly speaking they are not cells (no nucleus or organelles). They could be described as doughnut-shaped bags of haemoglobin (Hb), a RBC protein involved in gas transport (not just oxygen). Other proteins are present in the RBC most of which are involved in maintaining the RBC plasma membrane or promoting a change in the shape of the RBC. Frequent changes in morphology are required since the RBCs are constantly travelling through capillaries with lumen (vessel cavity) diameters ($8-10\mu m$) smaller/similar to themselves. Once they pass through the narrow vessels they normally return to their original biconcave shape.

E.1.2 Cardiovascular System

The cardiovascular system could be crudely considered as a pump with rigid pipes carrying blood around the body to all the bodies' cells. However this analogy oversimplifies the considerable dynamic nature of the various vessels, heart and organs involved in keeping the body in homeostasis.

Blood flow beginning at the heart is forcefully ejected from the right ventricle (oxygen-poor blood) through the pulmonary (*pulmonos = lung*) arteries and travels to the lungs. Here

blood collects oxygen (O_2) and releases carbon-dioxide (CO_2) and oxygen-rich blood arrives into the left atrium (*atrium = entryway*) via 4 pulmonary veins. Blood is then relatively gently pumped into the left ventricle (ventricle reaches 70% of its capacity without/prior to atrial contraction contributions) and is forcefully ejected from the heart via the aortic artery. This master artery splits into various arteries serving the rest of the body, including the brain. Blood from the aortic artery then travels sequentially into various arteries, leading into arterioles, then capillaries, venules, veins, and finally back to the heart via 3 veins - inferior vena cava (blood from below diaphragm), superior vena cava (blood from above diaphragm), and the coronary sinus (blood drained from the heart's myocardium). Blood relatively depleted in O_2 (typically ~70% saturated) returning to the heart then enters into the right atrium. Finally, the blood is gently pumped into the right ventricle to complete the cardiac cycle.

Some blood vessels in the cardiovascular system are constantly constricting and dilating (vasoconstriction and vasodilation, respectively) as ordered by the sympathetic nervous system. These processes are carried out in response and to compensate for undesired changes in blood pressure that can be caused by blood volume changes which itself is related to a myriad of conditions, such as high or low salt or water concentration levels in the blood.

E.1.3 Systemic Blood Pressure and Regulation

The blood vessels of the body differ in structure, size, function, O_2 content, and resistance to flow (resulting in pressure gradients). The contribution of each vessel type is described next.

E.1.3.1 Systemic arterial system

The arterial system contains essentially three types of artery - elastic, muscular, and arterioles. The elastic (conducting) arteries are located close to the heart with large lumens making them low resistance vessels. They do not engage in vasoconstriction but rather act as auxillary pumps or pressure reservoirs expanding and recoiling as blood is forced into them from the heart. This ensures that blood flowing through them does so continuously, rather than starting and stopping in synchrony with each heart beat. As a result the elastic arteries smoothen the pressure for the rest of the bodies' blood vessels to protect them from pressure-related damage. Muscular (distributing) arteries have lumen diameters of 10mm-0.3mm and are active in vasoconstriction but less distensible than elastic arteries. These are the main supply vessels distributing blood around the body.

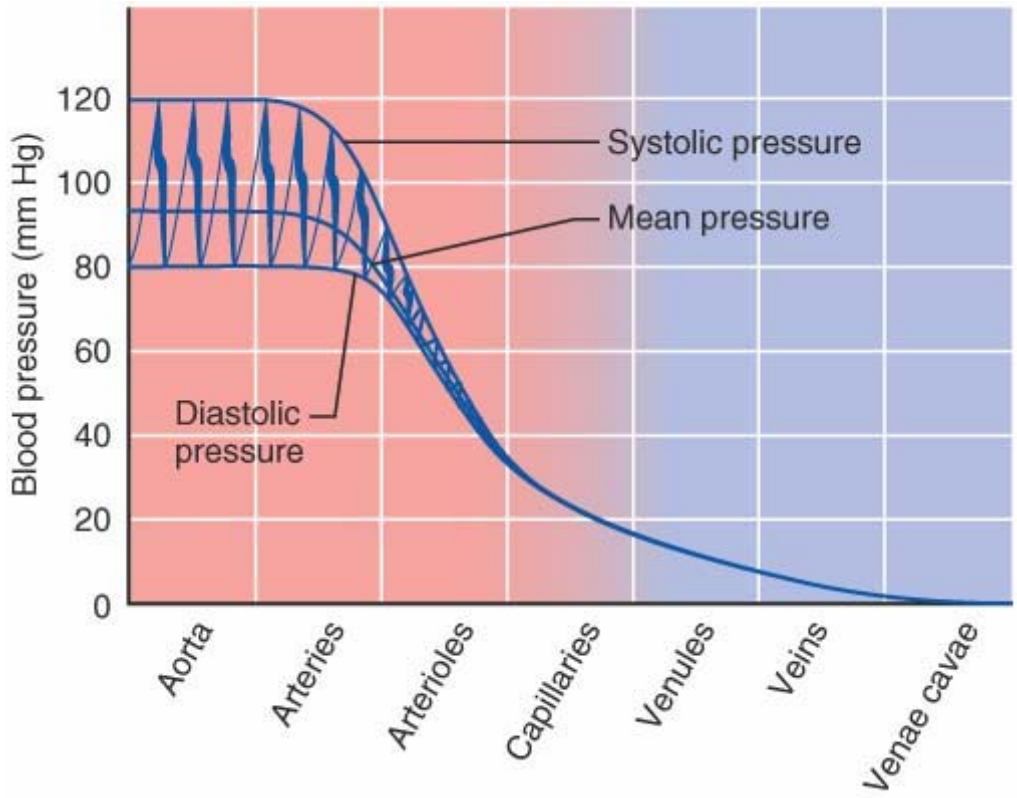

Figure E.1.1: Blood pressure in the various blood vessels of the cardiovascular system. (Reproduced from Marieb and Hoehn, 2006a)

Figure E.1.1 demonstrates the pulsatile nature of arterial blood pressure, especially close to the heart. As the left ventricle of the heart contracts, blood is forced into the aorta and other elastic arteries, which stretch under the pressure, and reach a pressure peak (systolic ~120 mmHg in a healthy human). Once the aortic valve closes preventing backflow of blood, these elastic arteries recoil with pressure decreasing to the diastolic pressure (~80 mmHg in a healthy human). The difference between the systolic and diastolic pressures is known as the pulse pressure (the effect of which incidently can be observed in the raw NIR signal analysis in Chapter 6 as systolic pressure levels are observed as an attenuation of more NIR light than diastolic pressures). Normal mean arterial pressure (MAP) is shown in the equation below (1.1) where the calculation caters for the pressure being diastole longer than systole. MAP is the pressure value that propels blood into the tissues of the body.

$$\begin{aligned} MAP &= diastolic\ pressure + \frac{pulse\ pressure}{3} \\ &= 80mmHg + \frac{40mmHg}{3} = 93mmHg \end{aligned} \tag{E.1}$$

Arterioles have the smallest arterial lumen diameters ($0.3mm - 10\mu m$). The smallest of these arterioles, which feed the capillary bed, have only a single layer of smooth muscle cells

surrounding the endothelial cell lining (this cell lining allows blood to flow further by reducing the friction between the vessel wall and the blood, and is found in all blood vessels). In terms of pressure gradients, arterioles have the most work to do, as can be seen in Figure E.1.2. This large gradient shift is required since the thin, fragile capillaries would rupture under pre-arteriole pressures. Sufficient arteriole constriction and closure of precapillary sphincters can induce a bypass of the capillary bed supplying the local tissue altogether, as shown in Figure E.1.2. One example of this is seen during vigorous exercise where the capillaries serving the intestines can be bypassed so as those capillaries suppling skeletal muscle may receive more blood (thus more O_2 delivery and increased waste removal). Note: Precapillary sphincters are absent in cerebral blood vessels where the arterioles have to supply the required pressure-reducing friction.

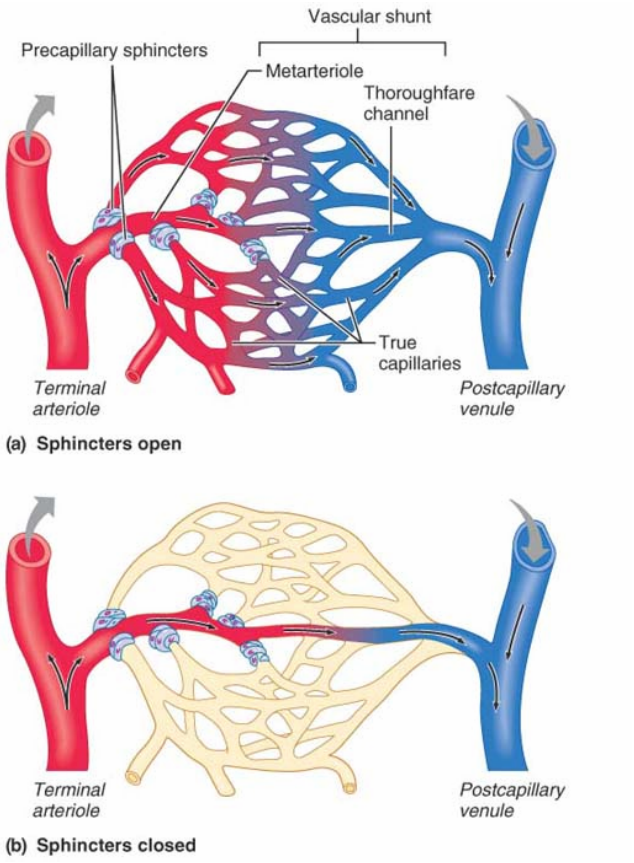

Figure E.1.2: Under precapillary sphincter constriction, the metarteriole acts as a shunt, bypassing the capillary bed (Reproduced from Marieb and Hoehn, 2006a).

E.1.3.2 Systemic capillary system

It can be seen from Figure E.1.1 that capillary blood pressure ranges from 35 mmHg in arterioles to ~15 mmHg on entering the venules. Since capillaries can be porous and highly permeable, these pressures are sufficient to force the solute-containing fluids into the interstitial space, where they can move (by osmosis) to tissues to supply nourishment.

E.1.3.3 Systemic venous system

The venous blood pressure gradient is normally too low (15 mmHg) to ensure blood returns to the heart terminating at the Vena Cavae. This is true even with the addition of backflow-reducing valves and large lumens. There is also no apparent pulsatile response (see Figure E.1.1), since the blood's kinetic energy has been dissipated (as heat) by the arterial and capillary system's peripheral resistance. Thus, three processes are in place to ensure venous return.

First is the 'respiratory pump' whereby when a person inhales, abdominal pressure increases, squeezing local veins and causing blood to return to the heart. During the same inhalation chest pressure decreases allowing thoracic veins to expand, thus speeding blood flow to the right atrium. Second is the more important 'muscular pump' whereby skeletal muscle activity surrounding deep veins milks blood from valve to valve, back to the heart. Third is the sympathetic nervous system controlling constriction of the smooth muscle layer around the veins, aiding venous return (the parasympathetic nervous system can operate for antagonistic vasodilation).

E.1.3.4 Maintenance of systemic blood pressure

The main physiological instruments in charge of maintaining homeostatic blood pressure and thus supply of blood to all cells in the body are the heart, blood vessels, and the kidneys, all operating under the control of the brain. Blood pressure manipulated by these is maintained principally via mechanisms controlling cardiac output (CO = stroke volume [ml/beat]*Heart-rate [beats/min]), peripheral resistance, and blood volume. Thus maintenance of blood pressure can be understood by analysis of how the body controls these three phenomena.

Cardiac output is the amount of blood pumped out by each ventricle in one minute (~5.25L/min in a healthy adult); where stroke volume is the amount of blood pumped out by one ventricle every beat (~70ml/beat). With a normal blood volume of ~5L, the whole blood supply passes through one side of the heart every minute. The factors determining CO are venous return, and neural and hormonal controls. Within the brainstem the cardioinhibitory centre's neural-controls in the medulla oblongata maintains a resting heart rate via the parasympathetic vagus nerves. Stroke volume is determined by venous return or end diastolic volume (volume of blood in a ventricle prior to contraction, during diastolic rest) during these resting periods. During stress however, the cardioacceleratory centre assumes command, activating the sympathetic nervous system increasing heart rate by acting on the SA node of the heart, and increasing stroke volume by increasing cardiac muscle

contractility (decreasing end systolic volume - volume of blood remaining in a heart ventricle after a full contraction). Again, since CO varies directly with heart rate and stroke volume, these processes describe CO enhancement and thus MAP increase.

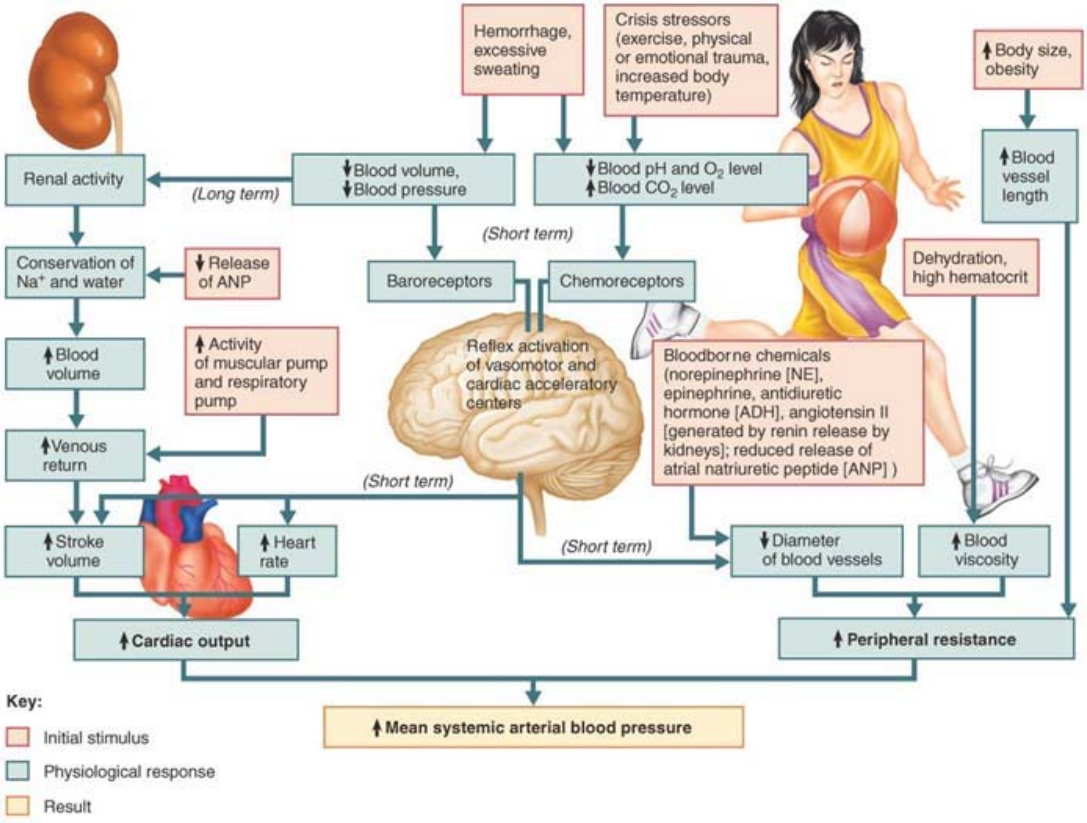

Figure E.1.3: Various processes that cause an increase in mean arterial blood pressure (MAP). Among the affecters (initial stimulus) are dehydration, large body size, high hematocrit, excessive sweating, emotional trauma, and particular bloodborne chemicals. The somatic responses to these affecters are changes in blood volume, pressure, pH, CO_2 and O_2 levels, and viscosity. Increases in cardiac output and peripherial resistance can be seen as the two chief intermediary physiological responses in the MAP hierarchal process. (Reproduced from Marieb and Hoehn, 2006a)

To picture these effects at work, Figure E.1.3 outlines how the mean arterial blood pressure is continuously tuned starting with the initiating stimuli followed by their corresponding physiological responses. Thus it can be seen how greatly varied MAP can be from one moment to the next depending on many effectors, such as hydration, hematocrit, body size, physical exertion etc. However, it can also be seen that there are both short-term (neural, hormonal) and long-term (renal) controls for maintainance of MAP.

E.1.3.4.1 Short-term controls

In the short-term, the brain implements neural controls which affect peripheral resistance and CO. Two neural controls are available:

1) The blood vessel diameter is altered. During low pressure conditions, blood vessel diameters supplying all parts of the body except the heart and brain are reduced, increasing systemic blood pressure to ensure blood supply to these vital organs.
2) In response to demand by various organs, blood distribution is altered, temporarily shunting/bypassing other organs, such as is seen during exercise where the stomach is bypassed to increase supply to skeletal muscle tissue (see Figure E.1.2).

The physiological circuitry for implementing these controls includes baroreceptors with afferent fibres, the vasomotor centre of the medulla oblongata, vasomotor fibres, and vascular smooth muscle. Finally, inputs from chemoreceptors and higher brain centres occasionally contribute to the neural control of MAP.

A cluster of neurons in the medulla oblongata known as the vasomotor centre, oversees changes in blood vessel diameter (peripherial resistance). This centre, along with the cardioacceleratory and cardioinhibitory centres described earlier make up the cardiovascular centre of the brain, which integrates blood pressure control by altering CO and blood vessel diameter via neural impulses. These impulses travel from the vasomotor centre along sympathetic efferents (vasomotor fibres) and innervate the smooth muscle of blood vessels, mainly arterioles. These arterioles are in a constant state of moderate constriction (vasomotor tone) and the degree of constriction is dependent on the supplied organ. The vasomotor fibres can also release vasoconstricting norepinephrine or, in some fibres such as occur in skeletal muscle, vasodilating acetylcholine which affects local blood flow. As already mentioned, vasomotor activity is also influenced by inputs from baroreceptors, chemoreceptors, and higher brain centres. Chemoreceptors respond to changes in blood levels of H^+ (blood pH), CO_2, and O_2. In the event of pH or O_2 level drop, or an increase in CO_2 in blood, chemoreceptors in the aortic arch and large arteries of the neck transmit impulses to the cardioacceleratory centre in the medulla to increase CO and also to the vasomotor centre, causing vasoconstriction. The resulting increase in blood pressure serves to speed the return of blood to the pulmonary circuit for increased O_2 replenishing and removal of CO_2. More important to acute (short-term) blood pressure control are baroreceptors. Baroreceptors are pressure-sensitive mechanoreceptors which react to changes in stretch and arterial pressure. They are found in the walls of the carotid sinuses (reflex regulation for brain blood supply), aortic arch and most large arteries of the neck and thorax. These neural receptors, when stretched, send rapid impulses to the vasomotor centre. This effect inhibits the centre resulting in vasodilation of arterioles, and veins, decreasing blood

pressure. Dilation of veins moves blood to venous reservoirs, reducing CO and venous return. At the same time, baroreceptor impulses also travel to the cardiac centres in the medulla stimulating parasympathetic activity, reducing heart rate and contractile force, and thus reducing systemic blood pressure. In higher brain centres such as the hypothalmus and cerebral cortex, some non-routine regulation of arterial pressure can occur via relays to the medulla centres. For example, if someone where talking to a person who makes them anxious, the hypothalmus could initiate a significant rise in blood pressure.

Another short-term control of MAP is via hormonal controls affecting peripheral resistance via hormones including Angiotensin II (arteriole vasoconstriction), antidiuretic hormone (ADH), atrial natriuretic peptide (ANP), and adrenal medulla hormones (epinephrine, norepinephrine). Interestingly, nicotine can stimulate large releases of the adrenal medulla hormones, causing intense vasoconstriction.

E.1.3.4.2 Long-term controls

The principle long-term regulation of MAP is via renal mechanisms. Blood volume is regulated close to 5L in a healthy person (dependent on age, body size, and sex). Baroreceptors can adapt to high or low blood pressure if prolonged (chronic), and they are thus inadequate for long-term control. In general, an increase in blood volume goes hand in hand with an increase in blood pressure, and similarly MAP decreases following a blood volume decrease. However, renal mechanisms such as elimination of water are used to keep blood volume and thus pressure within the desired range. Direct renal mechanisms stabilise blood volume whereby an increase in blood volume or blood pressure increases the rate at which fluid filters from the bloodstream into the kidney tubules. Since the kidneys cannot process the filtrate rapidly enough more is excreted in urine. This reduces MAP and blood volume (BV). In the opposite case of a decrease in MAP and BV, more water is conserved and returned to the bloodstream, increasing MAP and BV. Indirect renal mechanisms regulate blood volume via hormonal controls. In the event of inadequate renal perfusion, the kidneys release renin after being probed by the baroreceptors, a catalyst cascade resulting in the formation of Angiotensin II, stimulating the release of aldosterone (from the adrenal cortex), and ADH, both enhancing BV and thus MAP. Finally, to reduce BV and MAP, ANP antagonises ADH (from the posterior pituitary) and influences the kidneys to excrete more water and sodium from the body. A full illustration of the short-term and long-term MAP control can be seen in Figure E.1.3.

E.2 Introduction to the Human Nervous System

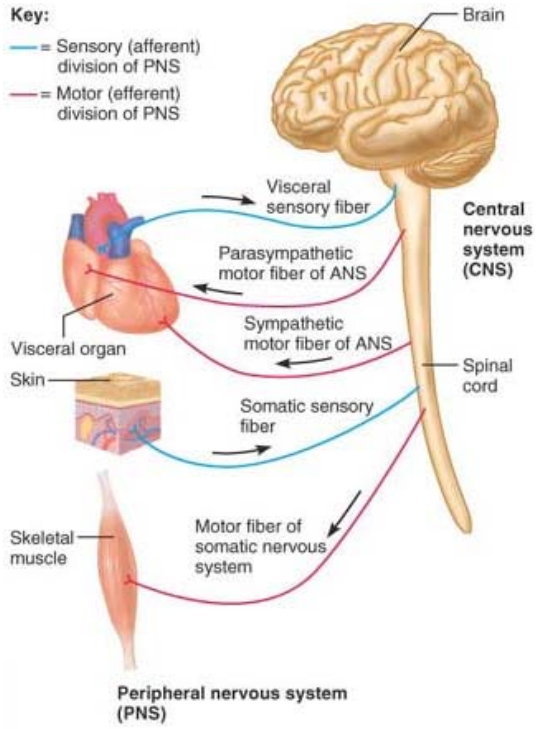

Figure E.2.1: Subdivisions of the human nervous system: CNS and PNS. (Reproduced from Marieb and Hoehn, 2006d)

The human nervous system controls and coordinates all the actions and reactions of the body. For this control a central command station is required known as the central nervous system (CNS) comprising the brain and spinal cord. Emanating from this is the peripheral nervous system (PNS). These systems work together gathering sensory input, integrating (processing and interpreting inputs) these inputs and finally making decisions on an appropriate response or motor output.

More specifically the CNS dictates motor responses based on reflexes, past experiences, and current inputs. Since the application of the optical brain-computer interface developed was as a communication aid for the severely disabled and since this device would be used to bypass the normal output pathways of the brain, the main impetus of physiological background of the nervous system will be on the brain of the CNS alone. However, a brief overview of the PNS is given next.

E.2.1 Peripheral Nervous System (PNS)

Bundles of axons or nerves protrude from the brain and spinal cord (CNS). Cranial nerves carrying impulses to and from the brain, and spinal nerves conducting impulses to and from the spinal cord connect all body parts in a highly integrated communication network. However these nerve fibres are specialised and some divisions of labour are shown in Figure

E.2.1. Figure E.2.2 below depicts the nerve impulse flow from the CNS to the various subdivisions of the PNS, and from the sensory divisions of the PNS to the CNS.

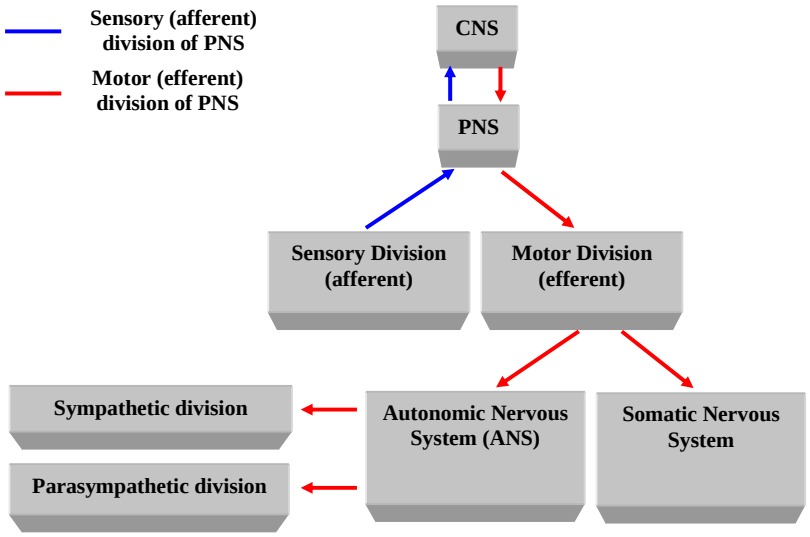

Figure E.2.2: Human nervous system subdivisions and nerve impulse flow direction. (Adapted from Marieb and Hoehn, 2006d)

The sensory afferent *("carrying towards")* division of the PNS carry nerve impulses toward the CNS from sensory receptors throughout the body. Specifically, somatic afferent fibres convey information from the skin, skeletal muscles, and joints. Visceral afferent nerve fibres carry impulses from the organs within the ventral body cavity. The sensory division impulses comprise the inputs to the CNS which it in turn must act on in an integrated manner.

The motor or efferent *("carrying away")* division of the PNS deal with nerve impulse traffic in the opposite direction: impulses from the CNS to the effector organs (glands and muscles). Impulses in this division control muscle movements and secretion of glands. The motor division however can be further classified and divided depending on whether the motor control is voluntary or not.

The somatic nervous system, also known as the voluntary nervous system, comprises axons (nerve fibres) which conducts the efferent impulses from the CNS to the skeletal muscles.

On the other hand, the autonomic nervous system (ANS) deals with the involuntary controls (aka involuntary nervous system). Cardiac muscles, smooth muscles (e.g. in blood vessels), and gland activity are modulated by axons in this system which is not under conscious control (e.g. heart beating). As mentioned in dealing with blood pressure, the ANS

is subdivided into the sympathetic and parasympathetic divisions. These tend to work in opposition, whereby the sympathetic division mobilises body systems such as constricting blood vessels to increase the mean arterial blood pressure, the parasympathetic division on the other hand is called into action to conserve energy and promotes regulation mechanisms during rest.

E.2.1.1 Neural Processing

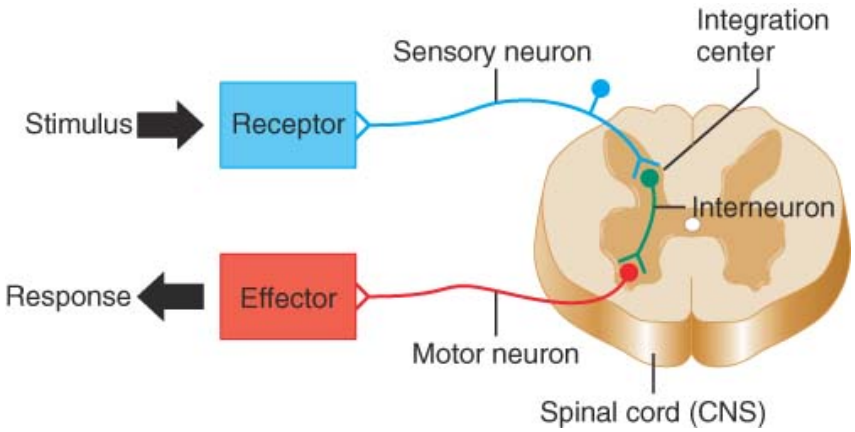

Figure E.2.3: Simple reflex arc. Five key components for processing a stimulus (input) are: the receptor; sensory neuron; CNS integration centre; motor neuron; and the effector (muscles or glands), producing a response. (Reproduced from Marieb and Hoehn, 2006d)

There are two methods of processing an input (stimulus): either serially or in parallel. In serial processing the impulse travels along one pathway. In parallel processing the input will travel multiple paths eventually integrated in different regions of the CNS. In general it is the brain's capability of parallel processing which makes it immensely powerful, although serial processing has its advantages.

Serial processing tends to involve spinal reflexes, although there are sensory straight-through pathways to the brain also. The reflex is the functional unit of the nervous system and is an automatic response to an input stimulus. It is highly repeatable and robust and contributes significantly to autonomic protection mechanisms of the body e.g. the rapid involuntary pulling of a hand away from a hot surface.

The reflex occurs over neural pathways known as reflex arcs. Five main components of this reflex arc from input stimulus to generating a response can be seen in Figure E.2.3: the receptor, sensory neuron, CNS integration centre, motor neuron, and the effector (muscles or glands). These arcs are known mainly for their somatic involvement (from the skin and muscles) but there are also visceral reflex arcs (with sensory fibres) that deal with irritation, stretch, and chemical changes of the viscera (internal organ). This visceral reflex arc is

similar to that shown in Figure E.2.3 except that it has an additional neuron in its motor component. Visceral pain can be felt as somatic in origin in some cases, since afferent nerve fibres for both somatic and visceral systems travel in the same pathways - a phenomenon known as referred pain. The most common example is from a heart attack where some of the pain is perceived in the medial part of the left arm, since the same spinal segments innervate both the heart and these portions of the left arm.

In parallel processing, the inputs travel into multiple pathways and are simultaneously processed in different parts of the brain, which are then integrated for a response. For example, on seeing something familiar, multiple associations of perhaps fear, perceived smell, and memories would all be simultaneously processed, and a response would be generated from an integration of these individual sub-processes. In addition, these parallel pathways are unique to each individual and the parallel processing is not repetitious since each subcircuit will process the input differently (Marieb and Hoehn, 2006d). This will be important when dealing with volitional thoughts of imaging moving an arm (in main document), which ultimately involves activation of multiple regions of the brain.

The 'top-down' description of the physiology of the brain so far has dealt with all the superficial cerebral layers from outside of the head inwards, and has given a broad overview of the human nervous system. The remainder of this subsection on brain anatomy and physiology will deal with the brain itself and the CNS, in particular giving an account of the cerebral cortex, since it is the main investigatory element in the optical measurements made.

E.3 Low-level structure and function of the nervous system

The nervous system is made up of mostly nervous tissue with extracellular space making up less than 20% of the CNS. The densely packed, highly cellular system is made up of only two cell types: supporting cells and neurons. The supporting cells are smaller than neurons and swaddle them providing structural support, whereas neurons transmit electrical signals throughout the nervous system.

E.3.1 Neuroglia - supporting cells

Neuroglia *("nerve glue")* are the cells supporting neurons and there are 6 types: 4 in the CNS (see Figure E.3.1(a)-(d)) and 2 in the PNS (see Figure E.3.1(e)). They function mainly to provide a supportive structure for neurons; however each has its own function. The CNS has astrocytes *("star cells")*, microglia, ependymal cells, and oligodendrocytes and they outnumber neurons by 10 to 1, making up half the mass of the brain (Marieb and Hoehn,

2006d). Astrocytes are the most abundant type in the CNS and as shown in Figure E.3.1(a) processes radiate from the cell body and cling to nearby neurons and the blood capillaries that the neurons exploit for nourishment. Astrocytes function is for neuron support, exchange between neurons and capillaries, synapse formation, determining capillary permeability, recycling released neurotransmitters, and removing leaked potassium ions. Microglial cells act as the pseudo-immune system of the brain since cells of the immune system of the body are not allowed into the CNS. They monitor the health of neurons and can transform to phagocytise dead neurons and invading microorganisms. Ependymal *("wrapping garment")* cells line the central cavities of the brain and spinal cord enforcing a permeable barrier between the CSF and the fluid bathing the brain tissue. Their cilia help in the circulation of CSF in the subarachnoid space and other cavities. Finally the oligodendrocytes *("few-branch-cells")* wrap themselves around thicker neuron fibres generating insulation in the form of myelin sheaths (discussed in section E.3.2). The two neuroglial cell types of the PNS are the satellite cells and Schwann cells. Satellite cells surround the neuron cell bodies, and the Schwann cells surround larger nerve fibres forming myelin sheaths for insulation - but this time in the PNS as shown in Figure E.3.1(e). They are also important to the regeneration of nerve fibres in the PNS.

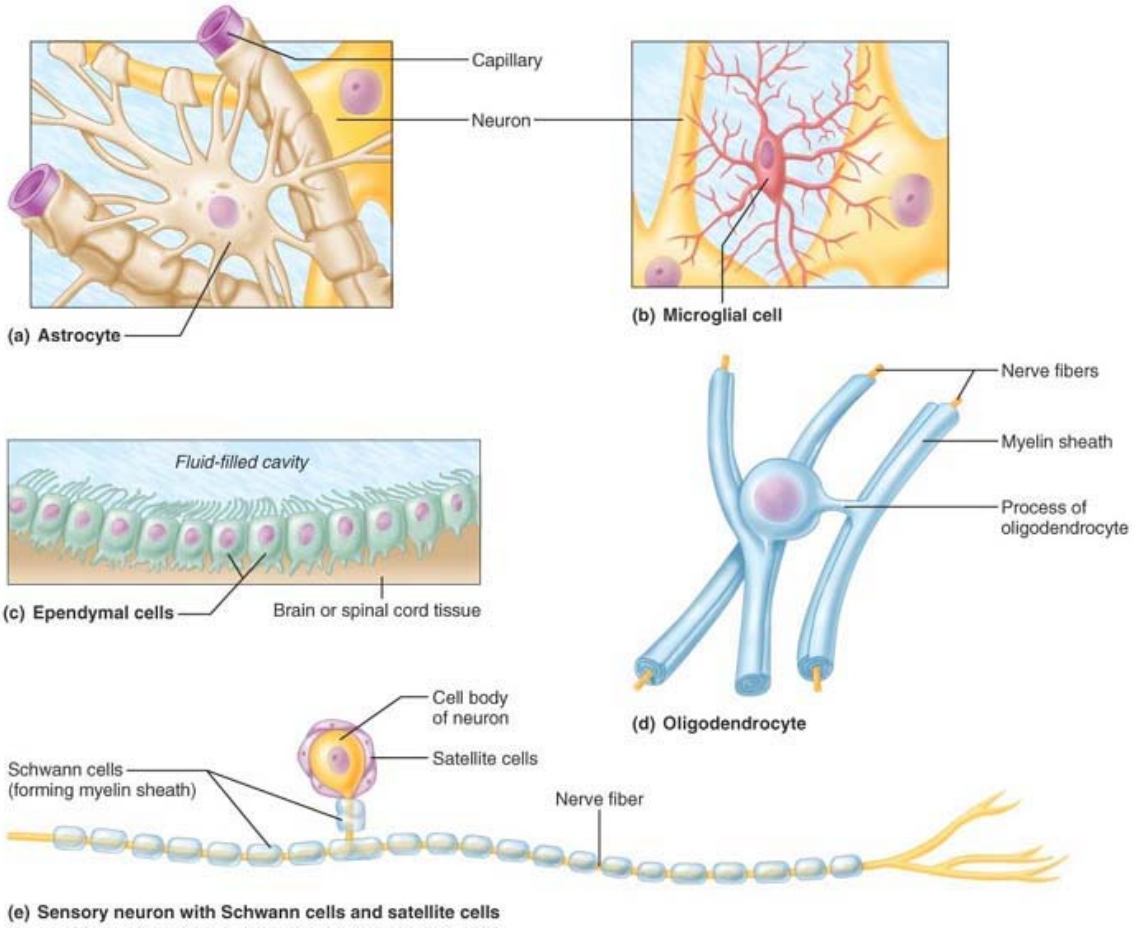

Figure E.3.1: Four types of supporting cells of the central nervous system. Neuroglia are smaller than neurons and outnumber them by 10 to 1, making up half the mass of the brain (Reproduced from Marieb and Hoehn, 2006d).

E.3.2 Neurons - excitatory cells

Neurons are the excitatory units in the circuitry of the human nervous system. Billions of them are found there, most in the CNS. There are various structural types of neurons as seen in Figure E.3.2. Common between the different types however, are a cell body and one or more outgrowths from this body. Apart from a few exceptions (relating to memory and smell regions), neurons are unable to divide once in place in communication links of the nervous system, and so they cannot be replaced once they die. They are highly metabolic requiring a continuous supply of oxygen and glucose, and can only survive a few minutes without oxygen. The plasma membrane of the neuron is the site of electrical signalling, where most neurons both accept and transmit impulses. The main components of the neuron-to-neuron chain are the cell body, the axon, dendrites, and synapses with myelination on some nerves.

Cell bodies of neurons are mostly found housed in the protective skull and vertebral column, and clusters of these in the CNS are called nuclei, whereas clusters in the PNS along nerves are called ganglia *("knot on a string")*. Two types of outgrowths or processes can

extend from these cell bodies: axons and/or dendrites. These processes differ in function and structure.

Dendrites are generally short with diffuse branching (as in Figure E.3.2), increasing the surface area for neighbouring neurons to link to. They are the receiver/input branches for the neuron, transmitting graded potentials (not action potentials) toward the cell body (discussed in section #). The ends of these dendrite branches thorn-outward with bulbous or spiky ends called dendritic spines. Synapses at these spines are where other neurons in close contact can transmit signals toward its neuron.

On the other hand each neuron has only one axon leaving its cell body (as in Figure E.3.2) and generally axons are the output branch that the cell body uses, conducting nerve impulses (action potentials) away from the cell body. Axons can be long or short, with long types known as nerve fibres, such as the 3-4 foot axon for the motor neuron extending from the big toe to the lumbar region of the spine. Axons do also have sub-branches called axon collaterals, but different to dendrites, they generally branch at right angles. The axon and its sub-branches also branch even more diffusely (10,000 or more) at their end, called telodendria. These telodendria have knoblike ending called synaptic knobs where the carried signal prepares for chemical transfer to the neighbouring neuron (or neighbouring neuron process). Under the influence of the incoming axonal signal, neurotransmitters are released into the extracellular space from vesicles at these synaptic knobs. These chemicals either excite or inhibit the neighbouring neurons (or effector cells) close to the knobs. Each neuron can simultaneously transmit to multiple neighbouring neurons due to the diffuse ending and surface area at the axon's end.

The synapse *(greek - syn "to join")* where neurotransmitters impose how the signal will continue can occur between; axons and cell bodies; and, axons and dendrites#. More uncommon are those between axons, between dendrites, and between dendrites and cell bodies. Some synapses however, provide electrical coupling, and are very rapid, such as those for jerky movements of the eyes and some for memory. Most are chemical synapses, facilitating the release and reception of neurotransmitters. Presynaptic and postsynaptic neuron's endings are spatially separated by a synaptic cleft (30-50um wide) filled with fluid. The axonal electrical signal is transduced to a chemical one via neurotransmitters, and back to an electrical signal at the postsynaptic cells.

The final major aspect of neurons is the selected myelination of certain nerve fibres (only axons). Long or thick fibres generally have a thick, fatty, and segmented white sheath called myelin sheath. These sheaths are produced by the neuroglia as mention in section

E.3.1- Schwann cells in the PNS and oligodendrocytes in the CNS. The function of these sheaths is for added protection, electrical insulation, and increasing the speed of the impulses travelling in the underlying nerve fibres. In the PNS gaps called nodes of Ranvier between the segments of myelin sheath of the fibres (~1mm) allow the axon collaterals to branch off the axon. In contrast, CNS myelination by oligodendrocytes can engulf up to 60 axons rather than one with wider spaced nodes. White matter of the brain and spinal cord are where myelination occurs in dense regions, usually primary fibre tracts.

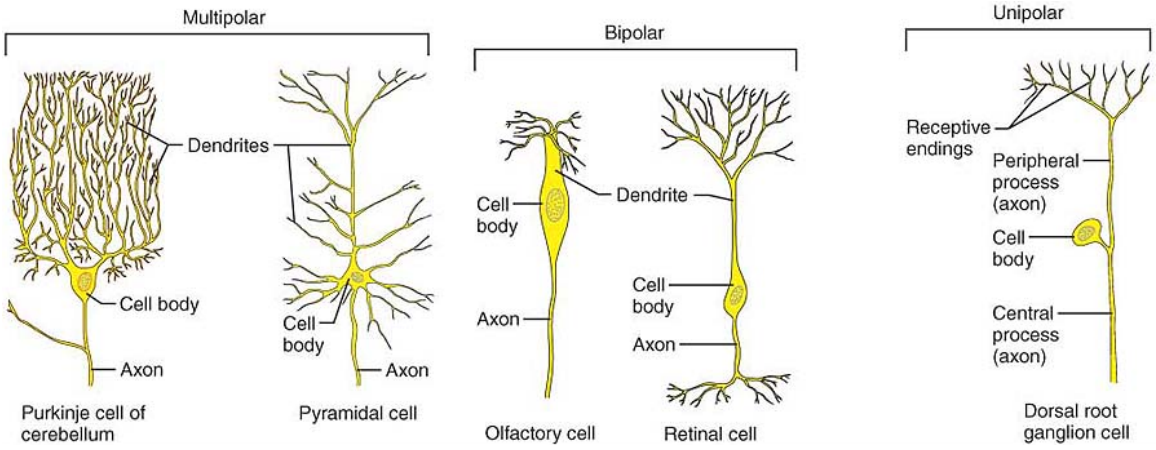

Figure E.3.2: Structural variations in neuron cell types. (Reproduced from Marieb and Hoehn, 2006d)

So in summary, the CNS is made of many neurons with cell bodies and processes. Conduction is mostly via axons and receiving signals via dendrites and cell bodies, with mostly chemical transducing of the electrical events at gaps between neurons called synapses.

Some of the major types of neurons as depicted in Figure E.3.2 are classified by structure and function. In terms of structure, neurons are classified depending on the number of processes coming from its cell body. As illustrated in Figure E.3.2, multipolar neurons have 3 or more processes leaving its cell, one of which is the axon. 99% of all neurons in the body are multipolar but vary in the dendritic pattern and length of processes. Most are interneurons conducting impulses within the CNS and some are motor neurons conducting along efferent pathways to muscles and glands. Bipolar neurons have one axon and one dendrite, found in special senses such as those from the retina of the eye and smell related receptors. These are generally sensory neurons. Unipolar or pseudounipolar neurons have a single process which splits into a t-junction of 2 processes: the central process and peripheral process, which are collectively known as the axon (no dendrites but they have sensory receptor endings). These are found in the PNS in afferents carrying impulses to the CNS.

Functionally, neurons can be sensory neurons, interneurons, or motor neurons. They are classified according to the direction of nerve impulse flow relative to the CNS. Sensory neurons carry impulses toward the CNS from sensory receptors of the periphery. Motor neurons carry impulse away from the CNS to muscles and glands. They are multipolar and their cell bodies are found within the CNS, apart from those of the ANS. Interneurons reside between motor and sensory neurons. They are responsible for nerve impulses within the CNS for integration, and most are multipolar as shown in Figure E.3.2 in the cerebellum and the pyramidal neurons discussed when considering the cerebral cortex lamination. Again, they make up most (99%) of the neurons of the body.

E.3.3 Neuronal activity

Last in the histological study of nervous tissue is a brief look at how neurons are involved in generating and conducting electrical signals. Although the human body is electrically neutral, different regions of the body may have some potential difference or voltage. Depending on the neuron type, a -40mV to -90mV (typically -70mV) potential exists at rest within the axon of the neuron, in reference to the surrounding extracellular space - the potential across the plasma membrane. This potential exists due to sodium and potassium ion gradients facilitated by intrinsic leakage diffusion and ATP-driven sodium-potassium pumps across the plasma membrane of the neuron. Thus, with this potential across the fatty cell plasma membrane, the neuron is said to be polarised.

Neurons are prone to being excited, and this can be a result of either a change in ion concentrations either side of the plasma membrane of the neuron, or a change in the permeability of the localised plasma membrane to ions, e.g potassium. The mode of communication for neurons is principally by alterations in the permeability of the membrane. This results in two possible signal types: graded potentials or action potentials. Graded potentials usually propagate over short distances, whereas action potentials (or nerve impulses) travel long distances down axons.

These potentials can either become more negative or less negative that the cell resting potential of ~-70mV. Thus, depolarisation is a reduction in the plasma membrane potential (towards zero and above), whereas hyperpolarisation is an increase (more negative) in this potential, e.g. from -70mV to -80mV.

Graded potentials are so called since their magnitude changes in proportion to stimulus strength. The resulting current flow reduces with distance from the localised stimulus, and so the stronger the stimulus, the further the current flow. These short millimeter potentials give rise to the long distance action potentials. Graded potentials giving rise to local currents

spread towards the axon from the dendritic and cell body membranes, whereby in many neurons, action potentials are then generated under the influence of these currents at the axon hillock (area between the cell body and the axon). Nevertheless, these local currents must exceed a certain threshold for the action potential to fire. The action potential is the same each time it is created: either it fires or it doesn't - known as the all-or-nothing phenomenon. In essence, once created it is independent of the stimulus strength.

The action potential is a reversal of potential of about 100mV (~from -70mV to +30mV) over a very brief period of 2-5msec. In this time there is a depolarisation phase from -70mV to +30mV, followed by a return to resting potential of -70mV, and finally a hyperpolarisation from -70mV to ~-80mV. This action potential spike is mainly produced as a result of a rapid influx of sodium ions at a focal area of the membrane. This produces local currents that open voltage gated channels in neighbouring membrane regions, whereby the action potential self-propagates down the axon from the axon hillock towards the axon terminals - like a domino effect. As a result, unlike the graded potential, the action potential doesn't decrease over distance from the initial stimulus. To understand this it can be said that the neuron itself is a poor conductor with decreases in current over distance, due to the membrane leaking ions to restore the resting membrane potential. In effect, the action potential is newly created at each adjacent membrane patch allowing the nerve impulse to propagate down the axon, rather than it actually conducting the impulse.

The CNS is able to interpret stimulus strength from the frequency of action potentials and not from the amplitude of the stimulus. As already mentioned the action potential amplitude is independent of stimulus strength and so it is the frequency of action potentials that is proportional to stimulus strength. So there will be more nerve impulses per unit time with a larger input stimulus. Finally the rate of nerve impulse propagation is determined by the degree of myelination and the axon diameter. The larger the axon diameter is, the less opposition to current flow and thus the faster the propagation. Myelination produces propagation of about 30 times that of unmyelinated fibres. Whereas unmyelinated fibres produce action potentials at each adjacent membrane patch, myelinated fibres only allow these to be generated at the nodes of Ranvier (the gaps between the myelinated segments of fibre - see section E.3.2). These occur every 1mm of axon, and the myelination acts as an insulator, limiting the ion exchange and thus current flow to these nodes. Group A fibres have the largest diameter and thickest myelination with speeds up to 150m/s - mostly in somatic sensory and motor fibres. Group B fibres with intermediate myelination and diameter size serving visceral organs and others propagate at 15m/s, with thin, unmyelinated Group C fibres pacing at 1m/s.

APPENDIX F

GLOSSARY

Term	Etymology	Comparative Meaning	Main Relevance
Inferior	Latin *īnferior* - lower	Below	Relative position reference
Superior	Latin *superus* - being above\over	Above	Relative position reference
Lateral	Latin *laterālis* - belonging to the side	To one side	Relative position reference
Ipsilateral	Latin *ipse* same; *latus* side	On the same side	Relative position reference
Contralateral	Latin *contra* against\ opposite; *latus* side	On the opposite side	Relative position reference
Dorsal	Latin *dorsum* - back	Toward the back or upper surface	Relative position reference
Ventral	Latin *venter* - abdomen	Toward the belly	Relative position reference
Anterior	Latin *ante* - before	Toward the front	Relative position reference
Posterior	Latin *post* - after	Toward the back	Relative position reference
Proximal	Latin *proximus* - nearest	Closest to main body unit, e.g. the shoulder	Relative position reference
Distal	Latin *distare* - to be distant	Farthest from main body unit e.g. the end tips of the hand	Relative position reference
Cranial	Greek *kranion* - skull		Relative position reference
Caudal	Latin *caudum* - tail	Same as inferior NOT posterior (in humans)	Relative position reference
Superficial	Latin *superficialis* - of or pertaining to the surface	Being at or near the surface	Relative position reference
Visceral\Deep		A long way inward	Relative position reference
Intermediate		In the middle of the range	Relative position reference

Parietal	Latin *parietalis* - of walls	Pertaining to the wall of a body part\cavity	Relative position reference
Basal		Forming the base	Relative position reference
Peripherial		On the periphery\ boundary	Relative position reference
Medial			Relative position reference
Sinister	Latin *sinister* - left	Towards the left	Relative position reference
Dexter	Latin *dexter* - right	Towards the right	Relative position reference
Palmar		In the direction of the palm	Relative position reference
Sagittal Plane		Splitting body into left and right halves	Plane of view. MRI imaging
Coronal Plane		Splitting body into front and back halves	Plane of view. MRI imaging
Transverse\Axial Plane		Splitting body into upper and lower halves	Plane of view. MRI imaging

REFERENCES

Allison, B. Z., McFarland, D. J., Schalk, G., Zheng, S. D., Jackson, M. M. and Wolpaw, J. R. (2008). "Towards an independent brain-computer interface using steady state visual evoked potentials." *Clin Neurophysiol* **119**(2): 399-408.

Allison, B. Z. and Pineda, J. A. (2003). "ERPs evoked by different matrix sizes: implications for a brain computer interface (BCI) system." *IEEE Trans Neural Syst Rehabil Eng* **11**(2): 110-3.

Allison, B. Z., Wolpaw, E. W. and Wolpaw, J. R. (2007). "Brain-computer interface systems: progress and prospects." *Expert Rev Med Devices* **4**(4): 463-74.

ALS_Association. (2008, Sept). "ALS Association." Retrieved 6th May, 2008, from http://www.alsa.org/als/.

Angelakis, E., Hatzis, A., Panourias, I. G. and Sakas, D. E. (2007). "Brain-computer interface: a reciprocal self-regulated neuromodulation." *Acta Neurochir Suppl* **97**(Pt 2): 555-9.

Aoyagi, T., Kishi, T., Yamaguchi, K. and Wantanabe, S. (1974). Improvement of ear-piece oximeter. *In: Abstracts of the 13th annual meeting of the Japanese Society for Medical Electronics and Biological Engineering*, Osaka.

Bauer, G., Gerstenbrand, F. and Rumpl, E. (1979). "Varieties of the locked-in syndrome." *Journal of Neurology* **221**(2): 77-91.

Bauernfeind, G., Leeb, R., Wriessnegger, S. C. and Pfurtscheller, G. (2008). "Development, set-up and first results for a one-channel near-infrared spectroscopy system / Entwicklung, Aufbau und vorlaufige Ergebnisse eines Einkanal- Nahinfrarot-Spektroskopie-Systems." *Biomed Tech (Berl)* **53**(1): 36-43.

Benaron, D. A., Hintz, S. R., Villringer, A., Boas, D., Kleinschmidt, A., Frahm, J., Hirth, C., Obrig, H., van Houten, J. C., Kermit, E. L., Cheong, W. F. and Stevenson, D. K. (2000).

"Noninvasive functional imaging of human brain using light." *J Cereb Blood Flow Metab* **20**(3): 469-77.

Berger, H. (1929). "Über das Elektroenkephalogramm des Menschen." *Archiv für Psychiatrie und Nervenkrankheiten* **87**: 527-570.

Berne, R. M. and Levy, M. N. (2000). *Cardiovascular Physiology*, Mosby.

Beverina, F., Palmas, G., Silvoni, S., Piccione, F. and Giove, S. (2003). "User adaptive BCIs: SSVEP and P300 based interfaces." *PsychNology Journal* **1**(4): 331-354.

Birbaumer, N. (2006). "Breaking the silence: brain-computer interfaces (BCI) for communication and motor control." *Psychophysiology* **43**(6): 517-32.

Birbaumer, N. and Cohen, L. G. (2007). "Brain-computer interfaces: communication and restoration of movement in paralysis." *J Physiol* **579**(Pt 3): 621-36.

Birbaumer, N., Ghanayim, N., Hinterberger, T., Iversen, I., Kotchoubey, B., Kubler, A., Perelmouter, J., Taub, E. and Flor, H. (1999). "A spelling device for the paralysed." *Nature* **398**(6725): 297-8.

Birbaumer, N., Kubler, A., Ghanayim, N., Hinterberger, T., Perelmouter, J., Kaiser, J., Iversen, I., Kotchoubey, B., Neumann, N. and Flor, H. (2000). "The thought translation device (TTD) for completely paralyzed patients." *IEEE Transactions on Rehabilitation Engineering* **8**(2): 190-193.

Blankertz, B. (2008, 24th June 2008). "BCI Competitions." from http://ida.first.fraunhofer.de/projects/bci/competitions/.

Blankertz, B., Dornhege, G., Krauledat, M., Müller, K.-R. and Curio, G. (2007). "The non-invasive Berlin Brain-Computer Interface: Fast acquisition of effective performance in untrained subjects." *Neuroimage* **37**(2): 539-550.

Blankertz, B., Dornhege, G., Lemm, S., Krauledat, M., Curio, G. and Müller, K. (2006). "The Berlin Brain-Computer Interface: Machine learning based detection of user specific brain states." *Journal of Universal Computer Science* **12**(6): 581–607.

Blankertz, B., Losch, F., Krauledat, M., Dornhege, G., Curio, G. and Muller, K. R. (2008). "The Berlin Brain--Computer Interface: accurate performance from first-session in BCI-naive subjects." *IEEE Trans Biomed Eng* **55**(10): 2452-62.

Boon, R. and de Montfort, G. (2004, 24th March). "Stages of Brain Development." Retrieved May, 2009, from http://www.learningdiscoveries.com.au/StagesofBrain Development.htm.

Bozkurt, A. and Onaral, B. (2004). "Safety assessment of near infrared light emitting diodes for diffuse optical measurements." *Biomed Eng Online* **3**(1): 9.

Braitenberg, V. and Schüz, A. (1991). *Anatomy of the cortex : statistics and geometry*. Berlin ; New York, Springer-Verlag.

Buxton, R. B. (2001). "The elusive initial dip." *Neuroimage* **13**(6 Pt 1): 953-8.

Buxton, R. B., Uludag, K., Dubowitz, D. J. and Liu, T. T. (2004). "Modeling the hemodynamic response to brain activation." *Neuroimage* **23 Suppl 1**: S220-33.

Chance, B., Cope, M., Gratton, E., Ramanujam, N. and Tromberg, B. (1998). "Phase measurement of light absorption and scatter in human tissue." *Review of Scientific Instruments* **69**(10): 3457-3481.

Chatterjee, A., Aggarwal, V., Ramos, A., Acharya, S. and Thakor, N. V. (2007). "A brain-computer interface with vibrotactile biofeedback for haptic information." *J Neuroeng Rehabil* **4**: 40.

Cheng, M., Gao, X., Gao, S. and Xu, D. (2002). "Design and implementation of a brain-computer interface with high transfer rates." *IEEE Trans Biomed Eng* **49**(10): 1181-6.

Choi, J., Wolf, M., Toronov, V., Wolf, U., Polzonetti, C., Hueber, D., Safonova, L. P., Gupta, R., Michalos, A., Mantulin, W. and Gratton, E. (2004). "Noninvasive determination of the optical properties of adult brain: near-infrared spectroscopy approach." *J Biomed Opt* **9**(1): 221-9.

Cohen, M. A. and Taylor, J. A. (2002). "Short-term cardiovascular oscillations in man: measuring and modelling the physiologies." *J Physiol* **542**(Pt 3): 669-83.

Colonnier, M. (1966). The structural design of the neocortex. *Brain and Conscious Experience*. J. C. Eccles. New York, Springer-Verlag**:** 1-23.

Cope, M. (1991). The application of NIRS to non-invasive monitoring of cerebral oxygenation in the newborn infant. Medical Physics and Bioengineering London, London. **PhD:** 342.

Cope, M. and Delpy, D. (1988). "System for long-term measurement of cerebral blood and tissue oxygenation on newborn infants by near infra-red transillumination." *Medical and Biological Engineering and Computing* **26**(3): 289-294.

Coyle, S. (2004). An optical brain computer Interface. *Cardiovasc Res*, September.

Coyle, S. (2004). Physiological noise in NIRS implifications for optical brain computer interfacing. *The 26th Annual International Conference of the IEEE Engineering in Medicine and Biology Society* San Francisco.

Coyle, S. (2005). Near-Infrared Spectroscopy for Brain Computer Interfacing. Engineering Kildare, Maynooth. **PhD Thesis** 222.

Coyle, S., Markham, C., Lanigan, W. and Ward, T. (2005). A mechanical mounting system for functional near-infrared spectroscopy brain imaging studies. *Opto-Ireland 2005: Optical Sensing and Spectroscopy*, Dublin, Ireland, SPIE.

Coyle, S., Ward, T. and Markham, C. (2003). Cerebral Blood Flow Changes related to Motor Imagery, using Near-infrared Spectroscopy (NIRS). *World Congress on Medical Physics and Biomedical Engineering* Sydney, Australia.

Coyle, S., Ward, T. and Markham, C. (2007). "Brain-Computer Interface using a simplified funcational near-infrared spectroscopy system." *J Neural Eng* **4**: 219-226.

Coyle, S., Ward, T., Markham, C. and McDarby, G. (2004). "On the suitability of near-infrared (NIR) systems for next-generation brain-computer interfaces." *Physiol Meas* **25**(4): 815-22.

Coyle, S., Ward, T., Markham, C., Roche, B., McDarby, G. and McCloone, S. F. (2003). The Use of Near-Infrared Spectroscopy in Measuring General Autonomic Arousal. *World Congress on Medical Physics and Biomedical Engineering*, Sydney, Australia.

Coyle, S. M., Ward, T. E. and Markham, C. M. (2007). "Brain-computer interface using a simplified functional near-infrared spectroscopy system." *J Neural Eng* **4**(3): 219-26.

Culver, J. P., Siegel, A. M., Franceschini, M. A., Mandeville, J. B. and Boas, D. A. (2005). "Evidence that cerebral blood volume can provide brain activation maps with better spatial resolution than deoxygenated hemoglobin." *Neuroimage* **27**(4): 947-59.

Cutler, M. (1929). "Transillumination as an aid in the diagnosis of breast lesions." *Surgery, Gynecology and Obstetrics* **48**: 721-29.

Daly, J. J. and Wolpaw, J. R. (2008). "Brain-computer interfaces in neurological rehabilitation." *Lancet Neurology* **7**(11): 1032-1043.

Decety, J., Jeannerod, M., Durozard, D. and Baverel, G. (1993). "Central activation of autonomic effectors during mental simulation of motor actions in man." *J Physiol* **461**(1): 549-563.

Dechent, P., Merboldt, K. D. and Frahm, J. (2004). "Is the human primary motor cortex involved in motor imagery?" *Brain Res Cogn Brain Res* **19**(2): 138-44.

Demirer, R. M., Ozerdem, M. S. and Bayrak, C. (2009). "Classification of imaginary movements in ECoG with a hybrid approach based on multi-dimensional Hilbert-SVM solution." *J Neurosci Methods* **178**(1): 214-8.

Dewilde, S., Mees, K., Kiger, L., Lechauve, C., Marden, M. C., Pesce, A., Bolognesi, M. and Moens, L. (2008). "Expression, purification, and crystallization of neuro- and cytoglobin." *Methods Enzymol* **436**: 341-57.

Dornhege, G., Blankertz, B., Curio, G. and Muller, K. R. (2004). "Boosting bit rates in noninvasive EEG single-trial classifications by feature combination and multiclass paradigms." *IEEE Trans Biomed Eng* **51**(6): 993-1002.

Duncan, A., Meek, J. H., Clemence, M., Elwell, C. E., Fallon, P., Tyszczuk, L., Cope, M. and Delpy, D. T. (1996). "Measurement of cranial optical path length as a function of age using phase resolved near infrared spectroscopy." *Pediatr Res* **39**(5): 889-94.

Duncan, A., Meek, J. H., Clemence, M., Elwell, C. E., Tyszczuk, L., Cope, M. and Delpy, D. T. (1995). "Optical pathlength measurements on adult head, calf and forearm and the head of the newborn infant using phase resolved optical spectroscopy." *Phys Med Biol* **40**(2): 295-304.

Edmund_Optics. (2009, 20th August 2009). "RT-830 glass BPF." 2009, from http://www.edmundoptics.com/techsupport/resource_center/product_docs/curv_46082.pdf.

Edvinsson, L., MacKenzie, E. and McCulloch, J. (2002). *Cerebral blood flow and metabolism*, Lippincott Williams & Wilkins Philadelphia, PA.

Elwell, C., Owen-Reece, H., Cope, M., Edwards, A., Wyatt, J., Reynolds, E. and Delpy, D. (1994). "Measurement of changes in cerebral haemodynamics during inspiration and expiration using near infrared spectroscopy." *Advances in Experimental Medicine and Biology* **345**: 619.

Elwell, C. E. (1995). *A practical users guide to near-infrared spectrocopy*. London, UK.

Evarts, E. (1966). "Pyramidal tract activity associated with a conditioned hand movement in the monkey." *Journal of Neurophysiology* **29**(6): 1011-1027.

Everdell, N. L., Gibson, A. P., Tullis, I. D. C., Vaithianathan, T., Hebden, J. C. and Delpy, D. T. (2005). "A frequency multiplexed near-infrared topography system for imaging functional activation in the brain." *Review of Scientific Instruments* **76**(9): -.

Fantini, S., Aggarwal, P., Chen, K. and Franceschini, M. A. (2001). "Monitoring brain activity using near-infrared light." *American Laboratory* **33**(20): 15-+.

Farwell, L. A. and Donchin, E. (1988). "Talking off the top of your head: toward a mental prosthesis utilizing event-related brain potentials." *Electroencephalogr Clin Neurophysiol* **70**(6): 510-23.

Fatourechi, M., Bashashati, A., Ward, R. K. and Birch, G. E. (2007). "EMG and EOG artifacts in brain computer interface systems: A survey." *Clinical Neurophysiology* **118**(3): 480-494.

Ferrari, M., Zanette, E., Giannini, I., Sideri, G., Nicola, A., Agostino, R. and Bucci, G. (1986). "Cerebral blood volume and haemoglobin oxygen saturation monitoring in neonatal brain by near infrared spectroscopy." *Advances in Experimental Medicine and Biology* **200**: 203-212.

Fetz, E. and Finocchio, D. (1975). "Correlations between activity of motor cortex cells and arm muscles during operantly conditioned response patterns." *Experimental Brain Research* **23**(3): 217-240.

Fox, E., Jobsis, F. F. and Mitnick, M. H. (1985). "Monitoring cerebral oxygen sufficiency in anaesthesia and surgery." *Advances in Experimental Medicine and Biology* **191**: 849-854.

Fox, P. and Raichle, M. (1986). "Focal physiological uncoupling of cerebral blood flow and oxidative metabolism during somatosensory stimulation in human subjects." *Proceedings of the National Academy of Sciences* **83**(4): 1140.

Franceschini, M., Fantini, S., Toronov, V., Filiaci, M. and Gratton, E. (2000). Cerebral Hemodynamics Measured by Near-Infrared Spectroscopy at Rest and During Motor Activation. *OSA In-Vivo Optical Imaging Workshop*, Washington, DC, Optical Society of America.

Franceschini, M. A. and Boas, D. A. (2004). "Noninvasive measurement of neuronal activity with near-infrared optical imaging." *Neuroimage* **21**(1): 372-86.

Franceschini, M. A., Fantini, S., Paunescu, L. A., Maier, J. S. and Gratton, E. (1998). "Influence of a superficial layer in the quantitative spectroscopic study of strongly scattering media." *Appl Opt* **37**(31): 7447-58.

Friedland, R. P. and Iadecola, C. (1991). "Roy and Sherrington (1890): a centennial reexamination of "On the regulation of the blood-supply of the brain"." *Neurology* **41**(1): 10-4.

Fuchino, Y., Nagao, M., Katura, T., Bando, M., Naito, M., Maki, A., Nakamura, K., Hayashi, H., Koizumi, H. and Yoro, T. (2008). "High cognitive function of an ALS patient in the totally locked-in state." *Neurosci Lett* **435**(2): 85-9.

Fukui, Y., Ajichi, Y. and Okada, E. (2003). "Monte Carlo prediction of near-infrared light propagation in realistic adult and neonatal head models." *Appl Opt* **42**(16): 2881-7.

Furdea, A., Halder, S., Krusienski, D. J., Bross, D., Nijboer, F., Birbaumer, N. and Kubler, A. (2009). "An auditory oddball (P300) spelling system for brain-computer interfaces." *Psychophysiology*.

Gao, X., Xu, D., Cheng, M. and Gao, S. (2003). "A BCI-based environmental controller for the motion-disabled." *IEEE Transactions on Neural Systems and Rehabilitation Engineering* **11**(2): 137-140.

Garry, D. J., Meeson, A., Yan, Z. and Williams, R. S. (2000). "Life without myoglobin." *Cellular and Molecular Life Sciences (CMLS)* **57**(6): 896-898.

Garry, D. J., Ordway, G. A., Lorenz, J. N., Radford, N. B., Chin, E. R., Grange, R. W., Bassel-Duby, R. and Williams, R. S. (1998). "Mice without myoglobin." *Nature* **395**(6705): 905-908.

Germon, T. J., Evans, P. D., Barnett, N. J., Wall, P., Manara, A. R. and Nelson, R. J. (1999). "Cerebral near infrared spectroscopy: emitter-detector separation must be increased." *Br J Anaesth* **82**(6): 831-7.

Gibson, A. P., Hebden, J. C. and Arridge, S. R. (2005). "Recent advances in diffuse optical imaging." *Phys Med Biol* **50**(4): R1-43.

Girouard, H. and Iadecola, C. (2006). "Neurovascular coupling in the normal brain and in hypertension, stroke, and Alzheimer disease." *J Appl Physiol* **100**(1): 328-35.

Gratton, G., Fabiani, M., Corballis, P. M., Hood, D. C., Goodman-Wood, M. R., Hirsch, J., Kim, K., Friedman, D. and Gratton, E. (1997). "Fast and localized event-related optical signals (EROS) in the human occipital cortex: comparisons with the visual evoked potential and fMRI." *Neuroimage* **6**(3): 168-80.

Gu, Y., Dremstrup, K. and Farina, D. (In Press, Corrected Proof). "Single-trial discrimination of type and speed of wrist movements from EEG recordings." *Clinical Neurophysiology* **In Press, Corrected Proof**.

Guan, J., Chen, Y., Lin, J., Yuan, Y. and Huang, M. (2005). N2 components as features for brain computer interface.

Guger, C., Daban, S., Sellers, E., Holzner, C., Krausz, G., Carabalona, R., Gramatica, F. and Edlinger, G. (In Press, Uncorrected Proof). "How many people are able to control a P300-based brain-computer interface (BCI)?" *Neurosci Lett* **In Press, Uncorrected Proof**.

Guger, C., Edlinger, G., Harkam, W., Niedermayer, I. and Pfurtscheller, G. (2003). "How many people are able to operate an EEG-based brain-computer interface (BCI)?" *IEEE Trans Neural Syst Rehabil Eng* **11**(2): 145-7.

Haensse, D., Szabo, P., Brown, D., Fauchere, J. C., Niederer, P., Bucher, H. U. and Wolf, M. (2005). "New multichannel near infrared spectrophotometry system for functional studies of the brain in adults and neonates." *Optics Express* **13**(12): 4525-4538.

Hamamatsu_Photonics_K.K. (2009, Sept 2007). "C5460-01 APD Module." 2009, from http://sales.hamamatsu.com/assets/pdf/parts_C/c5460_series_kacc1010e05.pdf.

He, B. J. and Raichle, M. E. (2009). "The fMRI signal, slow cortical potential and consciousness." *Trends Cogn Sci* **13**(7): 302-309.

Held, G. (2008). *Introduction to Light Emitting Diode Technology and Applications*, Auerbach Publications.

Herrmann, M. J., Ehlis, A. C. and Fallgatter, A. J. (2003). "Frontal activation during a verbal-fluency task as measured by near-infrared spectroscopy." *Brain Res Bull* **61**(1): 51-6.

Hinterberger, T., Birbaumer, N. and Flor, H. (2005). "Assessment of cognitive function and communication ability in a completely locked-in patient." *Neurology* **64**(7): 1307-8.

Hinterberger, T., Neumann, N., Pham, M., Kubler, A., Grether, A., Hofmayer, N., Wilhelm, B., Flor, H. and Birbaumer, N. (2004). "A multimodal brain-based feedback and communication system." *Exp Brain Res* **154**(4): 521-6.

Hinterberger, T., Schmidt, S., Neumann, N., Mellinger, J., Blankertz, B., Curio, G. and Birbaumer, N. (2004). "Brain-computer communication and slow cortical potentials." *IEEE Trans Biomed Eng* **51**(6): 1011-8.

Hirth, C., Obrig, H., Villringer, K., Thiel, A., Bernarding, J., Muhlnickel, W., Flor, H., Dirnagl, U. and Villringer, A. (1996). "Non-invasive functional mapping of the human motor cortex using near-infrared spectroscopy." *Neuroreport* **7**(12): 1977-81.

Hochberg, L. R., Serruya, M. D., Friehs, G. M., Mukand, J. A., Saleh, M., Caplan, A. H., Branner, A., Chen, D., Penn, R. D. and Donoghue, J. P. (2006). "Neuronal ensemble control of prosthetic devices by a human with tetraplegia." *Nature* **442**(7099): 164-71.

Horecker, B. (1943). "The absorption spectra of hemoglobin and its derivatives in the visible and near infrared regions." *Journal of Biological Chemistry* **148**: 173-83.

Hoshi, Y., Onoe, H., Watanabe, Y., Andersson, J., Bergström, M., Lilja, A., Långstöm, B. and Tamura, M. (1994). "Non-synchronous behavior of neuronal activity, oxidative metabolism and blood supply during mental tasks in man." *Neurosci Lett* **172**(1-2): 129-133.

Hoshi, Y. and Tamura, M. (1997). "Fluctuations in the cerebral oxygenation state during the resting period in functional mapping studies of the human brain." *Med Biol Eng Comput* **35**(4): 328-30.

Hudetz, A., Biswal, B., Shen, H., Lauer, K. and Kampine, J. (1998). "Spontaneous fluctuations in cerebral oxygen supply. An introduction." *Advances in Experimental Medicine and Biology* **454**: 551.

Huppert, T. J. and Boas, D. (2006). "HomER: NIRS data analysis software." Retrieved 28th May 2007, from http://www.nmr.mgh.harvard.edu/PMI/resources/homer/home.htm.

Huppert, T. J., Hoge, R. D., Diamond, S. G., Franceschini, M. A. and Boas, D. A. (2006). "A temporal comparison of BOLD, ASL, and NIRS hemodynamic responses to motor stimuli in adult humans." *Neuroimage* **29**(2): 368-82.

Ito, Y., Kennan, R. P., Watanabe, E. and Koizumi, H. (2000). "Assessment of heating effects in skin during continuous wave near infrared spectroscopy." *J Biomed Opt* **5**(4): 383-90.

Jackson, M., Mason, S. and Birch, G. (2006). "Analyzing Trends in Brain Interface Technology: A Method to Compare Studies." *Ann Biomed Eng* **34**(5): 859-878.

Jacobson, S. and Marcus, E. M. (2008). Cerebral Cortex Functional Localization. *Neuroanatomy for the Neuroscientist***:** 189-217.

Jasdzewski, G., Strangman, G., Wagner, J., Kwong, K. K., Poldrack, R. A. and Boas, D. A. (2003). "Differences in the hemodynamic response to event-related motor and visual paradigms as measured by near-infrared spectroscopy." *Neuroimage* **20**(1): 479-88.

Jobsis, F. F. (1977). "Noninvasive, infrared monitoring of cerebral and myocardial oxygen sufficiency and circulatory parameters." *Science* **198**(4323): 1264-7.

Joseph, D. K., Huppert, T. J., Franceschini, M. A. and Boas, D. A. (2006). "Diffuse optical tomography system to image brain activation with improved spatial resolution and validation with functional magnetic resonance imaging." *Appl Opt* **45**(31): 8142-51.

Julien, C. (2006). "The enigma of Mayer waves: Facts and models." *Cardiovasc Res* **70**(1): 12-21.

Kauhanen, L., Nykopp, T., Lehtonen, J., Jylanki, P., Heikkonen, J., Rantanen, P., Alaranta, H. and Sams, M. (2006). "EEG and MEG brain-computer interface for tetraplegic patients." *IEEE Trans Neural Syst Rehabil Eng* **14**(2): 190-3.

Kauhanen, L., Nykopp, T. and Sams, M. (2006). "Classification of single MEG trials related to left and right index finger movements." *Clin Neurophysiol* **117**(2): 430-9.

Kelly, S. P., Lalor, E. C., Reilly, R. B. and Foxe, J. J. (2005). "Visual spatial attention tracking using high-density SSVEP data for independent brain-computer communication." *IEEE Trans Neural Syst Rehabil Eng* **13**(2): 172-8.

Kennan, R., Horovitz, S., Maki, A., Yamashita, Y., Koizumi, H. and Gore, J. (2002). "Simultaneous recording of event-related auditory oddball response using transcranial near infrared optical topography and surface EEG." *Neuroimage* **16**(3): 587-592.

Kennedy, P. R. (1989). "The cone electrode: a long-term electrode that records from neurites grown onto its recording surface." *J Neurosci Methods* **29**(3): 181-93.

Kennedy, P. R., Bakay, R. A., Moore, M. M., Adams, K. and Goldwaithe, J. (2000). "Direct control of a computer from the human central nervous system." *IEEE Trans Rehabil Eng* **8**(2): 198-202.

Kennedy, P. R. and Bakay, R. A. E. (1997). "Activity of single action potentials in monkey motor cortex during long-term task learning." *Brain Res Cogn Brain Res* **760**(1-2): 251-254.

Kennedy, P. R., Kirby, M. T., Moore, M. M., King, B. and Mallory, A. (2004). "Computer control using human intracortical local field potentials." *IEEE Trans Neural Syst Rehabil Eng* **12**(3): 339-44.

Kennedy, P. R., Mirra, S. S. and Bakay, R. A. (1992). "The cone electrode: ultrastructural studies following long-term recording in rat and monkey cortex." *Neurosci Lett* **142**(1): 89-94.

Kiernan, M. C. (2009). "Identification of cognitive deficits in amyotrophic lateral sclerosis." *Clinical Neurophysiology* **120**(4): 645-646.

Klobassa, D. S., Vaughan, T. M., Brunner, P., Schwartz, N. E., Wolpaw, J. R., Neuper, C. and Sellers, E. W. (2009). "Toward a high-throughput auditory P300-based brain-computer interface." *Clinical Neurophysiology* **In Press, Corrected Proof**.

Koizumi, H., Yamamoto, T., Maki, A., Yamashita, Y., Sato, H., Kawaguchi, H. and Ichikawa, N. (2003). "Optical topography: practical problems and new applications." *Appl Opt* **42**(16): 3054-62.

Krauledat, M., Dornhege, G., Blankertz, B., Losch, F., Curio, G. and Muller, K. R. (2004). "Improving speed and accuracy of brain-computer interfaces using readiness potential features." *Conf Proc IEEE Eng Med Biol Soc* **6**: 4511-5.

Krepki, R., Curio, G., Blankertz, B. and Müller, K.-R. (2007). "Berlin Brain-Computer Interface--The HCI communication channel for discovery." *International Journal of Human-Computer Studies* **65**(5): 460-477.

Kronegg, J., Chanel, G., Voloshynovskiy, S. and Pun, T. (2007). "EEG-Based Synchronized Brain-Computer Interfaces: A Model for Optimizing the Number of Mental Tasks." *Neural Systems and Rehabilitation Engineering, IEEE Transactions on* **15**(1): 50-58.

Kubler, A., Furdea, A., Halder, S., Hammer, E. M., Nijboer, F. and Kotchoubey, B. (2009). "A brain-computer interface controlled auditory event-related potential (p300) spelling system for locked-in patients." *Ann N Y Acad Sci* **1157**: 90-100.

Lal, T. N., Schroder, M., Hill, N. J., Preissl, H., Hinterberger, T., Mellinger, J., Bogdan, M., Rosen, W., Hoffman, T., Birbaumer, N. and Scholkopf, B. (2005). A brain computer interface with online feedback based on magnetoencephalography. *Proceedings of the 22nd international conference on Machine learning*, Bonn, Germany, ACM.

Lebid, S., O'Neill, R., Markham, C., Ward, T. and Coyle, S. (2004). "Functional Brain Signals: A photon counting system for brain activity monitoring."

Lee, J. H., Ryu, J., Jolesz, F. A., Cho, Z. H. and Yoo, S. S. (2009). "Brain-machine interface via real-time fMRI: Preliminary study on thought-controlled robotic arm." *Neurosci Lett* **450**(1): 1-6.

Lenhardt, A., Kaper, M. and Ritter, H. J. (2008). "An adaptive P300-based online brain-computer interface." *IEEE Trans Neural Syst Rehabil Eng* **16**(2): 121-30.

Leuthardt, E. C., Schalk, G., Wolpaw, J. R., Ojemann, J. G. and Moran, D. W. (2004). "A brain-computer interface using electrocorticographic signals in humans." *J Neural Eng* **1**(2): 63-71.

Lule, D., Kurt, A., Jurgens, R., Kassubek, J., Diekmann, V., Kraft, E., Neumann, N., Ludolph, A. C., Birbaumer, N. and Anders, S. (2005). "Emotional responding in amyotrophic lateral sclerosis." *J Neurol* **252**(12): 1517-24.

Lunn, J. S., Hefferan, M. P., Marsala, M. and Feldman, E. L. (2009). "Stem cells: comprehensive treatments for amyotrophic lateral sclerosis in conjunction with growth factor delivery." *Growth Factors*: 1.

Luo, Q., Nioka, S. and Chance, B. (1996). Imaging on Brain Model by a Novel Optical Probe - Fiber Hairbrush. *Advances in Optical Imaging and Photon Migration*, Orlando, Florida, Optical Society of America TOPS.

Maclean, N. (1978a). The Distribution and Physiology of Haemoglobin. *The Institute of Biology's Studies in Biology no. 93: Haemoglobin*. London, Arnold**:** 72.

Maclean, N. (1978b). Haem and Globin - The Structure of Haemoglobin and its variations. *The Institute of Biology's Studies in Biology no. 93: Haemoglobin*. London, Arnold.

Madsen, P. L. and Secher, N. H. (1999). "Near-infrared oximetry of the brain." *Progress in Neurobiology* **58**(6): 541-560.

Margalit, E., Weiland, J., Clatterbuck, R., Fujii, G., Maia, M., Tameesh, M., Torres, G., D'Anna, S., Desai, S. and Piyathaisere, D. (2003). "Visual and electrical evoked response recorded from subdural electrodes implanted above the visual cortex in normal dogs under two methods of anesthesia." *Journal of Neuroscience Methods* **123**(2): 129-137.

Marieb, E. N. and Hoehn, K. (2006a). The cardiovascular system: blood vessels *Human Anatomy and Physiology*, Benjamin Cummings.

Marieb, E. N. and Hoehn, K. (2006b). The respiratory system. *Human Anatomy and Physiology*, Benjamin Cummings.

Marieb, E. N. and Hoehn, K. (2006c). The integumentary system. *Human Anatomy and Physiology*, Benjamin Cummings.

Marieb, E. N. and Hoehn, K. (2006d). Fundamentals of the nervous system and nervous tissue. *Human Anatomy and Physiology*, Benjamin Cummings.

Marieb, E. N. and Hoehn, K. (2006e). The central nervous system. *Human Anatomy and Physiology*, Benjamin Cummings.

Mason, S., Jackson, M. and Birch, G. (2005). "A General Framework for Characterizing Studies of Brain Interface Technology." *Ann Biomed Eng* **33**(11): 1653-1670.

Mason, S. G., Bashashati, A., Fatourechi, M., Navarro, K. F. and Birch, G. E. (2007). "A comprehensive survey of brain interface technology designs." *Ann Biomed Eng* **35**(2): 137-169.

Matthews, F., Pearlmutter, B. A., Ward, T. E., Soraghan, C. and Markham, C. (2008). "Hemodynamics for braincomputer interfaces." *Ieee Signal Processing Magazine* **25**(1): 87-94.

Matthews, F., Soraghan, C., Markham, C., Pearlmutter, B. and Ward, T. ((Under Development)). "Spread Spectrum Methods for Optical Modulation in Multichannel NIRS." *Journal of Neural Engineering*.

Matthews, F., Soraghan, C., Ward, T. E., Markham, C. and Pearlmutter, B. A. (2008). Software platform for rapid prototyping of NIRS brain computer interfacing techniques. *Conf Proc IEEE Eng Med Biol Soc*.

Mayhew, J., Askew, S., Zheng, Y., Porrill, J., Westby, G., Redgrave, P., Rector, D. and Harper, R. (1996). "Cerebral vasomotion: a 0.1-Hz oscillation in reflected light imaging of neural activity." *Neuroimage* **4**(3): 183-193.

Mayhew, J. E. W. (2003). "NEUROSCIENCE: A Measured Look at Neuronal Oxygen Consumption." *Science* **299**(5609): 1023-1024.

McFarland, D. J., Sarnacki, W. A. and Wolpaw, J. R. (2008). Electroencephalographic (EEG) control of three-dimensional movement. *Society for Neuroscience*, November, Washington, DC, USA.

Mellinger, J., Schalk, G., Braun, C., Preissl, H., Rosenstiel, W., Birbaumer, N. and Kubler, A. (2007). "An MEG-based brain-computer interface (BCI)." *Neuroimage* **36**(3): 581-93.

Merrick, E. and Hayes, T. (1976). "Continuous, non-invasive measurements of arterial blood oxygen levels." *Hewlett-Packard Journal* **28**: 2-9.

Miller, N. E. (1978). "Biofeedback and visceral learning." *Annu Rev Psychol* **29**: 373-404.

Muehlemann, T., Haensse, D. and Wolf, M. (2008). "Wireless miniaturized in-vivo near infrared imaging." *Opt. Express* **16**(14): 10323-10330.

Muller, N. G. and Knight, R. T. (2006). "The functional neuroanatomy of working memory: contributions of human brain lesion studies." Neuroscience **139**(1): 51-8.

Murphy, K., Secunda, J. and Rockoff, M. (1990). "Severe burns from a pulse oximeter." *Anesthesiology* **73**(2): 350.

Naito, M., Michioka, Y., Ozawa, K., Ito, Y., Kiguchi, M. and Kanazawa, T. (2007). "A communication means for totally locked-in ALS patients based on changes in cerebral blood volume measured with near-infrared light." *Ieice Transactions on Information and Systems* **E90d**(7): 1028-1037.

Nijholt, A. (2009). BCI for Games: A 'State of the Art' Survey. *Entertainment Computing - ICEC 2008***:** 225-228.

Nijholt, A. and Tan, D. (2008). "The state-of-the-art in BCIs." *IEEE Intelligent Systems* **23**(3): 72-74.

Obermaier, B., Neuper, C., Guger, C. and Pfurtscheller, G. (2001). "Information transfer rate in a five-classes brain-computer interface." *IEEE Trans Neural Syst Rehabil Eng* **9**(3): 283-8.

Obrig, H., Neufang, M., Wenzel, R., Kohl, M., Steinbrink, J., Einhaupl, K. and Villringer, A. (2000). "Spontaneous low frequency oscillations of cerebral hemodynamics and metabolism in human adults." *Neuroimage* **12**(6): 623-39.

Obrig, H. and Villringer, A. (2003). "Beyond the Visible-Imaging the Human Brain With Light." *J Cereb Blood Flow Metab* **23**(1): 1-18.

Obrig, H., Wenzel, R., Kohl, M., Horst, S., Wobst, P., Steinbrink, J., Thomas, F. and Villringer, A. (2000). "Near-infrared spectroscopy: does it function in functional activation studies of the adult brain?" *Int J Psychophysiol* **35**(2-3): 125-42.

Ogawa, S., Lee, T. M., Kay, A. R. and Tank, D. W. (1990). "Brain magnetic resonance imaging with contrast dependent on blood oxygenation." *Proc Natl Acad Sci U S A* **87**(24): 9868-72.

Ogawa, T., Tanaka, H. and Hirata, K. (2009). "Cognitive deficits in amyotrophic lateral sclerosis evaluated by event-related potentials." *Clinical Neurophysiology* **120**(4): 659-664.

Okada, E. and Delpy, D. T. (2003). "Near-infrared light propagation in an adult head model. I. Modeling of low-level scattering in the cerebrospinal fluid layer." *Appl Opt* **42**(16): 2906-14.

Okada, E. and Delpy, D. T. (2003). "Near-infrared light propagation in an adult head model. II. Effect of superficial tissue thickness on the sensitivity of the near-infrared spectroscopy signal." *Appl Opt* **42**(16): 2915-22.

Okui, N. and Okada, E. (2005). "Wavelength dependence of crosstalk in dual-wavelength measurement of oxy- and deoxy-hemoglobin." *J Biomed Opt* **10**(1): 11015.

Oldfield, R. (1971). "The assessment and analysis of handedness: the Edinburgh inventory." *Neuropsychologia* **9**(1): 97.

Owen-Reece, H., Smith, M., Elwell, C. E. and Goldstone, J. C. (1999). "Near infrared spectroscopy." *Br J Anaesth* **82**(3): 418-26.

Palaniappan, R. and Mandic, D. (2007). "Biometrics from brain electrical activity: a machine learning approach." *IEEE Transactions on Pattern Analysis and Machine Intelligence*: 738-742.

Patterson, J. R. and Grabois, M. (1986). "Locked-in syndrome: a review of 139 cases." *Stroke* **17**(4): 758-764.

Petersen, M. G., Dewilde, S. and Fago, A. (2008). "Reactions of ferrous neuroglobin and cytoglobin with nitrite under anaerobic conditions." *J Inorg Biochem* **102**(9): 1777-82.

Pfurtscheller, G., Leeb, R., Friedman, D. and Slater, M. (2007). "Centrally controlled heart rate changes during mental practice in immersive virtual environment: A case study with a tetraplegic." *Int J Psychophysiol*.

Pfurtscheller, G., Leeb, R., Keinrath, C., Friedman, D., Neuper, C., Guger, C. and Slater, M. (2006). "Walking from thought." *Brain Res* **1071**(1): 145-52.

Pfurtscheller, G., Leeb, R. and Slater, M. (2006). "Cardiac responses induced during thought-based control of a virtual environment." *Int J Psychophysiol*.

Pfurtscheller, G. and Neuper, C. (1997). "Motor imagery activates primary sensorimotor area in humans." *Neurosci Lett* **239**(2-3): 65-8.

Pfurtscheller, G., Neuper, C. and Birbaumer, N. (2005). Human brain-computer interface. *Motor Cortex in Voluntary Movements. A Distributed System for Distributed Functions*. A. Riehle and E. Vaadia. Boca Raton, Florida, CRC Press**:** 367-401.

Piantadosi, C. A., Hemstreet, T. M. and Jobsis-Vandervliet, F. F. (1986). "Near-infrared spectrophotometric monitoring of oxygen distribution to intact brain and skeletal muscle tissues." *Crit Care Med* **14**(8): 698-706.

Plichta, M. M., Herrmann, M. J., Ehlis, A. C., Baehne, C. G., Richter, M. M. and Fallgatter, A. J. (2006). "Event-related visual versus blocked motor task: detection of specific cortical activation patterns with functional near-infrared spectroscopy." *Neuropsychobiology* **53**(2): 77-82.

Porro, C. A., Cettolo, V., Francescato, M. P. and Baraldi, P. (2000). "Ipsilateral involvement of primary motor cortex during motor imagery." *Eur J Neurosci* **12**(8): 3059-63.

Porro, C. A., Francescato, M. P., Cettolo, V., Diamond, M. E., Baraldi, P., Zuiani, C., Bazzocchi, M. and di Prampero, P. E. (1996). "Primary motor and sensory cortex activation during motor performance and motor imagery: a functional magnetic resonance imaging study." *J Neurosci* **16**(23): 7688-98.

Posner, J. and Plum, F. (1966). *The diagnosis of stupor and coma*, Blackwell Scientific Publications.

Raggi, A., Iannaccone, S. and Cappa, S. F. (2009). "Event-related brain potentials in amyotrophic lateral sclerosis: A review of the international literature." *Amyotroph Lateral Scler*: 1-11.

Regan, D. (1989). *Human Brain Electrophysiology: Evoked Potentials and Evoked Magnetic Fields in Science and Medicine*. New York, Elsevier Science Ltd.

Richter, M., Zierhut, K., Dresler, T., Plichta, M., Ehlis, A.-C., Reiss, K., Pekrun, R. and Fallgatter, A. (2009). "Changes in cortical blood oxygenation during arithmetical tasks measured by near-infrared spectroscopy." *J Neural Transm Suppl* **116**(3): 267-273.

Robbins, R. A., Simmons, Z., Bremer, B. A., Walsh, S. M. and Fischer, S. (2001). "Quality of life in ALS is maintained as physical function declines." *Neurology* **56**(4): 442-4.

Rolfe, P. (2000). "In vivo near-infrared spectroscopy." *Annu Rev Biomed Eng* **2**: 715-54.

Ron-Angevin, R. and Diaz-Estrella, A. (2009). "Brain-computer interface: Changes in performance using virtual reality techniques." *Neurosci Lett* **449**(2): 123-7.

Ron-Angevin, R., Lopez, M. A. and Pelayo, F. J. (2009). The Training Issue in Brain-Computer Interface: A Multi-disciplinary Field. *IWANN (1)*, Springer.

Roy, C. S. and Sherrington, C. S. (1890). "On the Regulation of the Blood-supply of the Brain." *J Physiol* **11**(1-2): 85-158 17.

Ruei-Cheng, W., Sheng-Fu, L., Chin-Teng, L. and Chun-Fei, H. (2004). Applications of event-related-potential-based brain computer interface to intelligent transportation systems. *Networking, Sensing and Control, 2004 IEEE International Conference on*.

Sakatani, K., Yamashita, D., Yamanaka, T., Oda, M., Yamashita, Y., Hoshino, T., Fujiwara, N., Murata, Y. and Katayama, Y. (2006). "Changes of cerebral blood oxygenation and optical pathlength during activation and deactivation in the prefrontal cortex measured by time-resolved near infrared spectroscopy." *Life Sci* **78**(23): 2734-41.

Sassaroli, A., Tong, Y., Frederick, B. B., Renshaw, P. F., Ehrenberg, B. L. and Fantini, S. (2005). Studying brain function with concurrent near-infrared spectroscopy (NIRS) and functional magnetic resonance imaging (fMRI). *Optical Tomography and Spectroscopy of Tissue VI*, San Jose, CA, USA, SPIE.

Sato, H., Kiguchi, M., Kawaguchi, F. and Maki, A. (2004). "Practicality of wavelength selection to improve signal-to-noise ratio in near-infrared spectroscopy." *Neuroimage* **21**(4): 1554-62.

Sato, H., Kiguchi, M., Maki, A., Fuchino, Y., Obata, A., Yoro, T. and Koizumi, H. (2006). "Within-subject reproducibility of near-infrared spectroscopy signals in sensorimotor activation after 6 months." *J Biomed Opt* **11**(1): 014021.

Schalk, G. (2008). "Brain-computer symbiosis." *J Neural Eng*(1): P1.

Schalk, G., Kubanek, J., Miller, K. J., Anderson, N. R., Leuthardt, E. C., Ojemann, J. G., Limbrick, D., Moran, D., Gerhardt, L. A. and Wolpaw, J. R. (2007). "Decoding two-dimensional movement trajectories using electrocorticographic signals in humans." *J Neural Eng* **4**(3): 264-75.

Schalk, G., Miller, K. J., Anderson, N. R., Wilson, J. A., Smyth, M. D., Ojemann, J. G., Moran, D. W., Wolpaw, J. R. and Leuthardt, E. C. (2008). "Two-dimensional movement control using electrocorticographic signals in humans." *J Neural Eng* **5**(1): 75-84.

Schmidt, E. R. E., Pasterkamp, R. J. and van den Berg, L. H. (2009). "Axon guidance proteins: novel therapeutic targets for ALS?" *Progress in Neurobiology* **In Press, Accepted Manuscript**.

Schmidt, M., Bajic, D., Reichert, K., Martin, T., Meyer, G. and Whelan, H. (1996). "Light-emitting diodes as a light source for intraoperative photodynamic therapy." *Neurosurgery* **38**(3): 552.

Severinghaus, J. W. (2007). "Takuo Aoyagi: Discovery of Pulse Oximetry." *Anesth Analg* **105**(6S_Suppl): S1-4.

Seydnejad, S. R. and Kitney, R. I. (2001). "Modeling of Mayer waves generation mechanisms." *Ieee Engineering in Medicine and Biology Magazine* **20**(2): 92-100.

Shivapurkar, N., Stastny, V., Okumura, N., Girard, L., Xie, Y., Prinsen, C., Thunnissen, F. B., Wistuba, II, Czerniak, B., Frenkel, E., Roth, J. A., Liloglou, T., Xinarianos, G., Field, J. K., Minna, J. D. and Gazdar, A. F. (2008). "Cytoglobin, the newest member of the globin family, functions as a tumor suppressor gene." *Cancer Res* **68**(18): 7448-56.

Siemens-AG. (2009, 2009). "MAGNETOM Allegra." from http://www.medical.siemens.com/webapp/wcs/stores/servlet/PSGenericDisplay?storeId=10001&langId=-1&catalogId=-1&pageId=80968.

Sitaram, R., Zhang, H., Guan, C., Thulasidas, M., Hoshi, Y., Ishikawa, A., Shimizu, K. and Birbaumer, N. (2007). "Temporal classification of multichannel near-infrared spectroscopy signals of motor imagery for developing a brain-computer interface." *Neuroimage* **34**(4): 1416-27.

Sliney, D. and Wolbarsht, M. (1980). *Safety with Lasers and Other Optical Sources: A Comprehensive Handbook*. New York, Plenum Pub Corp.

Soraghan, C., Matthews, F., Kelly, D., Ward, T., Markham, C., Pearlmutter, B. and O'Neill, R. (2006). Viability of a dual channel optical BCI for use in a gaming environment. *CGAMES* Dublin Institute of Technology, Dublin, Ireland.

Soraghan, C., Matthews, F., Markham, C., Pearlmutter, B. A., O'Neill, R. and Ward, T. E. (2008). A 12-Channel, real-time near-infrared spectroscopy instrument for brain-computer interface applications. *Conf Proc IEEE Eng Med Biol Soc*.

Soraghan, C. J., Markham, C., Matthews, F. and Ward, T. E. (2009). "Triple wavelength LED driver for optical brain-computer interfaces." *Electronics Letters* **45**(8): 392-394.

Soraghan, C. J., Ward, T. E., Matthews, F. and Markham, C. (2008). Optical safety assessment of a near-infrared brain-computer interface. *Signals and Systems Conference, 208. (ISSC 2008). IET Irish*.

Soul, J. S. and du Plessis, A. J. (1999). "Near-infrared spectroscopy." *Seminars in Pediatric Neurology* **6**(2): 101-110.

Spinney, L. (2003). "Hear my voice." *New scientist* **22**(2383): 36-39.

Splinter, R. and Hooper, B. A. (2007). *An Introduction to Biomedical Optics*. New York, Taylor and Francis.

Sterman, M., Macdonald, L. and Stone, R. (1974). "Biofeedback training of the sensorimotor electroencephalogram rhythm in man: effects on epilepsy." *Epilepsia* **15**(3): 395-416.

Strangman, G., Boas, D. A. and Sutton, J. P. (2002). "Non-invasive neuroimaging using near-infrared light." *Biol Psychiatry* **52**(7): 679-93.

Strangman, G., Culver, J. P., Thompson, J. H. and Boas, D. A. (2002). "A quantitative comparison of simultaneous BOLD fMRI and NIRS recordings during functional brain activation." *Neuroimage* **17**(2): 719-31.

Sutter, E. E. (1992). "The Brain Response Interface - Communication through Visually-Induced Electrical Brain Responses." *Journal of Microcomputer Applications* **15**(1): 31-45.

Sutton, B. P., Ouyang, C., Karampinos, D. C. and Miller, G. A. (2009). "Current trends and challenges in MRI acquisitions to investigate brain function." *International Journal of Psychophysiology* **73**(1): 33-42.

Tachtsidis, I., Elwell, C. E., Leung, T. S., Lee, C. W., Smith, M. and Delpy, D. T. (2004). "Investigation of cerebral haemodynamics by near-infrared spectroscopy in young healthy volunteers reveals posture-dependent spontaneous oscillations." *Physiol Meas* **25**(2): 437-45.

Takahashi, T. (1994). *Atlas of the Human Body*. New York, HarperPerennial.

Thompson, J., Peterson, M. and Freeman, R. (2003). "Single-neuron activity and tissue oxygenation in the cerebral cortex." *Science* **299**(5609): 1070-1072.

Toronov, V., Franceschini, M. A., Filiaci, M., Fantini, S., Wolf, M., Michalos, A. and Gratton, E. (2000). "Near-infrared study of fluctuations in cerebral hemodynamics during rest and motor stimulation: temporal analysis and spatial mapping." *Med Phys* **27**(4): 801-15.

Tsubone, T., Tsutsui, K., Muroga, T. and Wada, Y. (2008). "Estimation of force motor command to control robot by NIRS-based BCI." *Neural Information Processing, Part Ii* **4985**: 969-978
1091.

Tungjitkusolmun, S. (1997). Design of Pulse Oximeters. J. G. Webster, Taylor and Francis Group, New York.

Udomphorn, Y., Armstead, W. M. and Vavilala, M. S. (2008). "Cerebral Blood Flow and Autoregulation After Pediatric Traumatic Brain Injury." *Pediatric Neurology* **38**(4): 225-234.

Uludag, K., Steinbrink, J., Kohl-Bareis, M., Wenzel, R., Villringer, A. and Obrig, H. (2004). "Cytochrome-c-oxidase redox changes during visual stimulation measured by near-infrared spectroscopy cannot be explained by a mere cross talk artefact." *Neuroimage* **22**(1): 109-19.

Utsugi, K., Obata, A., Sato, H., Aoki, R., Maki, A., Koizumi, H., Sagara, K., Kawamichi, H., Atsumori, H. and Katura, T. (2008). "GO-STOP Control Using Optical Brain-Computer Interface during Calculation Task." **E91-B**(7): 2133-2141.

Vaithianathan, T., Tullis, I. D. C., Everdell, N., Leung, T., Gibson, A., Meek, J. and Delpy, D. T. (2004). "Design of a portable near infrared system for topographic imaging of the brain in babies." *Review of Scientific Instruments* **75**(10): 3276-3283.

Vargas, C. D., Olivier, E., Craighero, L., Fadiga, L., Duhamel, J. R. and Sirigu, A. (2004). "The Influence of Hand Posture on Corticospinal Excitability during Motor Imagery: A Transcranial Magnetic Stimulation Study." *Cereb. Cortex* **14**(11): 1200-1206.

Varshni, Y. P. (1967). "Temperature dependence of the energy gap in semiconductors." *Physica* **34**(1): 149-154.

Vaughan, T. M., Heetderks, W. J., Trejo, L. J., Rymer, W. Z., Weinrich, M., Moore, M. M., Kubler, A., Dobkin, B. H., Birbaumer, N., Donchin, E., Wolpaw, E. W. and Wolpaw, J. R. (2003). "Brain-computer interface technology: a review of the Second International Meeting." *IEEE Trans Neural Syst Rehabil Eng* **11**(2): 94-109.

Vaughan, T. M., McFarland, D. J., Schalk, G., Sarnacki, W. A., Krusienski, D. J., Sellers, E. W. and Wolpaw, J. R. (2006). "The Wadsworth BCI Research and Development Program: at home with BCI." *IEEE Trans Neural Syst Rehabil Eng* **14**(2): 229-33.

Vaughan, T. M. and Wolpaw, J. R. (2006). "The Third International Meeting on Brain-Computer Interface Technology: making a difference." *IEEE Trans Neural Syst Rehabil Eng* **14**(2): 126-7.

Veldink, J. H., Kalmijn, S., Groeneveld, G.-J., Wunderink, W., Koster, A., de Vries, J. H. M., van der Luyt, J., Wokke, J. H. J. and Van den Berg, L. H. (2007). "Intake of polyunsaturated fatty acids and vitamin E reduces the risk of developing amyotrophic lateral sclerosis." *J Neurol Neurosurg Psychiatry* **78**(4): 367-371.

Vidal, J. J. (1973). "Toward direct brain-computer communication." *Annu Rev Biophys Bioeng* **2**: 157-80.

Vidal, J. J. (1977). "Real-Time Detection of Brain Events in EEG." *Proceedings of the IEEE* **65**(5): 633-641.

Villringer, A. and Chance, B. (1997). "Non-invasive optical spectroscopy and imaging of human brain function." *Trends Neurosci* **20**(10): 435-42.

Visser, K. R., Lamberts, R., Korsten, H. H. M. and Zijlstra, W. G. (1976). "Observations on blood flow related electrical impedance changes in rigid tubes." *Pflügers Archiv European Journal of Physiology* **366**(2): 289-291.

Waldert, S., Preissl, H., Demandt, E., Braun, C., Birbaumer, N., Aertsen, A. and Mehring, C. (2008). "Hand Movement Direction Decoded from MEG and EEG." *Journal of Neuroscience* **28**(4): 1000-1008.

Wang, Y., Wang, R., Gao, X., Hong, B. and Gao, S. (2006). "A practical VEP-based brain-computer interface." *IEEE Trans Neural Syst Rehabil Eng* **14**(2): 234-9.

Ward, T. E., Soraghan, C. J., Matthews, F. and Markham, C. (2007). "A Concept for Extending the Applicability of Constraint-Induced Movement Therapy through Motor Cortex Activity Feedback Using a Neural Prosthesis." *Comput Intell Neurosci*: 51363.

Weiskopf, N., Sitaram, R., Josephs, O., Veit, R., Scharnowski, F., Goebel, R., Birbaumer, N., Deichmann, R. and Mathiak, K. (2007). "Real-time functional magnetic resonance imaging: methods and applications." *Magn Reson Imaging* **25**(6): 989-1003.

Weiskopf, N., Veit, R., Erb, M., Mathiak, K., Grodd, W., Goebel, R. and Birbaumer, N. (2003). "Physiological self-regulation of regional brain activity using real-time functional magnetic resonance imaging (fMRI): methodology and exemplary data." *Neuroimage* **19**(3): 577-86.

Whelan, H., Buchmann, E., Dhokalia, A., Kane, M., Whelan, N., Wong-Riley, M., Eells, J., Gould, L., Hammamieh, R. and Das, R. (2003). "Effect of NASA light-emitting diode irradiation on molecular changes for wound healing in diabetic mice." *Journal of Clinical Laser Medicine & Surgery* **21**(2): 67-74.

Wittenberg, J. B. and Wittenberg, B. A. (2003). "Myoglobin function reassessed." *J Exp Biol* **206**(Pt 12): 2011-20.

Wolf, M., Bauschatz, A. S., Fauchere, J. C., Bucher, H. U., Niederer, P. and Haensse, D. (2004). "Near infrared spectrophotometry detects the neuronal activation induced by tactile, auditory and visual stimulation in term neonates." *Pediatric Research* **56**(3): 510-510.

Wolf, M., Ferrari, M. and Quaresima, V. (2007). "Progress of near-infrared spectroscopy and topography for brain and muscle clinical applications." *J Biomed Opt* **12**(6): 062104.

Wolfberg, A. J. and du Plessis, A. J. (2006). "Near-infrared spectroscopy in the fetus and neonate." *Clin Perinatol* **33**(3): 707-28, viii.

Wolpaw, J. R. (2007). "Brain-computer interfaces as new brain output pathways." *J Physiol* **579**(Pt 3): 613-9.

Wolpaw, J. R., Birbaumer, N., Heetderks, W. J., McFarland, D. J., Peckham, P. H., Schalk, G., Donchin, E., Quatrano, L. A., Robinson, C. J. and Vaughan, T. M. (2000). "Brain-computer interface technology: a review of the first international meeting." *IEEE Trans Rehabil Eng* **8**(2): 164-73.

Wolpaw, J. R., Birbaumer, N., McFarland, D. J., Pfurtscheller, G. and Vaughan, T. M. (2002). "Brain-computer interfaces for communication and control." *Clin Neurophysiol* **113**(6): 767-91.

Wolpaw, J. R. and McFarland, D. J. (2004). "Control of a two-dimensional movement signal by a noninvasive brain-computer interface in humans." *Proc Natl Acad Sci U S A* **101**(51): 17849-54.

Wolpaw, J. R., McFarland, D. J., Neat, G. W. and Forneris, C. A. (1990). "Development of an Electroencephalogram-Based Brain-Computer Interface." *Annals of Neurology* **28**(2): 250-251.

Wolpaw, J. R., McFarland, D. J. and Vaughan, T. M. (2000). "Brain-computer interface research at the Wadsworth Center." *IEEE Trans Rehabil Eng* **8**(2): 222-6.

Wriessnegger, S. C., Kurzmann, J. and Neuper, C. (2008). "Spatio-temporal differences in brain oxygenation between movement execution and imagery: A multichannel near-infrared spectroscopy study." *International Journal of Psychophysiology* **67**(1): 54-63.

Yasuma, F. and Hayano, J. (2004). "Respiratory Sinus Arrhythmia* Why Does the Heartbeat Synchronize With Respiratory Rhythm?" *Chest* **125**(2): 683-690.

Yoo, S. S., Fairneny, T., Chen, N. K., Choo, S. E., Panych, L. P., Park, H., Lee, S. Y. and Jolesz, F. A. (2004). "Brain-computer interface using fMRI: spatial navigation by thoughts." *Neuroreport* **15**(10): 1591-5.

Yoshimura, N. and Itakura, N. (2008). "Study on transient VEP-based brain-computer interface using non-direct gazed visual stimuli." *Electromyogr Clin Neurophysiol* **48**(1): 43-51.

Yousry, I., Naidich, T. P. and Yousry, T. A. (2001). "Functional magnetic resonance imaging: factors modulating the cortical activation pattern of the motor system." *Neuroimaging Clin N Am* **11**(2): 195-202, viii.

Yuen, T. G. H., Agnew, W. F. and Bullara, L. A. (1987). "Tissue response to potential neuroprosthetic materials implanted subdurally." *Biomaterials* **8**(2): 138-141.